The Loma Prieta, California, Earthquake of October 17, 1989—Strong Ground Motion

ROGER D. BORCHERDT, *Editor*

STRONG GROUND MOTION AND GROUND FAILURE
Thomas L. Holzer, *Coordinator*

U.S. GEOLOGICAL SURVEY PROFESSIONAL PAPER 1551-A

U.S. DEPARTMENT OF THE INTERIOR
MARCH 3, 1849

UNITED STATES GOVERNMENT PRINTING OFFICE, WASHINGTON : 1994

U.S. DEPARTMENT OF THE INTERIOR

BRUCE BABBITT, ***Secretary***

U.S. GEOLOGICAL SURVEY

Gordon P. Eaton, ***Director***

Manuscript approved for publication, October 6, 1993

Text and illustrations edited by George A. Havach

Library of Congress catalog-card No. 92–32287

For sale by U.S. Geological Survey, Map Distribution
Box 25286, MS 306, Federal Center
Denver, CO 80225

CONTENTS

THE LOMA PRIETA, CALIFORNIA, EARTHQUAKE OF OCTOBER 17, 1989: STRONG GROUND MOTION AND GROUND FAILURE

STRONG GROUND MOTION

SYNOPSIS

By Roger D. Borcherdt,
U.S. Geological Survey

CONTENTS

INTRODUCTION

Strong ground motion generated by the Loma Prieta, Calif., earthquake (M_S~7.1) of October 17, 1989, resulted in at least 63 deaths, more than 3,757 injuries, and damage estimated to exceed $5.9 billion. Strong ground motion severely damaged critical lifelines (freeway overpasses, bridges, and pipelines), caused severe damage to poorly constructed buildings, and induced a significant number of ground failures associated with liquefaction and landsliding. It also caused a significant proportion of the damage and loss of life at distances as far as 100 km from the epicenter. Consequently, understanding the characteristics of the strong ground motion associated with the earthquake is fundamental to understanding the earthquake's devastating impact on society. The papers assembled in this chapter address this problem.

Damage to vulnerable structures from the earthquake varied substantially with the distance from the causative fault and the type of underlying geologic deposits. Most of the damage and loss of life occurred in areas underlain by "soft soil." Quantifying these effects is important for understanding the tragic concentrations of damage in such areas as Santa Cruz and the Marina and Embarcadero Districts of San Francisco, and the failures of the San Francisco-Oakland Bay Bridge and the Interstate Highway 880 overpass. Most importantly, understanding these effects is a necessary prerequisite for improving mitigation measures for larger earthquakes likely to occur much closer to densely urbanized areas in the San Francisco Bay region (Housner and Penzien, 1990).

The earthquake generated an especially important data set for understanding variations in the severity of strong ground motion. Instrumental strong-motion recordings were obtained at 131 sites located from about 6 to 175 km from the rupture zone. This set of recordings, the largest yet collected for an event of this size, was obtained from sites on various geologic deposits, including a unique set on "soft soil" deposits (artificial fill and bay mud). These exceptional ground-motion data are used by the authors of the papers in this chapter to infer radiation characteristics of the earthquake source, identify dominant propagation characteristics of the Earth's crust, quantify amplification characteristics of near-surface geologic deposits, develop general amplification factors for site-dependent building-code provisions, and revise earthquake-hazard assessments for the San Francisco Bay region. Interpretations of additional data recorded in well-instrumented buildings, dams, and freeway overpasses are provided in other chapters of this report.

EARTHQUAKE RUPTURE AND CRUSTAL-PROPAGATION EFFECTS

Numerous models have been inferred regarding the characteristics and distribution of earthquake rupture responsible for generating the dominant features of the earthquake's seismic radiation field. Details of these models differ, but their general features, derived from both teleseismic and strong-motion data, are consistent. The models imply that (1) fault rupture initiated near the bottom (16–18-km depth) of a seismogenic zone in the San Andreas fault; (2) rupture propagated bilaterally at about 80 percent of the local shear velocity over an area extending about 15 km northwestward and 20 km southeastward along the fault and to within 2 to 3 km of the Earth's surface; and (3) slip was irregular but concentrated in two regions, with maximums exceeding 4 m and centered about 6 to 7 km on each side of rupture initiation and at a depth ranging from 10 to 14 km (Choy and Boatwright, 1990; Hartzell and others, 1991; Beroza, in press; Steidl and others, in press; Wald and others, in press).

An especially important characteristic of the rupture process is that the rupture proceeded bilaterally from its point of initiation. As a result, the rupture process was relatively brief, lasting only 6 to 8 s; waveforms of the dominant radiated energy are quite simple and of short duration, consistent with a relatively simple rupture process (for example, Beroza, in press, figs. 5, 6; see Borcherdt and Glassmoyer, this chapter, fig. 2). Damage could have been substantially greater had a unilateral or more complex rupture process occurred to increase the duration of shaking by at least 50 percent (see Somerville and others, this chapter). Kanamori and Satake (in press) point out that had a more complex rupture process occurred, as during the Armenia earthquake of December 7, 1988 (M=6.8), the resulting increase in duration of shaking could have caused substantially more damage.

Cormier and Su (this chapter) report that three-dimensional models of the Earth's crustal structure in the vicinity of the fault zone imply that ground motions may be focused to levels as much as 10 times greater than those implied by one-dimensional models. These findings, based on Green's function calculations derived from superimposed Gaussian beams, suggest at least a partial explanation for various evidence of severe ground shaking in and near the fault zone.

Stevens and Day (this chapter) found that a stochastic-subevent model predicts peak ground-motion parameters in reasonable agreement with values observed at 13 strong-motion stations within 30 km of the fault zone. Their model predicts substantial variations in peak ground motions due to random interference of waves generated by the assumed uniform distribution of subevents. Their model also predicts attenuation curves for peak acceleration and velocity inversely proportional to distance raised to the 1.5th power out to distances of 35 km. Beyond this distance, the attenuation curves are predicted to flatten, owing to reflected energy from the base of the crust.

Much of the loss of life and damage to major structures from the earthquake occurred in San Francisco and Oakland at distances of 90 to 105 km from the epicenter. The strong-motion data indicate that the shaking levels on sites underlain by rock exceeded those predicted by empirical curves derived from previous data by a factor of 2 to 3 (see Borcherdt and Glassmoyer, this chapter; Boore and Joyner, 1990). These elevated levels of motion can be attributed in part to crustal-propagation effects not necessarily documented well by strong-motion recordings of previous earthquakes. Specifically, observational data and model predictions provide convincing evidence that the shaking in San Francisco and Oakland was dominated by shear (*SH*)-wave energy reflected from the base of a relatively shallow Earth's crust (25 km thick) in the region (see Borcherdt and Glassmoyer, this chapter; Somerville and others, this chapter; Stevens and Day, this chapter; McGarr and others, 1991). Calculations suggest peak amplitudes for reflected waves as much as 2.5 times larger than for direct waves (see Somerville and others, this chapter).

The direction of dominant shaking observed at sites in San Francisco and Oakland was perpendicular to the strike of the San Andreas fault. This direction is readily apparent from ground motions inferred for this direction (see Borcherdt and Glassmoyer, this chapter, fig. 2) and from particle-motion plots for ground motions at periods longer than 1 s (see Vidale and Bonamassa, this chapter). This direction is predicted by simple source models (long-period focal-mechanism model; see Vidale and Bonamassa, this chapter) and inline crustal-propagation models of *SH*-wave energy. Particle-motion plots for periods of shaking shorter than 1 s indicate that significant proportions of the scattered energy arrived at the sites from various other propagation paths.

EFFECTS OF LOCAL GEOLOGIC DEPOSITS

Most of the damage and resulting loss of life from the earthquake was concentrated in areas underlain by "soft soil" conditions (Seed and others, 1990). Damage from the great San Francisco earthquake of April 18, 1906, also was concentrated in many of these same areas and was observed to depend chiefly on the geologic characteristics of the ground (Wood, 1908). The important role of local geologic deposits in influencing the amounts of damage and loss of life also has been reemphasized by tragic earthquakes of the 1980's in other parts of the world, especially those affecting Mexico City and Leninakan, Armenia. Consequently, the papers in this chapter, based on a unique new strong-motion data set, provide important results to help quantify the response of "soft soil" deposits for purposes of improved earthquake-resistant design and earthquake-hazard mitigation.

IMPLICATIONS OF STRONG-MOTION RECORDINGS

A regional assessment of the strong-motion recordings at 37 sites in the San Francisco Bay region (see Borcherdt and Glassmoyer, this chapter) reveals marked variations in ground-motion characteristics dependent on local geologic conditions. Comparative measurements for sites on various geologic units show that, in general, both peak amplitudes and duration of shaking were largest at sites on softer materials. Specifically, peak accelerations at sites on soil (alluvium, fill/bay mud), as normalized to peak values at local rock sites, are statistically larger than those at sites on hard rock. Peak acceleration, velocity, and displacement at sites on soft soil were as much as 6.1, 5.7, and 4.1 times larger, respectively, than at nearby rock sites. Spectral ratios show that local resonances developed at some soil sites, suggesting that peak amplifications near a factor of 15 occurred, though only over narrow period bands. Regression analyses show that the average horizontal spectral amplification is inversely proportional to mean shear velocity raised to some power. The absence of a statistical difference between regression curves derived using the strong-motion data and previously recorded, much smaller ground motions shows that mean shear velocity or weak-motion amplifications provided accurate predictions of amplification at damaging levels of ground shaking, as occurred during the earthquake.

The regression curves, derived from the Loma Prieta strong-motion data set (see Borcherdt and Glassmoyer, this chapter), provide rigorous empirical estimates of short-period (F_a) and midperiod (F_v) amplification factors for site-dependent building-code provisions. These factors, described by the relations

$$F_a = (v/997)^{-0.36}$$

and

$$F_v = (v/1{,}067)^{-0.64},$$

where v is the mean shear-wave velocity to 30 m (100 ft), permit estimates of site-dependent design spectra for input ground motion near 0.1 g (Borcherdt, 1993). These equations, together with new definitions of simplified site classes, are readily incorporated into revised building-code provisions.

Detailed geotechnical, geologic, and seismic data at strong-motion-recording sites provide an opportunity to evaluate methods for computing the response of soft-soil deposits. Two such sites of special importance analyzed in this chapter are Treasure Island and the Alameda Naval Air Station (ANAS). Both sites are underlain by reclaimed land composed of layers of hydraulic fill overlying interbedded layers of bay mud and sand. The sites are at comparable distances from the earthquake source (92, 97 km), near other sites on "rock" at which strong-motion recordings were obtained, and useful for understanding damage to such major structures as the San Francisco-Oakland Bay Bridge and the Interstate Highway 880 overpass. Recordings of horizontal ground motion at both sites show abrupt reductions in amplitude and changes in frequency content about 12 s after trigger time. These changes are consistent with the onset of liquefaction-induced ground failure at the sites. Peak horizontal ground accelerations recorded at the two sites were significantly larger than those recorded at nearby rock stations. They were 5.1 and 3.1 times larger in the radial direction and 1.6 and 2.1 times larger in the transverse direction (see Borcherdt and Glassmoyer, this chapter). Consequently, analyses of these recordings provide an important opportunity to evaluate models for calculating ground response at levels commensurate with the possible onset of ground failure.

Surface motions calculated by using the computer program SHAKE generally agreed with those observed at Treasure Island and the ANAS (see Carlisle and Rollins, this chapter; Rollins and others, this chapter; Idriss, 1990; Dickenson and Seed, 1991). In general, the conclusion is that reliable ground-response analyses can be performed for soft-soil sites at moderate acceleration levels, using the equivalent-linear method of the program SHAKE. Using the ground motions recorded in the east-west direction on Yerba Buena Island as input motion, Rollins and others (this chapter) report reasonably good agreement except at periods longer than 1 s at Treasure Island. They attribute this discrepancy either to the program's inability to model soil softening once liquefaction commences or to differences in the actual input motion at the base of the profile from that recorded on Yerba Buena Island. Their models utilize an extensive set of constitutive parameters for the soil profiles derived from detailed standard penetration tests, cone-penetration tests, geologic logs, and seismic shear-wave logs in boreholes to "rock."

The inferred soil-profile models and the program SHAKE predict that most of the amplification of acceleration at Treasure Island and the ANAS occurred in low-velocity materials (sand/bay mud) within about 10 to 12 m of the surface (see Carlisle and Rollins, this chapter; Rollins and others, this chapter). The models predict that a 10-percent variation in shear velocity may result in a significant (20 percent) variation in predicted acceleration. The models predict that spectral acceleration would be significantly higher for large earthquakes (M=7, 7.25, and 8.25) as might occur at much closer distances (11 km) on the Hayward fault. For these earthquakes, the models predict that nonlinearity will reduce the amplification by soft soils for periods shorter than 1 s, but for longer periods Carlisle and Rollins report that the reduction is small. Using several rock input motions recorded both near and at distances greater than about 80 km, they find that the ANAS soil profile and the program SHAKE predict a normalized surface-response spectrum, which exceeds the Structural Engineers Association of California design spectrum for an S3 site in the period range 0.5–1.0 s.

Detailed laboratory testing on a sample of bay mud obtained from the Marina District in San Francisco (see Sitar and Salgado, this chapter) suggests that soft silty clays may lose strength during periods of earthquake shaking and thereby contribute to permanent soil deformations and resulting soil failures. They find that static and cyclic, strain-controlled, undrained simple-shear tests on a sample of bay mud show that its behavior is generally consistent with that observed previously—namely, that its undrained strength is higher during the first cycle of loading than its static strength and that the modulus and reciprocal damping ratio decrease with increasing cyclic-shear strain. They also find, however, that the cyclic strength may decline during continuous cycles of loading to levels lower than the initial undrained strength.

The Loma Prieta strong-motion recordings provide a unique data set to help quantify the response of near-surface geologic deposits. However, because no downhole arrays were operational during the earthquake, important questions remain concerning the amplification and propagation of strong motion in "soft soils." To avoid this deficiency during future events, efforts are underway to install downhole arrays of instrumentation on Treasure Island (see de Alba and others, this chapter) and at three sites in the city of San Francisco. De Alba and others present the results of a comprehensive soil-testing program on Treasure Island and the design of an array currently being installed. Soil-testing results are especially useful for the interpretation of future data sets and modeling studies concerned with the response of similar "soft soil" deposits.

IMPLICATIONS OF AFTERSHOCK RECORDINGS

Aftershock experiments can provide additional insight regarding the interpretation of the main-shock records and useful information where no strong-motion data were recorded. The aftershock experiments described herein address problems concerned with (1) site response near the collapsed Interstate Highway 880 overpass, (2) the response of alluvial basins, (3) topographic amplification, and (4) site response in the city of Santa Cruz.

Field and others (this chapter) report on a site-response study conducted near the failed Interstate Highway 880 overpass (Hough and others, 1990). Hough and others reported evidence that the collapsed section of the overpass probably underwent stronger ground-motion amplification during the main shock than the section which did not collapse. The collapsed section was located in an area mapped as underlain by bay mud and previously predicted to be vulnerable to higher intensities than the adjoining area in which the overpass did not collapse (Borcherdt and others, 1975). Field and others report that subsequent studies have found that the young bay mud is thin in the area of collapse, that pile depths were longer in the bay-mud area, and that differences in performance may have been due to a set of complex soil-structure-interaction effects. They find that predominant peaks in the spectral amplifications observed for sites underlain by alluvium and bay mud over alluvium agree well with those predicted by one-dimensional models. They also report the previous observation that predicted amplifications are commonly less than those observed, but conclude that the aftershock data provide compelling evidence for at least the partial validity of one-dimensional models to account for the response of "soft soil" deposits.

Strong-motion recordings obtained at two sites in the Santa Clara Valley on thick sections of alluvium at distances of 44 to 46 km indicate that ground shaking (especially in the longer period range 1.5–5 s) was longer in duration and larger in amplitude than at sites at comparable distances underlain by "rock." Frankel and others (this chapter) report on an aftershock experiment conducted to better understand these distinctive characteristics of the strong ground motion in the valley. Using aftershocks recorded on a small-aperture array, they conclude that amplitudes and durations can be enhanced by (1) multiply reflected body waves arriving immediately after the arrival of the *S* wave and (2) long-period (1–6 s) surface-wave energy arriving with lower phase velocities. They point out that the surface-wave energy may have been converted from body-wave energy at the edge of the basin or been generated by the source. Average strong-motion amplifications with respect to "rock" observed at the two alluvial-basin sites were about 2.5 in the radial direction and 1.5 in the transverse direction. The absence of damage in the area indicates that structures were sufficiently strong to withstand the resulting ground motions.

Three-dimensional simulations of the sedimentary basin beneath the Santa Clara Valley (see Frankel and Vidale, this chapter) show that significant amounts of *S*-wave energy are converted to surface-wave energy at the edges of the basin. The synthetic seismograms show that the duration of shaking is prolonged most by these surface waves near the center of the basin and least along the edges. The synthetic seismograms qualitatively explain the amplifications in duration and amplitude recorded in the valley. Frankel and Vidale point out that these augmentations of the longer period energy in sedimentary basins may increase the seismic hazard for long-period structures, such as bridges and tall buildings.

Numerous examples of especially strong shaking in the epicentral area were initially thought to result from topographic amplification. Extensive aftershock studies conducted in the Santa Cruz Mountains (see Lindley and

Archuleta, this chapter) reveal that the observed site effects on recorded motion show a strong correlation with site geology but no correlation with site topography. Lindley and Archuleta find a relative deamplification of motion at ridgetop sites and amplification at valley sites. This unexpected result is interpreted to be due to the fact that most of the ridgetop sites are underlain by "harder" rocks of the Franciscan Complex, whereas the other sites are underlain by "softer" rocks. They find that seismic-wave attenuation and amplification were greatest at sites underlain by sedimentary rocks of Miocene and Pliocene age and least at sites on rocks of the Franciscan Complex.

Substantial damage and loss of life occurred in the city of Santa Cruz. Subsequent investigations showed that most of the damage and resulting loss of life occurred at vulnerable structures in the downtown area underlain by poor soil conditions. Comparative ground-motion measurements, using recordings of aftershocks obtained in the area (see Williams and others, this chapter), suggest significant amounts of horizontal amplification at frequencies less than 5 Hz. Williams and others report the results of a substantial effort to compare model predictions of ground response with those observed from aftershocks. Models of the velocity structure are derived from high-resolution seismic reflection and refraction data collected after the earthquake. They conclude that their modeling results are of only limited success in predicting the observed response. Model studies show that the effects of incidence angle, density, and attenuation were secondary in comparison with seismic velocity in influencing ground response.

IMPLICATIONS FOR SEISMIC HAZARD IN THE SAN FRANCISCO BAY REGION

Seismic-hazard assessments were made for major fault systems in California before the earthquake (Sykes and Nishenko, 1984; Wesnousky, 1986). These maps identified the Loma Prieta section of the San Andreas fault as an area of especially high seismic hazard. These evaluations were developed by using information on the size and location of historical earthquakes and the slip rates of Quaternary faults. The resulting maps (Wesnousky, 1986) displayed the probabilities that horizontal ground acceleration at hard-rock sites would exceed 0.1 *g* within the next 50 years. Since the preparation of these maps, additional information on slip rates has been acquired, rupture on the Loma Prieta segment of the fault has reduced inferred strain accumulations in the area, and strong motion recordings have provided quantitative measurements of the response of various geologic deposits in the area. Murphy and Wesnousky (this chapter) reevaluate the seismic hazard for the San Francisco Bay region by using this new information.

The updated seismic-hazard evaluation for sites underlain by hard rock in the San Francisco Bay region differs from an earlier evaluation (Wesnousky, 1986) in two principal respects, namely, an increased hazard in the East Bay due to new slip-rate information for the Rodgers Creek fault and the northern section of the Hayward fault, and a reduced hazard in the vicinity of the Loma Prieta section of the San Andreas fault. Both evaluations show that the probability for ground motions at rock sites to exceed 0.1 *g* within the next 50 years is high for most of the bay region. However, because many of the more densely urbanized areas are underlain by alluvium or fill overlying bay mud, they point out that these maps for rock are of only limited utility.

In reevaluating the seismic hazard for the San Francisco Bay region, Murphy and Wesnousky (this chapter) account for variations in surface geology on the basis of ground-motion-amplification factors derived from strong-motion recordings of the earthquake. They present maps showing the probabilities for peak ground velocity and acceleration exceeding 40 cm/s and 0.5 *g*, respectively, in the next 50 years. The resulting maps differ substantially from those derived for rock sites only. They show that in the San Francisco Bay region, the locations of highest seismic hazard may not be adjacent to and include the mapped active fault zone but, instead, may be located in areas along the margins of San Francisco Bay underlain by "soft soils" (fill/bay mud). Their maps also indicate that some other areas underlain by stiffer soils (Quaternary alluvium), if sufficiently close to faults, may also be assigned a higher level of hazard than areas on harder materials closer to the fault. Their hazard evaluation, incorporating the Loma Prieta strong-motion-amplification factors, illustrates that major new advances in the accuracy and resolution of seismic hazards in some urbanized areas can be made by incorporating the strong-motion-amplification effects of local geologic deposits.

GENERAL CONCLUSIONS

The earthquake occurred on a relatively remote section of the San Andreas fault in the Santa Cruz Mountains of central California. The earthquake generated strong ground motion sufficient to cause 63 deaths, more than 3,757 injuries, and damage exceeding $5 billion. Strong ground motion severely damaged critical lifelines, such as the San Francisco-Oakland Bay Bridge and structures of Interstate Highways 880 and 280 and the Embarcadero Freeway. It severely damaged numerous vulnerable buildings and triggered multiple ground failures associated with liquefaction and landsliding in the cities of San Francisco and Oakland at distances as much as 100 km or 60 miles from the epicenter. It caused most of the damage and loss of life in areas of soft-soil deposits. Although the impact of the earthquake on society was extensive, resulting in 10 counties being declared State and Federal disaster areas, it provides only a hint of the impact anticipated for future earthquakes expected with high probabilities of occurrence (67 percent for $M \geq 7$ in 30 years; Working Group on California Earthquake Probabilities, 1990) in or much closer to the densely urbanized areas of the San Francisco Bay region.

Fault rupture associated with the earthquake was brief (6–8 s). It proceeded bilaterally and resulted in strong shaking that lasted no more than 10 to 15 s at most sites. Consequently, damage from the 1989 Loma Prieta earthquake was less than that from commonly occurring earthquakes, whose rupture proceeds primarily in one direction and lasts twice as long. Energy reflected from the base of a relatively shallow Earth's crust accounted for the observed dominant transverse "bedrock" motions in San Francisco and Oakland and contributed to the amounts of damage observed at these distances. Levels of shaking in and near the fault zone appear to have been intensified by focusing due to intervening crustal structure. Substantial differences between observed levels of strong ground motion and those predicted by attenuation curves derived on the basis of previous data imply the need to update curves in current usage.

Analyses of strong-motion recordings reveal marked variations in shaking that depend on the geologic characteristics of the ground. Peak acceleration, velocity, and displacement were as much as 6.1, 5.7, and 4.1 times larger on soft-soil deposits than on nearby rock sites. On the average, horizontal ground motions were about 3.7 times larger at sites on soft soil than for sites on hard rock. These variations agree with those derived previously, using weak-motion or low-strain data. These data establish that soil amplification was a major contributor to levels of ground motion sufficient to cause damage to vulnerable structures in the San Francisco Bay region at distances near 100 km. They show, together with model studies, that ground-motion amplification by the soft deposits near the margins of San Francisco Bay, in general, was greater than anticipated by current design codes. They provide simple regression curves, which afford estimates of short-period and midperiod amplification as a function of mean shear-wave velocity for use in design for input ground-motion levels near 0.1 *g*. These curves form a basis for extrapolation to higher levels of motion. They provide, together with new definitions of simplified site classes, provisions that can be readily adopted into current design codes to better account for the amplification effects of local geologic deposits.

The reevaluation of the seismic hazard for the San Francisco Bay region, incorporating amplification factors inferred from strong-motion recordings, shows that the greatest hazard may not be in the fault zone, as indicated on previous maps prepared for a uniform ground condition, but, instead, in areas underlain by soft soils (fill/bay mud). This significant conclusion implies that important revisions in seismic-hazard evaluations may be needed for other urbanized seismic regions of the world.

REFERENCES CITED

Beroza, G.C., in press, Rupture history of the earthquake from high-frequency strong-motion data; implications for seismic hazard and earthquake-source mechanics, *in* Spudich, Paul, ed., The Loma Prieta, California, earthquake of October 17, 1989—main-shock characteristics: U.S. Geological Survey Professional Paper 1550–A.

Boore, D.M., and Joyner, W.B., 1990, Preliminary analysis of peak accelerations, *in* Benuska, Lee, ed., Loma Prieta earthquake reconnaissance report: Earthquake Spectra, v. 6, supp. 90–01, p. 50–58.

Borcherdt, R.D., in press, Simplified site classes and amplification factors for site-dependent code provisions: Workshop on National Earthquake Hazard Reduction Program site-dependent code provisions, Los Angeles, 1992, Proceedings.

Borcherdt, R.D., Gibbs, J.F., and Lajoie, K.R., 1975, Prediction of maximum earthquake intensity in the San Francisco Bay region, California, for large earthquakes on the San Andreas and Hayward faults: U.S. Geological Survey Miscellaneous Field Studies Map MF–709, scale 1:125,000, 11 p.

Choy, L.G., and Boatwright, John, 1990, Source characteristics of the Loma Prieta, California, earthquake of October 18, 1989 from global digital seismic data: Geophysical Research Letters, v. 17, no. 8, p. 1183–1186.

Dickenson, S.E., Seed, R.B., Lysmer, John, and Mok, C.M., 1991, Response of the soft soils during the 1989 Loma Prieta earthquake and implications for seismic design criteria: Pacific Conference on Earthquake Engineering, Auckland, New Zealand, 1991, Proceedings.

Hartzell, S.H., Stewart, G.S., and Mendoza, Carlos, 1991, Comparison of L_1 and L_2 norms in a teleseismic waveform inversion for the slip history of the Loma Prieta, California, earthquake: Seismological Society of America Bulletin, v. 81, no. 5, p. 1518–1539.

Hough, S.E., Friberg, P.A., Busby, R., Field, E.F., Jacob, K.H., and Borcherdt, R.D., 1990, Sediment-induced amplification and the collapse of the Nimitz Freeway: Nature, v. 344, no. 6269, p. 853–855.

Housner, G.W., and Penzien, J., 1990, Competing against time; report of the Governor's Board of Inquiry on the 1989 Loma Prieta Earthquake: Sacramento, Calif., 264 p.

Idriss, I.M., 1990, Response of soft soil sites during earthquakes, *in* H. Bolton Seed Memorial Symposium: Berkeley, Calif., BiTech, v. 2, p. 273–289.

Kanamori, Hiroo, and Satake, Kenji, in press, Broadband study of the source characteristics of the earthquake, *in* Spudich, Paul, ed., The Loma Prieta, California, earthquake of October 17, 1989—main-shock characteristics: U.S. Geological Survey Professional Paper 1550–A.

McGarr, A.F., Celebi, Mehmet, Sembera, E.D., Noce, T.E., and Mueller, C.S., 1991, Ground motion at the San Francisco International Airport from the Loma Prieta earthquake sequence, 1989: Seismological Society of America Bulletin, v. 81, no. 5, p. 1923–1944.

Seed, R.B., Dickenson, S.E., Reimer, M.F., Bray, J.D., Sitar, Nicholas, Mitchell, J.K., Idriss, I.M., Kayen, R.E., Kropp, A.L., Harder, L.F., Jr., and Power, M.S., 1990, Preliminary report on the principal geotechnical aspects of the October 17, 1989 Loma Prieta earthquake: Berkeley, University of California, Earthquake Research Center Report UCB/EERC–90/05, 137 p.

Steidl, J.H., and Archuleta, R.J., in press, Are geodetic measurements and rupture models consistent?, *in* Spudich, Paul, ed., The Loma Prieta, California, earthquake of October 17, 1989—main-shock characteristics: U.S. Geological Survey Professional Paper 1550–A.

Sykes, L.R., and Nishenko, S.P., 1984, Probabilities of occurrence of large plate rupturing earthquakes for the San Andreas, San Jacinto, and Imperial faults, California, 1983–2003: Journal of Geophysical Research, v. 89, no. B7, p. 5905–5927.

Wald, D.J., Helmberger, D.V., and Heaton, T.H., in press, Strong-motion and broadband teleseismic analysis of the earthquake for rupture-process and hazards assessment, *in* Spudich, Paul, ed., The Loma Prieta, California, earthquake of October 17, 1989—main-shock characteristics: U.S. Geological Survey Professional Paper 1550–A.

Wesnousky, S.G., 1986, Earthquakes, Quaternary faults, and seismic hazard in California: Journal of Geophysical Research, v. 91, no. B12, p. 12587–12631.

Wood, H.O., 1908, Distribution of apparent intensity in San Francisco, *in* Lawson, A.C., chairman, The California earthquake of April 18, 1906; report of the State Earthquake Investigation Commission: Carnegie Institution of Washington Publication 87, v. 1, p. 220–245.

Working Group on California Earthquake Probabilities, 1990, Probabilities of large earthquakes in the San Francisco Bay region, California: U.S. Geological Survey Circular 1053, 51 p.

THE LOMA PRIETA, CALIFORNIA, EARTHQUAKE OF OCTOBER 17, 1989: STRONG GROUND MOTION AND GROUND FAILURE

STRONG GROUND MOTION

STRONG-MOTION RECORDINGS

By A. Gerald Brady,
U.S. Geological Survey; and
Anthony F. Shakal,
California Division of Mines and Geology

CONTENTS

INTRODUCTION

Both the U.S. Geological Survey (USGS) and the California Division of Mines and Geology (CDMG) operate networks of permanently installed accelerographs within California. Cooperation at all levels has been maintained, particularly in the early stages of the CDMG's network development and in the selection of each network's instrumentation sites. Thus, the records recovered form a well-balanced set of data, both from a geographic standpoint and in the mix of ground-response stations and extensively instrumented structural stations. Within the San Francisco Bay region, the CDMG has a denser network, and the earthquake triggered more than twice as many CDMG as USGS stations. Details of the records from these two networks follow.

CDMG NETWORK

Strong-motion records were recovered from 93 stations in the CDMG's California Strong Motion Instrumentation Program (CSMIP) network, including 53 ground-response stations and 40 extensively instrumented structures. Of these stations, 25 were within 40 km of the epicenter; the most distant triggered stations were approximately 175 km from the epicenter. The 40 extensively instrumented structures include 33 buildings, 2 dams, 2 freeway bridges, a wharf, a tunnel, and an elevated rapid-transit structure. Shakal and others (1989) summarized the data for 125 records containing traces of 690 sensors (tables 1–3). The locations of the CSMIP stations that recorded the Loma Prieta main shock are shown in figures 1 and 2. The names corresponding to the CSMIP station codes used in figures 1 and 2 are listed in table 1. The geographic location, code, and site geology of each CSMIP station are listed in table 2. Stations are listed by epicentral distance for map areas 1 through 3 (fig. 1) in table 3—(1) San Jose and points south, (2) the west side of San Francisco Bay, and (3) the east side of the bay—along with a brief structural description, the earthquake trigger time, and the peak acceleration of each component at ground level and above ground for structural stations.

PROCESSING AND DISSEMINATION

CSMIP records, all on analog film, are processed at the Office of Strong Motion Studies headquarters in Sacramento, Calif. (fig. 1), where they are digitized on a rotating-drum scanner. A general description of the digitizing system, corrections, and the selection of filters for maximum useful frequency range were presented by Shakal and Ragsdale (1984).

Processed data are disseminated on tape or floppy disk in a standard format (Shakal and Huang, 1985); the station records in each tape are listed in table 4. Corresponding to these tapes is a series of three reports (California Strong Motion Instrumentation Program, 1991a–c) covering ground response (two tapes), building response (six tapes), and lifeline-structure response (two tapes) and containing plots of corrected acceleration, velocity, and displacement and response spectra.

USGS NETWORK

The National Strong-Motion Network (NSMN) operated by the USGS consists of approximately 1,000 stations

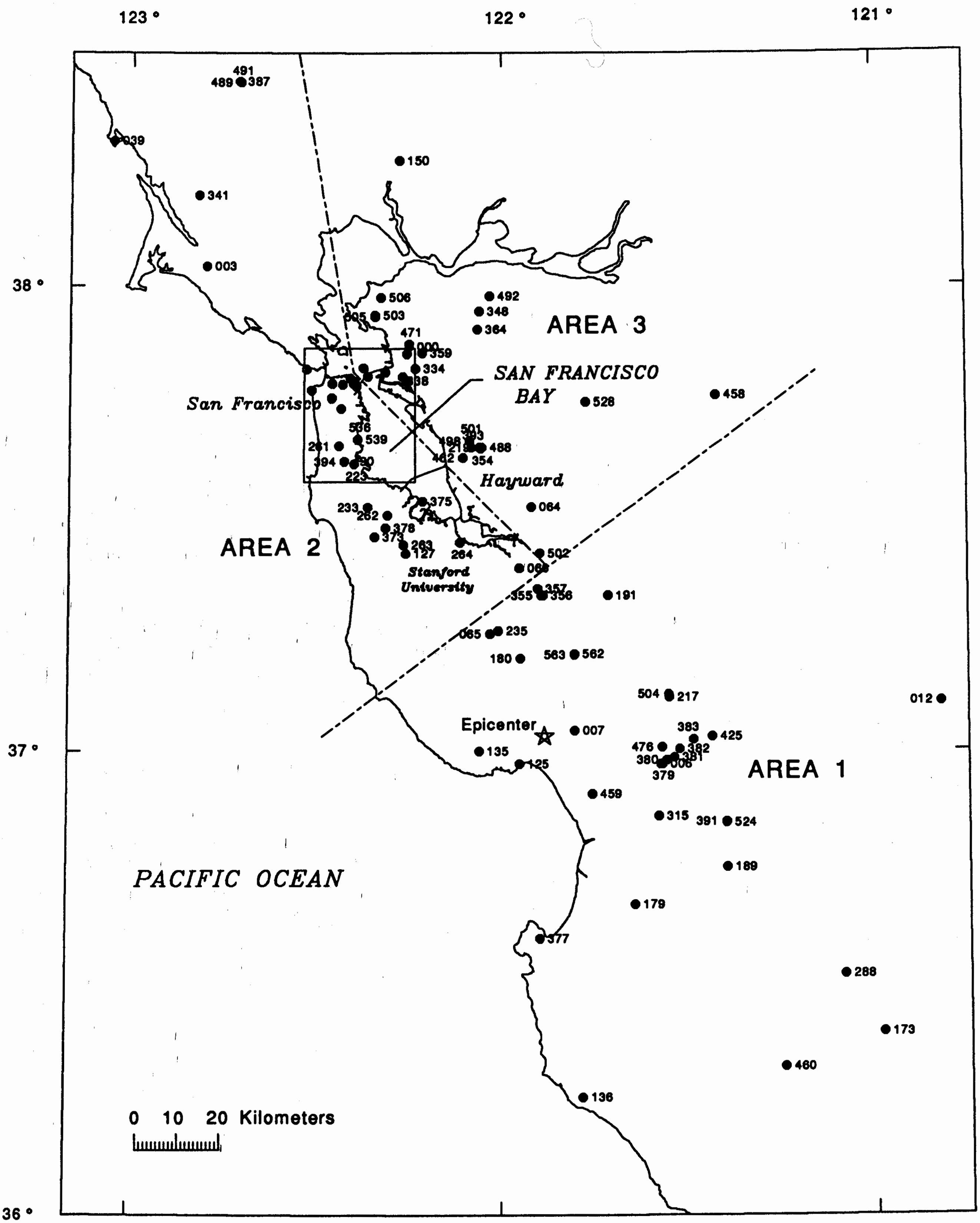

Figure 1.—San Francisco Bay region, showing locations of seismic stations (numbered dots) in California Strong Motion Instrumentation Program network that recorded earthquake. Rectangle delimits area of figure 2; areas 1 through 3 refer to sections of table 3. From Shakal and others (1989).

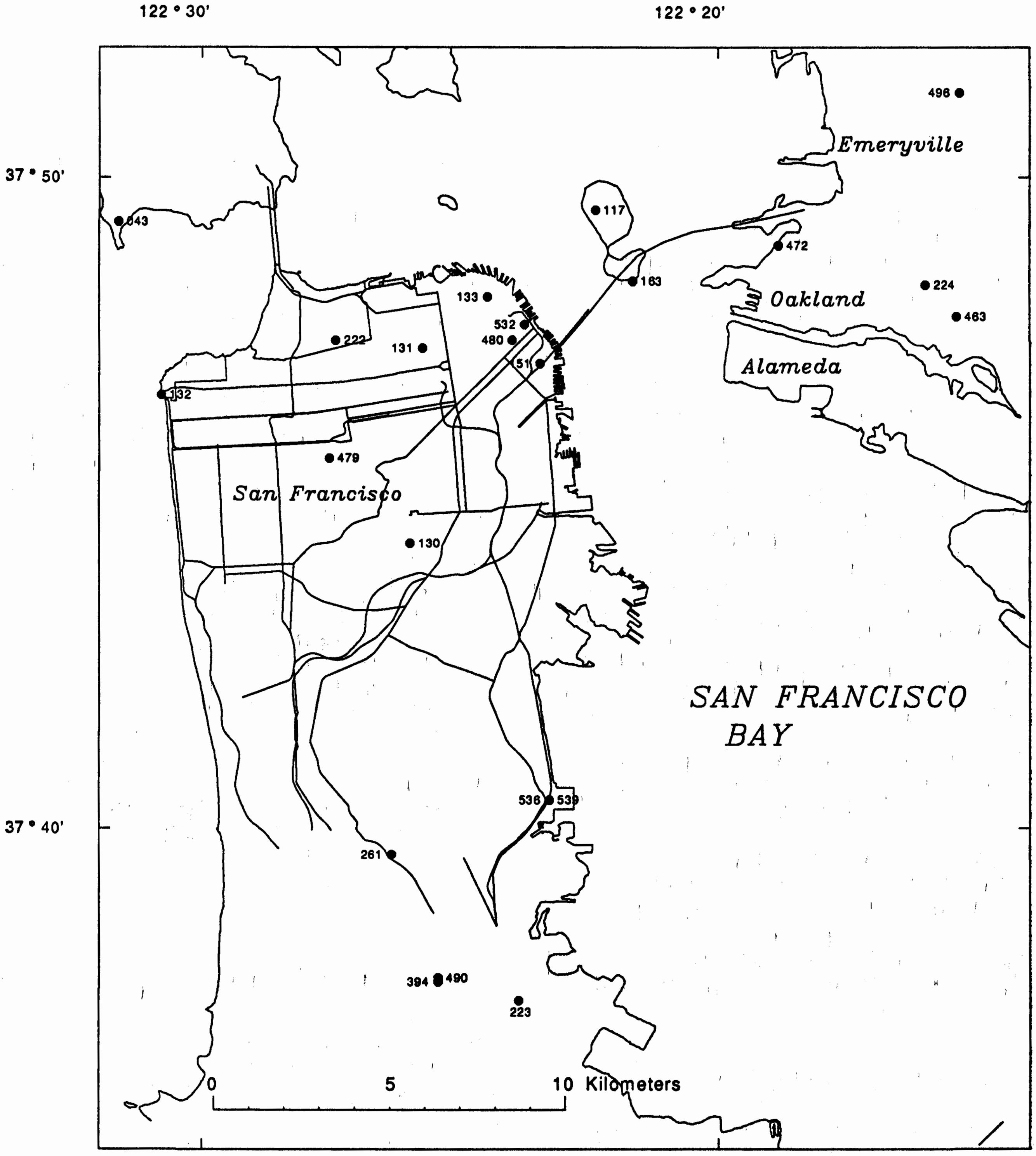

Figure 2.—San Francisco area, showing locations of seismic stations (numbered dots) in California Strong Motion Instrumentation Program network that recorded earthquake. From Shakal and others (1989).

in 41 States and Puerto Rico. The instrumentation is owned by numerous Federal, State, local, and private agencies and by private industry; specifically credited here are the Department of Veterans Affairs (formerly the Veterans' Administration), the California Department of Water Resources, the University of California, Berkeley, Stanford University, the Standard Oil Co., and the Bechtel Group, Inc. The primary objective of the USGS program is to record, on a national scale, strong ground motion and the response of engineered structures during large local earthquakes, and to disseminate the data to the earthquake-engineering research and design community.

The Loma Prieta main shock triggered accelerographs at 41 stations in the USGS network, although the records from 3 stations—namely, Milpitas-Rivera Street and Bear Valley stations 1 and 14—were not processed; epicentral distances ranged from 27 to 115 km (table 5). The 38 remaining stations consist of 26 ground stations (including 8 at the lowest levels of large buildings), 9 other large buildings (including 3 hospitals), 2 dams, and 1 bridge abutment. Six extensively instrumented structures recorded a response: five buildings and one dam. The number of channels at each station ranges from 3 in a triaxial package to 27, for example, in an extensively instrumented structure, the Pacific Park Plaza Building in Emeryville, Calif. (fig. 1). In such a deployment, acceleration sensors are placed in a structure and on the surrounding ground to record the dynamic response of the structure. Signals from the sensors are cabled to central recorders placed at locations convenient for installation, subsequent maintenance, and record retrieval.

The NSMN records are all on analog film, except for the digital record from the parking garage at Stanford University (fig. 1), which was obtained from a Seismotek digital recorder. A preliminary assessment of these records was presented by Maley and others (1989). Two stations that were omitted but that appear in the dissemination tapes are:

Stanford University: parking garage, basement
Bechtel Building, 50 Beale Street, San Francisco: basement, 12th, and 24th floors

Maley and others (1989) presented (1) descriptions of extensively instrumented structures; (2) notes on interesting records; (3) a table summarizing stations, instrumentation locations, and scaled peak accelerations; and (4) copies of film records, with a strip-chart copy of the digital record from the Stanford University parking garage.

PROCESSING AND DISSEMINATION

Records were processed from the 38 stations shown in figure 3 and listed in table 6. The film records were digitized by a commercial company, L.S. Associates (Santa Clara, Calif.), and, together with the digital record from the Stanford University parking garage, were processed for instrument correction and the removal of both high and low frequencies where noise was predominant. Converse and Brady (1992) described the USGS techniques for instrument correction and the high-frequency filter, and Basili and Brady (1978) and Brady (1989) presented general considerations of low-frequency-filtering decisions at the USGS. Examples of low-frequency-filter selection are contained in the reports by Hanks (1975) and Fletcher and others (1980). Recent conclusions regarding the selection of low-frequency filters for USGS Loma Prieta strong-motion data were drawn by Brady and Mork (1990) and Hanks and Brady (1991).

Brady and Mork (1990) presented plots of raw (or uncorrected) and processed data, and response and Fourier spectra, for 18 triaxial recorders at 12 stations. Corresponding digital data (but no Fourier spectral ordinates) are contained on a tape (USACA45) available from the National Geophysical Data Center (NGDC) in Boulder, Colo. Three subsequent tape pairs contain all the remaining records from the 38 stations. The location and direction of each acceleration component, with its corrected peak acceleration and the tape on which the data can be found, are listed in table 6, and a cross-reference to the contents of each tape in table 7. The addresses of the two data-disseminating agencies are as follows:

For CDMG data:
Data Reduction Manager
Office of Strong Motion Studies
Division of Mines and Geology
California Department of Conservation
801 K St., Mail Stop 13–35
Sacramento, CA 95814–3531
Telephone: 916–322–3105

For USGS data:
National Geophysical Data Center/NOAA,
325 Broadway, Mail Stop E/GC1
Boulder, CO 80303
Telephone: 303–497–6084

REFERENCES CITED

Basili, Mauro, and Brady, A.G., 1978, Low frequency filtering and the selection of limits for accelerogram corrections: European Conference on Earthquake Engineering, 6th, Dubrovnik, Yugoslavia, 1978, Proceedings, v. 1, p. 251–258.

Benuska, Lee, ed., 1990, Loma Prieta earthquake reconnaissance report: Earthquake Spectra, v. 6, supp. 90–01, 448 p.

Brady, A.G., 1989, Processing digitally-recorded seismic strong-motion accelerations: Workshop on Processing of Seismic Strong-Motion Records, 2d, Tokyo, 1988, Proceedings, p. 255–263.

Brady, A.G., and Mork, P.N., 1990, Loma Prieta, California, earthquake, October 18 (GMT), 1989; processed strong-motion records, volume 1: U.S. Geological Survey Open-File Report 90–247, 274 p.

California Strong Motion Instrumentation Program, 1991a, Plots of the accompany tapes; Loma Prieta 89–IG and –G (ground response data set): California Division of Mines and Geology, Office of

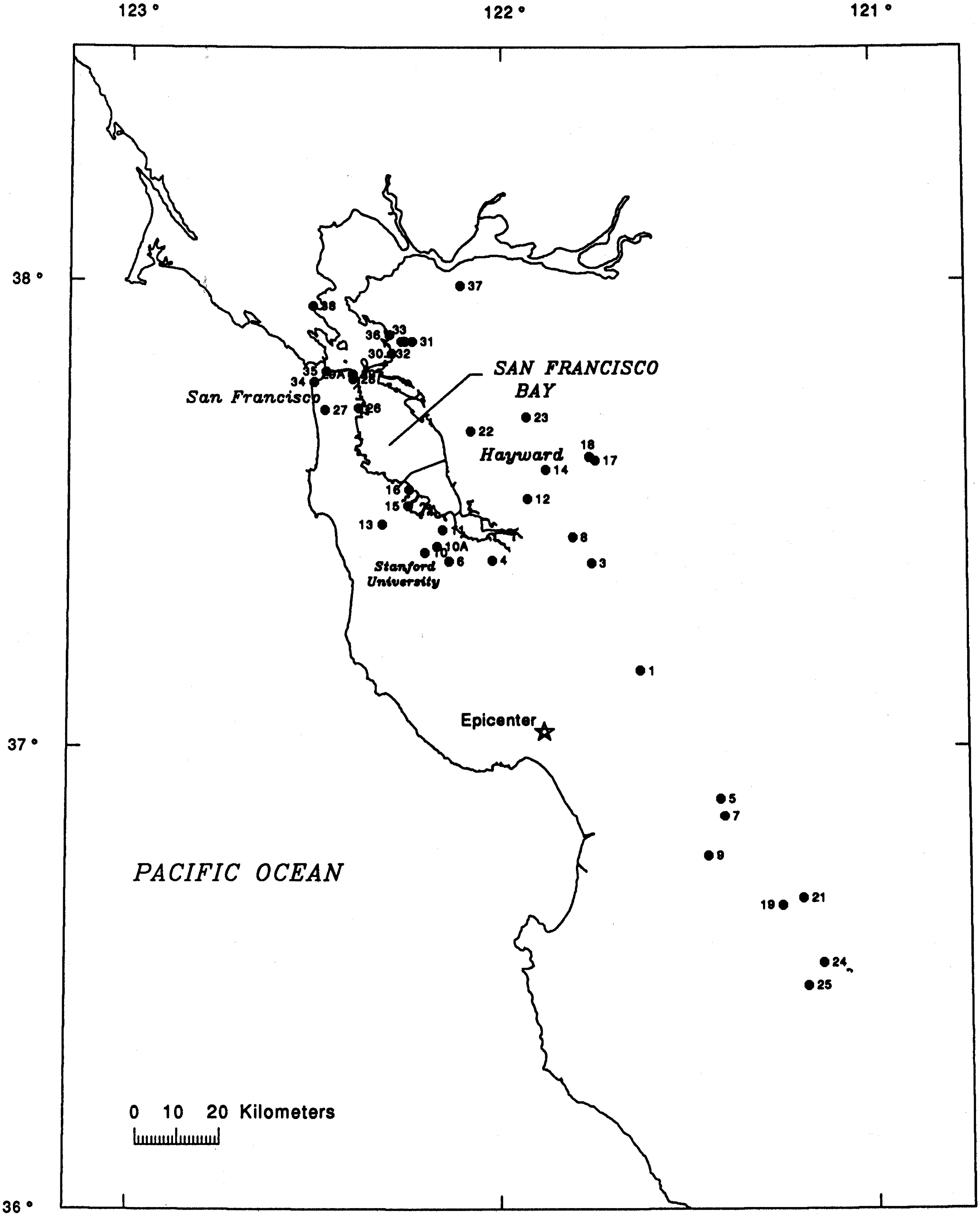

Figure 3.—San Francisco Bay region, showing locations of seismic stations (numbered dots) in U.S. Geological Survey network that recorded earthquake.

Strong Motion Studies Report OSMS 91–06.

———1991b, Plots of the accompany tapes; Loma Prieta 89–IB1, –IB2, –IB3, –IIB1, –IIB2 and –IIIB (building response data set): California Division of Mines and Geology, Office of Strong Motion Studies Report OSMS 91–07.

———1991c, Plots of the accompany tapes; Loma Prieta 89–IL and –L (lifeline structure response data set): California Division of Mines and Geology, Office of Strong Motion Studies Report OSMS 91–08.

Converse, A.M., 1992, BAP; basic strong-motion accelerogram processing software; version 1.0, *with a chapter on* Guidelines for selecting BAP run parameters, by A.M. Converse and A.G. Brady: U.S. Geological Survey Open-File Report 92–296–A.

Fletcher, J.B., Brady, A.G., and Hanks, T.C., 1980, Strong-motion accelerograms of the Oroville, California, aftershocks; data processing and the aftershock of 0350 August 6, 1975: Seismological Society of America Bulletin, v. 70, no, 1, p. 243–267.

Hanks, T.C., 1975, Strong ground motion of the San Fernando, California, earthquake; ground displacements: Seismological Society of America Bulletin, v. 65, no. 1, p. 193–225.

Hanks, T.C. and Brady, A.G., 1991, The Loma Prieta, California, earthquake, ground motion, and damage in Oakland, Treasure Island, and San Francisco: Seismological Society of America Bulletin, v. 81, no. 5, p. 2019–2047.

Maley, R.P., Acosta, A.V., Ellis, F., Etheredge, E.C., Foote, L.J., Johnson, D.A., Porcella, R.L., Salsman, M.J., and Switzer, J.C., 1989, U.S. Geological Survey strong-motion records from the northern California (Loma Prieta) earthquake of October 17, 1989: U.S. Geological Survey Open-File Report 89–568, 85 p.

Shakal, A.F., and Huang, M.J., 1985, Standard tape format for CSMIP strong-motion data tapes: California Division of Mines and Geology, Office of Strong Motion Studies Report OSMS 85–03.

Shakal, A.F., Huang, M.J., Reichle, M.S., Ventura, C., Cao, T., Sherburne, R.W., Savage, M., Darragh, R.B., and Peterson, C., 1989, CSMIP strong-motion records from the Santa Cruz Mountains (Loma Prieta), California earthquake of 17 October 1989: California Division of Mines and Geology, Office of Strong Motion Studies Report OSMS 89–06, 196 p.

Shakal, A.F., and Ragsdale, J.T., 1984, Acceleration, velocity, and displacement noise analysis for the CSMIP accelerogram digitization system, *in* Ground motion and seismicity: World Conference on Earthquake Engineering, San Francisco, 1984, Proceedings, v. 2, p. 111–118.

Switzer, J.C., Johnson, D., Maley, R.P., and Matthiesen, R.B., compilers, 1981, Western Hemisphere strong-motion accelerograph station list, 1980: U.S. Geological Survey Open-File Report 81–664.

TABLES 1–7

Table 1.—*Names of stations in the California Strong Motion Instrumentation Program network that recorded the earthquake*

[From Shakal and others (1989). See figures 1 and 2 for locations. BART, Bay Area Rapid Transit; bldg., building; CSUH, California State University, Hayward; LBL, Lawrence Berkeley Laboratory; UCSC, University of California, Santa Cruz; UCSF, University of California, San Francisco]

Code	Name	Code	Name
003	Olema—Point Reyes Ranger Station	359	Oakland—Caldecott Tunnel, Highway 24
006	Gilroy—Gavilan College, Physical Sciences Bldg.	364	Walnut Creek—10-story commercial bldg.
		373	Upper Crystal Springs Reservoir—Skyline Boulevard
007	Corralitos—Eureka Canyon Road		
012	Los Baños	375	Foster City—Redwood Shores
039	Bodega Head—Doran Beach	377	Monterey—City Hall
043	Point Bonita	378	Upper Crystal Springs Reservoir—Pulgas Temple
064	Fremont—Mission San Jose		
065	Saratoga—Aloha Avenue	379	Gilroy No. 1—Gavilan College, water tank
066	Agnew—Agnews State Hospital	380	Gilroy No. 2—Highway 101/Bolsa Road motel
117	Treasure Island—Naval Base fire station	381	Gilroy No. 3—sewage plant
125	Capitola—fire station	382	Gilroy No. 4 —San Ysidro School
127	Woodside—fire station	383	Gilroy No. 6—San Ysidro
130	San Francisco—Diamond Heights	387	Santa Rosa—5-story commercial bldg.
131	San Francisco—Pacific Heights	391	Hollister—1-story warehouse
132	San Francisco—Cliff House	393	Hayward—Muir School
133	San Francisco—Telegraph Hill	394	San Bruno—9-story government office bldg.
135	Santa Cruz—UCSC/Lick Observatory	425	Gilroy No. 7—Mantelli Ranch
136	Big Sur—Pfeiffer State Park	458	Tracy—sewage plant
150	Napa—Napa College	459	Watsonville—4-story commercial bldg.
151	San Francisco—Rincon Hill	460	Greenfield
163	Yerba Buena Island	462	Hayward—6-story office bldg.
173	Bitterwater	471	Berkeley—LBL
179	Salinas—John and Work Streets	472	Oakland—Outer Harbor Wharf
180	Lexington Dam	476	Gilroy—2-story historic commercial bldg.
189	Hollister—SAGO south	479	San Francisco—6-story UCSF bldg.
191	Halls Valley—Grant Park	480	San Francisco—18-story commercial bldg.
217	Coyote Lake Dam—abutment	483	Oakland—24-story residential bldg.
219	Hayward—CSUH stadium grounds	488	Hayward—4-story CSUH Science Bldg.
222	San Francisco—Presidio	489	Santa Rosa—14-story residential bldg.
223	San Francisco—International Airport	490	San Bruno—6-story office bldg.
224	Oakland—2-story office bldg.	491	Santa Rosa—Hendley and Tupper Streets
233	Lower Crystal Springs Dam	492	Concord—8-story residential bldg.
235	Saratoga—1-story school gymnasium	496	Berkeley—2-story hospital
261	South San Francisco—4-story hospital	498	Hayward—BART station parking lot
262	Belmont—2-story office bldg.	501	Hayward—BART elevated section
263	Redwood City—3-story school office bldg.	502	Milpitas—2-story industrial bldg.
264	Palo Alto—2-story office bldg.	503	Richmond—3-story government office bldg.
288	San Benito	504	Coyote Lake Dam—downstream
315	San Juan Bautista—Highway 101/156 overpass	505	Richmond—City Hall parking lot
334	Piedmont—3-story school office bldg.	506	Richmond—3-story office bldg.
338	Piedmont—Piedmont Junior High School grounds	524	Hollister—South Street and Pine Drive
341	San Rafael—3-story office bldg.	528	Livermore—Fagundes Ranch
348	Pleasant Hill—3-story commercial bldg.	532	San Francisco—47-story office bldg.
354	Hayward—13-story CSUH administration bldg.	536	South San Francisco—Sierra Point overpass
355	San Jose—10-story commercial bldg.	539	South San Francisco—Sierra Point
356	San Jose—10-story residential bldg.	562	San Jose—3-story office bldg.
357	San Jose—13-story government office bldg.	563	San Jose—Santa Teresa Hills

Table 2.—*Locations and site geology of stations in the California Strong Motion Instrumentation Program network that recorded the earthquake*

[From Shakal and others (1989). APEEL, Andreas Peninsula Earthquake Engineering Laboratory; BART, Bay Area Rapid Transit; bldg., building; CSUH, California State University, Hayward; SAGO, San Andreas Geophysical Observatory; UCB, University of California, Berkeley; UCSC, University of California, Santa Cruz; USGS, U.S. Geological Survey. Do., ditto]

Station	Lat (°N.)	Long (°W.)	Code (figs. 1,2)	Site geology
Agnew Agnews State Hospital	37.239	121.952	066	Alluvium.
Belmont 2-story office bldg.	37.512	122.308	262	Sandstone.
Berkeley Lawrence Berkeley Laboratory	37.876	122.249	471	Thin alluvium on shale, siltstone.
Berkeley 2-story hospital	37.855	122.256	496	Alluvium.
Berkeley UCB Memorial Stadium grounds	37.87	122.25	000	Fault gouge.
Big Sur Pfeiffer State Park	36.255	121.782	136	Alluvium.
Bitterwater	36.395	120.982	173	Do.
Bodega Head Doran Beach	38.311	123.052	039	Do.
Capitola fire station	36.974	121.952	125	Do.
Concord 8-story residential bldg.	37.979	122.032	492	Do.
Corralitos Eureka Canyon Road	37.046	121.803	007	Landslide deposits.
Coyote Lake Dam downstream	37.124	121.551	504	Alluvium.
Coyote Lake Dam—abutment (San Martin-Coyote Creek)	37.118	121.550	217	Fill over carbonate rocks.
Foster City—Redwood Shores (APEEL array sta. 1; USGS sta. 1001)	37.55	122.23	375	Alluvium, 210 m thick; serpentine.
Fremont Mission San Jose	37.530	121.919	064	Alluvium.
Gilroy 2-story historic commercial bldg.	37.009	121.569	476	---
Gilroy sta. 1—Gavilan College water tank (USGS sta. 1408)	36.973	121.572	379	Franciscan sandstone.
Gilroy sta. 2—Highway 101/Bolsa Road motel (USGS sta. 1409)	36.982	121.556	380	Alluvium.
Gilroy sta. 3 sewage plant (USGS sta. 1410)	36.987	121.536	381	Do.
Gilroy sta. 4 —San Ysidro School (USGS sta. 1411)	37.005	121.522	382	Do.
Gilroy sta. 6—San Ysidro (USGS sta. 1413)	37.026	121.484	383	Silty clay over sandstone.
Gilroy sta. 7 Mantelli Ranch	37.033	121.434	425	Alluvium over sandstone.
Gilroy Gavilan College, Physical Sciences Bldg.	36.973	121.568	006	Terrace deposits over sandstone.
Greenfield	36.321	121.243	460	Alluvium.
Halls Valley Grant Park	37.338	121.714	191	Do.
Hayward BART station parking lot	37.670	122.086	498	Do.
Hayward BART elevated section	36.671	122.087	501	---
Hayward 6-story office bldg.	37.635	122.104	462	Alluvium.

Table 2.—*Locations and site geology of stations in the California Strong Motion Instrumentation Program network that recorded the earthquake*—Continued

Station	Lat (°N.)	Long (°W.)	Code (figs. 1,2)	Site geology
Hayward 13-story CSUH administration Bldg.	37.655	122.056	354	Franciscan metavolcanic rocks.
Hayward 4-story CSUH Science Bldg.	37.657	122.053	488	Weathered metavolcanic rocks.
Hayward—CSUH stadium grounds (APEEL array sta. 3E; USGS sta. 1219)	37.657	122.061	219	Franciscan greenstone.
Hayward—Muir School (APEEL array sta. 2E; USGS sta. 1121)	37.657	122.082	393	Alluvium.
Hollister SAGO south	36.753	121.396	189	Granite.
Hollister South Street and Pine Drive	36.848	121.397	524	Alluvium.
Hollister 1-story warehouse	36.851	121.398	391	Do.
Lexington Dam	37.202	121.949	180	Slate and sandstone.
Livermore Fagundes Ranch	37.753	121.772	528	Alluvium.
Los Baños	37.106	120.825	012	Do.
Lower Crystal Springs Dam	37.529	122.361	233	Franciscan greywacke.
Milpitas 2-story industrial bldg.	37.430	121.897	502	Alluvium.
Monterey City Hall	36.597	121.897	377	Granite.
Napa Napa College	38.270	122.276	150	Alluvium.
Oakland Outer Harbor Wharf	37.816	122.314	472	Bay mud.
Oakland Caldecott Tunnel, Highway 24	37.857	122.214	359	Sandstone, shale, mudstone.
Oakland 2-story office bldg.	37.806	122.267	224	Alluvium.
Oakland 24-story residential bldg.	37.798	122.257	483	---
Olema Point Reyes Ranger Station	38.043	122.797	003	Alluvium.
Palo Alto 2-story office bldg.	37.453	122.112	264	Do.
Piedmont 3-story school office bldg.	37.823	122.233	334	Serpentinite.
Piedmont Junior High School grounds	37.823	122.233	338	Weathered serpentinite.
Pleasant Hill 3-story commercial bldg.	37.946	122.060	348	Alluvium, 2 m thick; sandstone.
Point Bonita	37.82	122.52	043	Broken rock and soil 2 m thick; sandstone.
Redwood City 3-story school office bldg.	37.448	122.265	263	Greenstone.
Richmond City Hall parking lot	37.935	122.342	505	Alluvium.
Richmond 3-story government office bldg.	37.938	122.342	503	---

Table 2.—*Locations and site geology of stations in the California Strong Motion Instrumentation Program network that recorded the earthquake*—Continued

Station	Lat (°N.)	Long (°W.)	Code (figs. 1,2)	Site geology
Richmond 3-story office bldg.	37.978	122.329	506	Alluvium.
Salinas John and Work Streets	36.671	121.642	179	Do.
San Benito	36.519	121.084	288	Do.
San Bruno 6-story office bldg.	37.628	122.424	490	---
San Bruno 9-story government office bldg.	37.627	122.424	394	Alluvium.
San Francisco Cliff House	37.78	122.51	132	Franciscan sandstone, shale.
San Francisco 18-story commercial bldg	37.792	122.400	480	Fill over bay mud.
San Francisco 47-story office bldg.	37.796	122.396	532	Fill.
San Francisco 6-story UCSF bldg.	37.762	122.459	479	---
San Francisco Diamond Heights	37.74	122.43	130	Franciscan chert.
San Francisco International Airport	37.622	122.398	223	Deep alluvium.
San Francisco Pacific Heights	37.79	122.43	131	Franciscan sandstone, shale.
San Francisco Presidio	37.792	122.457	222	Serpentine.
San Francisco Rincon Hill	37.79	122.39	151	Franciscan sandstone, shale.
San Francisco Telegraph Hill	37.80	122.41	133	Franciscan shale, sandstone.
San Francisco Bay Dumbarton Bridge	---	---	--	---
San Jose 10-story commercial bldg.	37.338	121.893	355	Alluvium.
San Jose 13-story government office bldg.	37.353	121.903	357	Do.
San Jose 3-story office bldg.	37.212	121.803	562	---
San Jose Santa Teresa Hills	37.210	121.803	563	Alluvium over serpentine.
San Jose 10-story residential bldg.	37.338	121.888	356	Alluvium.
San Juan Bautista Highways 101/156 overpass	36.862	121.578	315	Do.
San Rafael 3-story office bldg.	38.196	122.819	341	Franciscan sandstone and silts.
Santa Cruz UCSC/Lick Observatory Electronics Laboratory	37.001	122.060	135	Limestone.
Santa Rosa 5-story commercial bldg.	38.439	122.711	387	---
Santa Rosa 14-story residential bldg.	38.437	122.707	489	---
Santa Rosa Hendley and Tupper Streets	38.437	122.707	491	---
Saratoga Aloha Avenue	37.255	122.031	065	Alluvium.
Saratoga 1-story school gymnasium	37.262	122.009	235	Alluvium.

Table 2.—*Locations and site geology of stations in the California Strong Motion Instrumentation Program network that recorded the earthquake*—Continued

Station	Lat (°N.)	Long (°W.)	Code (figs. 1,2)	Site geology
South San Francisco 4-story hospital	37.660	122.439	261	Fill over sandstone.
South San Francisco Sierra Point	37.674	122.388	539	---
South San Francisco Sierra Point Overpass	37.674	122.388	536	---
Tracy sewage plant	37.766	121.421	458	Alluvium.
Treasure Island Naval Base fire station	37.825	122.373	117	Fill.
Upper Crystal Springs Reservoir Pulgas Temple (APEEL array sta. 7; USGS sta. 1160)	37.49	122.31	378	Sandstone.
Upper Crystal Springs Reservoir Skyline Blvd. (APEEL array sta. 10; USGS sta. 1107)	37.465	122.343	373	Do.
Walnut Creek 10-story commercial bldg.	37.907	122.065	364	Marine sedimentary rocks.
Watsonville 4-story commercial bldg.	36.909	121.756	459	Fill over alluvium.
Woodside fire station	37.429	122.258	127	Conglomerate.
Yerba Buena Island	37.81	122.36	163	Franciscan sandstone.

Table 3.—*Stations in the California Strong Motion Instrumentation Program network, arranged by epicentral distance*

[From Shakal and others (1989). Instrument-shelter types: A, small prefabricated metal or wood-frame building; D, small metal box; F, small one-story building; H, small fiberglass structure. Epicentral distances are listed relative to estimated main-shock location at lat 37.037° N., long 121.883° W. (by U.S. Geological Survey); numbers in brackets are distance to nearest point on the fault inferred from aftershock distribution. Accelerograph trigger times are listed in seconds after Loma Prieta main shock at 0004 G.m.t. October 18, 1989. RefN component is a convenient designation for the primary axis of a structure; for its true direction, see California Strong Motion Instrumentation Program (1989). APEEL, Andreas Peninsula Earthquake Engineering Laboratory; BART, Bay Area Rapid Transit; bldg., building; CSUH, California State University, Hayward; SAGO, San Andreas Geophysical Observatory; UCB, University of California, Berkeley; UCSC, University of California, Santa Cruz; UCSF, University of California, San Francisco; USGS, U.S. Geological Survey. Do., ditto]

Station	Structure type and size	Epicentral distance (km)	Trigger time (s)	Component (°)	Maximum Acceleration (g)	
					Ground	Structure
		Map area 1 (fig. 1)				
Corralitos	Instrument	7	20.4	90	0.50	---
Eureka Canyon Road	shelter F	[1]		Up	.47	---
				360	.64	---
Capitola	1-story bldg.	9	----	90	.47	---
fire station		[14]		Up	.60	---
Capitola Avenue				360	.54	---
Santa Cruz	do.	16	----	90	.44	---
UCSC/Lick Observatory		[16]		Up	.40	---
Electronics Laboratory				360	.47	---
Watsonville	4-story	18	21.6	45	.28	.81
4-story commercial bldg.	concrete bldg.	[7]		Up	.66	---
	(13 sensors)			135	.39	1.24
Lexington Dam	Earth dam	19	21.2	90	.41	.40
Lexington Reservoir	(9 sensors)	[5]		Up	.15	.22
(near Los Gatos)				360	.45	.45
San Jose	Instrument	21	18.3	225	.28	---
Santa Teresa Hills	shelter H	[10]		Up	.22	---
Bernal and Harry Roads				315	.27	---
San Jose	3-story	21	18.6	315	.20	.58
3-story office bldg.	steel bldg.	[10]		Up	.14	---
	(10 sensors)			45	.20	.67
Saratoga	1-story	27	----	270	.33	.87
1-story gymnasium	concrete gym	[9]		Up	.27	---
	(11 sensors)			360	.26	.77
Saratoga	1-story	27	----	90	.34	---
Aloha Avenue	bldg	[9]		Up	.41	---
				360	.53	---
Gilroy	2-story	28	23.4	250	.25	.55
2-story historic	masonry bldg.	[16]		Up	.15	---
commercial bldg.	(6 sensors)			160	.28	.99
Gilroy	1-story bldg.	29	----	67	.37	---
Gavilan College		[15]		Up	.20	---
Physical Sciences Bldg.				337	.33	---
Gilroy sta. 1	Instrument	29	23.9	90	.50	---
Gavilan College	shelter H	[15]		Up	.22	---
water tank				360	.43	---
Gilroy sta. 2	Instrument	30	23.8	90	.33	---
Highway 101/Bolsa Road	shelter F	[16]		Up	.31	---
motel				360	.37	---

Table 3.—*Stations in the California Strong Motion Instrumentation Program network, arranged by epicentral distance*—Continued

Station	Structure type and size	Epicentral distance (km)	Trigger time (s)	Component (°)	Maximum Acceleration (g)	
					Ground	Structure
		Map area 1 (fig. 1)—Continued				
Gilroy sta. 3	Instrument	31	23.9	90	0.37	---
Gilroy sewage plant	shelter H	[18]		Up	.38	---
				360	.55	---
Gilroy sta. 4	1-story bldg	32	24.1	90	.22	---
San Ysidro School		[20]		Up	.17	---
				360	.42	---
Gilroy sta. 6	Instrument	35	26.0	90	.17	---
San Ysidro	shelter A	[24]		Up	.10	---
microwave site				360	.13	---
Gilroy sta. 7	Instrument	40	----	90	.33	---
Mantelli Ranch	shelter F	[28]		Up	.12	---
Jamison Road				360	.23	---
Coyote Lake Dam	Instrument	31	24.6	285	.49	---
southwest abutment	shelter A	[21]		Up	.08	---
				195	.15	---
Coyote Lake Dam	Instrument	31	24.5	285	.19	---
downstream	shelter H	[21]		Up	.10	---
				195	.17	---
San Juan Bautista	Bridge	33	----	336	.15	.94
Highway 101/156 overpass	(12 sensors)	[19]		Up	.10	.27
				66	.14	.61
San Jose	10-story	33	----	150	.10	.37
10-story	concrete bldg.	[20]		Up	.09	---
residential bldg.	(13 sensors)			60	.13	.24
San Jose	do.	33	----	330	.09	.26
10-story		[20]		Up	.09	---
commercial bldg.				240	.11	.38
San Jose	13-story	35	----	337	.11	.35
13-story	steel bldg.	[21]		Up	.10	----
government office bldg.	(22 sensors)			67	.10	.36
Halls Valley	Instrument	37	24.9	90	.11	---
Grant Park	shelter A	[31]		Up	.06	---
Old ranch headquarters				360	.13	---
Salinas	1-story bldg.	46	25.9	250	.12	---
John and Work Streets		[34]		Up	.11	---
				160	.09	---
Hollister	Instrument	48	27.5	90	.18	---
South and Pine Streets	shelter H	[33]		Up	.20	---
				360	.38	---
Hollister	1-story tiltup	48	---	RefN	.36	.45
1-story warehouse	warehouse	[33]		Up	.18	---
	(13 sensors)			90	.25	.82
Monterey	1-story bldg.	49	27.6	90	.07	---
City Hall		[44]		Up	.03	---
				360	.07	---

Table 3.—*Stations in the California Strong Motion Instrumentation Program network, arranged by epicentral distance*—Continued

Station	Structure type and size	Epicentral distance (km)	Trigger time (s)	Component (°)	Maximum Acceleration (g)	
					Ground	Structure
Map area 1 (fig. 1)—Continued						
Hollister	Instrument	54	30.2	351	0.07	---
SAGO south	shelter A	[39]		Up	.06	---
Cienega Road				261	.07	---
Big Sur	1-story bldg.	87	33.7	90	.05	---
Pfeiffer State Park		[79]	Up	.03	---	
				360	.06	---
San Benito	Instrument	92	46.8	90	.05	---
	shelter A	[77]		Up	.02	---
				360	.05	---
Los Baños	do.	94	39.3	90	.05	---
		[83]		Up	.01	---
				360	.05	---
Greenfield	1-story bldg.	98	36.1	90	.08	---
police station		[85]		Up	.06	---
				360	.08	---
Bitterwater	Instrument	107	45.8	90	.06	---
Coalinga Road	shelter A	[93]		Up	.03	---
				360	.07	---
Map area 2 (fig. 1)						
Agnew	1-story bldg.	40	24.2	90	0.16	---
Agnews State Hospital		[25]		Up	.10	---
				360	.17	---
Palo Alto	2-story	50	----	37	.20	.38
2-story office bldg.	masonry bldg.	[32]		Up	.09	---
	(7 sensors)			127	.21	.55
Woodside	1-story bldg.	55	----	90	.08	---
fire station		[36]		Up	.05	---
				360	.08	---
Redwood City	3-story	57	----	217	.05	.19
3-story school	concrete bldg.	[38]		Up	.04	---
office bldg.	(6 sensors)			307	.09	.17
Upper Crystal	Instrument	63	----	90	.09	---
Springs Reservoir	shelter A	[44]		Up	.04	---
Skyline Boulevard				360	.10	---
(APEEL array sta. 10)						
Upper Crystal	do.	63	30.7	90	.09	---
Springs Reservoir		[44]		Up	.06	---
Pulgas Water Temple				360	.16	---
(APEEL array sta. 7)						
Redwood City	do.	63	29.2	90	.29	---
Redwood Shores		[44]		Up	.11	---
(APEEL array sta. 1)				360	.26	---
Belmont	2-story	65	----	345	.10	.20
2-story office bldg.	concrete bldg.	[46]		Up	.04	---
	(7 sensors)			75	.11	.19

Table 3.—*Stations in the California Strong Motion Instrumentation Program network, arranged by epicentral distance*—Continued

Station	Structure type and size	Epicentral distance (km)	Trigger time (s)	Component (°)	Maximum Acceleration (g)	
					Ground	Structure
Lower Crystal Springs Dam	Concrete	69	25.0	332	0.06	---
	gravity dam	[50]		Up	.03	.03
	(15 sensors)			242	.09	.07
San Francisco	1-story bldg.	79	34.1	90	.33	---
International Airport		[60]		Up	.05	---
service. bldg.				360	.24	---
near Highway 101						
San Bruno	9-story	81	----	65	.11	.32
9-story government	concrete bldg.	[62]		Up	.14	---
office bldg.	(16 sensors)			335	.16	.36
San Bruno	6-story	81	31.6	335	.14	.25
6-story office bldg.	concrete bldg.	[62]		Up	.12	---
	(13 sensors)			245	.12	.46
South San Francisco	Instrument	84	----	205	.11	---
Sierra Point	shelter H	[65]		Up	.05	---
				115	.06	---
South San Francisco	Isolated-deck	84		25	.09	.41
Sierra Point overpass	bridge	[65]		Up	.03	.11
Highway 101	(13 sensors)			115	.05	.22
South San Francisco	4-story	85	----	41	.14	.57
4-story hospital	steel bldg.	[66]		Up	.08	---
	(11 sensors)			311	.15	.68
San Francisco	2-story bldg.	92	----	90	.12	---
Diamond Heights		[73]		Up	.05	---
Digby Street fire station				360	.10	---
San Francisco	Instrument	95	35.7	90	.09	---
Rincon Hill	shelter A	[76]		Up	.03	---
Fremont and Harrison Streets				360	.08	---
San Francisco	6-story	95	35.0	345	.09	.28
6-story UCSF bldg.	concrete bldg.	[76]		Up	.04	---
	(13 sensors)			75	.07	.19
San Francisco	18-story steel/	95	33.1	90	.17	.27
18-story commercial bldg.	concrete bldg.	[77]		Up	.04	---
	(13 sensors)			RefN	.14	.27
San Francisco	47-story	96	33.9	RefN	.13	.48
47-story office bldg.	steel bldg.	[77]		Up	.08	---
	(18 sensors)			90	.20	.39
San Francisco	2-story bldg.	97	----	360	.05	---
Pacific Heights		[78]		Up	.03	---
California Street				270	.06	---
fire station						
San Francisco	do.	97	46.6	90	.08	---
Telegraph Hill		[78]		Up	.03	---
Stockton Street fire station				360	.06	---
San Francisco	Instrument	98	36.1	90	.21	---
Presidio	shelter H	[79]		Up	.06	---
Arguello Drive vista point				360	.10	---

Table 3.—*Stations in the California Strong Motion Instrumentation Program network, arranged by epicentral distance*—Continued

Station	Structure type and size	Epicentral distance (km)	Trigger time (s)	Component (°)	Maximum Acceleration (g)	
					Ground	Structure
Map area 2 (fig. 1)—Continued						
San Francisco	2-story bldg.	99	----	90	0.11	---
Cliff House		[80]		Up	.06	---
				360	.08	---
Point Bonita	Instrument	104	39.1	297	.07	---
	shelter A	[85]		Up	.03	---
				207	.07	---
San Rafael	3-story steel/	124	----	20	.04	.10
3-story office bldg.	concrete bldg.	[105]		Up	.03	---
	(16 sensors)			290	.04	.13
Olema	Instrument	138	42.5	90	.11	---
Point Reyes	shelter H	[119]		Up	.06	---
ranger station				360	.16	---
Santa Rosa	do.	171	12.9	69	.05	---
Hendley and Tupper Streets		[153]		Up	.03	---
				339	.04	---
Santa Rosa	14-story	171	12.1	340	.04	.21
14-story residential bldg.	concrete bldg.	[153]		Up	.02	---
	(16 sensors)			70	.05	.21
Santa Rosa	5-story	172	----	330	.06	.11
5-story commercial bldg.	concrete bldg.	[153]		Up	.03	---
	(16 sensors)			60	.06	.13
Bodega Head	1-story bldg.	175	----	180	.04	---
Doran Beach		[156]		Up	.02	---
				90	.04	---
Map area 3 (fig. 1)						
Milpitas	2-story	43	25.0	335	0.10	0.34
2-story industrial bldg.	tiltup bldg.	[29]		Up	.08	---
	(13 sensors)			245	.14	.58
Fremont	1-story bldg.	55	28.6	90	.11	---
Mission San Jose		[39]		Up	.09	---
fire station				360	.13	---
Hayward	6-story	69	29.5	335	.10	.24
6-story office bldg.	concrete bldg.	[51]		Up	.05	---
	(13 sensors)			65	.12	.45
Hayward	13-story	70	----	320	.08	.21
13-story CSUH	steel/concrete	[53]		Up	.05	---
Administration bldg.	(16 sensors)			50	.09	.24
Hayward	4-story	70	32.8	335	.05	.18
4-story CSUH	concrete bldg.	[53]		Up	.03	---
Science Bldg.	(16 sensors)			65	.04	.08
Hayward	Instrument	71	32.8	90	.08	---
CSUH Stadium grounds	shelter A	[53]		Up	.05	---
(APEEL array sta. 3E)				360	.08	---

Table 3.—*Stations in the California Strong Motion Instrumentation Program network, arranged by epicentral distance*—Continued

Station	Structure type and size	Epicentral distance (km)	Trigger time (s)	Component (°)	Maximum Acceleration (g)	
					Ground	Structure
		Map area 3 (fig. 1)—Continued				
Hayward	1-story bldg.	71	----	90	0.14	---
Muir School (APEEL array		[53]		Up	.10	---
sta. 2E) (USGS sta. 1121)				360	.18	---
Hayward	Instrument	73	----	310	.16	---
BART station	shelter H	[55]		Up	.08	---
parking lot				220	.16	---
Hayward—BART	Single-deck	73	31.3	310	.15	.26
elevated section	elevated rapid	[55]		Up	.05	----
	transit structure			220	.15	.60
	(16 sensors)					
Livermore	Instrument	80	35.6	92	.04	---
Fagundes Ranch	shelter H	[67]		Up	.02	---
North Livermore Avenue				2	.04	---
Tracy	1-story bldg.	91	40.3	90	.06	---
sewage plant		[83]		Up	.02	---
generator bldg.				360	.06	---
Oakland	24-story	91	35.1	305	.18	.38
24-story	concrete bldg.	[72]		Up	.04	.14
residential bldg.	(16 sensors)			35	.14	.25
Oakland	2-story masonry/	92	----	200	.20	.26
2-story office bldg.	steel bldg.	[73]		Up	.16	----
	(10 sensors)			290	.26	.69
Piedmont	3-story	93	----	315	.08	.18
Piedmont Junior High	concrete bldg.	[74]		Up	.04	----
3-story school bldg.	(11 sensors)			45	.07	.15
Piedmont	Instrument	93	----	45	.08	---
Piedmont Junior High	shelter H	[74]		Up	.03	---
School grounds				315	.07	---
Oakland	Concrete	95	35.0	35	.29	.45
Outer Harbor Wharf	wharf	[76]		Up	.07	----
14th Street	(12 sensors)			125	.27	.32
Yerba Buena Island	Instrument	95	----	90	.06	---
	shelter F	[77]		Up	.03	---
				360	.03	---
Treasure Island	1-story bldg.	98	----	90	.16	---
Naval Base		[79]		Up	.02	---
fire station				360	.11	---
Oakland	3,100-ft-long	96	37.0	251	----	.06
Caldecott Tunnel	tunnel	[77]		Up	----	.03
Highway 24	(24 sensors)			161	----	.06
Berkeley	2-story	97	36.5	345	.11	.28
2-story hospital	steel bldg.	[78]		Up	.04	----
	(12 sensors)			255	.12	.30
Walnut Creek	10-story	98	----	167	.10	.21
10-story	concrete bldg.	[81]		Up	.05	----
commercial bldg.	(16 sensors)			77	.05	.25

Table 3.—*Stations in the California Strong Motion Instrumentation Program network, arranged by epicentral distance*—Continued

Station	Structure type and size	Epicentral distance (km)	Trigger time (s)	Component (°)	Maximum Acceleration (g)	
					Ground	Structure
		Map area 3 (fig. 1)—Continued				
Berkeley Lawrence Berkeley Laboratory (LBL sta. 01) Cyclotron Road	Instrument shelter H	99 [80]	38.4	90	0.12	---
				Up	.04	---
				360	.05	---
Berkeley UCB Memorial Stadium grounds	Instrument shelter D	98 [80]	----	135	.13	---
				Up	.03	---
				225	.07	---
Pleasant Hill 3-story commercial bldg.	3-story concrete bldg. (12 sensors)	102 [85]	----	360	.08	.13
				Up	.03	----
				270	.13	.23
Concord 8-story residential bldg.	8-story masonry bldg. (13 sensors)	105 [89]	40.1	150	.06	.14
				Up	.03	----
				240	.06	.24
Richmond City Hall parking lot	Instrument Shelter H	108 [89]	38.4	280	.11	---
				Up	.04	---
				190	.13	---
Richmond 2-story government office bldg., City Hall	3-story concrete bldg. (13 sensors)	108 [89]	37.9	10	.12	.24
				Up	.04	----
				280	.09	.20
Richmond 3-story office bldg.	3-story steel bldg. (12 sensors)	112 [93]	36.9	360	.10	.32
				Up	.07	----
				270	.12	.29
Napa Napa College	1-story bldg.	141 [123]	----	90	.03	---
				Up	.02	---
				360	.03	---

Table 4.—*Stations in the California Strong Motion Instrumentation Program network whose earthquake records are contained in tapes processed by the California Division of Mines and Geology, Office of Strong Motion Studies*

[Types of records in tapes: LOMAPRIETA89–IG, ground-response stations; LOMAPRIETA89–IL, lifeline structures; LOMAPRIETA89–IB1 through LOMAPRIETA89–IB3, buildings. Tape LOMAPRIETA89–IG contains phase I (uncorrected acceleration) data; an accompanying tape, LOMAPRIETA89–G, contains phase II (corrected acceleration, velocity, and displacement) and phase III (spectra) data. Tape LOMAPRIETA89–IL contains phase I data; an accompanying tape, LOMAPRIETA89–L, contains phase II and phase III data. Tapes LOMAPRIETA89–IB1 through LOMAPRIETA89–IB3 contain phase I data; accompanying tapes, LOMAPRIETA89–IIB1 and LOMAPRIETA89–IIB2, contain phase II data, and tape LOMAPRIETA89–IIIB contains phase III data. BART, Bay Area Rapid Transit; bldg., building; CSUH, California State University, Hayward; SAGO, San Andreas Geophysical Observatory; UCSC, University of California, Santa Cruz]

Tape LOMAPRIETA89–IG

Corralitos—Eureka Canyon Road
Capitola—fire station
Santa Cruz—UCSC/Lick Observatory
Saratoga—Aloha Avenue
San Jose—Santa Teresa Hills
Gilroy—Gavilan College, Physical Sciences Bldg.
Gilroy sta. 1—Gavilan College, water tank
Gilroy sta. 2—Highway 101/Bolsa Road motel
Gilroy sta. 3—sewage plant
Gilroy sta. 4—San Ysidro School
Gilroy sta. 6—San Ysidro
Gilroy sta. 7—Mantelli Ranch
Coyote Lake Dam—southwest abutment
Coyote Lake Dam—downstream
Halls Valley—Grant Park
Hollister—South Street and Pine Drive
Hollister—SAGO South, Cienega Road
Salinas—John and Work Streets
Monterey—City Hall
Agnew—Agnews State Hospital
Woodside—fire station
Upper Crystal Springs Reservoir—Skyline Boulevard
Upper Crystal Springs Reservoir—Pulgas temple
Foster City—Redwood Shores
San Francisco Bay—Dumbarton Bridge
San Francisco International Airport
South San Francisco—Sierra Point overpass
San Francisco—Diamond Heights
San Francisco—Rincon Hill
San Francisco—Telegraph Hill
San Francisco—Pacific Heights
San Francisco—Presidio
San Francisco—Cliff House
Point Bonita
Olema—Point Reyes ranger station
Fremont—Mission San Jose
Hayward—CSUH stadium grounds
Hayward—Muir School
Hayward—BART station parking lot
Treasure Island
Yerba Buena Island
Berkeley—Lawrence Berkeley Laboratory
Piedmont Junior High School grounds
Richmond—City Hall parking lot

Tape LOMAPRIETA89–IL

San Juan Bautista—Highways 101/156 overpass (channels 1-12)
South San Francisco—Sierra Point overpass (channels 1-13)
South San Francisco—Sierra Point (channels 14-16)
Hayward—BART elevated section (channels 1-13)
Hayward—BART elevated section (channels 14-16)
Hayward—BART station (channels 17-19)
San Francisco Bay—Dumbarton Bridge (channels 1-13)
San Francisco Bay—Dumbarton Bridge (channels 14-26)
San Francisco Bay—Dumbarton Bridge west end free field (channels 1-3)
Lexington Dam (channels 1-3)
Lexington Dam (channels 4-6)
Lexington Dam (channels 7-9)
Lower Crystal Springs Dam (channels 1-12)
Lower Crystal Springs Dam (channels 13-15)
Oakland—Outer Harbor Wharf (channels 1, 3-12)

Tape LOMAPRIETA89–IB1

Watsonville—4-story commercial bldg. (channels 1-13)
Hollister—1-story warehouse (channels 1-13)
Hollister—South Street and Pine Drive (channels 1-3)
Gilroy—2-story historic commercial bldg. (channels 1-3)
Gilroy—2-story historic commercial bldg. (channels 4-6)
San Jose—3-story office bldg. (channels 1-10)
San Jose—Santa Teresa Hills (channels 1-3)
Saratoga—1-story school gymnasium (channels 1-11)
San Jose—10-story residential bldg. (channels 1-13)
San Jose—10-story commercial bldg. (channels 1-13)
San Jose—13-story government office bldg. (channels 1-12)
San Jose—13-story government office bldg. (channels 13-22)
Palo Alto—2-story office bldg. (channels 1-7)
Redwood City—3-story school office bldg. (channels 1-6)

Tape LOMAPRIETA89–IB2

Belmont—2-story office bldg. (channels 1-7)
San Bruno—9-story government office bldg. (channels 1-13)
San Bruno—9-story government office bldg. (channels 14-16)
San Bruno—6-story office bldg. (channels 1-13)
South San Francisco—4-story hospital (channels 1-11)
San Francisco 6-story school bldg. (channels 1-13)
San Francisco—18-story commercial bldg. (channels 1-13)
San Francisco—47-story office bldg. (channels 1-18)
Milpitas—2-story industrial bldg. (channels 1-13)
Hayward—6-story office bldg. (channels 1-13)
Hayward—13-story CSUH Administrative Bldg. (channels 1, 3-6, 8, 9, 11-13)
Hayward—13-story CSUH Administrative Bldg. (channels 14-16)

Tape LOMAPRIETA89–IB3

Hayward—4-story CSUH Science Bldg. (channels 1-13)
Hayward—4-story CSUH Science Bldg. (channels 14-16)
Oakland—24-story residential bldg. (channels 1, 3-5, 7-12)
Oakland—24-story residential bldg. (channels 14-16)
Oakland—2-story office bldg. (channels 1-10)
Piedmont—3-story school office bldg. (channels 1-11)
Piedmont Junior High School grounds (channels 1-3)
Berkeley—2-story hospital (channels 1-12)
Richmond—3-story government office bldg. (channels 1-13)
Richmond—City Hall parking lot (channels 1-3)
Richmond—3-story office bldg. (channels 1-12)
Walnut Creek—10-story commercial bldg. (channels 1-13)
Walnut Creek—10-story commercial bldg. (channels 14-16)
Pleasant Hill—3-story commercial bldg. (channels 1-12)
Concord—8-story residential bldg. (channels 1-10)
Concord—8-story residential bldg. (channels 11-13)

Table 5.—*Names and locations of stations in the U.S. Geological Survey's National Strong Motion Network that recorded the earthquake*

[From Switzer and others (1981) and Maley and others (1989). Instrument-shelter types: A, small prefabricated metal or wood-frame building; C, buried concrete vault; D, small metal box; H, small fiberglass structure. Data sources: BECH, Bechtel Group, Inc.; CDMG, California Division of Mines and Geology; CDWR, California Division of Water Resources; UCB, University of California, Berkeley; USGS, U.S. Geological Survey; USPS, U.S. Postal Service; VA, Veterans' Administration. APEEL, Andreas Peninsula Earthquake Engineering Laboratory; bldg., building; SAGO, San Andreas Geophysical Observatory; SFSU, San Francisco State University; SLAC, Stanford Linear Accelerator Center. Do., ditto]

Station name	Coordinates (lat °N., long °W.)	Epicentral distance (km)	Site geology	Structure type/size	Instrument location(s)	Data source
Morgan Hill Anderson Dam	37.166 121.626	27	---	Earth dam	Left abutment, crest, toe, middam, downstream	USGS
Cherry Flat Reservoir Calaveras Array	37.396 121.756	42	Franciscan volcanic and meta volcanic rocks.	Instrument shelter A	Ground level	USGS
Sunnyvale Colton Avenue	37.402 122.024	43	---	1-story wood-frame bldg.	do.	USGS
Milpitas Rivera Street	37.437 121.879	45	---	1-story reinforced concrete-block bldg.	do.	USGS
Hollister Differential array	36.888 121.413	45	---	Instrument shelter H	do.	USGS
Palo Alto VA Hospital, bldg. 1	37.40 122.14	46	Alluvium	6-story bldg.	Basement, roof.	VA
Hollister City Hall	36.851 121.402	47	---	---	Basement	USGS
Calaveras Reservoir South Calaveras Array	37.452 121.807	47	Older alluvium	1-story wood-frame bldg.	Ground level	USGS
Hollister SAGO Vault	36.765 121.446	49	---	Vault	do.	UCB
Palo Alto, Stanford SLAC Test Laboratory	37.419 122.205	51	---	---	do.	USGS
Stanford University parking garage	37.432 122.172	51	Alluvium	3-level garage	Basement	USGS
Menlo Park VA Hospital, bldg. 137	37.468 122.157	54	do.	3-story bldg.	Ground floor	VA
Fremont, Emerson Court Mission San Jose	37.535 121.929	56	Older alluvium	1-story wood-frame wood/stucco bldg.	Ground level	USGS
Crystal Springs Reservoir APEEL array Sta. 9	37.48 122.32	62	Sandstone	Instrument shelter A	do.	CDMG
Calaveras array Sunol Forest fire station	37.597 121.880	62	Alluvium	1-story steel I-beam bldg.	do.	USGS
Redwood City APEEL array sta. 2	37.52 122.25	63	Mud, 8-m depth; alluvium, 85-m depth.	Instrument shelter D	do.	USGS
Del Valle Dam	37.617 121.746	66	---	Earth dam	Toe, crest	CDWR
Foster City Menhaden Court	37.555 122.248	66	Mud and silt	2-story bldg.	Ground level	USGS

Table 5.—*Names and locations of stations in the U.S. Geological Survey's National Strong Motion Network that recorded the earthquake*—Continued

Station name	Coordinates (lat °N., long °W.)	Epicentral distance (km)	Site geology	Structure type/size	Instrument location(s)	Data source
Livermore VA Hospital, bldg. 62	37.625 121.762	66	Alluvium, 600-m deep; sandstone.	6-story bldg.	Basement, roof.	VA
Bear Valley Sta. 12 Williams Ranch	36.658 121.249	70	Nonmarine deposits.	1-story bldg.	Ground level	USGS
Bear Valley Sta. 5 Callens Ranch	36.673 121.195	73	do.	2-story bldg.	do.	USGS
Hayward City Hall 22300 Foothill Boulevard	37.679 122.082	74	Alluvium, 10-m deep; serpentine.	12-story bldg.	Ground, mall, 3rd and 12th floors.	USGS
Free field, north site	do.	74	---	Instrument shelter H	Ground level	USGS
Calaveras array Dublin fire station	37.709 121.932	75	Shallow alluvial deposits.	1-story wood-frame bldg.	do.	USGS
Bear Valley sta. 1 Fire station	36.573 121.184	81	Alluvium, nonmarine deposits.	1-story bldg.	do.	USGS
Bear Valley sta. 10 Webb residence	36.532 121.143	86	Alluvium	do.	do.	USGS
Bear Valley sta. 7 Pinnacles National Monument	36.483 121.184	88	Volcanic rocks	do.	do.	USGS
San Francisco Fire station 17	37.728 122.385	89	---	---	do.	USGS
Bear Valley sta. 14 Upper Butts Ranch	36.569 121.043	91	Marine deposits	1-story bldg.	do.	USGS
San Francisco—SFSU Thornton Hall	37.724 122.475	93	---	3-story reinforced concrete-block bldg.	do.	USGS
San Francisco Chevron bldg. 575 Market Street	37.79 122.40	95	---	41-story steel bldg.	2nd basement, 1st basement, 24th, 33rd, 41st floors.	USGS
San Francisco Transamerica Tower 600 Montgomery Street	37.80 122.40	96	---	49-story bldg. with 10-level tower	Basement, garage, plaza, 5th, 21st, 29th, 49th and 58th floors.	USGS
San Francisco Bechtel bldg. 50 Beale Street	---	95	---	24-story bldg.	Basement, 12th, 24th floors.	BECH
Emeryville 6363 Christie Avenue	37.844 122.295	97		30-story concrete-frame bldg.	Ground floor, 13th, 21st, 30th floors.	USGS
Free field, south site	do.	97	---	Instrument shelter H	Ground level	USGS
Berkeley Byerly Seismic Station (also called: Strawberry Canyon, UCB)	37.87 122.24	98		Instrument shelter C	do.	UCB
Berkeley UCB, Haviland Hall	37.87 122.26	98	Sandstone and chert	4-story bldg.	Basement	UCB

Table 5.—*Names and locations of stations in the U.S. Geological Survey's National Strong Motion Network that recorded the earthquake*—Continued

Station name	Coordinates (lat °N., long °W.)	Epicentral distance (km)	Site geology	Structure type/size	Instrument location(s)	Data source
Berkeley Great Western Bank	37.87 122.27	99		13-story bldg.	Basement, 4th floor, roof.	USGS
San Francisco VA Hospital	37.783 122.504	100	Franciscan assemblage	6-story bldg.	Basement, roof	VA
San Francisco Golden Gate Bridge Toll plaza	37.806 122.472	100	---	---	Ground level	USGS
Richmond Bulk Mail Center 2501 Rydin Street, SE.	37.884 122.302	101	---	3-story steel-frame bldg.	do.	USPS
Martinez VA Hospital	37.99 122.11	108	Shale and sandstone	4-story reinforced concrete bldg.	Basement	VA
Larkspur Ferry terminal	37.946 122.508	115	Marsh	Steel roof; concrete deck slab; piles	Ground, ferry dock	USGS

Table 6.—*Accelerations at stations in the U.S. Geological Survey's National Strong Motion Network that recorded the earthquake*

[For tape pairs (USACA46 and USACA47, USACA53 and USACA54, USACA55 and USACA56), the first contains raw or uncorrected data, and the second corrected data and spectra. Tape USACA45 includes preliminary versions of the ground-level, basement, and some upper-level structural records from the stations at Anderson Dam, 600 Montgomery Street in San Francisco, and 6363 Christie Avenue in Emeryville. Tape names are abbreviated to the last two digits. APEEL, Andreas Peninsula Earthquake Engineering Laboratory; bldg., building; CDWR, California Department of Water Resources; SAGO, San Andreas Geophysical Observatory; SLAC, Stanford Linear Accelerator Center; UCB, University of California, Berkeley; USGS, U.S. Geological Survey; VA, Veterans' Administration. Do., ditto]

Station			Corrected Acceleration		
Code (Fig. 3)	Name	Location	Direction (°)	Maximum (cm/s^2)	Tape
1	Anderson Dam Morgan Hill (USGS)	Crest	333	265	45, 46, 47
			Up	182	do.
			243	380	do.
		Downstream	333	240	do.
			Up	185	do.
			243	245	do.
		Left abutment	333	76.5	do.
			Up	52.7	do.
			243	64.6	do.
		Structure array:			
		Channel 1—middam, center	153	167	46, 47
		Channel 2—middam, center	243	149	do.
		Channel 3—middam, right	063	218	do.
		Channel 4—toe	333	116	do.
		Channel 5—toe	Up	126	do.
		Channel 6—toe	063	132	do.
		Channel 7—right crest	333	309	do.
		Channel 8—right crest	Up	176	do.
		Channel 9—right crest	063	412	do.
		Channel 10—center crest	333	314	do.
		Channel 11—center crest	Up	256	do.
		Channel 12—center crest	063	395	do.
3	Calaveras array Cherry Flat Reservoir (USGS)	---	360	78.2	55, 56
			Up	61.1	do.
			270	74.8	do.
4	Sunnyvale Colton Avenue (USGS)	---	360	215	45
			Up	111	do.
			270	210	do.
5	Hollister Airport differential array (USGS)	---	255	281	do.
			Up	156	do.
			165	277	do.
6	Palo Alto VA Hospital, bldg. 1 (VA)	Basement	302	342	45
			Up	193	do.
			212	378	do.
		Roof (7th level)	302	1,151	do.
			Up	635	do.
			212	823	do.
7	Hollister City Hall Annex basement (USGS)	---	180	217	do.
			Up	220	do.
			090	252	do.
8	Calaveras array Calaveras Reservoir south (USGS)	---	180	113	55, 56
			Up	62.4	do.
			090	68.7	do.
9	Hollister SAGO vault (USGS)	---	360	60.1	do.
			Up	42.7	do.
			270	36.3	do.

Table 6.—*Accelerations at stations in the U.S. Geological Survey's National Strong Motion Network that recorded the earthquake*—Continued

Station		Location	Corrected Acceleration		Tape
Code (Fig. 3)	Name		Direction (°)	Maximum (cm/s²)	
10	Stanford University	---	360	282	45
	SLAC Test Laboratory		Up	91.8	do.
	(USGS)		270	198	do.
10A	Stanford University	Basement	360	255	do.
	parking garage		Up	152	do.
			090	216	do.
11	Menlo Park	---	110	117	do.
	VA Hospital, bldg. 37		Up	96.4	do.
	(VA)		020	288	do.
12	Fremont	---	180	143	do.
	Emerson Court		Up	68.5	do.
	(USGS)		090	191	do.
13	APEEL array station 9	---	227	106	55, 56
	Crystal Springs Reservoir		Up	48.8	do.
	(USGS)		137	115	do.
14	Calaveras array	---	180	63.8	do.
	Sunol fire station		Up	29.8	do.
	(USGS)		090	82.9	do.
15	APEEL array sta. 2	---	133	223	45
	Redwood City		Up	84.5	do.
	(USGS)		043	272	do.
16	Foster City	---	360	117	55, 56
	Menhaden Court		Up	75.1	do.
	(USGS)		270	107	do.
17	Del Valle Dam	Crest	065	80.0	do.
	(CDWR)		Up	61.7	do.
			335	75.7	do.
		Toe	065	53.7	do.
			Up	27.4	do.
			335	39.7	do.
18	Livermore	Basement	125	56.2	do.
	VA Hospital, bldg. 62		Up	31.6	do.
	(VA)		035	46.4	do.
		Roof (7th)	125	84.9	do.
			Up	31.9	do.
			035	145	do.
19	Bear Valley sta. 12	---	310	166	do.
	Williams Ranch		Up	90.8	do.
	(USGS)		220	154	do.
21	Bear Valley sta. 5	---	310	69.7	do.
	Callens Ranch		Up	38.6	do.
	(USGS)		220	67.9	do.
22	Hayward City Hall	Ground floor	064	43.7	53, 54
	(USGS)		Up	31.9	do.
			334	54.0	do.
		Ground site north	064	48.7	do.
			Up	27.2	do.
			334	50.6	do.

Table 6.—*Accelerations at stations in the U.S. Geological Survey's National Strong Motion Network that recorded the earthquake*—Continued

Station		Location	Corrected Acceleration		Tape
Code (Fig. 3)	Name		Direction (°)	Maximum (cm/s²)	
		Structure array:			
		Channel 1—12th floor, west	334	91.3	53, 54
		Channel 2—12th floor, center	334	94.6	do.
		Channel 3—12th floor, center	064	125	do.
		Channel 4—7th floor, west	334	81.9	do.
		Channel 5—7th floor, center	334	75.9	do.
		Channel 6—7th floor, center	064	81.9	do.
		Channel 7—3rd floor, west	334	Inoperative	---
		Channel 8—3rd floor, center	334	56.6	do.
		Channel 9—3rd floor, center	064	72.0	do.
		Channel 10—3rd floor, southwest	Up	41.9	do.
		Channel 11—3rd floor, southwest	Up	41.6	do.
		Channel 12—ground floor, west	334	67.3	do.
23	Calaveras array	---	360	73.7	55, 56
	Dublin fire station		Up	52.3	do.
	(USGS)		270	71.8	do.
24	Bear Valley sta. 10	---	310	84.7	do.
	Webb residence		Up	50.3	do.
	(USGS)		220	119	do.
25	Bear Valley sta. 7	---	310	40.6	55, 56
	Pinnacles National		Up	26.3	do.
	Monument (USGS)		220	45.2	do.
26	San Francisco	---	360	104	do.
	1295 Shafter Street		Up	48.3	do.
	(USGS)		270	70.4	do.
27	San Francisco—SFSU	---	270	131	do.
	Thornton Hall		Up	36.7	do.
	(USGS)		180	116	do.
28	San Francisco	Basement	135	82.8	53, 54
	575 Market Street		Up	55.6	do.
	(USGS)		045	107	do.
		Structure array:			
		Channel 1—42d level, northwest	045	217	do.
		Channel 2—42d level, center	225	180	do.
		Channel 3—42d level, center	135	132	do.
		Channel 4—34th level, northwest	045	152	do.
		Channel 5—34th level, center	225	148	do.
		Channel 6—34th level, center	135	178	do.
		Channel 7—25th level, northwest	045	183	do.
		Channel 8—25th level, center	225	218	do.
		Channel 9—25th level, center	135	162	do.
		Channel 10—ground level	045	121	do.
		Channel 11—ground level	315	133	do.
29	San Francisco	Structure array:			
	600 Montgomery Street	Channel 1—21st floor, west central	351	194	46, 47
	(USGS)	Channel 2—21st floor, south central	351	177	do.
		Channel 3—21st floor, south central	081	215	do.
		Channel 4—5th floor, west central	351	263	do.
		Channel 5—5th floor, south central	351	264	do.
		Channel 6—5th floor, south central	081	219	do.
		Channel 7—SE corner, foundation	Up	73.1	do.
		Channel 8—ground level, west central	351	160	do.
		Channel 9—ground level, center	351	143	do.
		Channel 10—ground level, center	081	167	do.
		Channel 11—foundation, NW. corner	351	84.3	do.
		Channel 12—foundation, west side	351	90.1	do.
		Channel 13—foundation, SW. corner	Up	43.6	do.

Table 6.—*Accelerations at stations in the U.S. Geological Survey's National Strong Motion Network that recorded the earthquake*—Continued

Station		Location	Corrected Acceleration		Tape
Code (Fig. 3)	Name		Direction (°)	Maximum (cm/s²)	
		Basement	261	120	45
			Up	47.4	do.
			171	104	do.
		29th floor	261	156	do.
			Up	112	do.
			171	162	do.
		49th floor	261	306	do.
			Up	143	do.
			171	294	do.
29A	San Francisco Bechtel bldg. 50 Beale St.	Basement	135	147	53, 54
			Up	61.3	do.
			045	128	do.
		12th floor	135	150	do.
			Up	65.9	do.
			045	166	do.
		24th floor	135	126	do.
			Up	89.7	do.
			045	202	do.
30	Emeryville 6363 Christie Avenue (USGS)	Ground site, south	350	210	45, 46, 47
			Up	585	do.
			260	255	do.
		Structure array 1:			
		Channel 1—roof (31st level), west wing	350	260	46,47
		Channel 2—roof (31st level), south wing	050	301	do.
		Channel 3—roof (31st level), north wing	290	481	do.
		Channel 4—roof (31st level), central core	350	244	do.
		Channel 5—roof (31st level), central core	260	370	do.
		Channel 6—21st floor, central core	350	183	do.
		Channel 7—21st floor, west wing	350	186	do.
		Channel 8—21st floor, south wing	050	168	do.
		Channel 9—21st floor, north wing	290	236	do.
		Channel 10—13th floor, central core	350	266	do.
		Channel 11—13th floor, central core	260	253	do.
		Channel 12—21st floor, central core	260	239	do.
		Structure array 2:			
		Channel 1—13th floor, west wing	350	208	do.
		Channel 2—13th floor, south wing	050	223	do.
		Channel 3—13th floor, north wing	290	306	do.
		Channel 4—ground floor, west wing	Up	56.0	do.
		Channel 5—ground floor, south wing	Up	55.3	do.
		Channel 6—ground floor, central core	Up	37.5	do.
		Channel 7—ground floor, north wing	260	209	do.
		Channel 8—ground floor, north wing	Up	47.5	do.
		Channel 9—ground floor, north wing	350	174	do.
		Channel 10—ground site, north	350	181	do.
		Channel 11—ground site, north	Up	82.3	do.
		Channel 12—ground site, north	260	227	do.
31	Berkeley, UCB Strawberry Canyon (UCB)	---	135	47.3	55, 56
			Up	22.7	do.
			045	74.6	do.
32	Berkeley, UCB Haviland Hall basement (UCB)	---	135	24.7	do.
			Up	18.5	do.
			045	78.2	do.
33	Berkeley 2168 Shattuck Avenue (USGS)	Basement, east	261	92.6	53, 54
			Up	19.9	do.
			171	114	do.

Table 6.—*Accelerations at stations in the U.S. Geological Survey's National Strong Motion Network that recorded the earthquake*—Continued

Station		Location	Corrected Acceleration		Tape
Code (Fig. 3)	Name		Direction (°)	Maximum (cm/s²)	
		Basement, west	261	97.8	53, 54
			Up	22.5	do.
			171	91.5	do.
		Structure array:			
		Channel 1—13th floor, east core	171	124	do.
		Channel 2—13th floor, east core	261	228	do.
		Channel 3—13th floor, center	171	139	do.
		Channel 4—13th floor, roof, west core	171	175	do.
		Channel 5—13th floor, roof, west core	081	206	do.
		Channel 6—13th floor, southwest	081	226	do.
		Channel 7—13th floor, southwest	171	151	do.
		Channel 8—4th floor, southwest	171	223	do.
		Channel 9—4th floor, southwest	081	105	do.
		Channel 10—4th floor, west core	081	84.1	do.
		Channel 11—4th floor, west core	171	99.8	do.
		Channel 12—4th floor, east core	171	90.6	do.
34	San Francisco	Basement	185	78.0	55, 56
	VA Hospital		Up	56.4	do.
	(VA)		095	220	do.
		7th floor	185	335	do.
			Up	73.0	do.
			095	220	do.
35	San Francisco	---	360	124	45
	Golden Gate Bridge		Up	57.5	do.
	abutment (USGS)		270	239	do.
36	Richmond Bulk Mail	---	057	11.1	55, 56
	2501 Rydin Road		Up	35.9	do.
	(USGS)		327	104	do.
37	Martinez	---	020	65.6	do.
	VA Hospital		Up	34.3	do.
	basement (VA)		290	39.8	do.
38	Larkspur	---	360	94.6	do.
	ferry terminal		Up	59.1	do.
	(USGS)		270	135	do.

Table 7.—*Stations in the U.S. Geological Survey's National Strong Motion Network whose earthquake records are contained in tapes disseminated by the National Geophysical Data Center*

[The first tape in each pair contains uncorrected data for the listed stations; the second tape contains corrected data and spectra. Tape USACA45 contains all the data for the listed stations. APEEL, Andreas Peninsula Earthquake Engineering Laboratory; CRA, Central Recording Accelerograph; SAGO, San Andreas Geophysical Observatory; SFSU, San Francisco State University; SLAC, Stanford Linear Accelerator Center; UCB, University of California, Berkeley; VA, Veterans' Administration]

Tape USACA45
Anderson Dam, crest
Anderson Dam, left abutment
Anderson Dam, downstream
Sunnyvale
Hollister Airport
Palo Alto, VA Hospital, basement
Palo Alto, VA Hospital, roof
Hollister City Hall
SLAC
Stanford parking garage
Menlo Park VA Hospital
Fremont
Redwood City, APEEL array sta. 2
San Francisco, 600 Montgomery, basement
San Francisco, 600 Montgomery, 29th floor
San Francisco, 600 Montgomery, 49th floor
Emeryville, free field
Golden Gate Bridge, abutment

Tapes USACA46, USACA47
Anderson Dam, crest
Anderson Dam, downstream
Anderson Dam, left abutment
Anderson Dam, CRA-1, channels 1, 2, 3
Anderson Dam, CRA-1, channels 4, 5, 6
Anderson Dam, CRA-1, channels 7, 8, 9
Anderson Dam, CRA-1, channels 10, 11, 12
San Francisco, 600 Montgomery Street, CRA-1, channels 1, 2, 3
San Francisco, 600 Montgomery Street, CRA-1, channels 4, 5, 6
San Francisco, 600 Montgomery Street, CRA-1, channels 7, 8, 9
San Francisco, 600 Montgomery Street, CRA-1, channels 10, 11, 12
Emeryville, free field
Emeryville, CRA-1 sta. 1, channels 1, 2, 3
Emeryville, CRA-1 sta. 1, channels 4, 5, 6
Emeryville, CRA-1 sta. 1, channels 7, 8, 9
Emeryville, CRA-1 sta. 1, channels 10, 11, 12
Emeryville, CRA-1 sta. 2, channels 1, 2, 3
Emeryville, CRA-1 sta. 2, channels 4, 5, 6
Emeryville, CRA-1 sta. 2, channels 7, 8, 9
Emeryville, CRA-1 sta. 2, channels 10, 11, 12

Tapes USACA53, USACA54
Berkeley, 2168 Shattuck Avenue, channels 1, 2, 3
Berkeley, 2168 Shattuck Avenue, channels 4, 5, 6
Berkeley, 2168 Shattuck Avenue, channels 7, 8, 9
Berkeley, 2168 Shattuck Avenue, channels 10, 11, 12
Berkeley, 2168 Shattuck Avenue, east basement
Berkeley, 2168 Shattuck Avenue, west basement
San Francisco, 575 Market Street (Chevron Bldg.), channels 1, 2, 3
San Francisco, 575 Market Street (Chevron Bldg.), channels 4, 5, 6
San Francisco, 575 Market Street (Chevron Bldg.), channels 7, 8, 9
San Francisco, 575 Market Street (Chevron Bldg.), channels 10, 11
San Francisco, 575 Market Street (Chevron Bldg.), basement
Hayward City Hall, CRA-1, channels 1, 2, 3
Hayward City Hall, CRA-1, channels 4, 5, 6
Hayward City Hall, CRA-1, channels 8, 9
Hayward City Hall, CRA-1, channels 10, 11, 12
Hayward City Hall, ground level
Hayward City Hall, north ground site
San Francisco, 50 Beale Street (Bechtel Bldg.), basement.
San Francisco, 50 Beale Street (Bechtel Bldg.), 12th floor
San Francisco, 50 Beale Street (Bechtel Bldg.), 24th floor

Tapes USACA55, USACA56
APEEL array sta. 9
Bear Valley sta. 5
Bear Valley sta. 7
Bear Valley sta. 10
Bear Valley sta. 12
Berkeley, UCB, Haviland Hall
Berkeley, UCB, Strawberry Canyon
Calaveras Reservoir
Cherry Flat Reservoir
Del Valle Dam, crest
Del Valle Dam, toe
Dublin fire station
Foster City
Hollister, SAGO vault
Larkspur ferry terminal
Livermore, VA Hospital, basement
Livermore, VA Hospital, roof (7th level)
Martinez, VA Hospital, basement
Richmond, Bulk Mail Center, ground level
San Francisco, fire station 17, 1295 Shafter Street, ground level
San Francisco, SFSU, Thornton Hall
San Francisco, VA Hospital, basement
San Francisco, VA Hospital, 7th floor
Sunol fire station

THE LOMA PRIETA, CALIFORNIA, EARTHQUAKE OF OCTOBER 17, 1989: STRONG GROUND MOTION AND GROUND FAILURE

STRONG GROUND MOTION

EFFECT OF KNOWN THREE-DIMENSIONAL CRUSTAL STRUCTURE ON THE STRONG GROUND MOTION AND ESTIMATED SLIP HISTORY OF THE EARTHQUAKE

By Vernon F. Cormier and Wei-Jou Su,
University of Connecticut

CONTENTS

ABSTRACT

We synthesize the strong ground motion of the earthquake, using a known three-dimensional crustal model of the Loma Prieta region, a rupture model determined by assuming a laterally homogeneous structure, and Green's functions computed by superposition of Gaussian beams. Except for the waveforms at several stations where ray caustics intersect the fault plane, the principal effects of three-dimensional crustal structure are amplitude variations induced by focusing and defocusing. In contrast to results obtained by assuming a laterally homogeneous crust, stations within 30 km of the hypocenter and 5 km of the fault trace are predicted to be strongly focused by a factor of as much as 10 or more, whereas stations at the northeast edge of the Santa Clara Valley are predicted to be weakly defocused by a factor of 0.5. The focusing is caused by a zone of low-velocity material lying between the Zayante and San Andreas faults, and the defocusing by a wedge of high-velocity material between the San Andreas and Sargent faults. The magnitude of amplitude variations due to known three-dimensional structure is similar to that incorporated into site effects due to variations in surface impedance and shallow structure beneath receivers. Because these amplitude variations are strongly path dependent, a range of probable rupture histories, as well as a detailed three-dimensional structure, must be incorporated to make predictions useful for an assessment of earthquake hazard. If lateral homogeneity is assumed, the net effect of the predicted focusing and defocusing is to bias estimates of the relative slip in two high-slip regions found in inversions of local and teleseismic body waves. To match the observed waveforms with the structural model of Eberhart-Phillips and others (1990), we modify the slip model of Beroza (1991) by reducing the magnitude of northwest maximum slip by a factor of 0.7 and increasing the magnitude of southeast maximum slip by a factor of 2.5. These modifications are in the range of variations in the estimated slip history reported by investigators using different data sets and inversion procedures.

INTRODUCTION

The three-dimensional structure of the Earth's crust, especially the strong velocity contrasts and structural variation within and near major fault zones, may account for at least part of the strong variation and complexity of ground motions observed near fault traces (Cormier and Spudich, 1984; Rial and others, 1986; Cormier and Beroza, 1987; Ben-Zion, 1989). Because strong-ground-motion instruments are most commonly deployed and triggered close to mapped fault traces, the effects on ground motion of the known three-dimensional crustal structure surrounding a fault trace can commonly be quantified. The result of such an effort is important both to estimating earthquake hazard and to estimating slip history from waveform inversions. Can the effects of three-dimensional structure be identified in strong-motion data? If so, are these effects sufficiently large and predictable to be included in an assessment of earthquake hazard? If a laterally heterogeneous structure is assumed, to what extent can the neglect of three-dimensional structure bias the inversion of slip history from waveform data? What are the sizes, consistency, and types of these biases? To answer these questions, we synthesize strong ground motions in a three-dimensional model of the crust in the Loma Prieta region (Eberhart-Phillips and others, 1990), using a detailed model of the slip history of the earthquake (Beroza, 1991), and compare synthetic seismograms obtained for the three-dimensional structure with those calculated for a laterally homogeneous structure.

METHOD OF FORWARD MODELING

By changing the variables of integration in the elastic-source representation for slip on a plane, Bernard and Madariaga (1984) and Spudich and Frazer (1984) developed a fast technique for synthesizing strong ground motion. At each station, the ground motion at any point in time is simply the integrated motion radiated along an isochron of the fault surface corresponding to that time. The isochron is constructed from the sum of rupture time and propagation time of a body wave arriving at that station. This algorithm assumes that the complete record of ground motion consists of only a few body waves, each represented by a far-field ray-theoretical Green's function. The far-field approximation and the neglect of surface waves are not a severe limitation on synthesizing ground motion in the frequency band 1–10 Hz at distances of 5 km to several tens of kilometers from a crustal source. In practice, the neglect of surface waves generally can be extended to greater distances, owing to the strong scattering of high-frequency surface waves by topography and near-surface heterogeneity.

This algorithm was first applied in a laterally homogeneous structure and later extended with dynamic ray tracing (Cormier and Beroza, 1987) and superposition of Gaussian beams (Červený and others, 1987) to include the effects of three-dimensional crustal structure. Subsequently, Hu and McMechan (1988) applied the finite-difference method to model the elastic wavefield radiated by a spatially extended source in a laterally varying structure. Unlike the asymptotic ray and beam approaches, the finite-difference approach can be constructed to remain accurate for arbitrarily large ratios of wavelength to medium-scale length, where medium-scale length is measured by the ratio of velocity (or density) to the magnitude of the spatial gradient of velocity (or density gradient). The accuracy of asymptotic ray and beam approaches deteriorates, however, when these nondimensional ratios exceed several tenths (for example, Beydoun and Ben-Menahem, 1985). The numerical expense of the finite-difference technique has thus far limited its use to two-dimensional problems. The relatively cheap computational cost of asymptotic-ray theory, in contrast, makes three-dimensional problems tractable. The generalization of asymptotic-ray theory to the Gaussian-beam approach ensures regularity of the results in the vicinity of ray caustics. The steps in developing the Gaussian beam approach are initially similar to those used by Spudich and Frazer (1984). Both the ray and beam approaches start by considering the representation of far field displacement due to distributed slip on a plane; this representation integrates over the fault plane an integrand that includes the Green's function of a far-field body wave and a function specifying the slip history. The beam approach substitutes a superposition of Gaussian beams for the Green's function. A detailed derivation and the choice of free parameters in the beam method were given by Červený and others (1987). The results presented in the following sections were calculated by the narrow Gaussian beam approach described by Červený and others (1987).

MODEL INPUT

THREE-DIMENSIONAL STRUCTURE

Variation in the structure of the fault zones of the San Andreas fault system generally coincides with a variation in the style of slip among member fault segments within the system. Michael and Eberhart-Phillips (1991) found that cross sections of velocity perpendicular to the fault trace are generally simpler in form across creeping sections of the fault, with a single lateral discontinuity. A comparison of the San Andreas, Sargent, and Calaveras fault zones with the seismicity associated with each of these faults suggests that the absence of well-developed fault zones correlates with fault segments which remain locked over long periods of time (Mooney and Colburn, 1985; Mooney and Ginzburg, 1986). The crustal structure in the Loma Prieta region is consistent with this hypothesis. Three-dimensional inversions for velocity in the vicinity of the earthquake constrain any low-velocity zone surrounding the surface trace of the San Andreas to be less than 2 km wide. Surficial geology is consistent with a fault zone less than 1 km wide (McLaughlin and others, 1989). A well-developed low-velocity fault zone does not begin until the southeast termination of the Loma Prieta rupture zone (Thurber, 1983). Lying in the upper 4 km of the crust above the rupture zone, in the depth range within which well-developed low-velocity zones are observed elsewhere along the San Andreas fault, is a system of imbricate thrust faults, approximately 10 km wide, that includes both the surface trace of the San Andreas fault, the Sargent fault (fig. 1), and at least two other mapped faults (Seeber and Armbruster, 1990).

Not surprisingly, then, the most significant three-dimensional features resolved in high-resolution studies of the Loma Prieta region are associated not with zones of fault gouge but with the lithologic contrasts across fault planes. These features consist of a high-velocity wedge between the San Andreas and Sargent faults, a low-velocity zone between the San Andreas and Zayante faults, and a low-velocity zone coincident with the Santa Clara Valley east of the Sargent fault (Mooney and Colburn, 1985; Eberhart-Phillips and others, 1990; Lees, 1990). These features are all present in the *P*-wave-velocity model (fig. 2) of Eberhart-Phillips and others (1990).

The ray and Gaussian-beam calculations described below are performed in this model by using splines under tension to return continuous first and second spatial derivatives of velocity (Cline, 1981; Cormier, 1987). *S*-wave velocities are derived from *P*-wave velocities by assuming that $V_P/V_S=2$, consistent with average velocities measured in the upper crust along the San Andreas fault system (D.M. Eberhart-Phillips, oral commun., 1992). The amplitudes of synthetic waveforms are weak functions of the density model because density affects ray theoretical Green's functions only through factors containing the square root of density at ray end points. A constant density of 2.7×10^3 kg/m^3 is assumed, consistent with estimates for basement rocks surrounding the fault plane from stratigraphy and gravity studies (Clark and Rietman, 1973; Eberhart-Phillips and others, 1990).

Because our model is assumed to be continuous, reflected or converted body waves are omitted, as well as site effects due to reverberations in fine-layered structure near receivers. Although the maximum distance range of modeling is generally less than that in which *PmP* and *SmS* phases become important arrivals, near the distance at which these phases are critically reflected they are approximately represented as turning rays in a high-gradient region defining the transition to sub-Moho velocities.

SLIP HISTORY

Several inversions for the slip history of the earthquake using waveform data have been published (Beroza, 1991; Hartzell and others, 1991; Steidl and others, 1991; Wald

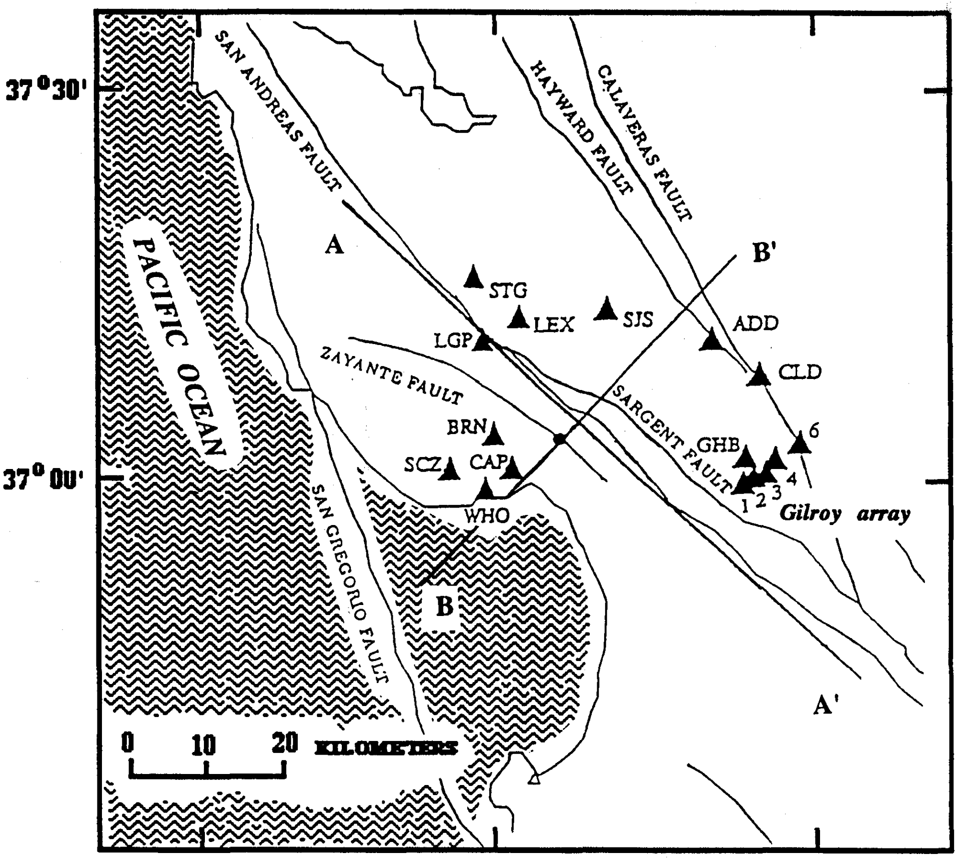

Figure 1.—Loma Prieta region, Calif., showing locations of strong-ground-motion stations (triangles) and major faults. *A–A'*, cross section along strike of the San Andreas fault; *B–B'*, cross section passing through hypocenter of 1989 Loma Prieta earthquake (dot) and intersecting the Zayante, San Andreas, and Sargent faults (see fig. 2).

and others, 1991). Although the distributions of slip orientation differ slightly and absolute slip magnitudes in similar regions of the fault plane differ by a factor of as much as 2, the principal features of the different slip models are remarkably similar. Each model consists of a bimodal distribution of high slip in a region northwest of the hypocenter with a high dip-slip component, and in a region southeast of the hypocenter with a primarily strike-slip component (fig. 3). The hypocentral or nucleation region is relatively deficient in slip. (Henceforth, the slip maximums in fig. 3 are referred to as the northwest and southeast slip maximums.) The authors of each source model noted that the differences between the models are attributable to different choices of data and (or) of the objective function to be minimized by the inversion procedure. The calculations described below use the slip model of Beroza (1991), summarized in figure 3, which was chosen because the ray-theoretical forward modeling used in its construction allowed a test of the Gaussian-beam method in the one-dimensional structural model of Beroza. Beam parameters and the angular increments of rays were chosen to reproduce the ray-theoretical synthetic seismograms obtained by Beroza in a one-dimensional structure. These beam and ray parameters were then used in the synthesis of ground motion in the three-dimensional structure of Eberhart-Phillips and others (1990), henceforth referred to as the EP model.

RESULTS

Figures 4 and 5, which compare theoretical with recorded data at the strong-ground-motion stations shown in figure 1 and listed in table 1, show the recorded trace at each station (top curve), followed by three synthetic seismograms, SYN1 through SYN3 (lower three curves), calculated by superposing narrow Gaussian beams for different models of the crustal structure and (or) slip history. The recorded and synthetic data are displacements bandpassed by a two-pole, zero-phase Butterworth filter with corner frequencies at 0.3 and 2 Hz. The horizontal

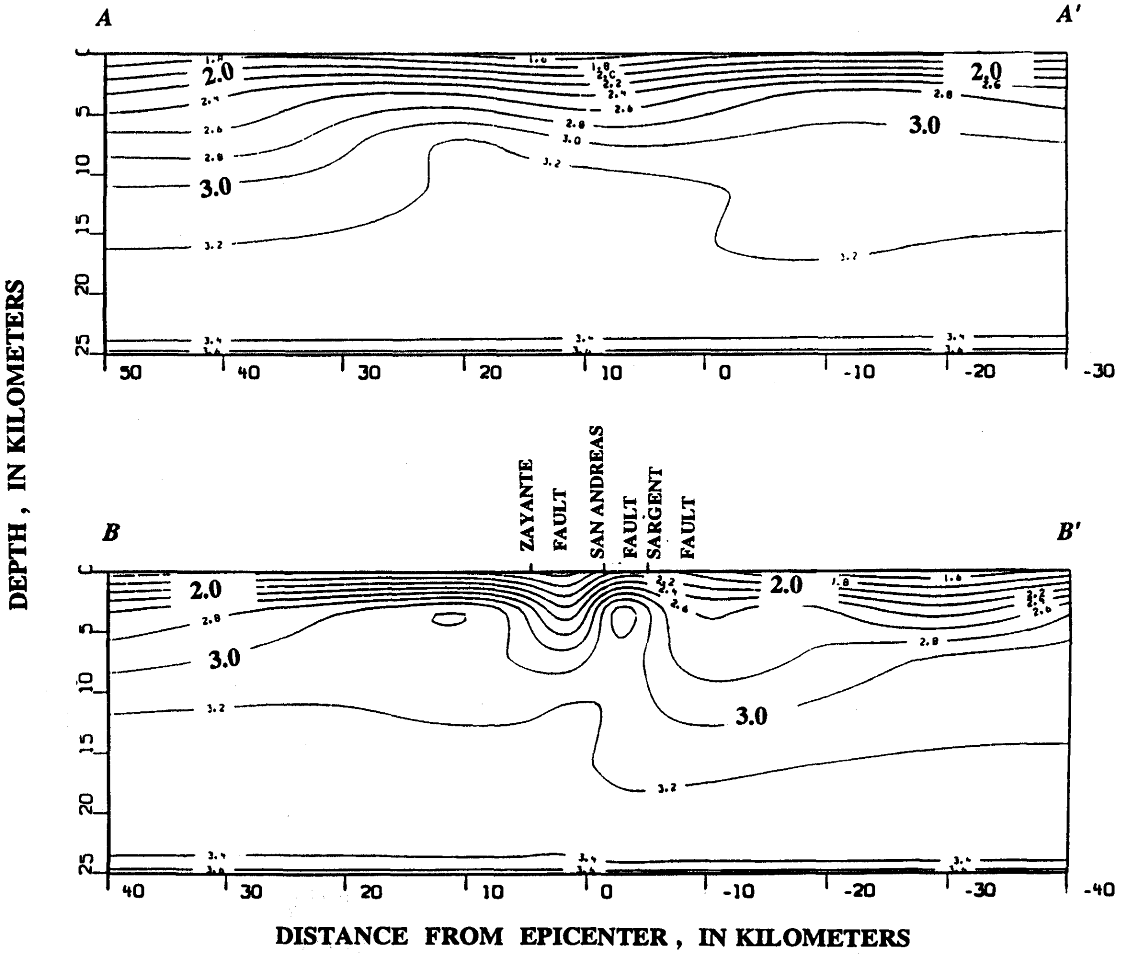

Figure 2.—*P*-wave-velocity contours (in kilometers per second) through cross sections *A–A'* and *B–B'* (fig. 1), as determined by Eberhart-Phillips and others (1990).

components of motion are rotated into a coordinate system with the x-axis parallel to the strike of the fault plane (130°), the z-axis pointing downward, and the y-axis forming a right-handed system (220°).

SYN1 seismograms were synthesized by using the one-dimensional (velocity a function of depth only) crustal structure and slip history determined by Beroza (1991) by minimizing an L_2 norm of the difference between the observed and synthetic waveforms. The seismograms shown by Beroza were synthesized by using ray-theoretical Green's functions with the algorithm described by Spudich and Frazer (1984), whereas the SYN1 seismograms in figure 4 were synthesized by the narrow-Gaussian-beam method described by Červený and others (1987). The SYN1 seismograms are indistinguishable from those synthesized by Beroza (1991), thus validating the Gaussian-beam superposition and our choice of parameters for beam width and ray increments.

SYN2 seismograms were synthesized for the three-dimensional EP structural model by using the slip model of Beroza (1991). SYN3 seismograms were also synthesized for the three-dimensional EP structural model, but the rupture model of Beroza was modified to obtain a better match to the peak amplitudes at stations close to the fault trace: LGP, LEX, STG, and the Gilroy array, G1 through G6 (fig. 1).

Both the amplitude and phase of the waveforms at stations close to Santa Cruz (stas. BRN, CAP, SCZ, WHO, fig. 1) are relatively insensitive to choice of either the one- or three-dimensional velocity model. The long duration and complexity of strong ground motion at these stations cannot be successfully modeled without invoking smaller-scale structures that induce scattering close to these stations.

The phases of the waveforms at stations LGP, LEX, and STG (fig. 1), which are all less than 5 km from the

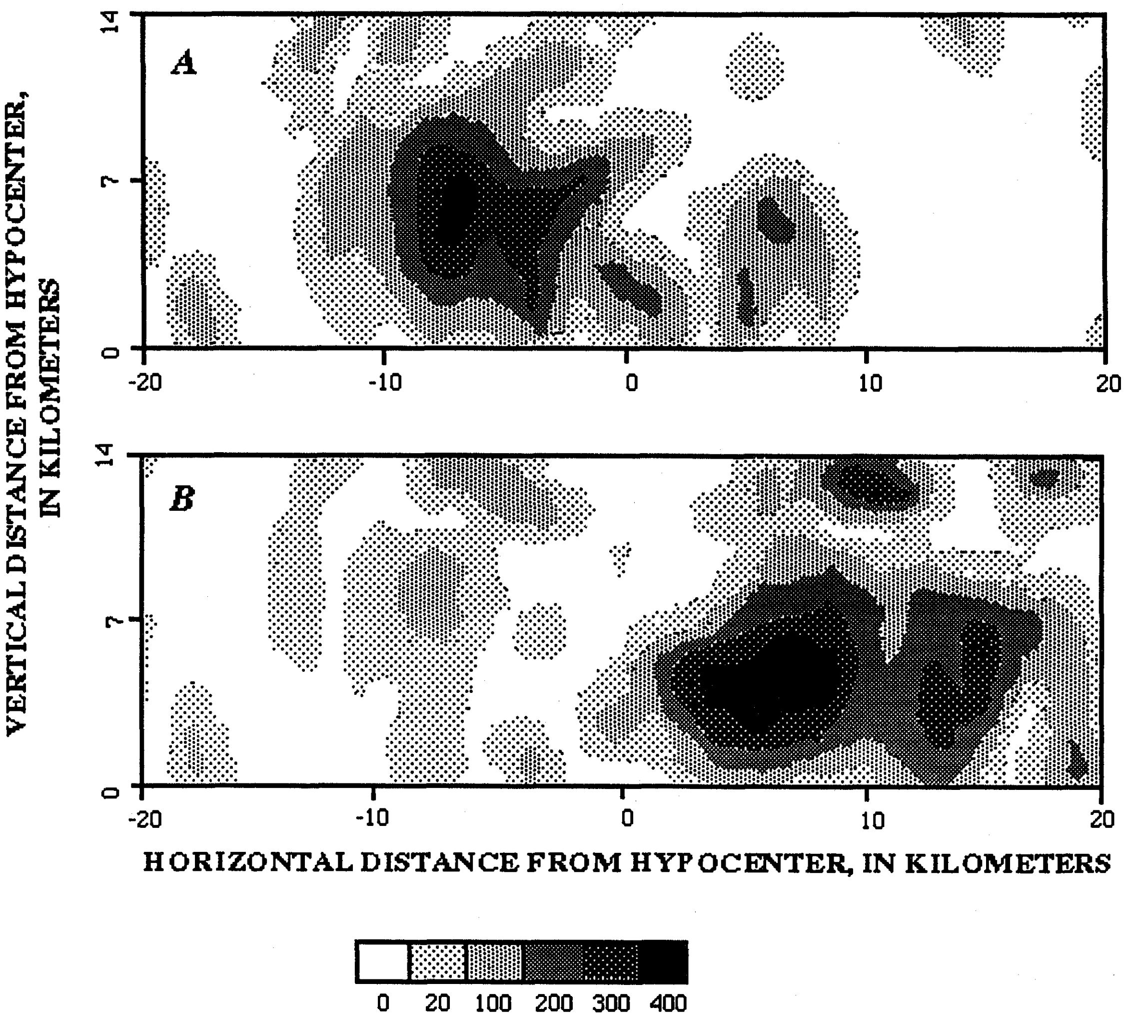

Figure 3.—Slip model of 1989 Loma Prieta earthquake, as determined by Beroza (1991), showing areas of dip-slip (*A*) and strike-slip (*B*) amplitude along fault plane. Shading denotes amount of slip (in centimeters) in different areas of fault plane. Depth to top of each plot is 4.8 km, above which slip is assumed to be zero.

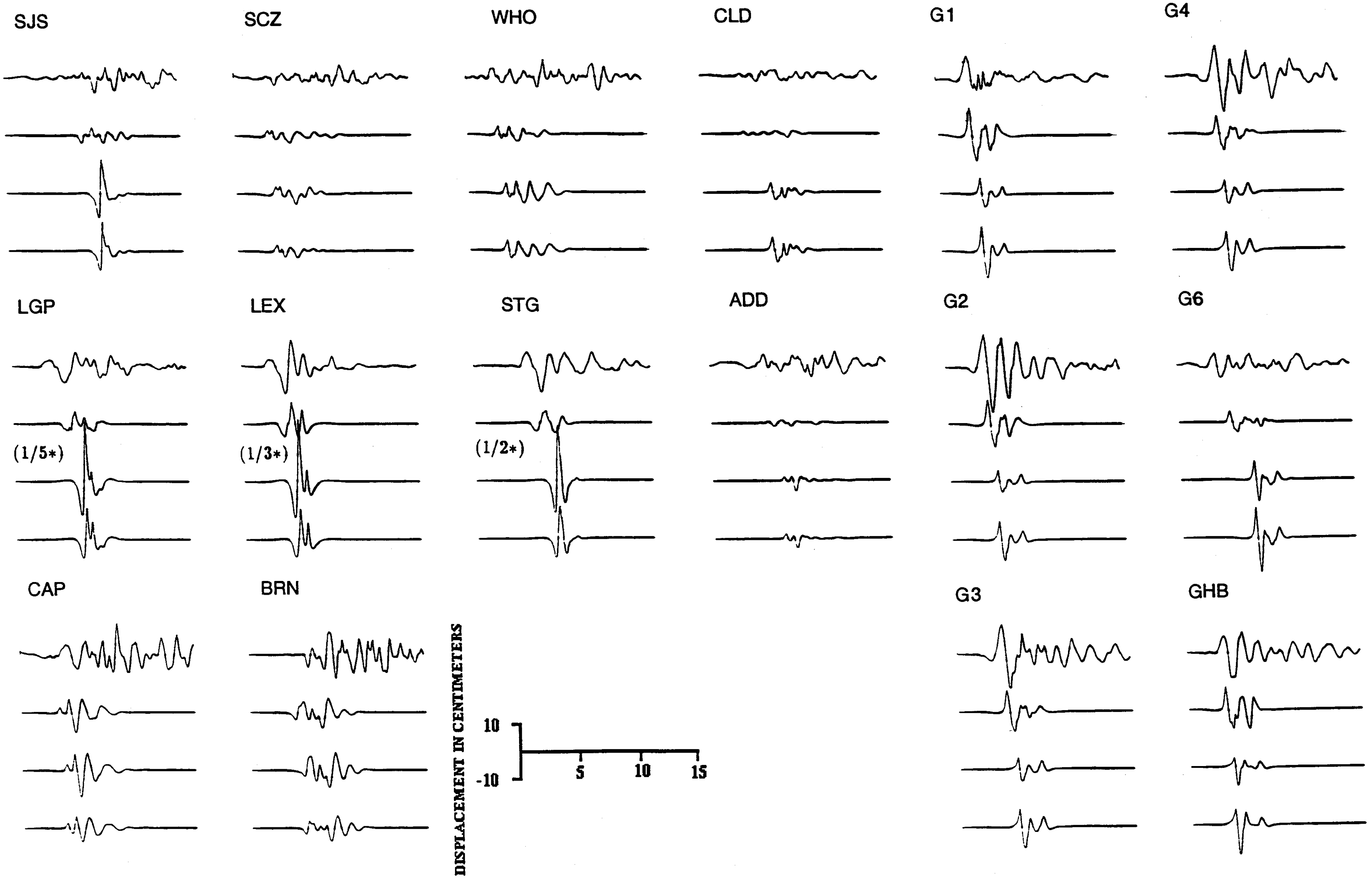

Figure 4.—Observed (top curve) and synthetic (SYN1–SYN3, lower three curves) seismograms for 220° component of ground motion (perpendicular to fault trace) at strong-ground motion stations shown in figure 1. All waveforms are filtered according to procedure of Beroza (1991); synthetic seismograms are computed by using narrow-Gaussian-beam method. SYN1 seismograms are computed by using slip model of Beroza (1991) in one-dimensional crustal model, SYN2 seismograms by using slip model of Beroza (1991) in three-dimensional crustal model of Eberhart-Phillips and others (1990), and SYN3 seismograms by using modified slip model in three-dimensional crustal model of Eberhart-Phillips and others (1990).

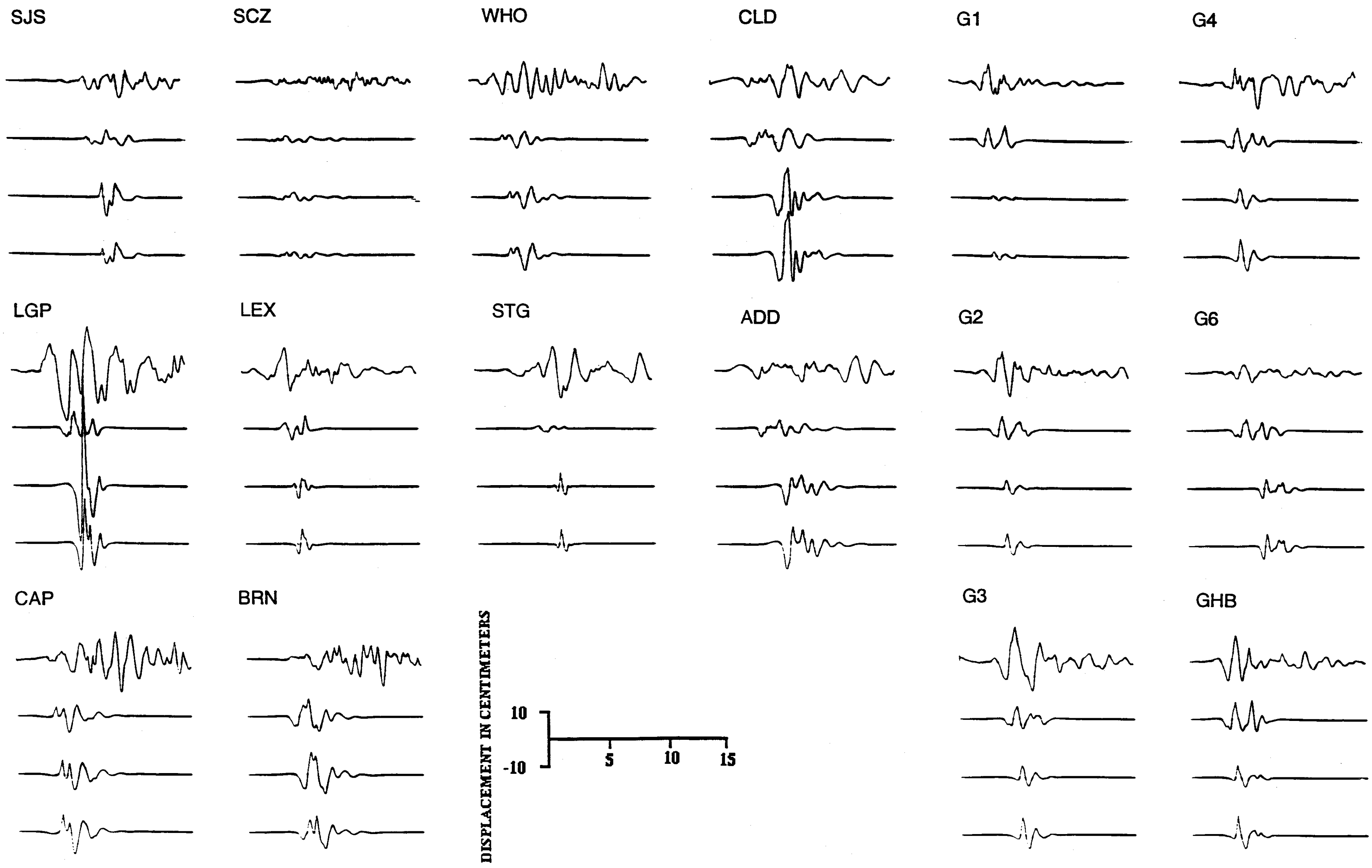

Figure 5.—Observed (top curve) and synthetic (SYN1–SYN3, lower three curves) displacements for 130° component of ground motion (parallel to fault trace) at strong-ground-motion stations shown in figure 1. All waveforms are filtered according to procedure of Beroza (1991); synthetic seismograms are computed by using narrow-Gaussian-beam method. SYN1 seismograms are computed by using slip model of Beroza (1991) in one-dimensional crustal model, SYN2 seismograms by using slip model of Beroza (1991) in three-dimensional crustal model of Eberhart-Phillips and others (1990), and SYN3 seismograms by using modified slip model in three-dimensional crustal model of Eberhart-Phillips and others (1990).

Table 1.—*Locations of strong-ground-motion stations*

[Owners: CDMG, California Division of Mines and Geology; UCSC, University of California, Santa Cruz; USGS, U.S. Geological Survey]

Station		Owner	Location	
Code	No.		Lat °N.	Long °W.
G1	47379	CDMG	121.572	36.973
G2	47380	CDMG	121.556	36.982
G3	47381	CDMG	121.536	36.987
G4	57382	CDMG	121.552	37.005
G6	57383	CDMG	121.484	37.026
GHB	47006	CDMG	121.883	37.037
CLD	47381	CDMG	121.550	37.118
ADD	1652A	USGS	121.628	37.166
SJS	57563	CDMG	121.785	37.167
LGP	---	UCSC	122.010	37.172
CAP	47125	CDMG	121.952	36.974
SCZ	58135	CDMG	121.060	37.011
LEX	57180	CDMG	121.949	37.202
BRN	---	UCSC	121.985	37.047
WHO	---	UCSC	121.995	36.973
STG	58065	CDMG	121.756	36.909

surface trace of the fault, are not strongly affected by the choice of either the one- or three-dimensional model. The body waves observed at these stations, however, are fundamentally higher in amplitude in the three-dimensional than in the one-dimensional model. These stations lie to the northwest of the hypocenter and so are more sensitive to the slip maximum northwest of the hypocenter. Thus, using the three-dimensional model, a reasonable match to the observed amplitudes at these stations can be achieved by reducing the amplitude of the northwest slip maximum in figure 3; a factor of 0.7 in slip amplitude was found to be optimal.

The body waves observed at the Gilroy array (stas. G1–G5, GHB, fig. 1), however, are fundamentally lower in amplitude in the three-dimensional than in the one-dimensional model. Because the Gilroy array is more sensitive to slip southeast of the hypocenter, observed amplitudes in the three-dimensional model can be matched by increasing the amplitude of the southeast slip maximum shown in figure 3; a factor of 2.5 was found to be optimal. An improvement in the match to the amplitude at station G6, however, cannot be made in this way because, unlike for the rest of the Gilroy array, the three-dimensional model focuses rather than defocuses body waves reaching this station from southeast region of the rupture zone (compare SYN1 and SYN2 seismograms at stas. G1–G6, fig. 4). We note that exceptional site effects have already been documented at station G06 from recordings of the April 24, 1984, Morgan Hill, Calif., earthquake and its aftershocks along the Hayward-Calaveras fault. Station G6 is centered within a well-developed low-velocity fault zone (Cormier and Spudich, 1984; Cormier and Beroza, 1987), more than 2 km wide near the surface. Cormier and Beroza suggested that focusing and multipathing within this fault zone account for the higher relative amplitudes at station G6 recorded for the 1984 Morgan Hill earthquake. The lower amplitudes recorded at station G6 relative to stations G1 through G5 and G7 for the 1989 Loma Prieta earthquake may somehow be related to the presence of the fault zone below station G6, where the different source-receiver geometry causes defocusing rather than focusing. For the 1984 Morgan Hill earthquake, both the rupture zone and station G6 lie within a fault-zone waveguide, whereas for the 1989 Loma Prieta earthquake, only station G6 lies within the fault-zone waveguide. The different behaviors at station G6 for these two earthquakes is consistent with a deeper propagation effect dependent on source-receiver geometry, rather than a site effect that can be modeled by a plane-layered structure. This propagation effect cannot be described exactly by the EP model because this model has insufficient resolution in the region of the Hayward-Calaveras fault to resolve structures with horizontal scale lengths of 2 km or less.

The effects of three-dimensional crustal structure on the strong ground motions produced by a distributed source can be illustrated in various ways. Thus far, we have compared only individual waveforms, whereby it is difficult to identify the particular three-dimensional structures inducing amplitude changes and to separate those changes from the effects of the radiation pattern. In addition, the sparse spatial sampling of the wavefield generally makes it difficult to discern the major amplitude trends induced by the three-dimensional structure. The sampling of Loma Prieta data, however, is sufficient to predict two significant effects of known three-dimensional structure: (1) focusing at stations close to the hypocenter and the surface trace of the San Andreas fault and (2) defocusing at stations northeast of the rupture zone in the vicinity of the Gilroy array (fig. 1). The geologic origin of these effects is not apparent without further analysis of the intermediate calculations used in synthesizing waveforms.

Spudich and Oppenheimer (1986) described an interpretational aid in which traction is contoured over the fault plane as a function of time. This approach is helpful for understanding the relative contribution of fault slip versus three-dimensional structure to the amplitudes observed at particular stations. However, because isochrons are neither sorted nor specifically identified in the modeling algorithm (Červený and others, 1987) used here, it is difficult to implement this interpretational aid in our analysis of the Loma Prieta data. Instead, we studied the geologic origin of amplitude variations by comparing the density of ray end points on the fault plane in the one- and three-dimensional models by plotting rays over contoured cross sections of the velocity structure. End-point density is closely related to geometric spreading; the precise relation is defined in reports describing the numerical calculation of geometric spreading (for example, Červený and others, 1977; Gajewski and Pšenčík, 1987). For a sequence of rays with constant increments in vertical and azimuthal takeoff angles, the square of the geometric spreading is proportional to the ratio of the product of any two distances between the end points of three neighboring rays, $\Delta X_1 \Delta X_2$, and the product of their azimuthal and vertical angular increments, $\Delta\gamma_1\Delta\gamma_2$. Plots of ray end points are also helpful in identifying regions of multipathing and in locating caustics. We describe a case study using plots of ray end points as an interpretational aid to locate structural effects for station CLD (fig. 1).

Station CLD is one of the few stations to exhibit large differences in both phase and amplitude between the seismograms in figure 5 calculated in the one- and three-dimensional models, neither of which in combination with the two different slip models provides an adequate

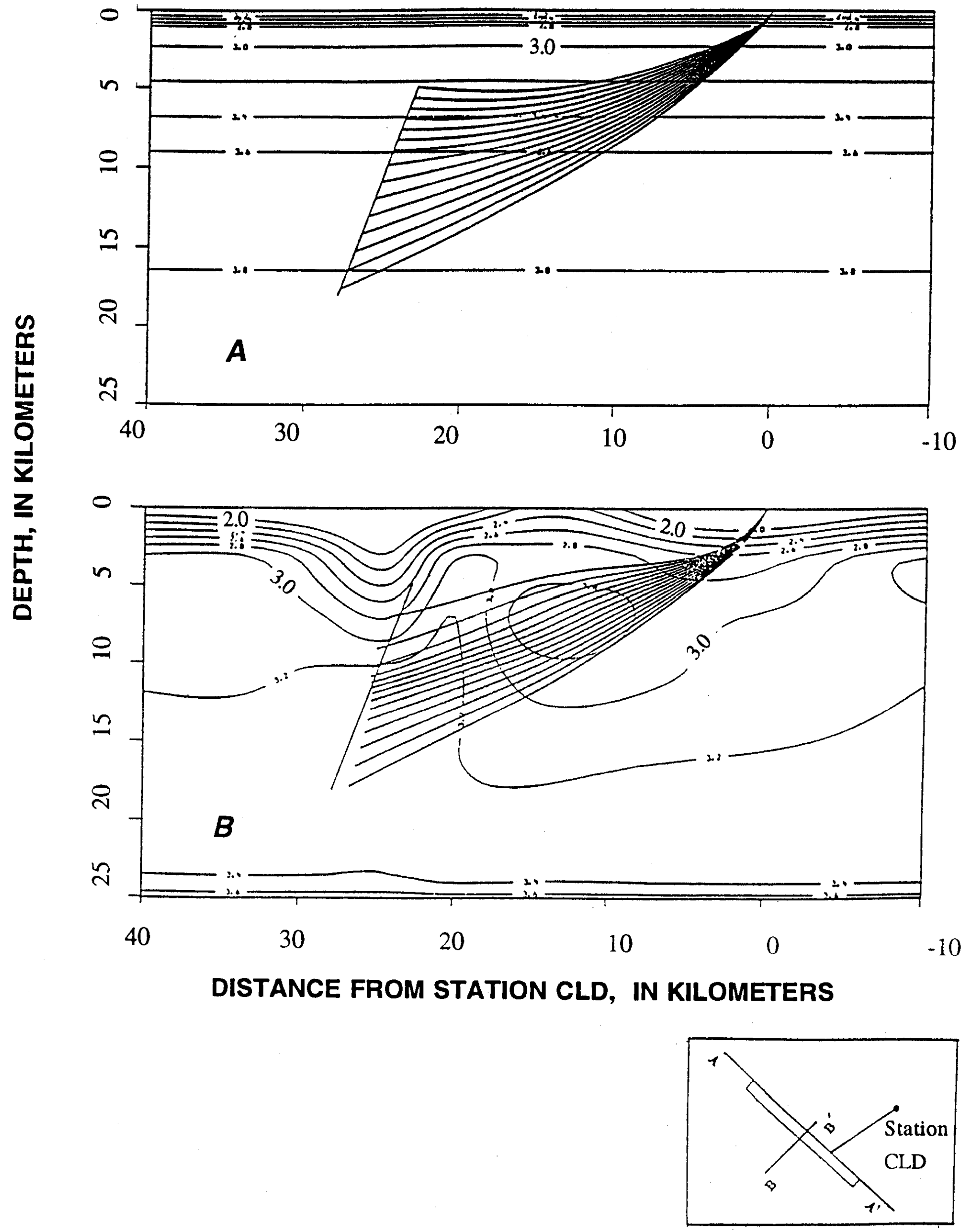

Figure 6.—Ray trajectories (contours of velocity in kilometers per second) projected onto cross-sectional plane defined by vertical and azimuth of station CLD (fig. 1) to center of southeast slip maximum for slip model shown in figure 3. *A*, One-dimensional model. *B*, Three-dimensional model. Inset shows surface trace of cross section relative to cross sections *A–A′* and *B–B′* (see fig. 1 for locations).

fit to the observed seismogram. The waveform may be better fitted with the EP model in combination with a slip model obtained by an iterative inversion that minimizes a misfit function. More subjectively, it may be argued that the results obtained in the three-dimensional model (SYN2 and SYN3 seismograms) better predict a broad negative excursion within the first 2 s.

The waveform at station CLD is primarily sensitive to the southeast slip maximum shown in figure 3. The structural cross sections shown in figure 6 are in a plane defined by station CLD and its local vertical, and by the centroid of the southeast slip maximum. In the one-dimensional model, rays that are initially shot along the azimuth defined by the intersection of the cross section and the surface remain in the plane of the cross section. Because rays wander out of this plane in the three-dimensional model, they do not appear to stop at the fault plane when projected onto the cross section. In the cross section through the EP model shown in figure 6, we can see a low-velocity basin to the west (left) of the fault, a high-velocity wedge to the east (right) of the fault, and a broader, low-velocity basin to the west of this high-velocity wedge. In cross section *B–B′* in figure 2, these structures can be identified as a basin bounded by the Zayante and San Andreas faults, a high-velocity wedge bounded by the San Andreas and Sargent faults, and the Santa Clara Valley. Rays traveling from the high-slip patch to station CLD are first defocused by the high-velocity wedge and then refocused by the low-velocity basin beneath the Santa Clara Valley. At station CLD, the focusing by the Santa Clara Valley is much stronger than the defocusing by the high-velocity wedge. In ray cross sections to the Gilroy array, however, the defocusing by the high-velocity wedge between the San Andreas and Sargent faults dominates the defocusing by the Santa Clara Valley.

At station CLD, the three-dimensional crustal structure generates multipathing and caustics, which are visible in the plot of end points of rays shot from station CLD to the fault plane shown in figure 7. The multipathing and caustics at station CLD account for the large differences seen in the synthetic seismogram for station CLD (fig. 5) computed in the one-dimensional structure versus the three-dimensional model. It is difficult to determine whether the multipathing and caustics predicted at station CLD are actually present in the data because the complexity of the slip model can be traded off with the waveform complexity induced by structure. There probably is not much tradeoff available, however, without degrading the fit to waveforms at other stations. For a smaller and simpler source, such as a small aftershock or foreshock located near the center of the high-slip patch, it would be determinable whether the predicted multipathing and caustics are realistic.

Station CLD is exceptionally situated in this structure. At most of the strong-ground-motion stations, the three-dimensional structure of the EP model does not induce multipathing or caustics in the direct body-wave arrivals. Instead, the principal effects are focusing and defocusing by a factor of as much as 2 or 3, which do not strongly affect the phase of waveforms radiated by a distributed source on the fault plane. In an inversion for slip history, we can expect that this focusing and defocusing will trade off with slip amplitude if an inappropriate one-dimensional crustal model is assumed, and errors by a factor of as much as 2 to 3 would occur in the predicted slip amplitude. Small errors will also occur in the location of zones of high slip, owing to ray bending in the three-dimensional structure. Tests with the one- and three-dimensional models reported here indicate that these errors are bounded by 2 km.

The waveform data plotted in figure 5 were all recorded less than 50 km from the hypocenter. Because destructive ground shaking occurred in the San Francisco Bay region at much greater distances from the Loma Prieta hypocenter, it would be of some interest to determine whether any known three-dimensional structures in the vicinity of the hypocenter affected strong-ground-motion amplitudes at these greater distances. The synthetic-modeling technique used for the one- and three-dimensional models, however, is restricted in validity to body-wave arrivals, and so it cannot include the effects of surface

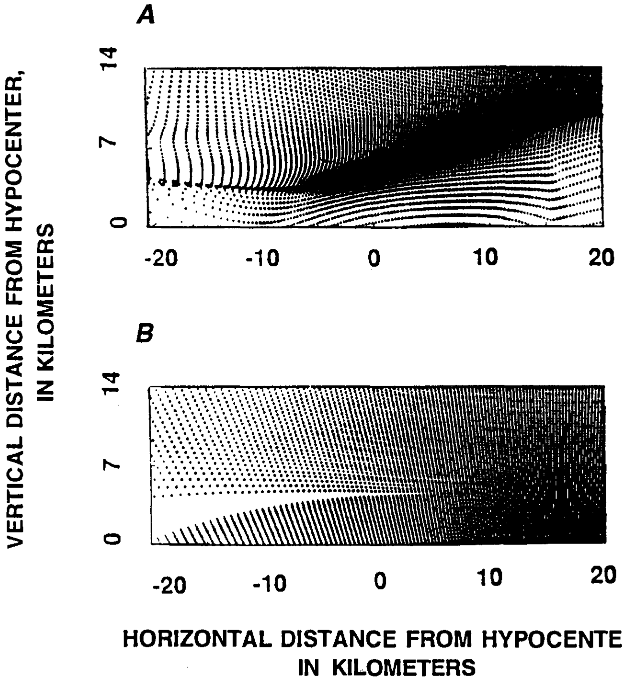

Figure 7.—End points on fault plane of *S*-wave rays shot from stations CLD (fig. 1) in one-dimensional (*A*) and three-dimensional (*B*) models. Increments of vertical and azimuthal takeoff are identical at station site. Dense areas of end points indicate regions of slip on fault plane that will contribute to motion at that station. Note that focusing zone in three-dimensional model in figure 7*B* emphasizes part of southeast slip maximum shown in figure 3.

waves that begin to be important arrivals at these greater distances, although plots of ray end points can be used to make some qualitative predictions for the body-wave arrivals. A longer range plot of ray end points at the surface (map view) from a source at the Loma Prieta hypocenter is shown in figure 8, where the hypocenter is used as the origin of the coordinate system and the starting point of the ray tracing. The *y*-axis coincides with cross section *A–A′* in figure 1. (The end points of rays traced from either the northwest or southeast slip maximums are largely similar.) The effect of three-dimensional structure in figure 8 is apparent in those regions that depart from the concentric rings predicted by a one-dimensional structure. The most striking feature is a defocusing zone on the northeast side of the fault trace, paralleling the fault trace at distances greater than 30 km. The location of this defocusing zone is bounded by the strike of the surface trace of the San Andreas fault in the rupture zone (*y*=0, fig. 8) and the strike of cross section *C–C′* in figure 8, which is approximately defined by the central axis of the San Francisco Bay trough. At lesser distances, this defocusing zone evolves into a nar-

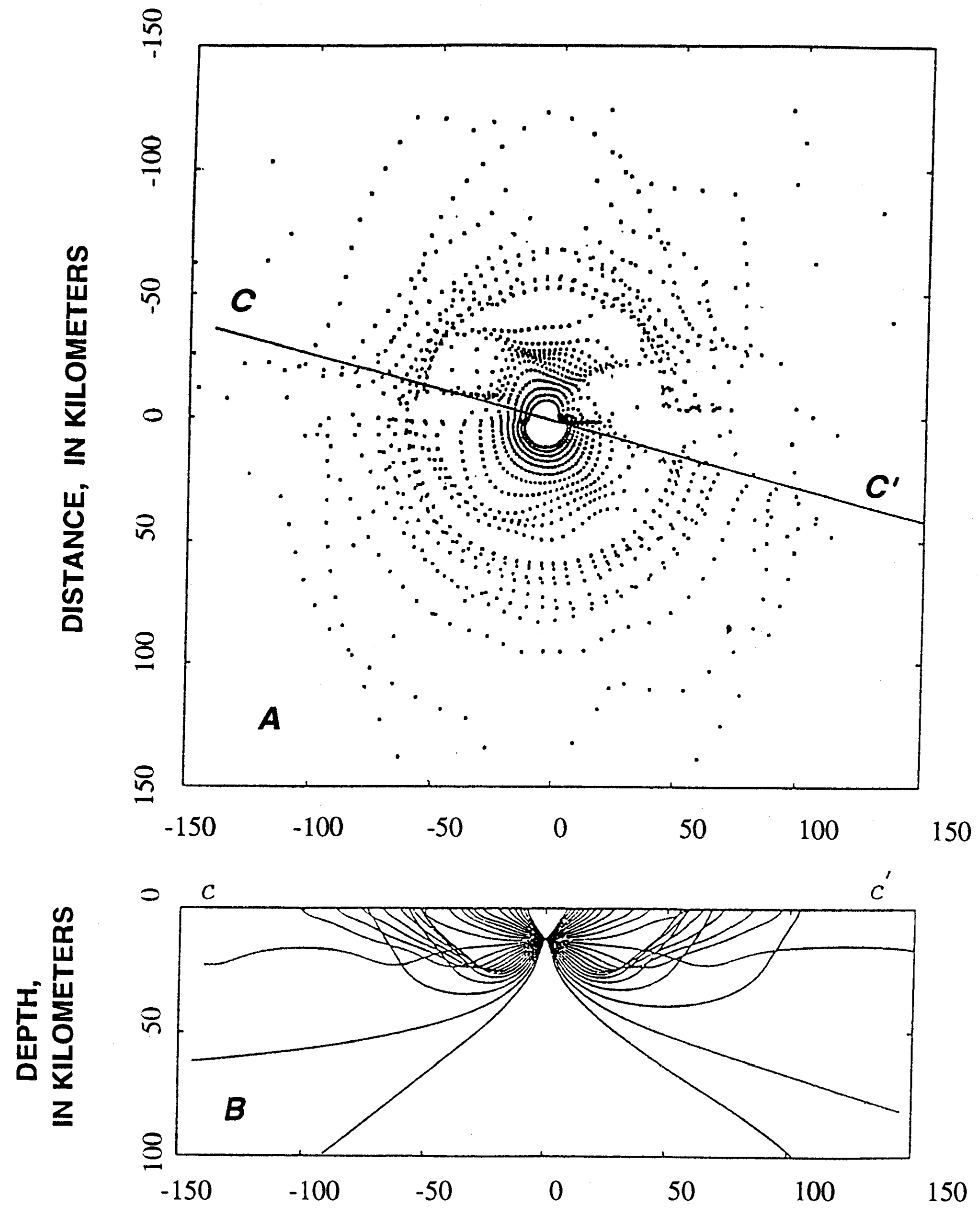

Figure 8.—Map view of end points (*A*) and cross section of trajectories (*B*) of rays shot from a point source located at hypocenter of Loma Prieta earthquake. (Patterns for point sources located within southeast or northwest slip maximum are similar in form.) *y*-axis coincides with surface trace of the San Andreas fault in rupture zone. Cross section *C–C′* is oriented along azimuth defined by epicenter of earthquake and center of San Francisco Bay trough.

rower focusing zone along the fault trace, consistent with the results discussed for stations LGP, LEX, and STG (fig. 1). The focusing at nearby stations is induced by the low-velocity zone bounded by the San Andreas and Zayante faults. At greater distances, the high-velocity wedge between the San Andreas and Sargent faults produces the broader defocusing zone paralleling and to the northeast of the surface trace of the San Andreas fault. Longer range data do not convincingly support the existence of such a defocusing zone and are likely dominated by the effects of structure local to each site. The relevant data would be from the soil sites in the west south bay described by Borcherdt and Glassmoyer (1992).

The importance of the *SmS* and *PmP* phase transitions to critical incidence, well documented by Sommerville and others (this chapter), is again evident in both the end-point plot and ray trace in cross section *C–C′* in figure 8. This is the region of high ray concentration occurring at distances of about 50 to 60 km from the hypocenter. Only the onset of the region of high amplitudes is predicted here, because the end-point plot cannot show the effect of postcritical incidence in a model in which the Moho is specified by a high-gradient zone rather than by a discontinuity. This increase in amplitude at distances greater than 50 km is principally governed by the depth to the Moho, which is taken to be constant in the EP model.

DISCUSSION

THREE-DIMENSIONAL STRUCTURE AND THE RESOLUTION OF SLIP HISTORY

The effects on slip-history inversion due to the neglect of three-dimensional structure depend on both the frequency band of inversion and the scale and intensity of true three-dimensional variations. It is widely recognized in applications of high-frequency seismology that an important change in either the statistics or spatial distribution of small-scale heterogeneities in the Earth's crust and upper mantle occurs somewhere near a frequency of 1 to 2 Hz. Below this band, inversions are successful for deterministic descriptions of source properties and structure, whereas above this band, such inversions are generally unsuccessful unless the path lengths of the data are much less 1 km. Numerous examples of this change in the behavior of seismic-wave scattering can be cited. For example, phase and amplitude fluctuations of teleseismic body waves at large-aperture arrays suggest the existence of a thin (1–2 km thick) layer in the upper crust that can account for high-angle scattering of 1-Hz body waves (Thomson, 1983). McLaughlin and others (1987) showed that strong stochastic dispersion of teleseismic body waves begins around 1 Hz, contributing to complex high-frequency codas. Bonamassa and Vidale (1991) reported that deterministic predictions of shear-wave polarization of the Loma Prieta strong ground motion deteriorate near 1 to 2 Hz. For these reasons, inversions of strong-ground-motion data for deterministic descriptions of slip history first low-pass-filter the data, removing the frequencies above 2 Hz. The one-dimensional structures used in subsequent waveform modeling may be viewed as approximate long-wavelength-equivalent models of the true structure.

One-dimensional structures consisting of three to four layers can provide an adequate description of the long-wavelength-equivalent structure, provided that the region of interest has no strong lateral heterogeneity with scale lengths between 1 to 10 km. We also note that this long-wavelength-equivalent structure generally will be anisotropic whenever preferential alignments of isotropic or anisotropic heterogeneities or cracks exist (Hudson, 1980, 1981; Crampin, 1984). Because strong-ground-motion data are commonly collected in regions with fault zones separating laterally differing structures that are associated with tectonically controlled basins and ridges, important scale lengths of heterogeneity in the range 1–10 km are the rule rather than the exception. Because 1- to 10-km spatial resolution is commonly achieved in regional tomographic studies of foreshock and aftershock data, in some regions the effects of at least isotropic heterogeneity at scale lengths equal to or larger than 1 km can be included. The results of our study suggest that neglect of the effects of lateral heterogeneity at these scale lengths may bias absolute-slip estimates by a factor of as much as 2.5 and locations of high-slip zones by as much as 2 km. From the viewpoint of spatially resolving high-slip zones separated by distances greater than 1 to 2 km, however, the most important features of the Loma Prieta slip history are not biased by the structural model: the two high-slip zones bordering a nucleation region with relatively small slip, and the different orientation of slip in each high-slip zone.

THREE-DIMENSIONAL STRUCTURE AND HAZARDS ASSESSMENT

In our study, the amplitude variations induced by the three-dimensional crustal structure of the Loma Prieta region are generally much larger than the factors by which the one-dimensional slip model was readjusted to fit the data, because the peak amplitudes at individual stations are not simply related to slip history along the fault plane. An example of this behavior is the difference between the SYN1 and SYN2 seismograms for stations

LGP, LEX, and STG in figure 5. With the slip model held constant, the SYN2 waveforms in the three-dimensional structure are 6 to 15 times larger in amplitude than the SYN1 waveforms in the one-dimensional model (Note in fig. 5 that reduction factors have been applied to the SYN2 seismograms for these stations to facilitate the comparison of features between waveforms.) In spite of these large amplifications, only a small adjustment in slip amplitude (×0.7) of the northwest slip maximum in figure 3 is needed to bring the amplitude of the predicted motions into close agreement with that of the observed motions. The true amplitude variation by a factor of 10 or more induced by resolvable three-dimensional structure is on the same order as the magnitude of amplitude variations that have been documented for variations in local site geology and nonlinear rheology (for example, Darragh and Shakal, 1991; Su and others, 1992). In principal, then, the effects of regional three-dimensional structure should be considered equal in importance to local site effects in hazard assessment. Unlike the more traditionally considered site effects, the effects of three-dimensional structure strongly depend on the paths between stations and high-slip patches. (Recall, for example, the contrasting behavior of sta. G6 and the rest of the Gilroy array for the 1984 Morgan Hill and 1989 Loma Prieta earthquakes.)

CONCLUSIONS

Ground-motion data from the earthquake were synthesized by the narrow-Gaussian-beam method for a distributed slip history and a known three-dimensional crustal structure with a scale length of heterogeneity of 1 to 10 km in the vicinity of the fault plane. The slip model was determined by Beroza (1991) from an inversion of strong ground motion by assuming a one-dimensional crustal model, and the three-dimensional structure model is that of Eberhart-Phillips and others (1990). The differences in ground motion predicted by using a three-dimensional versus a one-dimensional model are principally due to ray bending and focusing and defocusing. Focusing and defocusing produce variations by a factor of 2 to 3, more rarely 10, in peak amplitudes, in comparison with the amplitudes predicted by a one-dimensional structural model. Multipathing and caustics, which cause more severe waveform distortion, occur relatively infrequently within a typical observational range of less than 30 km. An exception would be the waveforms at stations lying along the strike of the fault or in a well-developed fault zone (Cormier and Spudich, 1984; Cormier and Beroza, 1987; Ben-Zion, 1989). This is not the case, however, at most of the strong-ground-motion stations that recorded the earthquake. The San Andreas fault zone is poorly developed in this area, a zone of imbricate thrust faults substituting for the broad low-velocity zone seen surrounding the surface trace of the fault in other places. Synthetic seismograms in a three-dimensional model of the Loma Prieta region suggest that ground motions at stations within 5 km of the fault trace are strongly affected by the presence of a high-velocity wedge between the San Andreas and Sargent faults. At distances greater than 50 km, this high-velocity wedge is predicted to defocus body waves radiated by the earthquake in a 10-km-wide zone northeast of and paralleling the strike of the San Andreas fault. At lesser distances, the same structure, in combination with an adjacent low-velocity zone between the Zayante and San Andreas faults, is predicted to strongly focus energy at stations within 5 km of the surface trace of the San Andreas fault. The Santa Clara Valley is predicted to weakly defocus Loma Prieta energy arriving near and at the Gilroy array (fig. 1). It is simple to demonstrate a focusing effect due to ray interaction with the Moho transition at distances beyond 50 km for energy radiated by either of the two slip maximums of the earthquake. Except for the Moho interaction, tradeoffs of the slip model with the structural model make it difficult to verify these predictions without carefully investigating the distribution of amplitudes in recordings of small aftershocks.

In inversions of slip history, the errors due to the inappropriate assumption of a one-dimensional crustal structure are comparable to the variations due to the use of different data sets or minimization criteria. In combination, these effects limit the resolution of the absolute size of discrete high-slip patches to a factor of 2 or more, and their location to within 1 to 2 km.

The amplitude variations due to resolvable three-dimensional crustal structure are similar in size to those predicted for variations in surface impedance, near-receiver reverberations, and nonlinear rheology. Thus, it is important to include the effects of known three-dimensional crustal structure in predictions of ground motion. The strong path dependence of these effects, however, makes them difficult to include in a hazard assessment without postulating reasonably detailed slip histories for probable earthquakes.

ACKNOWLEDGMENTS

This research was supported U.S. National Science Foundation grant EAR 90–11439. We thank Gregory Beroza and Donna Eberhart-Phillips for helpful discussions and for providing us with early versions of their Loma Prieta source and structural models. Paul Spudich offered many valuable suggestions for improving the manuscript.

REFERENCES CITED

Ben-Zion, Yehuda, 1989, The response of two jointed quarter spaces to SH line sources located at the material discontinuity interface: Royal Astronomical Society Geophysical Journal, v. 98, no. 2, p. 213–222.

Bernard, Pascal, and Madariaga, Raoul, 1984, A new asymptotic method for the modeling of near-field accelerograms: Seismological Society of America Bulletin, v. 74, no. 2, p. 539–557.

Beroza, G.C., 1991, Near-source modeling of the Loma Prieta earthquake; evidence for heterogeneous slip and implications for earthquake hazard: Seismological Society of America Bulletin, v. 81, no. 5, p. 1603–1621.

Beydoun, W.B., and Ben-Menahem, Ari, 1985, Range of validity of seismic ray and beam methods in general inhomogeneous media; I. General theory: Royal Astronomical Society Geophysical Journal, v. 82, no. 2, p. 207–234.

Bonamassa, Ornella, and Vidale, J.E., 1991, Directional site resonances observed from aftershocks of the 18 October 1989 Loma Prieta earthquake: Seismological Society of America Bulletin, v. 81, no. 5, p. 1945–1957.

Borcherdt, R.D., and Glassmoyer, G.M., 1992, On the characteristics of local geology and their influence on ground motions generated by the Loma Prieta earthquake in the San Francisco Bay region, California: Seismological Society of America Bulletin, v. 82, no. 2, p. 603–641.

Červený, Vlastislav, Molotkov, I.A., and Pšenčík, Ivan, 1977, Ray method in seismology: Prague, Univerzita Karlova, 214 p.

Červený, Vlastislav, Pleinerová, J., Klimeš, L., and Pšenčík, Ivan, 1987, High-frequency radiation from earthquake sources in laterally varying layered structures: Royal Astronomical Society Geophysical Journal, v. 88, no. 1, p. 43–79.

Clark, J.C., and Rietman, J.D., 1973, Oligocene stratigraphy, tectonics, and paleogeography southwest of the San Andreas fault, Santa Cruz Mountains and Gabilan Range, California Coast Ranges: U.S. Geological Survey Professional Paper 783, 18 p.

Cline, A.K., 1981, FITPAC—software package for curve and surface fitting employing splines under tension: Austin, University of Texas, Department of Computer Science.

Cormier, V.F., 1987, Focusing and defocusing of teleseismic P waves by known three-dimensional structure beneath Pahute Mesa, Nevada Test Site: Seismological Society of America Bulletin, v. 77, no. 5, p. 1688–1703.

Cormier, V.F., and Beroza, G.C., 1987, Calculation of strong ground motion due to an extended earthquake source in a laterally varying structure: Seismological Society of America Bulletin, v. 77, no. 1, p. 1–13.

Cormier, V.F., and Spudich, Paul, 1984, Amplification of ground motion and waveform complexity in fault zones; examples from the San Andreas and Calaveras faults: Royal Astronomical Society Geophysical Journal, v. 79, no. 1, p. 135–152.

Crampin, Stuart, 1984, Effective anisotropic elastic constants for wave propagation through cracked solids: Royal Astronomical Society Geophysical Journal, v. 76, no. 1, p. 135–145.

Darragh, R.B., and Shakal, A.F., 1991, The site response of two rock and soil station pairs to strong and weak ground motion: Seismological Society of America Bulletin, v. 81, no. 5, p. 1885–1899.

Eberhart-Phillips, D.M., Labson, V.F., Stanley, W.D., Michael, A.J., and Rodriguez, B.D., 1990, Preliminary velocity and resistivity models of the Loma Prieta earthquake region: Geophysical Research Letters, v. 17, no. 8, p. 1235–1238.

Gajewski, Dirk, and Pšenčík, Ivan, 1987, Computation of high-frequency seismic wavefields in 3-D laterally inhomogeneous anisotropic media: Royal Astronomical Society Geophysical Journal, v. 91, no. 2, p. 383–411.

Hartzell, S.H., Stewart, G.S., and Mendoza, Carlos, 1991, Comparison of L_1 and L_2 norms in a teleseismic inversion for the slip history of the Loma Prieta, California earthquake: Seismological Society of America Bulletin, v. 81, no. 5, p. 1518–1539.

Hu, L.-Z., and McMechan, G.A., 1988, Elastic finite-difference modelling and imaging for earthquake sources: Royal Astronomical Society Geophysical Journal, v. 95, no. 2, p. 303–313.

Hudson, J.A., 1980, Overall properties of a cracked solid: Cambridge Philosophical Society Proceedings, v. 88, p. 371–384.

———1981, Wave speeds and attenuation of elastic waves in material containing cracks: Royal Astronomical Society Geophysical Journal, v. 64, no. 1, p. 133–150.

Lees, J.M., 1990, Tomographic P-wave velocity images of the Loma Prieta earthquake asperity, Geophysical Research Letters, v. 17, no. 9, p. 1433–1436.

McLaughlin, R.J., Clark, J.C., and Brabb, E.E., 1989, Geologic map and structure sections of the Loma Prieta 7.5-minute quadrangle, Santa Clara and Santa Cruz Counties, California: U.S. Geological Survey Open-File Report 88–752, 32 p., scale 1:24,000, 2 sheets.

Michael, A.J., and Eberhart-Phillips, D.M., 1991, Relations among fault behavior, subsurface geology, and three-dimensional velocity models: Science, v. 253, no. 5020, p. 651–654.

Mooney, W.D., and Colburn, R.H., 1985, A seismic-refraction profile across the San Andreas, and Calaveras faults, west-central California: Seismological Society of America Bulletin, v. 75, no. 1, p. 175–191.

Mooney, W.D., and Ginzburg, A., 1986, Seismic measurements of the internal properties of fault zones: Pure and Applied Geophysics, v. 124, no. 1–2, p. 141–157.

Rial, J.A., Pereyra, V., and Wojcik, G.L., 1986, An explanation of USGS Station 6 record, 1979 Imperial Valley earthquake; a caustic induced by a sedimentary wedge: Royal Astronomical Society Geophysical Journal, v. 84, no. 2, 257–278.

Seeber, Leonardo, and Armbruster, J.G., 1990, Fault kinematics in the 1989 Loma Prieta rupture area during 20 years before that event: Geophysical Research Letters, v. 17, no. 9, p. 1425–1428.

Spudich, Paul, and Frazer, L.N., 1984, Use of ray theory to calculate high-frequency radiation from seismic sources having spatially variable rupture velocity and stress drop: Seismological Society of America Bulletin, v. 74, no. 6, p. 2061–2082.

Spudich, Paul, and Oppenheimer, D.H., 1986, Dense seismograph array observations of earthquake rupture, *in* Das, Shamita, Boatwright, John, and Scholz, C.H., eds., Earthquake source mechanics: American Geophysical Union Geophysical Monograph 37, p. 285–296.

Steidl, J.H., Archuleta, R.J., and Hartzell, S.H., 1991, Rupture history of the 1989 Loma Prieta, California earthquake, Seismological Society of America Bulletin, v. 81, no. 5, p. 1573–1602.

Su, Feng, Aki, Keiiti, Teng, Ta-liang, Zeng, Yuehua, Koyanagi, S.K., and Mayeda, Kevin, 1992, The relation between site amplification factor and surficial geology in central California: Seismological Society of America Bulletin, v. 28, no. 2, p. 580–602.

Thomson, C.J., 1983, Ray-theoretical amplitude inversion for laterally varying velocity structure below NORSAR: Royal Astronomical Society Geophysical Journal, v. 74, no. 2, p. 5525–558.

Thurber, C.H., 1983, Earthquake locations and three-dimensional crustal structure in the Coyote Lake area, central California: Journal of Geophysical Research, v. 88, no. B10, p. 8226–8236.

Wald, D.J., Helmberger, D.V., and Heaton, T.H., 1991, Rupture model of the 1989 Loma Prieta earthquake from the inversion of strong-motion and broadband teleseismic data: Seismological Society of America Bulletin, v. 81, no. 5, p. 1540–1572.

THE LOMA PRIETA, CALIFORNIA, EARTHQUAKE OF OCTOBER 17, 1989:
STRONG GROUND MOTION AND GROUND FAILURE

STRONG GROUND MOTION

SIMULATION OF STRONG GROUND MOTION

By Jeffry L. Stevens
Maxwell Laboratories, Inc.; and
Steven M. Day,
San Diego State University

CONTENTS

ABSTRACT

We model the strong ground motion from the earthquake by superimposing the ground motion from numerous subevents on the fault. The subevent source model is derived from finite-difference simulations of earthquakes. We model wave propagation by using geometric-ray theory for each subevent. The moment and geometry of the fault are constrained to the observed values. The free parameters in the model are the subevent radius and subevent stress drop. With a subevent radius of 1.3 km and a subevent stress drop of 200 bars, our model reproduces the ground motion quite well at 13 California Division of Mines and Geology stations within 30 km of the fault. This technique has been used previously to model the 1983 Coalinga, Calif., earthquake and two larger subduction-zone earthquakes in Mexico and Chile. The same parameters used to model the Loma Prieta data were also used to model the strong ground motion from the 1983 Coalinga earthquake. The subduction-zone events, however, required a lower subevent stress drop and larger subevent radius. This method provides a means for predicting strong ground motion at sites located close to hypothetical large earthquakes.

INTRODUCTION

The strong-motion recordings of the earthquake provide a unique opportunity to test and refine methods for predicting strong ground motion. In this paper, we simulate the strong ground motion of the earthquake at sites within approximately 50 km of the fault. The purpose of this study is not primarily to model the details of the earthquake but to use it as a test case of a general method for predicting ground motion from earthquakes that are expected but have not yet occurred. Such hypothetical earthquakes could include, for example, one on all or part of the Hayward fault, or on the San Andreas fault north of the Loma Prieta rupture zone (fig. 1).

The 1989 Loma Prieta earthquake was recorded by strong-motion instruments located in the Santa Cruz Mountains and surrounding areas. We have used recordings at 14 stations operated by the California Division of

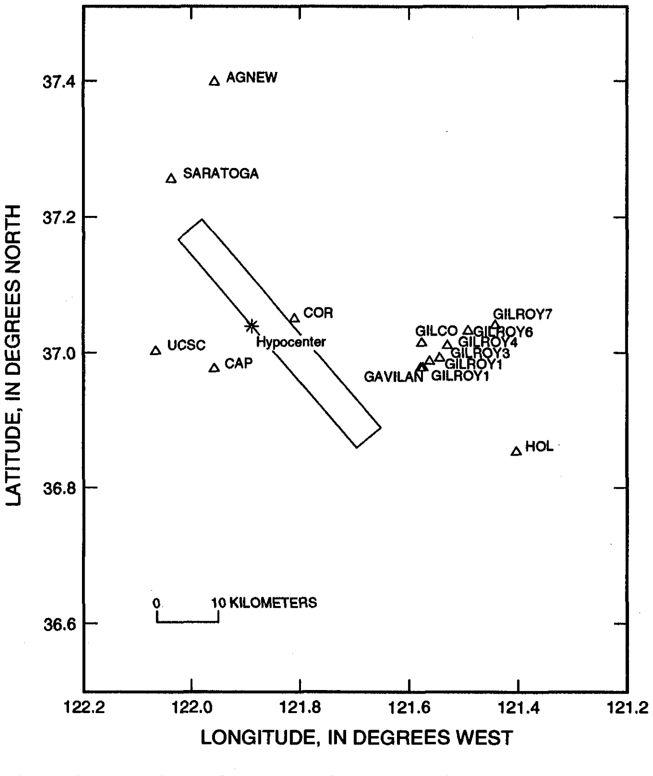

Figure 1.—Locations of strong-motion stations in California Division of Mines and Geology network within 30 km of hypocenter of 1989 Loma Prieta earthquake. Rectangle, surface projection of rupture zone.

Mines and Geology (CDMG) (Shakal and others, 1989; Huang and others, 1990) located within 30 km of the fault for comparison with our simulations. The locations of these stations are shown together with a surface projection of the fault plane in figure 1.

The method used to simulate strong ground motion is based on superposition of the seismic waves radiated by subevents that cover the fault plane. This method is similar to the barrier model proposed by Papageorgiou and Aki (1983a, b), with some additional features designed to make the model more realistic for simulating high-frequency ground motion from large earthquakes. In particular, the subevent radiation is modeled by using dynamic-crack theory (Day, 1982a, b; Stevens and Day, 1985); a stochastic component is included in the subregion dimensions, stress drops, and rupture times; and total slip duration is related to overall earthquake dimensions by allowing subregions to reload and undergo repeated stress drops as the rupture expands to cover the entire fault plane. The subevents are characterized by an average dimension and stress drop. These are the only free parameters in the simulations; all other parameters are constrained either by observations (for example, earth structure) or by hypothesis (for example, event dimensions for an expected earthquake).

Although numerous investigators have used some variant of subevent summation as a source representation for simulating strong ground motion, there is no consensus yet on the physical significance of the model parameters. As a result of the randomness in subevent rupture delays, the resulting ground motion has, at high frequency, approximately the characteristics of shot noise. At a minimum, then, the method can be viewed as a means of generalizing the band-limited-white-noise model of earthquake ground motion to account for the spatial extent and propagation of large ruptures. It provides a simple, but by no means unique, means of parametrizing the variations in slip and rupture velocity (that is, fault roughness) in an earthquake, thus determining the level of high-frequency seismic radiation. Day and Aki (1992) discussed further the problem of parametrizing fault roughness. Additional work is necessary to establish the extent to which subevent models can concurrently characterize both the low- and high-frequency components of ground motion.

The techniques used in this study to model the 1989 Loma Prieta earthquake have previously been applied to the 1985 M_w=8.0 Michoacán, Mexico, earthquake, the 1985 M_w=8.0 Valparaiso, Chile, earthquake, and the 1983 M_w=6.7 Coalinga, Calif., earthquake (Day and Stevens, 1987; Stevens and Day, 1987; Youngs and others, 1988). In each case, good agreement was obtained between the simulated and observed ground motion. The two subduction-zone earthquakes differed from the 1983 Coalinga earthquake, however, in local stress drop and subevent dimension. We found that the two subduction-zone earthquakes were modeled very well with a subevent stress drop of 40 bars and a subevent dimension of 2.6 km; the 1983 Coalinga earthquake, however, required a subevent stress drop of 200 bars and a subevent radius of 1.3 km. As we show below, the 1989 M_w=6.9 Loma Prieta earthquake is also modeled quite well with the subevent parameters that were appropriate for the 1983 Coalinga earthquake. Although more research is needed to determine the variations of these parameters in other events, our results suggest a difference in physical mechanism between subduction-zone events and crustal earthquakes that is reflected in the subevent parameters.

In the following sections, we first briefly describe the method used to simulate ground motion, then discuss the parameters used specifically to model the 1989 Loma Prieta earthquake and compare the predicted and observed ground motion. Finally, we discuss the implications of our results for the prediction of earthquake ground motion.

METHOD

We model strong ground motion by using the subevent-superposition method (Stevens and others, 1988; Youngs and others, 1988), as shown schematically in figure 2. The fault is divided into subregions that fail multiple times after the rupture front passes each subregion. As mentioned in the preceding section, each subregion has a characteristic size and stress drop, and a stochastic component that allows the size, stress drop, and rupture time to vary around the characteristic value. For the purpose of modeling an earthquake that has already occurred, the length and width of the fault and the earthquake moment are constrained to the observed values.

We model wave propagation by using geometric-ray theory. For stations within about 50 km of the fault rupture, the ground motion is dominated by direct arrivals and primary reflections, and so ray theory is adequate for these simulations. Wave-number integration is used to check the results to ensure that all arrivals that contribute significantly to the ground motion are included. The attenuation model is based on the work of Anderson and Hough (1984), who showed that attenuation depends weakly on the distance from the source to the receiver. We model this attenuation by including a low-Q layer in the uppermost kilometer of the crust, whereas Q remains high throughout the rest of the structure.

The radiation pattern of the subevents is represented by its rms average rather than the value corresponding to the specific departure angle of the ray path. Stevens and Day (1987), who studied aftershocks of the 1983 Coalinga earthquake to refine and validate the subevent model used in the earthquake simulations, found that the ground motion in the frequency band 1–10 Hz was more accurately represented by a "homogenized" radiation pattern than by the "exact" value. In particular, the nodes and peaks predicted by a double-couple radiation pattern are not observable in the aftershock records. More realistic simulations are therefore obtained by using an average radiation pattern in the subevent model.

The rise time of the earthquake, T_R, is defined by the relation $T_R=KW/V_r$, where $\frac{1}{2}<K<1$, V_r is the rupture velocity, and W is the width of the fault. This relation is based on dynamic modeling (Day, 1982a). The slip episodes in each subregion begin when the rupture front arrives, and are evenly divided over the time corresponding to the total rupture duration. The stochastic variation in rupture time, however, is sufficiently large to allow subevents to occur randomly throughout the rise time. In earlier tests, this consideration was found to be important to avoid destructive interference between arrivals caused by an artificial periodicity in the rupture times. In these simulations, we used a rise time comparable to the rupture duration. We note, however, that several studies based on the inversion of strong-motion data have found that the overall rise time of slip in large earthquakes is short in comparison with the predictions of crack theory. Heaton (1990), who reviewed the observational evidence pertaining to slip rise times, found that these times are typically about 10 percent of the overall duration of the rupture. For the 1989 Loma Prieta earthquake, Steidl and others (1991), estimated a slip rise time of approximately 1 s. The estimate by Wald and others (1991) is similar, and that by Beroza (1991) even shorter. Use of a more realistic slip rise time in the simulations might require some compensating adjustments to other model parameters (for example, subevent dimension and stress drop) to retain the agreement with strong-motion observations reported below.

The total number of slip episodes is defined by requiring that the sum of the moments of subevents equal the moment of the large earthquake. For a rectangular fault of length L, width W, and moment M_0 covered with circular subregions of average radius a and stress drop $\Delta\tau_L$, the moment of each subevent is $\frac{16}{7}\Delta\tau_L a^3$ (Neuber, 1958), the total number of subregions is $LW/4a^2$, and the total moment of the earthquake is given by

$$M_0 = \frac{4}{7} N \Delta\tau_L WLa,$$

where N is the number of slip episodes per event.

Additional complexity can be included in the model, such as spatial variations in local stress drop or irregular fault zones. Such detailed modeling could be used to refine the model to obtain a better data fit. However, because the main purpose of the method is to predict strong ground motion in places where these details are unlikely to be known in advance, our approach has been to use as simple a model as possible and then to use the

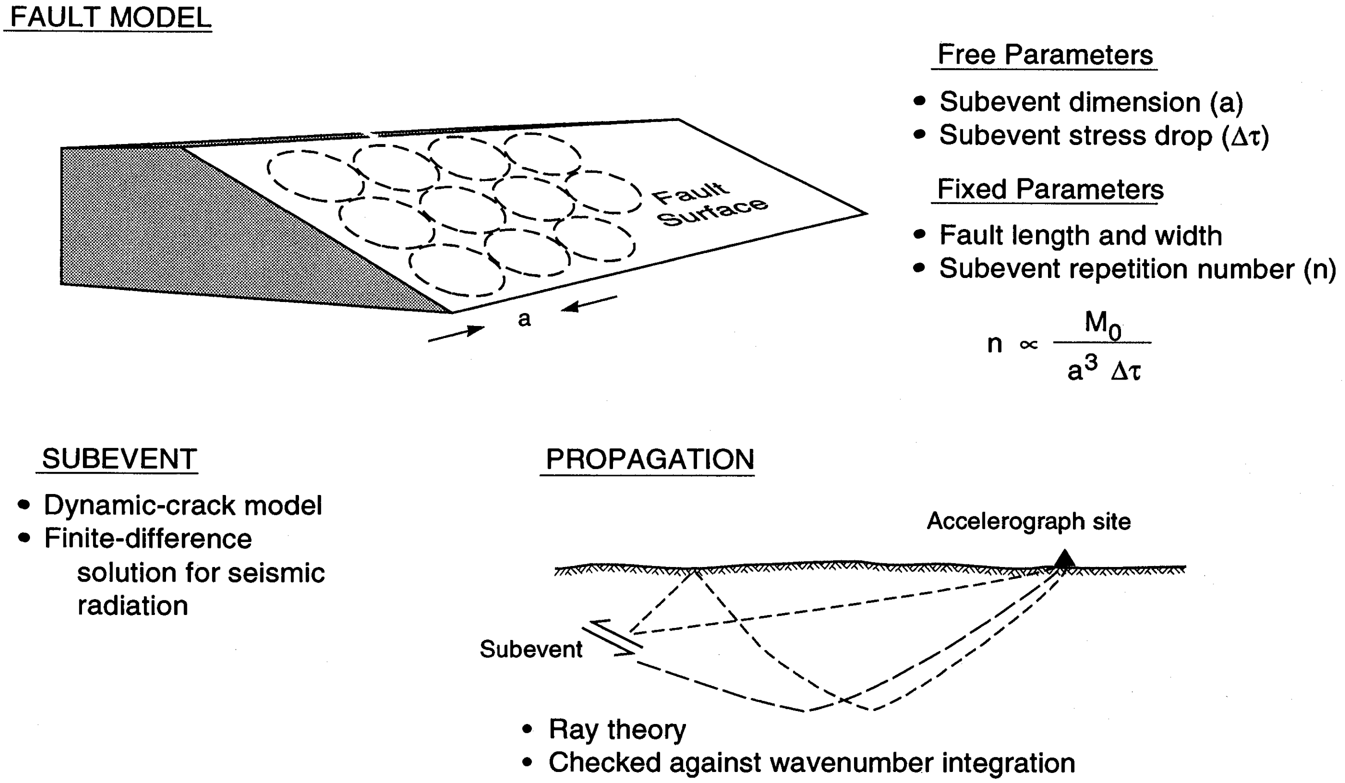

Figure 2.—Schematic diagram of method used to simulate ground motion from large earthquakes.

observed data misfit as a measure of the uncertainty in future predictions.

THE 1989 LOMA PRIETA EARTHQUAKE

The parameters used for the 1989 Loma Prieta earthquake were derived from several independent studies (Plafker and Galloway, 1989; Barker and Salzberg, 1990; Choy and Boatwright, 1990; Kanamori and Satake, 1990; Mueller and Johnston, 1990; Romanowicz and Lyon-Caen, 1990; Ruff and Tichelaar, 1990; Zhang and Lay, 1990). The hypocenter was located at lat 37.037° N., long 121.883° W., at 19-km depth. The moment of the event was 3.0×10^{19} N-m; the fault dimensions were 45 km long by 15 km wide; the strike, dip, and rake were 130°, 70°, and 135°, respectively; and the rupture velocity was 3.0 km/s. Using these parameters, a subevent stress drop of 200 bars, and a subevent radius of 1.3 km, the number of slip episodes per subregion is 3; we used a delay of 1.2±1.2 s between slip episodes. The earth model was the plane-layered model for the Loma Prieta region of Somerville and Yoshimura (1990), and we ran simulations using direct rays only, and direct rays plus reflections from the two largest discontinuities in the model. We used a (shear) Q value of 10 in the upper kilometer of the model, and a Q value of 1,000 at all greater depths.

Simulations were performed in two different ways. First, we performed calculations of the ground motion at the 14 CDMG stations that were shown in figure 1 to have a direct correlation of calculations with observations at these stations. Second, we performed numerous calculations on a grid extending 50 km from the fault center to generate synthetic ground motions over a wide area.

The predicted and observed peak horizontal accelerations and velocities at the 14 CDMG stations are plotted as a function of the distance to the closest point on the fault in figure 3. Both predictions and observations show a rapid decline in amplitude as a function of distance, and the calculated data match the observed data quite well at most stations. A notable exception is the station at Hollister, Calif. (HOL, fig. 1), which had a much higher than predicted peak velocity, apparently because of strong site effects. Response spectra calculated from the synthetic ground motion also matched the observations quite well. The simulated and observed response spectra for the station at Capitola, Calif. (CAP, fig. 1), are plotted in figure 4. This record is typical of most of the records that show a generally good fit to the data, but the observations lie above or below the calculations by about a factor of 2 in some frequency bands. The misfit between the predicted and observed data, averaged (frequency by frequency) over 13 CDMG stations (all except that at Hollister), is plotted in figure 5. Again, the fit to the data is quite good over a broad frequency range, and a somewhat larger misfit occurs near 1 Hz than at higher frequencies. This observed misfit can be used to estimate the uncertainty in future strong-ground-motion predictions.

The grid calculations were performed at 5-km intervals and used to generate contour plots of peak acceleration and velocity throughout the Loma Prieta region

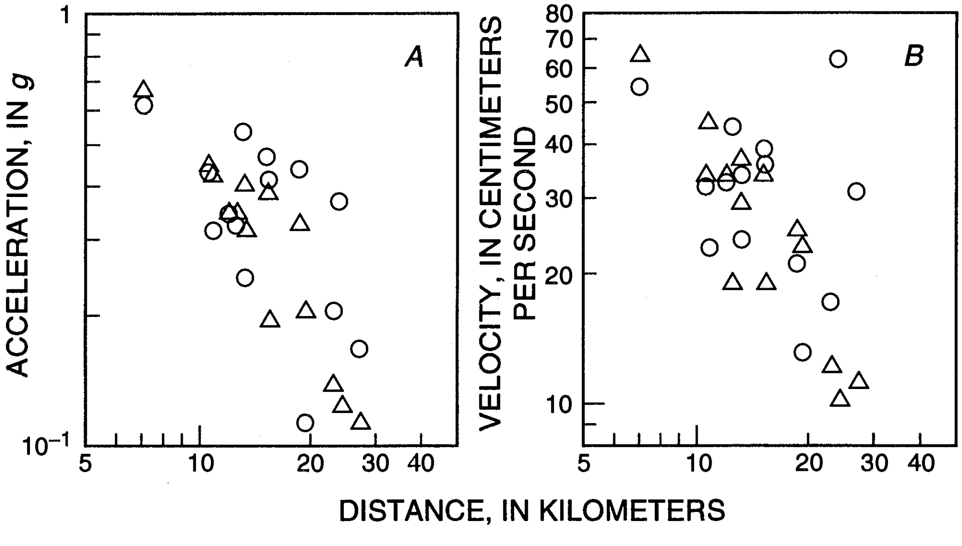

Figure 3.—Calculated (triangles) and observed (circles) peak horizontal acceleration (*A*) and velocity (*B*) at 14 California Division of Mines and Geology strong-motion stations as a function of distance to closest point on fault.

(figs. 6, 7). Variations in the ground motion caused by variations in the stochastic model parameters are easily seen in these plots. Even though the final slip distribution on the fault is nearly uniform, there is a substantial amount of variation in the predicted ground motion. These variations, which are caused by random interference between arrivals, are comparable in magnitude to observed variations over similar length scales.

The peak acceleration and velocity at all points on the grids in figures 6 and 7 are plotted as a function of distance to the closest point on the fault in figures 8 and 9. These plots provide a measure of the attenuation of these quantities as a function of distance *r*. Both the peak accelerations and peak velocities decrease rapidly at a rate of approximately $r^{-1.5}$ out to a distance of approximately 35 km, beyond which they become nearly constant at 0.1 *g* and 10 cm/s, respectively. This flattening of the attenuation curves is caused by mantle reflections, which begin to dominate the ground motion at that distance. This effect was previously noticed by Somerville and Yoshimura (1990), who used it to explain the high amplitudes of accelerations observed in the San Francisco area. For comparison, peak acceleration is plotted as a function of range calculated by using direct rays only in figure 10.

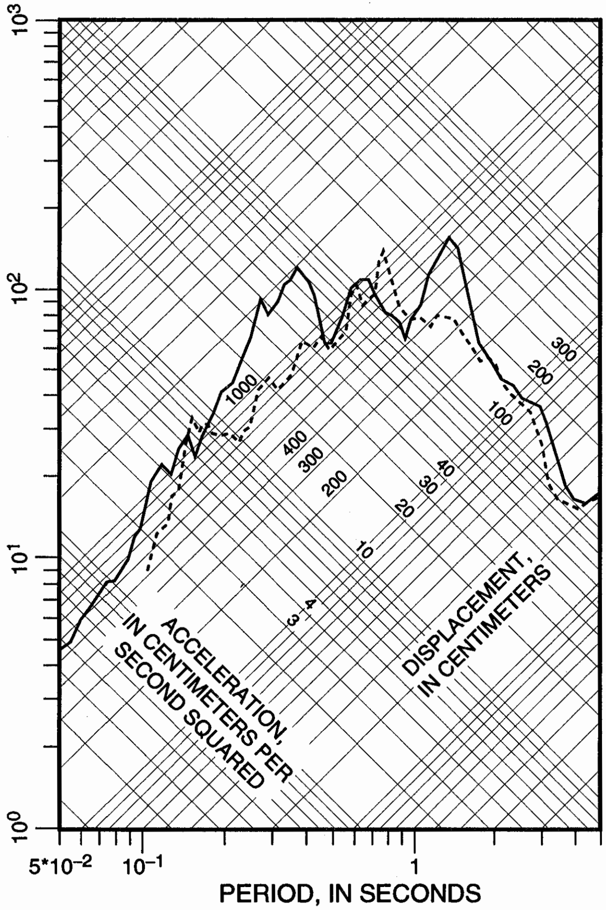

Figure 4.—Calculated (dashed curve) and observed (solid curve) 5-percent-damped response spectra at California Division of Mines and Geology strong-motion station in Capitola, Calif. (CAP, fig. 1)

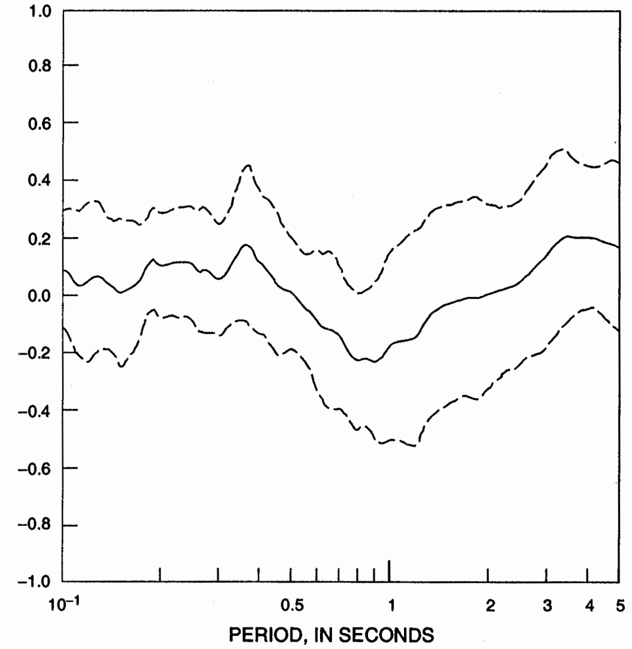

Figure 5.—Data misfit in 5-percent-damped response spectra averaged frequency by frequency over 13 California Division of Mines and Geology strong-motion stations. Dashed curves show ±1σ limits.

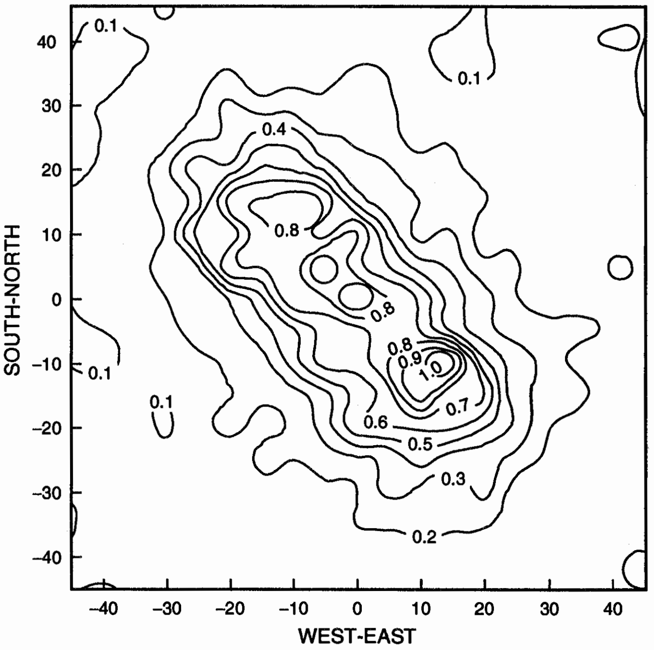

Figure 6.—Contour plot of peak horizontal acceleration (in *g*) on a grid with 5-km spacing. Coordinates in kilometers relative to center of Loma Prieta rupture zone (see fig. 1).

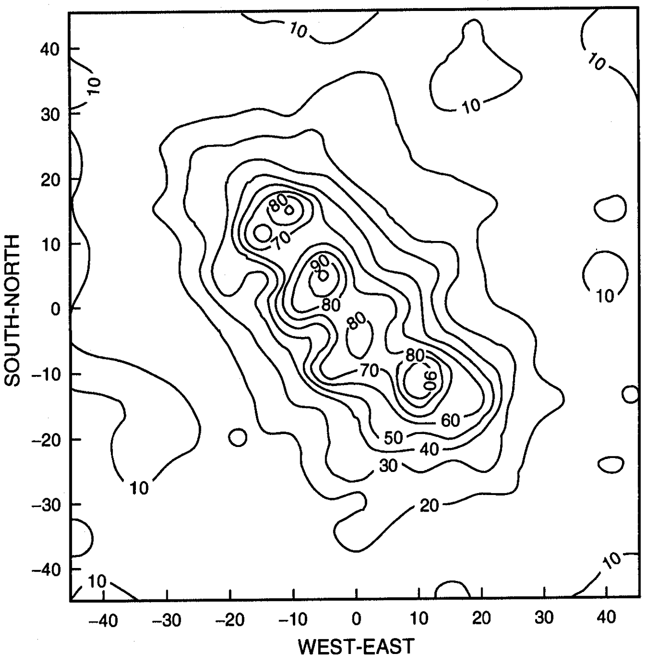

Figure 7.—Contour plot of peak horizontal velocity (in centimeters per second) on a grid with 5-km spacing. Coordinates in kilometers relative to center of Loma Prieta rupture zone (see fig. 1).

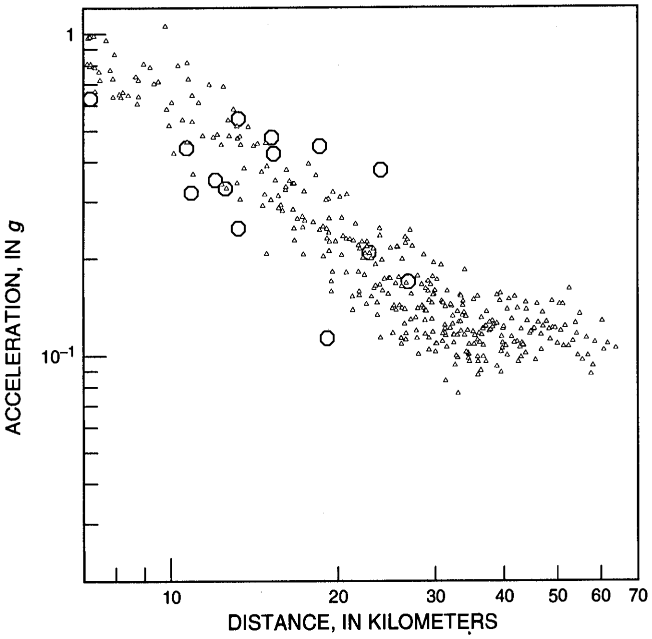

Figure 8.—Peak accelerations as a function of distance to closest point on fault, from contour plot in figure 6. Circles, observed peak accelerations at 14 California Division of Mines and Geology strong-motion stations; triangles, calculated peak accelerations. Flattening of curve at distances beyond 35 km is due to mantle reflections, which become dominant at that range.

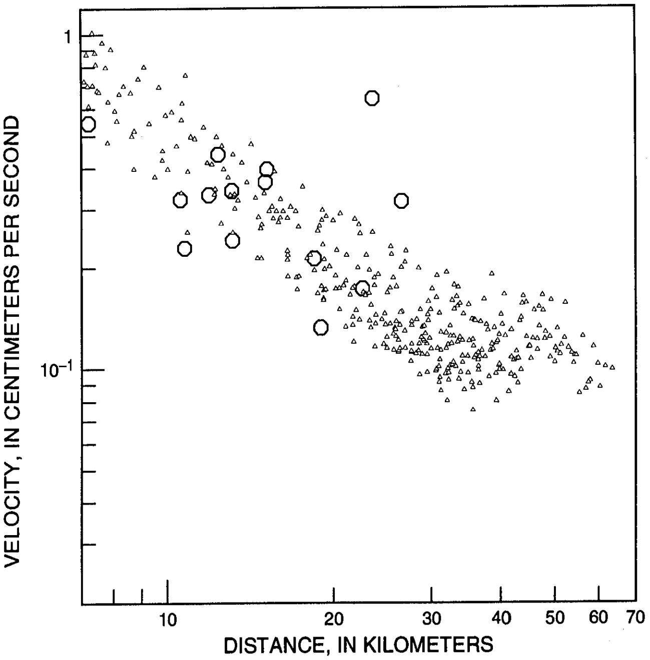

Figure 9.—Peak velocity as a function of distance to closest point on fault, from contour plot in figure 7. Circles, observed peak velocities at 14 California Division of Mines and Geology strong-motion stations; triangles, calculated peak velocities.

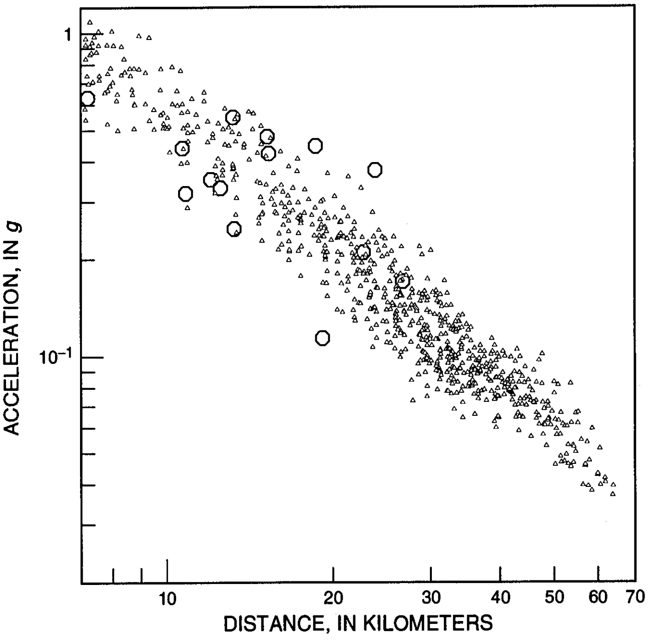

Figure 10.—Peak acceleration as a function of distance to closest point on fault, calculated using only direct rays with no mantle reflections. Circles, observed peak accelerations at 14 California Division of Mines and Geology strong-motion stations; triangles, calculated peak accelerations.

DISCUSSION AND CONCLUSIONS

We have modeled the strong ground motion from the 1989 Loma Prieta earthquake by using the subevent-superposition method. The results can be used to predict the ground motion from other hypothetical earthquakes. In addition, the observed misfit to the earthquake provides an estimate of the uncertainty in predictions of the ground motion from future earthquakes. In a recent study (Stevens and Day, 1990), this method was used to predict the strong ground motion and ground-motion uncertainty at a site 5 km from the San Andreas fault during a hypothetical M=7.5 earthquake.

We have modeled the earthquake slip distribution as uniform on a large scale; that is, we have incorporated small-scale roughness through the subevent parametrization but have not incorporated longer wavelength variation in slip amplitude. Models for this longer wavelength structure are available from inversion results (for example, Beroza, 1991; Steidl and others, 1991; Wald and others, 1991). We chose not to use such information, however, because we view simulations of the type reported here as a potential tool for assessing strong ground motion from potential future events, in which the distribution of slip will not be known in advance. Our intent was to assess the ability of a generic slip distribution to represent the observed ground motion. Thus, we allowed realistic uncertainties in the slip distribution to be fully subsumed in uncertainty estimates obtained from the data misfit.

Site effects were neglected in our study, as is evident, for example, in the very large misfit to the ground motion at Hollister. Corrections for site effects can readily be incorporated into the method if reliable site-amplification factors are available. For example, Chin and Aki (1991) used a subevent-summation approach to model the strong ground motion from the 1989 Loma Prieta earthquake but also incorporated corrections for local site amplification. They used site corrections measured from weak motion; however, they found that use of these corrections actually degraded the fit between recorded and simulated peak acceleration at sites within 50 km of the Loma Prieta rupture zone. Chin and Aki attributed this result to nonlinearity. In our study, unmodeled nonlinear effects and unmodeled site effects may have compensated each other somewhat.

The appropriate modeling of strong-motion site effects, including nonlinearity, is an important area for further research. We recommend additional research in three areas: (1) simulation of strong ground motion, using the subevent-superposition method for high-risk fault zones; (2) additional modeling of strong-motion-data sets from large earthquakes to provide validation and refinement of the method; and (3) incorporation of corrections for site amplification, using weak-motion records and theoretical modeling.

REFERENCES CITED

Anderson, J.G., and Hough, S.E., 1984, A model for the shape of the Fourier amplitude spectrum of acceleration at high frequencies: Seismological Society of America Bulletin, v. 74 , no. 5, p. 1969–1993.

Barker, J.S., and Salzberg, D.H., 1990, Long-period and broad-band teleseismic body-wave modeling of the October 18, 1989 Loma Prieta earthquake: Geophysical Research Letters, v. 17, no. 9, p. 1409–1412.

Beroza, G.C., 1991, Near-source modeling of the Loma Prieta earthquake: evidence for heterogeneous slip and implications for earthquake hazard: Seismological Society of America Bulletin, v. 81, no. 5, p. 1603–1621.

Chin, B.H., and Aki, Keiiti, 1991, Simultaneous study of the source, path, and site effects on strong ground motion during the 1989 Loma Prieta earthquake: a preliminary result on pervasive nonlinear site effects, Seismological Society of America Bulletin, v. 81, no. 5, p. 1859–1884.

Choy, G.L., and Boatwright, John, 1990, Source characteristics of the Loma Prieta, California, earthquake of October 18, 1989 from global digital seismic data: Geophysical Research Letters, v. 17, no. 8, p. 1183–1186.

Day, S.M., 1982a, Three-dimensional simulation of fault dynamics: rectangular faults with fixed rupture velocity, Seismological Society of America Bulletin, v. 72, no. 3, p. 705–727.

———1982b, Three-dimensional simulation of spontaneous rupture; the effect of nonuniform prestress: Seismological Society of America Bulletin, v. 72, no. 6, pt. A, p. 1881–1902.

Day, S.M., and Aki, Keiiti, 1992, Evaluation of the models: Workshop on Modeling Earthquake Ground Motion at Close Distances, Palo Alto, Calif., 1990, Proceedings.

Day, S.M., and Stevens, J.L., 1987, Simulation of ground motion from the 1985 Michoacan, Mexico earthquake [abs.]: Eos (American Geophysical Union Transactions), v. 68, no. 44, p. 1354.

Heaton, T.H., 1990, Evidence for and implications of self-healing pulses of slip in earthquake rupture: Physics of the Earth and Planetary Interiors, v. 64, p. 1–20.

Huang, M.J., Cao, T.Q., Vetter, U.R., and Shakal, A.F., 1990, Second interim set of CSMIP processed strong-motion records from the Santa Cruz Mountains, (Loma Prieta), California earthquake of 17 October 1989: California Division of Mines and Geology, Office of Strong Motion Studies Report OSMS 90–01.

Kanamori, Hiroo, and Satake, Kenji, 1990, Broadband study of the 1989 Loma Prieta earthquake: Geophysical Research Letters, v. 17, no. 8, p. 1179–1182.

Mueller, R.J., and Johnston, M.J.S., 1990, Seismomagnetic effect generated by the October 18, 1989, M_L 7.1 Loma Prieta, California, earthquake: Geophysical Research Letters, v. 17, no. 8, p. 1231–1234.

Neuber, Heinz, 1958, Theory of notch stresses; principles for exact calculation of strength with reference to structural form and material: U.S. Atomic Energy Commission, Office of Technical Information Report AEC–4547, 293 p.

Papageorgiou, S.P., and Aki, Keiiti, 1983a, A specific barrier model for the quantitative description of inhomogeneous faulting and the prediction of strong ground motion. I. Applications of the Model: Seismological Society of America Bulletin, v. 73, no. 3, p. 953–978.

———1983b, A specific barrier model for the quantitative description of inhomogeneous faulting and the prediction of strong ground motion. II. Applications of the model, Seismological Society of America Bulletin, v. 73, no. 4, p. 953–978.

Plafker, George, and Galloway, J.P., eds., 1989, Lessons learned from the Loma Prieta, California, earthquake of October 17, 1989: U.S. Geological Survey Circular 1045, 48 p.

Romanowicz, Barbara, and Lyon-Caen, Hélène, 1990, The Loma Prieta earthquake of October 18, 1989; results of teleseismic mantle and body wave inversion: Geophysical Research Letters, v. 17, no. 8, p. 1191–1194.

Ruff, L.J., and Tichelaar, B.W., 1990, Moment tensor rate functions for the 1989 Loma Prieta earthquake: Geophysical Research Letters, v. 17, no. 8, p. 1187–1190.

Shakal, A.F., Huang, M.J., Reichle, M., Ventura, C., Cao, T., Sherburne, R.W., Savage, M., Darragh, R.B., and Peterson, C., 1989, CSMIP Strong motion records from the Santa Cruz Mountains (Loma Prieta), California earthquake of 17 October 1989: California Division of Mines and Geology, Office of Strong Motion Studies, Report OSMS 89–06, 196 p.

Somerville, P.G., and Yoshimura, Joanne, 1990, The influence of critical Moho reflections on strong ground motions recorded in San Francisco and Oakland during the 1989 Loma Prieta earthquake: Geophysical Research Letters, v. 17, no. 8, p. 1203–1206.

Steidl, J.H., Archuleta, R.J., and Hartzell, S.H., 1991, Rupture history of the 1989 Loma Prieta, California, earthquake: Seismological Society of America Bulletin, v. 81, no. 5, p. 1573–1602.

Stevens, J.L., and Day, S.M., 1985, The physical basis of m_b:M_S and variable frequency magnitude methods for earthquake/explosion discrimination: Journal of Geophysical Research, v. 90, no. B4, p. 3009–3020.

———1987, Source characteristics of eight Coalinga aftershocks [abs.]: Eos (American Geophysical Union Transactions), v. 68, no. 44, p. 1361.

———1990, Simulation of strong ground motion from a magnitude 7.5 San Andreas earthquake: Workshop on Modeling Earthquake Ground Motion at Close Distances, Stanford, Calif., 1990, Proceedings.

Stevens, J.L., Day, S.M. and Barker, T.G., 1988, Simulation of strong ground motion from earthquakes: La Jolla, Calif., Maxwell Laboratories, Inc., S-Cubed Scientific Report SSS–TR–89–9988, 65 p.

Youngs, R.R., Day, S.M., and Stevens, J.L., 1988, Near-field ground motions for large subduction earthquakes, in Von Thun, J.L., ed., Proceedings; Earthquake Engineering and Soil Dynamics II—recent advances in ground-motion evaluation: American Society of Civil Engineers Geotechnical Special Publication 20, p. 445–462.

Wald, D.J., Helmberger, D.V., and Heaton, T.H., 1991, Rupture model of the 1989 Loma Prieta Earthquake from the inversion of strong-motion and broadband teleseismic data: Seismological Society of America Bulletin, v. 81, no. 5, p. 1540–1572.

Zhang, Jiajun, and Lay, Thorne, 1990, Source parameters of the 1989 Loma Prieta earthquake determined from long-period Rayleigh waves: Geophysical Research Letters, v. 17, no. 8, p. 1195–1198.

THE LOMA PRIETA, CALIFORNIA, EARTHQUAKE OF OCTOBER 17, 1989:
STRONG GROUND MOTION AND GROUND FAILURE

STRONG GROUND MOTION

INFLUENCE OF NEAR-SURFACE GEOLOGY ON THE DIRECTION OF GROUND MOTION ABOVE A FREQUENCY OF 1 HZ[1]

By John E. Vidale,
U.S. Geological Survey; and
Ornella Bonamassa,
University of California, Santa Cruz

CONTENTS

ABSTRACT

The direction of ground shaking observed at 13 California Division of Mines and Geology strong-motion stations across San Francisco and Oakland at frequencies below 1 Hz approximately agrees with a prediction calculated from the well-determined long-period focal mechanism. The directions of shaking at frequencies above 1 Hz, however, show little resemblance to this simple prediction, suggesting that the near surface geology interacts with the higher frequency seismic waves in a complex way. This propagational complexity, if a common feature, makes the recovery of source information from surface-recorded seismograms difficult and suggests that the focal mechanism commonly does not determine the direction of strongest shaking in an earthquake at this range of about 100 km at frequencies above about 1 Hz.

INTRODUCTION

The motion that an earthquake causes at the surface of the Earth is a combination of the details of faulting at depth and the complexities due to propagation through structures within the Earth of the seismic energy released by the faulting. Various ways of measuring the seismic source and propagational complexities have been described. There exists considerable literature that documents the usefulness of the concept of site response, whereby a particular site has a fixed set of frequencies which are amplified at that site no matter how the ground motion is induced (Borcherdt, 1970; Joyner and others, 1976; Joyner and others, 1981; Rogers and others, 1984). Seismic-wave interaction with such large-scale structures as major sedimentary basins can be described deterministically; these structures can be shown to distort seismic waves in a semipredictable way (Kagami and others, 1986; Vidale and Helmberger, 1988; Kawase and Aki, 1989). Bridging the gap between well-understood large-scale structures and fine structure where only the amplitude-versus-frequency behavior has been studied is the goal of considerable recent research.

This paper concentrates on empirically quantifying the distortion to the direction of strongest shaking caused by Earth structure, because it has been suggested that the direction of shaking is sometimes a feature of the recording site (a directional site resonance) rather than of the earthquake (Cranswick, 1988; Bonamassa and Vidale, 1991; Bonamassa and others, 1991; Vidale and others, 1991). These and other observations of horizontal ground motion above 1-Hz frequency (Abrahamson and others, 1989; Dietel and others, 1989) show very small lateral correlation distances—less than tens of meters for frequencies above a few hertz. Also, comparisons of seismograms written by surface and borehole instruments have shown that propagation through the shallowest tens of meters of the Earth can severely distort seismic pulses (Haukkson and others, 1987; Malin and others, 1988; Aster and Shearer, 1991a, b).

Although the near-surface layers of the Earth appear to scramble high-frequency waves, at long periods the Earth generally affects seismic waves in a predictable way that may be stripped off to study the earthquake source. This paper focuses on finding the transition frequency at

---

[1] Contribution No. 166, Institute of Tectonics, University of California, Santa Cruz, CA 95064.

which Earth structure, mainly near-surface geology, begins to obscure the signature of the seismic source at a distance of 100 km. We will find a transition frequency near 1 Hz.

DATA

The earthquake, which was the largest to strike the San Francisco Bay region since 1906, caused considerable damage and loss of life. On the positive side, it was captured by more than 100 strong-motion seismometers, providing an unprecedented opportunity to investigate details of the earthquake and earthquake hazards in general. Numerous investigators have reconstructed the spatial and temporal patterns of fault movements during the 5 to 10 s it took for the earthquake to occur.

This paper concentrates on observations of the effect of Earth structure on the seismic waves radiated by the earthquake. To this purpose, we examine the Loma Prieta main-shock records from 13 accelerometers located near San Francisco (fig. 1). The station numbers, names, locations, and geologic settings are listed in table 1; these stations are all free-field, basement, or first-floor installations, and all except station 480 are in two-story or lower structures. The recordings, which were originally captured on film, have been digitized and disseminated by the California Strong Motion Instrumentation Project, managed by the California Division of Mines and Geology (CDMG).

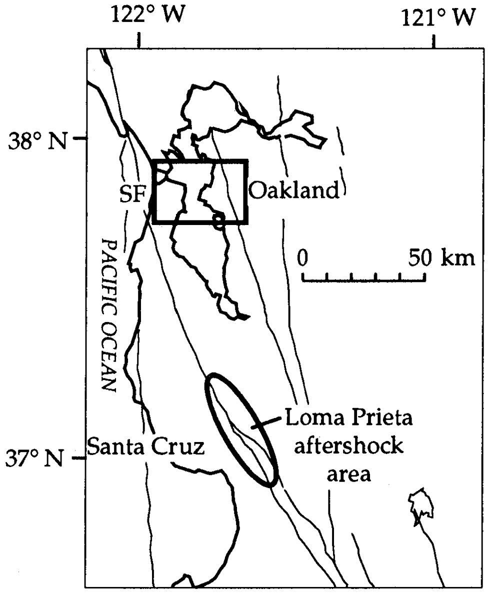

Figure 1.—San Francisco Bay region, showing locations of study area (rectangle) and Loma Prieta aftershock area. Irregular thin lines, faults. SF, San Francisco.

Table 1.—*Locations of and near-surface geology at 13 California Division of Mines and Geology strong-motion stations used in this study*

[See figure 2 for locations of stations. LBL, Lawrence Berkeley Laboratory; SF, San Francisco]

Station	Location	Near-surface geology
043	Point Bonita	2 m of broken rocks, sandstone.
117	Treasure Island	Fill.
130	SF, Diamond Heights	Franciscan chert.
131	SF, Pacific Heights	Franciscan sandstone, shale.
132	SF, Cliff House	Franciscan sandstone, shale.
151	SF, Rincon Hill	Franciscan sandstone, shale.
163	Yerba Buena Island	Franciscan sandstone.
222	SF, Presidio	Serpentine.
224	Oakland, 2-story building	Alluvium.
338	Piedmont, Junior High School	Weathered serpentine.
471	Berkeley, LBL	Thin alluvium on shale, siltstone.
472	Oakland, outer harbor wharf	Bay mud.
480	Oakland, 18-story building	Fill over bay mud.

These data are well suited for analysis of seismic-wave propagation because of the magnitude of the main shock and the close spacing of instrument sites relative to the epicentral distance. The earthquake generated sufficient long-period seismic energy that ground motion at a frequency of at least 0.2 Hz was reliably measured by strong-motion instruments. Similar periods were recovered from the 1971 San Fernando, Calif., earthquake, although fewer instruments were deployed at that time. The M_L=5.9 1987 Whittier Narrows, Calif., earthquake was recorded at a comparable number of stations, but strong-motion recordings did not have recoverable energy below 0.5 Hz. The group of 13 stations studied here lie within a 10- by 20-km area but are 60 to 100 km from the fault rupture, as estimated from aftershocks (Oppenheimer, 1990). Thus, the stations span only about 10°–15° in azimuth from the earthquake, and the signal that would be recorded across these stations would be similar in the absence of structural complexities, particularly in their direction of shaking.

The horizontal motion expected for a simple, layered structure is nearly perfectly linear polarization in the WSW–ENE direction, as shown in figure 2. These motions are calculated with a reflectivity simulation (Muller, 1985) and a simple source; the source mechanism and one-layer crustal structure assumed are listed in tables 2 and 3. The oblique thrust mechanism of the earthquake produced a large pulse of shear-wave energy on the transverse component and little motion on the radial and vertical components of motion at this azimuth and range, which is nearly directly along the San Andreas fault. A more complex earthquake extending tens of kilometers, such as the 1989 Loma Prieta earthquake, would produce more complex radiation, but it still would maintain a similar particle motion. The primary variation in particle motion predicted across the array is a rotation of the transverse direction of motion clockwise as one considers the stations more to the east. The large transverse pulse, which can also be thought of as an incipient Love wave, dominates all stations and appears on synthetic seismograms at all the frequencies considered in this paper.

The observed ground motions somewhat resemble the prediction of reflectivity simulations. The particle motion directions seen on the acceleration records in six different passbands are shown in figure 3. Comparison of the synthetic particle-motion directions with the observed directions shows a simple and unambiguous pattern: The directions of strongest motion at frequencies below 1 Hz shown in figure 3*A* generally agree with the directions expected from the simulation. Although longer period motion also shows the predicted pattern, it is not shown here because it is unclear up to what period the strong-motion recordings are accurate. The directions at frequencies above 1 Hz shown in figures 3*B* through 3*D* indicate directions of shaking that are increasingly unrelated to the direction expected. Although the highest frequency band shown, 3.2 to 6.4 Hz, shows some linear polarization, it does not correlate well with the prediction from the focal mechanism.

Some cautions must be noted. Time-domain information has been suppressed in this presentation, and so the initial *S*-wave arrivals may exhibit the polarization direction expected from the focal mechanism even at high frequencies, as observed for *S* waves by Bonamassa and Vidale (1991) and for *P* waves by Menke and Lerner-Lam (1991). Individual stations may record bizarre phenomena; for example, Treasure Island underwent liquefaction near the CDMG site (sta. 117, fig. 2), Cliff House (sta. 132) is located on steep topography (Borcherdt, 1990), Oakland (sta. 472) is located on a wharf that may be subject to water waves in the bay, and Oakland (sta. 480) is located in the basement of an 18-story building that may sway. Despite these potential outliers, the pattern is quite consistent across the array of strong-motion stations.

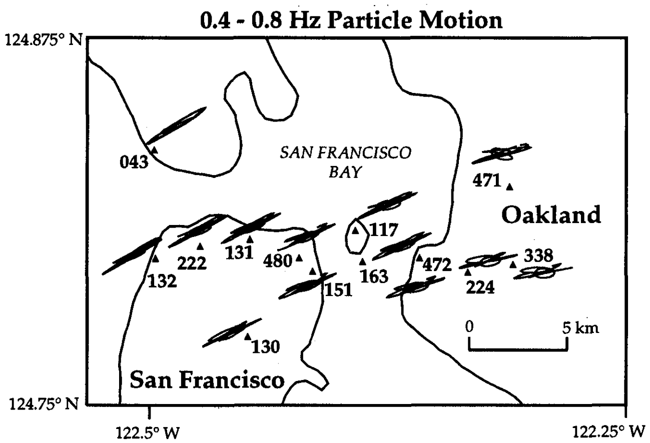

Figure 2.—Particle-motion diagrams for synthetic seismograms at 13 California Division of Mines and Geology strong-motion stations (numbered triangles; see table 1) in passband from 0.4 to 0.8 Hz (1.25- to 2.5-s period). Two passes of a three-pole Butterworth filter were applied.

Table 2.—*Source parameters of the earthquake*

Latitude	Longitude	Strike	Dip	Slip	Depth
37.036° N.	121.88° W.	130°	70°	135°	12 km

Table 3.—*One-layer model of crustal structure*

	Thickness (km)	*P*-wave velocity (km/s)	*S*-wave velocity (km/s)	$Q\alpha$	$Q\beta$	Density (g/cm^3)
Layer	25	6.2	3.60	200	150	2.66
Half space	- -	8.0	4.62	200	150	3.33

CONCLUSIONS AND UNANSWERED QUESTIONS

The relatively dense array of CDMG strong-motion stations across San Francisco and Oakland (fig. 2) provided one of the best fairly broadband (0.1–5.0 Hz) glimpses to date of the seismic wavefield generated by a large earthquake less than 100 km distant. The transition from particle motion that indicates source characteristics to particle motion that is strongly affected by propagation through the Earth clearly takes place near 1 Hz. This highly varying, high-frequency polarization is consistent with the results from most previous studies; Vidale (1989), Bonamassa and Vidale (1991), and Vidale and others (1991) saw a similar gross distortion of 2- to 20-Hz seismic waves, probably due to near-surface geology. As mentioned above, comparisons of seismic waves recorded on the surface and in boreholes document the scrambling effects of the near surface at high frequencies (Haukkson and others, 1987; Aster and Shearer, 1991a, b).

The coherence below 1 Hz is also consistent with previous work. Trifunac (1988) showed that the 0.5- to 1.0-Hz seismic waves generated by the 1987 Whittier Narrows earthquake were fairly coherent. Liu and Helmberger (1985) performed a similar analysis at a closer range of 5 to 20 km, with a comparable result of 2 Hz. Innumerable local, regional, and teleseismic earthquake source inversions have invariably proceeded on the assumption that seismic waves interact with Earth structure which is a stack of layers in the most complex case, and source studies commonly interpret seismic energy up to frequencies near 1 Hz as indicating details of rupture propagation.

In contrast, Ebel and Bonjer (1990) found that the 10-Hz particle motions of small earthquakes sometimes do reflect the focal mechanism. His study is in the stable craton in Germany, however, and so the confounding effect of the near surface may be strongest in such active tectonic regions as California, where all the other investigations were sited.

The questions that remain are, What geologic structures scramble the high-frequency polarization characteristics? The low spatial coherence suggests shallow structure, the borehole studies suggest shallow structure, and to the extent that common sense applies, the observation that the near surface is the least consolidated and most highly varying volume along the seismic-ray path suggests that the structures lie near the surface. Candidates for these near-surface structures include surface topography (Bard and Gariel, 1986; Kawase and Aki, 1989) and topography on the soil/rock interface (Bard and Tucker, 1985). Candidate for wave interactions include focusing through seismic velocity gradients acting as lenses (Langston and Lee, 1983; Rial, 1989); body- to surface-wave conversions at sharp, laterally heterogeneous velocity contrasts (Bard and Gariel, 1986; Vidale and Helmberger; 1988, Kawase and Aki, 1989); and energy that becomes trapped and reverberates between high-contrast interfaces (Novaro and others, 1990).

The task remaining is the construction of simulations with such methods as three-dimensional finite differences (Frankel and others, 1990; Frankel and Vidale, 1992) that reproduce the complexity we observe in the seismic wavefield, using realistic velocity models. This task relies on the equally difficult task of accurately estimating realistic three-dimensional velocity models of the near surface.

It is important to learn the processes affecting high-frequency seismic waves for earthquake-hazard mitigation, earthquake-source determination, and seismic-array-design goals. So far, three-dimensional site characterization is empirical, not based on an understanding of the physics involved. Clearly, optimal high-frequency seismic arrays that aim to study seismic sources must minimize the interference from Earth structure. Earthquake-source inversions must allow sufficient variance in the solutions to withstand the randomization of high-frequency waves by structure. Finally, site characterization for seismic-

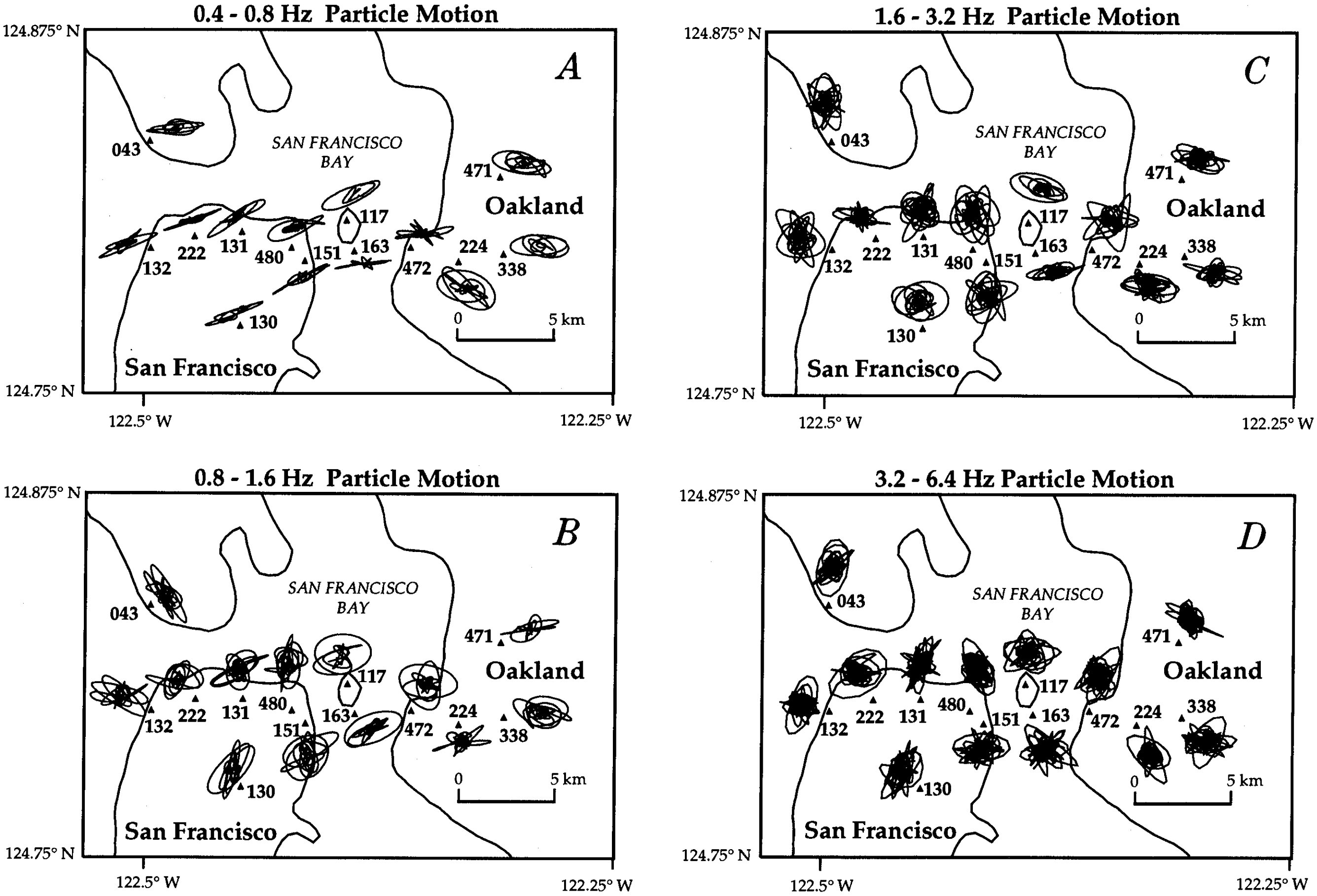

Figure 3.—Particle-motion diagrams for observations at 13 California Division of Mines and Geology strong-motion stations (numbered triangles; see table 1) in passbands (*A*) from 0.4 to 0.8 Hz (1.25- to 2.5-s period), (*B*) from 0.8 to 1.6 Hz, (*C*) from 1.6 to 3.2 Hz, and (*D*) from 3.2 to 6.4 Hz.

hazard mitigation might become a more precise science when phase as well as amplitude information is incorporated into predictions of shaking in future earthquakes.

ACKNOWLEDGMENTS

This research was supported by the California Strong Motion Instrumentation Program of the California Division of Mines and Geology under contract 8-9136 and by the Defense Advanced Research Projects Agency of the U.S. Department of Defense under contract F19628-89-K-0048. We thank Paul Spudich for his review of the manuscript. Charles Ammon ran the reflectivity code.

REFERENCES CITED

Abrahamson, N.A., Schneider, J.F., and Stepp, J.C., 1989, Spatial coherency of strong ground motion for application to soil structure interaction [abs.]: Seismological Research Letters, v. 60, no. 1, p. 3.

Andrews, D.J., 1986, Objective determination of source parameters and similarity of earthquakes of different size, *in* Das, Shamita, Boatwright, John, and Scholz, C.H., eds., Earthquake source mechanics: American Geophysical Union Geophysical Monograph 37, p. 259–267.

Aster, R.C., and Shearer, P.M., 1991a, High-frequency borehole seismograms recorded in the San Jacinto fault zone, southern California. Part 1. Polarizations: Seismological Society of America Bulletin, v. 81, no. 4, p. 1057–1080.

———1991b, High-frequency borehole seismograms recorded in the San Jacinto fault zone, southern California. Part 2. Attenuation and site effects: Seismological Society of America Bulletin, v. 81, no. 4, p. 1081–1100.

Bard, P.-Y., and Gariel, J.C., 1986, The seismic response of two-dimensional sedimentary deposits with large vertical velocity gradients: Seismological Society of America Bulletin, v. 76, no. 2, p. 343–360.

Bard, P.-Y., and Tucker, B.E., 1985, Underground and ridge site effects; a comparison of observation and theory: Seismological Society of America Bulletin, v. 75, no. 4, p. 905–922.

Bonamassa, Ornella, and Vidale, J.E., 1991, Directional site resonances observed from aftershocks of the 18 October 1989 Loma Prieta earthquake: Seismological Society of America Bulletin, v. 81, no. 5, p. 1945–1957.

Bonamassa, Ornella, Vidale, J.E., Houston, Heidi, and Schwartz, S.Y., 1991, Directional site resonances and the strong influence of near-surface geology on ground motion: Geophysical Research Letters, v. 18, no. 3, p. 901–904.

Borcherdt, R.D., 1970, Effects of local geology on ground motion near San Francisco Bay: Seismological Society of America Bulletin, v. 60, no. 1, p. 29–61.

———1990, Influence of local geology in the San Francisco Bay region, California on ground motions generated by the Loma Prieta earthquake of October 17, 1989: International Symposium on Safety of Urban Life and Facilities, Tokyo, 1990, Proceedings, p. 1.1–1.35.

Cranswick, Edward, 1988, The information content of high-frequency seismograms and the near-surface geologic structure of "hard rock" recording sites: Pure and Applied Geophysics, v. 128, no. 1–2, p. 333–363.

Dietel, Christopher, Chouet, Bernard, Aki, Keiiti, Ferrazzini, Valerie, Roberts, Peter, and Koyanagi, R.Y., 1989, Data summary for dense GEOS array observations of seismic activity associated with magma transport at Kilauea Volcano, Hawaii: U.S. Geological Survey Open-File Report 89–113, 171 p.

Ebel, J.E., and Bonjer, K.P., 1990, Moment tensor inversion of small earthquakes in southwestern Germany for the fault plane solution, Geophysical Journal International, v. 101, no. 1, p. 133–146.

Frankel, Arthur, Hough, S.E., Friberg, Paul, and Busby, R.W., 1990, Analysis and modeling of waveforms of Loma Prieta aftershocks recorded on a dense array in Sunnyvale, California [abs.]: Eos (American Geophysical Union Transactions), v. 71, no. 43, p. 1456.

Frankel, Arthur, and Vidale, J.E., 1992, A three-dimensional simulation of seismic waves in the Santa Clara Valley, California, from a Loma Prieta aftershock: Seismological Society of America Bulletin, v. 82, no. 5, p. 2045–2074.

Haukkson, Egill, Teng, T.-L., and Henyey, T.L., 1987, Results from a 1500 m deep, three-level downhole seismometer array; site response, low Q values, and f_{max}: Seismological Society of America Bulletin, v. 77, no. 6, p. 1883–1904.

Joyner, W.B., Warrick, R.E., and Fumal, T.E., 1981, The effect of Quaternary alluvium on strong ground motion in the Coyote Lake, California, earthquake of 1979: Seismological Society of America Bulletin, v. 71, no. 4, p. 1333–1349.

Joyner, W.B., Warrick, R.E., and Oliver, A.E., III, 1976, Analysis of seismograms from a downhole array in sediments near San Francisco Bay: Seismological Society of America Bulletin, v. 66, no. 3, p. 937–958.

Kagami, Hiroshi, Okada, Shigeyuki, Shiono, Keishi, Oner, Mete, Dravinski, Marijan, and Mal, A.K., 1986, Observation of 1- to 5-second microtremors and their application to earthquake engineering. Part III. A two-dimensional study of site effects in the San Fernando Valley: Seismological Society of America Bulletin, v. 76, no. 6, p. 1801–1812.

Kawase, Hiroshi, and Aki, Keiiti, 1989, A study on the response of a soft basin for incident *S*, *P*, and Rayleigh waves with special reference to the long duration observed in Mexico City: Seismological Society of America Bulletin, v. 79, no. 5, p. 1361–1382.

Langston, C.A., and Lee, J.-J., 1983, Effect of structure geometry on strong ground motions; the Duwamish River Valley, Seattle, Washington: Seismological Society of America Bulletin, v. 73, no. 6, p. 1851–1863.

Liu, H.-L., and Helmberger, D.V., 1985, The 23:19 aftershock of the 15 October 1979 Imperial Valley earthquake; more evidence for an asperity: Seismological Society of America Bulletin, v. 75, no. 3, p. 689–709.

Malin, P.E., Waller, J.A., Borcherdt, R.D., Cranswick, Edward, Jensen, E.G., and Van Schaak, J.R., 1988, Vertical seismic profiling of Oroville microearthquakes: velocity spectra and particle motion as a function of depth: Seismological Society of America Bulletin, v. 78, no. 2, p. 401–420.

Menke, William, and Lerner-Lam, Arthur, 1991, Observations of the transition from linear polarization to complex polarization in short-period compressive waves: Seismological Society of America Bulletin, v. 81, no. 2, p. 611–621.

Muller, G., 1985, The reflectivity method; a tutorial: Journal of Geophysics, v. 58, no. 1–3, p. 153–174.

Novaro, O., Seligman, T.H., Alvarez-Tostado, J.M., Mateos, J.L., and Flores, Jorges, 1990, Two-dimensional model for site effect studies of microtremors in the San Fernando Valley: Seismological Society of America Bulletin, v. 80, no. 2, p. 239–251.

Oppenheimer, D.H., 1990, Aftershock slip behavior of the 1989 Loma Prieta, California earthquake: Geophysical Research Letters, v. 17, no. 8, p. 1199–1202.

Rial, J.A., 1989, Seismic wave resonance in 3–D sedimentary basins:

Royal Astronomical Society Geophysical Journal, v. 99, no. 1, p. 81–90.

Rogers, A.M., Borcherdt, R.D., Covington, P.A., and Perkins, D.M., 1984, A comparative ground response study near Los Angeles using recordings of Nevada nuclear tests and the 1971 San Fernando earthquake: Seismological Society of America Bulletin, v. 74, no. 5, p. 1925–1949.

Trifunac, M.D., 1988, The Whittier Narrows, California earthquake of October 1, 1987—note on peak accelerations during the 1 and 4 October earthquakes: Earthquake Spectra, v. 4, no. 1, p. 101–114.

Vidale, J.E., 1989, Influence of focal mechanism on peak accelerations of strong ground motions for the Whittier Narrows, California, earthquake and an aftershock: Journal of Geophysical Research, v. 94, no. B7, p. 9607–9613.

Vidale, J.E., Bonamassa, Ornella, and Houston, Heidi, 1991, Directional site resonances observed from the 1 October 1987 Whittier Narrows, California, earthquake and the 4 October aftershock: Earthquake Spectra, v. 7, no. 1, p. 107–125.

Vidale, J.E., and Helmberger, D.V., 1988, Elastic finite-difference modeling of the 1971 San Fernando, California earthquake: Seismological Society of America Bulletin, v. 78, no. 1, p. 122–141.

THE LOMA PRIETA, CALIFORNIA, EARTHQUAKE OF OCTOBER 17, 1989:
STRONG GROUND MOTION AND GROUND FAILURE

STRONG GROUND MOTION

EFFECT OF CRITICAL REFLECTIONS FROM THE MOHO ON THE ATTENUATION OF STRONG GROUND MOTION

By Paul G. Somerville, Nancy F. Smith, and Robert W. Graves,
Woodward-Clyde Consultants

CONTENTS

ABSTRACT

The peak accelerations from the earthquake showed a more gradual attenuation with distance than predicted by standard attenuation relations. By analyzing profiles of main-shock and aftershock recordings with absolute times, and by generating profiles of synthetic strong-motion records, we have examined evidence for the effects of wave propagation in a layered crust on the attenuation of strong ground motions. At distances within about 50 km, the motions with the largest amplitudes were due to waves traveling directly upward from the source. Analysis of arrival time and phase velocity, however, indicates that the motions with the largest amplitudes at distances beyond about 50 km were critical reflections from interfaces beneath the source, predominantly the Moho. Further support for this interpretation is provided by recordings in San Francisco of explosions fired in the Loma Prieta epicentral area, which also show strong critical reflections from the Moho. Using strong-motion simulations, we estimate that in the San Francisco-Oakland area, the critically reflected waves had peak amplitudes about 2.5 times larger on average than the direct waves. These reflections were large and occurred at relatively close distances because of the relatively thin crust and deep earthquake-source depth, and they are a primary reason why the ground motions from the earthquake exceeded standard empirical predictions at distances beyond about 50 km for all categories of site conditions. Effects that further amplified ground motions in the San Francisco-Oakland area include rupture directivity and, at soft-soil sites, impedance contrast and resonance.

INTRODUCTION

Peak accelerations from the earthquake showed a more gradual attenuation with distance than predicted by standard attenuation relations, such as those summarized by Joyner and Boore (1988). Campbell (1991) reported that peak accelerations on alluvium showed no attenuation in the distance range 50–80 km, with distance defined as the closest distance to the rupture surface. Peak accelerations recorded in the San Francisco-Oakland area, at distances of about 80 to 100 km, exceeded those predicted by standard empirical attenuation relations, as shown in figure 1 (Boore and others, 1989) for all categories of site conditions. In these empirical attenuation relations, the effects of different focal depths and propagation paths on ground-motion attenuation are averaged to obtain a median estimate of the ground motions (solid curve, fig. 1). The variation in ground motions due to differences in wave-propagation conditions (such as earthquake-source depth and crustal structure) is included, together with other causes of variation, such as source and site effects, in the standard deviation of the median estimate (dashed curves, fig. 1). The objective of this paper is to investigate the influence of wave-propagation effects on the discrepancy between the observed ground-motion attenuation and that predicted by standard empirical attenuation relations.

WAVE-PROPAGATION ANALYSIS OF GROUND-MOTION ATTENUATION

The propagation of body waves in a horizontally layered crust is illustrated schematically in figure 2, as discussed by Burger and others (1987). At close distances, peak horizontal ground motions are controlled by direct upgoing shear waves. As distance increases, the reflections of the shear wave from interfaces below the source reach the critical angle and undergo critical reflection. The strong contrast in elastic moduli at these interfaces, especially the Moho, causes these critically reflected waves to have large amplitudes. Critically reflected waves are commonly observed in the *P*, and sometimes observed in the *S*, waves recorded during seismic-refraction experiments (for example, Gajewski and others, 1990), and such reflected waves are expected also to be present in earthquake ground motions. Bakun and Joyner (1984) found a positive residual in M_L values in central California at distances between 75 and 125 km and suggested that it may be due to Moho reflections. Somerville and others (1992) found evidence for the presence of critical Moho reflections, and a flattening in the ground-motion attenuation of individual earthquakes, in strong-motion recordings of most major California earthquakes. Critical reflections from the lower crust were found to dominate the amplitudes of strong-motion recordings of the October 25, 1988, Saguenay, Quebec, Canada, earthquake at distances beyond 65 km (Somerville and others, 1990).

The clearest evidence of the effect of critical reflections on ground-motion attenuation in the San Francisco Bay region comes from recordings of explosions and aftershocks, events that have briefer source processes than the main shock and thus provide a clearer representation of wave-propagation effects. Large critical reflections of *P* waves from the Moho were observed in a series of explosions that were detonated in the Loma Prieta area and near the north end of the Golden Gate Bridge in Marin County during summer 1991 (Catchings and Fuis, 1991). The data show large critical reflections in the northern part of the San Francisco Bay region (in the distance range 80–100 km) from the Loma Prieta shots, and in the Loma Prieta area from the Marin County shots. Critical Moho reflections were also observed in earlier seismic-refraction studies in coastal central California, as summarized by Walter and Mooney (1982).

Critical reflections were also identified in recordings of aftershocks of the 1989 Loma Prieta earthquake by McGarr and others (1991) and Somerville and Smith (1991). A profile of the east component of velocity recorded at stations northwest of the 1:30 a.m. P.s.t. November 5, 1989, aftershock, as described by Mueller and Glassmoyer (1990), is shown in figure 3*A*. All of the recordings have absolute times, allowing them to be aligned in time with a traveltime reduction of 3.5 km/s. Superimposed on this profile are the traveltimes for direct *S* waves, critical Conrad reflections (S_cS), and critical Moho reflection (S_mS). A profile of synthetic seismograms generated by using the reflectivity method, similar to that shown by Chin and Aki (1991, fig. 5), is shown in figure 3*B*.

Except at the closest station, the direct arrival has a small amplitude relative to later arrivals, and the first conspicuous phase has the arrival time of the critical Conrad reflection (S_cS). The largest phase at all stations except the closest station occurs soon after the expected arrival time of the critical Moho reflection (S_mS). These aftershock recordings indicate that at distances beyond about 50 km, the recorded peak ground-motion ampli-

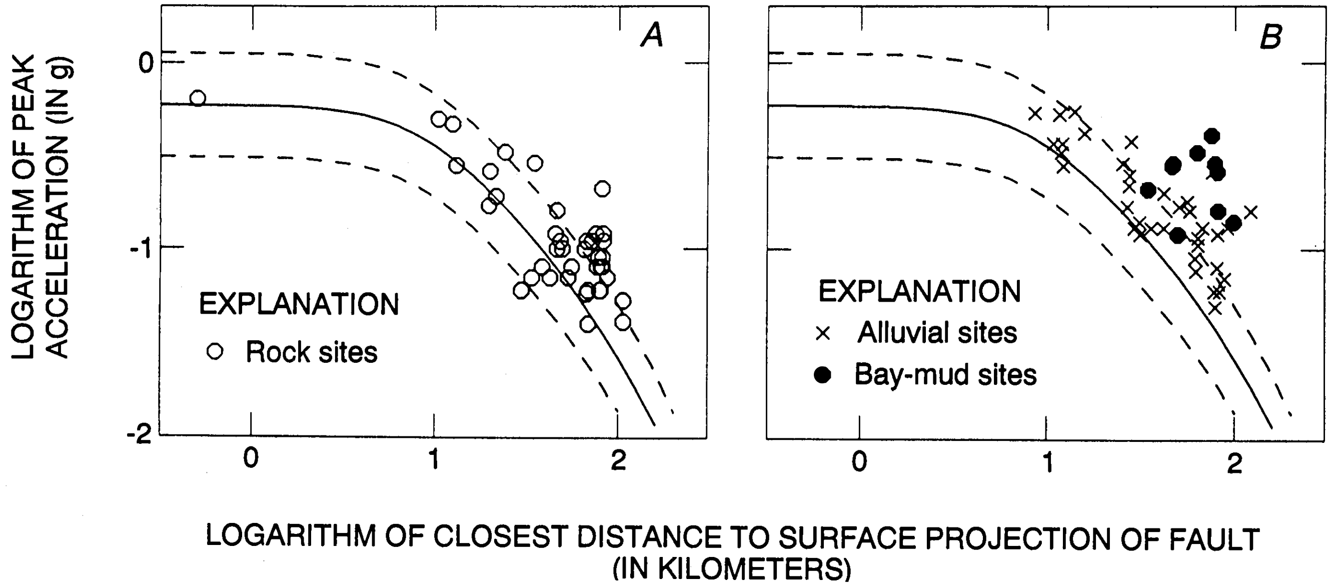

Figure 1.—Recorded peak horizontal acceleration as a function of distance from surface projection of Loma Prieta rupture zone for rock sites (*A*) and alluvium and bay-mud sites (*B*). Solid curve, median; dashed curves, standard deviation. From Boore and others (1989).

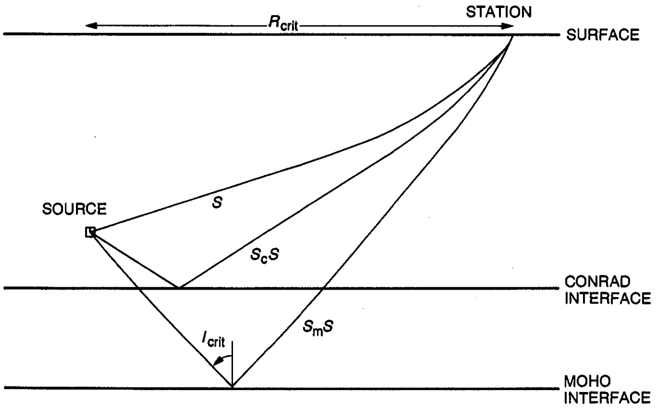

Figure 2.—Schematic diagram of wave-propagation model, showing direct waves (S) and reflected waves (S_cS and S_mS). At critical angle (i_{crit}), incident wave is totally reflected back to surface at distances starting at critical distance R_{crit}.

tudes are controlled not by the direct S wave but by the wave that is critically reflected from the Moho.

Preliminary analyses of the influence of critical reflections on the attenuation of strong ground motion from the Loma Prieta main shock were made by Somerville and Yoshimura (1990) and Somerville and Smith (1991). Somerville and Yoshimura used an assumed rupture model of the earthquake, whereas Somerville and Smith used the rupture model of Wald and others (1991), refined by using higher frequencies (P.G. Somerville and others, unpub. data, 1992). The analysis presented here is similar to that by Somerville and Smith but is further refined to include the effects of radiation-pattern differences between the direct and reflected rays.

A record section of accelerograms of the earthquake (fig. 4A) was compiled from all accelerograms to the

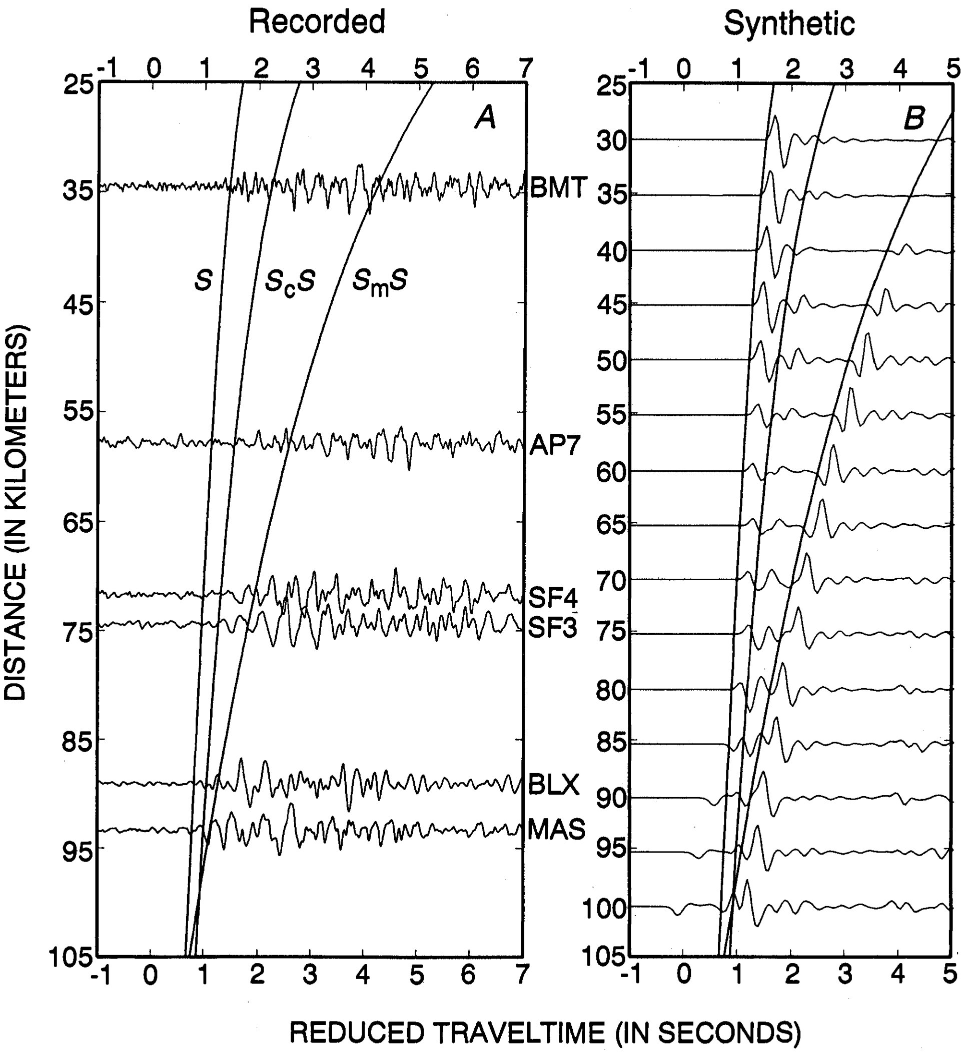

Figure 3.—Velocity profiles. A, Recorded velocity (east component) of 1:30 a.m. P.s.t. November 5, 1989, aftershock of 1989 Loma Prieta earthquake, compiled using epicentral distance and a traveltime reduction of 3.50 km/s. Arrival-time curves are explained in text. Symbols on right side of plot are U.S. Geological Survey station codes. B, Synthetic velocity seismograms.

north of the epicenter (that is, in the San Francisco Bay region) that have known trigger times (Maley and others, 1989; Shakal and others, 1989), using the origin time derived from strong-motion instruments. The recordings were obtained under various site conditions, as annotated in figure 4 and discussed further below. Arrival-time curves for three principal waves are also shown in figure 4: the direct shear wave (*S*), the shear wave reflected from the Conrad layer at a depth of 19 km (S_cS), and the shear wave reflected from the Moho at a depth of 25 km (S_mS). The smaller, lower frequency refracted arrivals S_c and S_n are shown by dashed lines. The curves were computed from the crustal-structure model listed in table 1 derived from that of Dietz and Ellsworth (1990), using a focal depth of 12 km to represent the center of energy release (Kanamori and Satake, 1990; Nábělek, 1990; Wald and others, 1991). To facilitate interpretation of the strong-motion data using these point-source traveltime curves, the accelerograms are plotted in the profile at their epicentral distances rather than at their closest distance to the fault.

To generate the synthetic accelerograms in figure 4, we used the method of Hadley and others (1982), as refined by Wald and others (1988) and described by Somerville and others (1991). For crustal earthquakes, the ground motions of the large event are obtained by summing the contributions from fault elements with dimensions of 3 by 4 km. Strong-ground-motion recordings very close to the source of an M=5.2 earthquake, scaled back to the source, are used to represent the source functions of the fault elements. Green's functions, including the direct *S* wave and primary reflections from interfaces, as calculated from the regional-structure model, are used to represent the propagation path. The contributions from each fault element are lagged, scaled, and summed so as to simulate rupture propagation over the fault surface. Asperities are modeled by weighting the contributions of the fault elements. The decrease in coherence of the radiation pattern that is observed to occur as frequencies increase is represented empirically by using a suite of empirical source functions. The reliability of this method in predicting the near-source motions

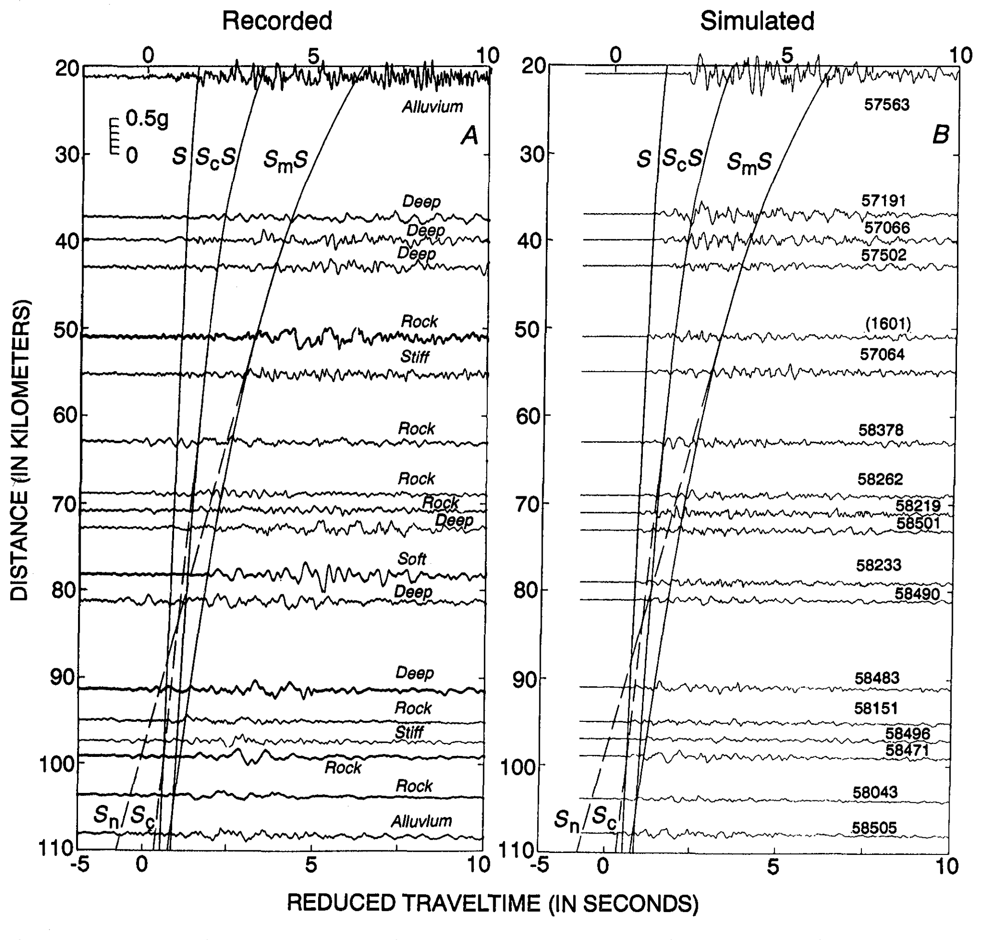

Figure 4.—Profiles of recorded (*A*) and simulated (*B*) accelerograms of 1989 Loma Prieta earthquake, compiled using epicentral distance and a traveltime reduction of 3.50 km/s. Arrival-time curves are explained in text. Soil conditions are annotated at right in figure 4*A*. Numbers in figure 4*B* are codes of stations in California Division of Mines and Geology's California Strong Motion Instrument Program network; numbers in parentheses are codes of stations in U.S. Geological Survey network.

Table 1.—*Loma Prieta velocity model, modified from crustal-structure model of Dietz and Ellsworth (1990).*

V_P (km/s)	V_S (km/s)	Density (g/cm3)	Depth (km)
1.730	1.00	1.50	0.10
3.380	1.95	1.55	.50
4.290	2.48	1.85	1.00
4.790	2.77	2.05	3.00
5.365	3.10	2.26	5.00
5.740	3.31	2.45	7.00
6.150	3.55	2.58	9.00
6.245	3.61	2.62	13.00
6.270	3.62	2.63	18.00
6.665	3.85	2.77	25.00
8.000	4.62	3.28	---

of the earthquake was estimated (P.G. Somerville and others, unpub. data, 1992), using the procedure of Abrahamson and others (1990).

We used a rupture model of the earthquake based on that of Wald and others (1991), refined by using higher frequencies (P.G. Somerville and others, unpub. data, 1992) from the inversion of near-source strong-motion data. The rupture surface is 40 km long by 15 km wide, and rupture spreads circularly from the 18-km-deep hypocenter at an average speed of 2.7 km/s that is independent of depth. Slip occurs in three time windows, each with 0.7-s duration and 0.1-s overlap. The seismic moment is 2.9×10^{26} dyne-cm, and the strike and dip are 128° and 70°, respectively (Kanamori and Satake, 1990). The rake varies on the fault plane. A near-source, range-independent component of anelastic absorption was represented empirically by that contained in the empirical source functions, which were derived from recordings of an M=5.2 aftershock of the 1979 Imperial Valley, Calif., earthquake (Liu and Helmberger, 1985) and an M=5.2 aftershock of the 1987 Whittier Narrows, Calif., earthquake (Joanne Yoshimura and C.K. Saikia, unpub. data, 1992). The peak-acceleration estimates are averages of separate simulations, using each of these two sets of empirical source functions.

We use arrival time and phase velocity to distinguish between different phases in the record section shown in figure 4. The onset of the largest accelerations at each station coincides with the arrival time of the critical Moho reflection (S_mS) at distances beyond about 50 km. The moveout of this onset with distance follows the S_mS traveltime curve and not that of the direct S wave. The duration of strong motion following the S_mS traveltime curve is about 5 s, which is compatible with the 6-s duration of the source observed teleseismically (Kanamori and Satake, 1990; Nábělek, 1990). We see a similar pattern in a profile of simulated accelerograms shown in figure 4*B*. These simulated accelerograms have large S_mS waves whose onset coincides with the S_mS traveltime curve and whose moveout is that of the S_mS arrival and not that of the direct S wave. The duration of strong motion of the simulated S_mS waves is about 5 s. In all of these respects, the simulated accelerograms resemble the recorded accelerograms, supporting the interpretation of the recorded accelerograms presented above. The simulated accelerograms were generated by using a crustal-structure model with a surface shear-wave velocity of 1 km/s, appropriate for soft-rock or stiff-soil conditions.

The peak accelerations on the simulated accelerograms trend similarly to those on the recorded accelerograms, as shown in figure 5, where the northerly profile of stations has been augmented by stations that lie within 30 km of the epicenter, demonstrating that the simulations agree well with the recorded data at close distances (P.G. Somerville and others, unpub. data, 1992). The peak accelerations attenuate normally to about 40 km but no further until reaching a distance of 80 km. In the distance range 60–100 km, the largest simulated motions at a given station are due to critical reflections, and we infer this interpretation also to be true of the recorded motions on the basis of the similarity in arrival times and phase

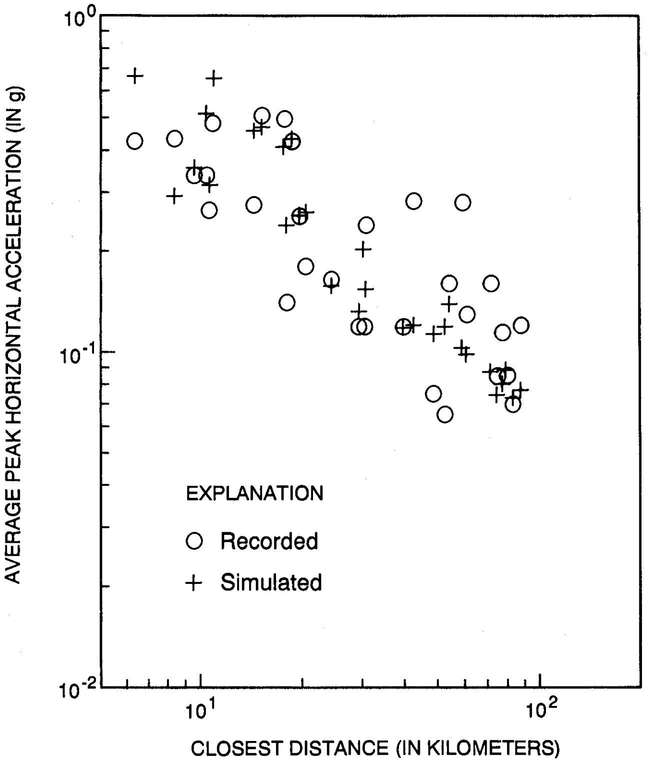

Figure 5.—Recorded (circles) and simulated (crosses) peak horizontal acceleration as a function of closest distance at sites within 30 km of epicenter and at sites within the San Francisco Bay region with known trigger times.

velocity described above. Although site conditions are presumably responsible for the larger scatter in recorded peak accelerations than in the simulated ones at a given distance, site conditions do not appear to explain the absence of attenuation between 40 and 80 km in both the recorded and simulated motions.

The relatively long source duration of the earthquake makes unambiguous identification of specific seismic phases, such as S_mS, difficult. However, in conjunction with the aftershock data plotted in figure 3 and the explosion data described by Catchings and Fuis (1991), the evidence based on traveltime and phase velocity from the main-shock strong motions strongly suggests that the motions were critical reflections.

COMPARISON OF CONTRIBUTIONS FROM DIRECT AND CRITICALLY REFLECTED RAYS

To examine the relative importance of direct and critically reflected rays, we performed separate simulations of the recorded ground motions for these rays. To minimize the effects of site conditions in comparing predictions with observations, we chose the set of 71 alluvial sites analyzed by Campbell (1991). In the set of critically reflected rays, we included the first critical reflection from each layer beneath the source. The attenuation of peak acceleration for each of these two sets of rays is plotted in figure 6*A*. The direct ray produces the largest peak accelerations out to a closest distance (*R*) of about 40 km. For closest distances greater than about 20 km, these peak accelerations attenuate more rapidly than 1/*R* because of geometric spreading of the upgoing wavefront as it propagates through lower velocity layers near the Earth's surface. The reflected rays produce the largest peak accelerations at distances beyond about 40 km. The peak acceleration of the reflected rays is approximately constant from the near-source region out to 80 km, with a broad peak centered at about 50 km, falling off rapidly beyond 80 km. The peak amplitudes of these reflected waves are larger than would be predicted from 1/*R* geometric spreading. In the San Francisco-Oakland area, peak amplitudes of the simulated critically reflected waves average about 2.5 times larger than those of the direct waves.

The peak accelerations of the complete simulations are compared with the recorded data and the attenuation relation derived from them by Campbell (1991) in figure 6*B*. The attenuation of the complete simulations re-

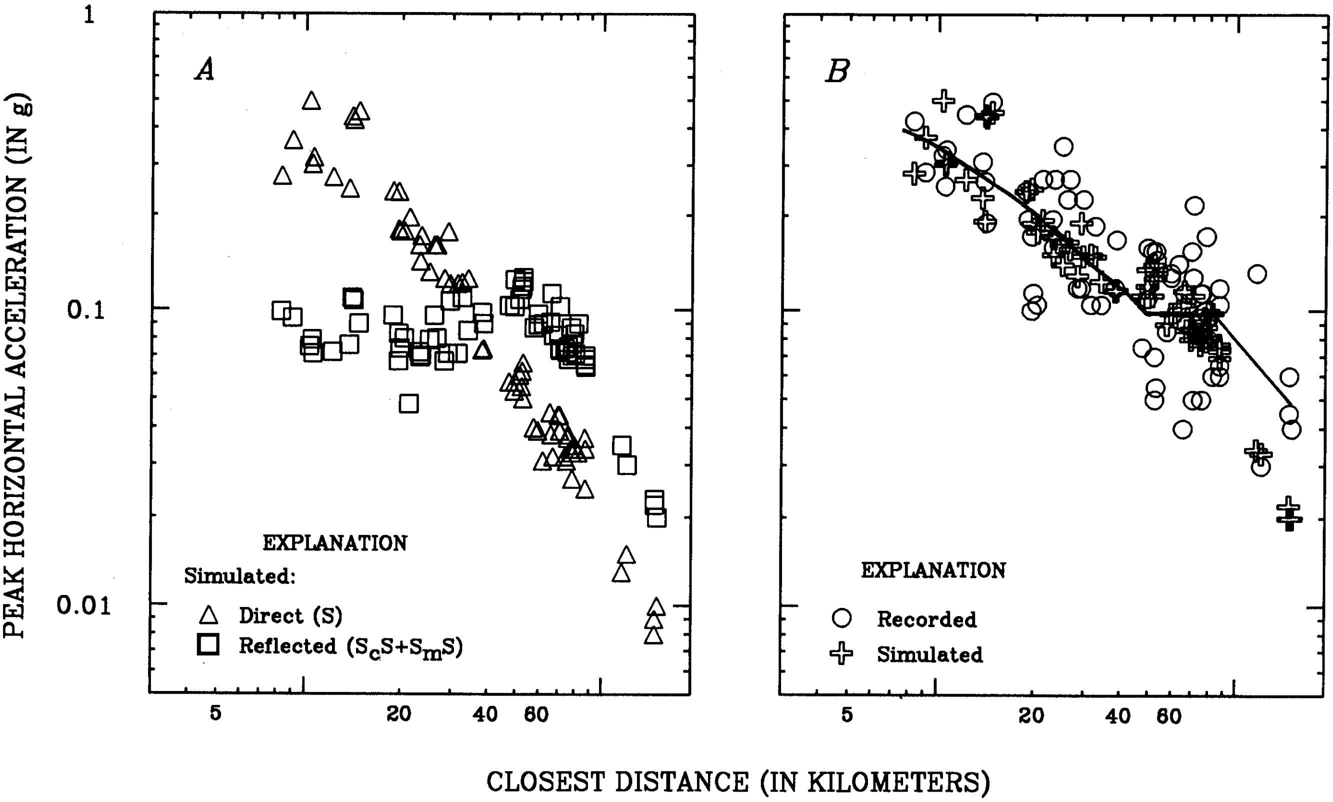

Figure 6.—Peak horizontal acceleration as a function of closest distance for 71 alluvial sites studied by Campbell (1991). *A*, Simulated direct (*S* wave; triangles) and critically reflected (S_cS and S_mS waves; squares) rays. *B*, Recorded (circles) and simulated (crosses) accelerations. Curve is attenuation relation fitted to recorded data by Campbell.

sembles the envelope of the attenuation of the individual ray sets in figure 6*A*. The flat trend of residuals of the simulated peak accelerations with respect to the recorded data, as shown in figure 7*A*, demonstrates that out to distances of 100 km, the simulated peak accelerations generally agree well with the recorded peak accelerations, although there is much more scatter in the recorded data than in the simulations, owing to the varying site conditions at the alluvial recording sites. The generally flat trend of residuals of the simulated peak accelerations with respect to the Campbell attenuation relation, as shown in figure 7*B*, indicates a flattening in the attenuation of the simulated peak accelerations, although the attenuation in the simulations is not so gradual as to be flat (like the Campbell relation) in the distance range 50–80 km.

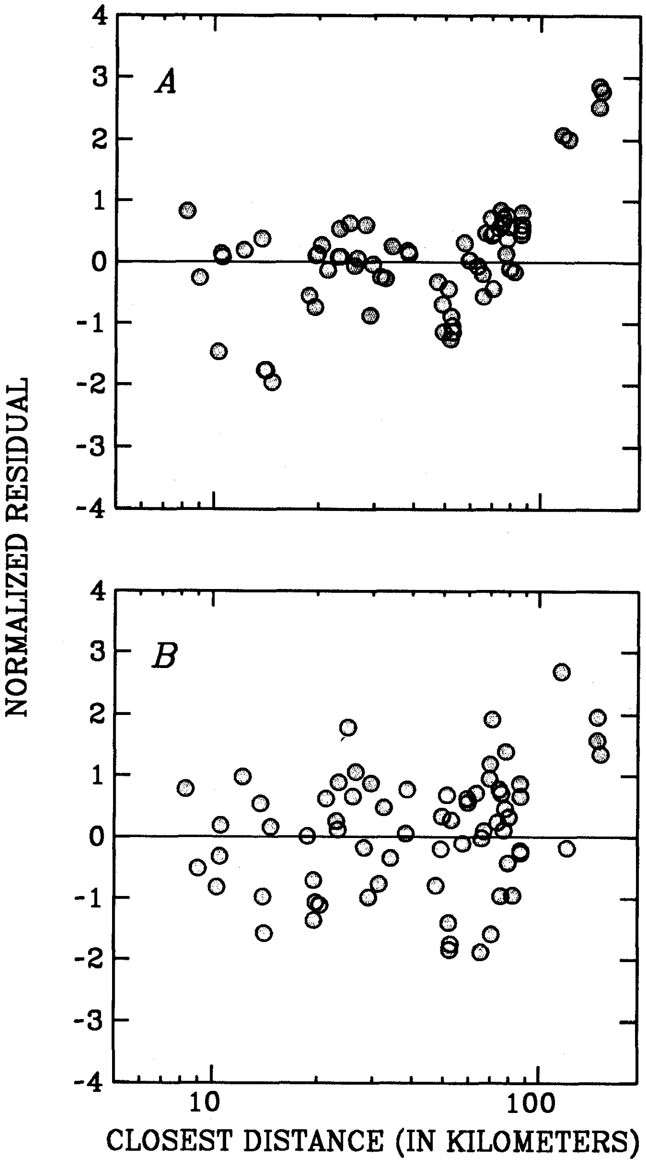

Figure 7.—Residuals between logarithms of recorded and simulated peak horizontal acceleration (*A*) and between attenuation relation of Campbell (1991) and simulated accelerations (*B*), normalized by standard error.

At distances beyond 100 km, the simulations significantly underpredict the data. Including additional rays, such as sS_mS, in the generation of synthetic seismograms improves the fit at these distances but cannot account for all the mismatch. Dreger and Helmberger (1991) showed a strong correlation between the strength of these additional phases and the source mechanism for moderate events. The empirical source functions used in our simulations are all from near-source recordings, where the radiation pattern can become smeared at high frequencies, owing to such effects as scattering and multipathing. At large distances, the radiation pattern may become more coherent for high frequencies, and so the empirical source functions we have used may not adequately model these effects. Other factors, such as the presence of a velocity gradient below the Moho or lateral variations in structure, can significantly affect the response at these distances. A complete discussion of these issues is beyond the scope of this paper.

DISCUSSION AND CONCLUSIONS

In the preceding analysis, we have concentrated on the effect of critical reflections from the base of a flat-layered crustal model as an explanation for the elevated ground-motion levels recorded in the San Francisco-Oakland area. Ground-motion amplitudes, however, are influenced by various of source, path, and site effects, several of which may coexist. It is important to identify which of these different effects was the predominant cause of the widespread elevation of recorded ground-motion amplitudes in San Francisco and Oakland.

Source effects.—The profile of simulated accelerograms shown in figure 4*B* includes the effects of strongly radiating patches (asperities) in the slip model of Wald and others (1991), refined by using higher frequencies (P.G. Somerville and others, unpub. data, 1992). Using a uniform slip model in place of this heterogeneous slip model reduces the overall amplitudes of the simulated motions, resulting in underprediction of the recorded motions. Such changes in the rupture model of the earthquake, however, do not change the shape of the simulated attenuation curve, indicating that its shape is not attributable to source complexity.

Directivity.—The systematic pattern of azimuthal variation observed by Campbell (1991) at distances beyond about 40 km shows peak accelerations about 20 percent above average recorded along strike to the northwest on the San Francisco peninsula and about 30 percent below average recorded to the north in the southeastern part of the San Francisco Bay region. This pattern, which is reproduced in our ground-motion simulations, is attributable to the effect of rupture directivity of the bilateral rupture, in which two-thirds of the seismic-moment release occurred to the northwest of the hypocenter. The different distribution of the distances of recording stations in these two directions tends to accentuate the flattening of the attenuation relation. In the closest distance range 20–50 km, where northerly stations predominate, the motions are reduced by the absence of directivity, whereas at distances beyond 50 km, where northwesterly stations predominate, the motions are enhanced by directivity. The data plotted in figure 6 predominantly represent the attenuation of direct rays in the northerly direction out to 50 km, and the attenuation of critically reflected rays in the northwesterly direction for distances beyond 50 km. The directivity of the earthquake resulted in relatively brief, large motions in the San Francisco Bay region. If the rupture had propagated unilaterally to the southeast, we calculate that the ground accelerations in the San Francisco-Oakland area would have been about 30 percent lower in amplitude and about 50 percent longer in duration. The effect of directivity on simulated peak accelerations in the near-source region is found to be insignificant in these calculations.

Site conditions.—The set of alluvial stations analyzed by Campbell (1991) was chosen to minimize the variation in the ground-motion-attenuation curve due to site conditions. As shown in figure 6, this relatively homogeneous data set shows a flattening in the attenuation curve, suggesting that it is unlikely that the shape of the curve is due to site effects. The profile of accelerograms with absolute times shown in figure 4*A* includes recordings under more diverse site conditions, with one accelerogram (from San Francisco International Airport, at an epicentral distance of 79 km) from a soft-soil site. Although these varying site conditions evidently caused local variations in ground-motion amplitude and frequency content, they do not explain the absence of attenuation between 50 and 80 km in the corresponding recorded peak acceleration plotted in figure 5.

ACKNOWLEDGMENT

This research was supported by U.S. National Science Foundation grant BCS–9011330.

REFERENCES CITED

Abrahamson, N.A., Somerville, P.G., and Cornell, C.A., 1990, Uncertainty in numerical strong motion predictions, in U.S. National Conference on Earthquake Engineering, 4th, Palm Springs, Calif., 1990, Proceedings: Berkeley, Calif., Earthquake Engineering Research Institute, v. 1, p. 407–416.

Bakun, W.H., and Joyner, W.B., 1984, The M_L scale in central California: Seismological Society of America Bulletin, v. 74, no. 5, p. 1827–1843.

Boore, D.M., Seekins, L.C., and Joyner, W.B., 1989, Peak accelerations from the 17 October 1989 Loma Prieta earthquake: Seismological Research Letters, v. 60, no. 4, p. 151–166.

Burger, R.W., Somerville, P.G., Barker, J.S., Herrmann, R.B., and Helmberger, D.V., 1987, The effect of crustal structure on strong ground motion attenuation relations in eastern North America: Seismological Society of America Bulletin, v. 77, no. 2, p. 420–439.

Campbell, K.W., 1991, An empirical analysis of peak horizontal acceleration for the Loma Prieta, California, earthquake of 18 October 1989: Seismological Society of America Bulletin, v. 81, no. 5, p. 1838–1858.

Catchings, R.D., and Fuis, G.S., 1991, Influence of crustal structure on the 1989 Loma Prieta earthquake and associated destruction [abs.]: Eos (American Geophysical Union Transactions), v. 72, no. 44, supp., p. 338.

Chin, B.-H., and Aki, Keiiti, 1991, Simultaneous study of the source, path and site effects on strong ground motion during the 1989 Loma Prieta earthquake; a preliminary result on pervasive nonlinear site effects: Seismological Society of America Bulletin, v. 81, no. 5, p. 1859–1884.

Dietz, L.D., and Ellsworth, W.L., 1990, The October 17, 1989, Loma Prieta, California earthquake and its aftershocks; geometry of the sequence from high-resolution locations: Geophysical Research Letters, v. 17, no. 9, p. 1417–1420.

Dreger, D.S., and Helmberger, D.V., 1991, Source parameters of the Sierra Madre earthquake from regional and local body waves: Geophysical Research Letters, v. 18, no. 11, p. 2015–2018.

Gajewski, Dirk, Stangl, R., Fuchs, K., and Sandmeier, K.J., 1990, A new constraint on the composition of the topmost continental mantle—anomalously different depth increases of P and S velocity: Geophysical Journal International, v. 103, no. 2, p. 497–507.

Hadley, D.M., Helmberger, D.V., and Orcutt, J.A., 1982, Peak acceleration scaling studies: Seismological Society of America Bulletin, v. 72, no. 3, p. 959–979.

Joyner, W.B., and Boore, D.M., 1988, Measurement, characterization, and prediction of strong ground motion, in Von Thun, J.L., ed., Proceedings; Earthquake Engineering and Soil Dynamics II—recent advances in ground motion evaluation: American Society of Civil Engineers Geotechnical Special Publication 20, p. 43–102.

Kanamori, Hiroo, and Satake, Kenji, 1990, Broadband study of the 1989 Loma Prieta earthquake: Geophysical Research Letters, v. 17, no. 8, p. 1179–1182.

Liu, H.-L., and Helmberger, D.V., 1985, The 23:19 aftershock of the October 1979 Imperial Valley earthquake; more evidence for an asperity: Seismological Society of America Bulletin, v. 75, no. 3, p. 689–708.

Maley, R.P., Acosta, A.V., Ellis, F., Etheredge, E.C., Foote, L.J., Johnston, D.A., Porcella, R.L., Salsman, M.J., and Switzer. J.C., 1989, U.S. Geological Survey strong-motion records from the Northern California (Loma Prieta) earthquake of October 17, 1989: U.S. Geological Survey Open-File Report 89–568, 85 p.

McGarr, A.F., Celebi, Mehmet, Sembera, E.D., Noce, Thomas, and Mueller, C.S., 1991, Ground motion at the San Francisco International Airport from the Loma Prieta earthquake sequence, 1989: Seismological Society of America Bulletin, v. 81, no. 5, p. 1923–1944.

Mueller, C.S., and Glassmoyer, G.M., 1990, Digital recordings of aftershocks of the October 17, 1989 Loma Prieta, California, earthquake: U.S. Geological Survey Open-File Report 90–503, 147 p.

Nábělek, J.L., 1990, Rupture process of the October 18, 1989 Loma Prieta earthquake from broadband teleseismic body waves, [abs.]: Seismological Research Letters, v. 61, no. 1, p. 46.

Shakal, A.F., Huang, M., Reichle, M.S., Ventura, C., Cao, T., Sherburne, R.W., Savage, M., Darragh, R.B., and Peterson, C., 1989, CSMIP strong-motion records for the Santa Cruz Mountains (Loma Prieta), California earthquake of 17 October 1989: California Division of Mines and Geology, Office of Strong Motion Studies Report OSMS 89–06, 196 p.

Somerville, P.G., McLaren, J.P., Saikia, C.K., and Helmberger, D.V., 1990, The 25 November 1988 Saguenay, Quebec, earthquake; source parameters and the attenuation of strong ground motion: Seismological Society of America Bulletin, v. 80, no. 5, p. 1118–1143.

Somerville, P.G., Sen, M.K., and Cohee, B.P., 1991, Simulation of strong ground motions recorded during the 1985 Michoacán, Mexico, and Valparaiso, Chile, earthquakes: Seismological Society of America Bulletin, v. 81, no. 1, p. 1–27.

Somerville, P.G., and Smith, N.F., 1991, Source, path and site effects on Loma Prieta strong motions: International Conference on Seismic Zonation, 4th, Stanford, Calif., 1991, Proceedings, v. 3, p. 335–342.

Somerville, P.G., Smith, N.F., and Dreger, D.S., 1992. The influence of critical Moho reflections on strong ground motion attenuation in California: report to California Division of Mines and Geology Strong Motion Instrumentation Program on contract 1090–514, 82 p.

Somerville, P.G., and Yoshimura, Joanne, 1990, The influence of critical Moho reflections on strong ground motions recorded in San Francisco and Oakland during the 1989 Loma Prieta earthquake: Geophysical Research Letters, v. 17, no. 8, p. 1203–1206.

Wald, D.J., Helmberger, D.V., and Heaton, T.H., 1991, Rupture model of the 1989 Loma Prieta earthquake from the inversion of strong-motion and broadband teleseismic data: Seismological Society of America Bulletin, v. 81, no. 5 p. 1540–1572.

Wald, D.J., Burdick, L.J., and Somerville, P.G., 1988, Simulation of acceleration time histories close to large earthquakes, *in* Von Thun, J.L., ed., Proceedings: Earthquake Engineering and Soil Dynamics II—recent advances in ground-motion evaluation: American Society of Civil Engineers Geotechnical Special Publication 20, p. 430–444.

Walter, A.W., and Mooney, W.D., 1982, Crustal structure of the Diablo and Gabilan Ranges, central California; a reinterpretation of existing data: Seismological Society of America Bulletin, v. 72, no. 5, p. 1567–1590.

THE LOMA PRIETA, CALIFORNIA, EARTHQUAKE OF OCTOBER 17, 1989: STRONG GROUND MOTION AND GROUND FAILURE

STRONG GROUND MOTION

INFLUENCES OF LOCAL GEOLOGY ON STRONG AND WEAK GROUND MOTIONS RECORDED IN THE SAN FRANCISCO BAY REGION AND THEIR IMPLICATIONS FOR SITE-SPECIFIC BUILDING-CODE PROVISIONS

By Roger D. Borcherdt and Gary Glassmoyer,
U.S. Geological Survey

CONTENTS

ABSTRACT

Strong ground motions recorded at 37 sites in the San Francisco Bay region during the earthquake show marked variations in characteristics dependent on crustal structure and local geologic conditions. Peak horizontal acceleration and velocity inferred for sites underlain by "rock" generally occur on the transverse component of motion; they are consistently greater, with lower attenuation rates than the corresponding mean values predicted by empirical curves based on previous strong-motion data. Theoretical amplitude distributions and synthetic seismograms calculated for 10-layer models suggest that "bedrock" motions were elevated partly because of the wide-angle reflection of *S*-wave energy from the base of a relatively thin (25 km thick) continental crust in the region. Average ratios of peak horizontal acceleration, velocity, and displacement increase with decreasing mean shear-wave velocity of near-surface deposits. Ratios of peak acceleration for sites on "soil" (alluvium, fill/bay mud) are statistically larger than those for sites on "firm to hard rock" (sandstone, shale, Franciscan Complex). Spectral ratios establish the existence of predominant site periods with peak amplifications near 15 for potentially damaging levels of ground motion at some sites underlain by "soil." Average spectral amplifications inferred for vertical and mean horizontal motions are not statistically different at the 2-percent-significance level from those inferred from previous low-strain data. Comparative weak- and strong-motion measurements show that mean shear-wave velocity or average low-strain spectral ratios are useful predictors of amplification at the damaging levels of ground motion observed during the earthquake. Analyses suggest that soil amplification and reflected crustal shear energy were major contributors to levels of ground motion sufficient to cause damage to vulnerable structures at distances near 100 km in the cities of San Francisco and Oakland. Regression curves for mean horizontal amplification of strong motion predict amplification for site-specific building-code considerations as a continuous function of shear-wave velocity v, for short-period motion (0.1–0.5 s) by $F_a=(v/997)^{-0.36}$ and for midperiod motion (0.4–2.0 s) by $F_v=(v/1{,}067)^{-0.64}$. Site classes and corresponding mean amplification factors, respectively, are as follows: (1) SC–I, hard and firm rock (SC–Ia, hard rock (0.8, 0.8); SC–Ib, firm to hard rock (1.0, 1.0)); (2) SC–II, soft rock and gravelly soils (1.3, 1.6); (3) SC–III, stiff clay and sandy soils (1.6, 2.3); (4) SC–IV, soft soils (2.0, 3.5) (SC–IVa, less than 120 ft; SC–IVb, special-study soils). These strong-motion-amplification factors provide rigorous estimates of amplification for improvements in site-

specific design spectra for building-code considerations either as a continuous function of site conditions or as a discrete function based on site classification. The revised site classes also provide a rigorous basis for mapping special-study zones for strong ground shaking, as implied by California law AB–3897.

INTRODUCTION

Damage and consequent loss of life from the earthquake were concentrated in areas underlain by "poor" soil conditions (Seed and others, 1990). Holmes and others (1990) concluded that damage to unreinforced-masonry buildings in San Francisco was greatest at sites underlain by soils with the highest potential for amplification. Damage from the great San Francisco earthquake of 1906 also was concentrated in many of these same areas and was observed to depend chiefly on the geological characteristics of the ground (Wood, 1908). The more significant damage in the heavily urbanized San Francisco Bay region occurred at distances near 100 km in areas of San Francisco and Oakland underlain by "poor" soil conditions. These concentrations of damage at considerable distances from the causative fault emphasize the need to quantify the factors contributing to ground-motion levels sufficient to induce soil and structural failures and consequent loss of life.

The free-field strong-motion data set as recorded at 34 sites in the San Francisco Bay region (Maley and others, 1989; Shakal and others, 1989) has been analyzed previously to quantify the influence of various deposits on strong ground motion (Borcherdt and Glassmoyer, 1992). Of these 34 sites, only 7 were located on the unit of most concern, namely, fill overlying bay mud. After these analyses, the data from three more sites located on fill/bay mud became available, along with additional, though not yet complete, information on geotechnical properties at several of the sites. For completeness of this paper, these previous analyses are included here in their entirety, with figures, tables, and conclusions updated to include the results from all 37 sites available to date. Recent comparative ground-motion measurements for both strong- and weak-motion data are also included here to augment previous results. In addition, the text is updated with respect to recent developments regarding the deformation of site classes for use in site-specific building codes. These developments are based, in part, on analyses of the amplification data presented herein.

Various data sets pertinent to assessing the influence of local deposits on ground shaking existed in the San Francisco Bay region before the 1989 Loma Prieta earthquake. These included intensity data from the 1906 San Francisco earthquake (Lawson and others, 1908), strong-motion data from 6 sites for the 1957 San Francisco earthquake (M=5.3) (Hudson and Housner, 1958), comparative ground-motion measurements at 99 sites from distant nuclear explosions (Borcherdt, 1970; Borcherdt and Gibbs, 1976), microtremor measurements at 50 sites (Gibbs and Borcherdt, 1974), and extensive compilations of seismic, geologic, geotechnical, and physical-property data compiled for regional planning purposes (Gibbs and others, 1975, 1976, 1977; Fumal, 1978; Helley and Lajoie, 1979; Wentworth and others, 1985). These measurements established that the amplitude and duration of weak ground motion generally increase with decreasing firmness of the deposits. They established the existence of predominant site periods for some sites and showed that strong relations exist between measured low-strain ground motions, intensities ascribed for the 1906 San Francisco earthquake, and shear-wave velocity. The data permitted the preparation of predicted-earthquake-intensity maps for the San Francisco Bay region (Borcherdt and others, 1975) and the development of procedures to map units with distinct seismic-response characteristics (Borcherdt and others, 1978; Fumal, 1978; Association of Bay Area Governments, 1982). The 1989 Loma Prieta earthquake provided the opportunity to evaluate the results of these earlier analyses in light of quantitative measurements of ground motion at levels commensurate with soil and structural damage.

This paper provides a comprehensive summary of the geotechnical, physical, and seismic properties of various geologic units in the San Francisco Bay region, as compiled and mapped to date, along with a correspondence between these units and recently proposed site classes for site-specific building-code provisions. Strong-motion recordings at sites underlain by various "rock" units are used to evaluate previously derived empirical attenuation curves and the influence of local crustal structure on recorded motions. The influences of local geologic deposits on recorded strong motions are analyzed with respect to those recorded at the nearest "rock" station. Comparative strong-motion measurements for various geologic and geotechnical units are provided for peak levels of ground acceleration, velocity, and displacement, and average spectral ratios for various period bands resolved into vertical, radial, and transverse components of motion. These comparative strong-motion measurements are compared with those from previous low-strain measurements from distant nuclear explosions. Empirical regression curves are derived between average ground response for various period bands and mean shear-wave velocity for both low-strain and strong ground motions. These regression curves are used to provide unambiguous estimates of amplification factors for the site classes being considered for site-specific building-code provisions.

GEOLOGIC AND SEISMIC CHARACTERISTICS OF LOCAL DEPOSITS

The San Francisco Bay trough is a northwest-trending graben bounded on the northeast and southwest by the active Hayward and San Andreas faults, respectively (fig. 1). San Francisco Bay, located in the center of this graben, is bounded by marshlands, alluvial plains, and, beyond 1 to 15 km, hills of the Coast Ranges. A wide variety of geologic units exist in close proximity throughout the region, ranging from Mesozoic sedimentary and plutonic rocks in the hills to Holocene alluvium and estuarine mud near the margins of the bay. Mesozoic and Tertiary rock units form the floor of the graben, containing a sedimentary sequence of which the lower part was initially designated "older bay sediments" and the upper part "younger bay mud" (Schlocker, 1968, p. 24).

Geologic characteristics, physical properties, and seismic shear-wave velocities for the various surficial units in the San Francisco Bay region are summarized in table 1. The six generalized geologic units in the region (fig. 1; col. 1, table 1) include Holocene bay mud (Qm), Quaternary alluvium (Qal), Tertiary and Quaternary sedimentary rocks (Qts) of the Santa Clara and Merced Formations, Mesozoic and Tertiary sedimentary rocks (TMs), Cretaceous granitic rocks (Kg), and the Cretaceous and Jurassic Franciscan Complex (KJf; K.R. Lajoie, in Borcherdt and others, 1975). These six units are further differentiated into 28 units on the basis of composition and physical properties (cols. 3–6, tables 1a, 1b). The unconsolidated units of bay mud and alluvium are differentiated and mapped according to composition, grain size, texture, and relative age (table 1a; Helley and Lajoie, 1979); the semiconsolidated units are differentiated and mapped according to composition, hardness, fracture spacing, and degree of weathering (table 1b; Wentworth and others, 1985). Seismic, geologic, and physical-property logs from boreholes to a depth of 30 m were compiled at more than 60 sites distributed throughout these various units (Gibbs and others, 1975, 1976, 1977). The number of measurements, mean shear-wave velocity, and standard deviation for each geologic unit are listed in tables 1a and 1b. Mean shear-wave velocities (to 30-m depth) are estimated for each of the strong-motion sites in table 2; the estimates were derived either from drill-hole logs at the site or from mean values derived at other sites with similar physical properties (Fumal, 1991).

The Holocene bay mud (unit Qhbm), which generally yields the largest amplifications of ground motion, is composed of unconsolidated, water-saturated, dark plastic clay and silty clay rich in organic material, with local lenses of well-sorted silt and sand and some beds of peat. It attains a thickness of 37 m beneath the bay and thins to zero along the margins of the bay. It generally contains more than 50 percent water (Helley and Lajoie, 1979). Measurements of shear-wave velocity range from 55 to 100 m/s in the depth interval 0–10 m and from 100 to 115 m/s in the depth interval 10–20 m (Fumal, 1978). The unit is overlain in urbanized areas along the margins of the bay by Quaternary artificial fill (unit Qaf), composed of hydraulically emplaced sand and clay or earth and rock emplaced with varying degrees of compaction. Limited measurements in the fills indicate shear-wave velocities ranging from 159 to 222 m/s.

The Quaternary alluvium (unit Qal) is composed of deposits widely varying in age and composition (see table 1a), including Holocene loose, well-sorted beach and dune sand; fine, medium, and coarse clay; silty clay; sand and sandy gravel; and various Pleistocene deposits ranging in composition from weakly to moderately consolidated, deeply weathered, poorly sorted, irregularly interbedded clay, silt, sand, and gravel to loose, well-sorted, fine to medium sand and subordinate silt (Helley and Lajoie, 1979). The unit reaches an overall thickness of as much as 400 to 500 m in the south bay beneath San Jose and is generally less than 200 m thick in the north bay beneath areas of San Francisco and Oakland. Shear-wave velocities range from 150–219 m/s for dune sand near the surface to 418–749 m/s for coarse-sandy gravel of late Pleistocene age (see table 1).

The semiconsolidated and consolidated units in the hills of the San Francisco Bay region include plutonic, volcanic, and a wide variety of sedimentary rocks (table 1b). Shear-wave velocities in these units range from about 425 m/s for soft sandstone to about 1,650 m/s for hard greenstone and fresh granite.

Previous ground-response studies (Borcherdt, 1970; Borcherdt and others, 1975, 1978; Borcherdt and Gibbs, 1976; Fumal, 1978) show that, in general, average amplification of ground motion increases with decreasing mean shear-wave velocity. Consequently, in terms of the generalized geologic units, these studies suggest that the largest amplifications generally can be expected on bay mud, lesser amounts on alluvium, and lesser but distinguishable amounts on the semiconsolidated units. Studies by Borcherdt and others (1978) and Fumal (1978) indicate that for mapping purposes, the unconsolidated bay-mud and alluvium can be classified into six categories distinguishable on the basis of seismic-response characteristics and physical properties. Similarly, the semiconsolidated and consolidated units can be classified into seven categories, which have been subsequently confirmed by using borehole data from 84 sites in the Los Angeles region (Fumal and Tinsley, 1985). The correspondence between these 13 categories and those differentiated

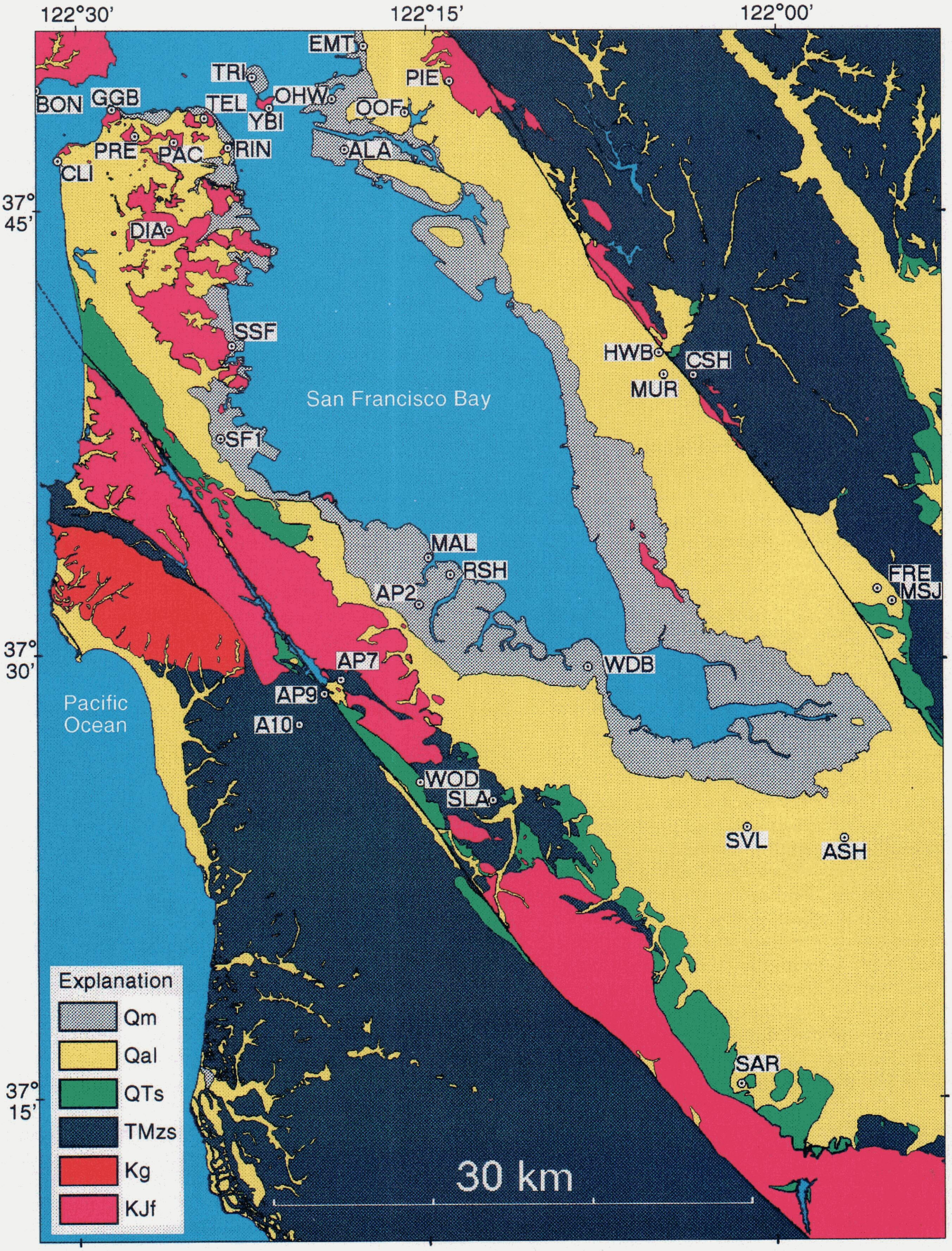

Figure 1.—Schematic map of the San Francisco Bay region, showing locations of 34 of 37 free-field stations that recorded earthquake, major faults (irregular heavy lines, dashed where inferred), and generalized geologic units (see tables 1a, 1b; from K.R. Lajoie, in Borcherdt and others, 1975).

Table 1a.—*Geologic, geotechnical, and physical properties of unconsolidated ("soil") units in the San Francisco Bay region*

[Generalized geologic units from K.R. Lajoie (in Borcherdt and others, 1975); differentiated geologic units, texture, and relative density and consistency generalized from Fumal (1978) and Helley and Lajoie (1970); shear-wave velocities from Gibbs and others (1975, 1976, 1977), Borcherdt and others (1978), and Fumal (1978); seismic units from Borcherdt and others (1978) and Fumal (1978); amplification capabilities from Borcherdt and others (1991); site classes from Borcherdt (in press)]

Generalized geologic units		Differentiated geologic units		Physical properties					Seismic unit	Site class	Amplification capability
						Shear Velocity					
Name	Symbol	Name	Symbol	Texture	Relative density	No.	Mean	S.d.			
				Holocene Deposits							
Bay mud (Younger bay mud)	Qm	Artificial fill	Qaf	Sand, sandy gravel, clay	Soft to very dense	3	196	27		SC-IV	High to very high.
		Estuarine bay mud	Qhbm	Clay to silty clay, minor sand, silt.	Very soft to soft:				i	SC-IV	
					Near surface	3	80	19			
					At depth	2	108	7			
Quaternary alluvium (Older bay sediment)	Qal	Beach and dune sand	Qhs	Sand	Loose to dense:				iv	SC-III	Intermediate to high.
					Near surface	3	173	32			
					At depth	3	311	13			
		Fine-grained alluvium	Qhaf	Clay to silty clay	Medium stiff to stiff	2	162	2	ii	SC-III	
		Medium-grained alluvium	Qham	Sand	Loose to dense	2	233	1	iv	SC-III	
		Coarse-grained alluvium	Qhac	Sandy gravel	Very dense	4	281	12	vi	SC-III	
				Pleistocene Deposits							
		Marine and continental	Qpmc	Sand, sandy silt, gravel	Dense to very dense:				v	SC-III	
					Near surface	2	280	29			
					At depth	5	505	37			
		Marine terrace	Qpmt	Sand to gravelly sand	Dense to very dense					SC-III	
		Late Pleistocene	Qpa								
		Dune sand (Merritt)	Qps	Sand	Dense to v. dense	1	350	--	v	SC-III	
		Fine grained		Clay to silty clay, sandy clay, silt.	Med. hard to hard:				ii,iii	SC-III	
					Near surface	6	199	27			
					At depth	11	343	48			
		Medium grained		Sand	Dense to v. dense:				v	SC-III	
					Near surface	2	349	11			
					At depth	7	367	71			
		Coarse grained		Sandy gravel	Very dense:				vi	SC-II	Low to intermediate.
					Near surface	2	451	46			
					At depth	5	606	123			

geologically is shown in tables 1a and 1b. This correspondence, together with recent strong-motion data, provides a rigorous basis to define site classes for seismic-zonation purposes.

The concept of amplification capability for four principal site classes was introduced as part of a methodology for mapping special-study zones for strong ground shaking in response to California law AB–3897 (Borcherdt and others, 1991). Subsequent building-code considerations have led to the rigorous specification of these site classes in terms of mean shear-wave velocity to a depth of 30 m (Borcherdt, in press). This specification permits an unambiguous classification of all sites, ranging from the hardest of rocks to the softest of soils (Borcherdt, in press). Agreement in results presented at a national site-response workshop held at the University of Southern California, Los Angeles, in 1992) by R.B. Seed, R. Dobry, and R.D. Borcherdt (written commun., 1992) led to a strong consensus regarding methodologies for incorporating amplification factors into site-specific response spectra. The site classes, as currently defined, provide a rigorous basis for both revised building codes and maps of special-study zones in conformance with California law AB–3897.

The physical description, range in mean shear-wave velocity, and amplification capability for the four main site classes (SC's; distinguished using roman numerals), respectively, are as follows: (1) SC–I, hard and firm rock, >650 m/s, very low to low; (2) SC–II, soft to firm rock and gravelly soils, 375 to 650 m/s, high to very high; (3) SC–III, stiff clays and sandy soils, 200 to 375 m/s, intermediate to high; and (4) SC–IV, soft soils, 100 to 200 m/s, high to very high (see Borcherdt and others, 1991, table 1; Borcherdt, in press, table 1). For building-code-provision considerations, the site class for rock is divided into two subclasses: SC–Ia, hard rock, 1,450 to 1,850 m/s; and SC–Ib, firm to hard rock, 650 to 1,450 m/s. The correspondence between these classes and the units differentiated geologically, assuming that they extend to a depth of 30 m, is specified in table 1.

To facilitate discussion, the terms "hard rock" and "soft rock" are here used to refer to the rock materials in

Table 1b.—*Geologic, geotechnical, and physical properties of semiconsolidated and consolidated ("rock") units in the San Francisco Bay region*

[Generalized geologic units and physical units from K.R. Lajoie (in Borcherdt and others, 1975); hardness, fracture spacing, and weathering generalized from Wentworth and others (1975) and Fumal (1978); shear-wave velocities from Gibbs and others (1975, 1976, 1977), Borcherdt and others (1978), and Fumal (1978); seismic units from Borcherdt and others (1978) and Fumal (1978); amplification capabilities from Borcherdt and others (1991); site classes from Borcherdt (in press)]

Generalized geologic units		Physical units (Composition)	Physical properties						Seismic unit	Site class	Amplification capability
Name	Symbol		Hardness	Fracture spacing	Weath-ering	Shear velocity m/s					
						No.	Mean	S.d.			
Quaternary and Tertiary sedimentary rocks:	QTs										
Santa Clara Formation		Predominately conglomerate, lesser sandstone, siltstone, claystone.	Firm to soft conglomerate, clasts hard.	Close to moderate in sandstone:						SC-II	Low to intermediate.
				Near surface	---	2	392	30	i		
				At depth	---	5	675	240	ii-iii, v		
Merced Formation		Sandstone, siltstone, claystone.	Firm to soft	Moderate to very wide in sandstone:						SC-II	Low to intermediate.
				Near surface	---	4	271	41	i		
				At depth	---	6	390	65	ii-ii		
Mesozoic and Tertiary sedimentary rocks	TMzs	Sandstone	Firm to soft	Very close to moderate	Moderate	4	470	85	i-iii	SC-II	Low to intermediate.
		Shale	Firm	Moderate to very wide	Fresh	5	560	105	ii-iii	SC-II	
		Sandstone, conglomerate	Hard to soft	Close to very close	Moderate	3	680	60	ii-iii	SC-II	
		Rhyolite, agglomerate	Hard to firm	Close to mod., locally wide	Fresh	4	1080	107	v	SC-Ib	
Cretaceous granitic rocks	Kg	Quartz diorite	Soft; hard masses	Close to very close	Moderate	4	600	30	ii	SC-II	
			Hard	Commonly close to v. wide	Fresh	1	1640	--	vii	SC-Ib	Low to very low.
Cretaceous and Jurassic Franciscan Complex	KJf	Sandstone (KJfss), shale (KJfsh), chert (KJfc).	Firm to soft	Very close to close	Moderate	6	718	158	iii	SC-Ib	
			Hard	Close, locally mod. to wide	Fresh	12	903	250	iii-vii	SC-Ib	
		Volcanic rocks, greenstone (KJfg).	Firm to hard	Close to locally moderate	Moderate	4	841	120	ii-iv	SC-Ib	
			Hard	Mod. to wide, locally v. wide	Fresh	1	1680	--	vii	SC-Ib	
		Serpentine (sp)	Firm to soft Blocks hard	Very close to close Mod. to wide in hard masses	Fresh	2	637	172	ii, iii	SC-II	

site classes SC–I and SC–II, respectively, and the term "soil" to the materials in both site classes SC–III and SC–IV. Most areas in the San Francisco Bay region are not underlain by soils composed of more than 25 percent gravel. Consequently, most areas mapped as Quaternary alluvium (unit Qal) in the San Francisco Bay region are classifiable as SC–III, provided the material is sufficiently thick.

STRONG-GROUND-MOTION DATA

The Loma Prieta strong-motion data set provides the first relatively complete set of strong-ground-motion measurements in the San Francisco Bay region at damaging levels of shaking. The recordings from various deposits throughout the region, including fill and bay mud, provide not only a unique opportunity to quantify the influence of local soft-soil deposits under damaging levels of ground motion but also an important opportunity to investigate the influence of crustal-propagation paths and resulting regional variations in bedrock motions. The locations of 34 of the combined set of 37 free-field stations analyzed herein are shown in figure 1.

To develop a uniform data set for our analyses, the digital time series for stations maintained by the U.S. Geological Survey (Maley and others, 1989) were uniformly reprocessed with standard AGRAM routines (Converse, 1984) to yield 50-sample-per-second acceleration-, velocity-, and displacement-time series comparable to those published by the California Strong Motion Instrumentation Program (CSMIP; Shakal and others, 1989) of the California Division of Mines and Geology. AGRAM routines were used to rotate the composite horizontal-component data at each site into components radial and transverse to the linear direction from epicenter to receiver.

Equiscaled plots of corresponding components of motion are useful for identifying characteristics of the source and the influences of crustal-propagation paths, local geology, and anomalous site or instrument characteristics (Borcherdt, 1970; Borcherdt and Gibbs, 1976). Plots of acceleration, velocity, and displacement, respectively, emphasize the short-, intermediate-, and long-period

Table 2.—*Peak acceleration, velocity, and displacement for the vertical, radial, and transverse components of ground motion at free-field stations in the San Francisco Bay region*

[1, California Strong Motion Instrumentation Program of the California Division of Mines and Geology; 2, Strong Motion Program of the U.S. Geological Survey. APEEL, Andreas Peninsula Earthquake Engineering Laboratory; BART, Bay Area Rapid Transit; bldg., building; CSUH, California State University, Hayward; LBL, Lawrence Berkeley Laboratory; SLAC, Stanford Linear Accelerator Center. Acc, acceleration; Disp, displacement; Dist, distance; E, epicentral; H, hypocentral; R, radial; T, transverse; Z, vertical. Average velocities from Fumal (1991). S.d., standard deviation for sites with velocities estimated from local geology]

Station		Distance			Vertical			Radial			Transverse					
Name	Code	Hyp. (km)	Epi. (km)	Rup. (km)	Acc. (cm/s/s)	Vel. (cm/s)	Disp. (cm)	Acc. (cm/s/s)	Vel. (cm/s)	Disp. (cm)	Acc. (cm/s/s)	Vel. (cm/s)	Disp. (cm)	Geologic unit	S.vel. (m/s)	S.d.*
Saratoga ^	SAR	33	27	12	353	26.3	15.5	458	39.0	9.6	297	54.3	31.8	QTs	440	55
Agnews State Hosp.^	ASH	44	40	27	82	9.7	4.9	159	29.3	17.5	169	17.4	12.9	Qhaf	240	35
Sunnyvale ^^	SVL	46	42	28	79	7.4	2.9	206	25.0	10.0	223	38.1	15.7	Qhaf/Qpa	240	35
SLAC ^^	SLA	54	51	35	90	9.2	2.9	214	19.9	4.0	242	45.9	10.7	QTs	320	*
Mission San Jose ^	MSJ	57	55	42	81	8.4	4.5	121	10.4	4.1	103	7.8	4.5	Qpa/QTs	285	10
Woodside Fire Station^	WOD	57	55	39	49	6.8	2.1	49	8.5	3.5	104	18.7	7.5	TMzs	440	55
Dumbarton Bridge West ^	WDB	58	55	40	57	5.9	2.0	99	14.6	4.4	117	24.7	7.7	Qhaf/Qhbm	149	--
Fremont ^^	FRE	58	55	42	68	4.6	1.3	143	10.2	2.2	181	10.4	2.6	Qpa	285	10
APEEL 9 (Crys.Spr. Res.) ^^	AP9	64	63	46	50	6.6	2.0	116	30.9	5.7	97	16.9	10.9	QTs	450	--
APEEL 10 (Skyline Blvd.) ^	AP10	65	63	47	36	7.8	2.5	68	11.2	5.5	107	20.0	7.2	TMzs	405	--
APEEL 7 (Pulgas Temple) ^	AP7	65	63	47	60	6.0	2.3	122	13.5	4.3	114	17.3	6.3	TMzs	435	--
APEEL 2 ^^	AP2	66	64	47	82	7.7	1.1	194	30.9	4.7	266	54.7	10.9	Qaf/Qhbm/Qpa	130	--
Redwood Shores (F. City) ^	RSH	67	65	47	101	8.4	3.6	280	33.7	9.3	284	43.1	13.8	Qaf/Qhbm	115	--
Maley Residence (F. City) ^^	MAL	68	66	50	74	3.6	.8	103	14.0	4.3	90	18.4	5.9	Qaf/Qhbm	130	--
CSUH Stadium Grounds ^	CSH	73	70	56	44	4.6	2.3	44	4.7	3.2	77	7.2	2.6	TMzs	525	--
Muir School (APEEL 2E) ^	MUR	73	71	57	91	3.8	2.1	91	15.7	4.2	125	12.6	3.5	Qpa	280	--
Hayward BART Station ^	HWB	74	72	58	81	4.7	1.7	81	11.1	2.8	187	11.3	3.7	Qpa	365	95
San Francisco Airport ^	SF1	81	79	63	63	5.3	1.8	223	19.6	3.1	378	34.5	5.4	Qaf/Qhbm	224	*
South San Francisco ^	SSF	85	84	76	31	4.4	1.4	31	6.4	1.3	105	8.8	3.0	KJfss	910	40
Alameda Naval Air Station ^	ALA	92	91	76	60	5.6	1.3	242	26.5	4.5	162	36.2	9.7	Qhaf/Qhbm	191	--
Oakland Office Bldg. ^	OOF	93	92	76	141	6.2	1.3	165	21.6	4.7	241	34.1	8.3	Qps/Qpa	295	--
Diamond Heights ^	DIA	94	92	76	42	6.7	1.4	96	7.3	.8	96	14.7	5.1	KJfsh	745	140
Piedmont Jr. High ^	PIE	94	92	77	25	2.1	1.0	47	4.9	1.7	98	12.3	3.1	KJfss	745	140
Oakland Harbor Wharf ^	OHW	96	94	79	65	10.5	1.8	261	25.9	5.3	322	48.0	12.9	Qaf/Qhbm/Qpa	251	--
Rincon Hill ^	RIN	96	94	79	28	4.0	1.9	68	4.1	1.4	98	13.2	5.5	KJfsh	745	140
Yerba Buena Island ^	YBI	97	96	80	27	4.2	1.1	40	4.4	1.4	68	14.3	4.3	KJfsh	880	--
Pacific Heights ^	PAC	98	96	81	31	5.9	2.3	38	4.6	.7	69	17.2	5.5	KJfsh	745	140
Emeryville ^^	EMT	98	97	81	57	4.9	.7	230	28.9	4.0	237	36.3	7.9	Qaf/Qhbm	245	--
Treasure Island ^	TRI	99	98	82	16	1.2	1.2	121	12.3	5.7	137	33.1	12.0	Qaf/Qhbm	171	--
Presidio ^	PRE	99	98	82	56	11.3	3.1	117	12.8	2.1	163	32.1	7.5	sp	515	5
Berkeley (Lawrence Lab.) ^	BKL	100	99	83	38	4.4	1.5	38	8.8	2.3	113	21.0	3.5	TMzs	610	*
Cliff House ^	CLI	101	99	83	61	7.5	1.6	86	11.7	2.1	90	22.0	7.2	KJfsh	745	140
Golden Gate Bridge ^^	GGB	101	100	83	55	11.6	2.6	134	19.2	3.9	204	32.3	6.3	Qal/sp	515	5
Bonita Point ^	BON	105	104	88	34	7.3	2.2	34	9.3	2.0	61	12.1	4.3	KJfss	745	140
Richmond City Hall ^	RCH	109	108	92	31	4.6	1.1	31	11.6	1.7	139	17.5	3.0	QTs	440	55
Larkspur Ferry Terminal ^^	LAR	116	115	99	59	3.6	1.2	110	16.6	3.1	123	18.6	4.3	Qhaf/Qhbm	130	--

^ CSMIP. ^^ USGS.

* Velocities with standard deviation and "*" estimated from geology (Fumal, 1991).

aspects of the recorded ground motions. Equiscaled plots of the velocity at free-field sites in the San Francisco Bay region are shown in figure 2, and of acceleration and displacement in figures 3 and 4. All the time-series plots were prepared by using the computer program PRS (Mueller, 1990).

To help identify the influences of propagation path and local deposits, the time series are classified into three groups (figs. 2–4): those sites in the San Francisco-Oakland area at comparable epicentral distances, those sites along the west side and south end of the bay, and those sites along the east side of the bay south of Oakland. The time series in each of these three groups are classified into "rock" and "soil" subgroups and arranged within each subgroup according to increasing distance. Station descriptions, distances, geologic classification, shear-wave velocity, and the peak value for each component of acceleration, velocity, and displacement are listed in table 2.

INFLUENCE OF CRUSTAL-PROPAGATION PATH (REGIONAL VARIATIONS IN "BEDROCK" MOTIONS)

Much more loss of life and structural damage occurred in San Francisco and Oakland at substantially greater distances (90–105 km) than in San Jose at close distances (35–45 km). Consequently, an important question for understanding the damage distribution concerns geographic variations in bedrock motions and their characteristics in areas of intense damage.

COMPARATIVE TIME-SERIES OBSERVATIONS

The time series and tabulated peak values (figs. 2–4; table 2) show distinct and characteristic differences between the various components of motion. They show that, in general, the largest peak amplitudes (acceleration, velocity, and displacement) occur on the transverse component of motion (except at stas. ALA, AP7, AP9, MAL, MUR, MSJ, ASH, and SAR, fig. 1). In the San Francisco-Oakland area and the east-bay hills, the dominant transverse motions are associated with a relatively simple pulse shape of 3- to 4-s period readily apparent in the velocity- and displacement-time series (figs. 3*A*, 4*A*). These time series show that the dominant transverse waveforms are most similar for sites underlain by rocks of the Franciscan Complex. This similarity in waveforms suggests a common crustal-propagation path for the dominant transverse motions, interpretable as *SH*-wave energy. It shows that the dominant motion on "bedrock" in San Francisco was similar and only slightly larger than that in the east-bay hills. These observations are consistent with observations by T.C. Hanks and G.A. Brady (oral commun., 1990) based on plots of the east-west components of motion. They noted for seven sites surrounding the San Francisco-Oakland Bay Bridge that the east-west component, which differs from the transverse component by about 26°–30°, was larger than the north-south component and that the dominant east-west waveforms were coherent.

Consistent and distinct differences in waveform shape and duration are apparent between the transverse component and the radial and vertical components recorded in the San Francisco-Oakland area. The vertical and radial components do not show the dominant 3- to 4-s short-

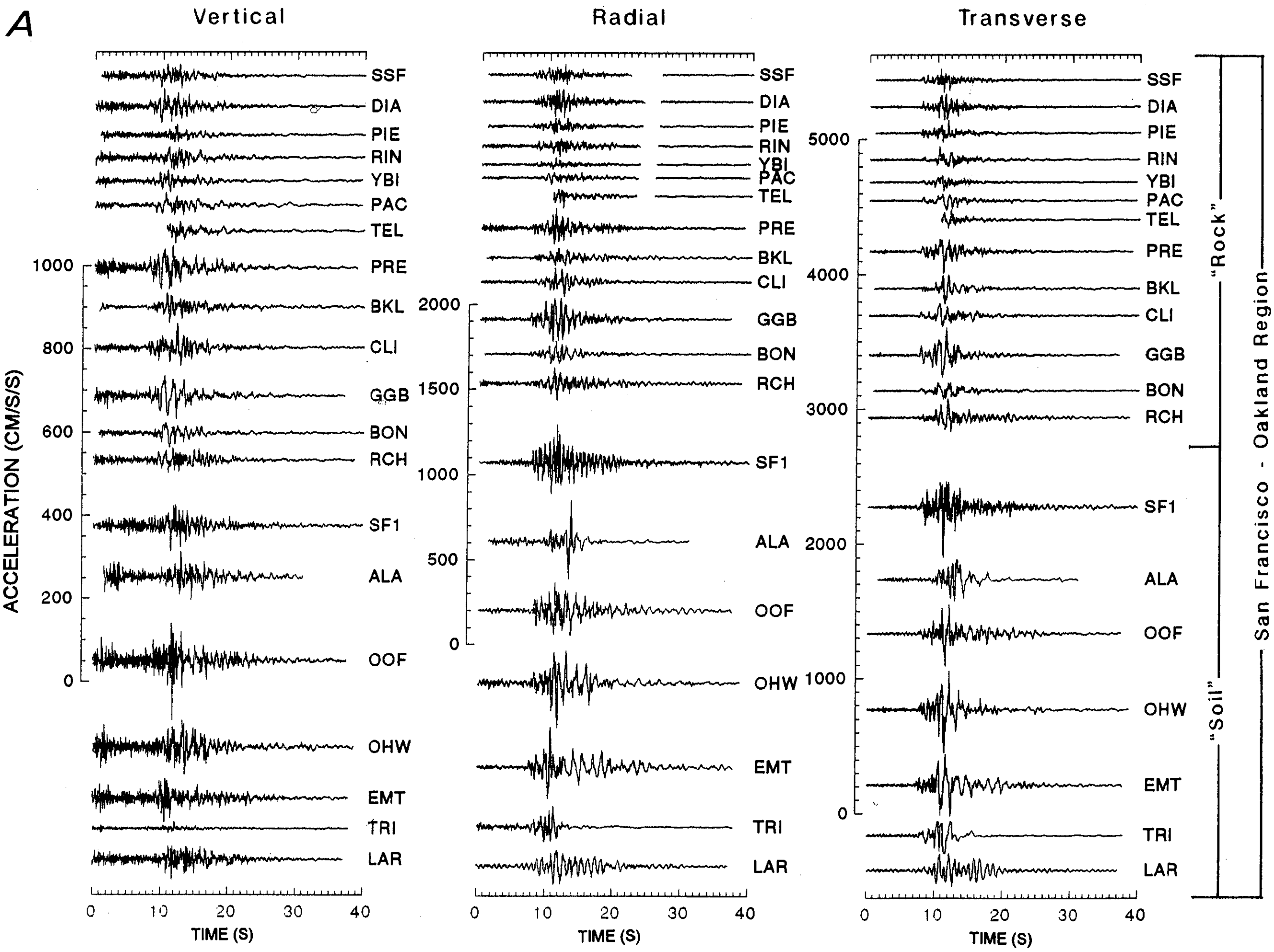

Figure 2.—Equiscaled plots of vertical, radial, and transverse components of ground acceleration as inferred for "rock" and "soil" sites in San Francisco-Oakland area (*A*) and sites in west, south, and east bay (*B*). Sites in each area, classified according to rock or soil, are arranged in order of increasing epicentral distance.

duration waveform apparent on the transverse component. Additional cycles of shaking on the vertical and radial components are consistent with the interpretation that the dominant forms of body-wave energy on the radial component are *SV* and converted *SV–P*.

The relatively simple, short-duration dominant motions in the San Francisco-Oakland area are consistent with a relatively simple source-rupture process for the earthquake, as inferred from teleseismic waveforms (Kanamori and Satake, 1990). They imply major energy release over a time period of about 6 s at a depth of 12 to 15 km along a relatively short (~35 km) segment of the fault. An important implication of these results, as pointed out by Kanamori and Satake (1990), is that the damage from the earthquake was less than might have occurred had the rupture process been more complex and the resulting duration of shaking longer.

Comparison of time series at rock sites on the west and east sides of the bay (for example, compare stas. AP7, AP9, and AP10 with sta. CSH in fig. 3*B*, and stas. RIN and PAC with stas. BKL and PIE in fig. 3*A*) shows that, in general, ground motions tend to be smaller on the east side than on the west side at comparable distances. Phases that correlate from site to site in each area suggest common crustal-propagation paths for dominant arrivals, and the absence of correlation from area to area suggests different crustal-propagation paths. For example, the radial and transverse components of motion at sites on both sides of the bay at intermediate epicentral distances of 45 to 70 km are longer in duration than those at sites in San Francisco at greater distances. These longer-duration signals indicate that the interarrival times for predominant crustal-propagation paths in the intermediate distance range are greater than those at larger distances.

COMPARATIVE ATTENUATION OBSERVATIONS

An important question concerning the damage in the San Francisco Bay region is whether the "bedrock" motions were larger than would have been predicted by using empirical curves derived from strong-motion data

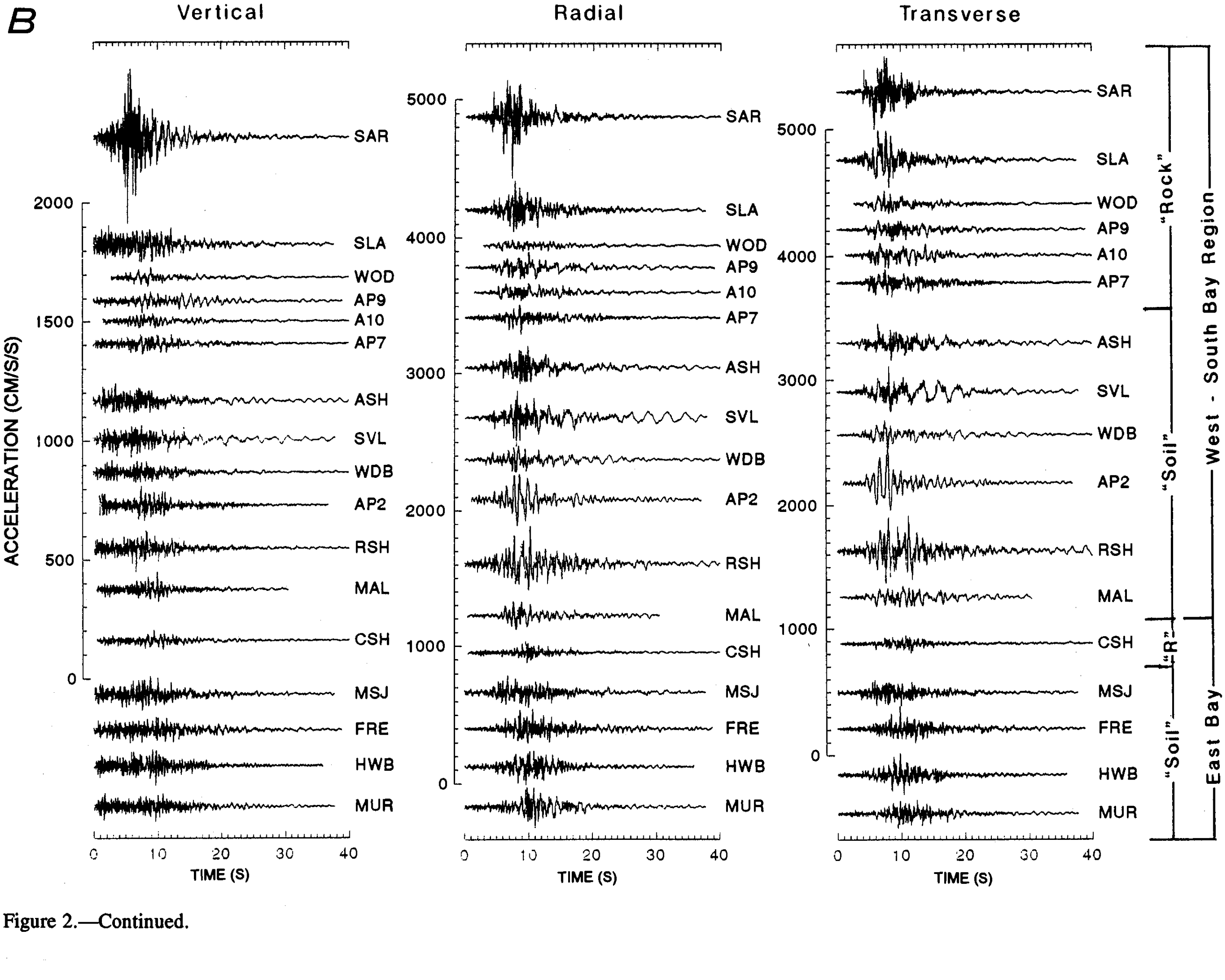

Figure 2.—Continued.

recorded during previous earthquakes, especially in light of the significant damage in the San Francisco-Oakland area at distances near 100 km. Early compilations of peak acceleration values by K.W. Campbell (oral commun., 1990) and Boore and Joyner (1990) indicate that the peak values at distances greater than 50 km generally exceed previously predicted values. To examine this question for the San Francisco Bay region, peak acceleration, velocity, and displacement amplitudes for the transverse component of motion recorded at "hard rock" and "soft rock" sites are plotted in figure 5 (see Borcherdt and Glassmoyer, 1992, for a corresponding plot of peak radial motion). (Stas. CLI and BON, fig. 1, are excluded from the "hard rock" classification because of possible influence of topography.) Superimposed on the plots of acceleration and velocity are the empirical mean and 1σ curves for maximum values on "rock" sites for an M_w=6.9 event (Joyner and Boore, 1988). (The independent variable for empirical curves is adjusted on the basis of a mean difference of 15.6 km between epicentral distance and closest distance to the projected rupture surface; D.M. Boore, oral commun., 1990.)

Comparison of the peak values with curves based on previous strong-motion data (fig. 5; Joyner and Boore, 1988) shows that the maximum peak horizontal accelerations and velocities are greater than the predicted mean peak amplitude at every site. Maximum peak velocities, in general, exceed the mean by more than one standard deviation. The amounts by which the peak amplitudes exceed their respective means increase with distance from the source. "Hard rock" peak motions at sites in San Francisco are more than 3 times greater than predicted.

Somerville and Yoshimura (1990) first suggested that amplitudes in the distance range 50–100 km were elevated because of wide-angle reflections from the base

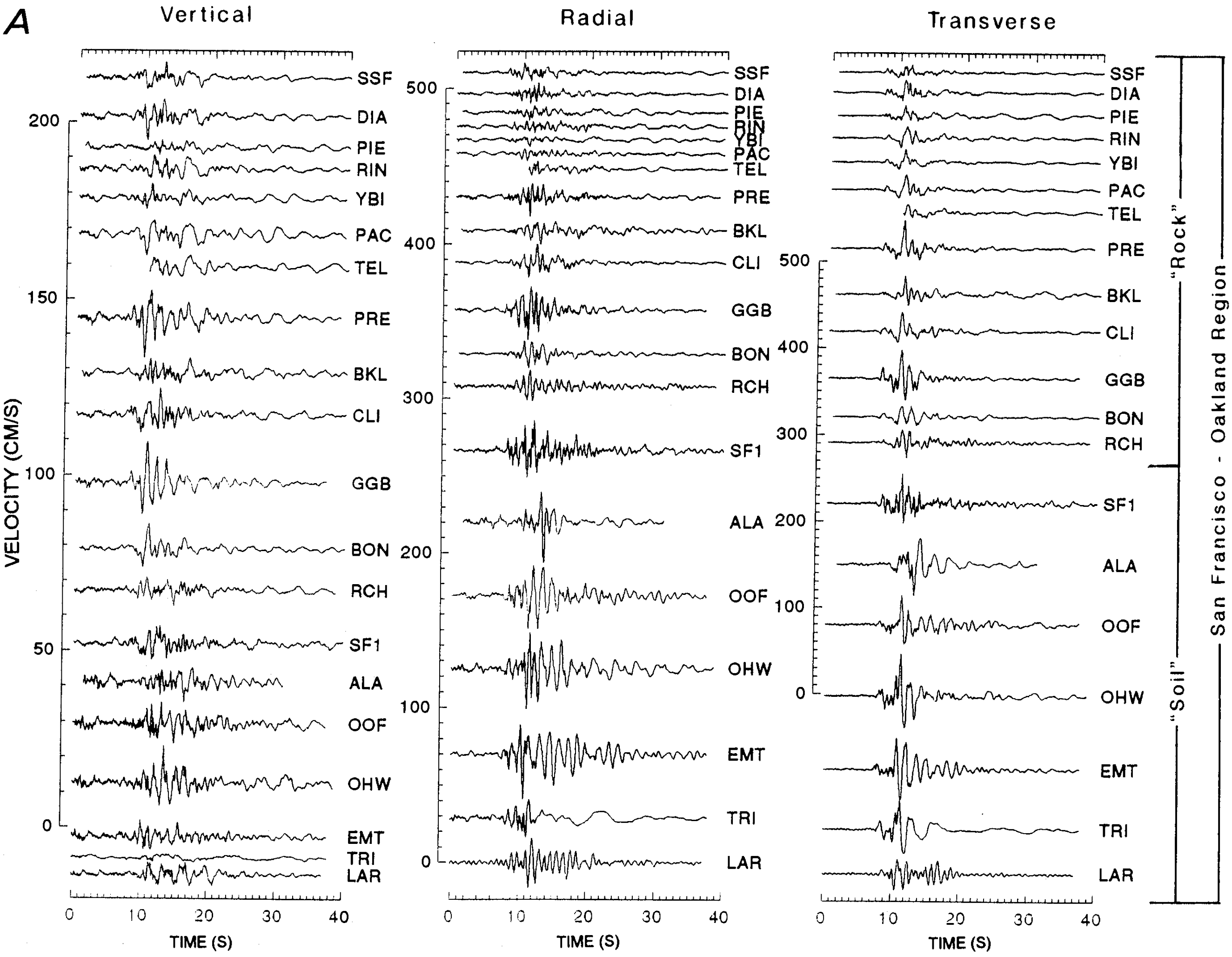

Figure 3.—Equiscaled plots of vertical, radial, and transverse components of ground velocity as inferred for "rock" and "soil" sites in San Francisco-Oakland area (*A*) and sites in west, south, and east bay (*B*). Sites in each area, classified according to rock or soil, are arranged in order of increasing epicentral distance.

of the Earth's crust. To evaluate the influence of this phenomenon, theoretical amplitude distributions (fig. 5) and synthetic seismograms (fig. 6*B*) were calculated for comparison with the observed peak amplitudes and derived record sections (figs. 6*A*, 6*C*).

The amplitude distributions (fig. 5) were calculated by assuming a point source at a depth of 13 km located directly updip from the hypocenter in a 10-layer viscoelastic *S*-wave model, derived from the *P*-wave model of Dietz and Ellsworth (1990) with a Poisson's ratio of 0.25. Homogeneous shear-wave *Q* values of 50, 100, and 200 were assigned to depths of 3, 7, and 25 km, respectively. They were computed using a ray-tracing technique (WAVES, MLAYER) recently developed with general anelastic-reflection/transmission coefficients for inhomogeneous wavefields (Borcherdt, 1977, 1982; Borcherdt and Wennerberg, 1985; Borcherdt and others, 1986). Calculations are provided for *SH* and *SV* waves (fig. 5) initiating as homogeneous waves from the source, traveling direct, intermediate-crustal-reflection (18-km depth), and Moho-reflection (25-km depth) paths. The synthetic seismograms (fig. 6) were computed by using a computer program for a 10-layer elastic model (RAYAMP3; David Crossley, written commun., 1990). Comparison of elastic- and anelastic-model predictions (Borcherdt and Glassmoyer, 1990) shows that the principal effect of anelasticity is an overall reduction in amplitude by about 30 percent near the Moho critical angle.

The theoretical amplitude distributions (fig. 5) predict that peak amplitudes for both the transverse and radial components of motion associated with *SH* and *SV* waves, respectively, should attenuate irregularly with distance. The curves predict that in the distance range 0–45 km, amplitudes for the direct wave should predominate but attenuate rapidly. At greater distances, amplitudes of the Moho reflection should predominate, with reflections from the intermediate crustal layer exceeding the direct wave at a distance of about 50 km.

The peak-amplitude data at "hard rock" and "soft rock" sites (fig. 5) do not define a rapid increase in amplitude at the expected critical angle because of scarcity of data; however, they do indicate trends in attenuation that are

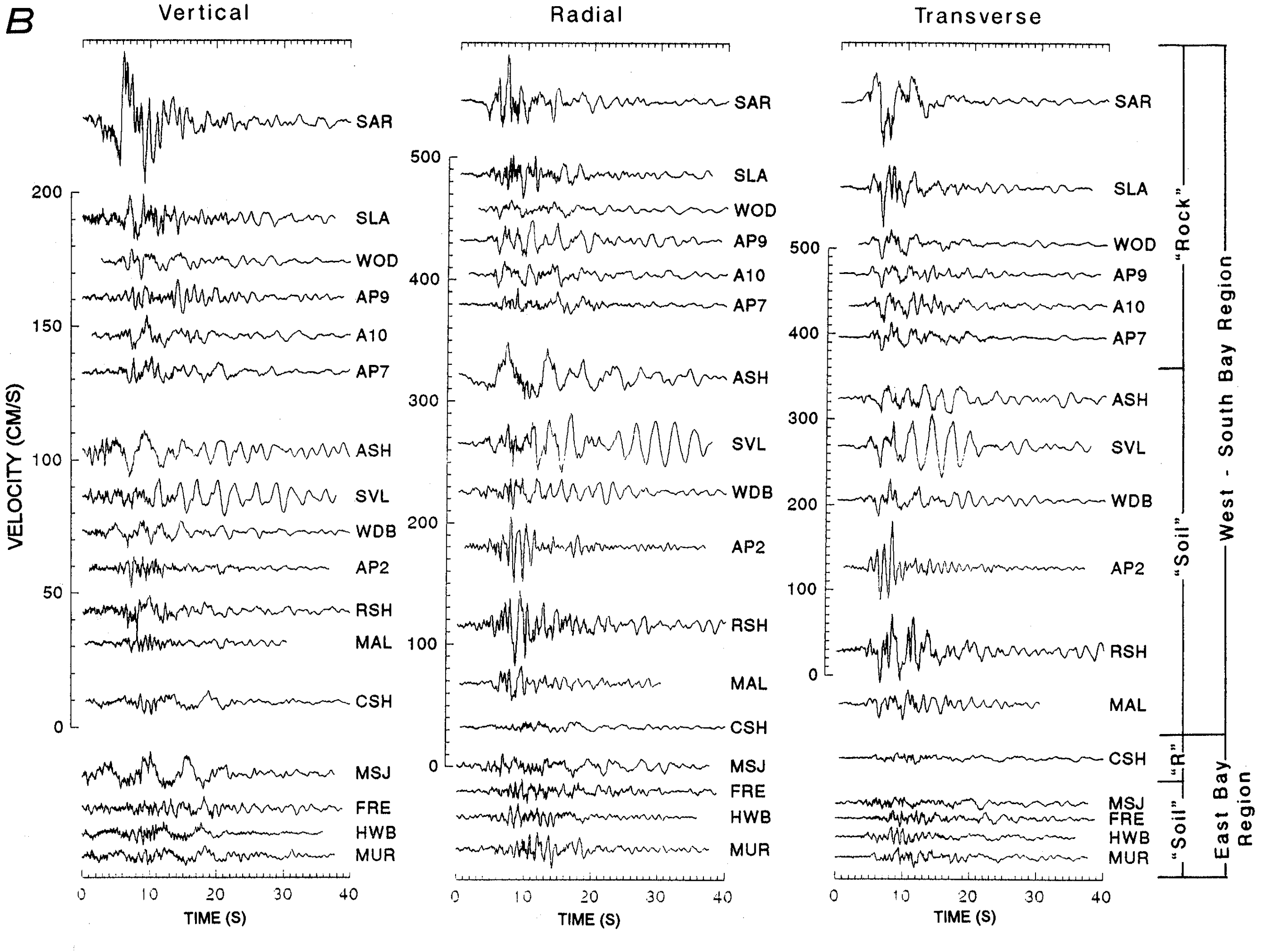

Figure 3.—Continued.

consistent with those predicted for *SV* and *SH* waves reflected beyond the critical angle. The peak amplitudes attenuate less with distance than predicted by empirical attenuation curves (Joyner and Boore, 1988), and less than predicted theoretically for the direct wave. The peak amplitudes for the transverse component of displacement are most consistent with empirical predictions, providing additional evidence that the relatively simple dominant waveform observed in San Francisco is *SH*-wave energy.

Record sections were prepared for the transverse components of velocity and displacement (fig. 6) by using the computer programs FROMGEOS (W.M. Kohler, written commun., 1990) and RID84 and RSEC88 (Luetgert, 1988a, b). These record sections are not as definitive as they might be because of a scarcity of sites with absolute timing and the necessity to include records from sites on thick soil deposits as well as "rock" sites. Locally generated surface-wave energy is evident as extended durations at some sites (sta. ASH, 39 km; sta. MSJ, 53 km; sta. CSH, 69 km; see fig. 1). Energy arrivals approximately consistent with predicted traveltimes for direct and reflected *S* waves are apparent, as are small arrivals about 2 s before the dominant arrival. These early arrivals are consistent with traveltimes computed by assuming a subevent located to the northwest of the hypocenter at a depth of 16 km, as inferred from teleseismic data (Choy and Boatwright, 1990). Peak displacement amplitudes suggest that the critical angle for the Moho reflection, though not well defined, must occur at distances less than about 55 km.

The synthetic seismograms (fig. 6) computed for *SH* waves, using a causal source pulse of 1.3 s, suggest a relatively simple waveform of short duration at distances near 100 km. They suggest that the dominant transverse arrival in San Francisco is reflected Moho energy and

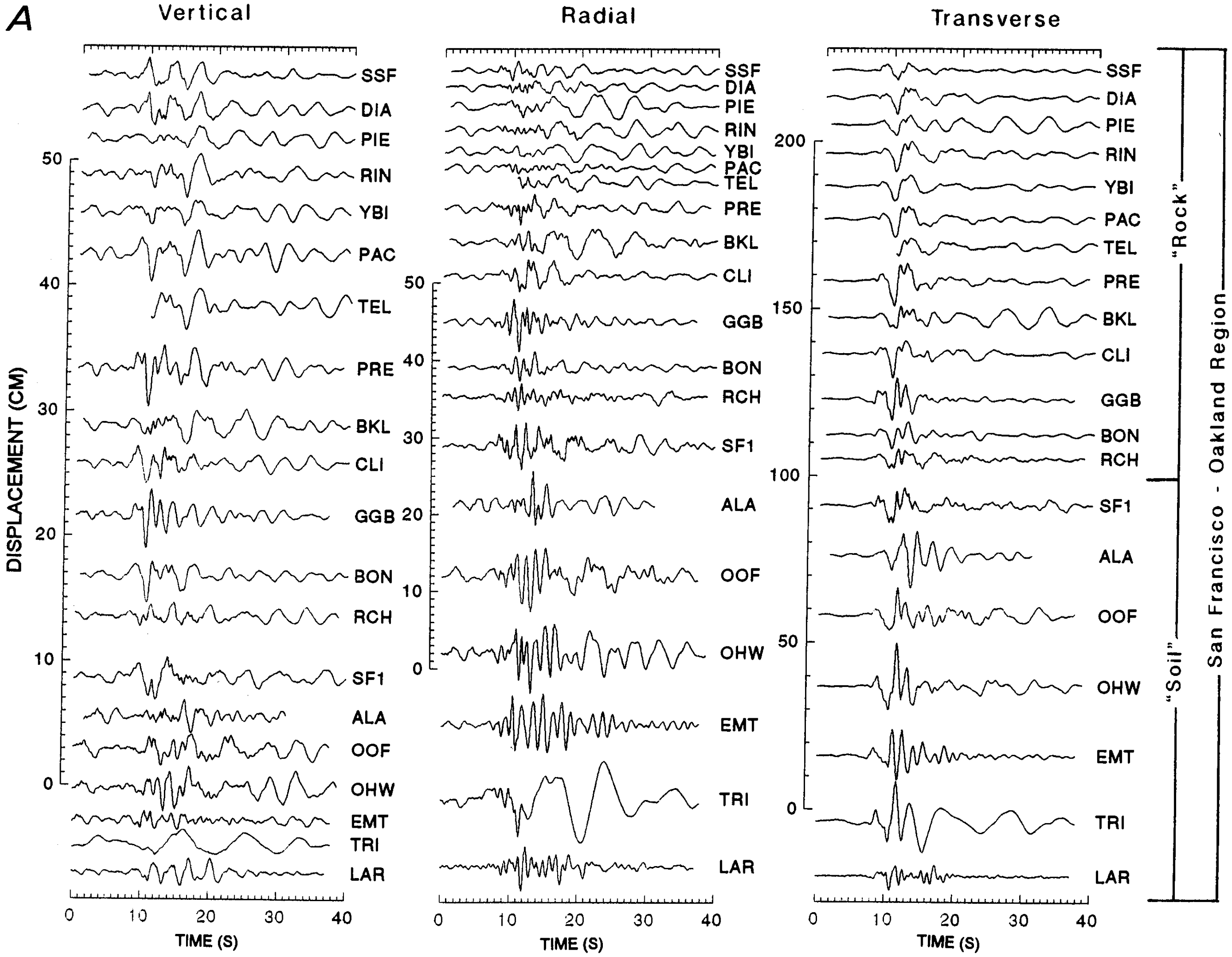

Figure 4.—Equiscaled plots of vertical, radial, and transverse components of ground displacement as inferred for "rock" and "soil" sites in San Francisco-Oakland area (*A*) and sites in west, south, and east bay (*B*). Sites in each area, classified according to rock or soil, are arranged in order of increasing epicentral distance.

that the observed interarrival-time intervals and durations should decrease with distance, consistent with earlier observations from the equiscaled plots of the recorded data (figs. 2–4).

Although the evidence for the Moho critical angle is not as pronounced in the observed data as predicted theoretically, several characteristics of the data argue for its existence, including simple dominant transverse waveforms in the San Francisco-Oakland area (figs. 4*A*, 6*C*), a trend for peak-amplitude data to attenuate less rapidly than predicted (fig. 5), signal duration decreasing with increasing distance beyond 60 km, and the consistency between theoretical and observed traveltimes (figs. 5, 6). Scatter in the data and deviations from model predictions suggest inadequacies in the inferred *S*-wave models.

In summary, strong-motion data indicate that the characteristics of "bedrock" shaking varied significantly throughout the San Francisco Bay region. In general, the level of shaking decreased with distance, but less rapidly than predicted on the basis of previous data. The strong-motion recordings indicate that the reflection of *SH*- and *SV*-wave energy from the base of the Earth's crust probably contributed to lower attenuation rates and to peak motions in the San Francisco-Oakland area more than 3 times greater than predicted. The largest "bedrock" motions generally occurred for *SH* waves in the transverse direction, perpendicular to the long axis of the San Francisco Bay trough. The recordings show characteristic differences indicative of the influence of various crustal-propagation paths and suggest that measurements of local "soil" response must be computed relative to chosen base stations so as to minimize these variations.

INFLUENCE OF LOCAL GEOLOGY

Previous comparative ground-motion studies at low strain levels (Borcherdt, 1970; Borcherdt and Gibbs, 1976) showed that thick sections of soft-soil deposits may increase significantly both the amplitude and duration of shaking in narrow but characteristic frequency

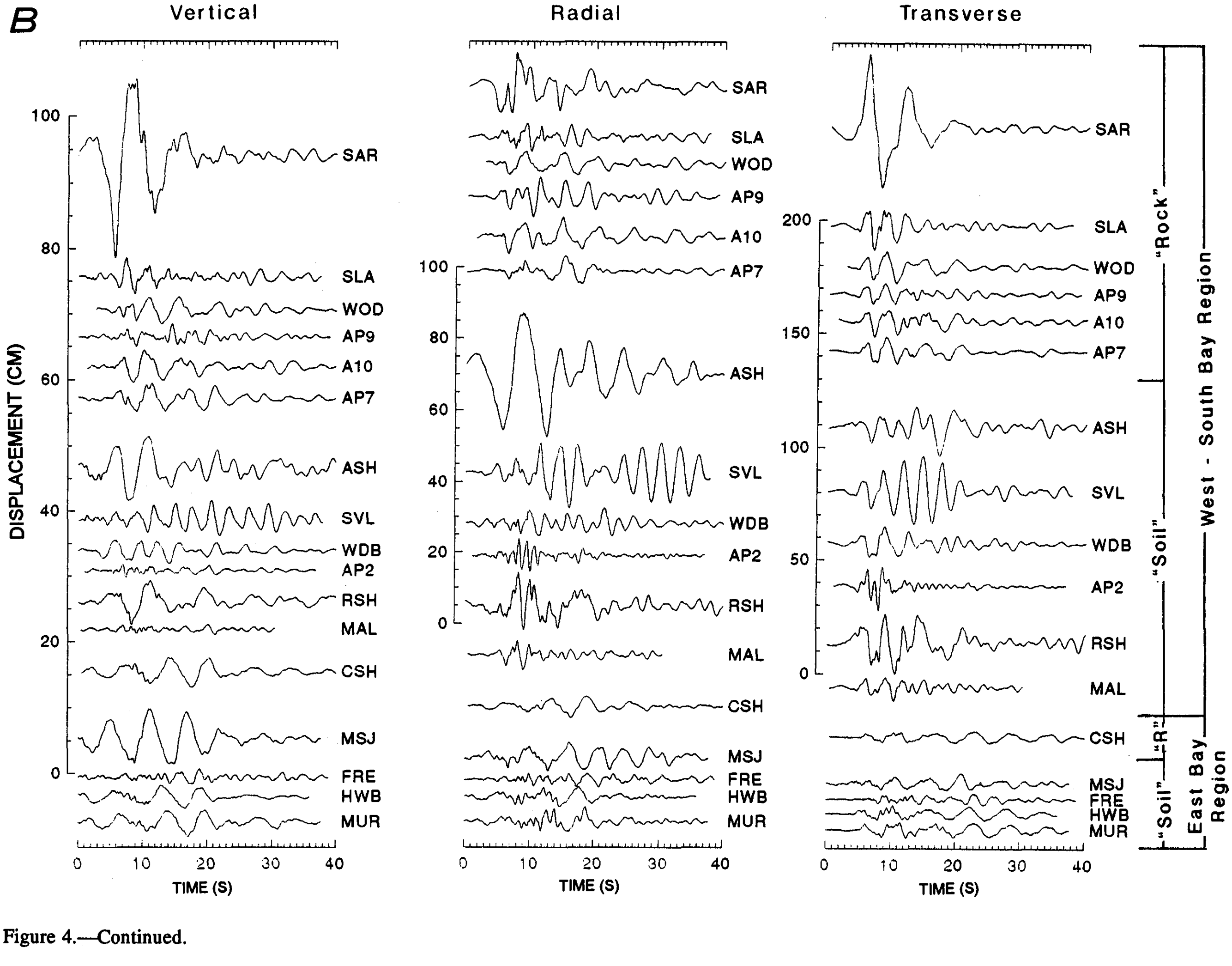

Figure 4.—Continued.

bands. Consequently, an important aspect of any causative damage evaluation for the 1989 Loma Prieta earthquake is the extent to which these effects can be quantified by using ground motions recorded at levels sufficient to induce soil and structural failures.

COMPARATIVE TIME-SERIES OBSERVATIONS

The plots of equiscaled time series (figs. 2–4) provide insight regarding the influence of local site conditions on recorded ground motions. The time histories generally show that peak amplitudes and the number of cycles of relatively strong shaking are larger at "soil" sites than at nearby "rock" sites. These amplifications are most apparent for the horizontal components of ground velocity shortly after the arrival of the *S*-wave energy; they are more apparent in the plots of velocity (fig. 3) and acceleration (fig. 2) than in the plots of displacement (fig. 4).

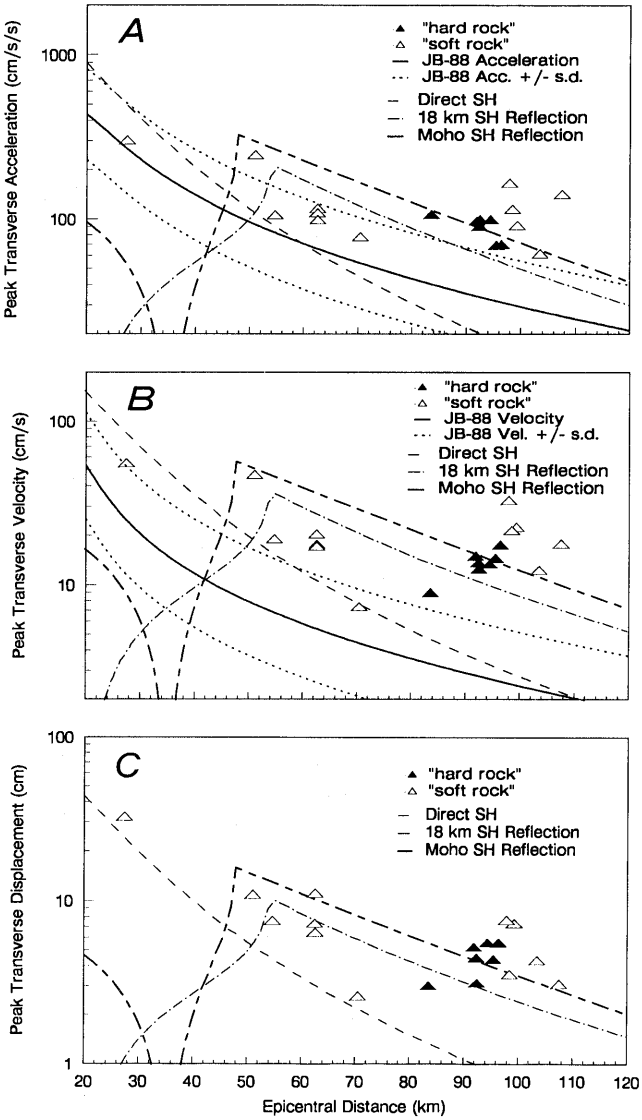

Figure 5.—Peak acceleration (*A*), velocity (*B*), and displacement (*C*) for transverse component of motion recorded at sites located on "hard rock" and "soft rock," empirical mean and 1s curves for corresponding peak horizontal motion (Joyner and Boore, 1988), and theoretical amplitude distributions for *SH* waves in a 10-layer viscoelastic model traveling direct paths and intermediate-crustal (18-km depth)- and Moho (25-km depth)-reflection paths.

The increased number of cycles of shaking recorded at the fill/bay-mud sites generally appear as a somewhat-monochromatic signal superimposed on longer period signals apparent in recordings from nearby "rock" sites (for example, stas. OHW, EMT, AP2, LAR, fig. 1; see fig. 2). These monochromatic-type signals, noted in previous low-strain studies (for example, Borcherdt, 1970), suggest that resonances in some near-surface soil layers also develop at high strain levels.

Horizontal acceleration (fig. 2*A*) and velocity (fig. 3*A*) time series at stations TRI and ALA (fig. 1) show abrupt reductions in amplitude and changes in frequency content at about 12 s after trigger time. These changes and the increase in long-period energy apparent on the inferred horizontal displacements (fig. 4*A*) are consistent with the onset of liquefaction-induced failure and possible lateral movement at the sites (Jarpe and others, 1989; Shakal and others, 1989). The time series for station AP2 (figs. 2*B*, 3*B*, 4*B*) also suggest rather abrupt reductions in amplitude, especially in the transverse component, after the onset of strong shaking. These reductions also may indicate some type of failure and (or) nonlinear soil behavior.

The time series for sites underlain by thick (300–500 m) sections of alluvium in the San Jose-Sunnyvale area (stas. ASH, SVL) are dominated by longer period motions (≥3 s), with substantially extended durations. These longer period ground motions, which are most apparent on the displacement-time series (fig. 4), suggest the existence of surface waves associated with the underlying alluvium. Subsequent modeling (see Frankel and Vidale, this chapter) suggests that some of the surface-wave energy is locally generated by *S*-wave energy incident on the boundary of the alluvial basin. Evidence for longer period energy near 5 to 6 s is also apparent in the recordings obtained at sites in the east bay (stas. CSH, MUR, MSJ, HWB, PIE, BKL, ALA; fig. 4*B*). The existence of these longer period motions on the east side, but not the west side, of the bay is consistent with east-northeastward propagation of surface waves in the sediment-filled San Francisco Bay trough.

COMPARATIVE PEAK-MOTION MEASUREMENTS

To quantify the influence of various geologic deposits on peak values, normalized ratios were computed for each site. Ratios of peak acceleration, velocity and displacement for the vertical, radial, and transverse components of motion are plotted in figure 7 and listed in table 3. The ratios are arranged according to type of underlying geologic deposit and plotted from left to right approximately according to decreasing mean shear-wave velocity (Fumal, 1991).

To minimize the influence of distance and propagation path, these ratios are computed with respect to the corresponding peak value observed at the nearest "rock" site (stas. WOD, AP7, CSH, RIN, PIE, fig. 1). Each ratio is normalized by the corresponding reciprocal ratio of hypocentral distances. Ratios for the normalization sites and for sites in San Francisco are computed with respect to the corresponding mean value determined for sites considered most representative of the Franciscan Complex in the San Francisco-Oakland area (namely, stas. RIN, SSF, YBI, PAC, DIA, PIE). Ratios initially were computed for 21 sites with respect to the mean value for sites on the Franciscan Complex in the San Francisco-Oakland area (Borcherdt, 1990; Borcherdt and Glassmoyer, 1990). However, because of the apparent dependence of the peak values on variations due to direct and reflected crustal-propagation paths, normalization to amplitudes from local "rock" sites is preferred. This procedure helps minimize the influence of different crustal-propagation paths, especially for soil sites in the east and south bay. The results for various normalization procedures are compared in the section below entitled "Comparison of Weak- and Strong-Motion Measurements of Ground Response."

Ratios of peak amplitude show the influence of local deposits in varying amounts for each component of motion (fig. 7; table 3). In general, ratios for vertical motion are less than those for horizontal motion. With the exception of three sites (stas. SAR, OOF, OHW, fig. 1), vertical ratios are less than a factor of 3 and show only a weak correlation with softness of the deposit. Ratios of peak horizontal amplitude show a definite tendency to increase with decreasing firmness of the site. Ratios for

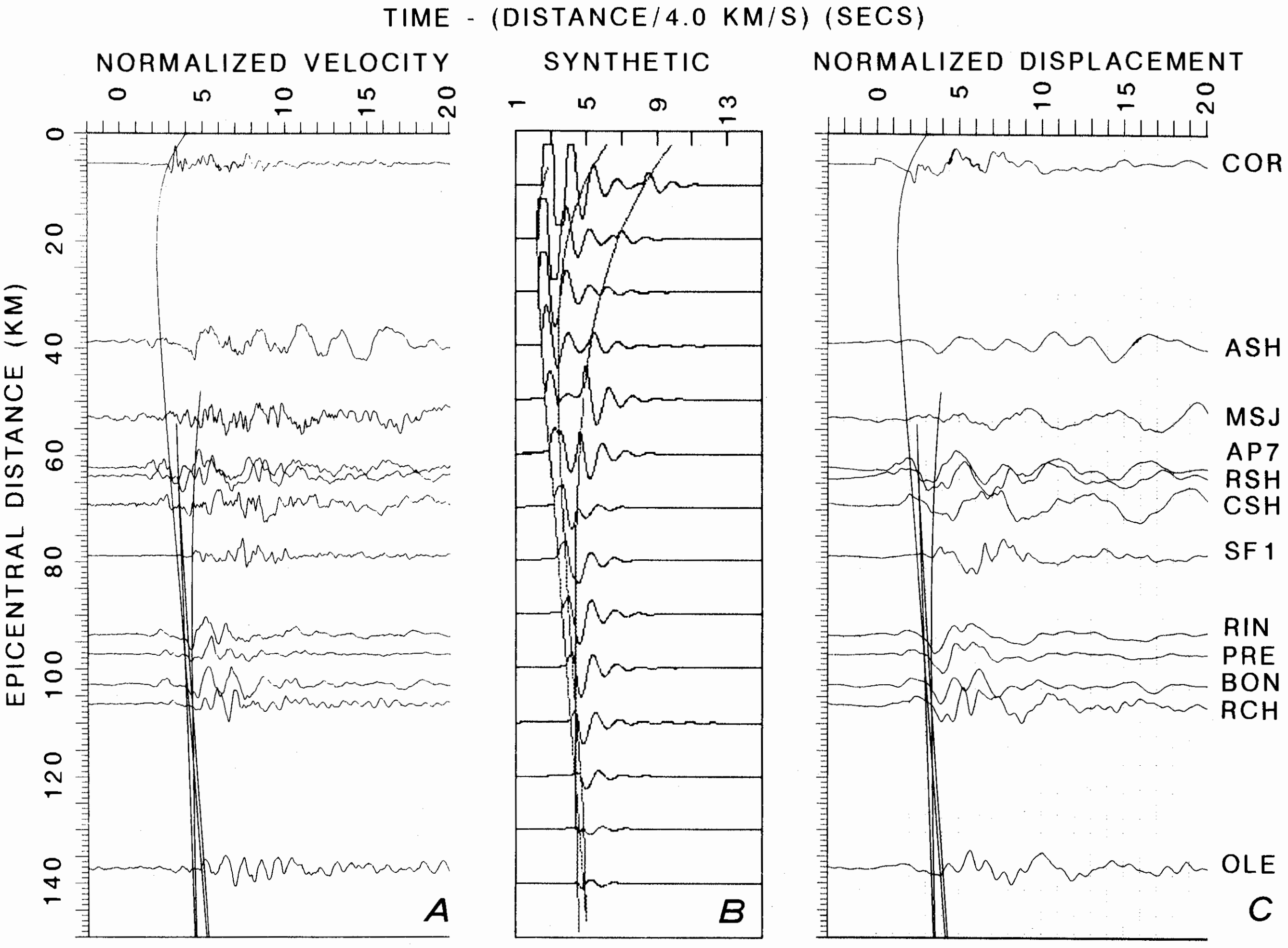

Figure 6.—Velocity (*A*) and displacement (*C*) record sections for transverse component of motion and synthetic recorded sections (*B*) calculated for 10-layer elastic model.

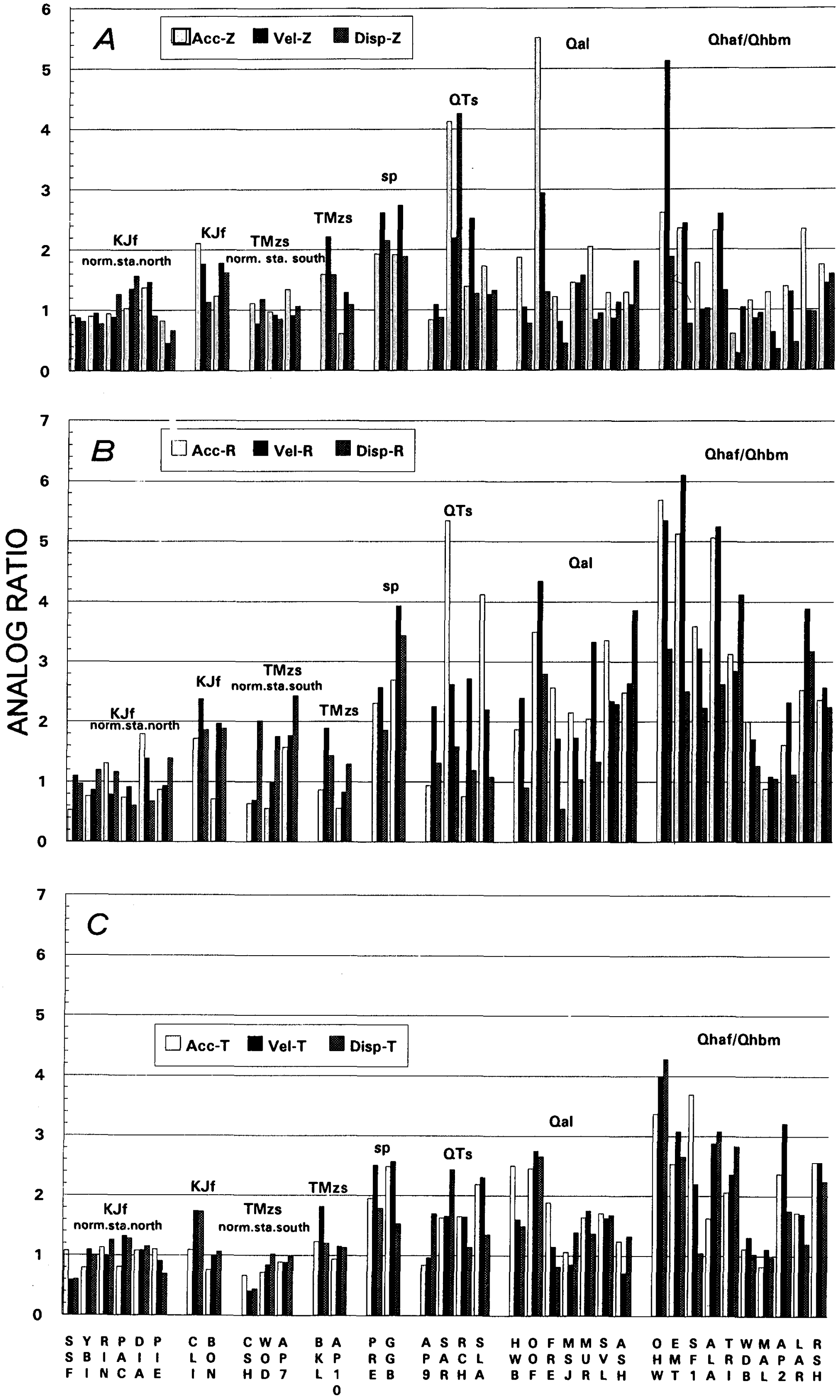

Figure 7.—Bar charts showing ratios of peak acceleration, velocity and displacement for the vertical (*A*), radial (*B*), and transverse (*C*) components of motion, as computed with respect to a "local rock" station and arranged according to geologic unit (see table 1).

Table 3a.—*Ratios of peak acceleration, velocity, and displacement for the vertical, radial, and transverse components of ground motion at "rock" sites normalized with respect to a "local rock" station*

[1, California Strong Motion Instrumentation Program of the California Division of Mines and Geology; 2, Strong Motion Program of the U.S. Geological Survey. APEEL, Andreas Peninsula Earthquake Engineering Laboratory; BART, Bay Area Rapid Transit; bldg., building; CSUH, California State University, Hayward; LBL, Lawrence Berkeley Laboratory; SLAC, Stanford Linear Accelerator Center. Acc, acceleration; Disp, displacement; Dist, distance; E, epicentral; H, hypocentral; R, radial; T, transverse; Z, vertical. Average velocities from Fumal (1991). S.d., standard deviation for sites with velocities estimated from local geology]

Station	Normalization station	H.dist. (km)	S. vel. to 30m	Vertical			Radial			Transverse		
				Acc	Vel	Disp	Acc	Vel	Disp	Acc	Vel	Disp
South San Francisco	SSF/KJf	85	910	0.92	0.88	0.82	0.53	1.10	0.97	1.08	0.59	0.60
Yerba Buena	YBI/KJf	97	880	.90	.95	.78	.76	.86	1.20	.79	1.09	1.00
Rincon Hill	RIN/KJf	96	745	.94	.89	1.27	1.31	.80	1.16	1.13	1.00	1.26
Pacific Heights	PAC/KJf	98	745	1.03	1.36	1.57	.74	.92	.60	.81	1.32	1.28
Diamond Heights	DIA/KJf	94	745	1.38	1.46	.91	1.79	1.39	.68	1.08	1.09	1.16
Piedmont Jr. High	PIE/KJf	94	745	.82	.46	.66	.87	.94	1.39	1.10	.91	.69
Mean			795	1.00	1.00	1.00	1.00	1.00	1.00	1.00	1.00	1.00
Standard deviation			78	.20	.36	.34	.47	.22	.31	.15	.24	.29
Cliff House	CLI/KJf	101	745	2.11	1.76	1.13	1.72	2.38	1.86	1.09	1.74	1.74
Bonita Point	BON/KJf	105	745	1.24	1.78	1.62	.71	1.97	1.88	.76	1.00	1.07
Mean			745	1.67	1.77	1.37	1.21	2.17	1.87	.93	1.37	1.40
CSUH Stadium Grounds	CSH/KJf	73	525	1.11	.78	1.18	.64	.69	2.01	.67	.41	.44
Woodside Fire Station	WOD/KJf	57	440	.97	.92	.85	.56	.98	1.75	.72	.84	1.02
APEEL 7 (Pulgas Temple)	AP7/KJf	65	435	1.34	.91	1.06	1.57	1.77	2.43	.89	.88	.98
Mean			467	1.14	.87	1.03	.92	1.15	2.07	.76	.71	.82
Standard deviation			51	.19	.08	.17	.56	.56	.34	.12	.26	.32
Berkeley (Lawrence Lab.)	BKL/PIE	100	610	1.59	2.21	1.58	.86	1.89	1.44	1.23	1.81	1.21
APEEL 10 (Skyline Blvd.)	AP10/AP7	65	405	.61	1.29	1.09	.55	.83	1.29	.94	1.15	1.13
Mean (TMzs)			508	1.10	1.75	1.33	.71	1.36	1.36	1.08	1.48	1.17
Presidio	PRE/KJf	99	515	1.93	2.62	2.15	2.31	2.57	1.86	1.95	2.51	1.79
Golden Gate Bridge	GGB/KJf	101	515	1.92	2.74	1.89	2.69	3.93	3.44	2.49	2.57	1.53
Mean (sp)			515	1.92	2.68	2.02	2.50	3.25	2.65	2.22	2.54	1.66
APEEL 9 (Crys.Spr. Res.)	AP9/AP7	64	450	.83	1.09	.87	.94	2.26	1.31	.84	.96	1.70
Richmond City Hall	RCH/PIE	109	440	1.39	2.52	1.27	.75	2.72	1.19	1.65	1.65	1.14
Saratoga	SAR/WOD	33	440	4.12	2.19	4.25	5.35	2.62	1.58	1.63	1.66	2.44
SLAC	SLA/WOD	54	320	1.72	1.26	1.32	4.11	2.21	1.08	2.19	2.31	1.35
Mean (QTs)			413	2.02	1.76	1.93	2.79	2.45	1.29	1.58	1.64	1.66
Standard deviation			62	1.45	.70	1.56	2.30	.26	.21	.56	.55	.57
Mean (Rock)			596	1.41	1.48	1.38	1.51	1.73	1.53	1.21	1.34	1.24
Standard deviation			160	.78	.69	.80	1.31	.89	.65	.52	.62	.46

the radial component of motion, approximately parallel to the central axis of the San Francisco Bay trough, tend to be larger than for transverse motion in all areas except the west bay, which are normalized to station AP7.

An important question concerns the influence of soil deposits on the various measures of peak ground motion, namely, acceleration, velocity, and displacement. Ratios of peak amplitude computed here for horizontal motion indicate that each of the three measures of ground motion were amplified by local soil deposits, with amplifications for peak acceleration and velocity exceeding those for displacement at most sites.

Regression analyses using previous strong-motion data sets by Joyner and Boore (1981, 1982) showed no statistically significant difference between rock and soil sites for peak horizontal acceleration but indicated that peak velocities at soil sites were higher by a factor of 1.5. Campbell (1981) used a separate category for sites on less than 10 m of soil; he found that peak horizontal accelerations for this shallow-soil classification were larger by an average factor of 1.8.

Mean values for ratios of peak horizontal (radial) acceleration computed here for the three general site classes of "rock" (SC–I, SC–II), alluvium (SC–III), and fill/bay mud (SC–IV) are nearly the same as for peak velocity (table 3). If the mean values for the "alluvium" sample are normalized by the corresponding mean values for the combined "rock" sample, then average factors of 1.7 and 1.5 are implied, respectively, for acceleration and velocity. These ratios are approximately consistent with the acceleration ratio derived by Campbell (1981) for shallow-soil sites and the velocity ratio derived by Joyner and Boore (1982) for their "soil" category. The analyses also show that the mean for the ratios of peak

Table 3b.—*Ratios of peak acceleration, velocity, and displacement for the vertical, radial, and transverse components of ground motion at "soil" sites normalized with respect to a "local rock" station*

[1, California Strong Motion Instrumentation Program of the California Division of Mines and Geology; 2, Strong Motion Program of the U.S. Geological Survey. APEEL, Andreas Peninsula Earthquake Engineering Laboratory; BART, Bay Area Rapid Transit; bldg., building; CSUH, California State University, Hayward; LBL, Lawrence Berkeley Laboratory; SLAC, Stanford Linear Accelerator Center. Acc, acceleration; Disp, displacement; Dist, distance; E, epicentral; H, hypocentral; R, radial; T, transverse; Z, vertical. Average velocities from Fumal (1991). S.d., standard deviation for sites with velocities estimated from local geology]

Station	Normalization	H.dist.	S. vel.	Vertical			Radial			Transverse		
	station	(km)	to 30m	Acc	Vel	Disp	Acc	Vel	Disp	Acc	Vel	Disp
Hayward BART Station	HWB/CSH	74	365	1.87	1.05	0.78	1.87	2.40	0.91	2.50	1.61	1.49
Oakland Office Bldg.	OOF/PIE	93	295	5.51	2.94	1.30	3.50	4.34	2.80	2.45	2.75	2.66
Fremont	FRE/CSH	58	285	1.22	.80	.45	2.57	1.72	.55	1.89	1.15	.81
Mission San Jose	MSJ/CSH	57	285	1.45	1.44	1.57	2.15	1.73	1.04	1.06	.86	1.39
Muir School (APEEL 2E)	MUR/CSH	73	280	2.05	.83	.94	2.05	3.33	1.33	1.64	1.76	1.36
Mean (Qpa)		71	302	2.42	1.41	1.01	2.43	2.71	1.32	1.91	1.62	1.54
Standard deviation		15	36	1.76	.89	.44	.65	1.13	.87	.60	.73	.68
Sunnyvale	SVL/WOD	46	240	1.28	.86	1.12	3.36	2.35	2.30	1.71	1.62	1.68
Agnew State Hosp.	ASH/WOD	44	240	1.29	1.08	1.81	2.49	2.64	3.86	1.24	.71	1.32
Mean (Qhaf)		45	240	1.28	.97	1.47	2.92	2.50	3.08	1.48	1.17	1.50
Mean (Qal)			284	2.10	1.29	1.14	2.57	2.65	1.83	1.79	1.49	1.53
Standard deviation			42	1.54	.76	.47	.64	.93	1.20	.55	.69	.56
Oakland Harbor Wharf	OHW/PIE	96	251	2.62	5.13	1.88	5.69	5.35	3.21	3.37	3.98	4.27
Emeryville Towers	EMT/PIE	98	245	2.35	2.44	.77	5.13	6.11	2.50	2.54	3.08	2.66
San Francisco Airport	SF1/KJf	81	224	1.77	1.00	1.02	3.59	3.21	2.23	3.69	2.20	1.04
Alameda Naval Air Station	ALA/PIE	92	191	2.32	2.60	1.32	5.06	5.25	2.62	1.63	2.88	3.08
Treasure Island	TRI/YBI	99	171	.60	.28	1.04	3.13	2.85	4.12	2.06	2.36	2.83
Dumbarton Bridge West	WDB/WOD	58	149	1.17	.87	.95	2.03	1.73	1.28	1.13	1.33	1.04
Maley Residence (F. City)	MAL/AP7	68	150	1.29	.63	.35	.88	1.09	1.05	.82	1.11	.98
APEEL 2	AP2/AP7	66	130	1.39	1.30	.46	1.61	2.32	1.12	2.37	3.21	1.75
Larkspur	LAR/KJf	116	130	2.35	.97	.97	2.53	3.89	3.18	1.72	1.70	1.20
Redwood Shores (F. City)	RSH/AP7	67	115	1.74	1.44	1.59	2.36	2.57	2.25	2.57	2.57	2.24
Mean (Qaf/Qhbm)		84	176	1.76	1.67	1.03	3.20	3.44	2.36	2.19	2.44	2.11
Standard deviation		19	50	.65	1.42	.47	1.63	1.67	1.00	.91	.89	1.10
Mean (Soil)			220	1.90	1.51	1.08	2.94	3.11	2.14	2.02	2.05	1.87
Standard deviation			71	1.07	1.18	.46	1.32	1.43	1.08	.79	.93	.94

acceleration for the alluvium sample is not statistically different from that for the "combined rock" sample. This conclusion, apparent in figure 7*B* and table 3, does not imply that peak accelerations were not significantly amplified by local "soil" deposits relative to "hard rock" sites, but instead, as pointed out by Campbell (1985), implies that samples from rock sites which include a wide variety of materials can result in significantly increased mean estimates for short-period components (peak accelerations) of strong ground motions and, in turn, reduced estimates of soil amplification.

COMPARATIVE SPECTRAL-RATIO OBSERVATIONS

Spectral ratios computed with respect to nearby rock sites provide estimates of the seismic-amplitude response of local deposits with the influences of source, crustal-propagation path, and recording instruments minimized (Borcherdt, 1970; Borcherdt and Gibbs, 1976). Spectral ratios, adjusted for hypocentral distance, are computed here with respect to nearby "rock" sites at stations RIN, PIE, CSH, AP7, and WOD (fig. 1), following the procedure used for computing ratios of peak amplitude. (Adjusted spectral ratios have also been computed for the initial data set with respect to a single site, sta. RIN; Borcherdt, 1990.) Spectral ratios are computed here as the ratio of the modulus of the discrete Fourier transforms derived from time series 40.96 s long. A leakage correction corresponding to a 10-percent cosine taper and triangular smoothing windows of 7 and 15 points have been applied, respectively, to the numerator and denominator.

Spectral ratios computed for the three components of motion show several characteristics that correlate with the type of local deposits. Equiscaled plots of the spectral ratios for the radial component of motion (fig. 8) serve to illustrate several of these characteristics. (Plots of the ratios for vertical and transverse motion are provided for the initial data set; Borcherdt, 1990.)

For sites in the general class of "rock" (SC–I, SC–II), the spectral ratios (fig. 8) suggest that, in general, amplification levels are least at sites underlain by the Franciscan Complex. At these sites, the spectral ratios for both horizontal and vertical motion are relatively constant with respect to frequency in the band 0.25–5 Hz. The average ratio for most sites is near 1. The spectral ratios computed for the normalization sites also are relatively constant with respect to frequency, suggesting that the normalized ground motions in the period band of interest at these sites were generally within a factor of 2 of those at sites on the Franciscan Complex. At sites on less consolidated materials (stas. PRE, GGB, BKL, AP10, AP7, RCH, SAR, SLA, fig. 1), average amplification levels and peak spectral amplitudes are notably larger. Substantial variations as a function of frequency are apparent at some sites (stas. GGB, RCH, SAR, SLA).

For sites in the general class of "soil" (SC–III, SC–IV), an important issue concerns the existence of predominant site periods at potentially damaging levels of strong ground motion. Examination of the spectral ratios shows well-defined predominant peaks for the alluvial site at station OOF near Lake Merritt and the fill/bay-mud sites at stations EMT, OHW, ALA, LAR, and AP2 (fig. 1). These peaks are evident in the radial component of motion but generally not in the transverse or vertical component. Spectral ratios computed for some of these sites with respect to station RIN (Borcherdt, 1990) show similar well-defined peaks. These peaks in the spectral ratios suggest the existence of local site resonances. They show that such resonances as observed previously for low-strain ground motions (Borcherdt, 1970) may also develop for ground motions of sufficient amplitude to damage vulnerable structures. The absence of well-defined resonant peaks at other soil sites (stas. HWB, FRE, MSJ, MUR, MAL, RSH, WDB) is consistent with low-strain observations and suggests that resonant motions do not uniformly develop at all "soft soil" (SC–IV) sites. The absence of such resonances on the transverse component of motion from the 1989 Loma Prieta earthquake may be due to the especially short duration of "bedrock" motion in this direction.

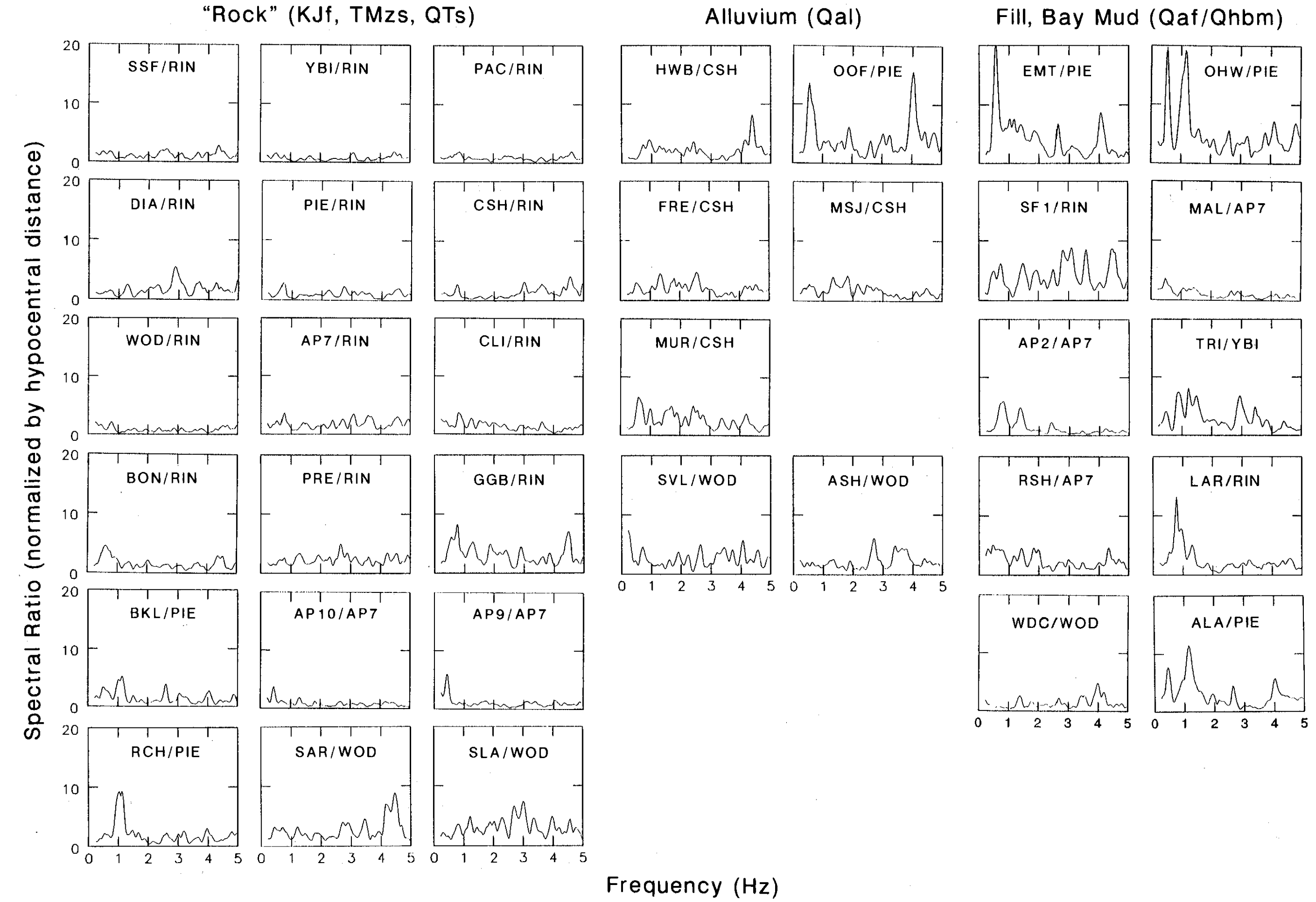

Figure 8.—Spectral ratios for the radial component of motion computed with respect to a "local rock" station and arranged according to type of near-surface geology (see table 1 for explanation).

COMPARATIVE AVERAGE SPECTRAL MEASUREMENTS

Averages of spectral ratios over specified period bands provide estimates of ground response useful for summarizing variations on a regional scale and variations pertinent for different types of structures (table 4). Averages of the spectral ratios for a short-period (0.1–0.5 s), an intermediate-period (0.5–1.5 s), and a long-period (1.5–5.0 s) band as computed with respect to local "rock" stations are listed in table 4 and plotted for the vertical, radial, and transverse components of motion in figure 9. These period bands tend to include the natural periods for structures 1 to 5, 5 to 15, and more than 15 stories high.

For vertical motion, the average spectral ratios (fig. 9*A*) suggest that the larger amplifications commonly occur in the short-period band. Means computed for the average spectral ratios for sites on alluvium and fill/bay mud (table 4) indicate that the average short-period vertical responses exceed the corresponding intermediate- and long-period responses. Corresponding mean values for "rock" sites show that the vertical responses in the various period bands are comparable. Greater vertical response for "soil" sites in the short-period band is consistent with the observation that the ratios of peak vertical acceleration and velocity commonly were greater than the ratios of peak displacement (fig. 7).

The average spectral ratios computed for horizontal motion at sites on fill/bay mud (site class SC–IV) suggest that the larger amplifications frequently occur in the intermediate- and long-period bands. For sites on alluvium, this distinction is apparent at several sites but less pronounced. Greater response for horizontal motion in the intermediate- and long-period bands is consistent at some sites with observations of larger ratios of peak velocity and displacement for corresponding components of motion (fig. 9). These results suggest that structures located on sites with resonant periods in these bands or structures whose periods lengthen into these bands once strong shaking commences are most vulnerable to the amplification effects of local deposits.

Average spectral ratios for the period band 0.4–2.0 s provide a useful parameter to summarize variations in ground response on a regional scale. Average spectral ratios computed with respect to local "rock" sites (fig. 10*A*; table 4) reconfirm that the largest influence of local deposits in general occurs for horizontal motion at sites underlain by alluvium and fill/bay mud. They also indicate, however, that average amplification levels greater than a factor of 2 commonly occur at sites on semiconsolidated units, with a relatively low shear-wave velocity that may be classified as rock (for example, sites on units sp, TMzs, and QTs, fig. 1; table 1b). They show that amplification in at least one horizontal direction consistently exceeded that in the vertical direction at soil sites, but at some rock sites, amplification in the vertical direction either slightly exceeded or was comparable to that in a horizontal direction.

At sites on alluvium and fill/bay mud, amplifications implied for the radial direction are consistently larger than those in the transverse direction in each area, except in the west bay near Foster City. The tendency for directional amplification in the San Francisco-Oakland area is consistent with a similar tendency implied by ratios of peak amplitude and may be associated with differences in the duration of the dominant signals in the two directions.

The maximum average spectral ratio with respect to a local "rock" site implied for sites on alluvium and fill/bay mud ranges from a factor of 1.4 to 6.6 (fig. 10*A*). This wide variation suggests the influence of various factors, including relative thickness of underlying soil layers, response characteristics of the normalization site, basin geometry, and type of dominant amplification. This wide variation must be accounted for in any attempt to generalize ground-response estimates according to mapped geologic units.

COMPARISON OF WEAK- AND STRONG-MOTION MEASUREMENTS OF GROUND RESPONSE

Estimates of the average ground response for various geologic units provide a basis for extrapolating site-specific response measurements to a regional scale for the purposes of seismic zonation. Previous measurements of ground response at 99 sites in the San Francisco Bay region provided a quantitative basis, together with modern geologic maps, for anticipating regional variations in earthquake intensity for large earthquakes on the San Andreas or Hayward fault (Borcherdt and others, 1975). Thus, an important aspect of the Loma Prieta data set concerns the extent to which ground-response variations anticipated on the basis of this larger weak-motion (low strain) data set agree with those that occurred during a local damaging earthquake.

Two important factors influencing measurements of ground response from the 1989 Loma Prieta earthquake, but not the low-strain data set, are attenuation and crustal structure. The distance range for the Loma Prieta data set implies rapid attenuation of body waves and includes critical distances for reflected crustal energy. The low-strain data were recorded at distances greater than 400 km. As a result, variations in distance to each of the recording sites were small in comparison with the total distance; therefore, variations due to geometric spreading and crustal structure are expected to be small (see Borcherdt, 1990, for discussion).

Table 4a.—*Average spectral ratios for the vertical, radial, and transverse components of ground motion at "rock" sites normalized with respect to a "local rock" station (RIN, AP7, CSH, PIE, YBI, or WOD, fig. 1)*

Station	H.dist (km)	S vel. (m/s)	Vertical period bands (secs)					Radial period bands (secs)					Transverse period bands (secs)				
			0.1-0.5	0.5-1.5	1.5-5.0	0.1-5.0	0.4-2.0	0.1-0.5	0.5-1.5	1.5-5.0	0.1-5.0	0.4-2.0	0.1-0.5	0.5-1.5	1.5-5.0	0.1-5.0	0.4-2.0
South San Francisco	85	910	1.07	1.00	0.69	1.04	0.96	1.06	1.02	1.31	1.07	1.07	1.18	0.82	0.53	1.12	0.85
Yerba Buena	97	880	.78	.98	.80	.81	.90	.69	.61	.97	.69	.58	.75	.85	.98	.77	.91
Rincon Hill	96	745	1.13	1.00	1.15	1.11	1.11	1.17	1.12	.93	1.15	1.04	.95	1.09	1.21	.98	.92
Pacific Heights	98	745	.72	.99	1.67	.81	1.07	.62	.99	.88	.69	.93	.56	1.01	1.44	.66	.98
Diamond Heights	94	745	1.38	1.44	1.20	1.38	1.39	1.62	1.26	.94	1.53	1.36	1.57	1.30	1.14	1.53	1.42
Piedmont Jr. High	94	745	.92	.61	.48	.85	.56	.84	1.01	.96	.86	1.02	.97	.92	.69	.95	.92
Mean (KJf ,norm.sta.north)		795	1.00	1.00	1.00	1.00	1.00	1.00	1.00	1.00	1.00	1.00	1.00	1.00	1.00	1.00	1.00
Standard deviation		78	.25	.27	.43	.23	.27	.37	.22	.15	.32	.25	.35	.18	.34	.30	.21
Cliff House	101	745	1.05	1.91	1.61	1.21	2.06	.78	2.24	1.71	1.04	1.90	.81	1.42	1.88	.92	1.34
Bonita Point	105	745	.79	1.28	1.72	.91	1.28	.89	1.94	2.62	1.12	1.90	.86	.77	1.98	.88	.96
Mean		745	.92	1.60	1.66	1.06	1.67	.83	2.09	2.16	1.08	1.90	.83	1.09	1.93	.90	1.15
CSUH Stadium Grounds	73	525	1.42	1.10	.52	1.34	1.06	1.49	.86	1.02	1.39	.76	1.38	.86	.55	1.28	.77
Woodside Fire Station	57	440	.82	.79	.87	.82	.77	.60	.91	1.28	.68	.82	.72	.99	1.10	.76	.91
APEEL 7 (Pulgas Temple)	65	435	1.78	1.00	.92	1.63	.97	1.19	1.65	1.57	1.28	1.60	1.48	1.29	1.18	1.45	1.22
Mean (norm.sta. south)		467	1.34	.97	.77	1.26	.94	1.09	1.14	1.29	1.12	1.06	1.19	1.05	.94	1.16	.96
Standard deviation		51	.48	.16	.22	.41	.15	.46	.44	.28	.38	.47	.42	.22	.34	.36	.23
Berkeley (Lawrence Lab.)	100	610	.90	2.90	1.80	1.20	2.60	.85	1.96	2.28	1.06	1.78	.68	2.34	1.87	.96	2.18
APEEL 10 (Skyline Blvd.)	65	405	.46	.97	1.05	.56	.99	.68	.88	1.86	.76	.82	.44	1.50	1.64	.63	1.54
Mean (TMzs)		508	.68	1.94	1.43	.88	1.80	.77	1.42	2.07	.91	1.30	.56	1.92	1.76	.80	1.86
Presidio	99	515	2.06	2.01	2.46	2.07	2.10	1.65	2.43	1.55	1.75	2.23	1.52	2.20	2.18	1.62	1.99
Golden Gate Bridge	101	515	1.56	1.82	2.88	1.66	2.03	1.70	4.34	3.64	2.18	4.05	1.18	3.13	2.90	1.48	2.66
Mean (sp)		515	1.81	1.92	2.67	1.87	2.06	1.68	3.39	2.60	1.96	3.14	1.35	2.67	2.54	1.55	2.33
APEEL 9 (Crys.Spr. Res.)	64	450	.73	1.37	1.46	.85	1.31	1.08	.93	2.94	1.15	.94	.97	1.06	1.18	.99	1.01
Saratoga	33	440	4.15	2.44	1.86	3.81	2.28	5.01	2.00	2.31	4.48	1.92	3.57	1.13	1.44	3.14	1.30
Richmond City Hall	109	440	2.00	2.60	2.30	2.10	2.50	2.07	3.53	1.54	2.25	2.70	1.61	3.46	1.59	1.87	2.72
SLAC	54	320	4.28	2.42	1.74	3.91	2.46	3.98	2.96	1.69	3.73	2.94	3.11	2.64	1.67	2.99	2.41
Mean (QTs)		413	2.79	2.21	1.84	2.67	2.14	3.04	2.36	2.12	2.90	2.13	2.32	2.07	1.47	2.25	1.86
Standard deviation		62	1.73	.56	.35	1.47	.56	1.78	1.14	.64	1.49	.90	1.23	1.18	.22	1.01	.83
Mean (Rock)		598	1.47	1.51	1.43	1.48	1.50	1.47	1.72	1.68	1.52	1.60	1.28	1.52	1.43	1.31	1.42
Standard deviation		185	1.12	.71	.53	.98	.67	1.23	.82	.64	1.07	.69	.86	.74	.45	.74	.59

Table 4b.—*Average spectral ratios for the vertical, radial, and transverse components of ground motion at "soil" sites normalized with respect to a "local rock" station (RIN, AP7, CSH, PIE, YBI, or WOD, fig. 1)*

Station	H.dist. (km)	S vel. (m/s)	Vertical period bands (secs)					Radial period bands (secs)					Transverse period bands (secs)				
			0.1-0.5	0.5-1.5	1.5-5.0	0.1-5.0	0.4-2.0	0.1-0.5	0.5-1.5	1.5-5.0	0.1-5.0	0.4-2.0	0.1-0.5	0.5-1.5	1.5-5.0	0.1-5.0	0.4-2.0
Hayward BART Station	74	365	3.01	1.00	0.74	2.64	1.38	2.09	2.44	1.04	2.09	2.30	2.23	1.78	0.84	2.11	1.88
Oakland Office Bldg	93	295	5.20	3.20	2.40	4.80	3.40	3.02	3.87	6.61	3.29	3.99	1.81	3.75	4.01	2.17	3.67
Fremont	58	285	1.58	1.04	1.82	1.52	1.14	1.58	2.33	1.89	1.69	2.40	1.45	1.52	1.54	1.46	1.67
Mission San Jose	57	285	2.08	1.03	1.31	1.91	1.27	1.39	2.23	2.07	1.54	2.16	1.47	1.12	1.24	1.42	1.20
Muir School (APEEL 2E)	73	280	2.76	1.06	1.11	2.45	1.06	1.85	3.40	3.05	2.11	3.43	1.82	1.65	1.88	1.80	1.78
Mean (Qpa)		302	2.93	1.47	1.48	2.66	1.65	1.99	2.85	2.93	2.14	2.86	1.76	1.96	1.90	1.79	2.04
Standard deviation		36	1.39	.97	.65	1.27	.99	.64	.74	2.18	.69	.81	.32	1.03	1.24	0.35	.95
Sunnyvale	46	240	2.60	1.10	2.05	2.37	1.23	3.04	2.16	3.43	2.94	2.07	2.40	1.14	1.99	2.21	1.17
Agnew State Hosp	44	240	2.33	1.22	1.47	2.14	1.31	2.78	1.63	1.81	2.58	1.50	2.17	.88	1.32	1.96	.91
MEAN (Qhaf)		240	2.47	1.16	1.76	2.26	1.27	2.91	1.90	2.62	2.76	1.79	2.29	1.01	1.66	2.09	1.04
Mean (Qal)		284	2.79	1.38	1.56	2.55	1.54	2.25	2.58	2.84	2.32	2.55	1.91	1.69	1.83	1.88	1.75
Standard deviation		42	1.16	.81	.57	1.06	.83	.69	.78	1.84	.64	.86	.37	.96	1.04	.33	.92
Oakland Harbor Wharf	96	230	4.10	3.40	5.30	4.00	4.00	3.38	7.02	8.30	4.11	6.62	2.48	6.34	7.23	3.23	5.61
Emeryville Towers	98	240	3.40	2.50	2.50	3.30	2.60	1.88	5.75	9.06	2.72	5.79	1.92	4.31	8.17	2.53	4.61
San Francisco Airport	81	180	1.78	1.51	.88	1.70	1.63	2.92	4.01	3.11	3.07	3.71	2.79	3.43	1.42	2.82	3.57
Alameda Naval Air Station	92	191	2.59	2.71	3.15	2.63	3.18	2.41	4.70	4.27	2.81	3.86	1.17	3.64	5.86	1.73	3.26
Treasure Island	99	130	.83	.31	.44	.74	.45	1.58	4.53	2.52	2.03	3.79	1.44	2.72	4.63	1.76	2.46
Dumbarton Bridge West	58	149	2.08	1.03	.98	1.89	.98	1.29	2.30	2.39	1.49	2.16	.92	1.47	1.35	1.02	1.44
Maley Residence (F. City)	68	150	1.25	1.11	1.00	1.22	1.10	.84	1.32	2.42	.98	1.23	.51	1.57	1.75	.71	1.40
APEEL 2	66	130	1.75	1.28	.78	1.65	1.50	.67	2.62	1.67	.97	2.22	.49	3.35	2.13	.94	2.81
Larkspur Ferry	116	130	3.56	1.22	1.64	3.13	1.32	1.41	3.87	1.36	1.76	2.81	1.12	4.51	3.32	1.61	3.02
Redwood Shores (F. City)	67	115	1.99	1.58	.99	1.89	1.58	2.93	3.18	4.32	3.02	2.91	2.12	3.26	3.29	2.32	3.21
Mean (Qaf/Qhbm)		165	2.33	1.67	1.77	2.22	1.83	1.93	3.93	3.94	2.30	3.51	1.50	3.46	3.91	1.87	3.14
Standard deviation		44	1.06	.93	1.50	1.02	1.09	.94	1.69	2.68	1.02	1.65	.80	1.43	2.47	.84	1.29
Mean (Soil)		214	2.52	1.55	1.68	2.35	1.71	2.06	3.37	3.49	2.31	3.11	1.67	2.73	3.06	1.87	2.57
Standard deviation		74	1.09	.86	1.18	1.02	0.97	.84	1.51	2.37	.86	1.43	.68	1.52	2.22	.66	1.32

To evaluate possible biases in the strong-motion data set due to attenuation and crustal structure, amplification ratios and samples of spectral ratios have been determined by three different normalization procedures. As a first procedure, the ratios were computed with respect to a local "rock" site, which corresponds for sites in the San Francisco-Oakland area to "firm to hard rocks" of the Franciscan Complex, and for sites in the west, east,

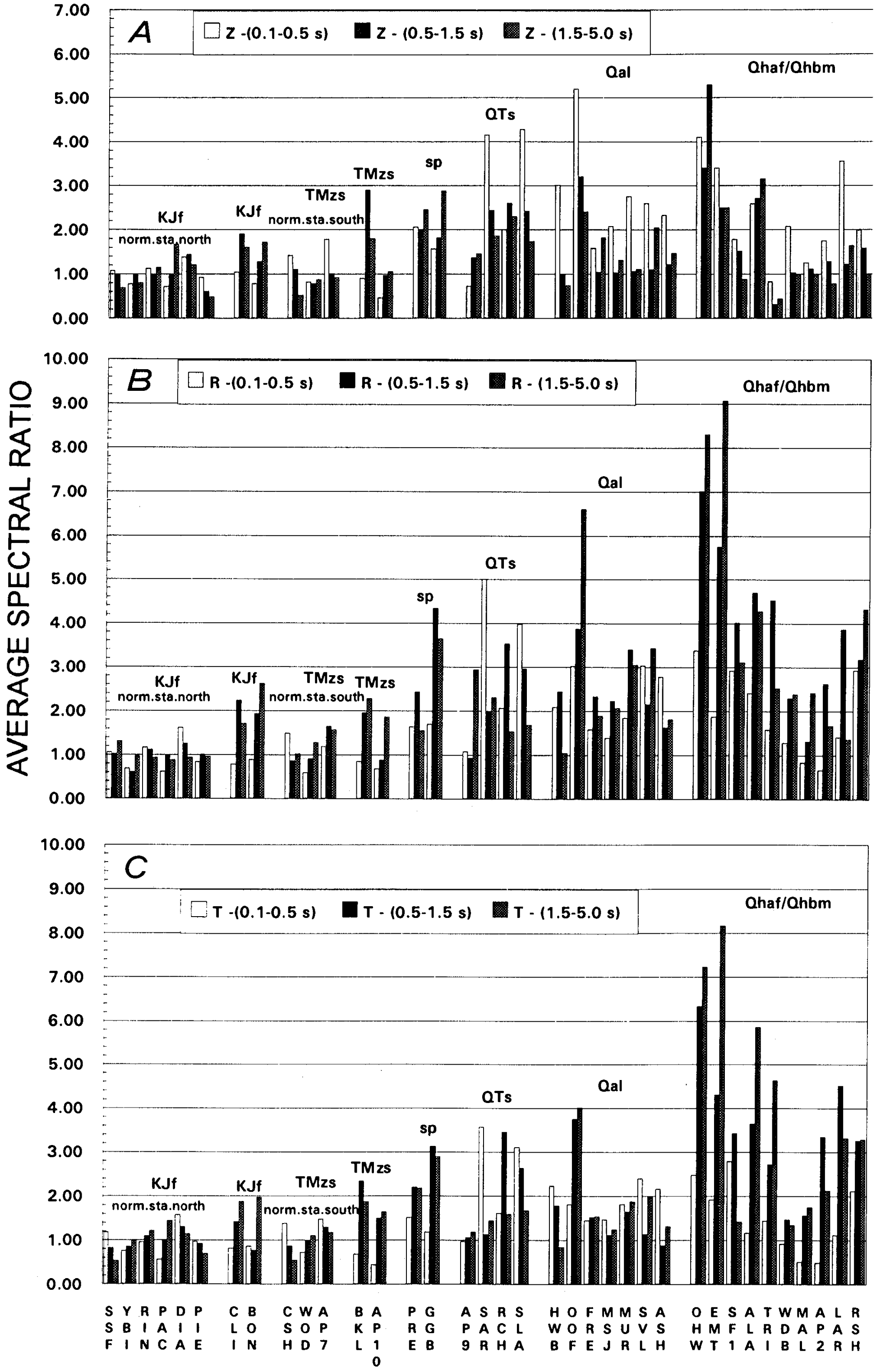

Figure 9.—Bar charts showing average spectral amplification in short-, intermediate- and long-period bands for vertical (*A*), radial (*B*), and transverse (*C*) components of motion, as computed with respect to a "local rock" station and arranged according to geologic unit (see table 1).

and south bay to "soft rock" of unit TMzs (table 1b). The average spectral ratios computed according to this procedure for each site are listed in tables 4a and 4b. As a second procedure, these ratios have been adjusted to the common ground condition of "firm to hard rock" corresponding to the Franciscan Complex. These adjusted values for each site and the corresponding scaling factors are summarized in tables 5a and 5b. As a third procedure, the ratios were initially computed with respect to the mean value determined for sites on the Franciscan Complex in the San Francisco and Oakland areas (Borcherdt and Glassmoyer, 1991). The statistics of each normalization procedure for each of the generalized geologic units are summarized in table 6.

Comparison of the mean values computed from the strong-motion data shows that the average response (vertical and horizontal) implied for units QTs and Qal (tables 1a, 1b) decreases if normalized to the mean value for sites on the Franciscan Complex. This decrease suggests that the procedure to normalize all sites to the mean value for sites on the Franciscan Complex (col. 3 for each component, table 6) does not adequately account for variations in distance between sites in the San Francisco-Oakland area and the sites on units QTs and Qal in the south bay. Comparison of the mean response values for the four sites in the west bay (stas. MAL, AP2, RSH, WDB, fig. 1) increase if the values are either adjusted with respect to a common local ground condition

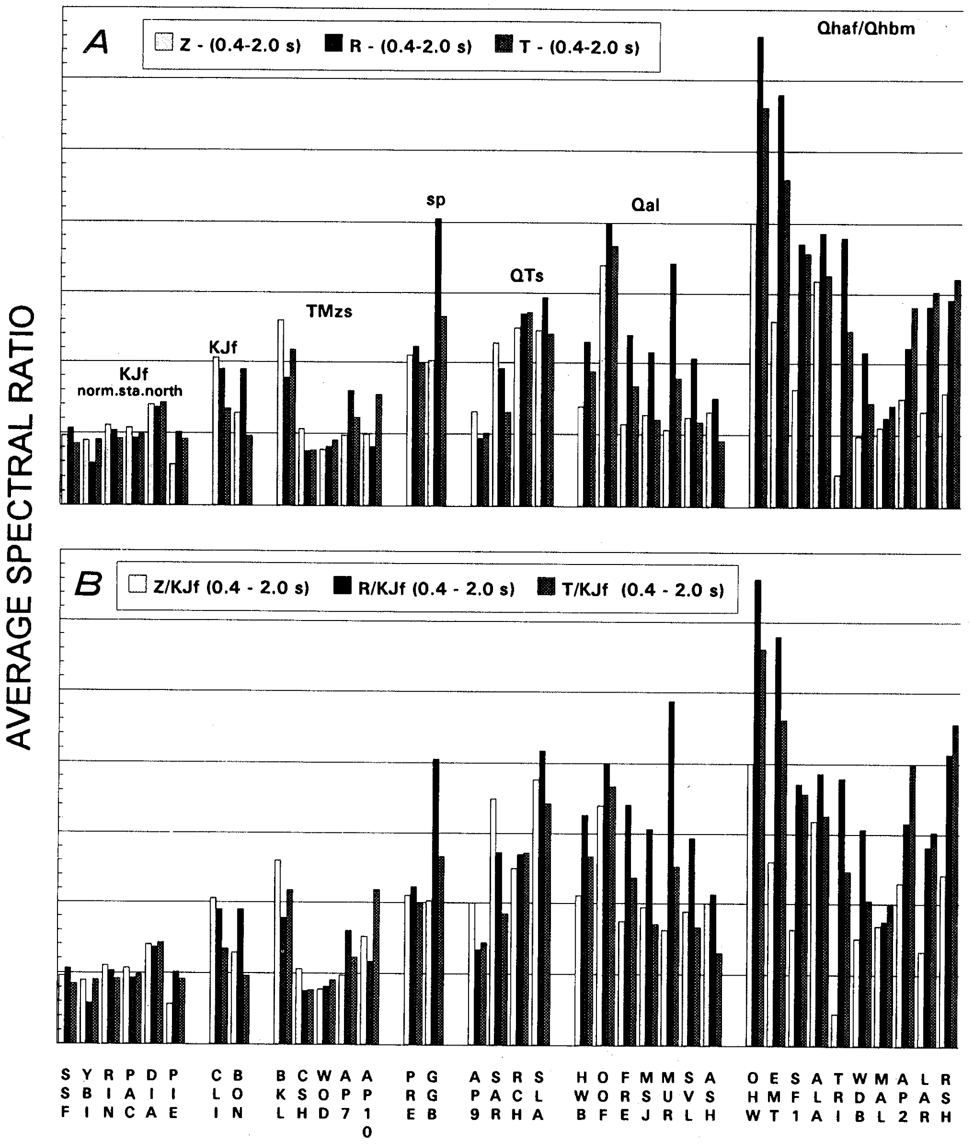

Figure 10.—Bar charts showing average horizontal spectral ratios for period band 0.4–2.0 s for vertical (Z), radial (R), and transverse (T) components of motion, as computed with respect to a "local rock" site (*A*) and normalized ("adjusted") with respect to a common ground condition (unit KJf, table 1b) (*B*). Average spectral ratios plotted in figure 10*B* provide preferred estimates of amplification at each site.

Table 5a.—*Average spectral ratios for specified period bands for "rock" sites, as normalized to "local rock" sites and adjusted to a common ground condition of "firm to hard rock" (unit KJf, table 1b)*

[1, California Strong Motion Instrumentation Program of the California Division of Mines and Geology; 2, Strong Motion Program of the U.S. Geological Survey. APEEL, Andreas Peninsula Earthquake Engineering Laboratory; BART, Bay Area Rapid Transit; bldg., building; CSUH, California State University, Hayward; LBL, Lawrence Berkeley Laboratory; SLAC, Stanford Linear Accelerator Center. Acc, acceleration; Disp, displacement; Dist, distance; E, epicentral; H, hypocentral; R, radial; T, transverse; Z, vertical. Average velocities from Fumal (1991). S.d., standard deviation for sites with velocities estimated from local geology]

Station	Geologic	Site	H.dist.	S velocity		KJf normalization factors			Vertical					Horizontal				
	unit	class	(km)	(m/s)	(ft/s)	Vertical	Horizontal		period bands (secs)					period bands (secs)				
							0.1-0.5	other	0.1-0.5	0.5-1.5	1.5-5.0	0.1-5.0	0.4-2.0	0.1-0.5	0.5-1.5	1.5-5.0	0.1-5.0	0.4-2.0
South San Francisco	KJfss	Ib	85	910	2985	1.00	1.00	1.00	1.07	1.00	0.69	1.04	0.96	1.12	0.92	0.92	1.09	0.96
Yerba Buena	KJfsh	Ib	97	880	2886	1.00	1.00	1.00	.78	.98	.80	.81	.90	.72	.73	.98	.73	.74
Rincon Hill	KJfsh	Ib	96	745	2444	1.00	1.00	1.00	1.13	1.00	1.15	1.11	1.11	1.06	1.11	1.07	1.07	.98
Pacific Heights	KJfsh	Ib	98	745	2444	1.00	1.00	1.00	.72	.99	1.67	.81	1.07	.59	1.00	1.16	.67	.96
Diamond Heights	KJfsh	Ib	94	745	2444	1.00	1.00	1.00	1.38	1.44	1.20	1.38	1.39	1.60	1.28	1.04	1.53	1.39
Piedmont Jr. High	KJfss	Ib	94	745	2444	1.00	1.00	1.00	.92	.61	.48	.85	.56	.91	.96	.83	.91	.97
Mean(KJf norm.: IV)				795	2608				1.00	1.00	1.00	1.00	1.00	1.00	1.00	1.00	1.00	1.00
Standard deviation				78	256				.25	.27	.43	.23	.27	.36	.18	.12	.31	.21
Cliff House	KJfsh	Ib	101	745	2444	1.00	1.00	1.00	1.05	1.91	1.61	1.21	2.06	.80	1.83	1.79	.98	1.62
Bonita Point	KJfsh	Ib	105	745	2444	1.00	1.00	1.00	.79	1.28	1.72	.91	1.28	.87	1.35	2.30	1.00	1.43
MEAN				745	2444				.92	1.60	1.66	1.06	1.67	.83	1.59	2.05	.99	1.53
CSUH Stadium Grounds	TMzs	II	73	525	1722	1.00	1.00	1.00	1.42	1.10	.52	1.34	1.06	1.44	.86	.78	1.34	.76
Woodside Fire Station	TMzs	II	57	440	1443	1.00	1.00	1.00	.82	.79	.87	.82	.77	.66	.95	1.19	.72	.86
APEEL 7 (Pulgas Temple)	TMzs	II	65	435	1427	1.00	1.00	1.00	1.78	1.00	.92	1.63	.97	1.33	1.47	1.37	1.36	1.41
Mean (TMzs; norm. south)				467	1531				1.34	.97	.77	1.26	.94	1.14	1.09	1.12	1.14	1.01
Standard deviation				51	166				.48	.16	.22	.41	.15	.43	.33	.30	.36	.35
Berkeley (Lawrence Lab.)	TMzs	II	100	610	2001	1.00	1.00	1.00	.90	2.90	1.80	1.20	2.60	.77	2.15	2.08	1.01	1.98
APEEL 10 (Skyline Blvd.)	TMzs	II	65	405	1328	1.53	1.25	1.42	.70	1.48	1.61	.86	1.51	.70	1.69	2.49	.99	1.68
Mean (TMzs)				508	1665				.80	2.19	1.70	1.03	2.06	.73	1.92	2.28	1.00	1.83
Presidio	sp	II	99	594	1948	1.00	1.00	1.00	2.06	2.01	2.46	2.07	2.10	1.58	2.32	1.87	1.69	2.11
Golden Gate Bridge	Qal/sp	II	101	515	1689	1.00	1.00	1.00	1.56	1.82	2.88	1.66	2.03	1.44	3.74	3.27	1.83	3.36
Mean (sp)				555	1819				1.81	1.92	2.67	1.87	2.06	1.51	3.03	2.57	1.76	2.73
Mean (TMzs, sp)				503	1651	1.53	1.25	1.42	1.32	1.59	1.58	1.37	1.58	1.13	1.88	1.86	1.28	1.74
Standard deviation				80	263	1.53	1.25	1.42	.52	.73	.87	.45	.68	.40	.98	.84	.40	.88
APEEL 9 (Crys.Spr. Res.)	QTs	II	64	450	1476	1.00	1.00	1.00	2.00	2.60	2.30	2.10	2.50	1.84	3.50	1.57	2.06	2.71
SLAC	QTs	III?	54	344	1128	1.53	1.25	1.42	2.85	.82	.29	2.45	.83	1.98	1.17	.59	1.94	1.00
Mean (QTs)				397	1302				2.42	1.71	1.30	2.28	1.66	1.91	2.33	1.08	2.00	1.86
Standard deviation				75	246				.60	1.26	1.42	.25	1.18	.10	1.64	.69	.09	1.21
Mean (QTs, TMzs, sp; SC-II)				480	1574				1.57	1.61	1.52	1.57	1.60	1.30	1.98	1.69	1.44	1.76
Standard deviation				88	288				.70	.77	.92	.57	.73	.49	1.05	.84	.47	.87
Mean (Rock; SC- Ib, SC-II)				622	2041				1.29	1.40	1.35	1.31	1.40	1.14	1.59	1.49	1.23	1.47
Standard deviation				183	601				.59	.66	.59	.49	.62	.45	.70	.58	.42	.54

or normalized with respect to the mean value for sites on the Franciscan Complex. Corresponding standard deviations are least for the sample adjusted to the local common ground condition. Each of these observations implies that the preferred estimate of ground response is provided by normalization to a common local ground condition.

Testing the null hypothesis that the mean for the low-strain samples equals the mean for the corresponding strong-motion sample, using a *t* distribution, indicates that the null hypothesis can be rejected at the 5-percent-significance level for some samples, depending on the normalization procedure used. For vertical motion, the null hypothesis cannot be rejected for any of the geologic samples with ratios computed with respect to a local "rock" site or adjusted by the mean for the low-strain samples. However, the null hypothesis can be rejected for the samples from units TMzs, Qal, and Qaf/Qhbm (tables 1a, 1b), corresponding to ratios normalized to the mean for the sample from unit KJf in San Francisco and Oakland, suggesting a bias of distance. For horizontal motion, the null hypothesis cannot be rejected at the 5-percent-significance level for the sample from unit Qaf/Qhbm. However, the null hypothesis cannot be rejected at the 2-percent-significance level for the sample from fill/bay mud consisting of ratios adjusted to a common ground condition. This implied difference in statistical significance depending on normalization procedure implies that estimates of mean response for the fill/bay mud derived from the Loma Prieta data set by normalizing to "local rock" or the mean value for unit KJf are biased by distance and the differences in rock type at the normalization sites. Therefore, the preferred estimates of mean response to the 1989 Loma Prieta earthquake are those associated with the spectral ratios adjusted to a common local ground condition, as plotted in figure 10 and listed in table 5.

To further compare the strong- and weak-motion data sets, average horizontal spectral amplifications (AHSA's) are plotted versus mean shear-wave velocity to 30-m depth for each site in figures 11*A* and 11*B*. Superimposed on each figure are best-fit, least-squares,

Table 5b.—*Average spectral ratios for specified period bands for "soil" sites, as normalized to "local soil" sites and adjusted to a common ground condition of "firm to hard rock" (unit KJf, table 1b)*

[1, California Strong Motion Instrumentation Program of the California Division of Mines and Geology; 2, Strong Motion Program of the U.S. Geological Survey. APEEL, Andreas Peninsula Earthquake Engineering Laboratory; BART, Bay Area Rapid Transit; bldg., building; CSUH, California State University, Hayward; LBL, Lawrence Berkeley Laboratory; SLAC, Stanford Linear Accelerator Center. Acc, acceleration; Disp, displacement; Dist, distance; E, epicentral; H, hypocentral; R, radial; T, transverse; Z, vertical. Average velocities from Fumal (1991). S.d., standard deviation for sites with velocities estimated from local geology]

Station	Geologic unit	Site class	H.dist. (km)	S velocity (m/s)	S velocity (ft/s)	KJf normalization factors Vertical	KJf normalization factors Horizontal		Vertical period bands (secs)					Horizontal period bands (secs)				
							0.1-0.5	other	0.1-0.5	0.5-1.5	1.5-5.0	0.1-5.0	0.4-2.0	0.1-0.5	0.5-1.5	1.5-5.0	0.1-5.0	0.4-2.0
Hayward BART Station	Qpa	III	74	365	1197	1.53	1.25	1.42	4.61	1.53	1.13	4.04	2.11	2.70	3.00	1.33	2.98	2.97
Oakland Office Bldg	Qps/Qpa	III	93	315	1033	1.00	1.00	1.00	5.20	3.20	2.40	4.80	3.40	2.42	3.81	5.31	2.73	3.83
Fremont	Qpa	III	58	285	935	1.53	1.25	1.42	2.42	1.59	2.78	2.33	1.74	1.89	2.73	2.44	2.24	2.89
Mission San Jose	Qpa	III	57	285	935	1.53	1.25	1.42	3.18	1.58	2.00	2.92	1.94	1.79	2.38	2.35	2.10	2.39
Muir School (APEEL 2E)	Qpa	III	73	280	918	1.53	1.25	1.42	4.22	1.62	1.70	3.75	1.62	2.29	3.59	3.50	2.78	3.70
Mean (Qpa)				306	1004				3.93	1.90	2.00	3.57	2.16	2.22	3.10	2.99	2.57	3.15
Standard deviation				36	117				1.12	.73	.64	.97	.72	.38	.59	1.51	.38	.60
Richmond City Hall	Qhaf	III	109	288	945	1.00	1.00	1.00	4.00	3.03	2.51	3.80	2.94	3.23	2.78	2.38	3.44	2.54
Sunnyvale	Qhaf	III	46	268	879	1.53	1.25	1.42	3.98	1.68	3.14	3.63	1.88	3.40	2.34	3.85	3.66	2.30
Agnew State Hosp	Qhaf	III	44	240	787	1.53	1.25	1.42	3.56	1.87	2.25	3.27	2.00	3.09	1.78	2.22	3.22	1.71
Mean (Qhaf)				265	870				3.85	2.19	2.63	3.57	2.28	3.24	2.30	2.82	3.44	2.19
Standard deviation				24	79				.25	.73	.46	.27	.58	.15	.50	.90	.22	.43
Mean (Qal: SC-III)				291	954				3.90	2.01	2.24	3.57	2.21	2.60	2.80	2.92	2.89	2.79
Standard deviation				37	120				.86	.69	.63	.74	.63	.61	.67	1.24	.55	.71
Oakland Harbor Wharf	Qaf/Qhbm	IV?	96	251	823	1.00	1.00	1.00	4.10	3.40	5.30	4.00	4.00	2.93	6.68	7.77	3.67	6.12
Emeryville Towers	Qaf/Qhbm	IV	98	196	643	1.00	1.00	1.00	3.40	2.50	2.50	3.30	2.60	1.90	5.03	8.62	2.63	5.20
San Francisco Airport	Qaf/Qhbm	IV	81	180	590	1.00	1.00	1.00	1.78	1.51	.88	1.70	1.63	2.86	3.72	2.27	2.95	3.64
Alameda Naval Air Sta.	Qaf/Qhbm	IV	92	191	626	1.00	1.00	1.00	2.59	2.71	3.15	2.63	3.18	1.79	4.17	5.07	2.27	3.56
Treasure Island	Qaf/Qhbm	IV	99	130	426	1.00	1.00	1.00	.83	.31	.44	.74	.45	1.51	3.63	3.58	1.90	3.13
Dumbarton Bridge West	Qaf/Qhbm	IV	58	149	489	1.53	1.25	1.42	3.18	1.58	1.50	2.89	1.50	1.38	2.68	2.66	1.78	2.56
Maley Res.(F. City)	Qaf/Qhbm	IV	68	150	492	1.53	1.25	1.42	1.91	1.70	1.53	1.87	1.68	.84	2.05	2.96	1.20	1.87
APEEL 2	Qaf/Qhbm	IV	66	130	426	1.53	1.25	1.42	2.68	1.96	1.19	2.52	2.30	.73	4.24	2.70	1.36	3.57
Larkspur Ferry	Qaf/Qhbm	IV	116	130	426	1.00	1.00	1.00	3.56	1.22	1.64	3.13	1.32	1.26	4.19	2.34	1.68	2.92
Redwood Shores	Qaf/Qhbm	IV	67	115	377	1.53	1.25	1.42	3.04	2.42	1.51	2.89	2.42	3.16	4.57	5.40	3.79	4.35
Mean (Qaf/Qhbm; SC-IV)				162	532				2.71	1.93	1.97	2.57	2.11	1.84	4.10	4.33	2.32	3.69
Standard deviation				42	138				.97	.87	1.40	.92	1.01	.87	1.26	2.31	.91	1.25
Mean (Soil; SC-IV, SC- III)				219	719				3.24	1.97	2.09	3.01	2.15	2.18	3.52	3.71	2.58	3.29
Standard deviation				76	250				1.08	.77	1.10	.97	.84	.84	1.21	1.99	.81	1.12

Table 6.—*Average spectral ratios for the period band 0.4–2.0 s for the vertical and mean horizontal components of ground motion determined from weak- and strong-motion data*

[Low-strain data normalized to the mean values for unit KJf (table 1b); strong-motion data normalized with respect to a "local rock" station, to a "local rock" station as adjusted by the mean value for the geologic unit at the normalization station, and to the mean value for unit KJf as determinable only from sites in the San Francisco-Oakland area (SF–O). S.d., standard deviation]

Geologic unit	S velocity (m/s)		Low-strain data Vertical KJf		Low-strain data Av. horizontal KJf		Strong-motion data Vertical "Rock"		Strong-motion data Vertical Adjusted to KJf		Strong-motion data Vertical KJf (SF-O)		Strong-motion data Average horizontal "Rock"		Strong-motion data Average horizontal Adjusted to KJf		Strong-motion data Average horizontal KJf (SF-O)	
	Mean	S.d.	Mean	S.d.	Mean	S.d.	Mean	S.d.	Mean	S.d.	Mean	S.d.	Mean	S.d.	Mean	S.d.	Mean	S.d.
KJf	795	78	1.00	0.26	1.00	0.38	1.00	0.27	1.00	0.27	1.00	0.27	1.00	0.21	1.00	0.21	1.00	0.21
TMzs	512	64	1.53	.35	1.42	.45	1.28	.75	1.39	.73	1.05	.26	1.24	.49	1.34	.52	1.32	.50
QTs	412	62	1.96	.68	1.70	.64	2.14	.56	2.94	.83	1.59	.30	1.99	.85	2.54	1.00	1.92	.64
Qal	284	42	2.19	.94	2.44	1.09	1.54	.83	2.10	.60	1.29	.33	2.15	.86	2.83	.76	1.79	.89
Qaf/Qhbm	174	51	2.45	1.15	5.67	3.31	1.83	1.09	2.11	1.01	1.37	.53	3.32	1.44	3.69	1.25	3.45	1.38

linear-regression lines with corresponding 95-percent-confidence limits for both the observed (standard error of the estimate) and the predicted (95-percent-confidence interval for the ordinate to the true regression line; Crow and others, 1960) values. The best-fit regression lines and their 95-percent-confidence limits for each data set are replotted in figure 11*C*. Testing the null hypothesis that the regression coefficients are significantly different shows that the null hypothesis cannot be rejected at significance levels well beyond 5 percent. The close agreement between the empirical curves for the two samples shows that measurements of either shear-wave velocity

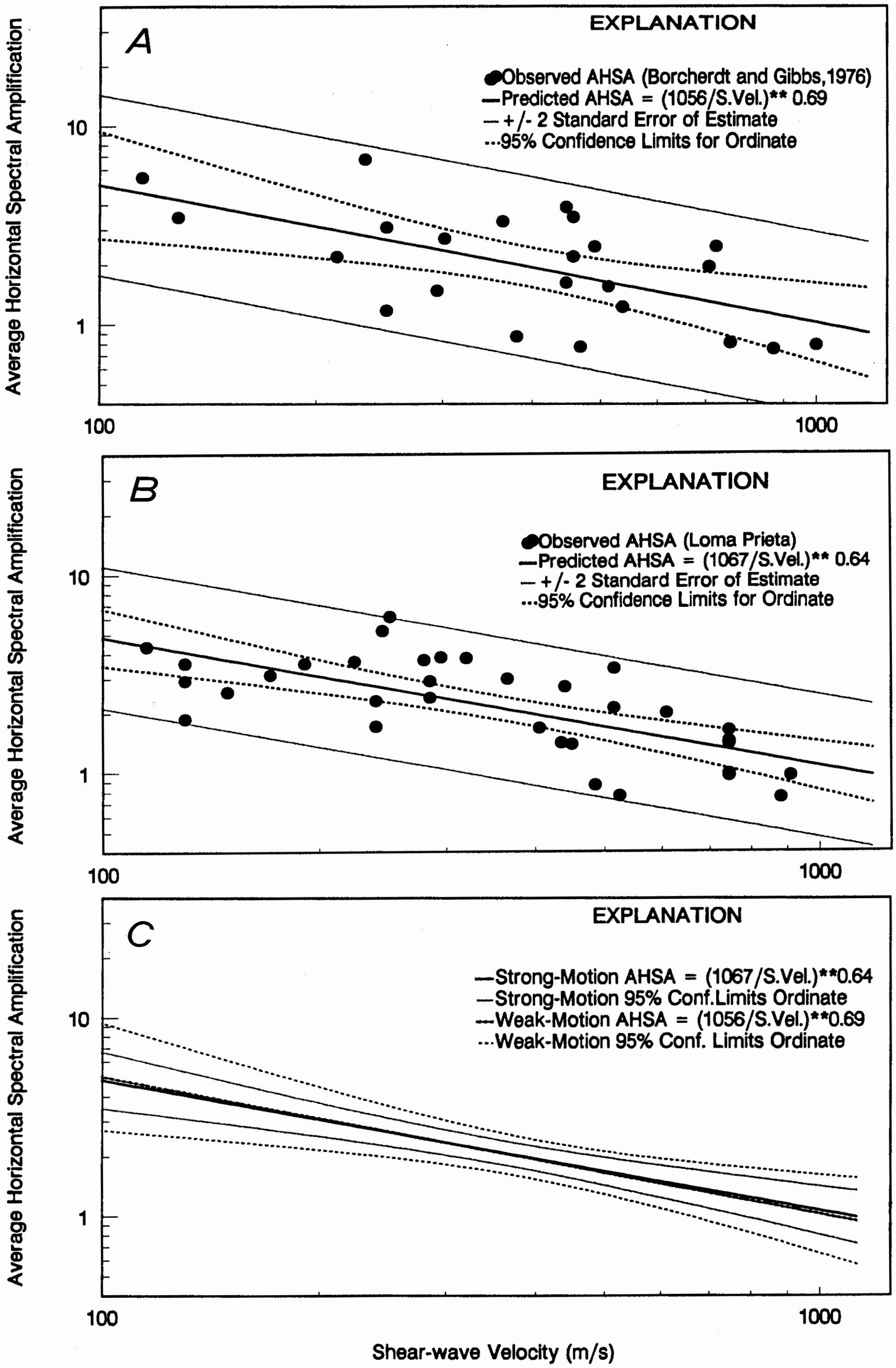

Figure 11.—Average horizontal spectral amplification versus mean shear-wave velocity to 30-m depth and empirical linear-regression curves with corresponding 95-percent-confidence limits for weak-motion (low strain) data (*A*), strong-motion data (*B*), and both data sets (*C*). Close agreement between the two sets of curves in figure 11*C* shows that either mean shear-wave velocity or weak-motion data could have been used to predict average amplifications observed for horizontal ground motion generated by 1989 Loma Prieta earthquake (see text).

Table 7.—*Site classes for site-dependent building-code provisions*

[Mean shear-wave velocity is to a depth of 30 m. Roman-numeral site-class designation from Borcherdt (in press); letter designation originally suggested by R.B. Seed (written commun., 1992).]

Site class		Classification criteria								
Name		(1) General description	(2) Mean shear-wave velocity						(3) Thickness	
			Minimum		Average		Maximum		Minimum	
			(ft/s)	(m/s)	(ft/s)	(m/s)	(ft/s)	(m/s)	(ft)	(m)
SC-I		Firm and hard rocks								
SC-Ia	A_0	Hard rocks (e.g. metamorphic rocks with very widely spaced fractures).	4600	1400	5300	1620	--	--	--	--
SC-Ib	A	Firm to hard rocks (e.g. granites, igneous rocks, conglomerates, sandstones, and shales with close to widely spaced fractures).	2300	700	3500	1050	4600	1400	--	--
SC-II	B	Gravelly soils and soft to firm rocks (e.g. soft igneous sedimentary rocks, sandstones, and shales, gravels, and soils with > 20% gravel).	1230	375	1800	540	2300	700	30	10
SC-III	C	Stiff clays and sandy soils (e.g. loose to v. dense sands, silt loams and sandy clays, and medium stiff to hard clays and silty clays (N>5 blows/ft)).	660	200	950	290	1230	375	20	5
SC-IV	D	Soft soils	--	--	500	200	660	200	--	--
SC-IVa	D1	Non-special-study soft soils (e.g. loose submerged fills and very soft to soft (N<5 blows/ft) clays and silty clays < 37 m (120 ft) thick).	--	--	--	--	--	--	10	3
SC-IVb	E	Special-study soft soils^ (e.g. liquefiable soils, quick and highly sensitive clays, peats, highly organic clays, very high plasticity clays (PI>75%), and soft soils more than 37 m (120ft) thick).	--	--	--	--	--	--	10	3

(^) Site-specific geotechnical investigations recommended for this class.

Table 8.—*Short-period (0.1–0.5 s) and midperiod (0.4–2.0 s) amplification factors predicted with respect to "firm to hard rock" (site class SC–IB) for revised site classes (table 7)*

[Revised site classes are defined in table 7. Amplification factors are predicted from the relations $F_a=(v/997)^{-0.36}$ and $F_v=(v/1{,}067)^{-0.64}$, where v is the mean shear-wave velocity to 30-m depth for each site class; amplification factors for each site class agree with those derived by R. Dobry and R.B. Seed (oral commun., 1992)]

Site class	Physical description	Shear velocity* (m/s)			Amplification**	
		Minimum	Mean	Maximum	F_a	F_v
SC-I	Rocks					
SC-Ia (A_0)	Hard rocks	1400	1620	--	0.8	0.8
SC-Ib (A)	Firm to hard rocks	700	1050	1400	1.0	1.0
SC- II (B)	Gravelly soils and soft to firm rocks	375	540	700	1.3	1.5
SC-III (C)	Stiff clays and sandy soils	200	290	375	1.6	2.3
SC-IV	Soft soils	--	150	200	2.0	3.5
SC-IVa (D)	Non-special-study soft soils					
SC-IVb (E)	Special-study soft soils					

or low-strain ground motion could have been used to predict within the uncertainty of the low-strain data set the responses observed during the 1989 Loma Prieta earthquake. Correlation coefficients for the strong- and weak-motion data sets are –0.7 and –0.6, respectively.

Preliminary empirical curves have been derived between amplification and the reciprocal of mean shear-wave velocity (Borcherdt and others, 1991). These curves provide a simple rule of thumb for predicting approximate levels of amplification; however, inhomogeneity of the residual distributions and a correlation coefficient of 0.5 indicate that the preferred empirical relation is that derived from linear regression on the logarithms of amplification and mean shear-wave velocity.

Inclusion of the three additional sites on fill/bay mud (stas. ALA, WDB, LAR, fig. 1) into the figures and tables of this paper has not significantly modified our general conclusions. However, comparison of the mean horizontal amplification in the midperiod band (0.4–2.0 s) computed for the sample from fill/bay mud (table 6) with that computed previously (see table 5; Borcherdt and Glassmoyer, 1992) shows that the mean horizontal spectral ratio for the expanded sample is reduced to 3.7 from its previous value of 4.0. This reduction is largely due to the low amplifications observed at the West Dumbarton Bridge site. Peak amplitude ratios (fig. 7; table 3) and average spectral ratios (fig. 10; table 4) compiled at this site and station MAL are relatively small in comparison with those computed for other sites on fill/bay mud. Most of the ratios for these sites are smaller than the corresponding means by more than 1σ. The relatively small responses observed at these sites also are less than predicted on the basis of geotechnical logs and the computer program SHAKE (S.E. Dickenson and R.B. Seed, oral commun., 1992). The apparently reduced motions at these sites suggests that other, yet-undocumented factors, such as crustal structure or soil-sensor interaction, may be influencing the observed ground motions.

AMPLIFICATION MEASUREMENTS FOR SITE-SPECIFIC BUILDING-CODE PROVISIONS

Amplification factors derived from the Loma Prieta strong-motion data set provide an important characterization of ground response for use in revised building codes. This characterization (Borcherdt and Glassmoyer, 1992), as updated herein and presented and reviewed at a recent national site-response workshop (Borcherdt, in press), is summarized here for completeness.

Average amplification factors for vertical and average horizontal ground motion, as inferred at each of 36 free-field sites in the San Francisco Bay region, are listed in table 5. These factors, best represented by the average spectral ratios for various period bands, are listed for the short-period band (0.1–0.5 s), intermediate-period band (0.5–1.5 s), long-period (1.5–5.0 s), midperiod (0.4–2.0 s), and entire-period (0.1–5.0 s) bands. Each ratio has been normalized by hypocentral distance and adjusted to a common local ground condition, namely, "firm to hard rock" of the Franciscan Complex (unit KJf, table 1b). The statistics for each sample, corresponding to the generalized geologic units and site classes, is listed in tables 5a and 5b. Corresponding ratios of peak acceleration, velocity, and displacement and average spectral ratios for the individual radial and transverse components of motion, scaled to a common local ground condition, are readily derivable from the results listed in tables 3 and 4 (also the results of Borcherdt and Glassmoyer, 1992). Mean shear-wave velocities to a depth of 30 m, as either measured or estimated for each site by Fumal (1991), are summarized in tables 1a and 1b.

Regression curves relating average horizontal spectral amplification to mean shear velocity for the midperiod band (0.4–2.0 s) are plotted in figure 10 together with corresponding 95-percent-confidence limits. Corresponding regression curves for the short-, intermediate-, and long-period bands show that the intermediate- and long-period dependencies are similar to that for the midperiod band. This important observation suggests that site response is best characterized by two factors, one for the short-period band and one for the other bands.

The average horizontal-amplification factors F_a and F_v for the short-period (0.1–0.5 s) and midperiod (0.4–2.0 s) bands, respectively, at a site with mean shear-wave velocity v to a depth of 30 m are given by

$$F_a = (v/997)^{-0.36}$$

and

$$F_v = (v/1{,}067)^{-0.64}$$

These regression curves provide a rigorous basis to predict site amplification continuously, for site conditions ranging from the softest of soils to the hardest of rock. These empirical regression curves were derived by assuming a linear relation between the logarithms of average amplification and mean shear-wave velocity. The resulting equations imply that the amplification at each site is proportional to some power of the impedance ratio for an approximate average soil profile at the site to rock. The mean velocities implied for rock by the empirical regression curves are consistent with measured values for "firm to hard" rocks and consistent with the midpoint of 1,050 m/s chosen for site class SC–Ib. These empirical relations, based on the Loma Prieta strong-motion data set, are considered most valid for "bedrock" input motions less than or near 0.1 *g*.

Physical descriptions, mean-shear-wave-velocity intervals, and minimum thicknesses for site classes SC–I through SC–IV are summarized in table 7. The mean amplification factor predicted for each site class for horizontal motion in the short-period and midperiod bands is listed in table 8. These factors are predicted by substituting the midpoint of the mean-shear-wave-velocity interval for each site class into the empirical regression curves described by equations 1a and 1b. These mean amplification factors agree closely with the factors derived independently by R.B. Seed (written commun., 1992) and R. Dobry (written commun., 1992). These factors, as implied by the Loma Prieta strong-motion data set, are the first estimates of site-specific amplification factors for consideration in revised building codes based on a substantiative set of inplace measurements of site response for input ground-motion levels near 0.1 *g*.

CONCLUSIONS

Several conclusions implied by the Loma Prieta strong-motion data set are consistent with those derived previously from low-strain and the 1906 San Francisco earthquake-intensity data.

1. Damage from both earthquakes in the San Francisco-Oakland area was concentrated in the areas underlain by fill/bay mud ("soft soil").
2. Ascribed intensities for both earthquakes in San Francisco varied by three units, from the highest for sites in the Embarcadero, China Basin, and the Marina District as it existed in 1906 to the lowest for sites underlain by the Franciscan Complex. (This variation in intensity is consistent with that predicted for these sites by using the relation established between low-strain amplifications and intensity increment; Borcherdt and others, 1975; see Borcherdt and Glassmoyer, 1990, and Borcherdt, 1991.)
3. Ratios of peak amplitude and average spectral ratios for horizontal motion generally increase with decreasing firmness of the deposit and generally are largest for sites underlain by fill/bay mud.
4. Amplification of horizontal motion is greater than that of vertical motion for sites on alluvium and fill/bay mud.
5. Horizontal-spectral-amplification curves define predominant frequencies for both low-strain and strong ground motions at some sites on fill/bay mud (for example, stas. EMT, OHW, AP2, ALA, fig. 1) and some sites on alluvium (for example, stas. OOF, SVL); other sites on these deposits show irregular amplification as a function of frequency and several less well defined peaks.
6. Horizontal and vertical spectral amplifications for sites on "hard rock" are approximately constant as a function of frequency in the period band 0.2–4 s; some sites on "soft rock" (units TMzs, sp, QTs, tables 1a, 1b) show higher average amplification levels and increased amplification over narrow frequency bands.
7. Means of the average horizontal spectral amplifications inferred for the various geologic units do not differ statistically from those based on weak-motion data, except for samples of Loma Prieta amplifications derived by various normalization procedures considered biased by distance and normalization procedure.

Several additional conclusions related to characteristics of the source and geographic variations in "bedrock" motions are unique to the Loma Prieta strong-motion data set.

1. Duration of shaking was relatively short, consistent with bilateral rupture for a dominant main event and less damage than might have occurred for unilateral rupture over a similar fault length.
2. Transverse (*SH*) motions were larger than radial (*P–SV*) motions, which, in turn, were larger than vertical motions at most sites.
3. Peak horizontal accelerations and velocities at all sites in the San Francisco Bay region were greater, and attenuation rates less, than those predicted empirically on the basis of previous strong-motion data.
4. A contributory factor to larger peak motions and, in turn, increased damage levels in the San Francisco-Oakland area was the wide-angle reflection of *S*-wave energy from the base of a relatively shallow (25 km deep) Earth's crust in the region.

The following conclusions pertain to the response of local geologic units in the San Francisco Bay region.

1. Peak accelerations at sites on soil (units Qal, Qaf/Qhbm, tables 1a, 1b) are statistically larger than those at sites on "hard rock" (unit KJf) but not necessarily larger than those at sites on "soft rock" (units sp, QTs).
2. Each measure of peak motion (acceleration, velocity, and displacement) for horizontal motion increases on average with decreasing mean shear-wave velocity, with amplifications inferred for radial motion at "soil" sites commonly greater than those for transverse motion.
3. Average ratios of peak acceleration, velocity, and displacement for radial motion are, respectively, 2.6, 2.6, and 1.8 times larger at sites on alluvium (unit Qal) and 3.2, 3.4, and 2.4 times larger at sites on fill/bay mud sites (unit Qaf/Qhbm) than at nearby "rock" sites.
4. Average spectral ratios (0.4–2.0 s) suggest that the mean strong-motion responses with respect to a uniform bedrock condition (unit KJf) for vertical and horizontal motion are, respectively, 2.1 and 2.8 for unit Qal and 2.1 and 3.7 for unit Qaf/Qhbm.

The following conclusions pertain to ground-response measurements for consideration in site-specific building-code provisions.

1. The strong-motion recordings of the 1989 Loma Prieta earthquake are an important empirical data set from

which to consider site-specific building-code provisions, because they provide the first substantive set of inplace ground-response measurements for a wide variety of geologic materials, from soft clay to hard rock, in close proximity, so that influences of source and wave propagation are minimal or identifiable.

2. Average horizontal spectral amplifications determined from weak- and strong-motion measurements imply that amplification factors for a short-period (F_a; 0.1–0.5 s) and a midperiod (F_v; 0.4–2.0 s) band characterize site response as a continuous function of mean shear-wave velocity.
3. Empirical equations describing short-period (F_a) and midperiod (F_v) amplification factors for strong ground motion as a function of mean shear-wave velocity (v) are

$$F_a = (v/997)^{-0.36}$$

and

$$F_v = (v/1{,}067)^{-0.64}\,.$$

4. The physical description, range in mean shear-wave velocity, amplification capability, and amplification factors implied for the short-period and midperiod bands for the revised site classes being considered in site-specific building-code provisions (Borcherdt, in press) are, respectively: SC–Ib, firm to hard rock, 700 to 1,400 m/s, very low to low (1.0, 1.0); SC–II, soft to firm rock and gravelly soils, 375 to 700 m/s, low to intermediate (1.3, 1.6); SC–III, stiff clays and sandy soils, 200 to 375 m/s, intermediate to high (1.6, 2.3); and SC–IV, soft soils, 100 to 200 m/s, high to very high (2.0, 3.5), where the amplification factors are considered most appropriate for input ground-motion levels less than or near 0.1 *g*.

ACKNOWLEDGMENTS

We appreciate the significant efforts of the California Strong Motion Instrumentation Program of the California Division of Mines and Geology (Shakal and others, 1989) and the Strong Motion Program of the U.S. Geological Survey (Maley and others, 1989). T.E. Fumal graciously provided estimates of mean shear-wave velocity and geologic classifications for each of the sites, and assisted with tables 1 and 7 on the basis of his earlier work as a student with the first author. K.R. Lajoie helped with updating the computer-scanned version of his original generalized geologic map, suggested table 1 as a geologic summary, and provided helpful review comments. L.G. Wennerberg provided computations for the empirical curves in figure 3. S.E. Dickenson kindly provided copies of data at three bay-mud sites to expedite updating the figures and tables. R.B. Seed and R. Dobry graciously contributed their thoughts and results concerning site-specific building-code provisions. We appreciate reviews of the manuscript by H.P. Liu, W.B. Joyner, R.D. Brown, and E. Şafak. Carol Sullivan pleasantly transformed the text by using the computer program TEX.

REFERENCES CITED

Association of Bay Area Governments, 1982, Using earthquake intensity and related damage to estimate earthquake intensity and cumulate damage potential from earthquake ground shaking: Berkeley, Calif., Working Paper 17, 59 p.

Boore, D.M., and Joyner, W.B., 1990, Preliminary analysis of peak accelerations, *in* Benuska, Lee, ed., Loma Prieta earthquake reconnaissance report: Earthquake Spectra, v. 6, supp. 90–01, p. 50–58.

Borcherdt, R.D., 1970, Effects of local geology on ground motion near San Francisco Bay: Seismological Society of America Bulletin, v. 60, no. 1, p. 29–61.

———1977, Reflection and refraction of type-II *S* waves in elastic and anelastic media: Seismological Society of America Bulletin, v. 67, no. 1, p. 43–67.

———1982, Reflection-refraction of general *P* and type-I *S* waves in elastic and anelastic solids: Journal of Geophysical Research, v. 70, no. 3, p. 621–638.

———1990, Influence of local geology in the San Francisco Bay region, California on ground motions generated by the Loma Prieta earthquake of October 17, 1989: International Symposium on Safety of Urban Life and Facilities, Tokyo, 1990, Proceedings, p. 1.1–1.35.

———1991, On the observation, characterization, and predictive GIS mapping of strong ground shaking for seismic zonation—a case study for San Francisco Bay region: New Zealand National Society Earthquake Engineering Bulletin, v. 24, p. 287–305.

———in press, Materials in support of working committee proposals to draft NEHRP site dependent response provisions: National Workshop to Draft NEHRP Site-Dependent Response Provisions, Los Angeles, 1992, Proceedings.

Borcherdt, R.D., and Gibbs, J.F., 1976, Effects of local geological conditions in the San Francisco Bay region on ground motions and the intensities of the 1906 earthquake: Seismological Society of America Bulletin, v. 66, no. 2, p. 467–500.

Borcherdt, R.D., and Glassmoyer, G.M., 1990, Local geology and its influence on strong ground motion generated by the Loma Prieta earthquake of October 17, 1989, *in* Putting the pieces together; National Conference; The Loma Prieta Earthquake One Year Later: Oakland, Calif., Bay Area Earthquake Preparedness Project, p. 11–32.

———1992, On the characteristics of local geology and their influence on ground motions generated by the Loma Prieta earthquake in the San Francisco Bay region, California: Seismological Society of America Bulletin, v. 82, no. 2, p. 603–641.

Borcherdt, R.D., and Wennerberg, L.G., 1985, General *P*, type-I *S*, and type-II *S* waves in anelastic solids; inhomogeneous wave fields in low-loss solids: Seismological Society of America Bulletin, v. 75, no. 6, p. 1729–1763.

Borcherdt, R.D., Gibbs, J.F., and Fumal, T.E., 1978, Progress on ground motion predictions for the San Francisco Bay region, California, *in* Brabb, E.E., ed., Progress in seismic zonation in the San

Francisco Bay region: U.S. Geological Survey Circular 807, p. 13–25.

Borcherdt, R.D., Gibbs, J.F., and Lajoie, K.R., 1975, Prediction of maximum earthquake intensity in the San Francisco Bay region, California, for large earthquakes on the San Andreas and Hayward faults: U.S. Geological Survey Miscellaneous Field Studies Map MF–709, 11 p., scale 1:125,000.

Borcherdt, R.D., Glassmoyer, G.M., and Wennerberg, L.G., 1986, Influence of welded boundaries in anelastic media on energy flow, and characteristics of general *P*, *S*–I, and *S*–II body waves; observational evidence for inhomogeneous body waves in low-loss solids: Journal of Geophysical Research, v. 91, no. B11, p. 11503–11518.

Borcherdt, R.D., Wentworth, C.M., Glassmoyer, G.M., Fumal, T.E., Mark, R.K., and Gibbs, J., 1991, Methodology for predictive GIS mapping of special study zones for strong ground shaking in the San Francisco Bay region, CA: International Conference on Seismic Zonation, 4th, Stanford, Calif., 1991, Proceedings, v. 3, p. 545–552.

Campbell, K.W., 1981, Near-source attenuation of peak horizontal acceleration: Seismological Society of America Bulletin, v. 71, no. 6, p. 2039–2070.

———1985, Strong motion attenuation relations; a ten-year perspective: Earthquake Spectra, v. 1, no. 4, p. 759–804.

Choy, G.L., and Boatwright, John, 1990, Source characteristics of the Loma Prieta, California, earthquake of October 18, 1989 from global digital seismic data: Geophysical Research Letters, v. 17, no. 8, p. 1183–1186.

Crow, E.L., Davis, F.A., and Maxfield, M.W., 1960, Statistics manual: New York, Dover, 288 p.

Converse, April, 1984, AGRAM; a series of computer programs for processing digitized strong-motion accelerograms; version 2.0: U.S. Geological Survey Open-File Report 84–525, 104 p.

Dietz, L.D., and Ellsworth, W.L., 1990, The October 17, 1989, Loma Prieta, California, earthquake and its aftershocks; geometry of the sequence from high-resolution locations: Geophysical Research Letters, v. 17, no. 9, p. 1417–1420.

Ellen, S.D., and Wentworth, C.M., in press, Hillside materials and slopes of the San Francisco Bay region, California: U.S. Geological Survey Professional Paper 1357.

Fumal, T.E., 1978, Correlations between seismic wave velocities and physical properties of near-surface geologic materials in the southern San Francisco Bay region, California: U.S. Geological Survey Open-File Report 78–1067, 114 p.

———1991, A compilation of the geology and measured and estimated shear-wave velocity profiles at strong-motion stations that recorded the Loma Prieta, California, earthquake: U.S. Geological Survey Open-File Report 91–311, 163 p.

Fumal, T.E., and Tinsley, J.C., 1985, Mapping shear-wave velocities of near surface geologic materials, *in* Ziony, J.I., ed., Evaluating earthquake hazards in the Los Angeles region—an earth-science perspective: U.S. Geological Survey Professional Paper 1360, p. 127–149.

Gibbs, J.F., and Borcherdt, R.D., 1974, Effects of local geology on ground motion in the San Francisco Bay region, California—a continued study: U.S. Geological Survey Open-File Report 74–222, 146 p.

Gibbs, J.F., Fumal, T.E., and Borcherdt, R.D., 1975, In-situ measurements of seismic velocities at twelve locations in the San Francisco Bay region: U.S. Geological Survey Open-File Report 75–564, 87 p.

———1976, In-situ measurements of seismic velocities in the San Francisco Bay region, part II: U.S. Geological Survey Open-File Report 76–731, 145 p.

Gibbs, J.F., Fumal, T.E., Borcherdt, R.D., and Roth, E.F., 1977, In-situ measurements of seismic velocities in the San Francisco Bay region . . . part III: U.S. Geological Survey Open-File Report 77–850, 143 p.

Helley, E.J., and Lajoie, K.R., 1979, Flatland deposits of the San Francisco Bay region, California—their geology and engineering properties, and their importance to comprehensive planning: U.S. Geological Survey Professional Paper 943, 88 p.

Holmes, W.T., Lizundia, B., Brinkman, S., Conrad, J., Reitherman, R., Dong, W., Burton, J., and Bailey, A., 1990, Preliminary report on damage to unreinforced masonry buildings. The Loma Prieta earthquake: San Francisco, Rutherford and Chekene, 34 p.

Hudson, D.E., and Housner, G.W., 1958, An analysis of strong-motion accelerometer data from the San Francisco earthquake of March 22, 1957: Seismological Society of America Bulletin, v. 48, no. 3, p. 253–268.

Jarpe, S.P., Hutchings, L.J., Hauk, T.F., and Shakal, A.F., 1989, Selected strong- and weak-motion data from the Loma Prieta earthquake sequence, Seismological Research Letters, v. 60, no. 4, p. 167–176.

Joyner, W.B., and Boore, D.M., 1981, Peak horizontal acceleration and velocity from strong motion records including records from the 1979 Imperial Valley, California, earthquake: Seismological Society of America Bulletin, v. 71, no. 6, p. 2011–2038.

———1982, Prediction of earthquake response spectra: U.S. Geological Survey Open-File Report 82–977, 16 p.

———1988, Measurement, characterization, and prediction of strong ground motion, *in* Von Thun, J.L., ed., Proceedings; Earthquake Engineering and Soil Dynamics II—recent advances in ground-motion evaluation: American Society of Civil Engineers Geotechnical Special Publication 20, p. 43–102.

Kanamori, Hiroo, and Satake, Kenji, 1990, Broadband study of the 1989 Loma Prieta earthquake: Geophysical Research Letters, v. 17, no. 8, p. 1179–1182.

Lawson, A.C., chairman, 1908, The California earthquake of April 18, 1906; report of the State Earthquake Investigation Commission: Carnegie Institution of Washington Publication 87, 2 v.

Luetgert, J.H., 1988a, User's manual for RID84; interactive modeling of one-dimensional velocity-depth functions: U.S. Geological Survey Open-File Report 88–247, 30 p.

———1988b, User's manual for RJEC88; interactive computer programs for plotting seismic refraction record sections: U.S. Geological Survey Open-File Report 88–262, 89 p.

Maley, R.P., Acosta, A.V., Ellis, F., Etheridge, E.C., Foote, L.J., Johnson, D.A., Porcella, R.L., Salsman, M.J., and Switzer, J.C., 1989, U.S. Geological Survey strong-motion records from the northern California (Loma Prieta) earthquake of October 17, 1989: U.S. Geological Survey Open-File Report 89–568, 85 p.

Mueller, C.S., 1990, Computer programs for analyzing digital seismic data: U.S. Geological Survey Open-File Report 90–35, 100 p.

Schlocker, Julius, 1968, The geology of the San Francisco Bay area and its significance in land-use planning, in Danehy, E.A., and Harding, R.C., eds., Urban environmental geology in the San Francisco Bay region: Sacramento, Calif., Association of Engineering Geologists, p. 7–24.

Seed, R.B., Dickenson, S.E., Riemer, M.F., Bray, J.D., Sitar, Nicholas, Mitchell, J.K., Idriss, I.M., Kayen, R.E., Kropp, Alan, Harder, L.F., Jr., and Power, M.S., 1990, Preliminary report on the principal geotechnical aspects of the October 17, 1989 Loma Prieta earthquake: Berkeley, University of California, Earthquake Engineering Research Center Report UCB/EERC–90/05, 137 p.

Shakal, A.F., Huang, M., Reichle, M.S., Ventura, C., Cao, T., Sherburne, R.W., Savage, M., Darrah, R.B., and Petersen, C., 1989, CSMIP strong-motion records from the Santa Cruz Mountains (Loma Prieta), California earthquake of 17 October 1989: California Division of Mines and Geology, Office of Strong Motion Studies Report OSMS 89–06, 196 p.

Somerville, P.G., and Yoshimura, Joanne, 1990, The influence of critical Moho reflections on strong ground motions recorded in San Francisco and Oakland during the 1989 Loma Prieta earthquake: Geophysical Research Letters, v. 17, no. 8, p. 1203–1206.

Wennerberg, L.G., Glassmoyer, G.M., and Borcherdt, R.D., 1984, Effects of anelasticity; wide angle reflections [abs.]: Eos (American Geophysical Union Transactions), v. 65, no. 45, p. 1008.

Wentworth, C.M., Ellen, S.D., Frizzell, V.A., and Schlocker, Julius, 1985, Map of hillside materials and description of their engineering character, San Mateo County, California, U.S. Geological Survey Miscellaneous Investigations Map I–1257–D, scale 1:62,500, 2 sheets.

Wood, H.O., 1908, Distribution of apparent intensity in San Francisco, *in* Lawson, A.C., chairman, The California earthquake of April 18, 1906; report of the State Earthquake Investigation Commission: Carnegie Institution of Washington Publication 87, v. 1, p. 220-245.

THE LOMA PRIETA, CALIFORNIA, EARTHQUAKE OF OCTOBER 17, 1989: STRONG GROUND MOTION AND GROUND FAILURE

STRONG GROUND MOTION

GROUND RESPONSE ON TREASURE ISLAND

By Kyle M. Rollins and Michael D. Mchood,
Brigham Young University;
Roman D. Hryciw and Matthew Homolka,
University of Michigan; and
Scott E. Shewbridge,
Tensar, Inc.

CONTENTS

ABSTRACT

During the earthquake, ground motions recorded on Treasure Island, a manmade fill in San Francisco Bay, were considerably greater than at the adjacent rock outcrop on Yerba Buena Island. This difference provided an opportunity to evaluate existing methods for computing ground response. To perform the analyses, soil-profile data and shear-wave-propagation velocities were measured by seismic cone-penetration testing at several sites on Treasure Island, including the ground-motion-recording station. Measured shear-wave velocities at the recording station agreed well with subsequent velocity measurements using other procedures. Ground motions on Treasure Island were computed with the program SHAKE90, using the Yerba Buena Island data as the rock-outcrop motion. Reasonable agreement was observed between the computed and recorded accelerations at the recording station. Sensitivity studies were performed to evaluate the influence of various parameters, including base rock velocity, soil layering, and shear-wave-velocity profile at depth. Ground-response analyses were also performed at other sites on Treasure Island, and the computed peak accelerations ranged from 0.13 to 0.20 *g*. The degree of damage in various places on the island correlated somewhat with the computed peak accelerations.

INTRODUCTION

The 1985 Mexico City earthquake and the 1989 Loma Prieta earthquake both provided ample evidence of the effects of local geologic conditions on the intensity of ground shaking. A notable example of soil amplification during the 1989 Loma Prieta earthquake was provided by the ground motions recorded on Yerba Buena Island and Treasure Island. Yerba Buena Island is a rock outcrop in San Francisco Bay, whereas Treasure Island is a manmade hydraulic fill placed on Yerba Buena shoals, a sandbar immediately northwest of Yerba Buena Island. Although both islands are at essentially the same distance from the epicenter of the earthquake, they had significantly different ground response owing to foundation conditions. Thus, these data provide an excellent opportunity to examine soil amplification and to evaluate methods for computing ground response.

Idriss (1990) performed a ground-response analysis for Treasure Island, utilizing the best available estimates of the depth to bedrock and shear-wave-propagation velocities (v_s). A similar study was performed by Seed and others (1990), using better data on depth to bedrock. For the present study, seismic cone-penetration tests (CPT's) were conducted on Treasure Island to accurately determine v_s values. Tests were performed as deep as 29 m (95 ft) immediately adjacent to the seismic recording station, as well as at five other locations on the island. At greater depths, shear-wave velocities were measured by using the downhole technique. Analyses were performed by using the equivalent-linear program SHAKE90.

CONSTRUCTION HISTORY OF TREASURE ISLAND

Treasure Island is a 400-acre manmade island immediately northwest of the rock outcrop on Yerba Buena Island in San Francisco Bay (fig. 1). It was constructed in 1936–37 for activities celebrating the construction of the Golden Gate Bridge and the San Francisco-Oakland Bay Bridge. Subsequently, it was the site of an international exposition. During World War II, it was commissioned as a naval installation, and it serves as such today. The original surface soils included a shallow-water sandbar or spit extending northwestward from Yerba Buena Island, and soft silty clay known as bay mud surrounding the sandbar to the north and east. Approximately 65 percent of the island was built on the sandbar, and the rest on bay mud (Lee, 1969).

Treasure Island was constructed by hydraulic and clamshell dredging. A perimeter rock dike was built in two to four stages on a bed of coarse sand placed over bay mud. This dike acted as a retaining system for the sand that was pumped or placed inside. The structure is thus essentially an upstream-constructed hydraulic fill.

SOIL STRATIGRAPHY

The soils on Treasure Island may be grouped into four broad categories: fill, native shoal sand, recent bay sedimentary deposits, and older bay sedimentary deposits. Both the fill and the native shoal sand consists predominantly of sand and varying amounts of clay, silt, and gravel; however, the fill is somewhat looser and locally exhibits a lower CPT tip resistance (q_c) than does the native shoal sand. Typical q_c values for the fill range from 1 to 5 MPa, and for the native shoal sand from 4 to 10 MPa. The recent bay sedimentary deposits consist predominantly of bay mud, a relatively soft, medium-plastic, silty clay with a q_c value increasing with depth and ranging from 0.8 to 1.4 MPa. The cone-friction ratio of bay mud is about 1 percent. At the southeast end of the island, nearest to Yerba Buena Island, the recent bay sedimentary deposits include a mixture of bay mud interbedded with sand. A relatively dense sand generally underlies the bay mud, which is underlain by relatively stiff sandy or silty clay of Pleistocene age.

The depth and thickness of soil layers vary significantly around the island. The thickness of the fill and native shoal sand ranges from 10.7 m (35 ft) at the south end to 15.2 m (50 ft) in the north. The depth of recent bay sedimentary deposits ranges from 10.7m (35 ft) in the south to only about 15.2 m (50 ft); however, in the southeast corner of the island, the deposits, which include both bay mud and interlayered sands, are as much as 36.6 m (120 ft) deep. In the north, the bay mud ranges in depth from 13.7 m (45 ft) to 16.8 m (55 ft) to as much as 21.3 m (70 ft) in the northeast corner to 48.8 m (160 ft) in the west corner of the island.

Bedrock elevation has been confirmed at a depth of 85 m (280 ft) at the location shown in figure 1; this is the only confirmed depth to bedrock on Treasure Island at this time. Nevertheless, from this point and the rock outcrop on Yerba Buena Island, the bedrock surface is estimated to dip 2° NW.

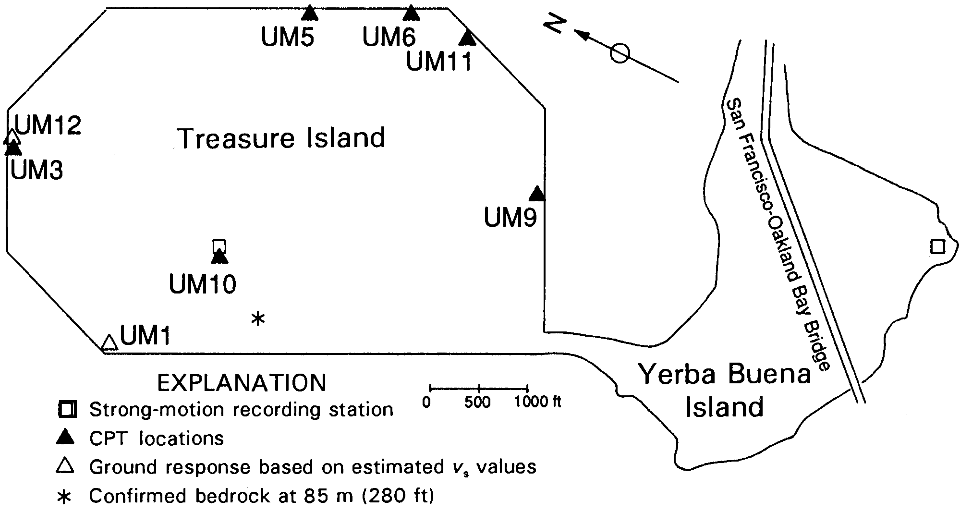

Figure 1.—Sketch map of Yerba Buena Island and Treasure Island in San Francisco Bay, showing locations of sites where ground-response analyses were performed. CPT, core-penetration test; v_s, shear-wave velocity.

RECORDED GROUND MOTIONS ON YERBA BUENA ISLAND AND TREASURE ISLAND

The seismographs on Yerba Buena Island and Treasure Island are both located on the floors of small one-story buildings and oriented to record motions in the north-south, east-west, and vertical directions. The epicentral distances are 95 km for Yerba Buena Island and 98 km for Treasure Island. The strongest ground motions were in the east-west direction, as shown in figure 2. Peak accelerations in this direction were 0.06 *g* on Yerba Buena Island and 0.16 *g* on Treasure Island. In the north-south direction, the peak accelerations were smaller (0.03 *g* on Yerba Buena Island and 0.11 *g* on

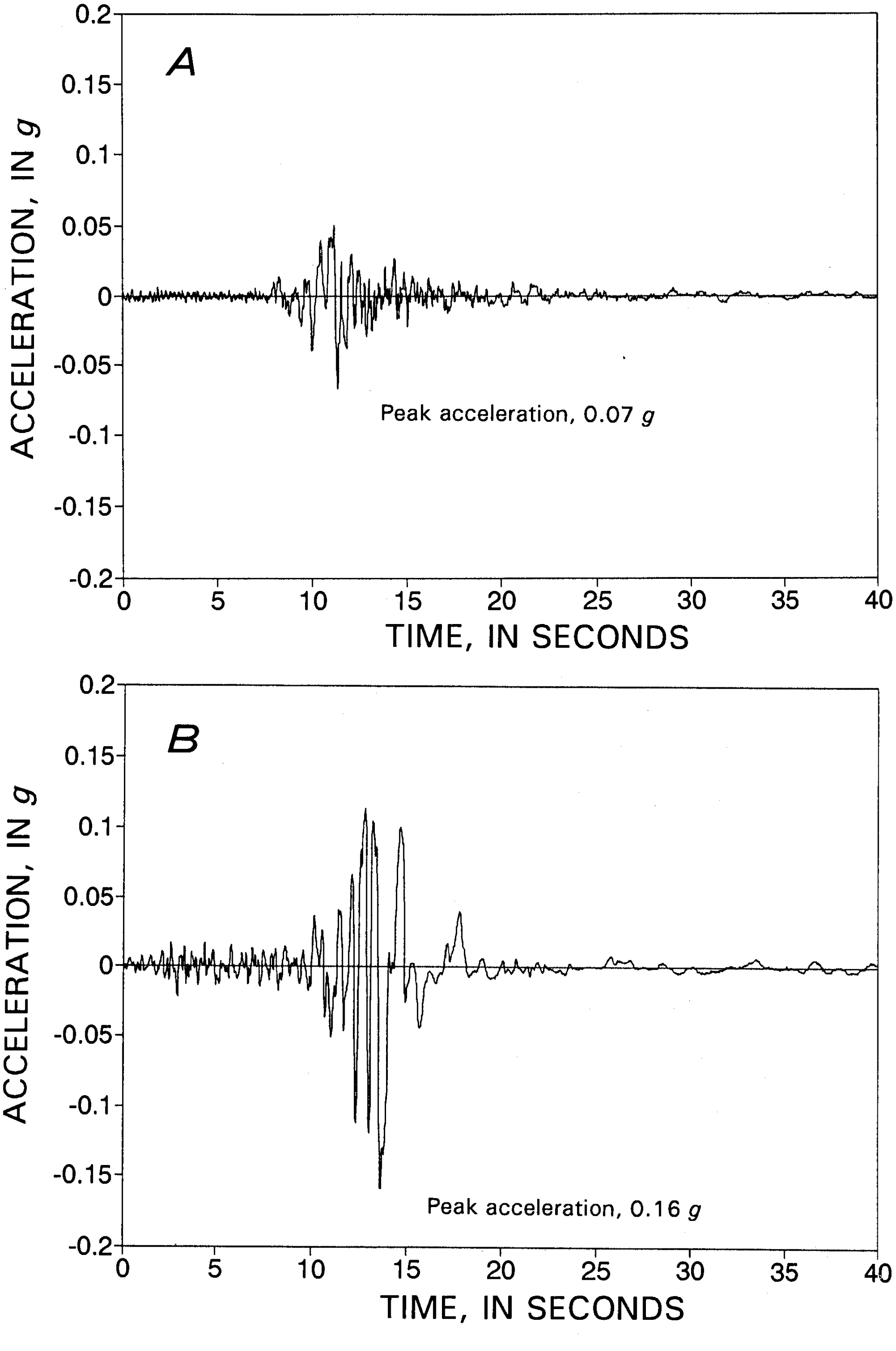

Figure 2.—Recorded ground motion in east-west direction on Yerba Buena Island (*A*) and Treasure Island (*B*).

Treasure Island). The duration of strong shaking was approximately 4 s.

EARTHQUAKE DAMAGE

An extensive postearthquake assessment of damage to the retaining system on Treasure Island was performed by Shewbridge and others (1990). Seed and others (1990) discussed damage to the interior of the island. Damage features to the levee system included lateral spreads, slope failures, pavement cracking and collapse, and soil settlement. Evidence of soil liquefaction was pervasive in the interior of the island, and numerous large sand boils were observed. Settlements of as much as 30 cm (12 in.) occurred, accompanied by numerous pipe breaks and water ponding at the surface.

The best ground-motion performance was observed at site UM1 (fig. 1), where no to very little damage was evident. Although no damage was evident at site UM3, some liquefaction did occur in adjacent inland areas, and a large slump in the levee system was observed at site UM12. This site is particularly noteworthy because during construction of the island, a 120-m (400 ft)-wide trench was dug to a depth of 6 to 9 m (20–30 ft) below the original bay bottom and backfilled with heavy sand before placing the seawall here. Site UM3 was estimated to be located at the inland fringe of this trench.

As much as 9 cm (3.5 in.) of vertical settlement was observed adjacent to a building approximately 60 m (200 ft) inland from site UM9. At site UM5, 9 cm (3.5 in.) of horizontal displacement of the soil was observed; in addition, 5 cm (2 in.) of vertical settlement was observed 30 m (100 ft) away. At site UM6, sand boils and 12 to 15 cm (5–6 in.) of horizontal movement of the levee were evident. Liquefaction was observed at site UM11; however, soils in an area immediately south of site UM11 had been improved by vibroflotation and sustained no damage whatsoever.

SEISMIC CONE-PENETRATION TESTING AND RESULTS

Shear-wave-propagation velocities in the fill and the recent bay sedimentary deposits were measured by seismic CPT's utilizing the University of Michigan's 20-ton rig. The University of Michigan CPT system is based on a pseudointerval concept, whereby a single receiver in the cone records shear-wave-arrival times. The signals were generated at the surface by horizontally directed hammerblows to one of the CPT rig-leveling pads. Measurements were made at 1-m (3 ft)-depth intervals. Reversed-signal-polarity traces and digital recordings provided a high degree of confidence in the identification of shear-wave arrivals.

Shear-wave-propagation velocities in the older bay sedimentary deposits could not be determined by seismic CPT because tip resistances in the sand immediately below the bay mud were much higher than in the bay mud. As a result, attempted penetration of the sand caused severe rod bending through the bay mud and precluded further penetration.

At several other sites, seismic CPT soundings were terminated before reaching the older bay sedimentary deposits. Thus, models of v_s versus depth needed to be developed for the bay mud and for the fill and native shoal sand. Wave-propagation profiles at other depths and sites could then be calculated from these models and from the known stratigraphy, as determined by Shewbridge and others (1990).

The shear-wave-propagation velocities in the fill and native shoal sand (fig. 3) exhibit considerable scatter, as would be expected for a manmade deposit. Nevertheless, the best-fit equation

$$v_s = 150 + 4z\ , \tag{1}$$

where z is the depth (in meters), was used to estimating v_s (in meters per second) at sites UM1 and UM12 (fig. 1).

The shear-wave-propagation velocities in the bay mud are plotted in figure 4. To supplement the data from Treasure Island with the v_s values for bay mud at shallower depths, an additional seismic CPT was performed at the Alameda Naval Air Station (ANAS), which is located approximately 5 km (3 mi) southeast of Yerba Buena Island. Our best fit equation,

$$v_s = 30z^{0.55}\ , \tag{2}$$

agrees very well with the shear-wave-propagation velocities in bay mud collected by Seed and Sun (1989) from seven previously published sources.

After the seismic CPT's, downhole shear-wave velocity was also measured at the seismic recording station (site UM10, fig. 1) by Redpath (1991); the results are plotted in figure 5. Measurements were made at 3-m (10 ft) intervals inside a 125-mm (5 in.)-diameter polyvinyl chloride casing grouted into a 250-mm (10 in.)-diameter hole that extended to a depth of 90 m (300 ft). Redpath was unable to measure shear-wave velocities in the basement rock. The seismic CPT's and downhole shear-wave velocities at site UM10 are compared in figure 5. Although the seismic CPT velocities are somewhat higher, agreement is typically within 20 percent. The differences may be attributable to the shorter measurement interval (1 versus 3 m) used for the seismic CPT's and the smaller hole size (57 versus 250 mm), which would tend to reduce disturbance. Shear-wave velocities measured by crosshole testing performed at the site (see de Alba and others, this chapter) agree very well with the seismic CPT results (fig. 5).

As shown below, the ground-response analysis is rather insensitive to the assumed v_s values in the older bay sedimentary deposits. Nevertheless, because v_s values in these layers were unavailable except at site UM10 (fig. 1), an assumed relation of v_s versus depth for the stiff clay was adopted for the full thickness of the older bay sedimentary deposits. This relation,

$$v_s = 240 + 1.6z\ , \qquad (3)$$

agrees reasonably well with the shear-wave velocities in the older bay sedimentary deposits measured at this and other sites (Joyner and others, 1976; Redpath, 1991).

Layer depths at the test locations and the depths of seismic CPT's are summarized in table 1. Below the maximum test depths, equations 1 through 3 were used to compute v_s except at site UM10 (fig. 1). The propagation velocities at sites UM1 and UM12 are based entirely on equations 1 through 3.

GROUND-RESPONSE ANALYSES

PROCEDURES

At each of the sites shown in figure 1, the ground response was determined by using the computer program SHAKE90, an updated version of SHAKE (Schnabel and others, 1972) that assumes equivalent-linear soil response. Dynamic soil properties are iteratively adjusted until they are compatible with the computed cyclic strain. Normalized shear modulus and damping as a function of shear strain are plotted in figure 6. The data for fill are from Seed and others (1986), and the data for the bay mud and the older bay sedimentary deposits from Lodde (1982). The average cyclic shear strain was taken as 0.65 times the maximum shear strain. The recorded time histories at Yerba Buena Island were used as "outcropping" rock input motions, which were transferred to the base rock by using the procedure of Schnabel and others (1972).

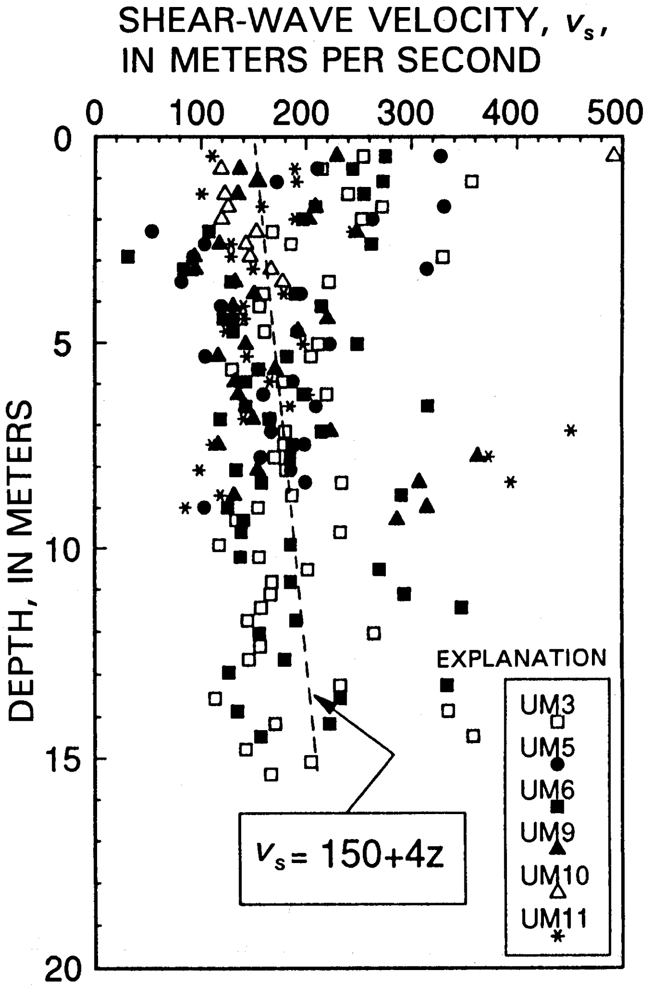

Figure 3.—Shear-wave velocity versus depth in fill and native shoal sand at sites on Treasure Island (see fig. 1 for locations).

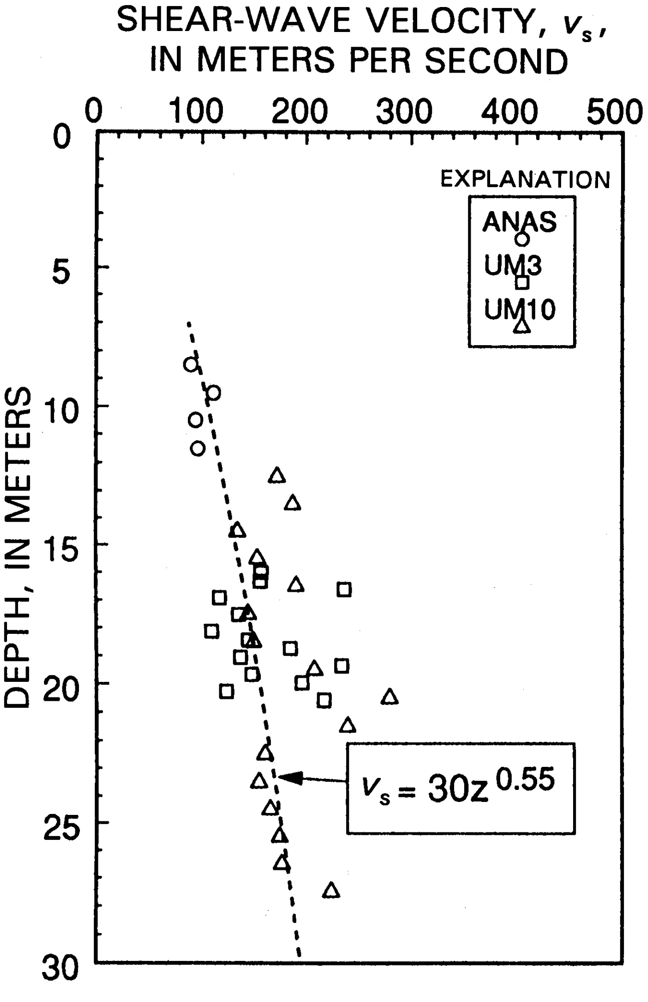

Figure 4.—Shear-wave velocity versus depth in bay mud at sites on Treasure Island (see fig. 1 for locations).

SENSITIVITY ANALYSES

Because wave-propagation velocities in the older bay sedimentary deposits were unavailable at all the sites (fig. 1), a sensitivity analysis was performed to gage the possible errors due to misestimation of v_s in these soils. The acceleration-response spectra at site UM10 (fig. 1) was computed by using several different assumptions, including v_s varying with depth, as measured by Redpath (1991); v_s varying with depth, as measured by Redpath but without the two low-velocity layers; and v_s constant at 300, 335, 365, and 400 m/s. Except for the assumption of low-velocity layers, the computed ground motions are insensitive to the assumed v_s values for the older bay sedimentary deposits. Therefore, the equation developed for v_s in the older bay sedimentary deposits should allow a reasonable estimation of the ground response at the sites where measurements are unavailable.

The inclusion of low-velocity layers reduces the agreement between measured and computed response (fig. 7). These low-velocity layers act as shock absorbers and significantly attenuate ground motions across the entire period range of interest. B.B. Redpath (oral commun., 1992) indicated that there is sufficient uncertainty in interpreting the velocities in these layers to question whether they truly exist, particularly considering their effect on the computed response. This question will likely be resolved by crosshole shear-wave measurements, which are planned for the site UM10. Low-velocity layers were omitted from the analyses at other sites.

Because the shear-wave velocity in the basement rocks was not measured, a sensitivity analysis was also performed for this parameter. The response spectra computed for bedrock velocities ranging from 610 to 1,830 m/s (2,000–6,000 ft/s), which cover the range of velocities measured in Franciscan bedrock, are shown in figure 8. An increase in bedrock velocity progressively increases the response; although this technique improves the agreement at a period of 0.7 s, it worsens it at a period of 1.3 s. The best fit with the measured data is obtained when the elastic half-space representing the basement rock was assumed to have a shear-wave velocity of 1,220 m/s (4,000 ft/s), in reasonably good agreement with the velocity commonly used for basement rocks in geotechnical practice in the San Francisco Bay region and here used for all subsequent analyses.

COMPUTED GROUND MOTIONS AND RESPONSE SPECTRA FOR RECORDED ACCELERATION LEVELS

Using the seismic CPT shear-wave profile in combination with Redpath's (1991) shear-wave profile (neglecting low-velocity zones), final response calculations were performed for the site UM10 (fig. 1). A typical acceleration-time history computed by the program SHAKE90 for site UM10 is compared with the recorded motion in figure 9. The computed time history is similar in form to the recorded motions up to about 14 s, but then the differences become substantial, and the pulses no longer match. These differences are likely due to the onset of liquefaction in the fill, which the program SHAKE is unable to model.

Response spectra computed for the east-west and north-south directions are compared with the measured spectra in figure 10. The shapes of the spectra for the east-west and north-south components, which correspond to motions transverse and radial to the direction of fault rupture, differ considerably. In the east-west direction, the agreement between the measured and computed response is quite good: The computed spectral accelerations are generally within 10 to 30 percent of the recorded values, and the periods of the peaks in the recorded and computed ground motions match well. The agreement is much poorer in the north-south direction, however, and for periods longer than 1 s the computed response is less than 50 percent of the measured response.

The fact that the computed response is quite good for the east-west direction but quite poor for the north-south direction suggests that the north-south rock motion below Treasure Island may differ significantly from that on Yerba Buena Island. We note that the peak acceleration in the north-south direction on Yerba Buena Island is more than 1σ below the mean value expected at this source distance (78 km) on the basis of attenuation relations (Idriss, 1990). Better agreement with the recorded spectrum is obtained when the peak acceleration in the input record is increased from 0.03 to 0.045 *g* (fig. 10). A peak acceleration of 0.045 *g* is slightly less than the mean acceleration at this distance. These difficulties point out the desirability of placing downhole instruments to define the input motion at the base of the soil profile, as is being done at this site (see de Alba and others, this chapter).

The ranges of the computed response spectra for all eight sites are shown in figure 11, along with the spectra of the recorded motions on Yerba Buena Island and Treasure Island. The computed peak ground accelerations in the east-west and north-south directions at all sites are summarized in table 2. The differences in stratigraphy around the island clearly resulted in different computed ground motions; for example, the peak accelerations in the east-west direction ranged from of 0.13 *g* at site UM3 to 0.20 *g* at site UM9.

The variation in maximum acceleration is related to the natural period at each site. Higher ground accelerations occur where the site period approaches peaks in the spectral acceleration of the input rock motion (at 0.7 and

1.3 s), and lower ground accelerations correspond to troughs. For example, the shallowest site (UM9, fig. 1), with a natural period (0.9 s) closest to the predominant period of the rock input motion, had the highest computed peak acceleration, whereas the deepest site (UM3), with the longest computed period (1.7 s), had the lowest computed peak acceleration. It appears that overburden thicknesses were too large to be in resonance with the predominant input accelerations at a period of 0.7 s, although some amplification due to the peaks at 1.3 s was observed at the seismic recording station (site UM10). We note that the period of the second mode of vibration at the recording site was about 0.65 s, which is close to the highest peak of the input spectrum. It also appears that the peak accelerations correlated somewhat with the fill thickness, or depth to bay mud, although it is unclear whether this correlation was due to soil amplification or is just a coincidental trend that paralleled the effects of site period.

Some correlation between peak ground acceleration and damage was observed. Lower ground motions were computed for the northwestern part of the island, where damage was least noticeable. The excavation performed during island construction at site UM12 (fig. 1) resulted in larger ground motions than at the adjacent site UM3. Extensive ground settlement was observed near site UM9, where the largest accelerations were computed. On the east side of the island, where damage was also significant, accelerations ranged from 0.16 to 0.19 *g*. These correlations, however, are somewhat incomplete without consideration of the liquefaction susceptibility of the soil profiles. Future work will likely include such analysis.

Table 1.—*Layer thicknesses and depths of seismic cone-penetration tests at sites on Treasure Island*

[All values in meters. CPT, cone-penetration test; n.d., no data]

Site (fig.1)	Depth to top of layers (m)			Seismic CPT depth
	Bay mud	Older bay sedimentary deposits	Bedrock	
UM1	13.5	48.5	97	n.d.
UM3	15.5	33.9	110	21.0
UM5	11.9	15.6	79	8.3
UM6	14.6	17.0	64	14.6
UM9	9.3	28.0	46	9.3
UM10	11.7	28.9	85	29.0
UM11	14.0	28.0	59	9.0
UM12	21.0	33.0	107	n.d.

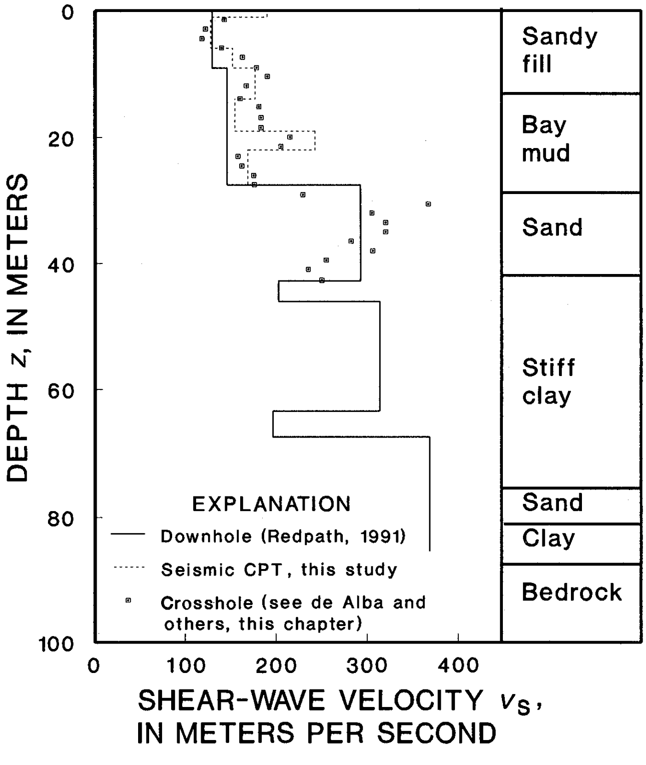

Figure 5.—Shear-wave velocity versus depth at seismic recording station on Treasure Island (see fig. 1 for location). CPT, cone-penetration test.

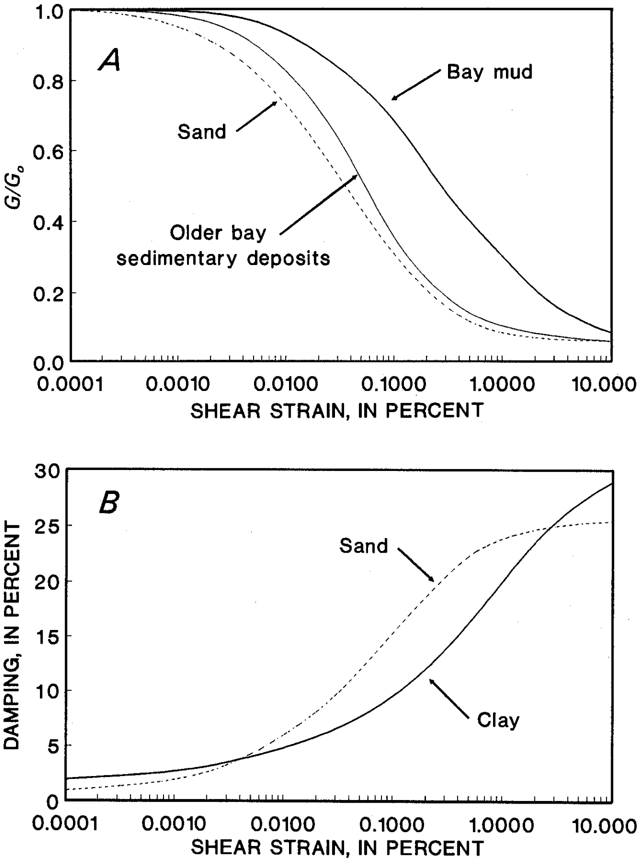

Figure 6.—Normalized shear modulus (*A*) and damping (*B*) versus shear strain. Data from Lodde (1982), Seed and others (1986), and Seed and Sun (1989).

The SHAKE90 analyses revealed several additional interesting features of ground amplification on Treasure Island. The peak accelerations at site UM10 (fig. 1) are plotted versus depth in figure 12. At this site, the older bay sedimentary deposits apparently contributed very little to ground amplification, the bay mud contributed somewhat, but the fill contributed by far the most. However, this observation should not be understood to mean that the fill is inherently more prone to amplification than the bay mud, but rather that the fill is under lower confining pressure and, by its surcharging effect, provides the bay mud with higher shear stiffness. To support this hypothesis, an additional SHAKE90 run was performed for site UM10, assuming that the fill and native shoal sand were replaced by bay mud. The wave-propagation velocity of bay mud was modeled by equation 2. The result is a peak acceleration of 0.18 *g* (east-west), which is equivalent to the peak acceleration for the actual stratigraphy shown in figure 12. Thus, at this site, the loose sandy fill at the surface was just as effective in amplifying ground motions as the bay mud, and the response would have been about the same even if the bay mud had extended to the ground surface.

COMPUTED GROUND RESPONSE FOR FUTURE HIGHER ACCELERATION LEVELS

Future earthquakes may subject Treasure Island to significantly higher peak acceleration levels. On the basis of the attenuation relations of Seed and Idriss (1983), an M=7.0 earthquake on the Hayward fault at a distance of 11 km would generate a peak acceleration of about 0.45 *g* on rock, 7.5 times higher than the peak acceleration recorded on Yerba Buena Island during the 1989 Loma Prieta earthquake. Because of the good agreement between the measured and computed response at lower accelerations, a reasonable estimation of the ground response at higher acceleration levels may be possible, using the SHAKE90 analysis techniques for the same profile. This evaluation has been performed by using eight time histories recorded at stations Gilroy No. 1, Santa Cruz, Corralitos, and Capitola as "outcropping" input motions. These recordings are all on rock or stiff soil sites at an average source distance of 11 km and show an average peak acceleration of 0.45 *g*.

The computed mean response spectrum is shown by the solid curve in figure 13, and the mean$\pm 1\sigma$ spectra by the dotted curves. We note that the computed mean peak acceleration is only 0.43 *g*, slightly lower than the mean peak acceleration of the input records. These analyses indicate that soil nonlinearity will prevent the threefold amplification of peak acceleration observed at low accelerations from occurring for these higher accelerations. Thus, although an earthquake closer to Treasure Island would generate significantly higher spectral accelerations than those recorded during the 1989 Loma Prieta earthquake, it is improper to simply scale up the recorded response spectra by any linear ratio of accelerations.

SUMMARY

1. Seismic CPT's were conducted on Treasure Island to determine the shear-wave-propagation velocities of the fill and bay mud. Models for wave propagation in these materials were developed for use in other places where seismic CPT data were unavailable.
2. The ground motions and response spectra computed by the program SHAKE90 agreed reasonably well with those recorded on Treasure Island, except for periods greater than 1 s. The disagreement may be due to SHAKE90's inability to model softening of the soil after the onset of liquefaction, or to differences between the rock motion at the base of the soil profile and that recorded at the rock outcrop on Yerba Buena Island.
3. The analyses at other sites revealed that response spectra and peak accelerations probably varied on Treasure Island during the earthquake. Computed peak accelerations in the east-west direction range from 0.13 to 0.20 *g*. This variation is related to the period of the soil deposit in relation to the peaks in the input motion spectra.
4. Some correlation is possible between peak ground acceleration and observed earthquake damage. The greatest damage was observed on the southeast side of the island, where the largest ground motions are believed to have occurred. The least damage was observed in the northwest, corresponding to the areas where the smallest ground motions occurred.
5. Because of the low shear-wave-propagation velocity in the loose sandy fill at the seismic recording station (site UM10, fig. 1), the sand was as effective in amplifying peak accelerations as if the bay mud extended to the ground surface.
6. Analyses indicate that future earthquakes closer to Treasure Island will result in significantly higher spectral accelerations than those recorded during the 1989 Loma Prieta earthquake. However, soil nonlinearity will prevent the same degree of amplification (soil to rock) observed at lower accelerations from occurring for higher accelerations.

ACKNOWLEDGMENTS

This research was supported by U.S. National Science Foundation grants BCS–9011121, DOI–G–14–08–0001–G1865, CES–8807134, and BCS–9011294 to Brigham

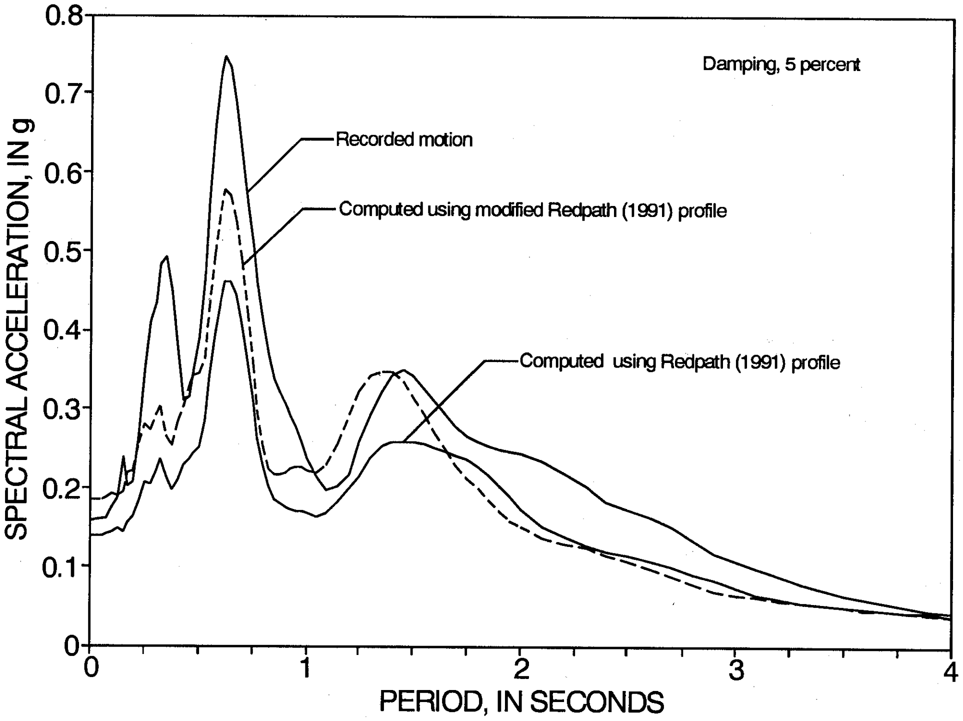

Figure 7.—Computed response spectra in east-west direction at site UM10 (fig. 1) for older bay sedimentary deposits with and without low-velocity layers.

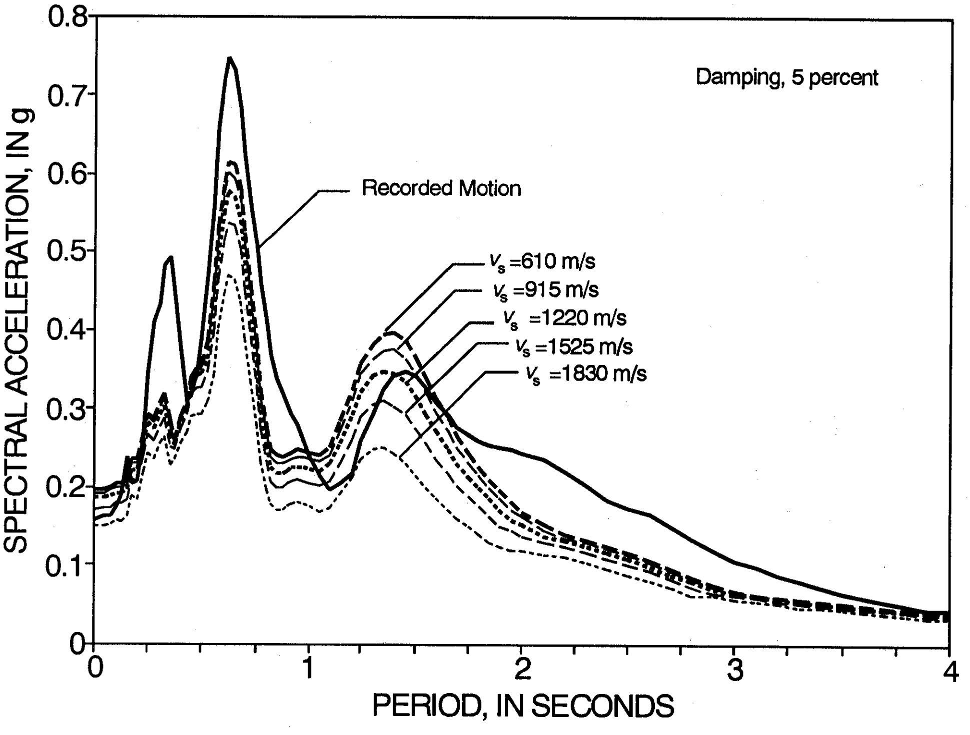

Figure 8.—Computed response spectra in east-west direction at site UM10 (fig. 1), using various assumptions for shear-wave velocity in basement rocks.

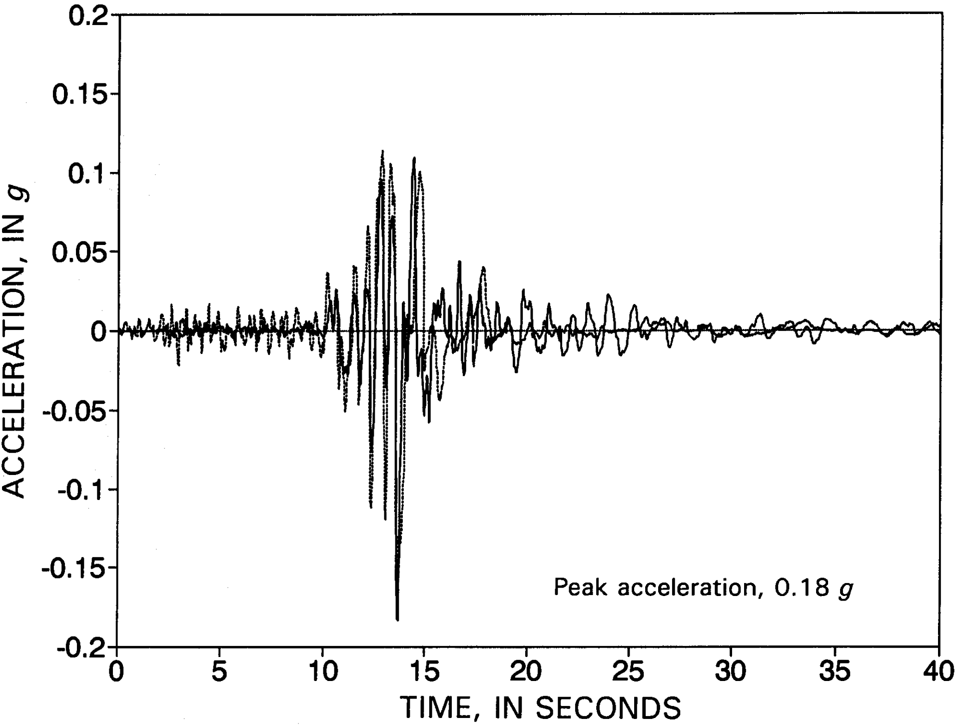

Figure 9.—Acceleration-time history in east-west direction at site UM10 (fig. 1), as recorded (dotted curve) and computed by program SHAKE90 (solid curve).

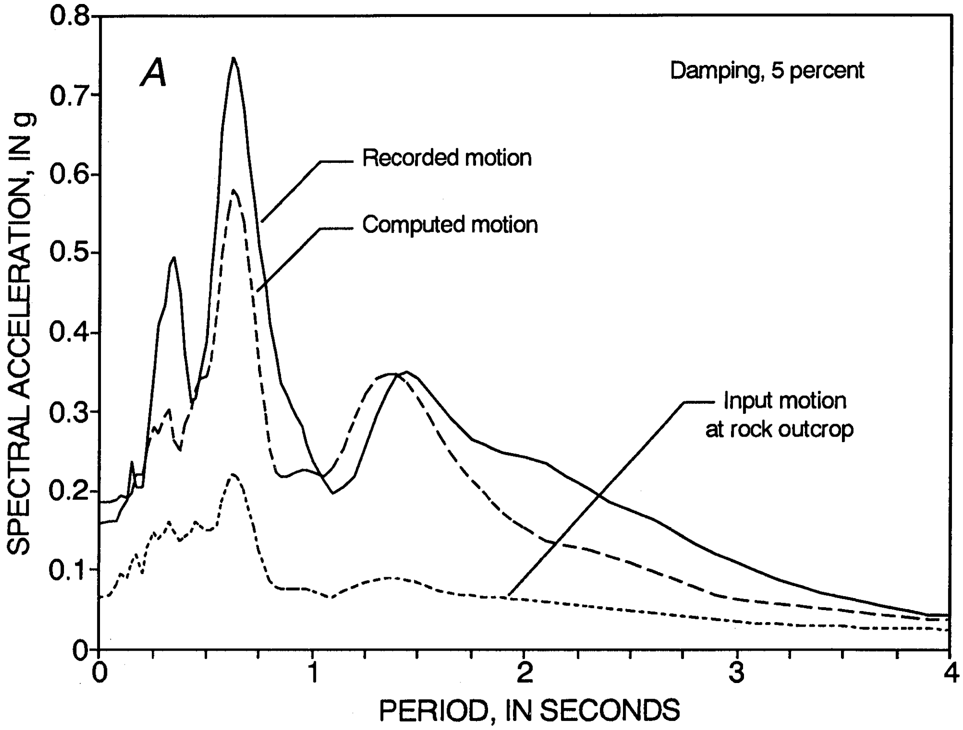

Figure 10.—Response spectra in east-west (*A*) and north-south (*B*) directions at site UM10 (fig. 1), recorded by seismic cone-penetration testing and computed using modified shear-wave velocities of Redpath (1991)

Young University. We thank John A. DeBecker of the Western Division, Naval Facilities Engineering Command, and his staff for their support, and we appreciate the assistance of Geomatrix Consultants, Inc., of San Francisco.

REFERENCES CITED

Idriss, I.M., 1990, Response of soft soil sites during earthquakes, *in* H. Bolton Seed Memorial Symposium: Berkeley, Calif., BiTech, v. 2, p. 273–289.

Joyner, W.B., Warrick, R.E., and Oliver, A.A., 1976, Analysis of seismograms from a downhole array in sediments near San Francisco Bay: Seismological Society of America Bulletin, v. 66, n. 3, p. 937–958.

Lee, C.H., 1969, Bay mud developments; case history 2, Treasure Island fill, *in* Geologic and engineering aspects of San Francisco Bay fill: California Division of Mines and Geology Special Report 97, p. 69–72.

Lodde, P.F., 1982, Dynamic response of San Francisco Bay Mud: Austin, University of Texas, M.S. thesis, 283 p.

Redpath, B.B., 1991, Seismic velocity logging in the San Francisco Bay area: Palo Alto, Calif., Electric Power Research Institute final report under agreement RP 3014–06, 34 p.

Schnabel, P.B., Lysmer, John, and Seed, H.B., 1972, SHAKE; a computer program for earthquake response analysis of horizontally layered sites: Berkeley, University of California, Earthquake Engineering Research Center Report EERC 72–12, 88 p.

Seed, H.B., and Idriss, I.M., 1983, Ground motions and soil liquefaction during earthquakes: El Cerrito, Calif., Earthquake Engineering Research Institute, 134 p.

Seed, H.B., and Sun, J.I., 1989, Implications of site effects in the Mexico City earthquake of Sept. 19, 1985 for earthquake resistant design criteria in the San Francisco Bay area of California: Berkeley, University of California, Earthquake Engineering Research Center Report UCB/EERC–89/03, 124 p.

Seed, H.B., Wong, R.T., Idriss, I.M., and Tokimatsu, Kohji, 1986, Moduli and damping factors for dynamic analyses of cohesionless soils: Journal of Geotechnical Engineering, v. 112, no. 11, p. 1016–1032.

Seed, R.B., Dickenson, S.E., Riemer, M.F., Bray, J.D., Sitar, Nicholas, Mitchell, J.K., Idriss, I.M., Kayen, R.E., Kropp, Alan, Harder, L.F., Jr., and Power, M.S., 1990, Preliminary report on the principal geotechnical aspects of the October 17, 1989 Loma Prieta earthquake: Berkeley, University of California, Earthquake Engineering Research Center Report UCB/EERC–90/05, 51 p.

Shewbridge, S.E., Power, M.S., and Basore, C., 1990, Perimeter dike stability evaluation, Naval Station Treasure Island: San Bruno, Calif., Western Division Naval Facilities Engineering Command, 23 p.

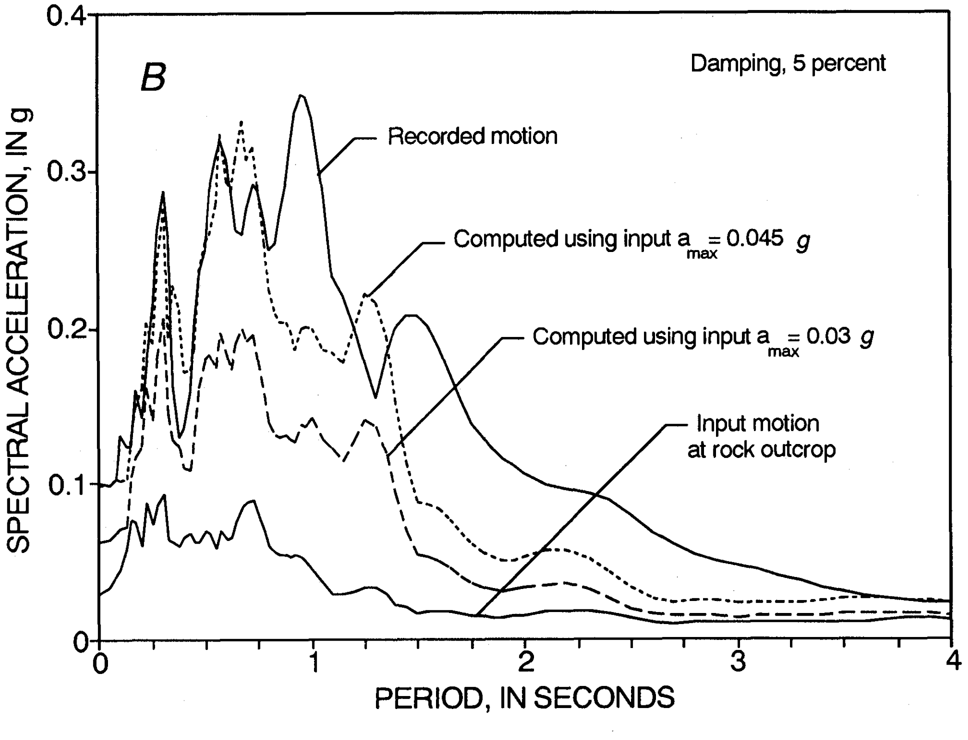

Figure 10.—Continued.

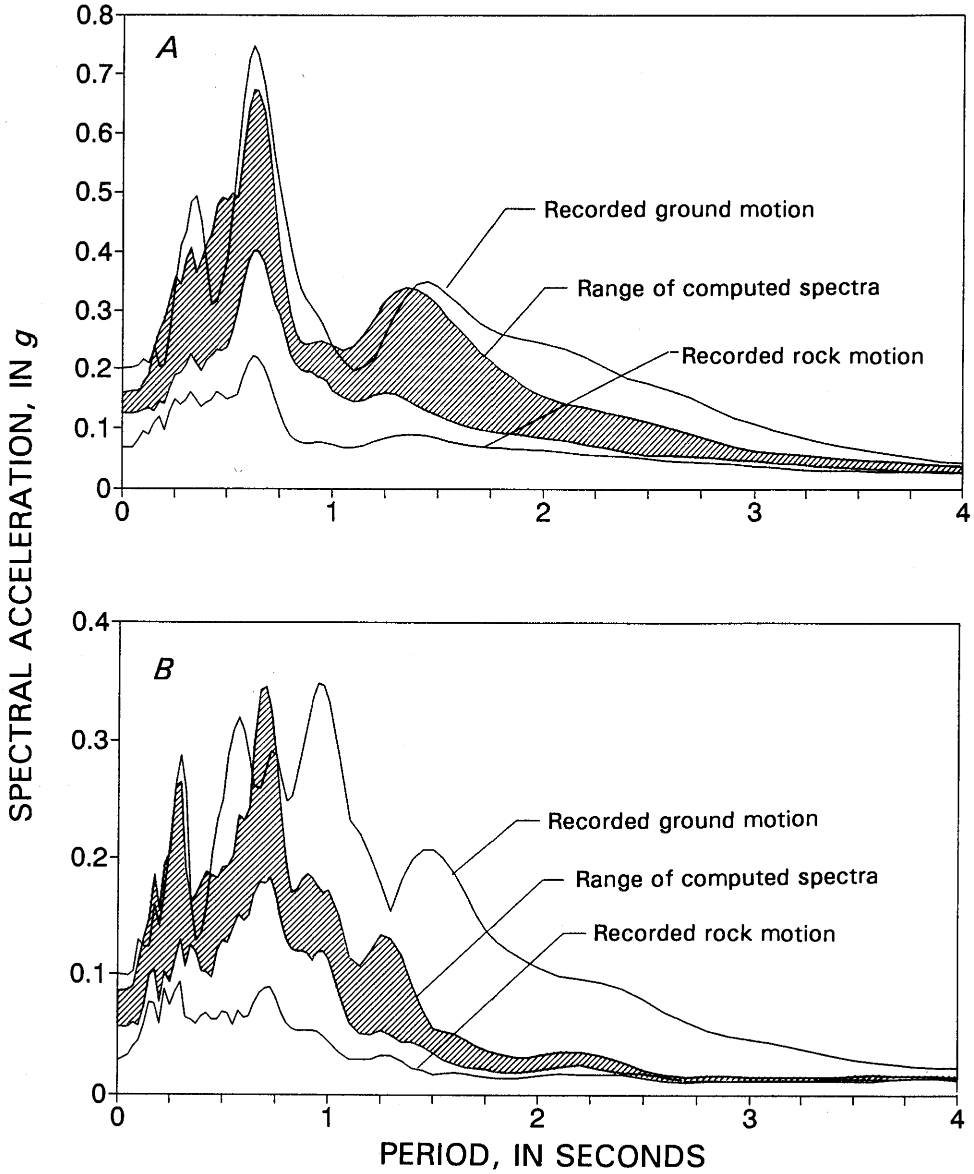

Figure 11.—Ranges of computed response spectra in comparison with recorded spectra in east-west (*A*) and north-south (*B*) directions on Treasure Island.

Table 2.—*Computed peak ground accelerations at sites on Treasure Island*

[All values in percent of gravity]

Site (fig.1)	Direction	
	East-West	North-South
UM1	0.16	0.06
UM3	.13	.06
UM5	.19	.07
UM6	.17	.08
UM9	.20	.09
UM10	.18	.06
UM11	.16	.07
UM12	.16	.06

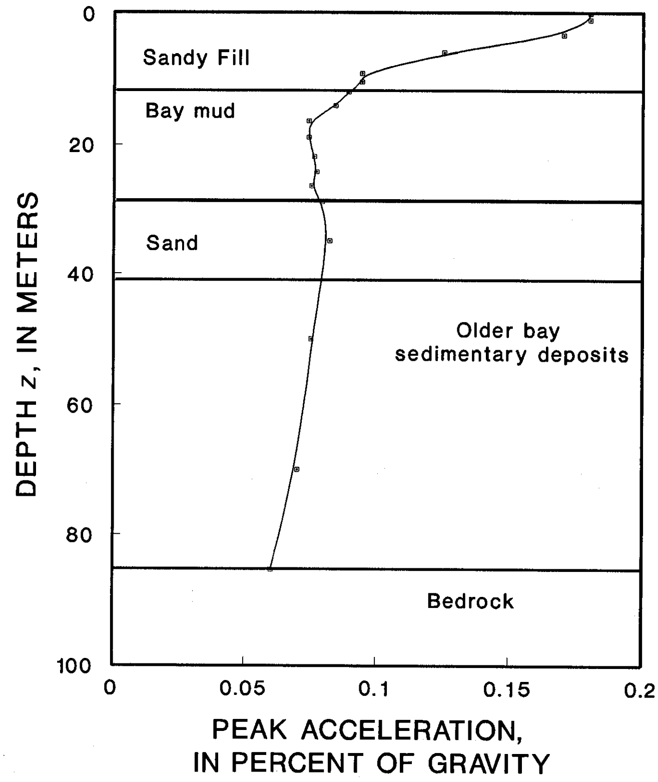

Figure 12.—Computed peak acceleration versus depth at site UM10 (fig. 1).

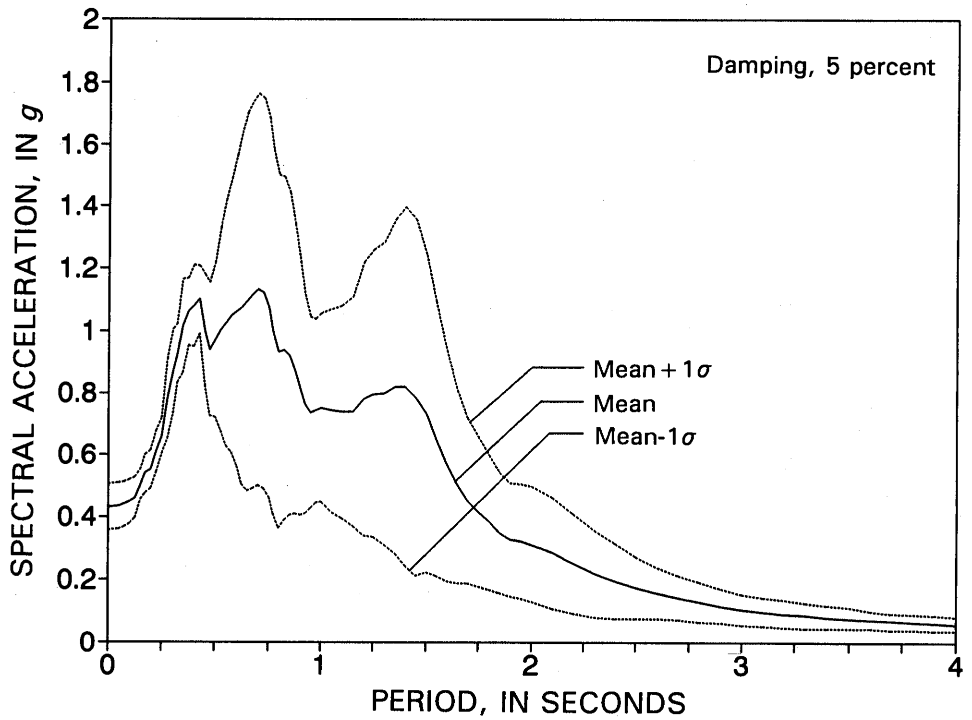

Figure 13.—Computed mean and mean±1s acceleration-response spectra on Treasure Island for eight near-field Loma Prieta input motions with a mean peak acceleration of 0.45 *g*.

THE LOMA PRIETA, CALIFORNIA, EARTHQUAKE OF OCTOBER 17, 1989:
STRONG GROUND MOTION AND GROUND FAILURE

STRONG GROUND MOTION

GROUND-RESPONSE STUDIES AT THE ALAMEDA NAVAL AIR STATION

By Harvey Carlisle,
U.S. Naval Civil Engineering Laboratory; and
Kyle M. Rollins,
Brigham Young University

CONTENTS

ABSTRACT

The ground motions recorded at the Alameda Naval Air Station, a soft-soil site, during the earthquake were more than 3 times higher than on rock at the adjacent rock outcrop on Yerba Buena Island, even though the two sites were at similar epicentral distances. These recordings enable us to verify the ability of the program SHAKE to compute ground response in soft soils. To perform these analyses, the soil profile was determined by drilling a borehole to bedrock at a depth of 470 ft (143.3 m) and obtaining samples for laboratory testing. Field testing included cone-penetration tests, standard penetration tests, and shear-wave-velocity logging, using both downhole methods and a seismic cone penetrometer. Ground-response analyses were performed by using the program SHAKE, and the computed ground motions agreed well with the measured values. Analyses were also performed for the higher accelerations that might result from an earthquake closer to the site. Statistical evaluations were made for several near- and far-field rock records, and mean spectrum shapes and spectral ratios were determined. Motions were also recorded at the roof level of the building housing the seismographs. A dynamic analysis was performed for the building by using a modified version of the program FLUSH; the computed time history was quite similar to the recorded time history.

INTRODUCTION

The striking contrast between ground motions at soft-soil and rock sites in the San Francisco Bay region during the earthquake has awakened interest in ground-response analysis. Although the computer program SHAKE (Schnabel and others, 1972) has been shown to provide reasonable estimates of ground response for Mexico City soils (Seed and others, 1987), its value for more common soil types still needs to be proved. Additional research on the ground response at soft-soil sites has been made possible by numerous accelerograms that were recorded during the earthquake.

In this study, ground-response analyses were performed at the Alameda Naval Air Station (ANAS), using the computer program SHAKE for various rock-input motions. At ANAS, a soft-deep-soil site, recorded ground motions were significantly higher than at the adjacent rock outcrop on Yerba Buena Island, even though the distances from the fault rupture are nearly identical. This closely spaced pair of accelerograms make it possible to verify the accuracy of the equivalent-linear method for ground-response analysis. The computed response spectra at ANAS compare favorably with the measured values. In addition, accelerograms recorded on the roof of an aircraft-maintenance hangar allow an evaluation of the ability of the computer program FLUSH (Lysmer and others, 1975) to model the response of the structure to earthquake shaking.

RECORDED GROUND MOTIONS

During the earthquake, accelerograms were recorded in the east-west, north-south, and vertical directions at ANAS, situated on a deep-soft-soil profile, and on Yerba Buena Island, a rock outcrop in San Francisco Bay approximately 3 mi (5 km) northwest of ANAS (fig. 1). The epicentral distance is 59 mi (95 km) to Yerba Buena Island and 57 mi (92 km) to ANAS. The east-west components of the ground motion are plotted in figure 2.

Although the epicentral distances to both sites are nearly identical, the recorded motions differed significantly. In the east-west direction, the peak ground acceleration recorded on Yerba Buena Island was about 0.07 *g*, however, at ANAS a peak acceleration of 0.21 *g* was recorded, a value 3.5 times greater than on Yerba Buena Island. In the north-south direction, the peak ground acceleration recorded on Yerba Buena Island was only 0.03 *g*, whereas at ANAS a peak acceleration of 0.26 *g* was recorded. Ground motions were recorded in two locations at ANAS: at the ground floor and the roof of building 23, a one-story steel-frame aircraft hangar. The peak accelerations in the east-west and north-south directions at the roof level were 0.36 and 0.45 *g*, respectively.

SITE CHARACTERISTICS

GEOLOGY OF THE SAN FRANCISCO BAY REGION

Rogers and Figuers (1992) constructed subsurface maps of the San Francisco Bay region by assembling information from more than 200 deep-well logs. They presented geologic cross sections of San Francisco Bay and described the processes that formed the various deposits. One of their geologic cross sections through ANAS is shown in figure 3.

The bedrock unit underlying most of the San Francisco Bay region is the Franciscan Complex, a diverse assemblage of sedimentary, volcanic, and metamorphic rocks that in the vicinity of ANAS consists primarily of shale and graywacke sandstone. Above the Franciscan basement lies the Alameda Formation, which was deposited when the region began subsiding about 1–0.5 Ma. The lower part of this formation consists of continental facies (deposits in alluvial fans, lakes, flood plains, streams, and swamps).

The sea entered the depression about 0.5–0.4 Ma and left marine deposits that constitute the upper part of the Alameda Formation. The Pacific Ocean reentered San Francisco Bay during Pleistocene time approximately 115 ka, depositing the Yerba Buena Mud Member of the San Antonio Formation. Above this layer lie estuarine and alluvial sedimentary deposits of the San Antonio Formation, in which Rogers and Figuers (1992) included the Posey Formation and Merritt Sand. Sea level rose again during Holocene time between 11 and 8 ka, and estuarine mud, known informally as bay mud, was deposited over the San Antonio Formation.

CONSTRUCTION HISTORY AT ANAS

ANAS was constructed between 1939 and 1940 by placing dredged Merritt Sand from nearby channels over the shallow estuarine mud, using hydraulic-filling techniques. The fill was placed behind a hand-stacked rockfill seawall that enclosed an area of about 2 mi^2 (5.2 km^2) (Rogers and Figuers, 1991).

SOIL PROFILE AT ANAS STRONG-MOTION STATION

To define the soil profile at ANAS, a test borehole (BYU1, fig. 1) was drilled to bedrock immediately east of building 23, which houses the two seismographs. A simplified diagram of the soil profile, based on logging by Thomas E. Fumal of the U.S. Geological Survey, is shown in figure 4. Sampling was performed at approximately 10-ft (3 m) intervals to a depth of 110 ft (33.5 m), using 3-in. (75 mm)-diameter, thin-walled Shelby tubes and a standard split-spoon sampler. Below the sampling depth, the soil profile was based on a description of drill cuttings and the reaction of the drill rig.

The upper 16 ft (4.87 m) of the profile was found to consist of loose sandy fill, and ground water was located at a depth of 8 ft (2.44 m). The sandy fill is underlain by a 30-ft (9.14 m)-thick layer of bay mud. Immediately below the bay mud is a 45-ft (13.7 m)-thick layer of dense Merritt Sand. Beneath the Merritt Sand lie stiff-clay deposits that extend to a depth of 422 ft (128.7 m). Gravelly-sand layers penetrate the clay deposits at depths of 238 to 256 ft (72.6–78.0 m), the likely boundary between the Yerba Buena Mud Member and clays of the

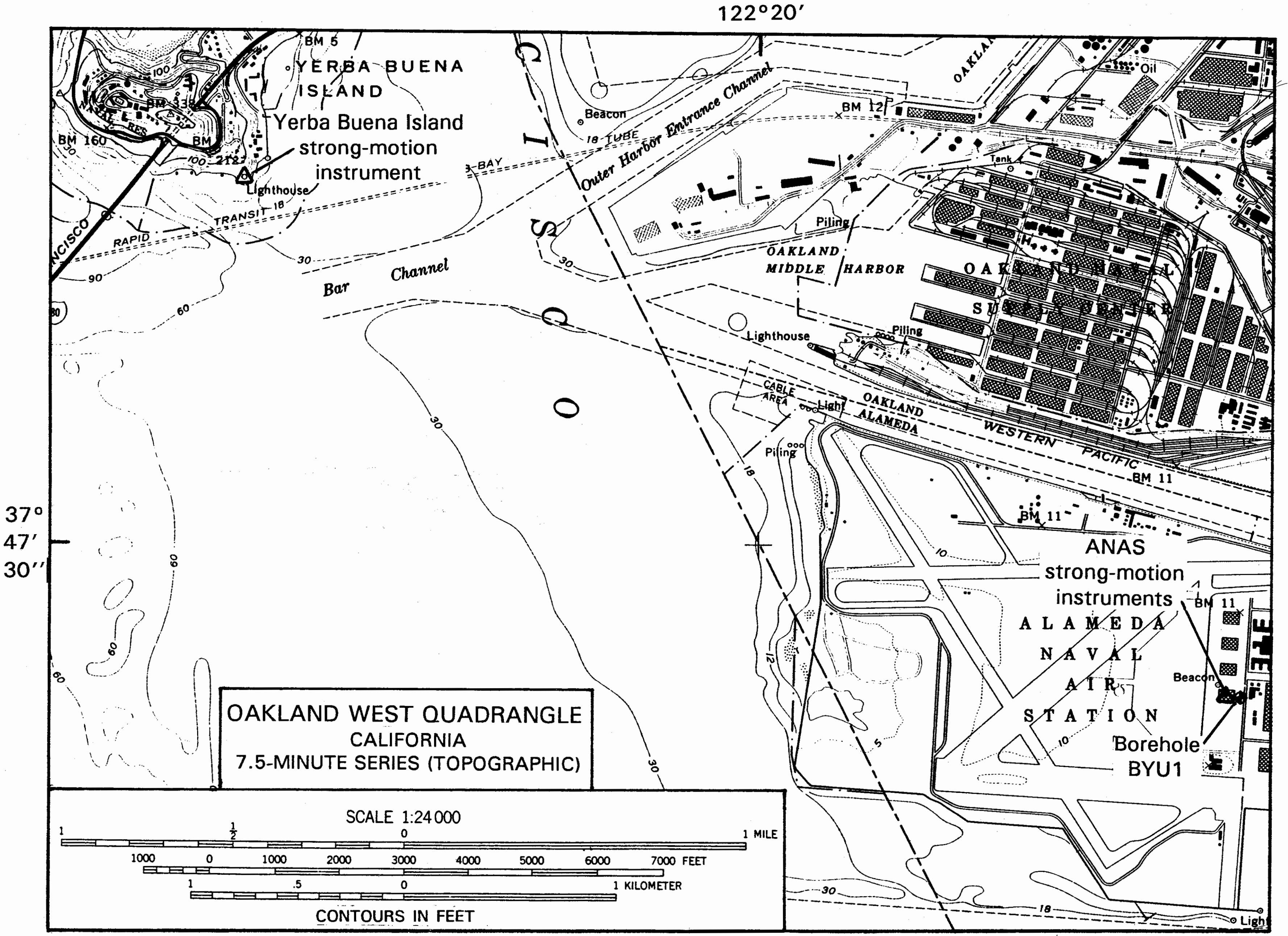

Figure 1.—Part of San Francisco Bay, showing location of strong-motion instruments on Yerba Buena Island and at Alameda Naval Air Station (ANAS).

Alameda Formation. According to the geologic cross section provided by Rogers and Figuers (1991), the boundary should lie at a depth of approximately 240 ft (73.1 m). Gravel, sand, and clay layers extend from 422 ft (128.7 m) to the Franciscan bedrock at 466 ft (142.0 m), which consists of hard black shale.

Other boreholes at ANAS suggest that the soil profile is relatively horizontal and uniform. The log for a water well that extended to bedrock at a depth of 455 ft (138.7 m) at a location about 2,000 ft (610 m) northwest of the recording site is nearly identical to that for borehole BYU1. As part of a geotechnical investigation for a proposed hangar on the south side of building 23, Harding Lawson Associates (1984) drilled 11 holes and sampled to a depth of 95 ft (29.0 m). An east-west cross section through their drill holes (fig. 5) shows that the soils

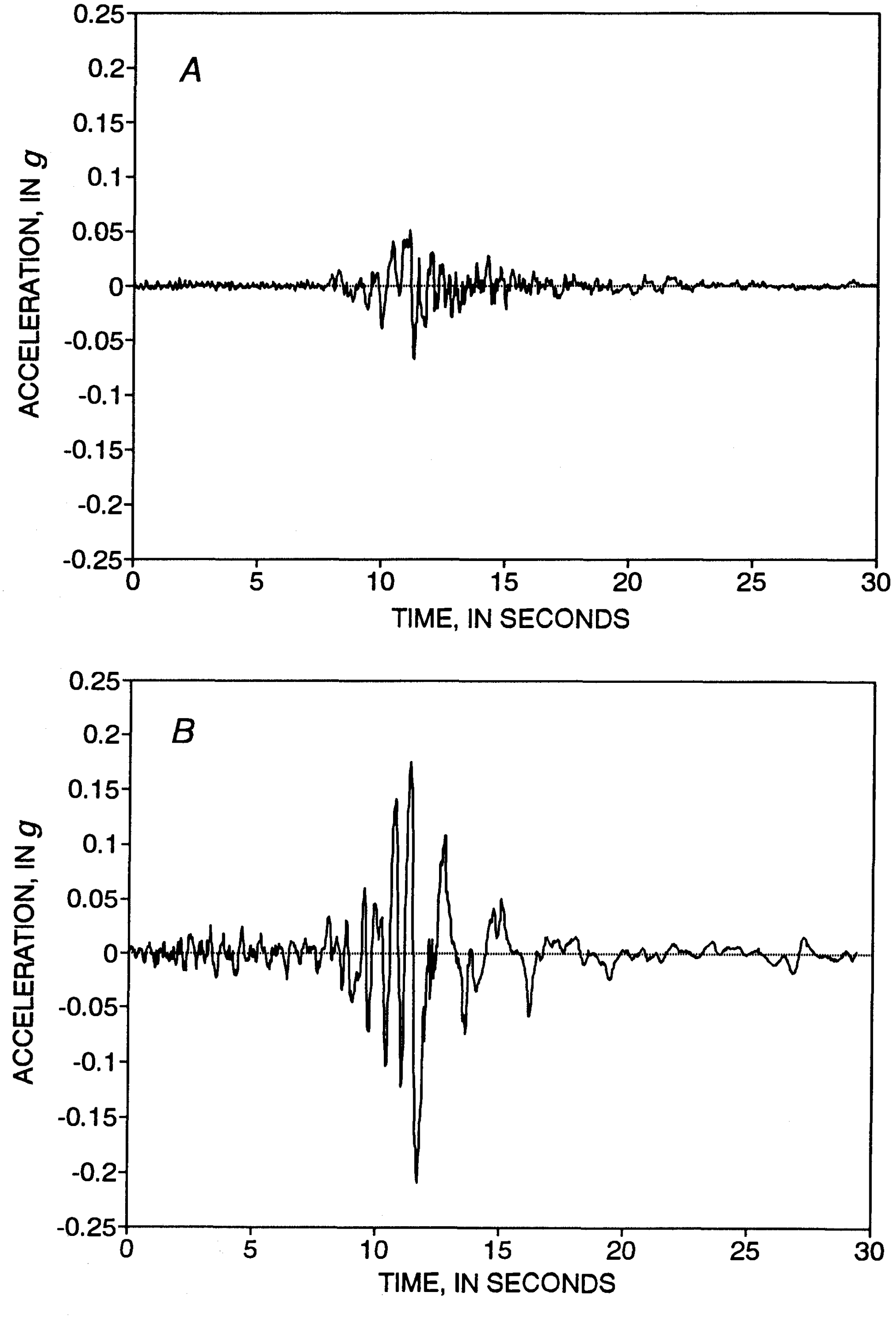

Figure 2.—Recorded east-west ground motion at stations on Yerba Buena Island (*A*) and at Alameda Naval Air Station (*B*).

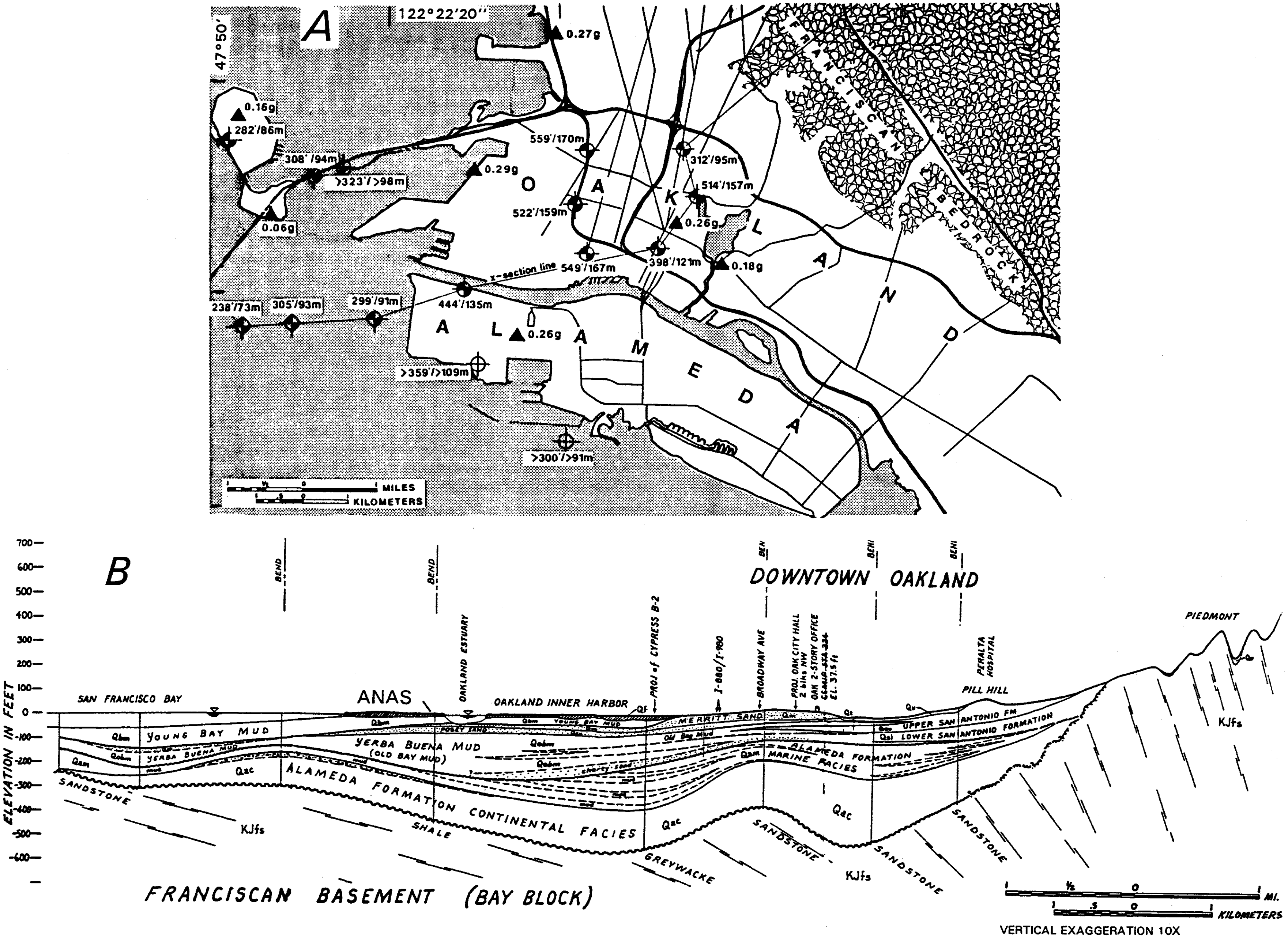

Figure 3.—Geology of the San Francisco Bay region. *A*, Schematic map of Oakland-Alameda area, showing locations of boreholes (crossed circles) and strong-motion-recording stations (triangles). *B*, Geologic cross section through Alameda Naval Air Station (ANAS). From Rogers and Figuers (1991).

generally are horizontally bedded, and the profile is nearly identical to that at borehole BYU1 (fig. 1).

RESULTS OF STANDARD PENETRATION TESTS

The results of standard penetration tests (SPT's) conducted at borehole BYU1 (fig. 1) and at an adjacent hangar (Harding Lawson Associates, 1984) are plotted as a function of depth in figure 6. More than 60 uncorrected *N* values were available from Harding Lawson Associates, and the data points shown in figure 6 represent the averages at each depth. The sandy fill is relatively loose, with average SPT *N* values of 10 to 20, whereas the Merritt Sand is moderately dense to dense, with average *N* values of 40 to 60 in the lower part of the profile.

RESULTS OF CONE-PENETRATION TESTS

A seismic cone-penetration-test (CPT) sounding adjacent to borehole BYU1 (fig. 1) was made by Roman D. Hryciw of the University of Michigan; tip resistance, q_c, as a function of depth is plotted in figure 6. The seismic CPT data extend only to a depth of 50 ft (15.2 m) because penetration into the dense sand below a depth of 45 ft (13.7 m) caused the rods to bend excessively in the relatively soft bay mud immediately above the sand. Tip resistances in the sandy fill range from 20 tons/ft^2 (2 MPa) in the looser layers to about 90 tons/ft^2 (9 MPa) in the denser layers. Tip resistances in the bay mud are typically about 6 tons/ft^2 (600 kPa), with a friction ratio of 1 percent.

RESULTS OF LABORATORY TESTING

Laboratory testing of samples from borehole BYU1 (fig. 1) included Atterberg limits, shear strength, and consolidation on the fine-grained samples and mechanical analyses on the coarse-grained samples. Densities of the clay samples were determined by measuring the weight of each sample in a consolidation ring before performing consolidation tests. The results of the laboratory testing are summarized in table 1. Undrained shear strength as a function of depth is plotted in figure 6, and dry density, natural-moisture content, Atterberg limits, and compression characteristics as a function of depth are plotted in figure 7. The data of Harding-Lawson Associates (1984) are presented along with the data from borehole BYU1 where appropriate.

The soil samples of bay mud taken at depths of 25, 30, and 40 ft (7.6, 9.1, and 12.2 m) were generally found to consist of normally consolidated, high-plasticity silt and clay. A peaty-clay layer about 1 ft (0.3 m) thick was penetrated at a depth of 32 ft (9.75 m); this layer had a plasticity index (PI) of 107 percent, a natural-moisture content of 133 percent, and an organic-matter content of

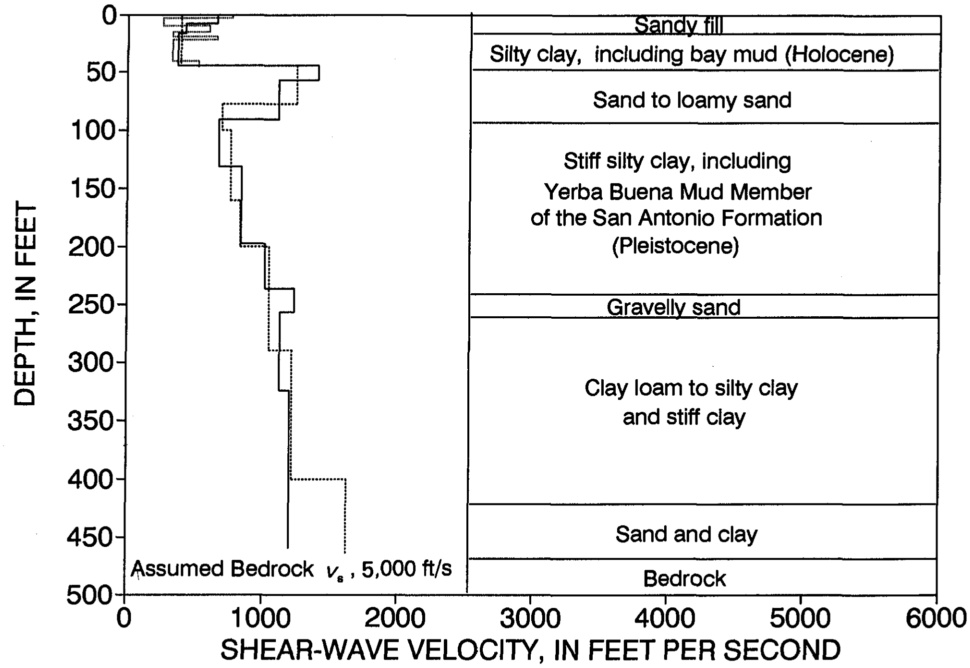

Figure 4.—Shear-wave velocity (v_s) versus depth at building 23 at Alameda Naval Air Station. Short-dashed curve, seismic cone-penetration-test measurements by Roman D. Hryciw of the University of Michigan; long-dashed curve, downhole measurements of Redpath (1991); solid curve, downhole measurements by U.S. Geological Survey.

26 percent. Unconsolidated undrained triaxial shear tests performed on samples at depths of 24, 32, and 42 ft (7.3, 9.8, and 12.8 m) revealed relatively low shear strengths of 378, 636, and 838 lb/ft^2 (18.1, 30.5, and 40.1 kPa), respectively. The ratio of undrained shear strength to vertical effective stress (s_u/σ'_0) was 0.22 to 0.32 for the bay mud and about 0.27 for the Yerba Buena Mud Member of the San Antonio Formation.

The layer of Merritt Sand underlying the bay mud was determined to be a poorly graded fine sand containing less than 10 weight percent silt. Clay of the Yerba Buena Mud Member between depths of 90 and 110 ft (27.4 and 33.5 m) has a high PI of about 40 percent. The clay was found to be overconsolidated, with an overconsolidation ratio of about 2. The undrained shear strengths of samples at depths of 90 and 100 ft (27.4 and 30.5 m) were both about 1,700 lb/ft^2 (81.4 kPa).

SHEAR-WAVE-VELOCITY PROFILE

Shear-wave velocities at ANAS were measured by the downhole seismic method and by seismic CPT's. Downhole velocity measurements were first performed by Gibbs and others (1992); later, Redpath Geophysics was hired to perform a second set of measurements. Before the downhole testing, a 4-in. (10 cm)-diameter polyvinyl chloride (PVC) casing was tremie grouted in place within the 8-in. (20 cm)-diameter borehole. In downhole testing, a sensor is secured in the hole with a packer, and measurements are taken with the sensor at depth intervals of 10 to 20 ft (3–6 m). A shear-wave impulse is generated at the ground surface, and the velocity at each depth can be determined by recording the time when the impulse arrives at the sensor. Reversing the polarity of the shear-wave impulse greatly facilitates determination of the arrival time.

The shear-wave-velocity profile determined by Gibbs and others (1992) is shown in figure 4. Gibbs and others reported some difficulty in interpreting arrival times below a depth of 328 ft (100 m) because of interference from tube waves, even though a large air-powered horizontal hammer was used to generate shear waves at the ground surface. Redpath (1991) found that tube-wave interference can be eliminated by lowering the water table inside the casing by about 100 ft (30.5 m) before testing. This procedure was employed at ANAS, and tube waves were not observed.

Redpath (1991) also used an innovative method that allowed him to rotate the downhole sensor after inflation of the packer, so that the shear-wave impulse was recorded at the same orientation to the surface plank at each depth. This procedure, in combination with a preamplifier in the sensor, provided remarkably clear arrival times, using only a horizontal sledgehammer impact on a plank at the surface to generate the shear wave. The shear-wave-velocity profile determined by Redpath (fig. 4) agrees relatively well with that of Gibbs and others (1992); however, Redpath showed an increase in shear-wave velocity at a depth of 400 ft (122 m), which Gibbs and others (1992) may not have observed because of tube-wave interference.

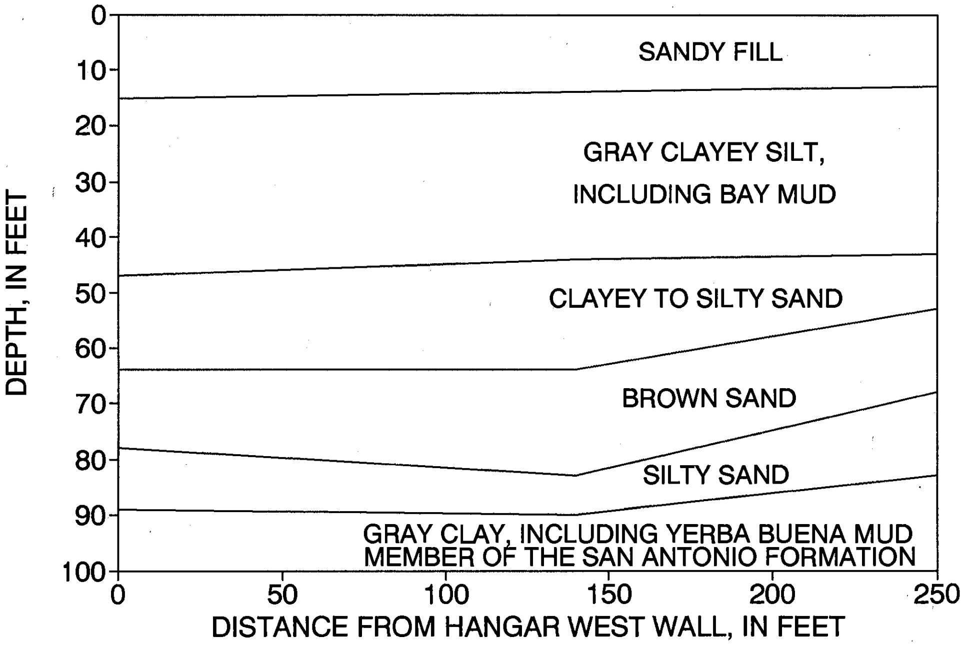

Figure 5.—East-west cross section of soil profile south of aircraft-maintenance hangar (building 23) at Alameda Naval Air Station, as determined by Harding Lawson Associates' (1984) subsurface investigation.

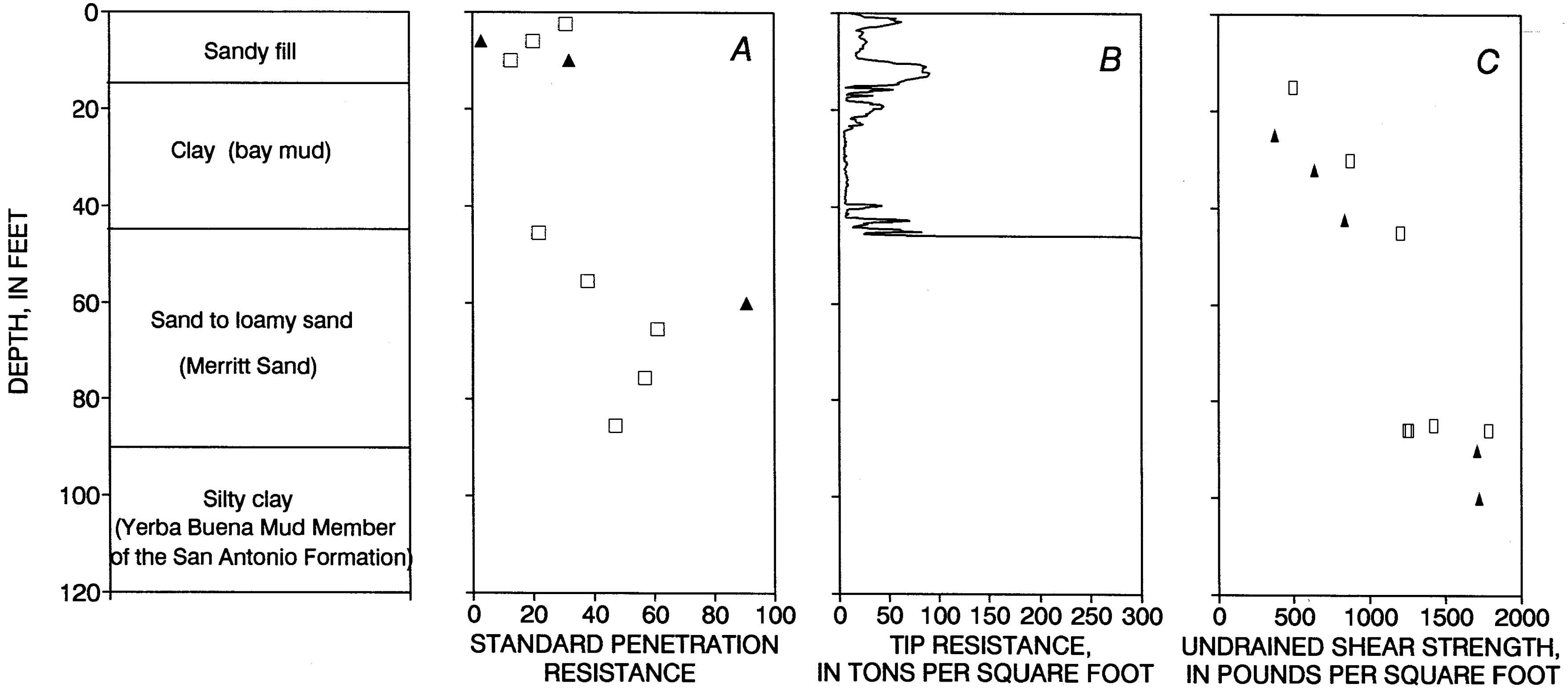

Figure 6.—Standard penetration resistance (*A*), tip resistance (*B*), and undrained shear strength (*C*) versus depth at Alameda Naval Air Station. Squares, averages of data of Harding Lawson Associates (1984); triangles, downhole measurements in borehole BYU1 (fig. 1).

Table 1.—*Results of laboratory tests on soil samples from borehole BYU1 (fig. 1) at the Alameda Naval Air Station*

[Unified Soil Classification System soil types: CH, inorganic clays of high plasticity; CL, inorganic clays of low to medium plasticity; MH, inorganic silts of high plasticity; SM, silty sands, sand-silt mixtures; SP, poorly graded sands. Do., ditto; n.a., not analyzed]

Depth (ft)	Description	Liquid limit (percent)	Plastic limit (percent)	Plasticity index (percent)	USCS soil type	Undrained shear strength (lb/ft^2)	Natural-moisture content (percent)	Dry density (lb/ft^3)	Effective stress (lb/ft^2)	Preconsolidation pressure (lb/ft^2)
24-26	Sandy clay----------	42	26	16	CL	378	38.5	78.9	1,753	1,600-1,800
30	Sandy silt-----------	51	30	21	MH	---	---	---	1,988	-----
32	Clayey silt----------	184	77	107	MH	636	132.6	34.1	2,082	1,800-2,100
40-43	Silty clay (soft)-----	54	25	29	CH	838	---	---	2,551	-----
50-52	Poorly graded sand	n.a.	n.a.	n.a.	SP-SM	---	19.7	103.6	3,046	-----
70-72	Sand-----------------	n.a.	n.a.	n.a.	SP	---	21.6	113.5	4,558	-----
90-92	Stiff clay------------	40	19	21	CL	1,711	20.0	108.4	5,995	10,000-11,000
100-102	do--------------------	72	32	40	CH	1,722	50.4	70.6	6,738	11,000-12,000
110-112	do--------------------	79	34	45	CH	---	51.9	74.0	7,176	-----

Roman D. Hryciw also measured shear-wave velocities at the site, using a seismic CPT rig: The seismic cone was pushed into the ground, and measurements were taken at 3.3 ft (1 m) intervals. Similar to the downhole method, a shear-wave impulse was generated at the ground surface by striking one of the leveling pads beneath the rig; a single receiver in the cone recorded the shear-wave-arrival times. The results of these seismic CPT's are also plotted in figure 4. These data show much more variation in shear-wave velocity above a depth of 46 ft (14 m) than the conventional downhole methods, possibly owing to greater resolution with the shorter measurement interval and greater accuracy, because sample disturbance is minimized with the smaller diameter hole. In the ground-response analysis, the seismic CPT results were used for the upper 46 ft (14.0 m) of the profile, and the downhole results of Redpath (1991) were used for the rest of the profile.

CORRELATION OF SHEAR-WAVE VELOCITY AND UNDRAINED SHEAR STRENGTH

Because shear-wave-velocity measurements are not always economically feasible for a project, reasonable correlations with basic soil properties are desirable. Correlations between shear-wave velocity and undrained shear strength were suggested by Dickenson and others (1991), as shown in figure 8, which is based on data collected from several sites in the San Francisco bay region. Data from the shear tests at ANAS agree reasonably well with the proposed v_s-versus-s_u relation.

No correlation could be established between the maximum shear modulus G_{max} at small strains (10^{-4} percent) and the undrained shear strength because of the large scatter in the data. None of the data points had a G_{max}/s_u ratio higher than 1,400.

GROUND-RESPONSE ANALYSES

Ground-response analyses were performed for the ANAS site by using a modified version of the computer program SHAKE (Schnabel and others, 1972), which can handle as many as 50 layers and 13 G/G_{max} curves. SHAKE computes the response of horizontally layered soil profiles due to rock-input motions, using wave-propagation techniques; thus, it is particularly suited for the ANAS site. Because the shear modulus of soil decreases nonlinearly with increasing shear strain, whereas the damping ratio increases nonlinearly with increasing shear strain, the program iterates until the shear modulus and damping ratio are compatible with the calculated shear strains. This procedure is known as the equivalent-linear method. The program SHAKE has been widely used to calculate the response of soil sites. Studies of the ground response in Mexico City during the September 1985 earthquake (Seed and others, 1987) indicated that SHAKE could provide reasonable estimates of ground motions on soft-soil sites when appropriate shear-modulus-degradation curves were employed.

SHAKE INPUT DATA

Required input to the program SHAKE includes soil-layer thickness, density, low-strain shear modulus, and the variation of shear modulus and damping with cyclic

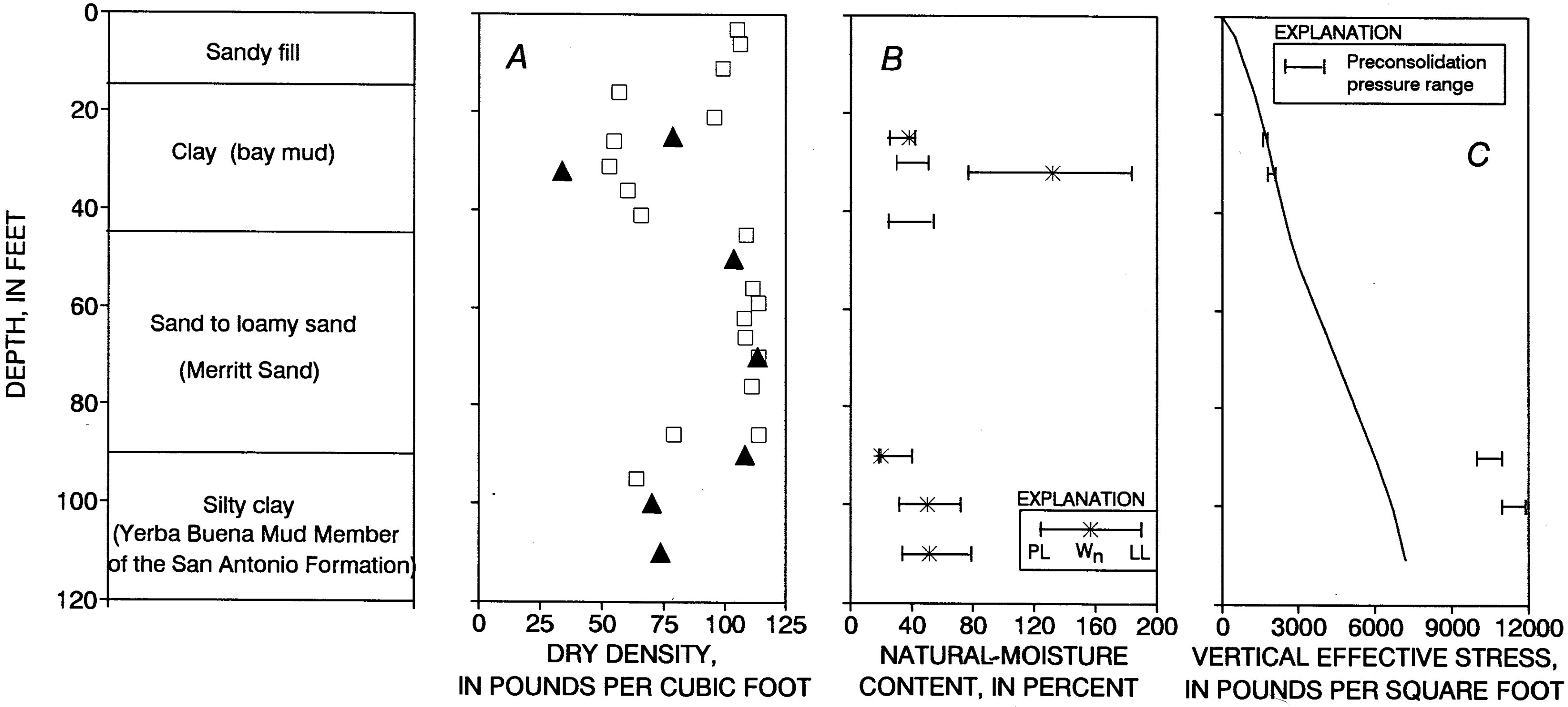

Figure 7.—Dry unit weight (*A*), natural-moisture content (*B*), and vertical effective stress (*C*) versus depth at Alameda Naval Air Station. Squares, measurements at borehole BYU1 (fig. 1). LL, liquid limit; PL, plastic limit; W_n, natural-moisture content.

shear strain. Layer thicknesses and density data were available or could be estimated with reasonable accuracy from the borehole logs, and low-strain shear moduli were calculated directly from the shear-wave-velocity data. A shear-wave velocity of 5,000 ft/s (1,520 m/s) was assumed for the Franciscan bedrock.

The modulus degradation and damping curves developed by Lodde (1982) were used for the bay mud, however, modulus reduction and damping curves corresponding to PI (Sun and others, 1989) were used for the deeper clay layers in the profile. Curves corresponding to PI's of 20 to 40 were assumed for the clay layers below a depth of 110 ft (33.5 m). Modulus-degradation curves correlated to effective overburden pressure (Seed and others, 1986) were used for the cohesionless soil layers in the profile.

COMPUTED GROUND MOTIONS AND RESPONSE SPECTRA FOR RECORDED ACCELERATION LEVELS

Many accelerograms on rock sites were available to use as input motions; however, the recording station on Yerba Buena Island, just 3 mi (5 km) from ANAS, is the closest. Use of the east-west accelerogram from this station as the rock-outcrop-input motion produced a spectrum shape that most closely matched that of the recorded east-west spectrum.

The recorded acceleration-response spectrum at ANAS is plotted in figure 9. The measured peak ground acceleration was 0.21 *g*, and the peak spectral acceleration of 0.93 *g* occurred at a period of 0.65 s. Included in figure 9 are two spectra computed by using the accelerogram from the station on Yerba Buena Island and the modulus reduction curves mentioned previously as input to the program SHAKE. One spectrum was calculated by using shear-wave velocities based on Redpath's downhole seismic method for the whole profile, and the other by using shear-wave velocities determined by the seismic CPT's for the upper soil layers and Redpath's downhole seismic method for the remaining part of profile. Although both calculated curves plot below the recorded curve, the periods of the peak spectral accelerations match very well. Use of the detailed shear-wave velocities determined by the detailed seismic CPT's for the upper soil layers results in a somewhat-better match. The curve calculated by using strictly the downhole shear-wave velocities has a computed peak ground acceleration of 0.17 *g* and a peak spectral acceleration of 0.56 *g* at a period of 0.65 s, whereas the curve calculated by using seismic CPT shear-wave velocities has a computed peak ground acceleration of 0.20 *g* and a peak spectral acceleration of 0.66 *g* at a period of 0.63 s.

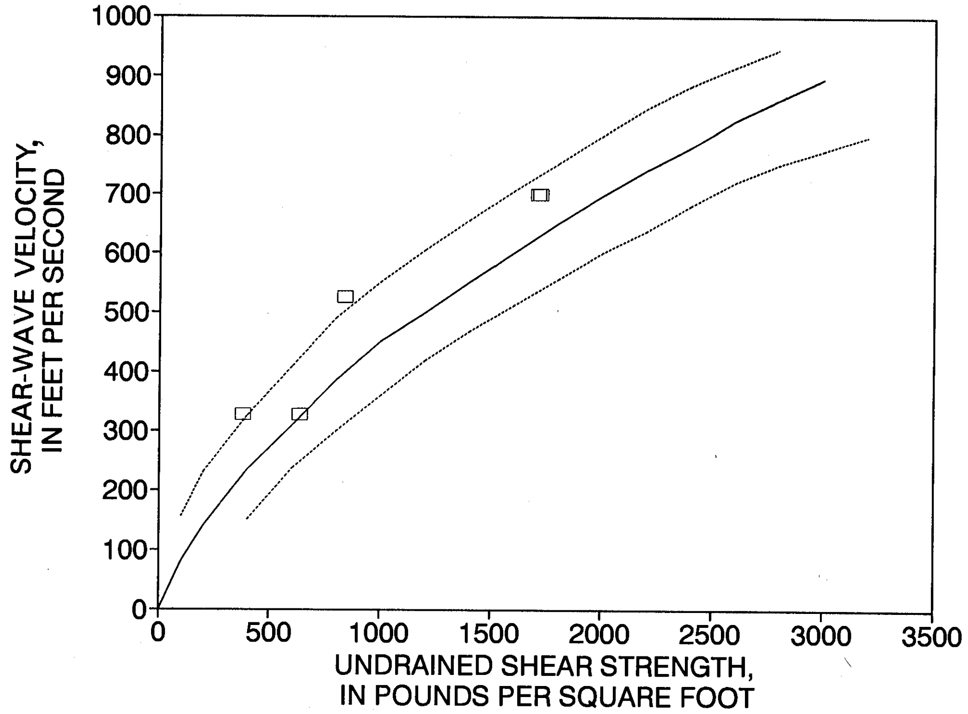

Figure 8.—Computed mean (solid) and mean±1σ (dashed) curve of undrained shear strength versus shear-wave velocity at Alameda Naval Air Station. Squares, downhole measurements in borehole BYU1 (fig. 1). From Dickenson and others (1991).

EFFECTS OF CHANGES IN SHEAR-WAVE VELOCITIES AND INPUT MOTIONS

During their investigation of ground amplification in Mexico City, Seed and others (1987) found that some sites were sensitive to small changes in input parameters, such as shear-wave velocities and bedrock-input motions. Owing to the possible uncertainties in shear-wave velocity and bedrock-motion amplitude, Seed and others (1987) suggested allowing a 10-percent variance from measured downhole shear-wave velocities and a 20-percent variance from measured bedrock-motion amplitude. For the ANAS site, it could be argued that the variation would be upward on both accounts. First, ANAS is closer to the epicenter than Yerba Buena Island and thus would be expected to have slightly higher accelerations; additionally, the measured $a_{\max}$ value at the station on Yerba Buena Island falls at the low end of the "regional average" for rock sites at similar epicentral distance and azimuth. Second, disturbance and stress changes associated with drilling and placement of the PVC casing would tend to reduce the measured shear-wave velocities from their true values.

To evaluate the sensitivity of these results to variations in shear-wave velocity and input-motion amplitude, additional ground-response analyses were performed. The shear-wave velocities measured by seismic CPT's for the upper soil layers at ANAS were held constant, but the measured velocities below a depth of 46 ft (14.0 m) determined by Redpath's (1991) downhole seismic method were changed by ±10 percent. The response spectra computed by the program SHAKE are plotted in figure 10.

The 10-percent increase in shear-wave velocities generally increased the computed spectral accelerations by about 20 percent for periods less than 2 s. The peak ground acceleration increased from 0.20 to 0.24 *g*, which is greater than the recorded peak ground acceleration of 0.21 *g*. The peak spectral acceleration increased from 0.66 to 0.80 *g*, which is still lower than the peak acceleration on the recorded spectrum. The 10-percent decrease in shear-wave velocities decreased the computed peak ground acceleration to 0.17 *g* and the peak spectral acceleration to 0.52 *g*.

Finally, analyses were performed by using input motions scaled by ±10 percent. The best agreement with the measured response was achieved by using an input motion increased by 10 percent, along with the soil profile with shear-wave velocities increased by 10 percent. The computed response spectrum agrees very well (fig. 11). The computed peak ground acceleration is 0.26 *g*, 0.05 *g* higher than the recorded peak ground acceleration; and the computed peak spectral acceleration is 0.86 *g*, 0.07 *g* less than the peak acceleration on the recorded spectrum. Thus, with only minor adjustments, ground motions can be computed in very good agreement with the measured values. This example, coupled with similar results from other sites (see Rollins and others, this chapter; Idriss,

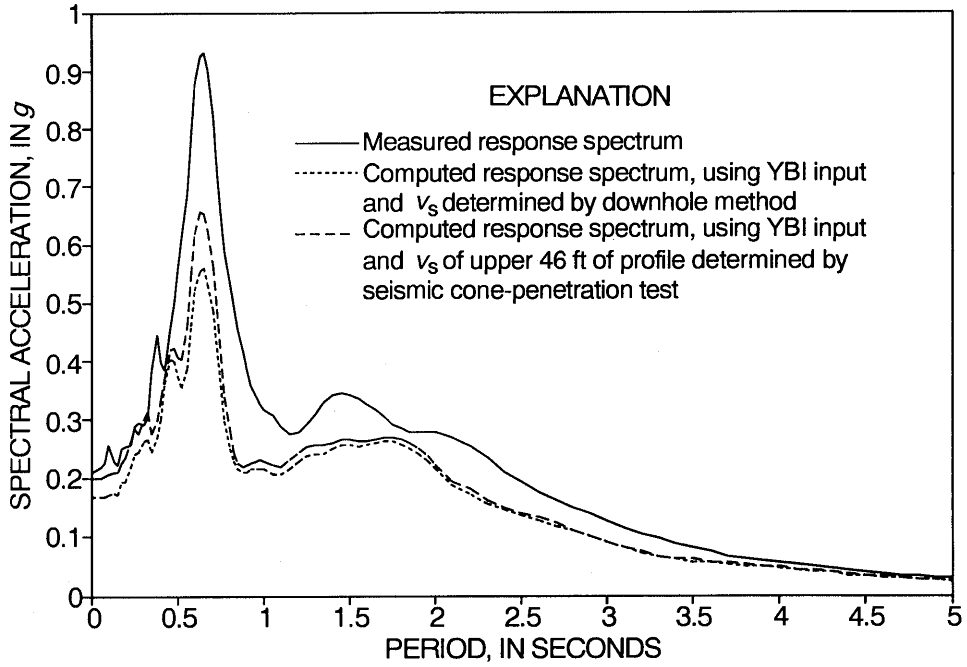

Figure 9.—Recorded and computed acceleration-response spectra in east-west direction at Alameda Naval Air Station. v_s, shear-wave velocity; YBI, Yerba Buena Island. 5-percent damping.

1990; Dickenson and others, 1991), indicates that reliable ground-response analyses can be performed for soft-soil sites at moderate accelerations by using the equivalent-linear method implemented in the program SHAKE.

Although the agreement between the measured and computed motions in the east-west direction is very good, the computed motions differ significantly from the measured motions in the north-south direction. Similar difficulties were noted for the north-south motions in analyses at the Treasure Island site (see Rollins and others, this chapter). The good agreement in the east-west direction and the poor agreement in the north-south direction at both Treasure Island and ANAS suggests that the north-south rock motion recorded on Yerba Buena Island may differ significantly from that at bedrock under these two sites. For example, if the recorded surface motions on Treasure Island are deconvolved to bedrock and then propagated through the soil profile at ANAS, the agreement between computed and measured response spectra is quite good. This example points out the need for downhole accelerometers that can provide rock-input records at soft-soil sites in the future. T.V. McEvilly of the University of California, Berkeley, plans to install a six-component accelerometer at the base of borehole BYU1 (fig. 1) at ANAS: Three components have an acceleration range from 1×10^{-7} to 0.5 g and a frequency range of 0.5 to 500 Hz, and the other three components are standard 4.5-Hz geophones.

PEAK ACCELERATION VERSUS DEPTH

Although the entire soil profile affects the site period and eventual ground response, it is of interest to determine which layers in the profile increase the peak acceleration. The program SHAKE was also used to compute peak accelerations at various depths throughout the ANAS profile, and a plot of peak acceleration versus depth is shown in figure 12. Peak accelerations were slightly amplified in the deeper soil layers and strongly amplified in the bay mud and sandy fill at the surface. The computed peak accelerations increased by more than 150 percent in the upper 50 ft (15.2 m) of the profile, similar to the computed results on Treasure Island (see Rollins and others, this chapter).

COMPUTED GROUND MOTIONS AND RESPONSE SPECTRA FOR FUTURE HIGHER ACCELERATION LEVELS

Because ANAS is only 5.5 mi (9 km) from the Hayward fault and 11 mi (18 km) from the San Andreas fault, future earthquakes could produce significantly higher accelerations than were recorded during the 1989 Loma Prieta earthquake. On the basis of the attenuation relations of Seed and Idriss (1982), M=7.25 and 8.25 earthquakes on these faults would produce peak ground accelerations of 0.45 to 0.55 g, respectively. To evaluate

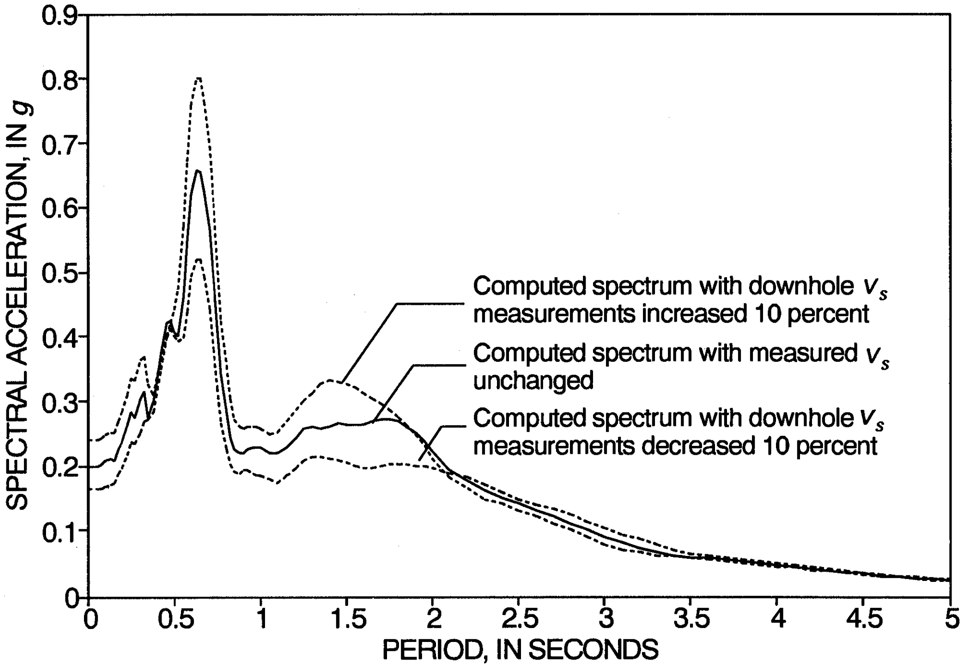

Figure 10.—Computed acceleration-response spectra in east-west direction at Alameda Naval Air Station, with shear-wave velocities (v_s) modified by 10 percent. 5-percent damping.

the response of the ANAS soil profile to stronger earthquake shaking, SHAKE analyses were performed by using synthetic acceleration-time histories representative of an M=7.25 earthquake with a peak acceleration of 0.45 *g* developed by Seed and Sun (1989) and an M=8.25 earthquake with a peak acceleration of 0.55 *g* developed by Seed and Idriss. Because a 10-percent increase in shear-wave velocities in the lower part of the profile resulted in a better match with the recorded spectrum, these higher velocities were used in all subsequent analyses.

The response spectra computed at the ground surface are plotted in figure 13 along with the measured spec-

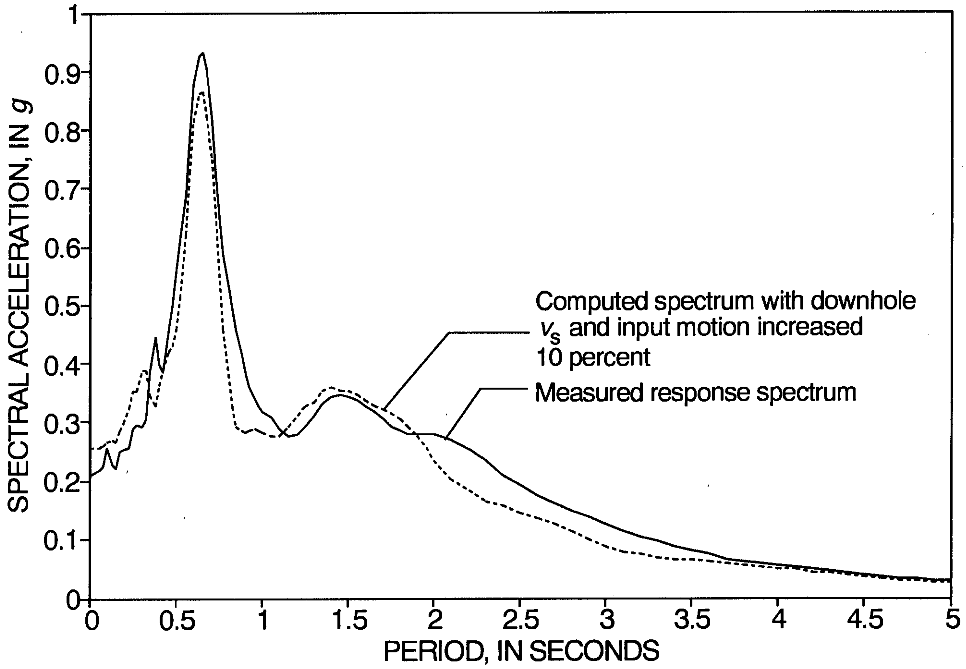

Figure 11.—Computed acceleration-response spectrum in east-west direction at Alameda Naval Air Station that agrees best with recorded spectrum. v_s, shear-wave velocity. 5-percent damping.

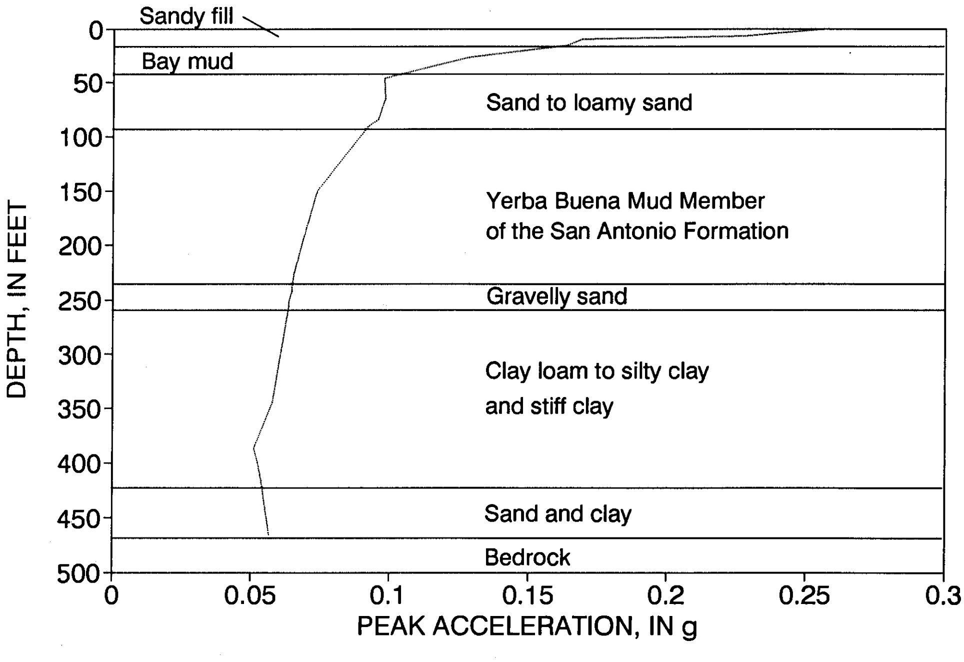

Figure 12.—Peak acceleration versus depth at Alameda Naval Air Station.

trum from the 1989 Loma Prieta earthquake. Although the peak ground accelerations are not amplified to the same extent as for the Loma Prieta records, the spectral accelerations are significantly higher for the closer earthquakes. The M=8.25 earthquake produced a peak spectral acceleration of 2.7 g at a period of 0.85 s, and the M=7.25 earthquake a peak spectral acceleration of 1.61 g at a period of 0.68 s. Peak ground accelerations computed for the M=8.25 and 7.25 earthquakes were 0.65 and 0.41 g, respectively. We note, however, that SHAKE analyses do not account for the effect of liquefaction in the upper sand layers and the resulting decrease in shear modulus in the liquefied zone. Liquefaction would tend to reduce the acceleration and lengthen the fundamental period of the soil deposit.

STATISTICAL COMPARISON OF RESPONSE TO NEAR- AND FAR-FIELD EARTHQUAKES

To provide a statistical evaluation of the ground response at ANAS that accounts for the variation in the rock-input records, SHAKE runs were performed for 12 far-field and 9 near-field records. The 12 far-field rock-input records were recorded at stations Diamond Heights, Rincon Hill, Pacific Heights, Telegraph Hill, Presidio (all in San Francisco), and Yerba Buena Island. These records, which were recorded at a mean epicentral distance of 59.3 mi (95.7 km), have a mean peak acceleration of 0.086 g, with a standard deviation of 0.04 g. The nine near-field rock and stiff-soil records consist of Seed and Sun's (1989) synthetic M=7.25 record, along with the motions recorded at stations Gilroy No. 1, Santa Cruz, Corralitos, and Capitola. These records, which were recorded at a mean epicentral distance of 9.4 mi (15.3 km), have a mean peak acceleration of 0.46 g, with a standard deviation of 0.07 g.

COMPUTED MEAN RESPONSE SPECTRUM

The computed mean response spectra at ANAS for the near- and far-field records are plotted in figure 14. Although the mean peak input acceleration for the near-field records is 5.3 times higher than that for the far-field records, the computed near-field spectral accelerations typically are only 2 to 3 times higher than the far-field spectral accelerations because of soil nonlinearity and differences in the shape of the near- and far-field rock-input spectra.

Mean normalized spectra shapes were also determined for near- and far-field motions by dividing the spectral accelerations by the peak ground acceleration. The spectra are shown in figure 15, in comparison with the design-spectrum shape recommended for S3 sites, such as that at ANAS, by the 1992 Structural Engineers Association of California (SEAOC) code. Because the ANAS profile contains from 20 to 40 ft (6.1–12.2 m) of soft clay, it

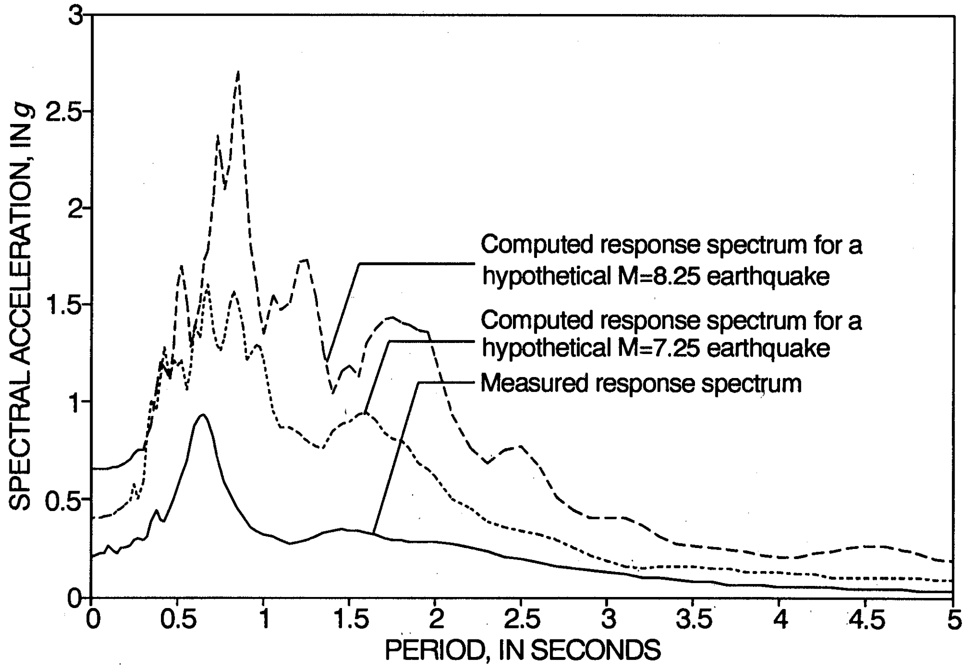

Figure 13.—Computed acceleration-response spectra in east-west direction for hypothetical M=7.25 and 8.25 earthquakes near Alameda Naval Air Station. 5-percent damping.

classifies as an S3 site. In general, the computed spectrum is below the design spectrum; however, in the period range 0.5–1.0 s the design spectrum is exceeded, and so a design based on it would be somewhat unconservative in this period range. The design spectrum is even more unconservative in comparison with the mean±1σ spectrum, which is 30 to 50 percent higher than the mean spectrum.

COMPUTED SPECTRAL RATIOS

Spectral ratios were also computed for each input record used, by dividing the values in the computed ground-surface-response spectrum by the values in the response spectrum for the corresponding rock-outcrop-input motion. The mean±1σ spectral ratios at ANAS for near- and far-field records are plotted in figure 16.

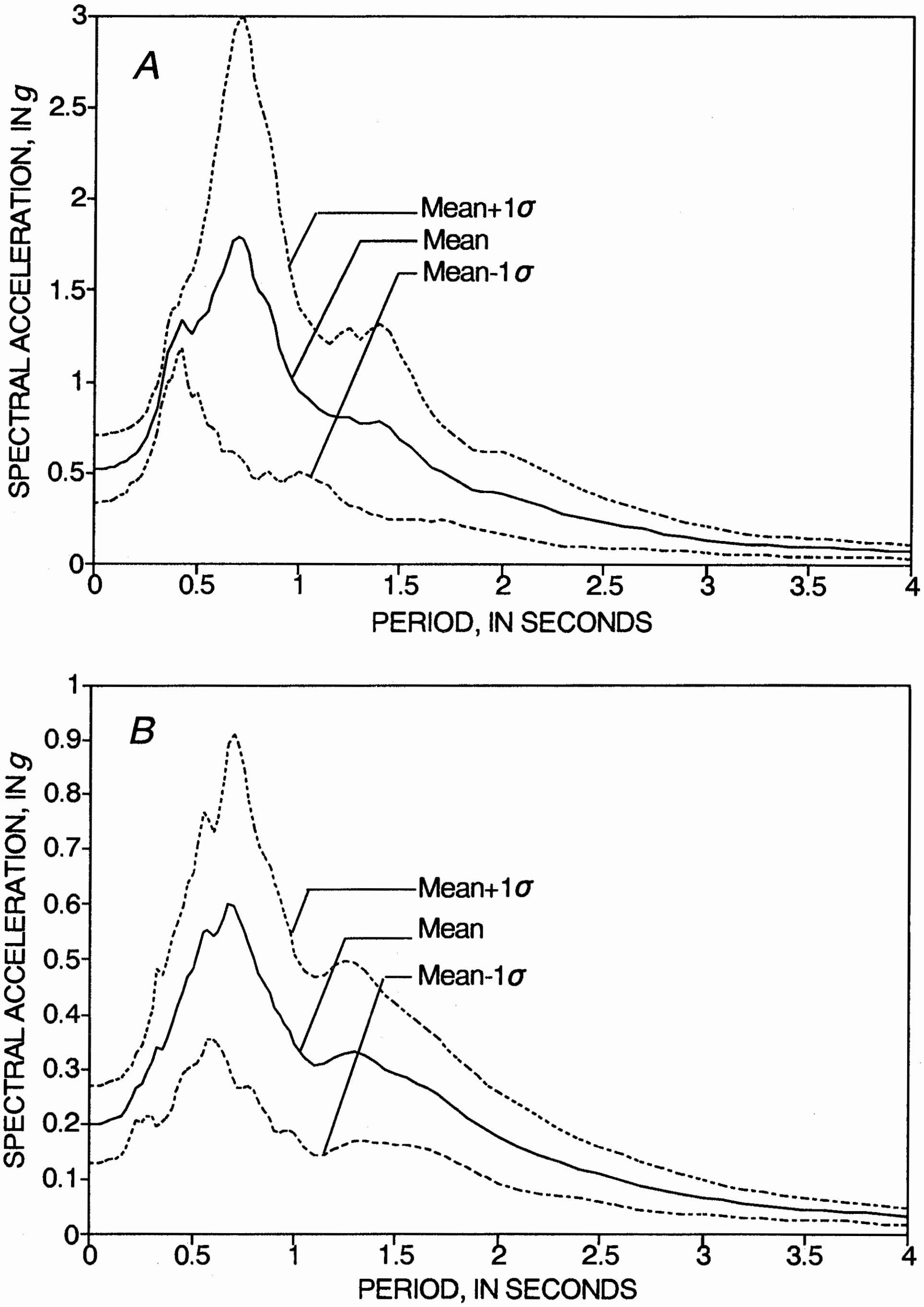

Figure 14.—Computed mean and mean±1σ acceleration-response spectra for near-field (*A*) and far-field (*B*) records at Alameda Naval Air Station. 5-percent damping.

The spectral-ratio curves indicate that the peak ground acceleration at ANAS during the earthquake averaged about 2.7 times as great as the peak acceleration at nearby rock sites. In particular, the far-field spectral-ratio curve peaked at 3.8 and 4.1 at periods of 0.68 and 1.7 s, respectively.

The computed spectral ratios for near-field events are significantly lower than for far-field events at periods less than 0.5 s. Therefore, if a fault rupture were located closer to ANAS, the peak ground acceleration would be only slightly amplified (see fig. 14*A*). Structures located with periods of 0.05 to 0.36 s would undergo lower peak accelerations than if they were located on rock sites. The near-field mean spectral-ratio curve increases from about 1.0 *g* at a period of 0.36 s to 3.12 *g* at a period of 0.85 s and, after a slight decrease, to 3.35 *g* at a period of 2.2 s. The reduction in computed spectral ratios at higher accelerations is attributable to soil nonlinearity, which causes an increase in damping and a reduction in shear modulus when computed shear strains increase.

DYNAMIC ANALYSIS OF BUILDING 23 AT ANAS

Two strong-motion accelerographs were installed at the center column of an aircraft-maintenance hangar (building 23) at ANAS; one was bolted to the center column at the ground floor, and the other at the center column at the midheight of the roof truss (33 ft [10m]), as shown in figure 17. These recordings permit an assessment of the ability of the dynamic finite-element program FLUSH (Lysmer and others, 1975) to evaluate the structural response of a simple building. Although the hangar did not sustain any structural damage due to the earthquake, the floor slab settled 1 to 2 in. (2.5–5 cm) relative to the column footings, apparently owing to liquefaction of the loose sandy fill. The footings for each column, which are supported by pile foundations that extend to dense Merritt Sand at a depth of 80 ft (24.4 m), did not settle.

DETERMINATION OF THE NATURAL PERIOD OF THE STRUCTURE

To determine the natural period of the structure, the spectral accelerations for the roof recording were divided by those for the ground-surface recording. The ratio reached a peak at a period of 0.35 s that defines the natural period of vibration of the building when subjected to the earthquake.

FLUSH MODEL OF BUILDING 23

A two-dimensional dynamic analysis was performed for the east-west cross section in figure 17, using a version

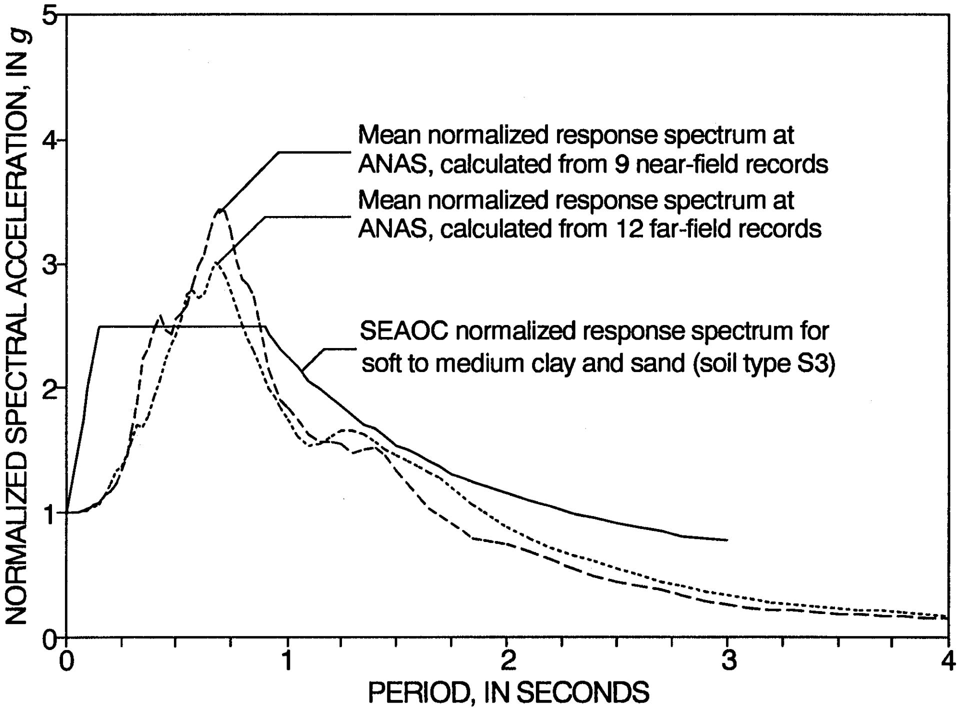

Figure 15.—Computed mean normalized acceleration-response spectra for near- and far-field records at Alameda Naval Air Station (ANAS), in comparison with design spectrum recommended for an S3 site by Structural Engineers Association of California (SEAOC). 5-percent damping.

of the computer program FLUSH modified for use on a microcomputer. The member sizes for the basic steel-frame components of the aircraft-maintenance hangar are also shown in figure 17 (Lew, 1990). At this stage of our study, the effects of soil-structure interaction were ignored, and the columns were treated as if they were founded on rock. Although this assumption is only an approximation, the computed results are nevertheless quite good.

The program FLUSH requires the user to input the building stiffness for a typical 1-ft (0.3 m)-long strip through the building. A total of 11 W12X40 columns and 11 W24X80 columns are spaced at 20-ft (6.1 m) intervals

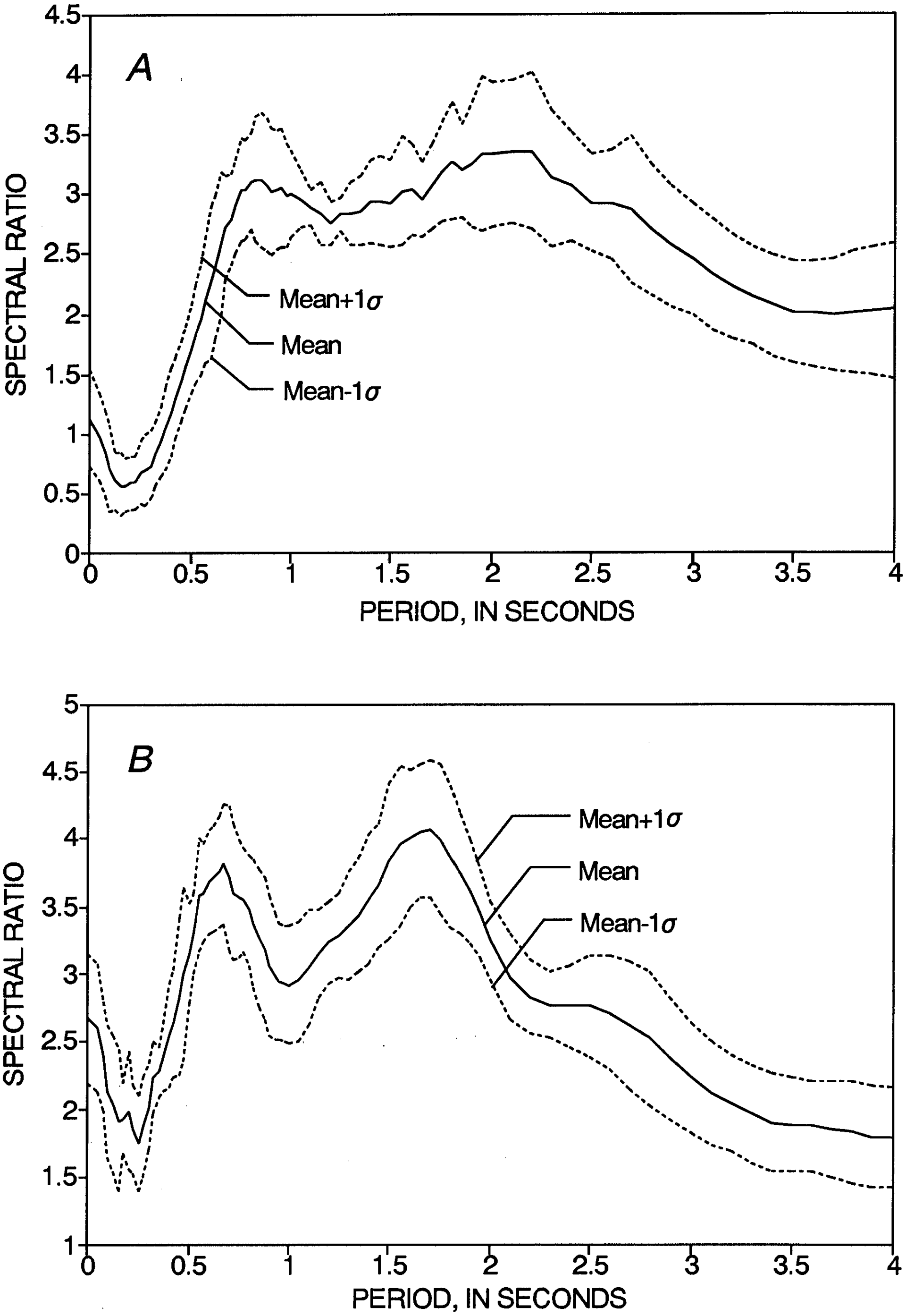

Figure 16.—Computed mean and mean±1σ spectral ratios versus time for near-field (*A*) and far-field (*B*) records at Alameda Naval Air Station.

on center in the north-south direction on the east and west sides of the building. At the centerline of the building, however, one W21X122 column is located at the center, and two W21X68 columns at both the north and south sides. To appropriately model the stiffness at the centerline of the building, an equivalent moment of inertia about the centerline was calculated by summing the moments of inertia of the columns and beams in each bay and dividing by the building length in the north-south direction. The steel sections were assumed to behave linearly with a modulus of elasticity of 29 million lb/in^2 (20 GPa) and a material damping ratio of 5 percent. Finally, line loads representing dead weight were applied to the roof truss and to the beams supporting the mezzanine floor.

COMPUTED ACCELERATIONS AND RESPONSE SPECTRA AT ROOF LEVEL

The acceleration-time history computed for the roof level, using the measured ground-surface time history as input, is shown in figure 18 along with the measured acceleration-time history. The agreement is quite good throughout the entire record and serves to validate the computer program for this simple model. The computed response spectrum at the roof level is compared with the measured spectrum in figure 19, and again the agreement is good. On the basis of the computed roof-level spectrum, the building period is calculated to be 0.34 s, very close to the measured period. The agreement between measured and computed response diminishes somewhat when the computed ground-surface time history is used as the input motion; however, the agreement is still relatively good.

The structure was also analyzed by using computed ground motions for an M=7.25 earthquake as described above. The computed peak acceleration at the roof level was 0.77 *g*, very close to the acceleration predicted by the response spectrum computed by the program SHAKE (see fig. 13). This result indicates that the building is behaving as a single-degree-of-freedom structure.

CONCLUSIONS

1. Agreement between the computed and measured responses at ANAS is very good. This example, coupled with similar results from other sites (see Rollins and others, this chapter; Idriss, 1990; Dickenson and others, 1991), indicates that reliable ground-response analyses can be performed for soft-soil sites at moderate accelerations by using the equivalent-linear method implemented in the computer program SHAKE.
2. Because small variations in measured shear-wave velocity and rock-input motion can result in significant variations in the computed response, ground-response studies should always consider the effect of these variations. Appropriate variations might consist of 10-percent changes in measured shear-wave velocity and 20-percent changes in acceleration.
3. Although the entire thickness of the soil profile affects the potential for soil amplification, most of the increases in computed peak acceleration at ANAS were concentrated near the ground surface.
4. Although the spectral acceleration levels due to a near-field M=7.25 earthquake would be significantly higher at ANAS than those recorded during the 1989 Loma Prieta earthquake, SHAKE analyses indicate that soil nonlinearity will result in lower spectral ratios ($S_{a,soil}$ to $S_{a,rock}$) for periods less than 2.0 s than for far-field events, such as the 1989 Loma Prieta earthquake. This reduction in spectral ratios is, however, relatively small for periods greater than 1.0 s.
5. Soil amplification at ANAS, which classifies as an S3 site, will produce ground-surface-response-spectrum shapes that exceed the SEAOC design spectrum for an S3 site in the period range 0.5–1.0 s.
6. Agreement between the computed and measured responses at the roof level of an aircraft-maintenance hangar at ANAS also is very good. This example indicates that dynamic analyses using the computer program FLUSH can provide reasonable estimates of the structural response for simple structures at accelerations where the structure responds elastically.

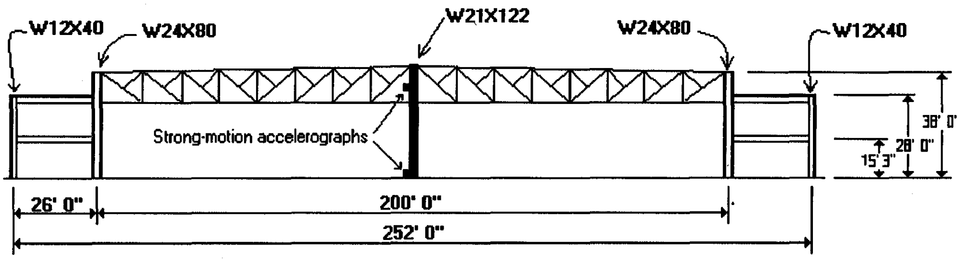

Figure 17.—East-west cross section of aircraft-maintenance hangar (building 23) at Alameda Naval Air Station, showing locations of strong-motion accelerographs.

ACKNOWLEDGMENTS

This research was supported by U.S. National Science Foundation grant BCS–9011121; we appreciate supplemental funding provided by I.M. Idriss of the University of California, Davis. In addition, we thank Mr. Richard Ferris and his staff at the Western Division, Naval Facilities Engineering Command, and Mark Barressi of the Facilities Management Office at ANAS for their support and assistance. Finally, we appreciate the assistance provided by Joseph Sun of Woodward-Clyde Consultants in coordinating the field investigations.

REFERENCES CITED

Dickenson, S.E., Seed, R.B., Lysmer, John, and Mok, C.M., 1991, Response of soft soils during the 1989 Loma Prieta earthquake and implications for seismic design criteria: Pacific Conference on Earthquake Engineering, Auckland, New Zealand, 1991, Proceedings, v. 3, p. 191–203.

Gibbs, J.F., Fumal, T.E., Boore, D.M., and Joyner, W.B., 1992, Seismic velocities and geologic logs from borehole measurements at seven strong-motion stations that recorded the 1989 Loma Prieta earthquake: U.S. Geological Survey Open-File Report 92–287, 139 p.

Harding Lawson Associates, 1984, Geotechnical investigation, paint and finishing hangar (P–704), naval air rework facility, Naval Air Station, Alameda, California: report on job No. 13078,004.04, 52 p.

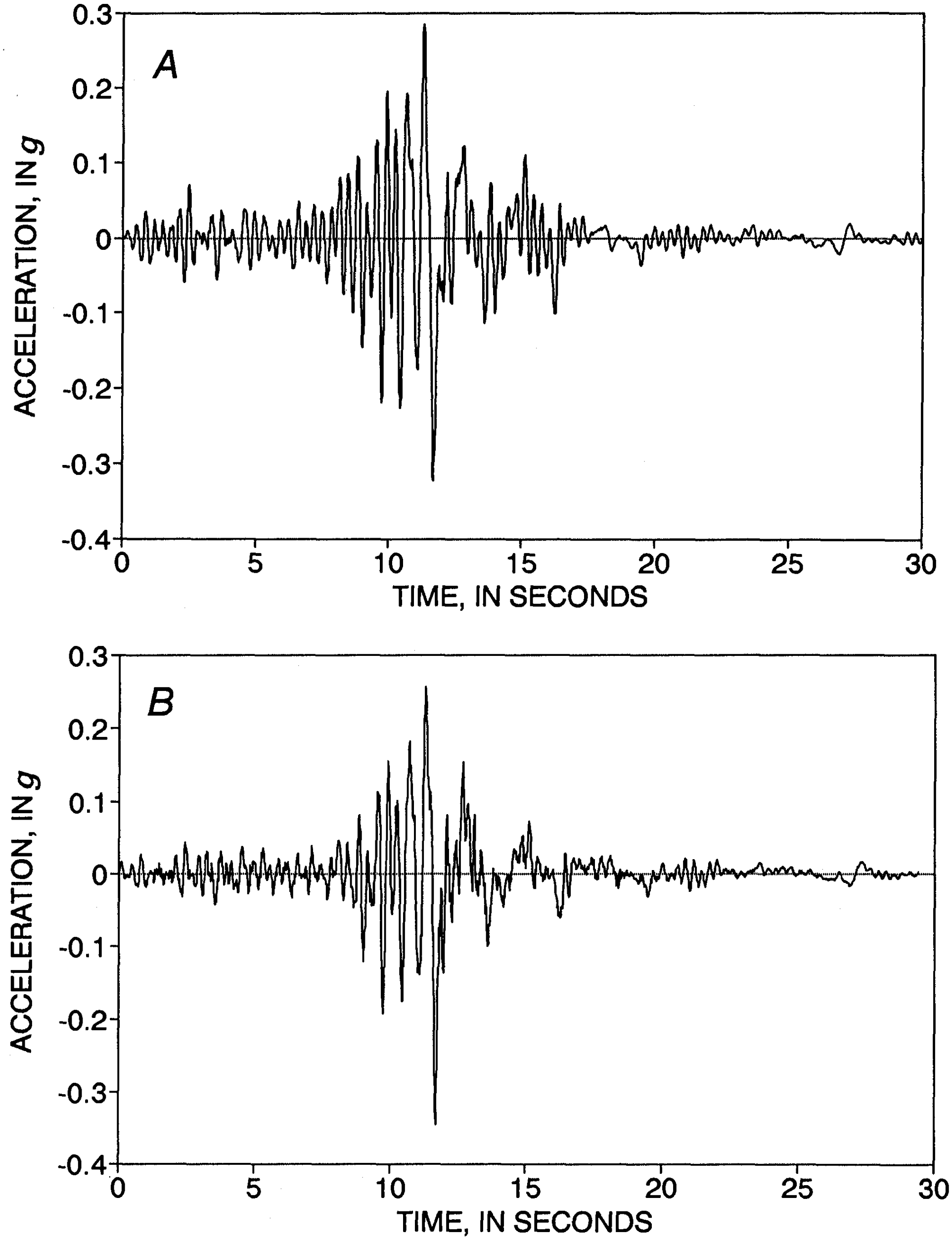

Figure 18.—Compute (*A*) and recorded (*B*) acceleration-time history in east-west direction at roof level of building 23 at Alameda Naval Air Station.

Idriss, I.M., 1990, Response of soft soil sites during earthquakes, *in* H. Bolton Seed Memorial Symposium: Berkeley, Calif., BiTech, v. 2, p. 273–289

Lew, T.K., 1990, Earthquake preparedness; an analysis of the 1989 Loma Prieta earthquake and isoseismal maps for selected historic earthquakes in the San Francisco Bay region: Port Hueneme, Calif., U.S. Naval Civil Engineering Laboratory Technical Memorandum 51–90–07, 13 p.

Lodde, P.F., 1982, Dynamic response of San Francisco Bay Mud: Austin, University of Texas, M.S. thesis, 283 p.

Lysmer, John, Udaka, T., Tsai, C.F., and Seed, H.B., 1975, FLUSH; a computer program for approximate 3–D analysis of soil-structure interaction problems: Berkeley, University of California, Earthquake Engineering Research Center Report EERC 75–30, 83 p.

Redpath, B.B., 1991, Seismic velocity logging in the San Francisco Bay area: Palo Alto, Calif., Electric Power Research Institute final report under agreement RP 3014–06, 34 p.

Rogers, D.J., and Figuers, S.H., 1991, Site stratigraphy and near shore development effects on soil amplification in the greater Oakland area, *in* Baldwin, J.E., and Sitar, Nicholas, eds., 1989 Loma Prieta earthquake: U.S. Association of Engineering Geologists Special Publication 1, p. 123–150

———1992, Engineering geologic site characterization of the greater Oakland-Alameda area, Alameda and San Francisco counties, California: final report to U.S. National Science Foundation, 52 p.

Schnabel, P.B., Lysmer, John, and Seed, H.B., 1972, SHAKE; a computer program for earthquake response analysis of horizontally layered sites: Berkeley, University of California, Earthquake Engineering Research Center Report EERC 72–12, 88 p.

Seed, H.B. and Idriss, I.M., 1982, Ground motions and soil liquefaction during earthquakes: El Cerrito, Earthquake Engineering Research Institute, 134 p.

Seed, H.B., Romo, M.P., Sun, J.I., and Jaime, A., 1987, Relationships between soil conditions and earthquake ground motions in Mexico City in the earthquake of Sept. 19, 1985: Berkeley, University of California, Earthquake Engineering Research Center Report UCB/EERC–87/15, 112 p.

Seed, H.B., and Sun, J.I., 1989, Implications of site effects in the Mexico City earthquake of Sept. 19, 1985 for earthquake resistant design criteria in the San Francisco Bay area of California: Berkeley, University of California, Earthquake Engineering Research Center Report UCB/EERC–89/03, 124 p.

Seed, H.B., Wong, R.T., Idriss, I.M., and Tokimatsu, Kohji, 1986, Moduli and damping factors for dynamic analyses of cohesionless soils: Journal of Geotechnical Engineering,, v. 112, no. 11, p. 1016–1032.

Sun, J.I., Golesorkhi, Ramin, and Seed, H.B., 1988, Dynamic moduli and damping ratios for cohesive soils: Berkeley, University of California, Earthquake Engineering Research Center Report UCB/EERC–88/15, 38 p.

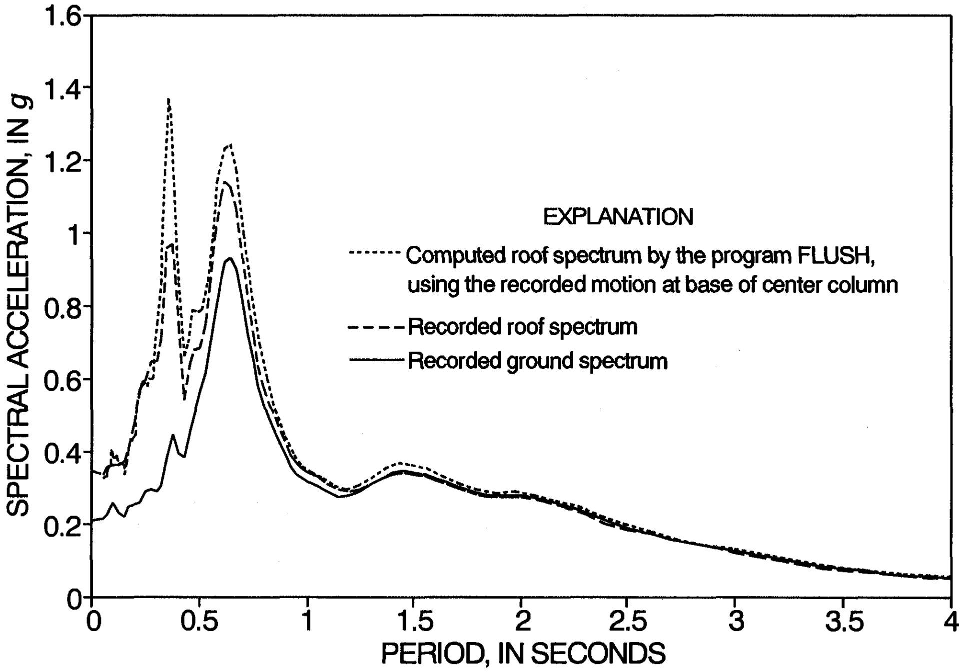

Figure 19.—Computed and recorded acceleration-response spectra in east-west direction at roof level of building 23 at Alameda Naval Air Station, in comparison with recorded spectrum at ground level. 5-percent damping.

THE LOMA PRIETA, CALIFORNIA, EARTHQUAKE OF OCTOBER 17, 1989:
STRONG GROUND MOTION AND GROUND FAILURE

STRONG GROUND MOTION

BEHAVIOR OF YOUNG BAY MUD FROM THE MARINA DISTRICT OF SAN FRANCISCO UNDER STATIC AND CYCLIC SIMPLE SHEAR

By Nicholas Sitar and Rodrigo Salgado,
University of California, Berkeley

CONTENTS

ABSTRACT

A sample of young bay mud obtained from a U.S. Geological Survey borehole in the Marina District of San Francisco was tested in a series of static and cyclic, strain-controlled, undrained simple shear tests. The young bay mud at this site has a higher than average silt content, a lower plasticity index, and a lower compressibility than are typical of this deposit elsewhere. Under cyclic loading, this soil exhibits a strength about 40 percent higher than its static undrained strength during the first cycle of loading. During successive cycles of loading, the cyclic strength decreases significantly and becomes lower than the initial static strength after about five cycles of loading at strains greater than 1 percent. During future major earthquakes, such loss of strength could lead to possible large deformations and (or) failures along the lateral margins of fills and embankments founded on young bay mud, unless the potential for strength loss is explicitly accounted for in design.

INTRODUCTION

Shortly after the earthquake, the U.S. Geological Survey drilled an exploratory borehole at Winfield Scott School at Beach and Divisadero Streets in the Marina District of San Francisco. The purpose of this borehole was to obtain information on site stratigraphy, soil properties, and inplace shear-wave velocities, and to install a downhole accelerometer for investigating the amplification of ground motions at the site (Kayen and others, 1990). Hydraulically pushed, 78-mm-diameter Shelby tube samples were recovered at intervals throughout the entire profile, providing an opportunity for laboratory determination of soil properties. A portion of one sample tube containing Holocene bay mud, referred to in this paper and in geotechnical practice as young bay mud, from a depth of 7.6 to 8.6 m (WSS5; Kayen and others, 1990) was tested in static and cyclic simple shear to evaluate the strength characteristics of young bay mud under cyclic loading.

SOIL DESCRIPTION, INDEX PROPERTIES, AND CONSOLIDATION-TEST RESULTS

The unit stratigraphically identified as young bay mud at the site is a gray, clayey silt containing shells and shell fragments that occasionally interfere with sample trimming. The natural-moisture content determined from sample trimmings used for consolidation and simple-shear tests ranges from 52 to 54.8 percent. The liquid and plastic limits were measured to be 55 and 30 percent, respectively, giving a plasticity index of 25 percent; the soil can be classified using the U.S. Soil Conservation Service System as MH–CH, silty clay/clayey silt of high plasticity. Overall, the natural moisture content and Atterberg limits are substantially lower than typical values for young bay mud—for example, a natural-moisture content of 90 percent, a liquid limit of 88 percent, and a plasticity index of 40 percent at Hamilton Air Force Base (table 1).

We performed a continuous-loading consolidation test, using the method of Janbu and others (1981). The test was only partly successful, however, owing to difficulties with the loading device, and could not be repeated because of limited sample amount. The laboratory and field consolidation curves obtained from this test are shown in figure 1. The preconsolidation pressure, p_c, determined by using the Casagrande construction, is 267 kPa, suggesting an overconsolidation ratio (OCR) of about 3.3, based on an estimated inplace effective overburden pressure $p_0 \equiv \sigma_v' = 80$ kPa. Although this OCR appears to be a fairly high, it is not unusual for desiccated bay mud from the tidal zone (Bonaparte and Mitchell, 1979) and is consistent with a natural moisture content lower than the liquid limit. The field compression index, $C_c = 0.28$, obtained from the consolidation test, however, is significantly lower than typical values for young bay mud, which range from 1.2 to 1.8. One possible factor responsible for this difference is the substantially lower clay-size fraction, 33 percent versus 44–48 percent, and correspondingly higher silt content in comparison with, for example, young bay mud with a similar OCR at Hamilton Air Force Base (table 1). The coarser gradation would be consistent with a shallow, near-beach environment postulated on the basis of the index tests and based on the geography of the site.

Table 1.—*Properties of young bay mud*

Location	Hamilton Air Force Base	Marina District
Saturated unit weight (kN/m^3)	14.8	16.6
Natural-moisture content (percent)	90	52-54.8
Silt/clay content (percent)	54/46	67/33
Liquid limit (percent)	88	55
Plasticity index (percent)	44	25
Liquidity index	≈ 1	.88-0.99
Overconsolidation ratio	3 (in the crust)	3.3
Compression index	.8-0.9	.28
Undrained strength ratio, s_u/p (test dependent).	.29-0.42	.24 (OCR = 1), .54-0.57 (OCR = 3.3)

SIMPLE-SHEAR TESTS

DESCRIPTION OF THE TEST DEVICE

Our simple-shear device is designed for testing short cylindrical samples encased in a flexible membrane and enclosed in a pressure chamber. The axial load is applied by a vertical piston connected to the top platen, and the shear load is applied by a horizontal piston connected to the bottom platen. The loads are measured by internal load cells, and both pistons are pneumatically operated. The chamber pressure is independently controlled, and air is used as the confining fluid in relatively short-duration tests, such as those described herein.

Both vertical and horizontal displacements are measured by means of linearly variable differential transformers (LVDT's). The horizontal LVDT is located inside the cell between the top platen and an arm fixed to the horizontal piston; the vertical LVDT is placed between the top of the vertical piston and a fixed frame. The drainage lines coming out of each platen meet in a single line connected to a volume-change device, which is designed to measure pore pressure during undrained tests and volume change during consolidation.

Data acquisition and control software, the Automatic Testing System (ATS; Sousa and Chan, 1991), and an accompanying data acquisition and control system enable either manual or preprogrammed, automatic control of the axial and shear loads. The ATS collects and stores vertical and horizontal loads and displacements, volume change, pore pressure, cell pressure, and effective confining stress, and it also provides a real-time graphical display of the data during a test. Both stress- and strain-controlled static and cyclic tests can be performed.

SAMPLE PREPARATION

The soil was carefully extruded from the Shelby tube by using a hydraulic extruder. A length about 50 percent

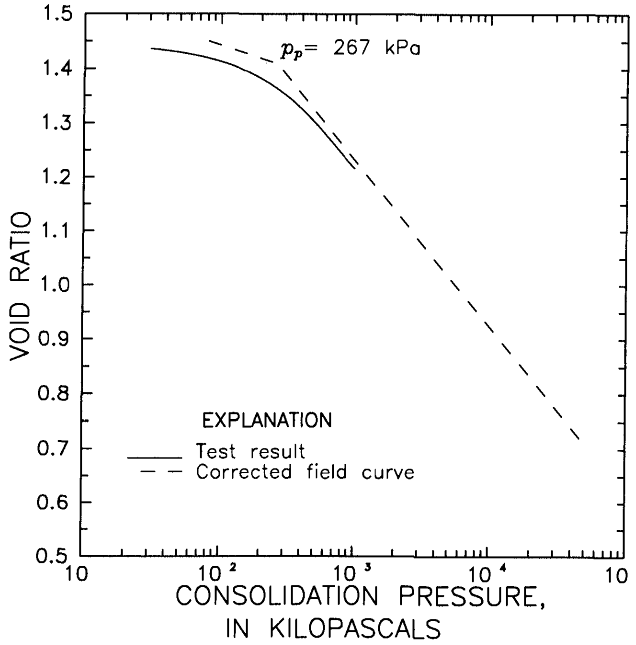

Figure 1.—Consolidation pressure versus void ratio for young bay mud from the Marina District of San Francisco.

greater than the desired height of the sample was extruded and cut off with a wire saw for each test; part of the excess soil was used for moisture-content determinations. Once extruded, each sample was placed in a mold and cut down to size, using a thin-wire saw and a metal leveler. The sample was then weighed, measured, and placed between the platens. A latex membrane was stretched over the sample and sealed against the platens, using rubber O-rings. The drainage lines were then connected to the platens, and the sample was subjected to a low vacuum (typically a third of an atmosphere) to remove trapped air and to check for possible leaks through the membranes or O-rings. The sample was then installed inside the device, and the chamber was closed.

The sample was deaired by evacuating both the sample and the chamber, to maintain the effective confining stress at a third of an atmosphere. Thus, the pressure inside the sample could be decreased to almost −100 kPa without the risk of overconsolidating the sample. The sample was kept under vacuum until air bubbles were no longer coming out (about 1 hour). Then, the backpressure was gradually increased, and water was allowed to enter the sample, while maintaining constant effective stress, until the sample was saturated.

TESTING PROCEDURE

After saturation, the samples were anisotropically consolidated at K_0=0.6, which is near the upper bound of the range 0.47–0.65 measured at Hamilton Air Force Base (Bonaparte and Mitchell, 1979). The tests were carried out at two consolidation-stress levels: (1) the current inplace effective vertical stress, σ_v', of 80 kPa (OCR=3.3); and (2) an effective vertical stress of 280 kPa, just greater than the preconsolidation pressure. Thus, the influence of OCR on the observed strength and stress-strain characteristics could be evaluated.

All tests were performed undrained, with pore-pressure measurements. The static tests were carried out at a constant strain rate of 0.2 percent per minute. In the cyclic tests, 30 cycles of loading were applied at a rate of 1 Hz at each strain level; therefore, the strain rate increased proportionally with the strain level. Owing to the limited number of samples available for testing, the samples subjected to cyclic loading were tested at progressively increasing strain levels, without dissipation of pore pressure between the tests. This procedure has been successfully used by other investigators for similar reasons (for example, Ishihara and Yasuda, 1980). Postcyclic static tests were attempted whenever possible to evaluate the influence of cyclic loading on the undrained strength of the soil. Constant vertical (axial) load was maintained throughout all the tests.

STATIC-TEST RESULTS

The stress-strain curves obtained from static simple-shear tests on samples consolidated at the two different effective vertical stresses are shown in figure 2. The stress-strain curves from the two tests at the inplace effective vertical stress, σ_v', of 80 kPa are characterized by monotonically increasing strength, even at strains

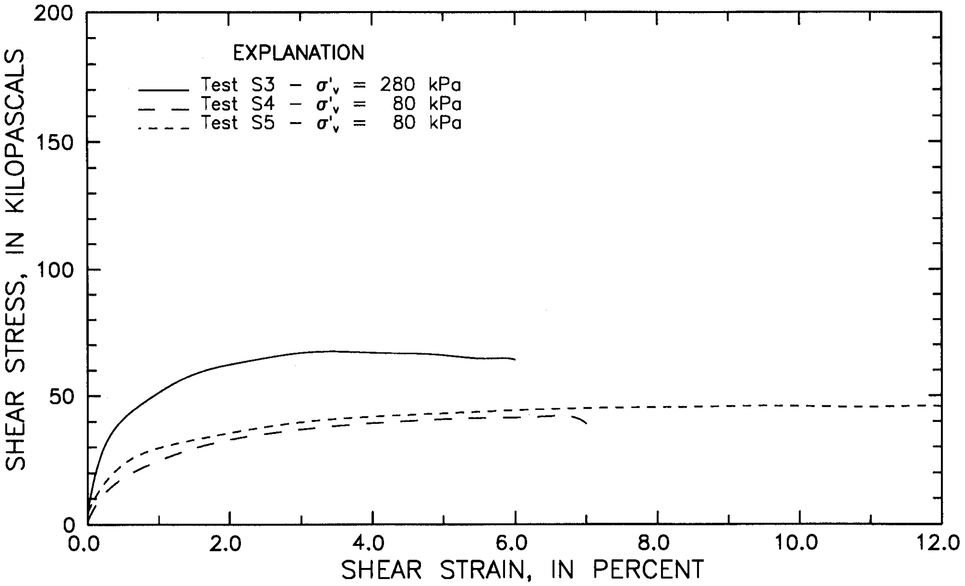

Figure 2.—Stress-strain curves from undrained static simple-shear tests on samples of young bay mud from the Marina District of San Francisco. σ_v', effective vertical stress.

beyond 6 percent. The sample tested at σ_v'=280 kPa reached its peak strength at a strain of about 3 percent, followed by essentially plastic deformation and no appreciable strain softening. The s_u/p ratios from the two tests at σ_v'=80 kPa (OCR=3.3) are 0.54 and 0.57, respectively. These ratios are higher than previously obtained from isotropically and anisotropically consolidated, undrained triaxial tests on young bay mud. In contrast, the s_u/p ratio from the test at σ_v'=280 kPa (OCR≈1) is 0.24, somewhat lower than is typical of young bay mud (Bonaparte and Mitchell, 1979). All of these s_u/p ratios, however, fall well within the range obtained by Ladd and others (1977) for clays tested in anisotropically consolidated, direct simple-shear tests.

CYCLIC-TEST RESULTS

Three samples were tested in a series of cyclic tests at an effective vertical stress, σ_v', of 280 kPa. The first sample was subjected to cyclic tests at strains of 0.25, 0.5, and 1 percent, followed by a static test to failure; the second sample was tested at strains of 0.5, 1, and 2 percent, again followed by a static test to failure; and the third sample was dynamically tested at a strain of 5 percent. Only one sample was consolidated at the inplace effective vertical stress of 80 kPa (OCR=3.3); it was tested at strains of 0.5 and 1.5 percent.

The stress-strain hysteresis loops for the 1st and 30th cycle at the various cyclic strains are plotted together with the corresponding undisturbed static and postcyclic static stress-strain curves in figures 3 and 4, respectively, for the samples consolidated at σ_v'=280 kPa, and in figures 5 and 6 for the samples consolidated at σ_v'=80 kPa. Although the test data are limited, several important observations can be made. The undrained shear strength and, thus, the shear modulus during the first cycle of loading can significantly exceed the static shear strength of the soil at a given stress level. This increase in strength, by as much as 40 percent in our tests, results from an increased rate of loading in the cyclic tests. Note that all the cyclic tests were performed at 1 Hz, and so the strain rate increases with increasing cyclic shear strain; the corresponding increase in undrained shear strength with increasing strain rate during the first cycle of loading is readily apparent in figure 3.

The ratio of the maximum cyclic shear strength, τ_c, to the static shear strength, τ_s, versus the cyclic-shear-strain amplitude is plotted in figure 7, which shows the already-mentioned increase in cyclic shear strength with increasing strain amplitude and (or) strain rate during the first cycle of loading; however, this trend is reversed during the fifth and succeeding cycles of loading. Overall, figure 7 shows that the cyclic shear strength degrades with increasing number of cycles and the rate of degradation increases with increasing cyclic shear strain. These trends are consistent with the results obtained by Seed and Chan (1966) and Arango and Seed (1974).

The normalized shear modulus, G/G_{max}, and damping ratio versus cyclic shear strain are plotted in figures 8 and 9, respectively. The maximum shear modulus, G_{max}, was computed from the measured inplace shear-wave velocity of 140 m/s (Kayen and others, 1990). In addition, the data were normalized to account for the higher

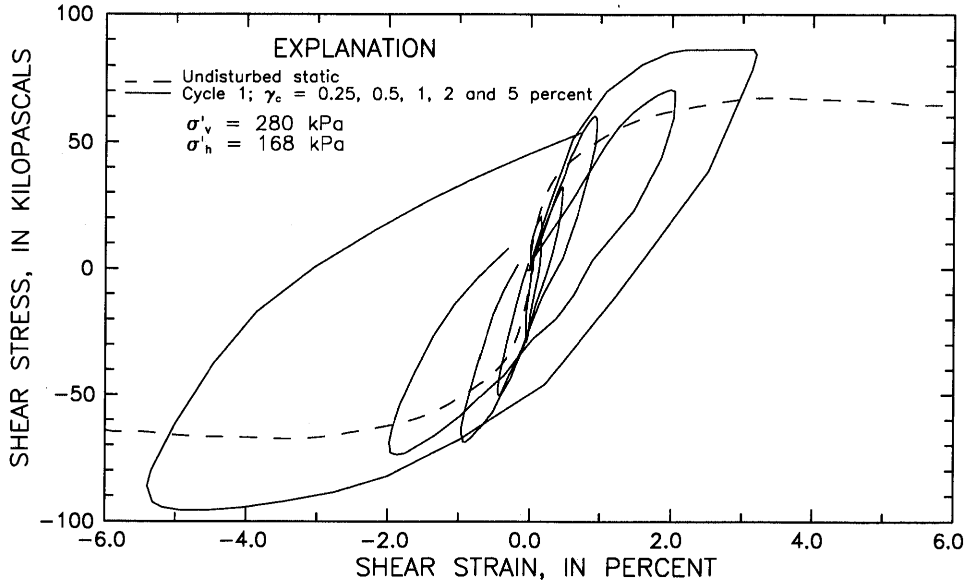

Figure 3.—Hysteresis loops during first cycle of loading at effective vertical stress, σ_v', of 280 kPa from undrained cyclic simple-shear tests on samples of young bay mud from the Marina District of San Francisco. σ_h', effective horizontal stress; γ_c, cyclic shear strain.

consolidation stresses in the tests consolidated at σ'_v=280 kPa, using the relation $G_{max1}/G_{max2}=(\sigma'_{m1}/\sigma'_{m2})^{0.5}$, where σ'_m is the mean normal stress. Vucetic and Dobry (1991) developed a series of normalized modulus-reduction curves for soils with different plasticities (C1–C5, fig. 8). The normalized data from our tests follow these trends and generally fall well within the bounds for soils with comparable plasticities defined by Vucetic and Dobry. Similarly, the damping ratios generally fall within the range established for soft clayey soils by Sun and others (1988). The damping ratio tends to increase with increasing cyclic shear strain; however, at any given strain level, the maximum damping ratio occurs during the first cycle of loading and then decreases with increasing number of cycles at a given strain level. Similar behavior of young bay mud was noted by Isenhower (1979).

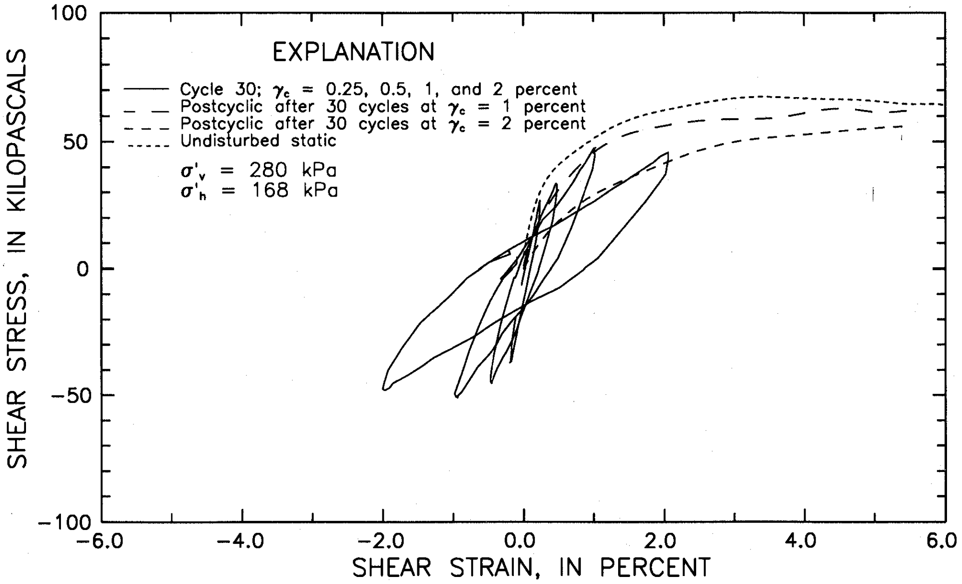

Figure 4.—Hysteresis loops during 30th cycle of loading at effective vertical stress, σ'_v, of 280 kPa from undrained cyclic simple-shear tests on samples of young bay mud from the Marina District of San Francisco. σ'_h, effective horizontal stress; γ_c, cyclic shear strain.

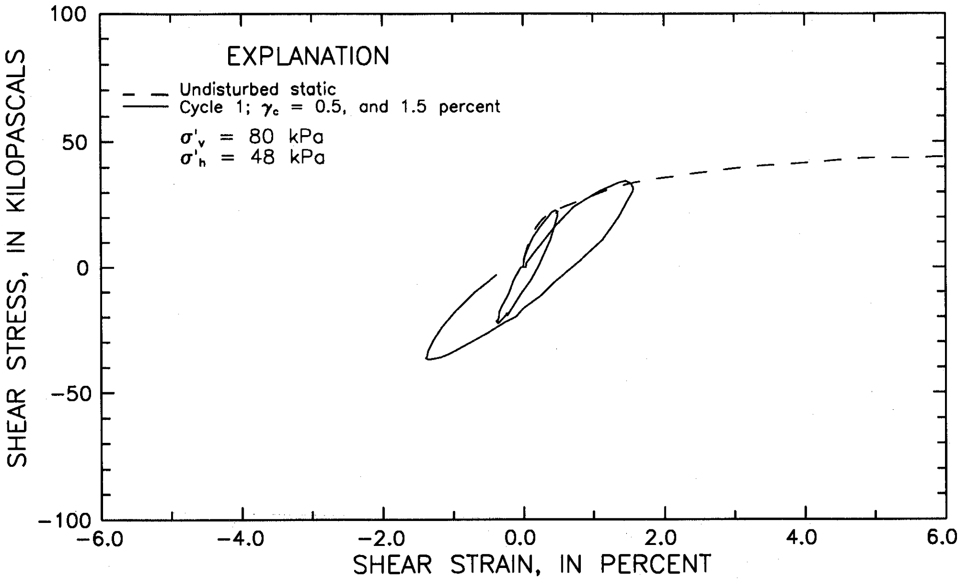

Figure 5.—Hysteresis loops during first cycle of loading at effective vertical stress, σ'_v, of 80 kPa from undrained cyclic simple-shear tests on samples of young bay mud from the Marina District of San Francisco. σ'_h, effective horizontal stress; γ_c, cyclic shear strain.

DISCUSSION

The most interesting aspect of the results presented here is the effect of relatively few cycles of loading on the cyclic strength of young bay mud. The data plotted in figure 7 indicate that the cyclic strength of the tested soil may decrease well below its static strength after about five cycles of loading at strains greater than 1 percent. In addition, the postcyclic static strength of the soil will be equal to the shear strength reached during the last cycle of loading at the maximum strain sustained during the loading interval, as shown in figure 4. These

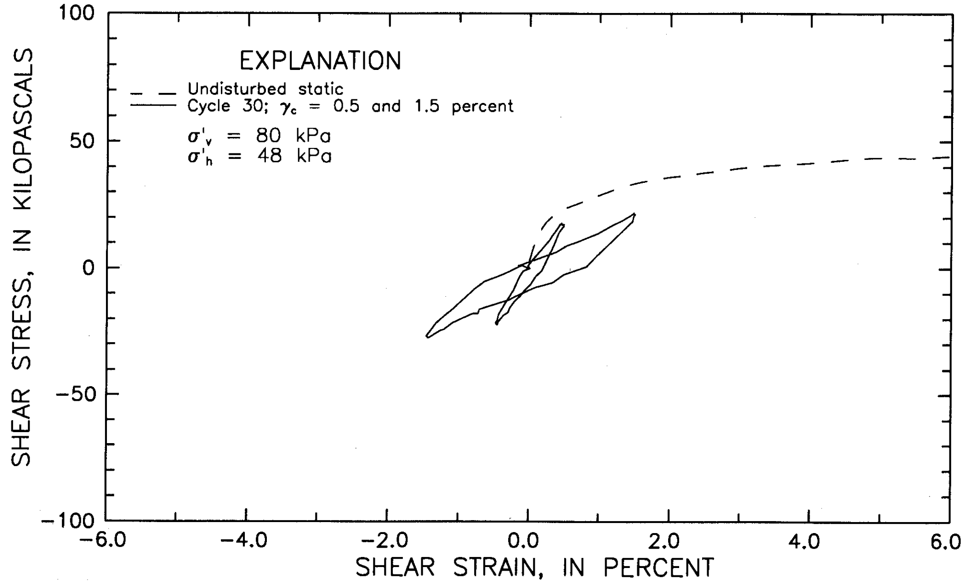

Figure 6.—Hysteresis loops during 30th cycle of loading at effective vertical stress, σ'_v, of 80 kPa from undrained cyclic simple-shear tests on samples of young bay mud from the Marina District of San Francisco. σ'_h, effective horizontal stress; γ_c, cyclic shear strain.

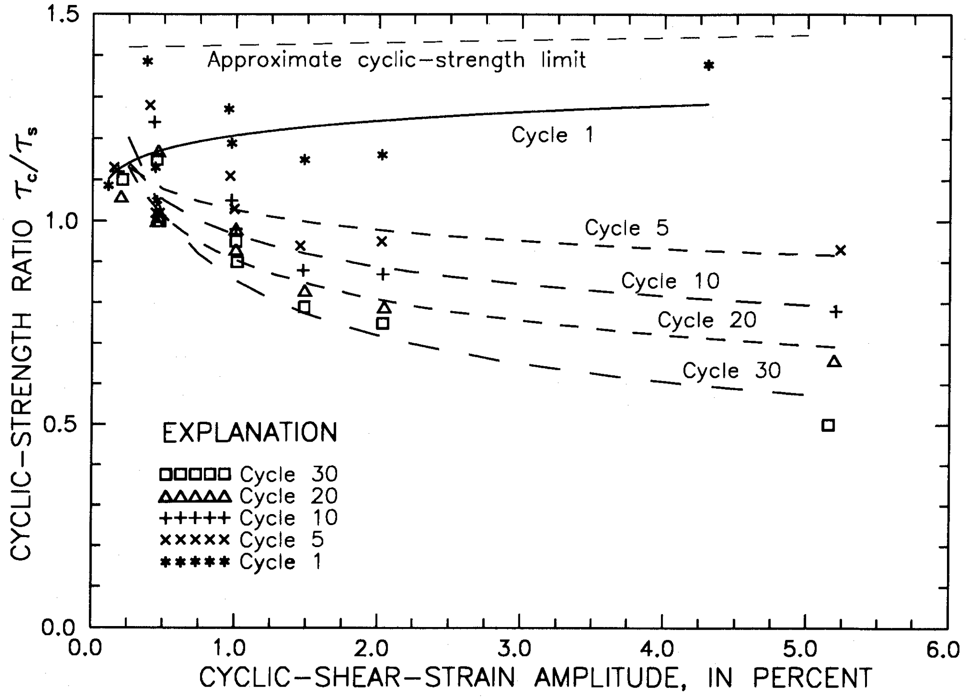

Figure 7.—Cyclic-strength ratio versus cyclic-shear-strain amplitude and number of loading cycles from tests on samples of young bay mud from the Marina District of San Francisco.

results have implications particularly for assessment of the seismic performance of lateral margins of fills and embankments overlying young bay mud during major seismic events. Because only relatively few cycles of loading at strains greater than 1 percent can lead to a significant reduction in the undrained strength of this deposit, excessive deformations and (or) outright slope failures during a major earthquake could be postulated, particularly if the design slope-stability computations have been made by assuming a high cyclic-shear strength, which is characteristic of the first cycle of loading.

Interestingly, to our knowledge the degree of strength degradation observed in our tests has not been typically reported for young bay mud and, apparently, may be related to the relatively low plasticity—that is, high silt

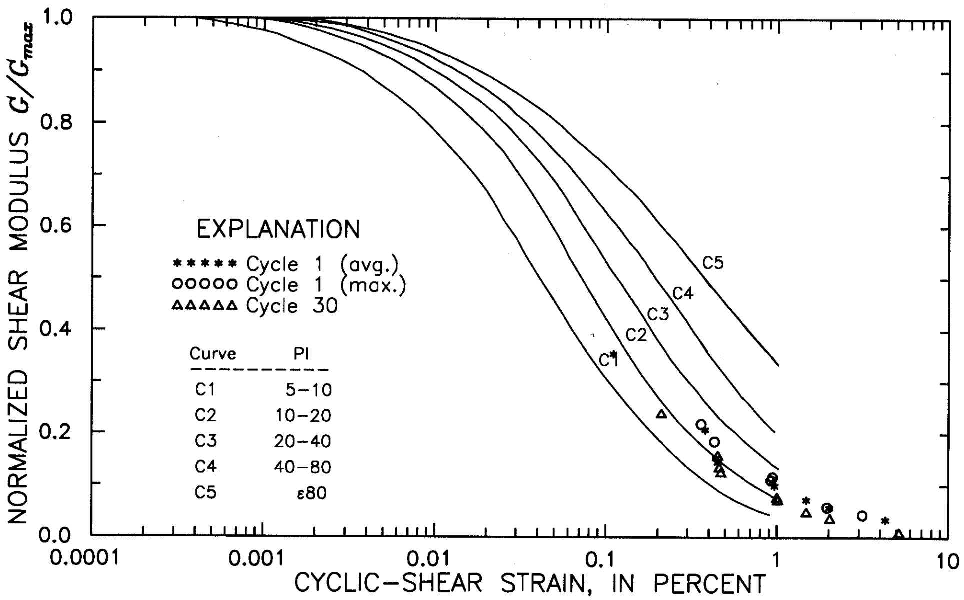

Figure 8.—Normalized shear modulus versus cyclic shear strain and plasticity index (PI) from tests on samples of young bay mud from the Marina District of San Francisco. Curves C1 through C5 after Vucetic and Dobry (1991).

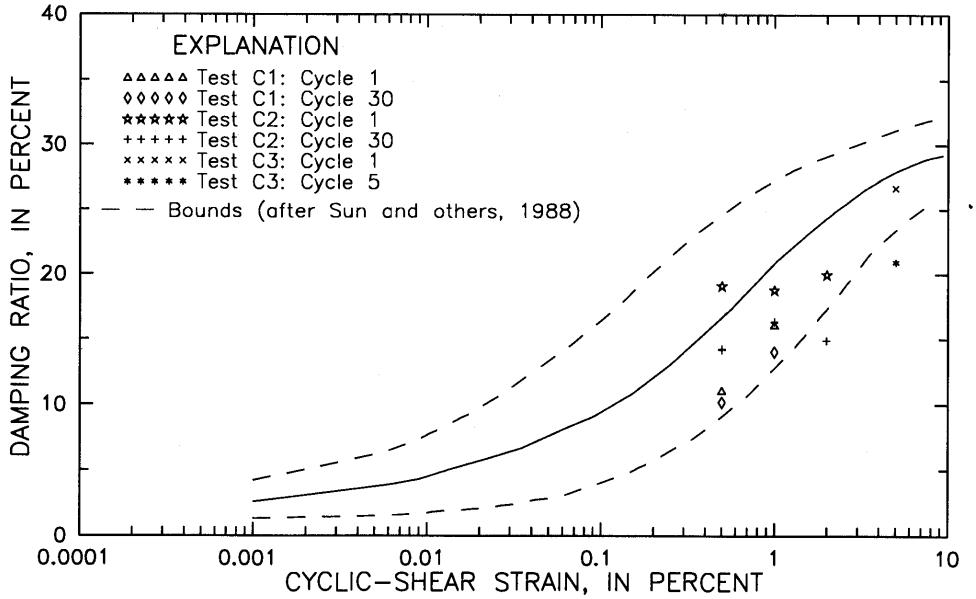

Figure 9.—Damping ratio versus cyclic shear strain and number of loading cycles from tests on samples of young bay mud from the Marina District of San Francisco.

content—of the samples. The relation of the modulus reduction to the plasticity index in cohesive soils was pointed out by Vucetic and Dobry (1991), and Ishihara and Yasuda (1980) suggested that the degree of strength loss under cyclic loading increases with decreasing soil plasticity. The data of Ishihara and Yasuda (1980), however, reproduced in figure 10, do not account for the cyclic-strain amplitude. The importance of cyclic-strain amplitude was shown previously in figure 7 and is also illustrated by superimposing the data from our tests onto figure 10.

Finally, we consider whether the composition of the soil samples from the Marina District can be considered representative of young bay mud in general. In this respect, we note that young bay mud is actually a clayey silt by its gradation, and layers or laminations with higher silt content are not unusual. Because potential slope failures can occur along very narrow failure planes, the presence of even a single silty zone exhibiting the behavior observed in our tests could significantly influence the seismic slope stability.

CONCLUSIONS

The results of static and cyclic, strain-controlled, undrained simple-shear tests on a sample of young bay mud from the Marina District of San Francisco show that its behavior is generally consistent with that observed previously. Its undrained strength during the first cycle of loading is significantly higher than its static strength, and the shear modulus decreases and the damping ratio increases with increasing cyclic shear strain. Our test results also show, however, that the cyclic strength can decline quite significantly with an increasing number of cycles of loading, possibly resulting in a residual postcyclic strength that is, in fact, lower than the initial undrained shear strength. These results have implications particularly for the design of fills and embankments along the margins of San Francisco Bay because the loss of strength of the underlying soft silty clays during a major earthquake could lead to excessive deformation and possible failures.

ACKNOWLEDGMENTS

This research was supported in part by U.S. National Science Foundation grant BCS–9003529. We thank Monique Nykamp for her assistance with the laboratory testing.

REFERENCES CITED

Arango, Ignacio, and Seed, H.B., 1974, Seismic stability and deformation of clay slopes: American Society of Civil Engineers Proceedings, Geotechnical Engineering Division Journal, v. 100, no. GT2, p. 139–156.

Bonaparte, Rudolph, and Mitchell, J.K., 1979, The properties of San Francisco Bay Mud at Hamilton Air Force Base, California: Berkeley, University of California, Department of Civil Engineering Geotechnical Engineering Report, 179 p.

Isenhower, W.M., 1979, Torsional simple shear/resonant column properties of San Francisco Bay Mud: Austin, University of Texas, M.S. thesis, 307 p.

Ishihara, Kenji, and Yasuda, Susumu, 1980, Cyclic strengths of undisturbed cohesive soils of western Tokyo, *in* International Sympo-

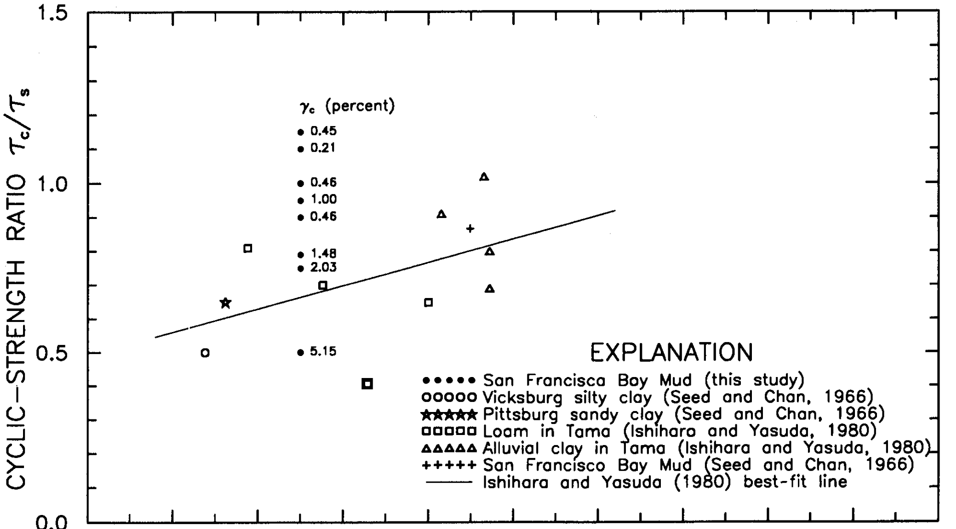

Figure 10.—Cyclic-strength ratio versus plasticity index after 30 loading cycles from tests on clays (after Ishihara and Yasuda, 1980). γ_c, cyclic shear strain.

sium on Soils Under Cyclic and Transient Loading, Swansea, U.K., 1980, Proceedings: London, A.A. Balkema, p. 57–66.

Janbu, Nilmar, Tokheim, O., and Senneset, Kaare, 1981, Consolidation tests with continuous loading: International Conference on Soil Mechanics and Foundation Engineering, 10th Stockholm, 1981, Proceedings, p. 645–654.

Kayen, R.E., Liu, H.-P., Westland, R.E., Warrick, R.E., Gibbs, J.F., Fumal, T.E., and Lee, H.J., 1990, Engineering and seismic properties of the soil column at Winfield Scott School, Marina District of San Francisco, California, chap. G *of* Effects of the Loma Prieta earthquake on the Marina District, San Francisco, California: U.S. Geological Survey Open-File Report 90–253, p. G1–G18.

Ladd, C.C., Foott, Roger, Ishihara, Kenji, Schlosser, F., and Poulos, H.G., 1977, Stress-deformation and strength characteristics: International Conference on Soil Mechanics and Foundation Engineering, 9th, Tokyo, 1977, Proceedings, v. 2, p. 421–482.

Seed, H.B., and Chan, C.K., 1966, Clay strength under earthquake loading conditions: American Society of Civil Engineers Proceedings, Soil Mechanics and Foundations Division Journal, v. 92, no. SM2, p. 53–78.

Sousa, J.B., and Chan, C.K., 1991, Computer applications in the UCB geotechnical laboratories, in Geotechnical Engineering Congress, Boulder, Colo., 1991, Proceedings: American Society of Civil Engineers Geotechnical Special Publication 27, v. 1, p. 531–543.

Sun, J.I., Golesorkhi, Ramin, and Seed, H.B., 1988, Dynamic moduli and damping ratios for cohesive soils: Berkeley, University of California, Earthquake Engineering Research Center Report UCB/EERC–88/15, 48 p.

Vucetic, Mladen, and Dobry, Ricardo, 1991, Effect of soil plasticity on cyclic response: Journal of Geotechnical Engineering, v. 117, no. 1, p. 87–107.

THE LOMA PRIETA, CALIFORNIA, EARTHQUAKE OF OCTOBER 17, 1989:
STRONG GROUND MOTION AND GROUND FAILURE

STRONG GROUND MOTION

DEEP INSTRUMENTATION ARRAY AT THE TREASURE ISLAND NAVAL STATION

By Pedro de Alba, Jean Benoît, Daniel G. Pass, and John J. Carter,
University of New Hampshire;
T. Leslie Youd,
Brigham Young University; and
Anthony F. Shakal,
California Division of Mines and Geology

CONTENTS

ABSTRACT

High levels of rock-motion amplification by soft-soil deposits of various thicknesses were observed during the earthquake. These observations raise questions about how earthquake motion at bedrock was transmitted through the overlying soil deposits, and emphasize once again the need for deep instrument arrays that would enable investigators to observe the transmission of earthquake motion from bedrock. Such an array is currently operating at the Treasure Island Naval Station in San Francisco Bay. In this paper, we present the results of the extensive soils-exploration program performed during instrument installation and the rationale for the instrumentation program. Downhole accelerometers have been installed below the bedrock surface (91-m [300 ft] depth) and at four intermediate locations in the soil profile, complemented by existing surface instruments both at the site and on the adjacent bedrock outcrop at Yerba Buena Island.

INTRODUCTION

A crucial observation to emerge from the wealth of ground-surface records generated by the earthquake is that motion amplification on soft-soil sites was unexpectedly high. Idriss (1991a) reported horizontal accelerations 200 to 600 percent higher at soft-soil sites than at rock sites at comparable epicentral distances. Although similar behavior, at lower accelerations, was observed in the 1985 Mexico City earthquake, this behavior was attributed to the exceptionally elastic response of Mexico City clays over a wide strain range (Romo and Jaime, 1986).

In the San Francisco Bay region, for a "well behaved" clay, such as the young bay mud of geotechnical usage, this behavior is somewhat more difficult to explain in the absence of direct observations of the propagation of bedrock motion upward through the soil column to the ground surface. Some analytical procedures suggest that the observed behavior is controlled by the thickness of young bay mud at a particular site and that the properties of the materials underlying the softer clay have only a minor influence on the calculated surface motions (Hryciw and others, 1991). Other investigators, pointing to the large amplifications recorded at sites where the young bay mud is relatively thin, suggest that the underlying old bay clay plays an important role or that major amplification may be due simply to the impedance contrast between stiffer and softer sedimentary deposits. Adding to these uncertainties is the long-standing controversy over the correct way to transform rock-outcrop motion to bedrock motion at the base of the soil profile to be analyzed. Such controversial points can best be clarified by installing deep arrays of accelerometers between bedrock and the ground surface; however, no such arrays were in place in the San Francisco Bay region at the time of the earthquake.

We have conducted an extensive review of potential sites in the San Francisco Bay region for establishing such an array. A basic requirement was that the site chosen fit into the framework of the proposed network of U.S. Geotechnical Test Sites (Benoît and de Alba, 1988).

The ideal site should, besides the requirements of security, meet the following conditions: (1) be sufficiently large as to allow future research for development of new soil-testing and site-characterization techniques, and (2) remain accessible to other researchers over a period of at least 30 years.

After considering several candidate sites, we identified an area adjoining fire station 1 (building 157) at the Treasure Island Naval Station as the best site meeting these conditions. From the viewpoint of potential for strong motion, it is about 12.8 km (8 mi) from the Hayward fault (fig. 1) and 29 km (18 mi) from the near-

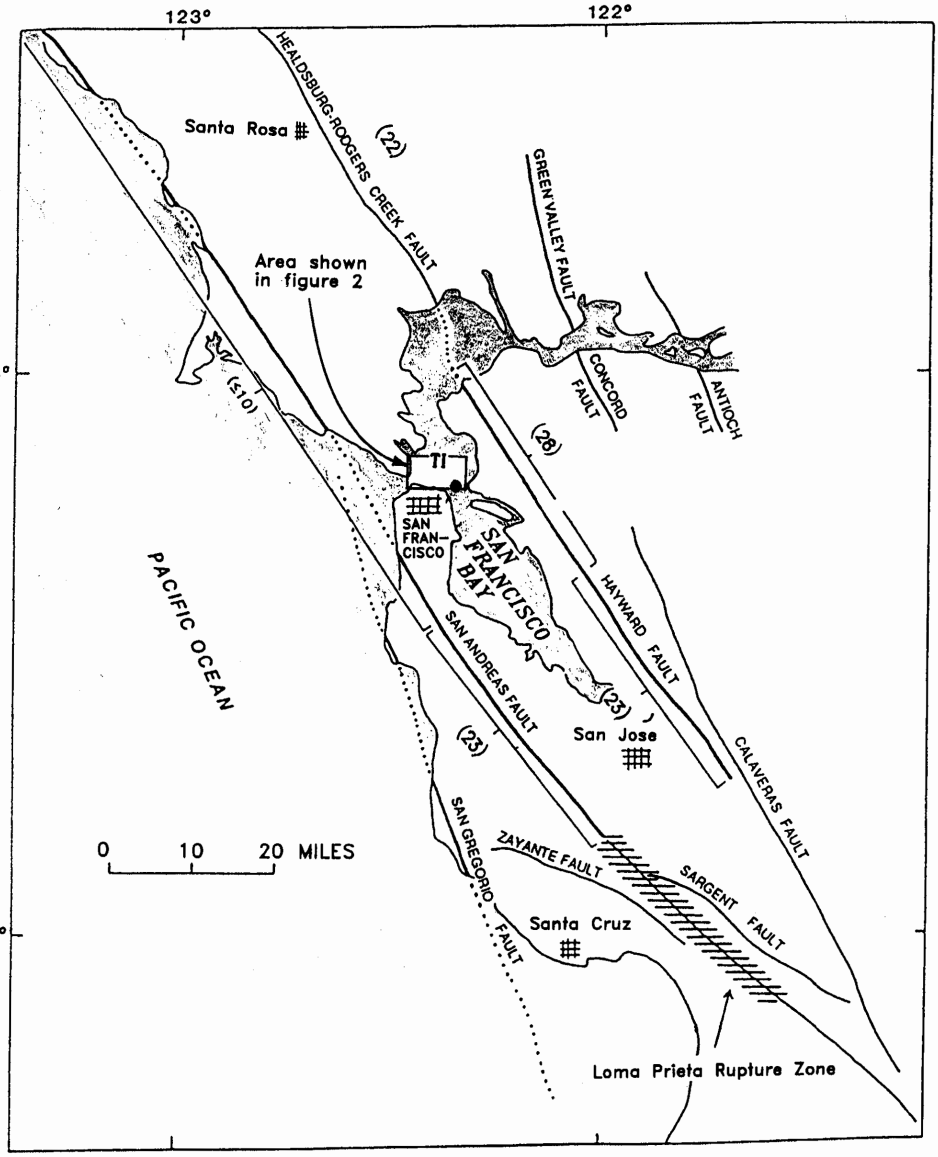

Figure 1.—San Francisco Bay region, showing locations of major faults (dotted where inferred). Numbers in parentheses indicate 30-year probability of an M=7+ earthquake on particular fault segment (Working Group on California Earthquake Probabilities, 1990). TI, Treasure Island. Box shows area of figure 2. Modified from Housner and Penzien (1990).

est point on the peninsular section of the San Andreas fault, which are both considered the major potential causative faults for a future M=7+ earthquake in the San Francisco Bay region (Working Group on California Earthquake Probabilities, 1990).

From a geotechnical viewpoint, the site is located on a deep soil profile, consisting of approximately 12 m (40 ft) of potentially liquefiable silty sand overlying about 15 m (50 ft) of medium-stiff young bay mud over dense sand and hard old bay clay, with bedrock at 91-m (300 ft) depth. The presence of a liquefiable-sand deposit of significant thickness made it possible to study the pore pressures and changes in soil stiffness in a liquefying granular soil, as well as the clay response. Another feature that made this site particularly attractive was that the California Strong Motion Instrumentation Program (CSMIP) of the California Division of Mines and Geology (CDMG) maintains a surface accelerograph at the fire station, which recorded the Loma Prieta earthquake motion, and plans to install a bedrock instrument at 98-m (320 ft) depth. In addition, the CSMIP has a surface instrument on the adjacent bedrock outcrop at Yerba Buena Island.

Therefore, we proposed to the U.S. National Science Foundation's Earthquake Hazard Mitigation Program that accelerometers be installed at various depths in the soil profile to complement the CSMIP instruments on Treasure Island. This installation would include several piezometers in the upper sand layers and be preceded by an extensive site-characterization study. Subsequently, in view of the obvious benefits of working in collaboration, we successfully proposed to the CSMIP that they take over the eventual operation of the site, as well as the processing and distribution of records and other information that might be obtained.

SITE DESCRIPTION

Treasure Island is a 162-ha (400 acre) artificial island formed by hydraulic filling in 1936–37, as the site of the 1939 Golden Gate International Exposition. The island was constructed over a natural-sand spit and young bay mud adjacent to a natural-rock outcrop of the Franciscan Complex, Yerba Buena Island (fig. 2). The island was formed by filling behind a perimeter rock dike, which served to retain the sand, and was raised by the "upstream" method, that is, by building subsequent dike sections over the previously placed hydraulic fill (Lee, 1969).

The hydraulic fill consists of silty fine sand, with a few clayey zones. By the nature of the placement method, the material is relatively loose. Liquefaction of this loose material was observed during the earthquake, accompanied by extensive sand boiling and lateral spreading in the vicinity of the perimeter dike. Maximum reported settlements were about 0.3 m (1 ft) (Seed and others, 1990). The peak ground-surface acceleration recorded at Treasure Island by the CSMIP instrument for the earthquake was only 0.16 *g*. Thus, the potential for major damage at higher intensity levels is evident.

There was no surface evidence of liquefaction at the fire station during the earthquake. However, the surface-acceleration record obtained at this site, in contrast to those at other soft-soil sites, shows a sudden drop about 15 s into the record and practically no response after 16

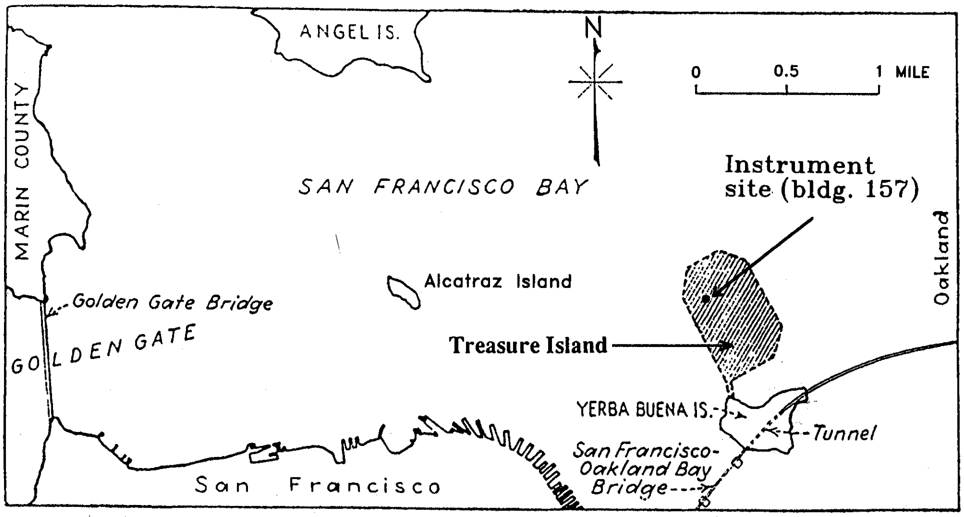

Figure 2.—Northern part of San Francisco Bay (see fig. 1), showing location of instrumented area near fire station at the Treasure Island Naval Station. Bldg., building. Modified from Seed and others (1990).

s (Idriss, 1991b). This behavior is almost certainly due to liquefaction of the underlying sand. We note that the peak ground-surface acceleration at the adjacent bedrock outcrop on Yerba Buena Island was only 0.067 *g*, indicating a significant amplification of bedrock motion by the soil deposits underlying Treasure Island.

SITE CHARACTERISTICS

An extensive site-characterization program was carried out (in August 1991) while preparing the site for installation of additional instruments. Onsite testing included standard penetration tests (SPT's), cone-penetration tests (CPT's) by piezocone, self-boring-pressuremeter (SBPM) tests, dilatometer tests (DMT's), field-vane tests (FVT's), and crosshole shear-wave-velocity measurements.

Subsoil information had previously been obtained for this site in November 1990 from a 103.6-m (340 ft)-deep borehole drilled by Woodward-Clyde Consultants, Inc., as part of a joint effort with the Electric Power Research Institute of Palo Alto, Calif., the University of California, Davis, the CDMG, and the U.S. Geological Survey (USGS). SPT's were carried out in the upper sand layers, and tube samples of the hydraulic fill and young bay mud were recovered. A simplified soil profile, based on observations from this deep borehole and from the current study, is shown in figure 3.

Analysis of the site response during the earthquake (Hryciw and others, 1991; Idriss, 1991a) suggests that the soils above the old bay clay had the greatest influence on the ground-surface motion. Therefore, this new study was intended to explore the horizontal variation of these soils across the site, as well as to provide more extensive

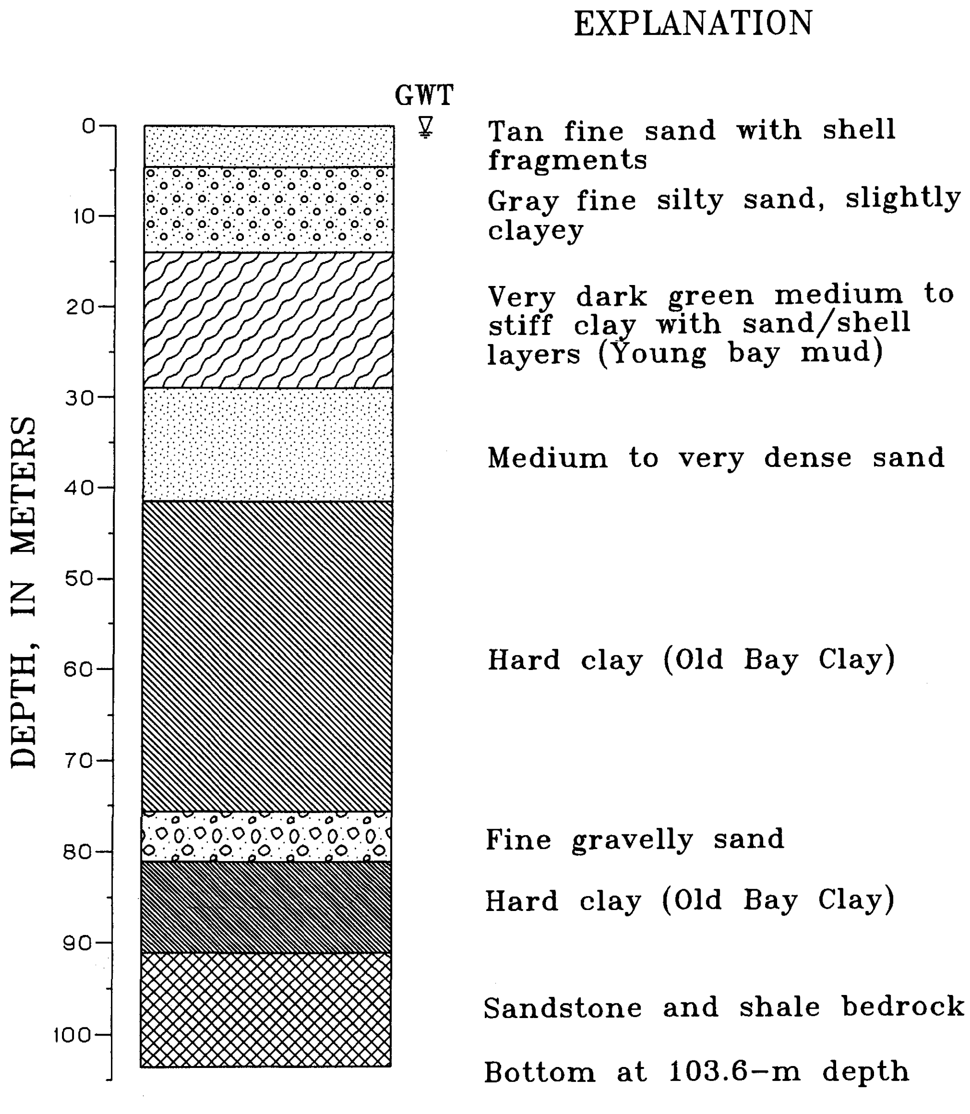

Figure 3.—Schematic soil profile at fire station at the Treasure Island Naval Station. GWT, ground-water table.

quantitative field information on the materials down to the old bay clay, using various onsite testing techniques.

The locations of tests at the site are shown in figure 4. Boreholes B–1 through B–4 were used for SPT's and thin-wall-tube sampling; these boreholes were subsequently cased for installation of accelerometers. Borehole B–CDMG is the deep borehole described above. Explorations generally showed an upper sand deposit extending to a depth of about 12.2 m (40 ft), followed by a transition zone to a depth of about 13.7 m (45 ft) into a greenish-gray clay deposit (young bay mud) that reaches a depth of approximately 29 m (95 ft) and is underlain by a series of dense sand deposits, about 9 m (30 ft) thick, over hard old bay clay.

The SPT's indicated two distinct sublayers in the upper sand deposit. The upper 4.5 m (15 ft) consists of a tan fine silty sand. Numerous rock/concrete fragments were struck at depths to 1.5 m (5 ft) that impeded drilling, suggesting that this part might be a dumped rather than a hydraulic fill. A silt seam was penetrated at a depth of about 4 m (13 ft); below this layer was gray fine sand, evidently hydraulic fill. Grain-size curves for the samples recovered from SPT's (see fig. 9) show fines contents ranging from about 6 to 20 percent in the upper tan sand and from 13 to 40 percent in the gray sand; the fines are predominantly nonplastic. However, materials at depths of about 7 to 9 m (23–29 ft) are predominantly SC in the Unified Soil Classification System.

SPT results for the sand layers are summarized in figure 5. These tests were carried out according to the general recommendations of Seed and others (1984); a baffled drag bit was used to advance a 100-mm (4 in.)-diameter borehole stabilized with drilling mud. The split spoon was provided with a liner to give a constant internal diameter. A-size drilling rods were used, and the spoon was advanced with a safety hammer. Energy measurements were carried out during selected tests at depths of 9.8 to 11.0 m (32–36 ft), using a Binary Instruments SPT calibrator and a piezoelectric load cell. The results from 17 successful tests indicated an average energy ratio (fraction of maximum theoretical energy) of 68 percent, somewhat higher than conventionally expected from a safety hammer but well within the range reported by Farah (1991) for this equipment. Values of $(N_1)_{60}$ (blow count normalized to an effective overburden stress of 95.8 kPa [1 ton/ft^2] and an energy ratio of 60 percent) based on this energy ratio are plotted as a function of depth in figure 5. We note that, even if the blow count is increased by 3 to 4 blows per foot (bpf) to account for increased liquefaction resistance due to the

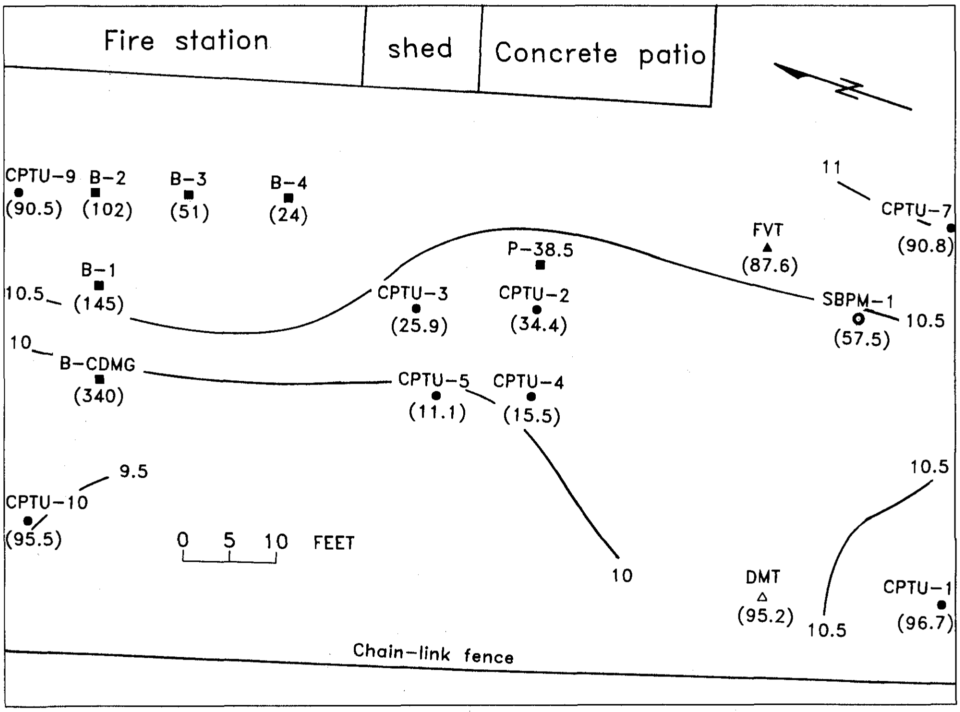

Figure 4.—Area near fire station at the Treasure Island Naval Station, showing locations of inplace borehole tests: B, accelerometer boring; CPTU, piezocone; DMT, dilatometer; FVT, field vane; SBPM, self-boring pressuremeter. Standard penetration tests were also performed in boreholes B–1, B–3, and P–38.5. Curved lines, contours of elevation of ground surface (in feet above mean lower low water). Numbers in parentheses indicate exploration depth (in feet). CDMG, California Division of Mines and Geology.

fines content of the sand, as suggested by Seed (1986), this deposit would still fall into the "high damage potential" range for an M=7.5 earthquake proposed by Seed and others (1984).

The deepest piezocone profile at borehole CPTU–1 (fig. 4) is shown in figure 6. Soil conditions were found to be quite uniform within the study area, and the results of other CPT's substantially replicate those at borehole CPTU–1, as shown in figure 7. Although the sand deposits show the variation in tip resistance expected in such materials, the general trends are the same, with a decrease in q_t (cone-tip resistance corrected for unequal areas) to a depth of about 6 m (20 ft), where a well-defined series of clayey seams was penetrated, followed by an increase in q_t below a depth of 9 m (29 ft) and an abrupt decrease in q_t at a depth of about 12.2 m (40 ft), where the sand/clay transition zone was penetrated.

The cone-tip resistance and pore-pressure readings agree well with the dilatometer material index (I_D, fig. 8), indicating numerous small silty and clayey seams throughout the sand deposit, as well as the better defined clayey zone mentioned above. Grain-size curves for the upper and lower sand layers are shown in figure 9.

Crosshole shear-wave-velocity measurements were carried out at the site by Earth Technology Corp. Three cased boreholes (B–1, B–2, B–CDMG, fig. 4), were used to the maximum cased depth of borehole B–2 (31.1 m [102 ft]), and two boreholes to the maximum depth of borehole B–1 (44.2 m [145 ft]). The results, as summarized in figure 10, show that velocities in the sandy fill

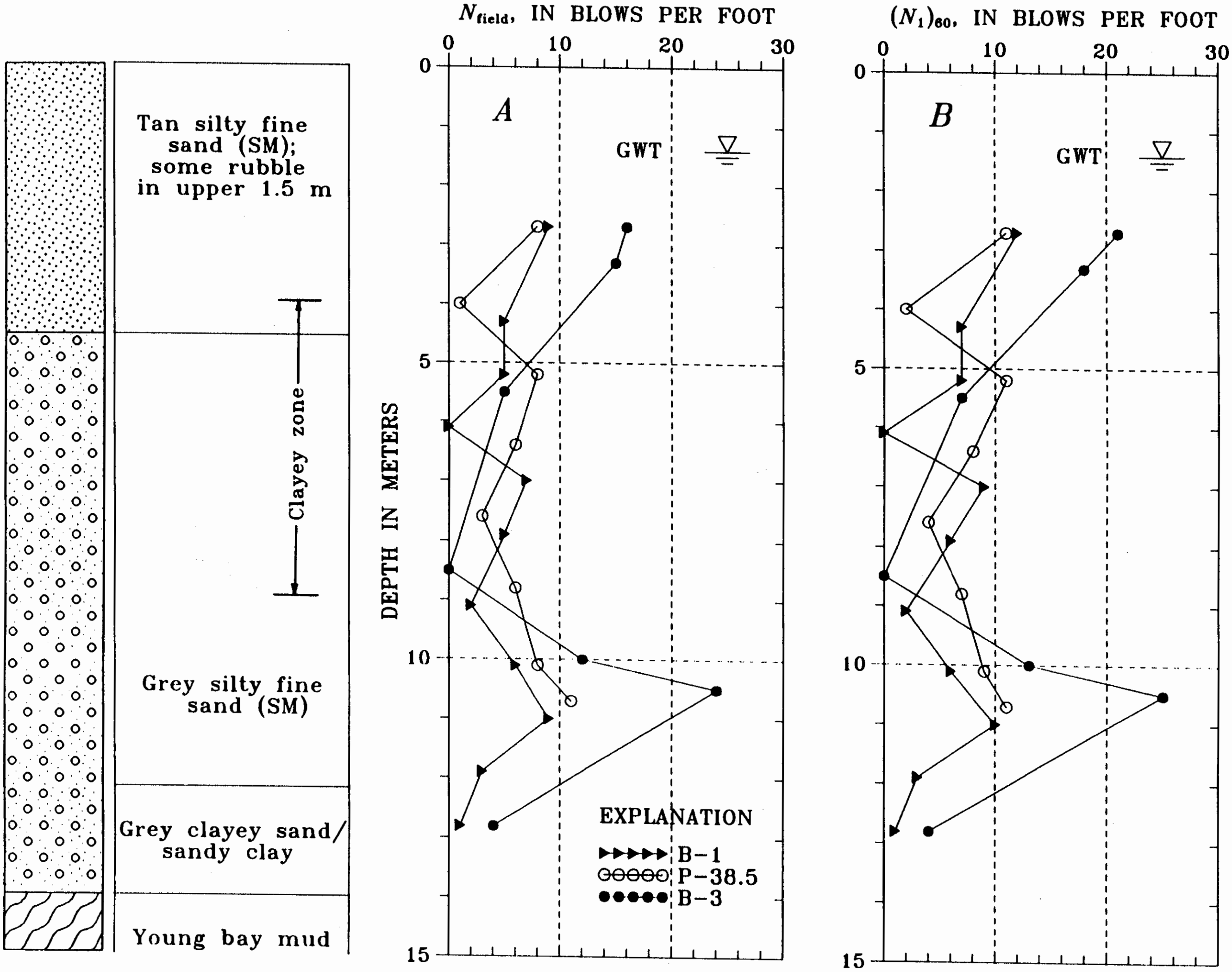

Figure 5.—Field (*A*) and normalized (*B*) blow counts from standard penetration tests at the Treasure Island Naval Station. GWT, ground-water level.

are relatively low, with a maximum of 190 m/s and a minimum of 120 m/s. We note that crosshole tests using the same boreholes were subsequently repeated by K.H. Stokoe of the University of Texas, Austin (oral commun., 1991), with essentially the same results.

As previously noted, a transition zone, about 1.5 m (5 ft) thick, was penetrated between the hydraulic-fill sand and the young bay mud. This transitional material changes in gradation from a clayey sand (SC) to a sandy lean clay (CL) and exhibits a low penetration resistance, as shown in figure 5.

The results of a dilatometer sounding (borehole DMT, fig. 4) carried out to a depth of 29 m (95 ft) near borehole CPTU–1 are shown in figure 8 in terms of material index I_D, lateral-stress index K_D, and DMT modulus E_D. These results indicate that the I_D profile at borehole DMT agrees well with the tip-resistance and pore-pressure results at borehole CPTU–1 (figs. 6, 7), in that numerous small silty and clayey seams were found throughout the sand deposit and a well-defined clayey zone was identifiable. The E_D measurements clearly show the change in stiffness between the sand deposits and the underlying young bay mud, as well as identifying a few soft, thin seams within the sand deposits.

An SBPM was used at the site to evaluate at-rest horizontal stresses in the sand deposits and the upper part of the young bay mud. Grounding problems between the probe and the onsite power supply did not permit automatic data acquisition, and so each test had to be recorded manually, significantly decreasing its accuracy. The average at-rest horizontal-stress coefficient, K_0, as a function of depth is plotted in figure 11 as a range calculated from the maximum and minimum horizontal stresses measured by each of the strain sensors on the SBPM. Also shown are K_0 values obtained using the empirical relation of Jáky (1944) for normally consolidated soils: $K_0=1-\sin\phi'$, where ϕ' is the effective-stress friction angle. The ϕ' values for the sand deposits were calculated from the CPTU tip resistance, using the procedure of Robertson and Campanella (1983). For the young bay mud, we used the ϕ' values reported by Bonaparte and Mitchell (1979) on young bay mud at Hamilton Air Force Base.

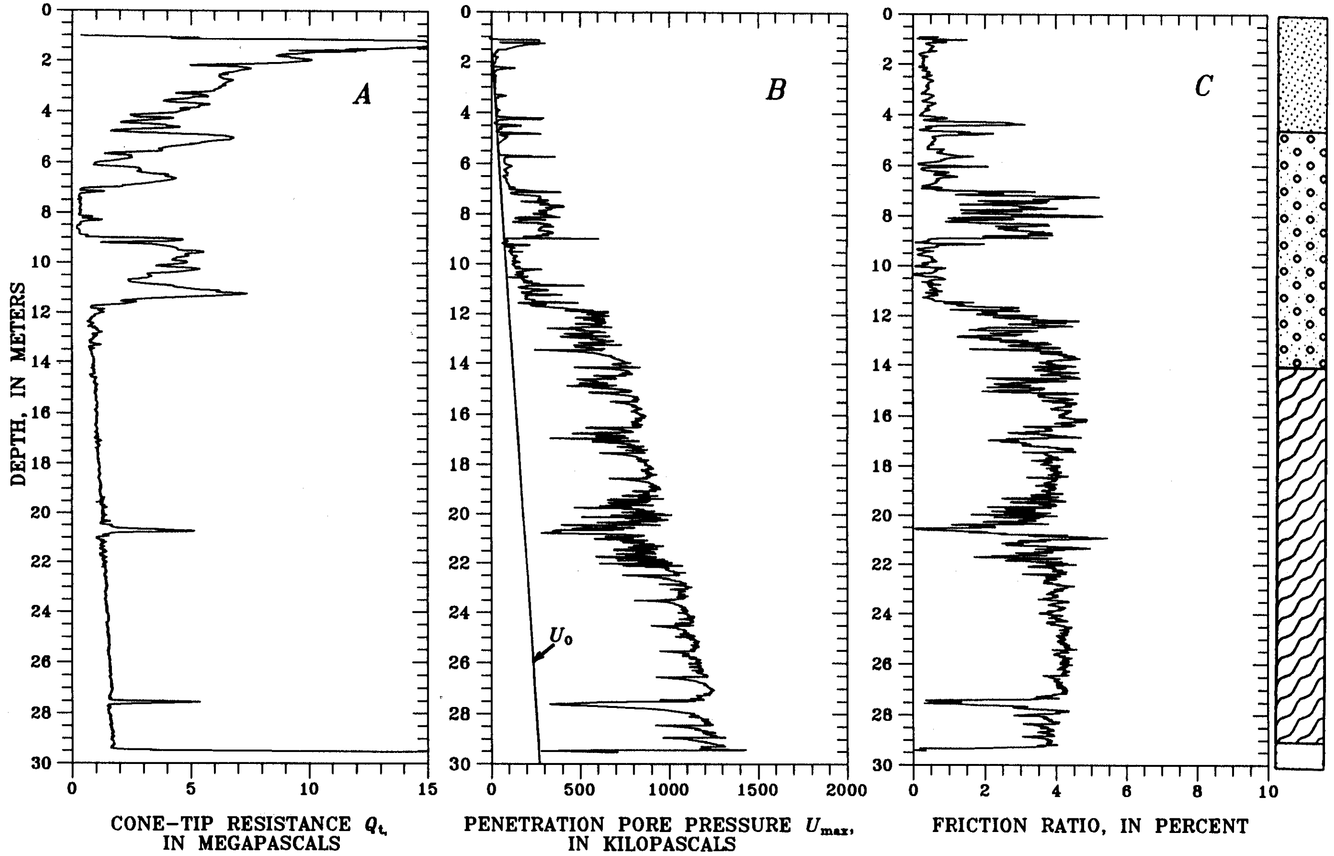

Figure 6.—Cone-tip resistance (*A*), penetration pore pressure (*B*), and friction ratio (*C*) versus depth from cone-penetration tests in borehole CPTU–1 at the Treasure Island Naval Station (see fig. 4 for location and fig. 3 for soil symbols). Elevation of ground surface is 10.8 ft (3.28 m) above mean lower low water. μ_0, hydrostatic pressure.

We then compared the SBPM results with the values interpreted from the DMT, using available empirical relations based on the values of I_D and K_D. In the sand deposits (I_D>1.2), K_0 was evaluated by Schmertmann's (1983) method, using CPT data from an adjacent CPTU borehole. In the clay and clayey sand deposits (I_D<1.2), we used the method of Marchetti (1980) directly. Our results show that the K_0 values estimated from Jáky's (1944) empirical relation are consistently lower than those calculated from either the DMT or SBPM results. The DMT and SBPM results agree relatively well, and the average SBPM results fall somewhere between the DMT results and Jáky's (1944) values. The DMT results suggest high K_0 values near the ground surface: Both the SBPM and DMT results indicate a K_0 value of 0.55 to 0.65 between depths of 3 and 11 m (10 and 36 ft); the DMT results show K_0 values increasing below a depth of 11 m (36 ft) to about 0.65–0.85, whereas the K_0 values from the SBPM results average 0.6. Below a depth of 18 m (59 ft) to the maximum depth of the DMT sounding, the K_D value is nearly constant, suggesting that the K_0 value remains relatively constant in the young bay mud.

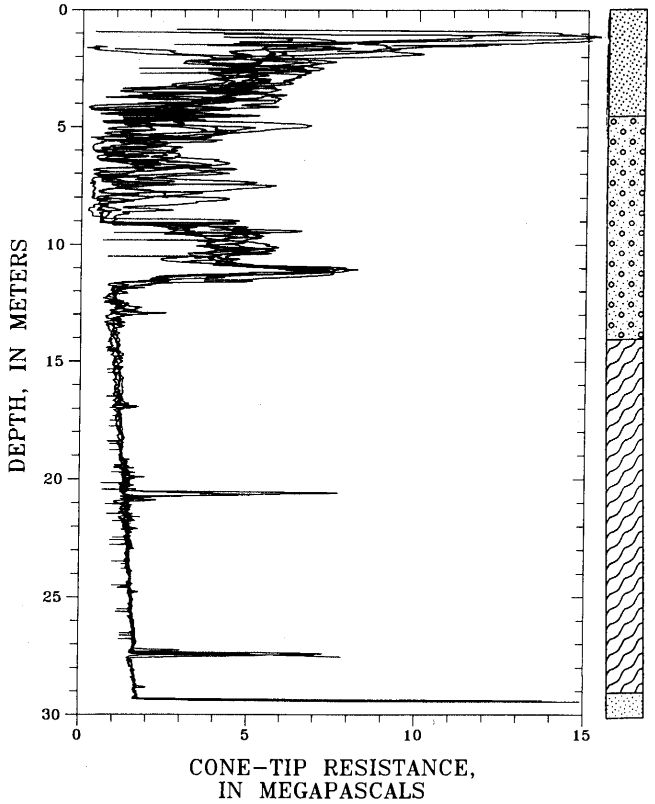

Figure 7.—Cone-tip resistance versus depth for selected cone-penetration tests at the Treasure Island Naval Station. See figure 3 for soil symbols.

The young bay mud can be described as medium stiff to stiff, on the basis of the FVT results plotted in figure 12. These results, which have been corrected by using the method of Åas and others (1986), show undrained shear strength steadily increasing from 27 kPa (3.9 lb/in^2) near the transition zone to 61 kPa (8.8 lb/in^2) near the base of the young bay mud. We note that some FVT tests may have been affected by lenses of shell fragments, which are common in these deposits; these results were omitted from the corrected data set. The ratio of corrected undrained shear strength, S_u, to vertical effective stress, σ'_{vo}, was found to be about 0.26.

At the bottom of the young bay mud, at a depth of about 29.3 m (96 ft), there is a clearly defined transition to a dense gray fine-sand deposit, finely interlayered in its upper 3.6 m (12 ft) with shell fragments. SPT blow counts in this upper sublayer range from 52 to 82 bpf. This sand deposit is underlain by about 1.8 m (6 ft) of less shelly sand, somewhat less dense, with an SPT blow count of 33, followed by another shell-rich sand layer at a depth of 34.8 m (114 ft), very dense, with a blow count of more than 100 bpf. This deposit becomes somewhat siltier and less dense with depth (thin-walled-tube samples were obtainable below a depth of 39 m [128 ft]). The bottom of this deposit is at 42.4 m (139 ft), where there is a sharp boundary with the old bay clay.

INSTRUMENTATION

PIEZOMETERS

Exploration results indicate that, if the site undergoes significant levels of earthquake motion, earthquake-induced excess pore pressures may markedly alter the hydraulic-fill response as the earthquake progresses. Therefore, we installed eight piezometers in August 1991 at depths ranging from 3 to 11.7 m (10–38.5 ft) (fig. 13) to monitor dynamically induced pore pressure in the sand deposits.

Because long-term survivability in a brackish-groundwater environment was a major concern in the selection of these instruments, we chose transducers with titanium casings. To protect them during installation, they were encased in specially designed nylon tips (fig. 14). In this design, the sensitive face of the transducer is in contact with an internal water-filled cavity, connected to the ground water through porous plastic inserts in the tip.

Each piezometer tip was carefully saturated and installed by inserting the base of the tip section into a steel holder attached to the end of the drill string. The piezometer was then lowered to the bottom of a drilling-mud-stabilized borehole and pushed about 30 cm (1 ft) into undisturbed soil. During this operation, the piezometer tip was protected by placing it in a water-filled plastic bag attached to a retrieval cord, which made it possible to tear off the bag once the point was engaged in the undisturbed soil. A second, heavier cord that had been looped through holes at the base of the tip section (fig. 14) was left in place when the insertion tool was withdrawn. This cord can be used to retrieve the piezometer for replacement or recalibration after recording pore pressure during an earthquake. After installation, each piezometer boring was grouted with a weak cement/bentonite mixture (1 part bentonite to 0.25 parts cement to 12.5 parts water), designed to remain plastic and allow for piezometer retrieval, as described above. To complement the pore-pressure observations and measure permanent displacements, an inclinometer casing was installed to a depth of 18.3 m (60 ft) (fig. 13).

ACCELEROMETERS

The distribution of accelerometers is designed to trace the propagation of strong earthquake motion from bedrock through the soil profile. Triaxial downhole accelerometers have been installed in boreholes B–1 through B–4 (fig. 4), at depths ranging from 6.4 to 97.6 m (21–320 ft). The locations of these instruments at the site are shown in figure 14, and a schematic distribution of the accelerometers and piezometers with depth in figure 15. Acceleration data will thus be obtained below the bedrock surface, near the top of the old bay clay, near the top of the dense gray sand, near the top of the young bay mud, and in the hydraulic fill. All the accelerometers are installed in 127-mm (5 in.)-internal-diameter polyvinyl chloride (PVC) pipe, grouted in place. The instruments are secured by using the CSMIP orientation and locking system (Shakal and Petersen, 1992). As previously noted, a surface accelerometer is already in operation at the site. All the recorders have been interconnected for precise timing. The installation was completed in January 1993.

FUTURE WORK

We are aware of the potential importance of three-dimensional effects on the site response; bedrock slopes upward from the site toward Yerba Buena Island to the

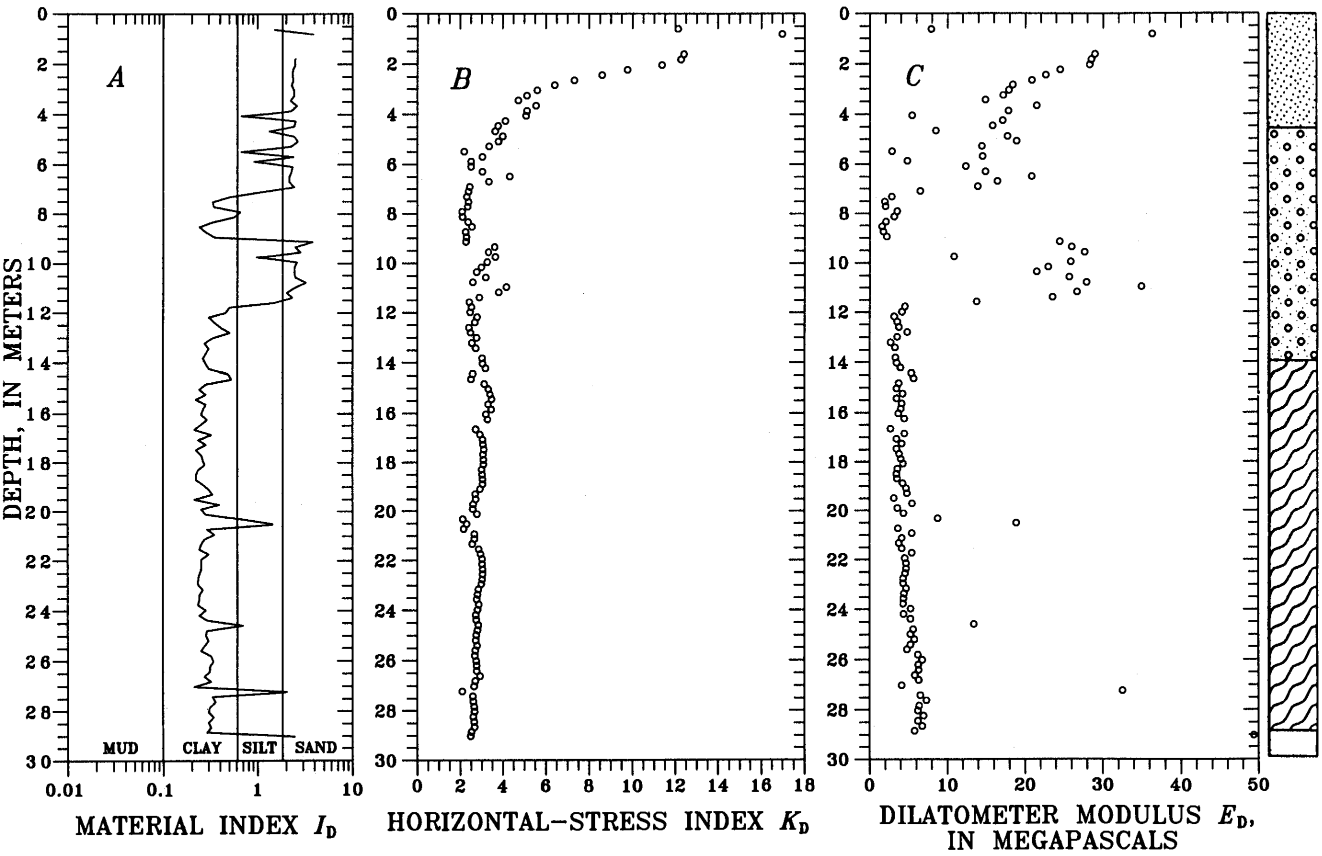

Figure 8.—Material index (*A*), horizontal-stress index (*B*), and dilatometer modulus (*C*) versus depth from Marchetti dilatometer tests at the Treasure Island Naval Station. Elevation of ground surface is 10.3 ft (3.14 m) above mean lower low water. See figure 3 for soil symbols.

south. Future studies will include a refraction survey to characterize the bedrock surface, as well as studies and potential instrumentation of locations on the island that were improved by vibroflotation or compaction piles and that behaved well during the earthquake.

ACKNOWLEDGMENTS

This research was supported by U.S. National Science Foundation grants BCS–9011332 and BCS–9016470 under the Earthquake Hazard Mitigation Program. The project's advisory panel, Thomas L. Holzer, Izzat M. Idriss, J. Carl Stepp, Kenneth H. Stokoe, and Richard D. Woods, provided valuable input during the planning stages for the installation. Richard Faris and his staff at the Geotechnical Branch of the U.S. Naval Facilities Engineering Command, Western Division, were most helpful in supplying soils information at various naval installations; Thomas C. Cuckler and his Planning Division staff at the Treasure Island Naval Station greatly facilitated our work there. The SPT calibrator was loaned by the U.S. National Institute of Standards and Technology, through the good offices of George Gobel of the University of Colorado, Boulder.

REFERENCES CITED

Åas, Gunnar, Lacasse, Suzanne, Lunne, Tom, and Høeg, Kaare, 1986, Use of in situ tests for foundation design in clay, *in* Proceedings of In Situ '86, a specialty conference; use of in situ tests in geotechnical engineering: American Society of Civil Engineers Geotechnical Special Publication 6, p. 1–30.

Benoît, Jean, and de Alba, Pedro, Editors, 1988, Designated sites for geotechnical experimentation in the United States: workshop at the University of New Hampshire, September 1988, 165 p.

Bonaparte, Rudolph, and Mitchell, J.K., 1979, The properties of San Francisco Bay Mud at Hamilton Air Force Base, California: Berkeley, University of California, Department of Civil Engineering Geotechnical Engineering Report, 179 p.

Farah, J.A., 1991, Field energy measurements of standard penetration testing: Boulder, University of Colorado, M.S. thesis, 399 p.

Housner, G.W., and Penzien, J., 1990, Competing against time; report of the Governor's Board of Inquiry on the 1989 Loma Prieta earthquake: Sacramento, Calif., 264 p.

Hryciw, R.D., Rollins, K.M., Homolka, Matthew, Shewbridge, S.E., and McHood, M.D., 1991, Soil amplification at Treasure Island during the Loma Prieta earthquake: International Conference on

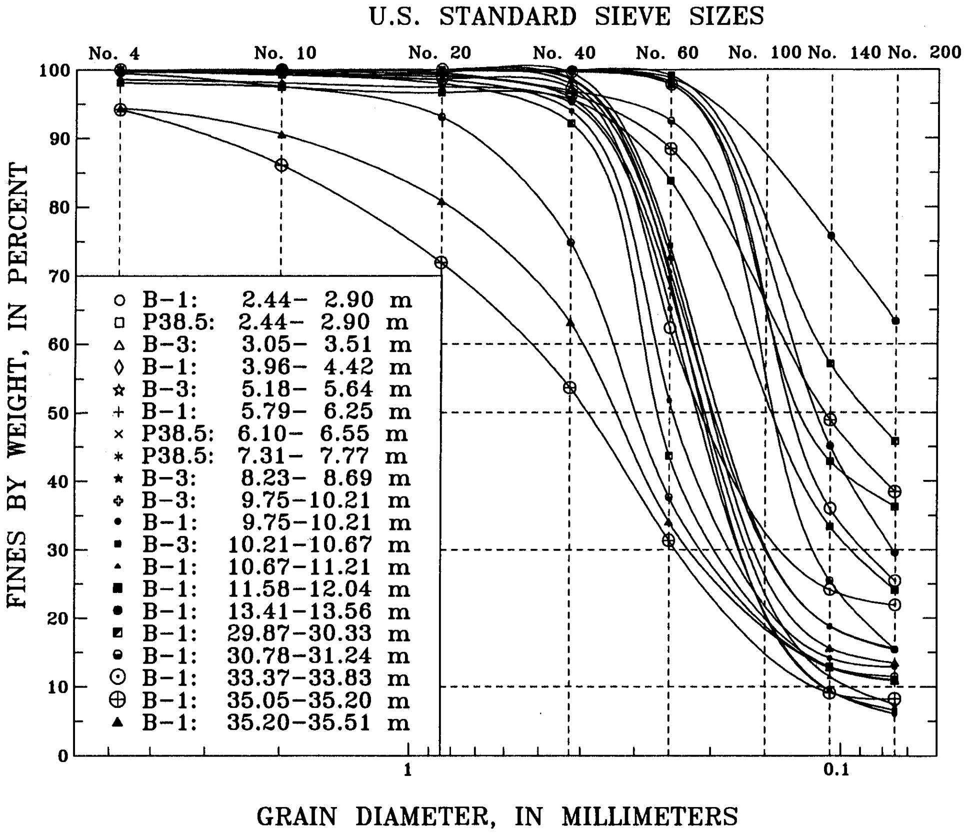

Figure 9.—Grain size versus fines content in upper and lower sand layers at fire station at the Treasure Island Naval Station.

Recent Advances in Geotechnical Earthquake Engineering and Soil Dynamics, 2d, St. Louis, Mo., 1991, Proceedings, v. 2, p. 1679–1685.

Idriss, I.M., 1991a, Earthquake ground motions at soft soil sites: International Conference on Recent Advances in Geotechnical Earthquake Engineering and Soil Dynamics, 2d, St. Louis, Mo., 1991, Proceedings, v. 3, p. 2265–2273.

———1991b, Response of soft soil sites during earthquakes, *in* H. Bolton Seed Memorial Symposium: Berkeley, Calif., BiTech, v. 2, p. 273–289.

Jáky, J., 1944, [The coefficient of earth pressure at rest]: Society of Hungarian Architects and Engineers Journal, v. 78, no. 22, p. 355–358 [in Hungarian].

Lee, C.H., 1969, Case history 2. Treasure Island fill, *in* Lee, C.H., and Praszker, Michael, Bay mud developments and related structural foundations, *in* Goldman, H.B., ed., Geologic and engineering aspects of San Francisco Bay fill: California Division of Mines and Geology Special Report 97, p. 69–72.

Marchetti, Silvano, 1980, In situ tests by flat dilatometer: American Society of Civil Engineers Proceedings, Geotechnical Engineering Division Journal, v. 106, GT3, p. 299–321.

Robertson, P.K., and Campanella, R.G., 1983, Interpretation of cone penetration tests—part I (sand): Canadian Geotechnical Journal, v. 20, no. 4, p. 718–773.

Romo, M.P., and Jaime, Alberto, 1986, Characteristicas dinamicas de algunas arcillas del Valle de México y análisis de la respuesta sismica del suelo [Dynamic characteristics of some clays in the Valley of Mexico and analysis of the seismic response of the soil]: Universidad Nacional Autónoma de México, Instituto de Ingeniería, 43 p.

Schmertmann, J.H., 1983, Revised procedure for calculating K_0 and OCR from DMT's with ID>1.2 and which incorporate the penetration force measurement to permit calculating the plane strain friction angle: DMT Workshop, Gainesville, Fla., 1983.

Seed, H.B., 1986, Design problems in soil liquefaction: Berkeley, University of California, Earthquake Engineering Research Center Report UCB/EERC–86/02, 33 p.

Seed, H.B., Tokimatsu, Kohji, Harder, L.F. and Chung, R.M., 1984, The influence of SPT procedures in soil liquefaction resistance evaluations: Berkeley, University of California, Earthquake Engineering Research Center Report UCB/EERC–84/15, 50 p.

Seed, R.B., Dickinson, S.E., Reimer, M.F., Bray, J.D., Sitar, Nicholas, Mitchell, J.K., Idriss, I.M., Kayen, R.E., Kropp, Alan, Harder, L.F. and Power, M.S., 1990, Preliminary report on the principal geotechnical aspects of the October 17, 1989 Loma Prieta earthquake: Berkeley, University of California, Earthquake Engineering Research Center Report UCB/EERC–90/05, 137 p.

Shakal, A.F., and Petersen, C., 1992, Downhole strong-motion accelerometry; objectives and techniques: Seismological Society of America Annual Meeting, Santa Fe, N.Mex., 1992.

Working Group on California Earthquake Probabilities, 1990, Probabilities of large earthquakes in the San Francisco Bay region, California: U.S. Geological Survey Circular 1053, 51 p.

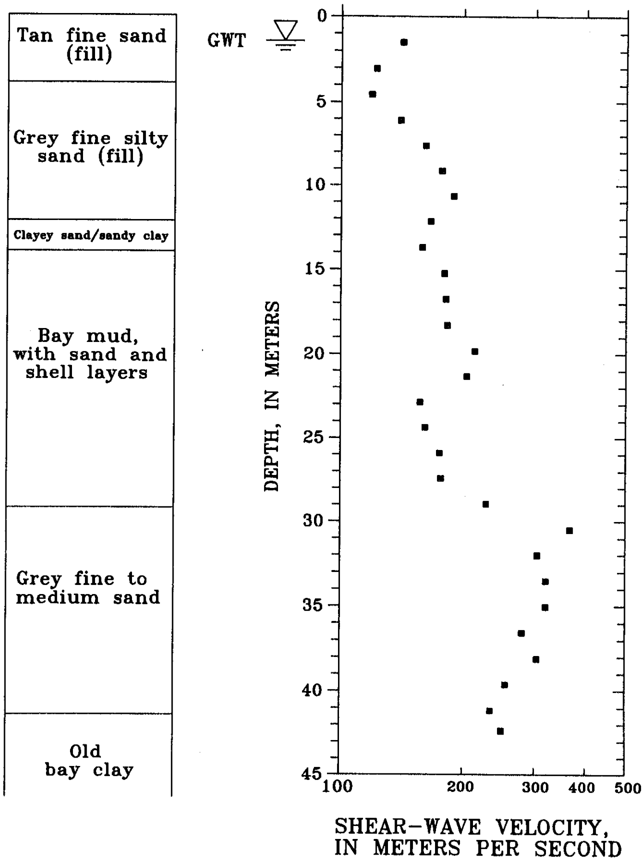

Figure 10.—Shear-wave velocity versus depth from crosshole tests at fire station at the Treasure Island Naval Station. GWT, ground-water table.

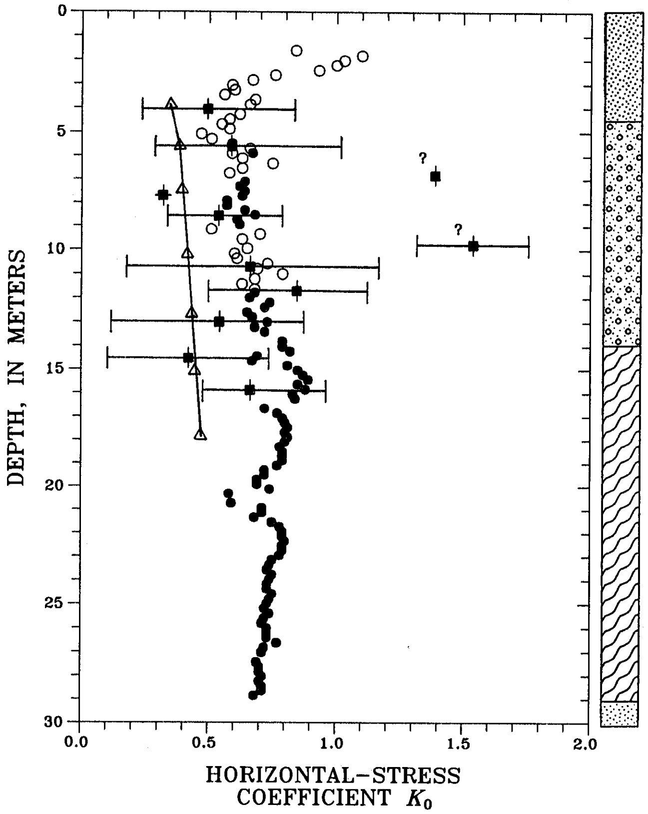

Figure 11.—At-rest horizontal-stress coefficient from self-boring pressuremeter (SBPM) tests (squares), Marchetti dilatometer (DMT) tests (dots, $I_D<1.2$; circles, $I_D>1.2$), and empirical relation of Jáky (1944) (triangles). Bars show error limits of SBMP data. See figure 3 for soil symbols.

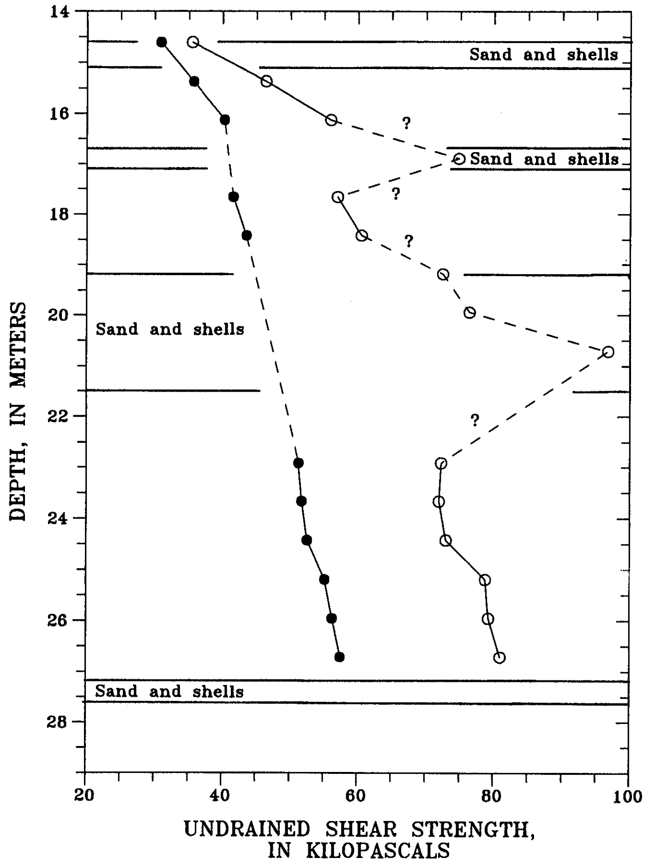

Figure 12.—Undrained shear strength versus depth in young bay mud at fire station at the Treasure Island Naval Station. Circles, field data; dots, data corrected according to Åas and others (1986). Some data points may be affected by shell lenses.

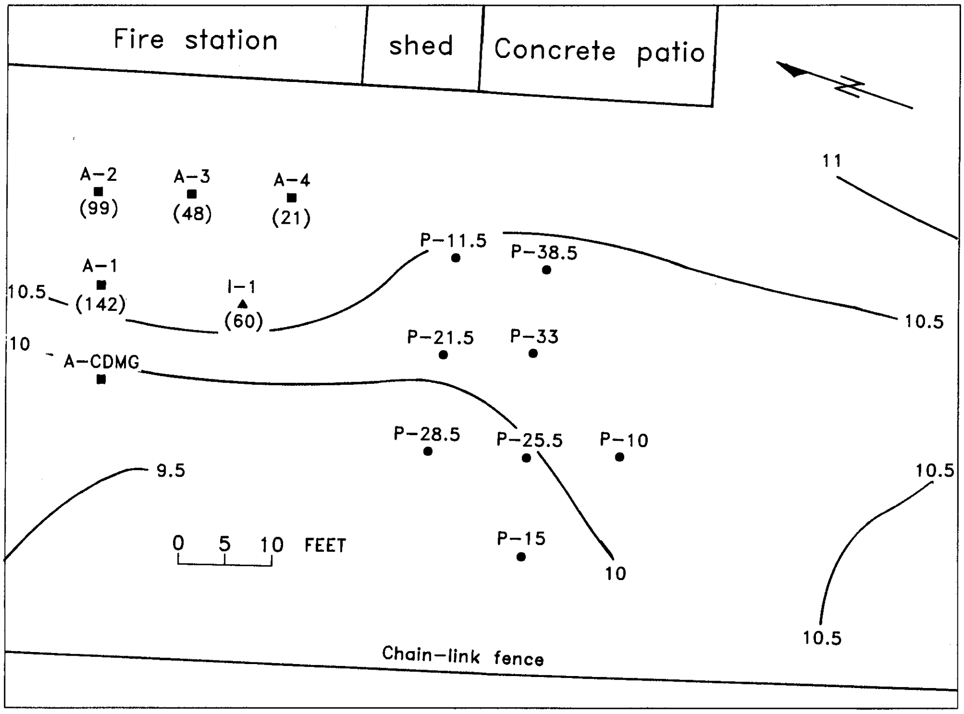

Figure 13.— Area near fire station at the Treasure Island Naval Station, showing locations of piezometers (P–), accelerometers (A–), and inclinometer (I-1). Curved lines, contours of elevation of ground surface (in feet above mean lower low water). Numbers in parenthesis indicate depth of tip (in feet). CDMG, California Division of Mines and Geology.

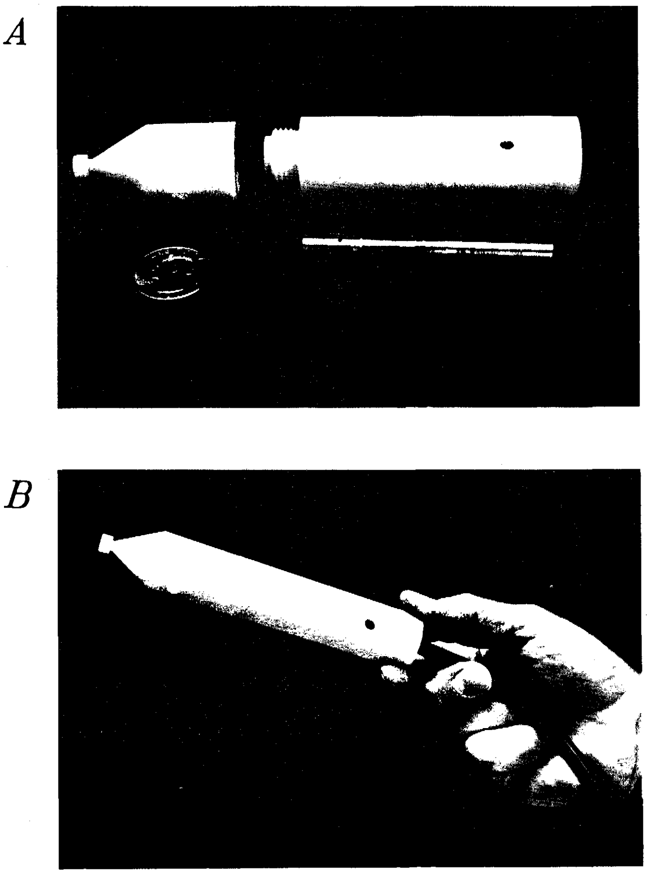

Figure 14.—Piezometer. *A*, Disassembled, showing Druck PDCR 35/D transducers and nylon tip. Sensing face of piezometer is sealed in lower section by O-rings. Note porous plastic inserts. *B*, Assembled. Note holes for attaching retrieval cord.

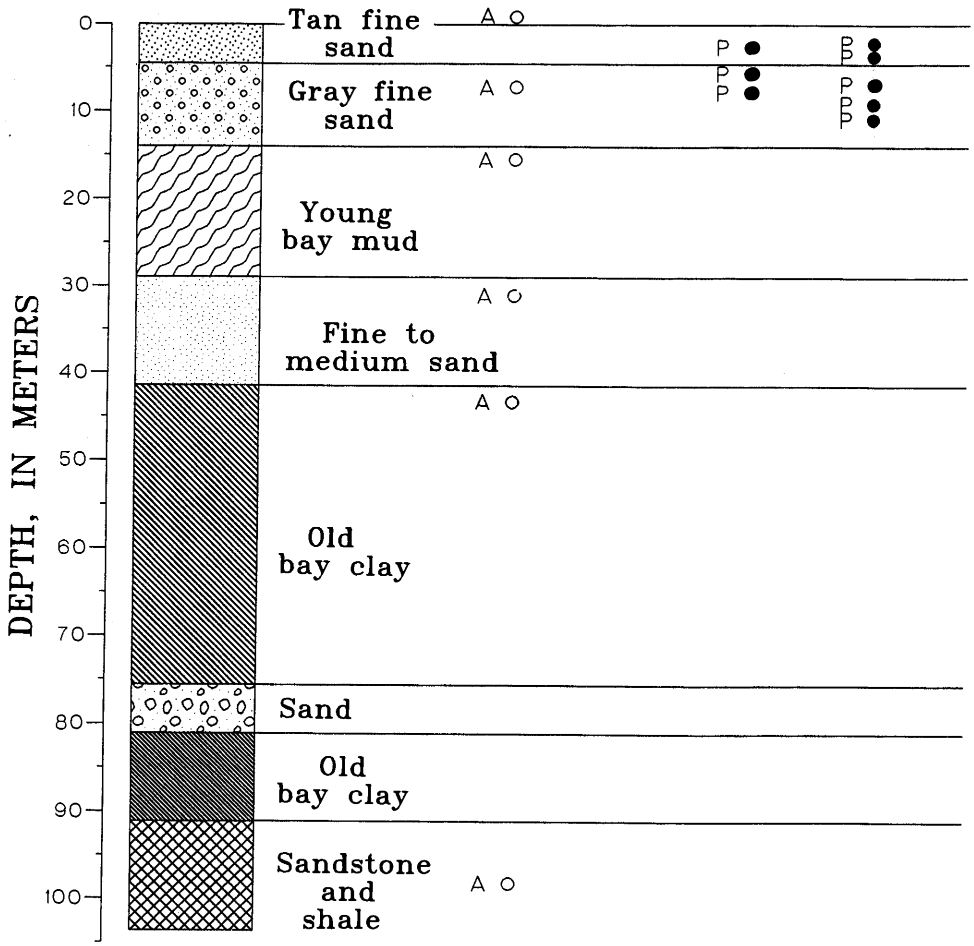

Figure 15.—Schematic soil profile at fire station at the Treasure Island Naval Station, showing distribution of accelerometers (A) and piezometers (P).

THE LOMA PRIETA, CALIFORNIA, EARTHQUAKE OF OCTOBER 17, 1989:
STRONG GROUND MOTION AND GROUND FAILURE

STRONG GROUND MOTION

SITE RESPONSE IN OAKLAND, CALIFORNIA, NEAR THE FAILED SECTION OF THE NIMITZ FREEWAY

Edward H. Field, Susan E. Hough, Klaus H. Jacob, and Paul A. Friberg,
Columbia University, Lamont-Doherty Earth Observatory

CONTENTS

ABSTRACT

We present the results of a site-response study performed near the failed Nimitz Freeway in Oakland, Calif., after the earthquake. We use the method of spectral ratios to estimate the ground-motion amplification at soft-soil sites, relative to hard-rock sites. Although individual spectral ratios of aftershocks vary widely, average spectral ratios exhibit stable peaks that agree remarkably well with the resonances predicted by one-dimensional models whose parameters were determined independently. The predicted amplifications, however, are more than half those observed, and we still lack a conclusive explanation for this discrepancy. Spectral ratios of Loma Prieta strong-motion records exhibit clear amplifications, but details of the strong-motion site response are obscured by uncertainties in the estimates. Given the success of one-dimensional models in predicting the resonances and overall shape of average weak-motion spectral ratios, we believe that such site-response studies can contribute valuable information to assessments of site-specific earthquake hazard.

INTRODUCTION

The severe consequences of sediment amplification have been observed in numerous earthquakes. Although our understanding of this phenomenon has been enhanced by several studies (for example, Borcherdt, 1970; Borcherdt and Gibbs, 1976), our ability to accurately predict it in advance is still in the developmental stage. In this paper, we present the results of a sediment amplification study performed in Oakland, Calif., after the 1989 Loma Prieta earthquake. Weak-motion site response was estimated from the average spectral ratios of aftershock recordings. The results are compared with predictions from one-dimensional models and with the spectral ratios of strong-motion records obtained for the main shock at nearby sites.

EXPERIMENT

Working under the auspices of the National Center for Earthquake Engineering Research and the Incorporated Research Institute for Seismology, seismometers were deployed at five sites in Oakland, Calif., after the earthquake (fig. 1). This deployment was chosen to investigate what role sediment amplification may have played in the collapse of the Cypress Overpass section of the Nimitz Freeway. These five sites include one on alluvium (S3), three on mud over alluvium (S1, S2, S5), and a reference site (S4) located on the Franciscan Complex, which constitutes the bedrock in the San Francisco Bay region.

Between October 20 and October 27, 1989, 18 aftershocks were recorded at the bedrock site S4 and at least one of the soft-soil sites. The locations of these aftershocks are shown in figure 2, and pertinent information is listed in table 1. Body-wave magnitudes ranged from 2.2 to 4.4, and epicentral distances to site S4 ranged from 75.5 to 118 km.

The earthquakes were recorded at 100 samples per second, using three-component Mark Products L22–D geophones paired with Refraction Technology (REFTEK) digital recorders. Each recording was corrected by replacing the actual geophone response, determined experimentally by Menke and others (1991), with the nominal response, which is flat to velocity above 2 Hz and falls off at 12 dB per octave below.

WEAK-MOTION OBSERVATIONS

The particle-velocity-time series observed at sites on bedrock (S4, fig. 1) and alluvium (S3) and at one site on mud over alluvium (S1) for a typical aftershock are plotted in figure 3. Horizontal-amplitude spectra for a 20-s-long shear-wave segment are plotted in figure 4, along with spectra of the preevent noise (dotted curves). These spectra were computed by using the high-resolution multitaper method of Thomson (1982) and Park and others (1987), which produces an equivalent smoothing width of 0.4 Hz.

Spectral ratios for sites on alluvium (S3) and mud over alluvium (S1) with respect to the site on bedrock (S4) for the same aftershock are plotted in figure 5. These curves contain many peaks that might be attributable to site-response resonances. As discussed extensively by Field and others (1992), however, we must be careful in interpreting site-response estimates from single spectral ratios because signal-generated noise from scattering can cause the actual input motion to differ significantly, both in amplitude and phase, from that observed at a nearby reference site. The presence of this noise, which is typically much greater than the ambient seismic/instrumental noise, gives rise to peaks and troughs in the spectral ratio that are completely unrelated to the site response.

The transverse-component spectral ratios obtained from all the events recorded at the sites on alluvium (S3, fig. 1) and mud over alluvium (S1) are plotted in figure 6. These plots, computed for the first 20 s of the shear-wave arrival, show substantial variation among the spectral ratios. In addition to the uncertainty associated with each individual estimate, this observed scatter may also be due to an intrinsic variation in the site response with source location. As discussed by Field and others (1992), this intrinsic variation should be small for this study, given the similar epicentral distances and azimuths among the aftershocks (see fig. 1). Therefore, most of the observed scatter in figure 6 is probably due to signal-generated noise, which obscures the individual site-response estimates.

The geometric averages of the spectral ratios, with respect to the site on bedrock (S4, fig. 1), for the site on alluvium (S3) and the three sites on mud over alluvium (S1, S2, S5) are plotted in figure 7, along with the standard deviation of the means. These plots represent our best estimates of the observed site response. The results are not significantly different, however, if we use other shear-wave segment lengths, spectral estimates with different smoothing widths, or other averaging procedures.

To investigate the possibility of nonlinear behavior, the average site response at each site was computed over three different source-magnitude ranges: $m_b \leq 3.0$, $3.0 < m_b \leq 4.0$, and $m_b > 4.0$. The site-response estimates from each of these ranges were found not to be statistically different at the 95-percent-confidence level, forcing us to accept the null hypothesis that the response among the different magnitude ranges is the same.

MODELING

Although the individual spectral ratios (fig. 6) vary widely, the geometric averages (fig. 7) reveal several significant peaks. We add credibility to these site-response estimates if we can substantiate their features by a reasonable theoretical model. In this effort, we start with the simplest of models and work toward fitting more and more complex models as the data warrant.

After the earthquake, two borehole studies were performed near the failed section of the Nimitz Freeway (Redpath, 1990): one (borehole 2 at bent 43) near the site on alluvium (S3, ~250 m to the northwest) and the other (borehole 8 at bent 91) near the site on mud over alluvium (S1, ~750 m to the southeast). These studies included shear-wave-velocity measurements of the alluvium, using both downhole and surface sources (measurements of the mud were not obtained). Redpath (1990) presented the results as a recommended alluvium-layer-velocity model composed of seven sublayers at borehole 2 and five sublayers at borehole 8. To reduce the uncertainty in these estimates, and to provide a single alluvium shear-wave velocity at each site, the sublayer velocities were combined by averaging the sublayer slownesses weighted by the sublayer thicknesses (the total alluvium thickness divided by the time taken for a shear wave to traverse the layer stack).

With the alluvium thickness and average shear-wave velocity obtained for borehole 2, a one-dimensional linear transfer function was computed for the site on alluvium (S3, fig. 1), using the method of Kennett and Kerry (1979). This site was approximated as a single layer over a half-space subjected to a vertically incident shear wave. The result is plotted in figure 8, along with the average transverse-component spectral ratio observed at the site (the transverse component is shown because it is the least likely to be affected by *P*- to *S*-wave conversions). The physical parameters used in the calculation are listed in table 2. The shear-wave velocity of the Franciscan Complex was obtained as the unweathered value reported by Rogers and Figuers (1991), the densities are those reported by Trask and Rolston (1951), and the quality factor (*Q*) is that used by Joyner and others (1976) for similar deposits on the southwest shore of San Francisco Bay.

The comparison in figure 8 shows that the three prominent peak frequencies agree well with the frequencies of the first three resonant modes in the single-layer model. The slight discrepancy in frequency for the fundamental mode near 0.6 Hz is probably due to sensor-response falloff below 2 Hz (as evidenced by the fact that the low-frequency tail of the fundamental mode appears to be cut off).

A similar calculation was made for the site on mud over alluvium (S1, fig. 1), approximated as a two-layer stack (mud and alluvium) overlying a half-space, subjected to a vertically incident shear wave. The result is plotted in figure 9, along with the average transverse-component spectral ratios. The physical parameters used in the calculation are listed in table 3. The depth to bedrock and average alluvium-layer velocity were obtained from the data collected at borehole 8 (Redpath, 1990). The mud depth at site S1 and all the densities are those reported by Trask and Rolston (1951). Rogers and Figuers (1991) reported that the shear-wave velocities of bay mud range from 90 to 150 m/s. We chose the lower value of 90 m/s because the mud layer is relatively thin at this site. The half-space velocity was obtained as before, and the quality factors are again those used by Joyner and others (1976), who reported similar values for both the mud and alluvium.

The comparison in figure 9 shows a good agreement in frequency between the first four prominent peaks, with the fifth and sixth peaks differing by ~0.15 and 0.3 Hz, respectively. These peaks are associated with resonances of the two-layer stack, and the broad peak near 3.5 Hz with a fundamental resonance of the mud. Again, the slight discrepancy for the first peak is probably due to instrument-response falloff (the low-frequency tail of this peak also appears to be cut off).

Although the peak frequencies agree well, the amplitudes predicted by the models are less than half those observed. Such amplitude discrepancies have been found in other studies as well (for example, Mueller, 1986;

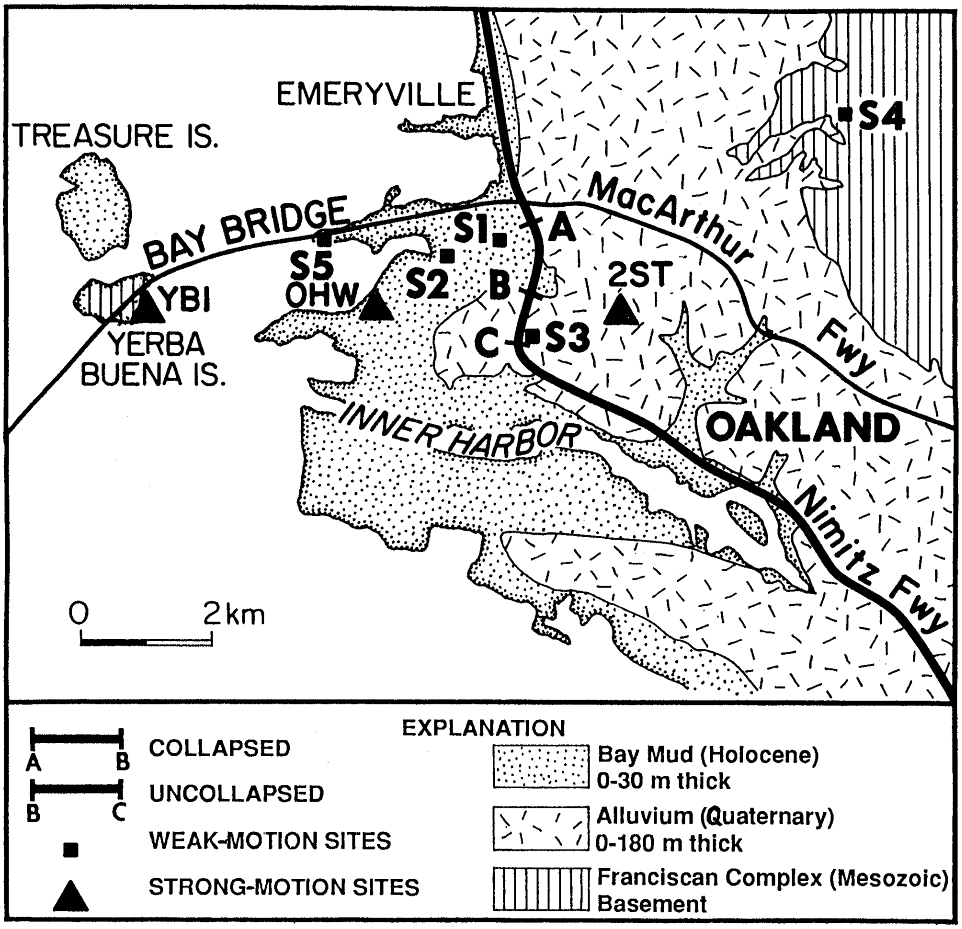

Figure 1.—Oakland, Calif., area, showing locations of the Nimitz Freeway and of weak- and strong-motion-recording sites used in this study.

Table 1.—*Information on aftershocks used in this study*

[See figure 1 for locations of sites. Event times, locations, and magnitudes from U.S. Geological Survey's Northern California Seismic Network (Calnet) data. Asterisks, recorded at that site]

Julian day	Hour: minute	Latitude (° N.)	Longitude (° W.)	Depth (km)	Magnitude (m_b)	Site S1	Site S2	Site S3	Site S4	Site S5
294	00:49	37.038	238.141	11.6	4.1	*	*	*	*	---
298	01:27	37.068	238.178	9.4	4.2	*	*	*	*	*
297	04:48	37.046	238.199	4.2	3.2	*	*	*	*	*
298	05:38	37.074	238.175	9.7	2.8	*	*	---	*	*
297	07:02	37.171	238.045	5.0	2.8	---	*	*	*	*
295	08:17	37.171	237.929	13.2	2.6	---	*	*	*	*
294	08:32	37.112	238.006	13.0	2.7	---	*	*	*	---
297	08:56	37.178	238.041	4.9	2.5	---	---	*	*	*
299	09:01	37.039	238.118	10.8	3.6	*	*	*	*	---
295	09:44	36.916	238.328	6.0	3.3	*	*	*	*	*
294	10:57	37.158	238.017	7.2	2.6	---	*	*	*	---
294	12:54	37.137	238.065	5.3	3.1	*	*	*	*	---
295	12:55	37.057	238.210	6.8	2.2	---	*	---	*	*
298	13:00	36.889	238.363	3.7	3.7	*	*	*	*	*
300	13:29	36.952	238.275	13.9	3.0	*	*	---	*	---
295	14:24	36.984	238.190	15.0	3.7	*	*	*	*	*
298	22:01	36.987	238.191	14.7	3.7	*	*	*	*	---
294	22:14	37.055	238.121	12.7	4.4	*	*	*	*	*

Borcherdt and others, 1989). As discussed by Field and others (1992), producing a good fit between observed and predicted site response is hampered by several factors. One factor is observational uncertainty from random noise in the data. Biases due to the estimation technique and (or) a possible site response at the reference site would also exacerbate modeling problems. As discussed above, stable site-response estimates are obtained only after averaging the spectral ratios from several events (the individual spectral ratios do not, themselves, agree well with the models shown in figs. 8 and 9). This averaging, however, causes additional difficulty in fitting observations to a model because the site response itself may vary with source location. As also mentioned previously, this should not be a problem with our data, given the distribution of source locations relative to the recording sites. Another factor influencing the match between observations and data is that the models may be oversimplified with respect to the incident waves and the assumed velocity structure. For example, models generally assume a single incidence angle and azimuth, whereas in reality, scattering will cause shear-wave arrivals from various incidence angles and azimuths.

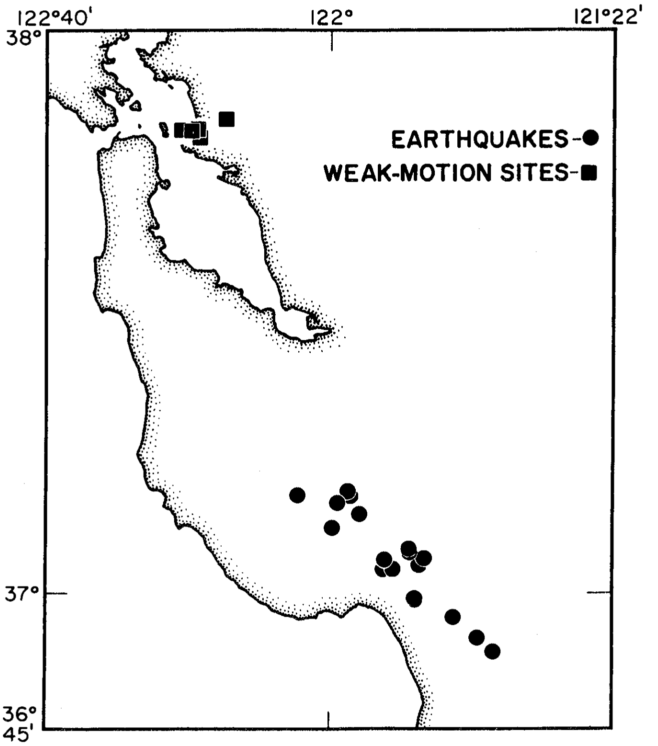

Figure 2.—San Francisco Bay region, showing locations of aftershocks and weak-motion recording sites used in this study.

One-dimensional transfer functions were also computed for the case where the alluvium was composed of the sublayers suggested by Redpath (1990). We found negligible differences between the two cases, in terms of fitting our observations, suggesting that the main features of the site response are insensitive to fine details in the velocity structure. The comparison shown in figures 8 and 9 might be improvable by a trial-and-error adjustment of the other one-dimensional model parameters. Varying the incidence angle and quality factors within a reasonable range, however, does not produce a significant change. If the shear-wave velocity of the Franciscan Complex in Oakland is more than a factor of 2 greater than the typical value of 1,200 m/s reported by Rogers and Figuers (1991), then the increased impedance contrast would remove the observed amplitude discrepancy. We have no seismic data, however, to substantiate such an anomalously high shear-wave velocity for the bedrock in this area.

The most likely explanation for the amplitude discrepancy seen in figures 8 and 9 may be that one-dimensional models do not account for boundary-layer topography or lateral wave propagation. Therefore, two- or three-dimensional modeling might produce a better fit to our observations. The sedimentary deposits in Oakland, however,

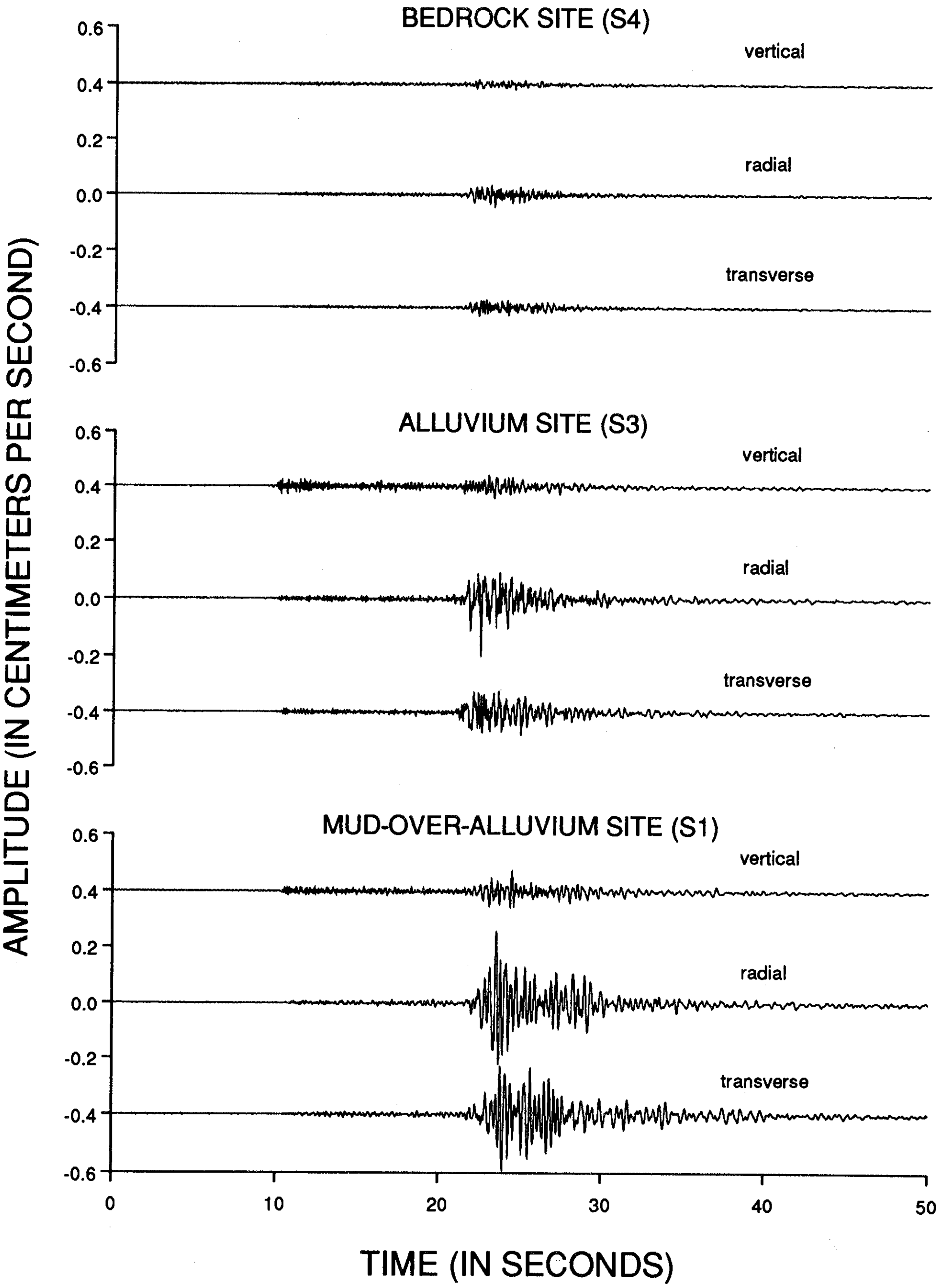

Figure 3.—Particle-velocity time series for an M=4.2 aftershock that occurred at 01:27 G.m.t October 25 (Julian day 298), 1989 (see table 1). Plots contain an instrument response that is flat to velocity above 2 Hz and falls off at 12 dB per octave below.

lack the shape ratio necessary to produce the type of two-dimensional resonance phenomena discussed by Bard and Bouchon (1985). Surface-wave generation at the basin edges might produce the observed high amplifications. The question then becomes whether the site response, with lateral wave propagation, is simply the one-dimensional response times a frequency-independent multiplicative factor. We know of no studies that substantiate such a claim. The sedimentary deposits in this area fill a channel between the east edge of Oakland and Yerba Buena Island (fig. 1). The axis of this channel trends northwest and plunges southeast (S.H. Figuers, written commun., 1991). An adequate model of this situation would probably have to be three dimensional. We know of no such models that can examine the amplitude of modes above the fundamental, because of computational constraints. In addition, our knowledge of the velocity structure in Oakland is probably not detailed enough to warrant such an effort. Therefore, multidimensional effects remain as a highly likely but unsubstantiated cause of the observed discrepancy.

The important point is that simple one-dimensional models, for which the parameters were chosen completely independently of our observations, match the frequency of peaks and the overall shape of the observed spectral ratios remarkably well. The discrepancy in amplitude remains unexplained and may involve a combination of several factors.

STRONG-MOTION OBSERVATIONS

During the Loma Prieta main shock, the California Strong Motion Instrumentation Program of the California Division of Mines and Geology obtained strong-motion records at two soft-soil sites in Oakland (fig. 1): one at a two-story office building located on alluvium (2ST), and the other at the Oakland Outer Harbor Wharf (OHW), which is on mud over alluvium. Strong-motion records were also obtained at a site on Franciscan bedrock on Yerba Buena Island (YBI). The horizontal-component spectral ratios of the strong-motion records at sites 2ST and OHW, relative to site YBI, are shown in figure 10. These ratios show a general amplification with several peaks that may be related to soft-soil resonances. However, attributing specific resonance modes to the individual peaks, as was done previously for the average weak-motion estimates (figs. 8, 9), cannot be easily done here. A similar conclusion was drawn by Hanks and Brady (1991), who found that a spectral-ratio analysis of the Loma Prieta strong-motion data set tends to "confuse" our understanding of the role of sediment amplification. This problem could arise for several reasons. One reason is that the response at the strong-motion sites could be more complex than at our weak-motion sites, making an interpretation more problematic. Furthermore, there could be possible soil-structure interactions of the wharf at site OHW and of the two-story building at site 2ST.

Another factor inhibiting an interpretation of the strong-motion records is the uncertainty associated with the spectral ratios. As discussed previously, spectral ratios vary widely when the input is estimated from a record obtained on bedrock some distance away, owing to the difference between the true and estimated input motions. Given the unrealistically high amplification factor of 35 implied by the radial-component spectral ratio at the site on mud over alluvium (2ST), these site-response estimates are probably affected by this problem. This result underscores the fact that extreme caution is needed when interpreting site response from individual spectral ratios.

We may be tempted to clarify the situation by examining the individual spectra used to calculate the ratio. If a spectral-ratio peak arises from a trough in the reference-site spectrum, rather than a peak in the sediment-site spectrum, we might conclude that the peak is unrelated to site response. However, it is not unlikely that the true input motion may have a spectral trough at the same frequency as a site-response resonance, thereby preventing a peak in the corresponding sediment-site spectrum. Therefore, such a conclusion should probably be avoided without corroborating evidence.

A final factor complicating our strong-motion spectral-ratio interpretations are possible nonlinear effects, especially with respect to the bay mud. Observational evidence for such effects has recently been presented (Aki and Irikura, 1991; Chin and Aki, 1991; Darragh and Shakal, 1991). Given the observational uncertainties discussed above, however, identifying nonlinear effects from individual spectral ratios is problematic at best.

DISCUSSION AND CONCLUSIONS

Although the weak-motion spectral ratios vary widely, the geometric averages exhibit features that are explained well by one-dimensional models based on independent physical-parameter determinations. In particular, the three prominent peaks observed at the site on alluvium (S3, fig. 1) and the first four peaks observed at the site on mud over alluvium (S1) agree well in frequency with the resonances predicted by the simple one-dimensional models. Although geotechnical data are unavailable for the other sites on mud over alluvium (S2, S5), the average spectral ratios observed at those sites display similar features to the two-layer site response observed at site S1 (fig. 7). Interestingly, the relative shift in resonant frequencies among sites S1, S2, and S5 is consistent with the belief that the contact between alluvium and Franciscan Complex is characterized by a channel whose axis of maximum depression passes near site S2 (S.H. Figuers, written commun., 1991). That the alluvium thickness is therefore greatest at site S2 agrees with the fact that the observed resonant frequencies are slightly lower at this site.

The site-response amplitudes predicted by the one-dimensional models are less than half those observed. Part of this discrepancy may be due to observational biases. As shown by Field and others (1992), however, spectral ratios should provide unbiased estimates of the site response. Nevertheless, we plan to compare the results presented here with those of other site-response-estimation techniques, such as that of Boatwright and others (1991). Other possible reasons for the amplitude discrepancy are that the half-space velocity used is too low, or that

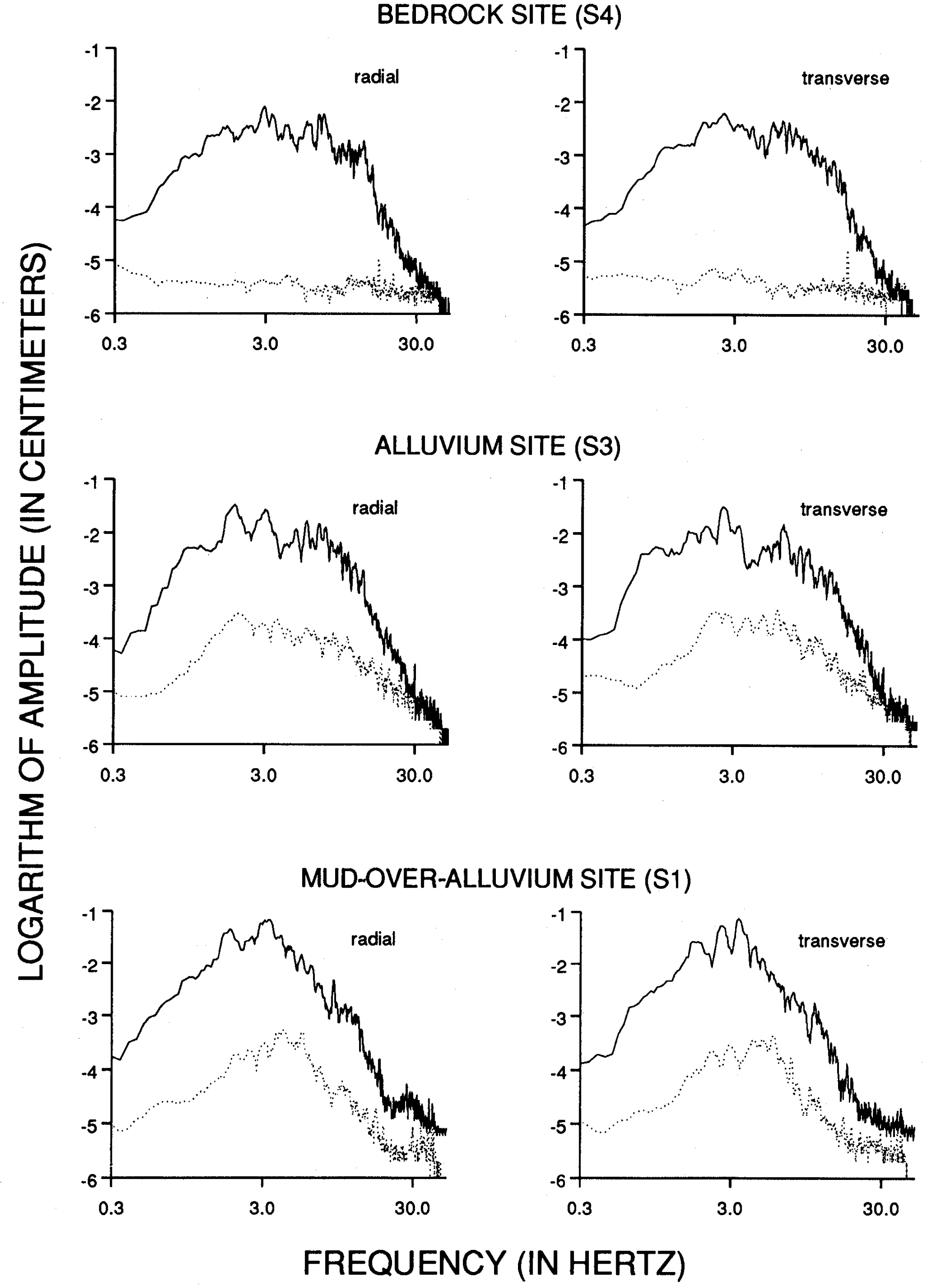

Figure 4.—Horizontal-component amplitude spectra of particle-velocity-time series shown in figure 3. Solid curve, 20-s segment of shear-wave starting at its arrival; dotted curve, preevent noise sample.

the model is inadequate because of multidimensional effects. The good match between observed and predicted peak frequencies, however, provides compelling evidence for at least the partial validity of the one-dimensional models.

The strong-motion spectral ratios clearly demonstrate an overall sediment amplification, as well as several possible resonances, although the details of the site response cannot be ascertained from these individual estimates, given the observational uncertainties. Attempts to fit the details of the spectral ratios to a model would certainly lead to erroneous conclusions.

On the basis of a preliminary examination of the data presented here, Hough and others (1990) presented evidence that the contrast between the collapsed and relatively intact sections of the Nimitz Freeway corresponded to an enhanced amplification by bay mud at the collapsed section but not at the uncollapsed section. From subsequent borehole studies performed at the failed section, some investigators have concluded that the bay mud was too thin at this site to have contributed to the collapse via sediment amplification (S.H. Figuers, oral commun., 1991). As discussed by Housner and Penzien (1990) and Rogers (1991), the distinguishing characteristic may be a design difference involving differential pile depths (owing to the bay mud), which would give rise to different structural responses between the two sections. The collapse itself probably involved a combination of effects in terms of a complex soil-structure interaction. In addition to the influence of the mud, the 2.5-Hz natural frequency of the structure (Housner, 1990) may well have been tuned to one of the higher alluvium-layer modes so prevalent in our observations. Even if the structural resonance was not exactly tuned to an alluvium-layer resonance, the overall amplification in that frequency range would likely have contributed to the collapse.

The sedimentary resonances and general amplification observed in this study have important consequences with respect to site-specific seismic-hazard assessment. Be-

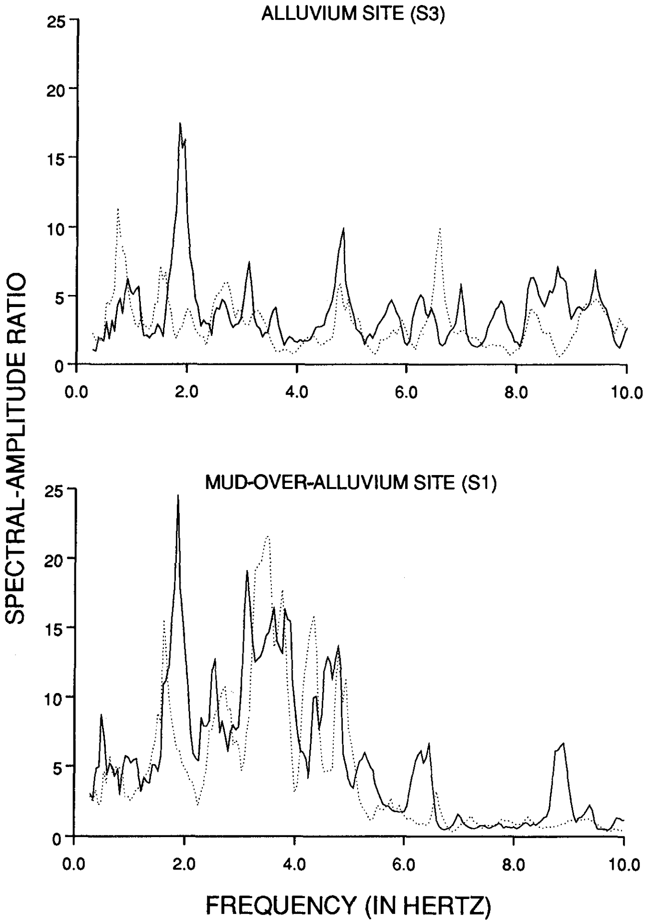

Figure 5.—Ratios of sediment-site spectra shown in figure 3 with respect to bedrock-site spectra. Solid curve, radial component; dotted curve, transverse component.

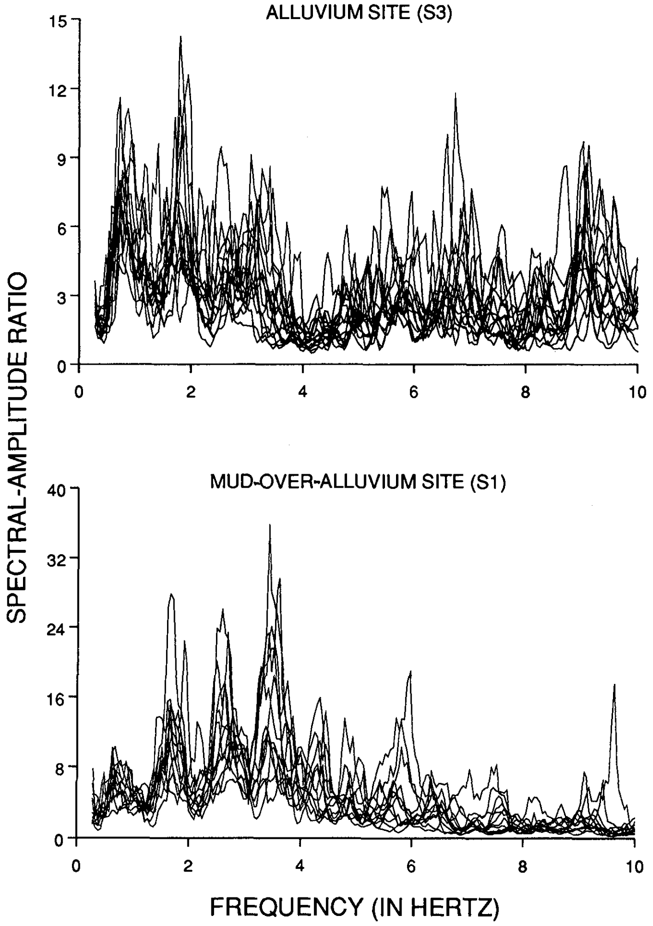

Figure 6.—Transverse-component spectral ratios for all events recorded at sites on alluvium (S3, top) and mud over alluvium (S1, bottom) with respect to site on bedrock (S4). See figure 1 for locations.

fore our results can be applied with any reliability, however, certain questions must be addressed. For example, how stable are these observed amplifications with respect to changes in source location? Another question concerns the role of nonlinear effects and how they can be accounted for. If these questions can be addressed, site-response studies will provide valuable information to assessments of site-specific seismic hazard.

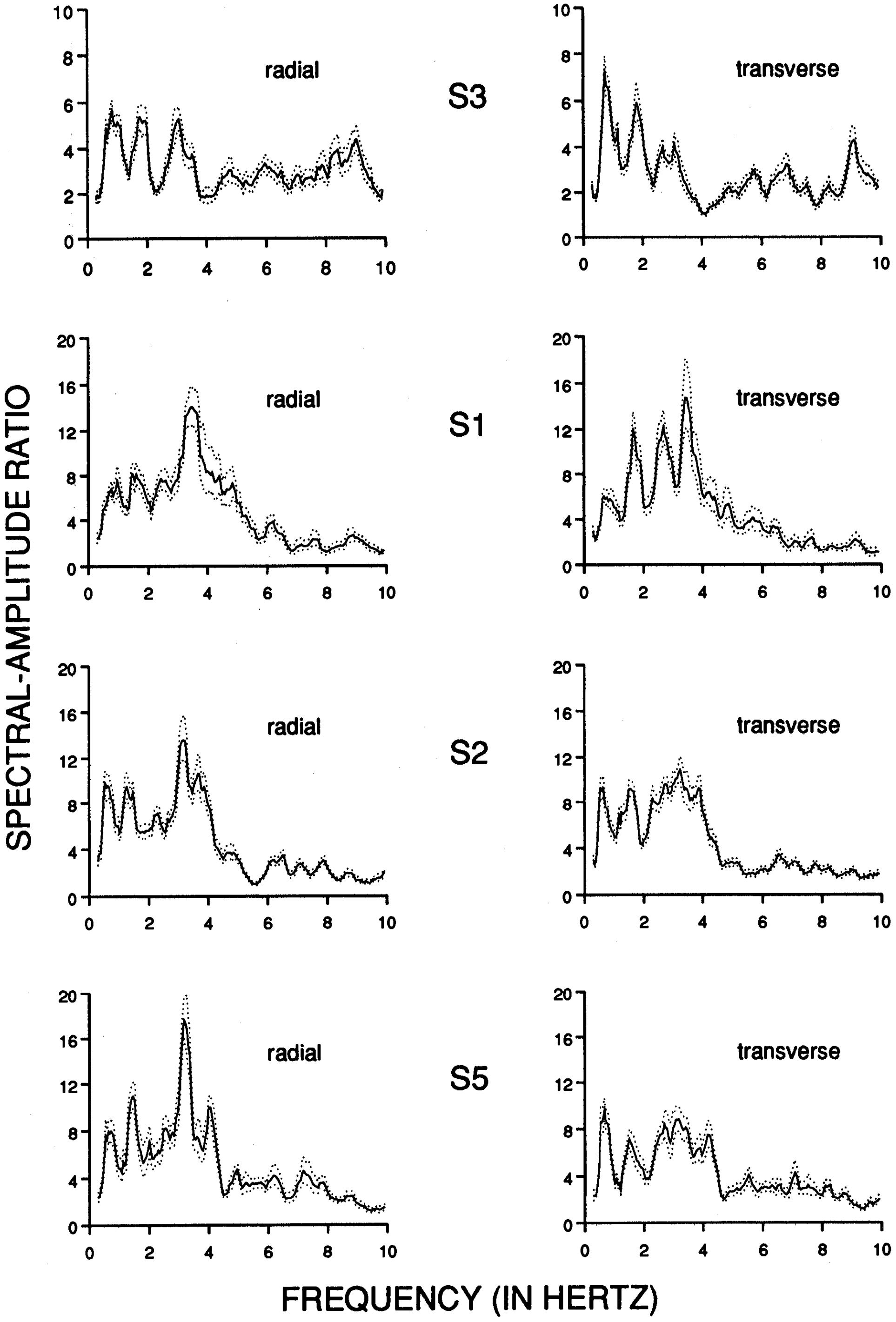

Figure 7.—Horizontal-component geometric-average spectral ratios observed at all sediment sites. Dotted curve, ±1σ of mean.

ACKNOWLEDGMENTS

We thank Robert Busby and all the others who participated in the fieldwork after the earthquake. We also thank William Menke, Geoffrey Abers, George Havach, and Roger Borcherdt for their helpful comments in reviewing the manuscript. This research was supported by National Center for Earthquake Engineering Research grants 89–1301 (scope B), 89–1306, and 90–1306; U.S. National Science Foundation grant EAR90–11783; and Incorporated Research Institutions for Seismology award 0133 (scope DA).

Table 2.—*Parameters of one-dimensional model used for the site on alluvium (S3, fig. 1)*

[β, shear-wave velocity; ρ, density; *Q*, quality factor]

	Thickness (m)	β (m/s)	ρ (g/cm^3)	*Q*
Layer-----------	159	384	2.0	16
Half-space------	---	1,200	2.4	---

REFERENCES CITED

Aki, Keiiti, and Irikura, Kojiro, 1991, Characterization and mapping of earthquake shaking for seismic zonation: International Conference on Seismic Zonation, 4th, Stanford, Calif., 1991, Proceedings, v. 1, p. 61–110.

Bard, P.Y., and Bouchon, Michel, 1985, The two-dimensional resonance of sediment-filled valleys: Seismological Society of America Bulletin, v. 75, no. 2, p. 519–541.

Boatwright, John, Seekins, L.C., and Mueller, C.S., 1991, Ground motion amplification in the Marina: Seismological Society of

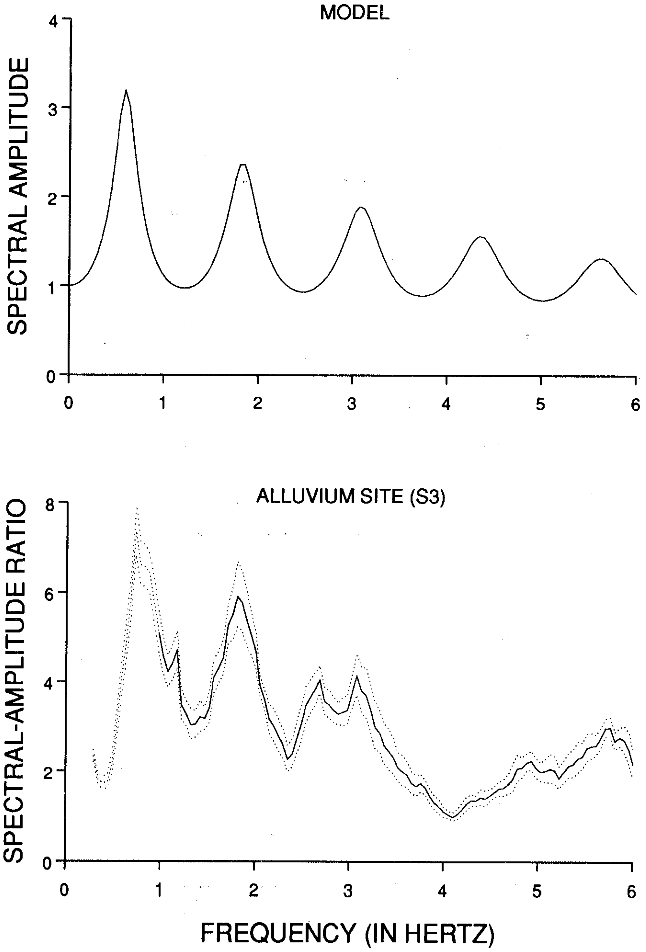

Figure 8.—Transfer function of single-layer-over-a-half-space model for site S3 (top) and average transverse-component spectral ratio observed at this site (bottom) (see fig. 1 for location). Dotted curves below 1 Hz in lower plot serve as a reminder that spectral ratios become less reliable in this range below 2-Hz natural frequency of sensor.

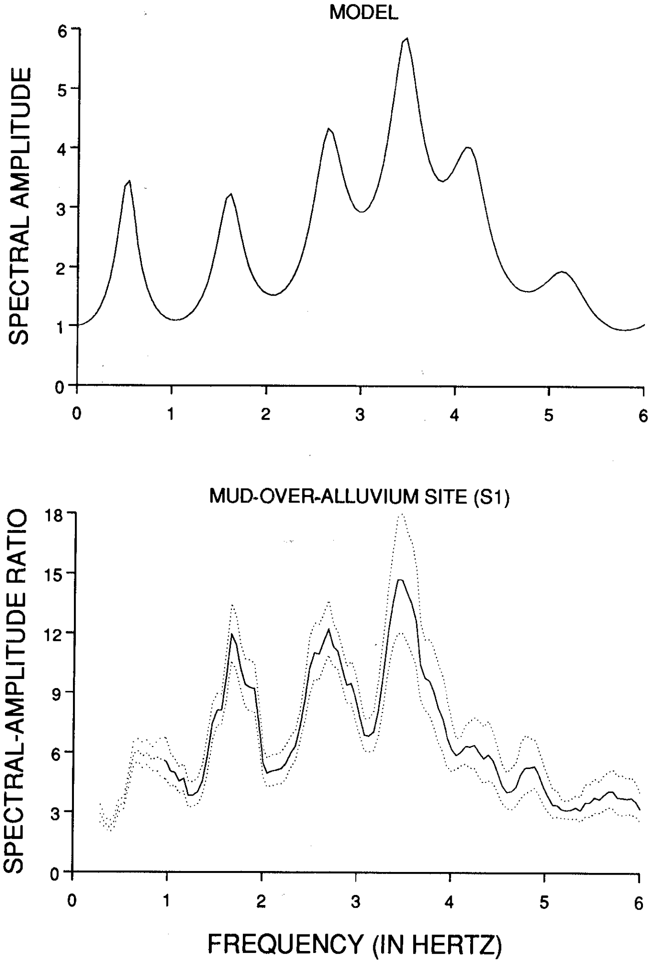

Figure 9.—Transfer function of two-layer (mud over alluvium) model for site S1 (top) and average transverse-component spectral ratio observed for this site (bottom) (see fig. 1 for location). Dotted curves below 1 Hz in lower plot serve as a reminder that spectral ratios become less reliable in this range below 2-Hz natural frequency of sensor.

Table 3.—*Parameters of one-dimensional model used for the site on mud over alluvium (S1, fig. 1)*

[β, shear-wave velocity; ρ, density; Q, quality factor]

	Thickness (m)	β (m/s)	ρ (g/cm^3)	Q
Layer 1----------	6.1	90	1.6	16
Layer 2----------	164.0	384	2.0	16
Half-space------	---	1,200	2.4	---

America Bulletin, v. 81, no. 5, p. 1980–1997.

Borcherdt, R.D., 1970, Effects of local geology on ground motion near San Francisco Bay: Seismological Society of America Bulletin, v. 60, no. 1, p. 29–61.

Borcherdt, R.D., and Gibbs, J.F., 1976, Effects of local geological conditions in the San Francisco Bay region on ground motions and the intensities of the 1906 earthquake: Seismological Society of America Bulletin, v. 66, no. 2, p. 467–500.

Borcherdt, R.D., Glassmoyer, G.M, Andrews, M.C., and Cranswick, Edward, 1989, Effect of site conditions on ground motion and damage, *in* Wyllie, L.A., Jr., and Filson, J.R., eds., Armenia earthquake reconnaissance report: Earthquake Spectra, special supp., p. 23–42.

Chin, B., and Aki, Keiiti, 1991, Simultaneous study of the source, path, and site effects on strong ground motion during the 1989 Loma Prieta earthquake; a preliminary result on pervasive nonlinear site effects: Seismological Society of America Bulletin, v. 81, no. 5, p. 1859–1884.

Darragh, R.B., and Shakal, A.F., 1991, The site response of two rock and soil station pairs to strong and weak ground motion: Seismological Society of America Bulletin, v. 81, no. 5, p. 1885–1899.

Field, E.H., Jacob, K.H., and Hough, S.E., 1992, Earthquake site response estimation; a weak motion case study: Seismological Society of America Bulletin, v. 82, no. 6, p. 2283–2307.

Hanks, T.C., and Brady, A.G., 1991, The Loma Prieta earthquake, ground motion, and damage in Oakland, Treasure Island, and San Francisco: Seismological Society of America Bulletin, v. 81, no. 5, p. 2019–2047.

Hough, S.E., Friberg, P.A., Busby, Robert, Field, E.F., Jacob, K.H., and Borcherdt, R.D., 1990, Sediment-induced amplification and the collapse of the Nimitz Freeway: Nature, v. 344, no. 6269, p. 853–855.

Housner, G.W., and Penzien, J., 1990, Competing against time; report of the Governor's Board of Inquiry on the 1989 Loma Prieta earthquake: Sacramento, Calif., 264 p.

Joyner, W.B., Warrick, R.E., and Oliver, A.A., III, 1976, Analysis of seismograms from a downhole array in sediments near San Francisco Bay: Seismological Society of America Bulletin, v. 66, no. 3, p. 937–958.

Kennett, B.L.N., and Kerry, N.J., 1979, Seismic waves in a stratified half space: Royal Astronomical Society Geophysical Journal, v. 57, no. 3, p. 557–583.

Menke, William, Shengold, Larry, Guo, Hongsheng, Ge, Hu, and Lerner-Lam, A.L., 1991, Performance of the short-period geophones of the IRIS/PASSCAL array: Seismological Society of America Bulletin, v. 81, no. 1, p. 232–242.

Mueller, C.S., 1986, The influence of site conditions on near-source high-frequency ground motion; case studies from earthquakes in Imperial Valley, Ca., Coalinga, Ca., and Miramichi, Canada: Stanford, Calif., Stanford University, Ph.D. thesis, 239 p.

Park, Jeffrey, Lindberg, C.R., and Vernon, F.L., III, 1987, Multitaper spectral analysis of high-frequency seismograms: Journal of Geophysical Research, v. 92, no. B12, p. 12675–12684.

Redpath, B.B., 1990, Borehole velocity surveys at the Embarcadero in San Francisco and the Cypress Structure in Oakland: report to California Department of Transportation.

Rogers, D.J., 1991, Site stratigraphy and its effects on soil amplification in the greater Oakland area during the October 17, 1989 Loma Prieta earthquake: International Conference on Recent Advances in Geotechnical Earthquake Engineering and Soil Dynamics, 2d, St. Louis, Mo., 1991, Proceedings.

Rogers, D.J., and Figuers, S.H., 1991, Site stratigraphy effects on soil amplification in the vicinity of Oakland, California: International Conference on Seismic Zonation, 4th, Stanford, Calif., 1991, Proceedings, v. 1, p. 61–110.

Thomson, D.J., 1982, Spectrum estimation and harmonic analysis: Institute of Electrical and Electronic Engineers Proceedings, v. 70, p. 1055–1096.

Trask, P.D., and Rolston, J.W., 1951, Engineering geology of San Francisco Bay, California: Geological Society of America Bulletin, v. 62, no. 9, p. 1079–1110.

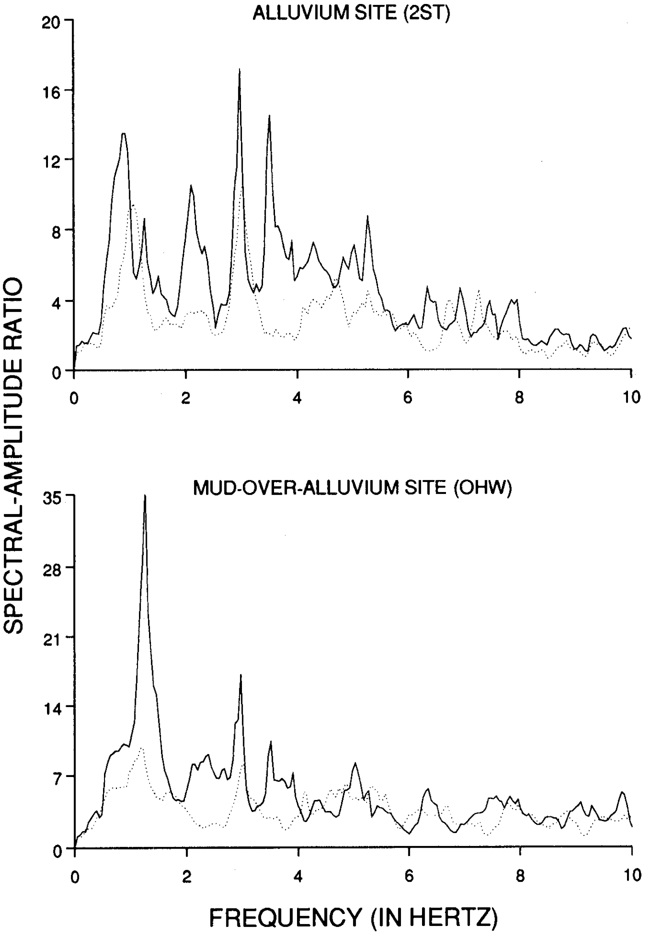

Figure 10.—Spectral ratios of 20-s shear-wave segments of Loma Prieta strong motion recordings obtained at sites 2ST and OHW with respect to observations on Franciscan bedrock at site YBI (see fig. 1 for locations). Solid curve, radial component; dotted curve, transverse component.

AFTERSHOCK OBSERVATIONS FROM A DENSE ARRAY IN SUNNYVALE, CALIFORNIA

By Arthur Frankel,
U.S. Geological Survey; and
Susan E. Hough, Paul A. Friberg, and Robert Busby,
Columbia University, Lamont-Doherty Earth Observatory

CONTENTS

ABSTRACT

We deployed a small-aperture (≈300 m) four-station array in Sunnyvale, Calif., for 5 days to record aftershocks of the earthquake. The purpose of this deployment was to study the seismic response of the alluvium-filled Santa Clara Valley and the role of surface waves in the seismic shaking of sedimentary basins. Strong-motion records of the Loma Prieta main shock indicate that surface waves produced the peak velocities and displacements at some sites in the Santa Clara Valley. We use the recordings from our dense array to determine the apparent velocity and backazimuth (direction of propagation) for various arrivals in the seismograms of four aftershocks of M=3.6 to 4.4. Apparent velocities are generally observed to decrease over time after the *S*-wave arrival. Phases arriving less than 8 s after the *S* wave have apparent velocities comparable to that of the *S* wave and appear to be body waves multiply reflected from under the station or by crustal interfaces. For times 10 to 30 s after the direct *S* wave, we observe long-period (1–6 s) arrivals, with apparent velocities decreasing from 2.5 to 0.8 km. We interpret these arrivals to be surface waves and conclude that they produced the long duration of shaking observed on the aftershock records. Much of the energy in the 40 s after the *S*-wave arrival is coming approximately from the direction to the source, although some arrivals have backazimuths as much as 60° different from the backazimuth to the epicenter. Two aftershocks show arrivals coming from 30°–40° more easterly than the epicenters; this energy may have been scattered from outcrops along the southeast edge of the basin. In contrast, the deepest aftershock studied (17-km depth) displays later arrivals, with backazimuths 30°–40° more westerly than the backazimuth to the epicenter. A distinct arrival for one aftershock propagates from the southwest, possibly scattered from the west edge of the basin. Synthetic seismograms calculated from a plane-layered crustal model do not show the long-period Love waves observed in the waveforms of an M_L=4.4 aftershock. These Love waves may be generated by the conversion of incident *S* waves or Rayleigh waves near the edge of the basin.

INTRODUCTION

It is well known that the seismic shaking at sites in sedimentary basins is larger in amplitude at low frequencies (<5 Hz) and longer in duration than at sites on rock. This observation has generally been thought to result from the amplification and reverberation of *S* waves by the low-velocity sedimentary layer (Kanai, 1952; Haskell, 1960; Borcherdt and Gibbs, 1976; Joyner and others, 1981), although this explanation is only partial. Surface waves can be an important component of seismic shaking in sedimentary basins for periods of about 1 s and longer. These surface waves can increase the duration and amplitude of long-period shaking in basins.

Many population centers are located in sedimentary basins near the source regions of expected large earthquakes. A knowledge of the seismic response of sedimentary basins at periods of 1 s and longer is crucial for assessing the vulnerability of buildings 10 or more stories high and such extended structures as highway overpasses, bridges, and pipelines that are located in such basins.

Recent studies using numerical methods have demonstrated that sizable surface waves in sedimentary basins can be generated by the conversion of incident *S* waves at the edges of the basins (Harmsen and Harding, 1981; Ohtsuki and Harumi, 1983). Vidale and Helmberger (1988) used a two-dimensional finite-difference method to show how the 1971 San Fernando, Calif., earthquake generated surface waves in the San Fernando and Los Angeles Basins from incident *S* waves. Bard and others (1988) and Kawase and Aki (1989) pointed out how regional *S* waves from the 1985 Michoacán, Mexico, earthquake could have been converted to surface waves at the edge of the lakebed basin containing the area of Mexico City that was damaged during the earthquake. These surface waves can account for the increased duration of shaking observed in this area. Frankel and others (1989) presented evidence from recordings of aftershocks of the 1988 Armenia earthquake that surface waves contributed to the damage of buildings in the Leninakan Basin during the main shock.

The aftershock sequence of the 1989 Loma Prieta earthquake provided us with an opportunity to study the seismic response of the alluvium-filled Santa Clara Valley (fig. 1). Our motivation for deploying an array in Sunnyvale, Calif., stemmed from examining the strong-motion records of the main shock obtained from the U.S. Geological Survey (USGS)'s strong-motion station (SMA, fig. 1) at Colton Avenue in Sunnyvale (Maley and others, 1989). Acceleration, velocity, and displacement seismograms for the main shock are shown in figure 2. The velocity and displacement records were high-pass filtered, with a corner at 0.1 Hz. The acceleration records show a peak at about 11 s (fig. 2), signifying the *S*-wave arrival from the major episode of rupture. The velocity and displacement records exhibit sizable long-period signals arriving at about 14 s, a few seconds after the *S* waves. These arrivals, which have a period of about 3 s, make up the peak displacements and velocities on both horizontal components. The late arrival of these waves and their long-period characteristics suggest that they are surface waves. The long duration of the seismograms shown in figure 2 underscore the importance of understanding these long-period arrivals. Similar long-period arrivals are observed on the displacement records obtained from the nearby California Division of Mines and Geology (CDMG) strong-motion station at Agnews State Hospital (fig. 1).

We designed the four-station array in Sunnyvale (fig. 1) with a small aperture, so that we could determine the apparent velocity and backazimuth (direction of propagation) for waves propagating in the valley. This paper presents our initial analysis of four of the largest aftershocks recorded by the array.

ARRAY CHARACTERISTICS AND GEOLOGIC SETTING

The Sunnyvale dense array is mapped in figure 3. The stations were arranged in a triangle, with one station inside the triangle. The average length of the sides of the triangle was 290 m. The seismometers were placed on concrete pads or patios adjacent to one-story houses. We used three-component seismometers with 5-s natural periods; this relatively long natural period made the seismometers suitable for studying surface waves. At each station, the signals from the seismometers were fed into a Reftek PASSCAL recording system. The signals were digitized at a rate of 200 samples per second, with 16-bit resolution; each record was 90 s long. The digitized data were stored on a computer at each station. Each station had an OMEGA time receiver, and so the absolute timing was accurate to about 0.001 s. The array operated for 5 days between October 22 and October 27, 1989.

The Santa Clara Valley is a northwest-striking basin filled with alluvium of Pliocene, Pleistocene, and Holocene age (fig. 1). The thickness of alluvium in the cen-

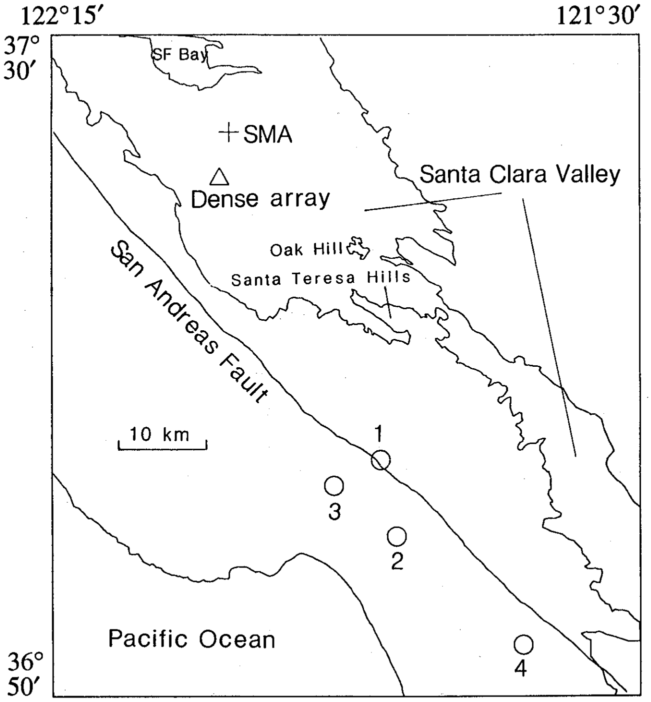

Figure 1.—Sketch map of Santa Clara Valley, showing locations of Sunnyvale dense array, U.S. Geological Survey strong-motion station at Colton Avenue in Sunnyvale (SMA), and epicenters of aftershocks used in this study (numbered circles; events 1–4, table 1). Valley boundary is formed by contact between alluvium and consolidated rocks (California Division of Mines and Geology, 1969).

tral part of the valley is unknown, although it must be greater than about 500 m, the maximum depth of water wells in the central part of the valley (California Department of Water Resources, 1967), none of which reached bedrock. Consolidated rocks that form the bottom of the basin are of two groups: (1) metamorphic rocks of the Franciscan Complex and (2) Tertiary sedimentary rocks overlying the Franciscan Complex.

The depth to bedrock beneath the Sunnyvale dense array is probably 280 to 470 m. Along the west edge of the valley, well data show the alluvium thickening to about 300 m within a few kilometers of the edge (California Department of Water Resources, 1967). A well located about 2 km west of the array penetrated consolidated rock (Tertiary shale) at a depth of 250 m. However, neither a 280-m-deep well located 1 km southwest of the array nor a 305-m-deep well located 2 km north of the array reached bedrock. A well at Moffett Field (fig. 1) located about 5 km north of the array penetrated basement at a depth of 470 m (E.J. Helley, oral commun., 1990).

Some parts of the valley near San Francisco Bay are covered with a thin layer of bay mud with a very low shear-wave velocity. The Sunnyvale dense array was located on older alluvium, well removed from the bay mud.

GENERAL OBSERVATIONS

Displacement seismograms for the four aftershocks studied (M_L=3.6–4.4) are shown in figure 4. The locations of their epicenters are shown in figure 1, and their characteristics are listed in table 1, based on USGS determinations. The original horizontal seismograms were rotated to the transverse and radial components and then corrected for instrument response to yield ground displacement. All the displacement seismograms shown in this paper were high-pass filtered at 0.1 Hz by a phaseless filter applied in the frequency domain.

The most obvious feature of the displacement seismograms in figure 4 is the substantial motion for times as long as 30 s after the *S*-wave arrival, motion commonly as large as that of the *S* wave. Given that the source duration for earthquakes in this magnitude range should be no more than about 1 s, the prolonged duration of shaking is noteworthy. Some of the seismograms display long-period arrivals with periods of 3 to 6 s. A distinct train of such arrivals is observed on the transverse component for event 1 between 12 and 28 (fig. 4*A*); this event had the largest magnitude of those studied. The transverse seismograms for event 4 also show large,

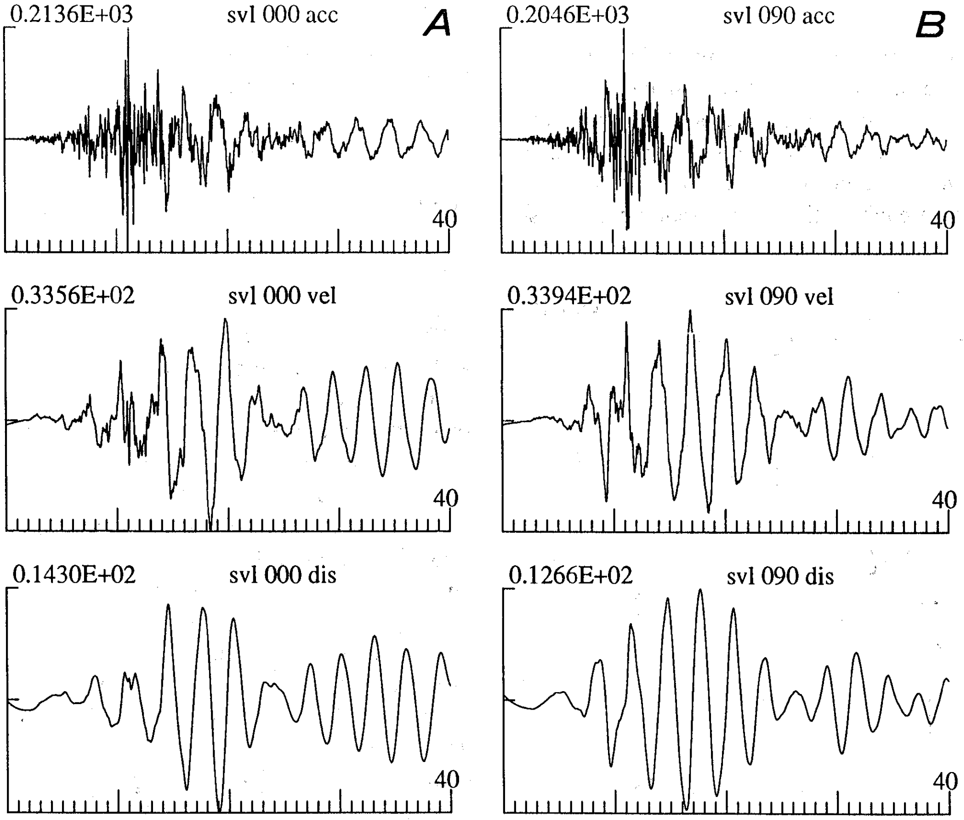

Figure 2.—Seismograms of acceleration (top), velocity (middle), and displacement (bottom) for Loma Prieta main shock recorded at U.S. Geological Survey strong-motion station (SMA, fig. 1). *A*, 0° horizontal component. *B*, 90° horizontal component.

long-period arrivals; this aftershock had the greatest distance and shallowest depth of those studied, and so we would expect more surface-wave energy from this event. Some secondary arrivals are observed for two or more events, such as the arrival on the transverse component 5 s after the *S* wave and the arrival on the radial component 10 to 11 s after the *S* wave (events 1–3, table 1).

The uncorrected seismograms for event 1 (M_L=4.4) from the three array stations at the corners of the triangle (fig. 3) are shown in figure 5. These are essentially proportional to velocity. The seismograms show many arrivals that are coherent between stations, particularly the lower frequency arrivals. The seismograms also show a decrease in frequency content over time. The horizontal components of the *S* waves are much more impulsive than the vertical components. The amplitude of the vertical components builds after the *P*-wave arrival and reaches a maximum significantly after the *S*-wave arrival on the horizontal components. The displacement seismograms for event 1 (fig. 6) contain many arrivals that can be correlated between stations, as discussed below.

METHOD FOR DETERMINING VECTOR SLOWNESS OF ARRIVALS

We used the waveforms from the Sunnyvale dense array to determine the apparent velocity and backazimuth for coherent arrivals in the seismograms. We calculated the average cross-correlation between waveforms as a function of east-west and north-south slownesses. First, the seismogram from each station was windowed. Cross-correlation calculations were performed for a range of values of east-west slowness p_x and north-south slowness p_y. For each slowness vector, the time delay *t* for each station was calculated from the relation

$$\Delta t = p_x \Delta x + p_y \Delta y,$$

where Δx and Δy are the east-west and north-south distances, respectively, between a station and some arbitrary reference point. Then, the windowed seismogram for each station was shifted in time by the value of $-\Delta t$ calculated for that station. The cross-correlation was calculated between each pair of shifted seismograms. Given seismograms $u(t)$ and $v(t)$ for two stations, the zero-lag cross-correlation is given by

$$x_{\mathrm{corr}} = \frac{\Sigma[u(t)v(t)]}{\Sigma[u(t)u(t)][v(t)v(t)]},$$

where the sums are taken over the number of time points in the windowed seismograms. Finally, the average cross-correlation between all pairs of stations was calculated, providing a measure of the coherence of the windowed seismograms for the particular p_x and p_y values. Where the average cross-correlation is a maximum, the particular p_x and p_y, values for the arrival in the windowed seismograms can be estimated. The apparent velocity V_{app} is given by

$$V_{\mathrm{app}} = (\sqrt{p_x^2 + p_y^2})^{-1},$$

and the backazimuth ϕ (clockwise from north) by

$$\phi = \tan^{-1}(p_x/p_y).$$

The average cross-correlation as a function of the p_x and p_y values for the *P* wave from event 1 is plotted in figure 7. Here, we used a 0.4-s window of the *P* wave from the uncorrected (velocity) seismograms, encompassing the first half-cycle of the *P* wave. The average cross-correlation was determined over intervals of 0.01 km in slowness by calculating the average cross-correlation for a 100-by-100 grid of slowness values. For this and subsequent slowness analyses described in this paper, we used the seismograms from stations SUNC, SUND, and SUNJ (fig. 3). The seismograms from station SUNM were omitted because this station was located only 80 m from station SUNC and we thought that using the seismogram from station SUNM would be equivalent to double-weighting station SUNC.

The cross-correlation plot for the *P* wave (fig. 7) has a maximum corresponding to an apparent velocity of approximately 6.3 km/s and a backazimuth of 145°, similar to the backazimuth to the epicenter, which is 150°. This

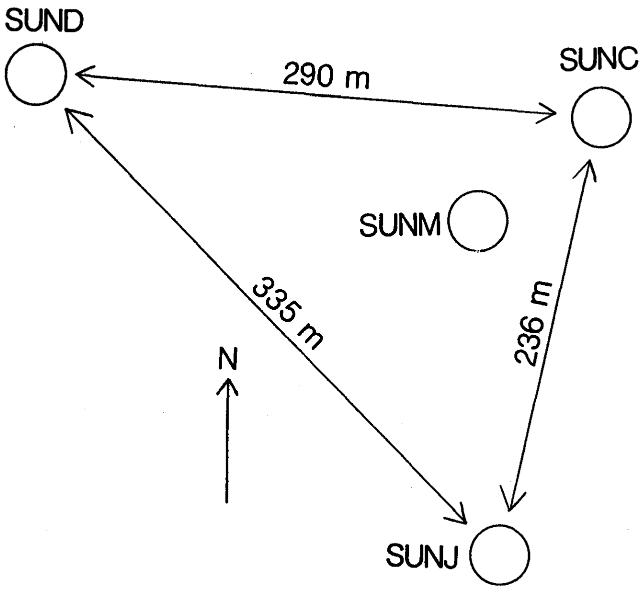

Figure 3.—Schematic map of four stations in Sunnyvale dense array (fig. 1).

apparent velocity is quite reasonable for a *P* wave at this distance.

The average cross-correlation for the *S* wave from event 1, derived from a 0.3-s window encompassing the first half-cycle on the uncorrected radial components, is plotted in figure 8. The maximum cross-correlation is found at an apparent velocity of 3.3 km/s and a backazimuth of 154°, very close to the backazimuth to the epicenter.

All the contours of the cross-correlation plots are elongate approximately north-northeast, corresponding to the shortest side of the array triangle (fig. 3). The determination of the apparent velocity parallel to this side of the triangle has the poorest resolution.

Arrivals later in the seismograms have lower frequency content, and so the resolution of slowness is not as good as with the initial arrivals. The low-frequency arrivals are clearest on the displacement seismograms. The average cross-correlation for a 2-s window of the transverse-displacement seismograms for event 1 is plotted in figure 9*A*. Here, the window begins at 15 s, approximately 10 s after the *S*-wave arrival. The average cross-correlation was calculated over a 50-by-50 grid of slownesses, ranging from −1 to +1 s/km for the east-west and north-south slownesses. The maximum cross-correlation is observed for an apparent velocity of 2.4 km/s and a backazimuth of 110°. This apparent velocity

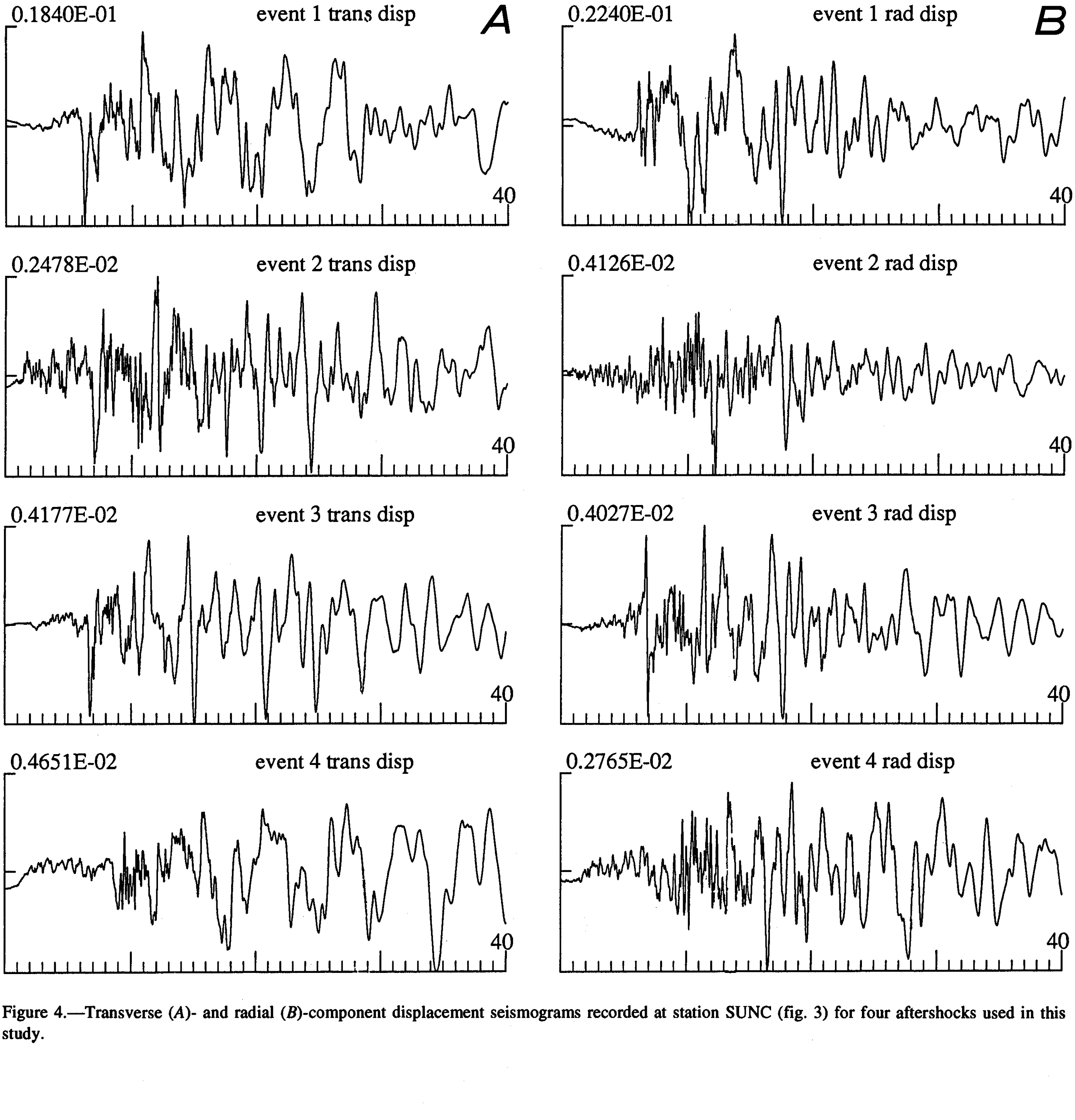

Figure 4.—Transverse (*A*)- and radial (*B*)-component displacement seismograms recorded at station SUNC (fig. 3) for four aftershocks used in this study.

Table 1.—*Details of aftershocks used in this study*

Event	Origin time (G.m.t.)	M_L	Depth (km)	Epicentral distance (km)	Back-azimuth
1	0127 Oct. 25, 1989	4.4	10.2	36.7	150°
2	2201 Oct. 25, 1989	3.7	17.4	45.0	154°
3	0901 Oct. 26, 1989	3.6	12.4	37.0	160°
4	1300 Oct. 25, 1989	3.8	5.7	62.8	147°

is significantly lower than that of the initial *S* wave, and this backazimuth is 40° from the backazimuth to the epicenter. The contours are more widely spaced in figure 9 than in the figures 7 and 8 because of the lower frequency content of the signal.

The average cross-correlation for a 2-s window beginning at 17 on the transverse-displacement records for event 1 is plotted in figure 9*B*. The maximum cross-correlation is found at an apparent velocity of 1.6 km/s and a backazimuth of 146°. This apparent velocity is significantly lower than that in the window 2 s earlier on the record, and the backazimuth differs by 36° (compare figs. 9*A* and 9*B*). The low apparent velocities found for both windows implies that the arrivals in these windows are surface waves.

To estimate the resolution of this method, we performed tests on synthetic pulses. Random noise was added to a sine wave with a period of 1 s and a duration of 1 cycle. The noise had an rms amplitude equal to 10 percent of the peak amplitude of the sine wave. The resulting pulses had a signal-to-noise ratio similar to that of the data. The synthetic pulses were shifted in time, corresponding to a particular apparent velocity and backazimuth and the station geometry of the Sunnyvale dense array. Then, we used the method described above to estimate the apparent velocity and backazimuth. The estimates were within 10 percent of the apparent velocity and 10° of the backazimuth. Thus, we believe that differences of 20° in the true backazimuth can be resolved by this method with the configuration of the Sunnyvale dense array, for arrivals with periods of about 1 s. The method works best when only one phase is present within the time window chosen, but not so well when two or more phases with different slownesses are present.

The above method was applied to successive time win-

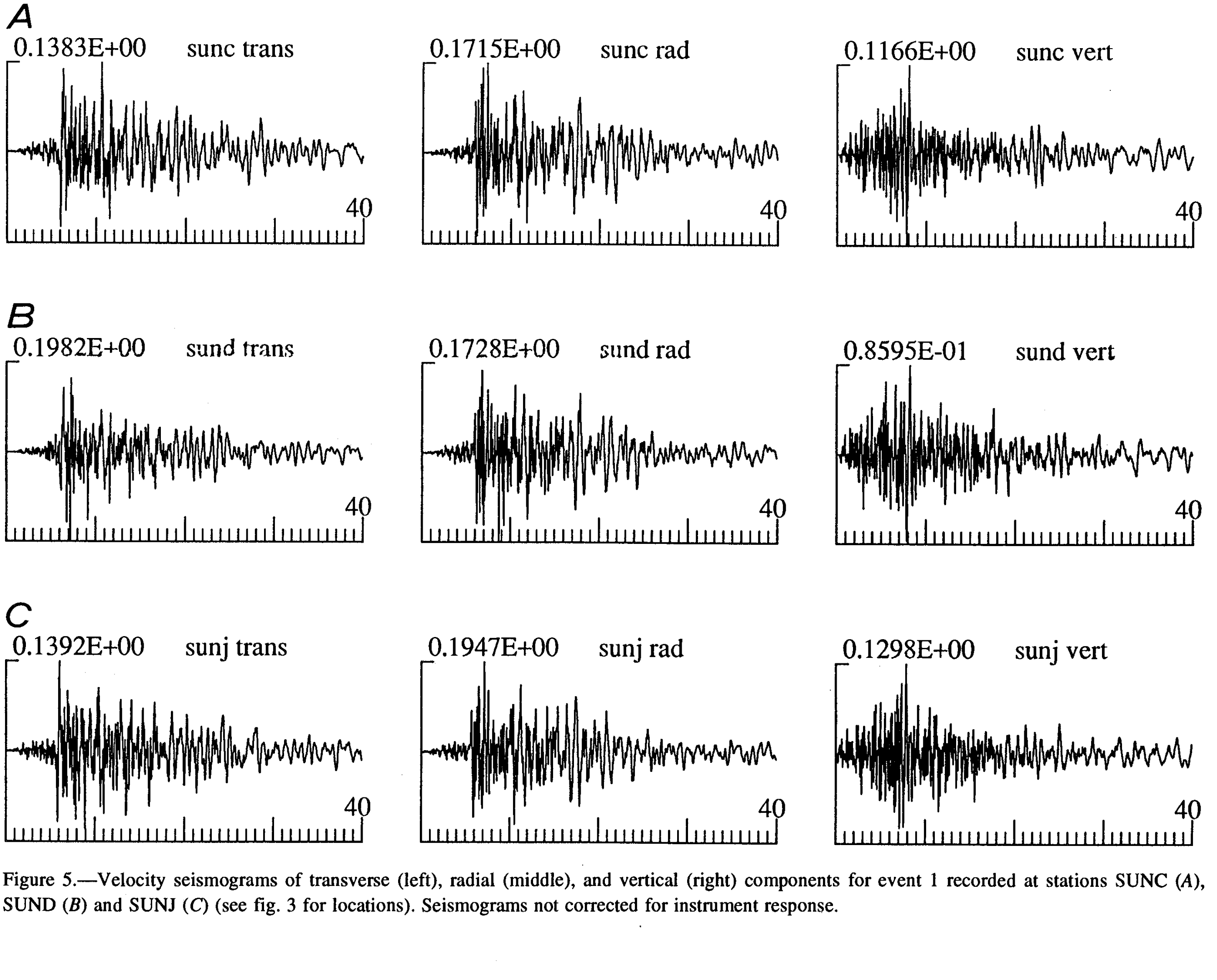

Figure 5.—Velocity seismograms of transverse (left), radial (middle), and vertical (right) components for event 1 recorded at stations SUNC (*A*), SUND (*B*) and SUNJ (*C*) (see fig. 3 for locations). Seismograms not corrected for instrument response.

dows to determine the apparent velocity and backazimuth as a function of time in the seismograms. We chose a window length to 2 s. The centerpoint of successive windows differed by 1 s, giving a 1-s overlap of adjacent windows. For each window, a 50-by-50 grid of slownesses was used, encompassing east-west and north-south slownesses ranging from −1 to +1 s/km.

APPARENT VELOCITIES AND BACKAZIMUTHS OF ARRIVALS

EVENT 1

The results of the moving-window analysis of the transverse component displacement seismograms for event 1 (M_L=4.4) are plotted in figure 10*A*. Here we have plotted the values only when the cross-correlation was at least 0.9. Thus, the waveforms for these windows are well correlated between the three stations. At 10 to 30 s, the displacement seismograms are characterized by arrivals with periods of 1 to 2 s superimposed on a longer period wavetrain with periods of 4 to 6 s (fig. 10*A*). The 2-s window used in the moving-window analysis generally allows an estimate of the slowness of these 1- to 2-s pulses, rather than that of the longer period wave; a slowness determination for the 4- to 6-s energy is presented below.

The apparent velocities plotted in figure 10*A* generally decrease over time on the seismograms. The direct *S* wave has an apparent velocity of about 3.0 km/s when a 2-s window is used on the displacement seismograms. The large positive arrival at 11 s also has a relatively high apparent velocity of 3 to 4 km/s. Because this arrival is observed at the same time after the direct *S* wave on the transverse-component displacement records from three aftershocks with different depths (fig. 4*A*) and has a high apparent velocity, we conclude that it is a body wave multiply reflected under the station. For times later than 8 s after the direct *S* wave, the apparent velocities decrease to less than 2.5 km/s. The arrivals at 17 to 28 s have apparent velocities ranging from about 1 to 2 km/s. By 30 s after the *S* wave arrival, the apparent velocities of the phases on these seismograms decrease to 0.8 km/s.

The low apparent velocities of less than 2.5 km/s and the long-period (T≥1 s)characteristics of the energy ar-

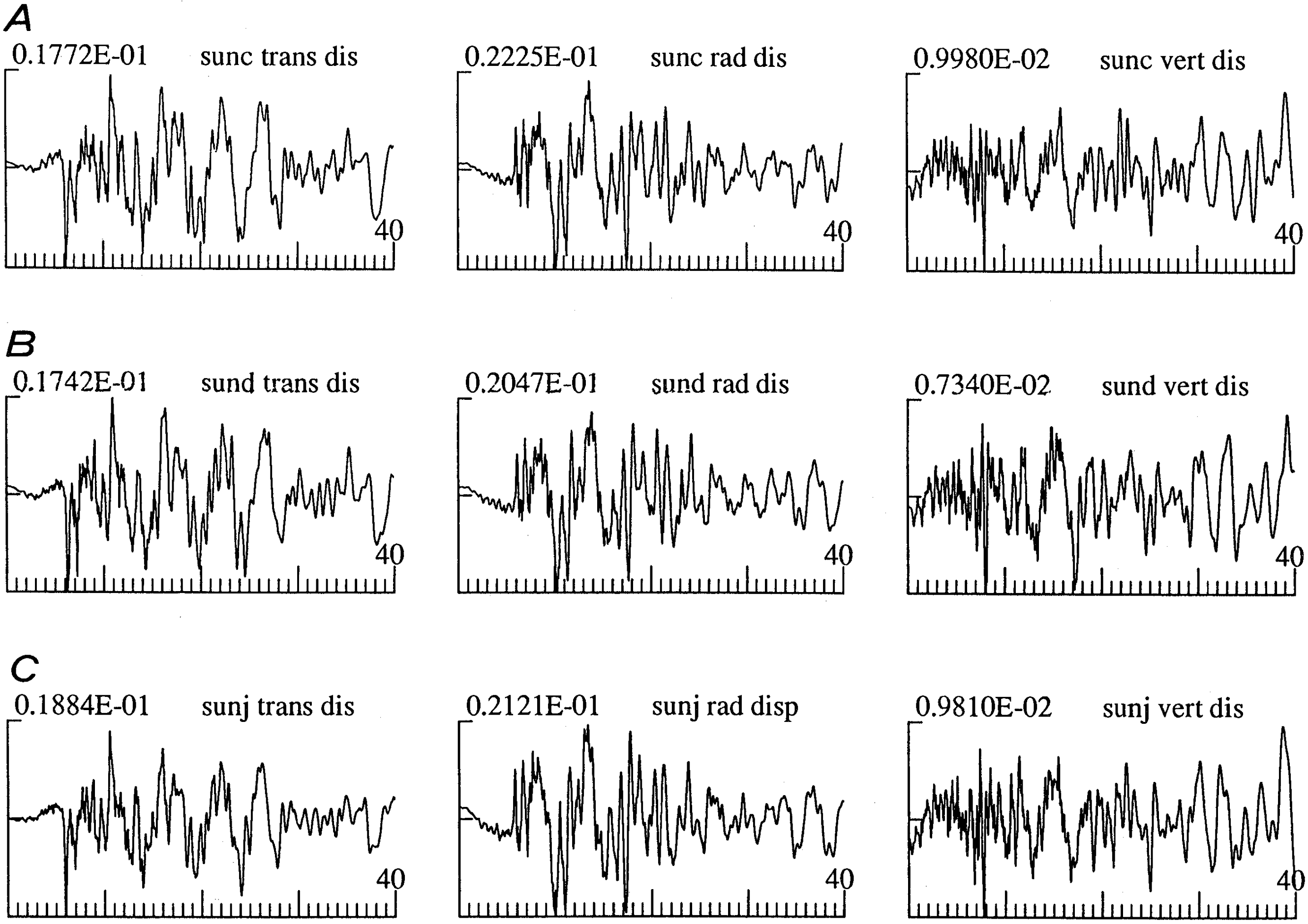

Figure 6.—Displacement seismograms of transverse (left), radial (middle), and vertical (right) components for event 1 recorded at stations SUNC (*A*), SUND (*B*), and SUNJ (*C*) (see fig. 3 for locations). Seismograms not corrected for instrument response.

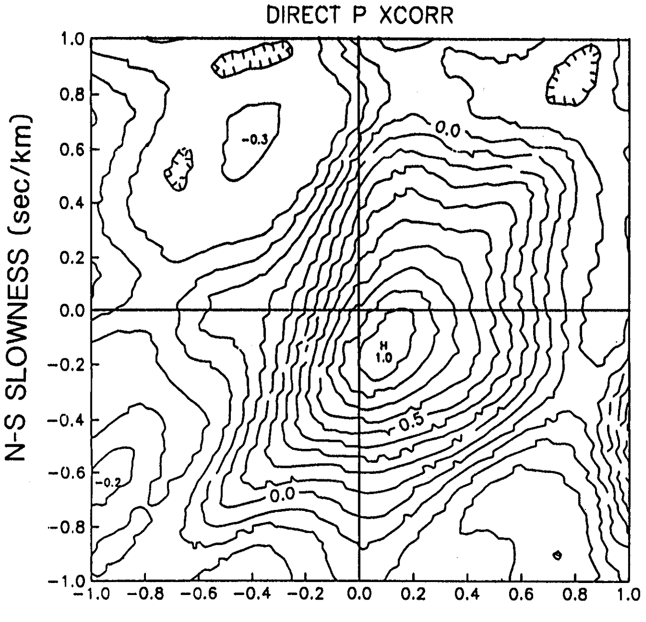

Figure 7.—Cross-correlation as a function of slowness for *P* wave of event 1 from 0.4-s window of uncorrected vertical-component seismograms recorded at three stations in Sunnyvale dense array (see fig. 1 for location). Contour interval, 0.1. H, position of peak cross-correlation, corresponding to apparent velocity of 6.3 km/s and backazimuth of 145°. Backazimuth to epicenter is 150°.

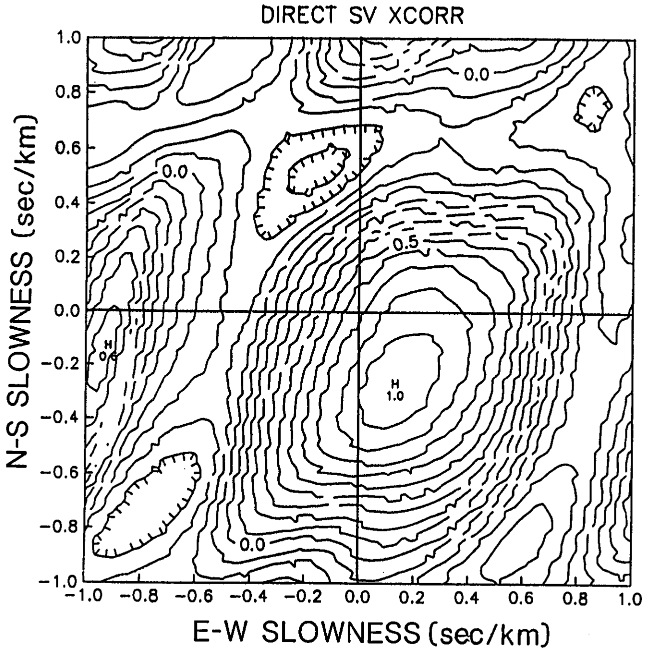

Figure 8.—Cross-correlation as a function of slowness for *S* wave of event 1 from 0.3-s window of uncorrected radial-component seismograms recorded at three stations in Sunnyvale dense array (see fig. 1 for location). Contour interval, 0.1. H, position of peak cross-correlation, corresponding to apparent velocity of 3.3 km/s and backazimuth of 150°. Backazimuth to epicenter is 150°.

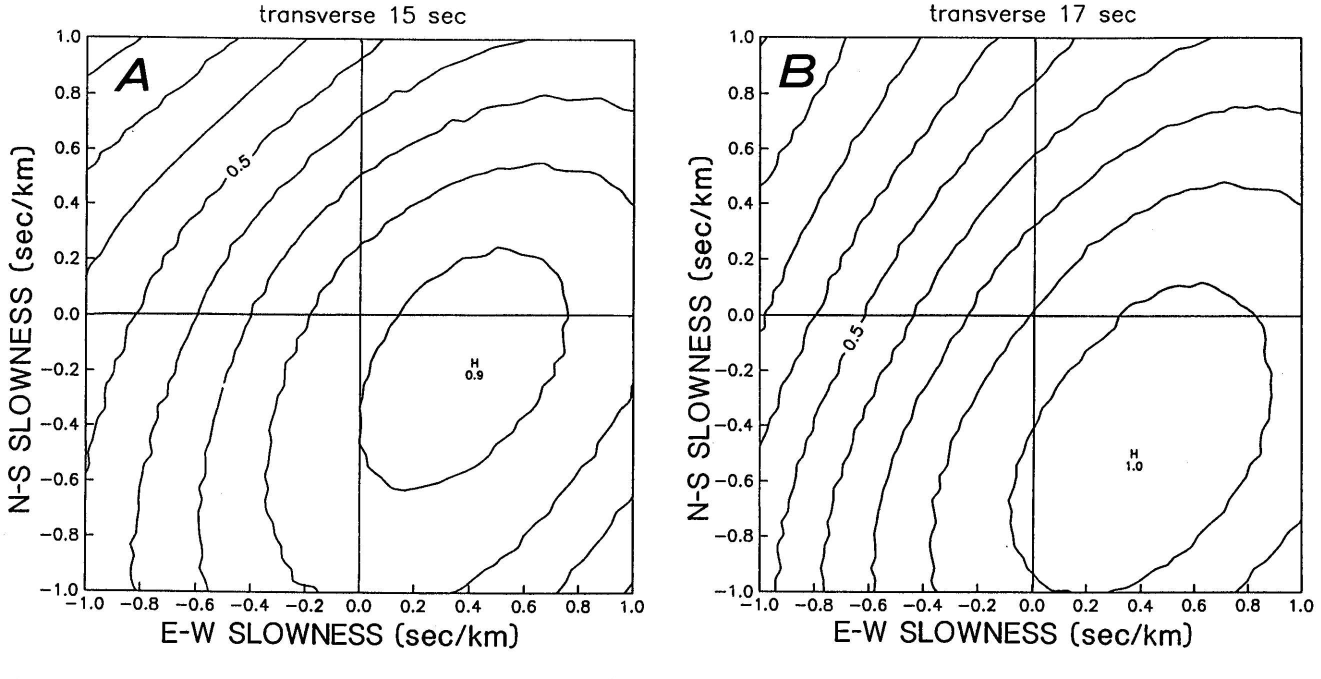

Figure 9.—Cross-correlation as a function of slowness for event 1 from transverse-component displacement seismograms. Contour interval, 0.1. H, position of peak cross-correlation. *A*, 2-s window starting at 15 s. Point H corresponds to apparent velocity of 2.4 km/s and backazimuth of 110°. *B*, 2-s window starting at 17 s. Point H corresponds to apparent velocity of 1.6 km/s and backazimuth of 146°.

riving later than 8 s after the *S* wave indicate that these arrivals are primarily surface waves. The *S*-wave velocity at the hypocenter is estimated at 3.6 km/s, on the basis of traveltimes from earthquakes (Dietz and Ellsworth, 1990). We would expect direct *S* waves to have apparent velocities of about 3.6 to 4 km/s, given the source-receiver

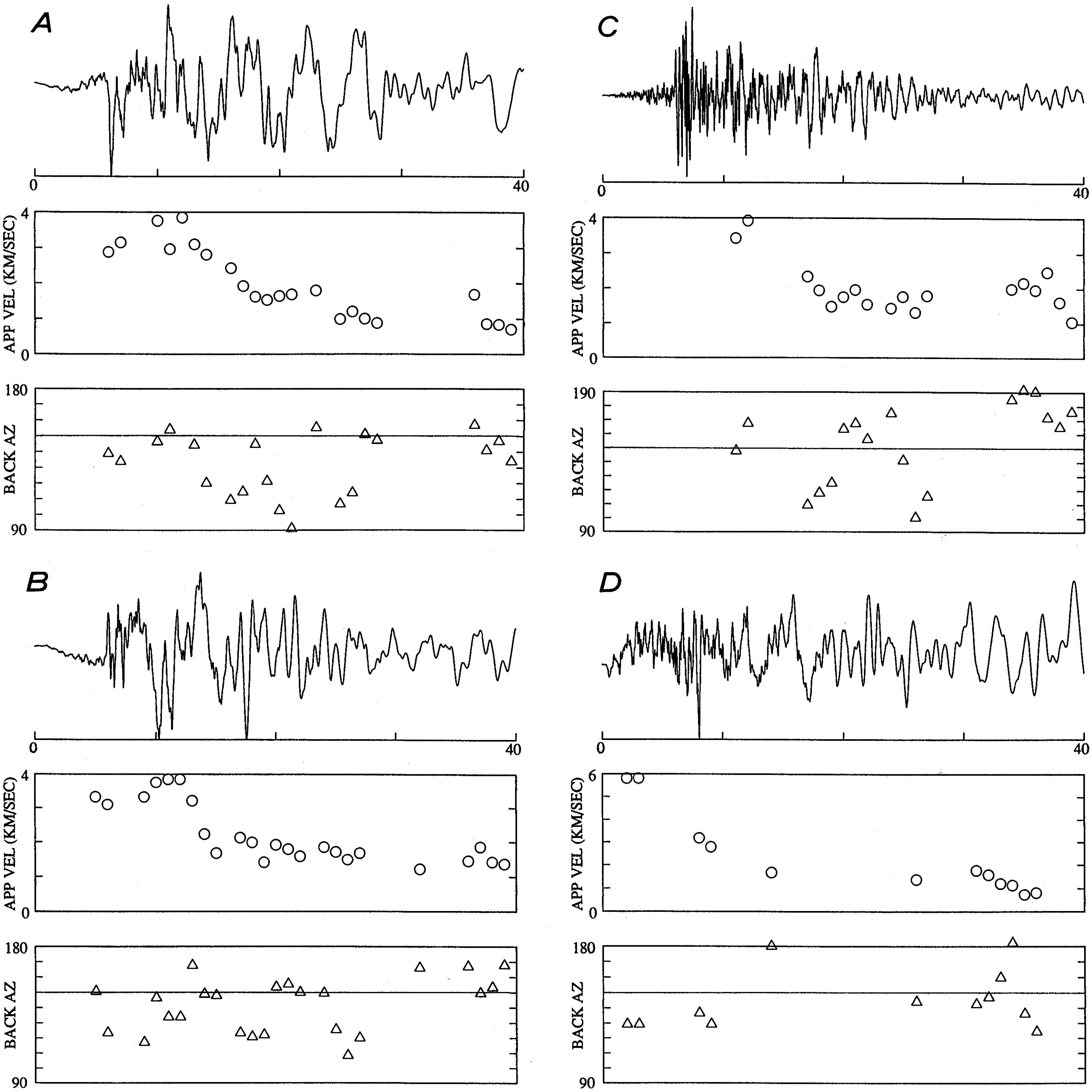

Figure 10.—Results from moving-window analysis of seismograms (top) recorded at station SUNC (fig. 3) for four aftershocks used in this study, showing apparent velocity (middle) and backazimuth (bottom) versus time. Horizontal line in backazimuth plots indicates backazimuth to epicenter. *A*, Transverse component of displacement for event 1. Only data with cross-correlation of at least 0.9 are plotted. *B*, Radial component of displacement for event 1. Only data with cross-correlation of at least 0.9 are plotted. *C*, Uncorrected radial component of velocity for event 1. Only data with cross-correlation of at least 0.9 are plotted. *D*, Vertical component of displacement for event 1. Only data with cross-correlation of at least 0.9 are plotted. *E*, Transverse component of displacement for event 2. Only data with cross-correlation of at least 0.85 are plotted. *F*, Radial component of displacement for event 2. Only data with cross-correlation of at least 0.85 are plotted. *G*, Radial component of displacement for event 3. Only data with cross-correlation of at least 0.9 are plotted. *H*, Radial component of displacement for event 4. Only data with cross-correlation of at least 0.9 are plotted.

distance of 37 km and the depth of 10 km. Here, we assume that the *S* wave traverses horizontal interfaces, and so its apparent velocity remains unchanged by transmission across each interface. Although the apparent velocity might be lowered by transmission or reflection from dipping interfaces, the long-period characteristics of the phases with apparent velocities of 2.5 km/s or less support the notion that these arrivals are surface waves.

The apparent velocities of these waves are generally consistent with those expected for Love waves trapped in the alluvium. The apparent velocity determined from the array is equivalent to the phase velocity. Love waves trapped in sedimentary deposits would have phase velocities between the lowest shear-wave velocity of the deposits and the shear-wave velocity of the underlying bedrock. Joyner and others (1976, 1981) measured the velocities of the alluvium at two sites in the Santa Clara Valley; they found the lowest shear-wave velocity to be about 300 m/s. Joyner and others (1981) reported a shear-wave velocity of 2.0 km/s for Franciscan bedrock

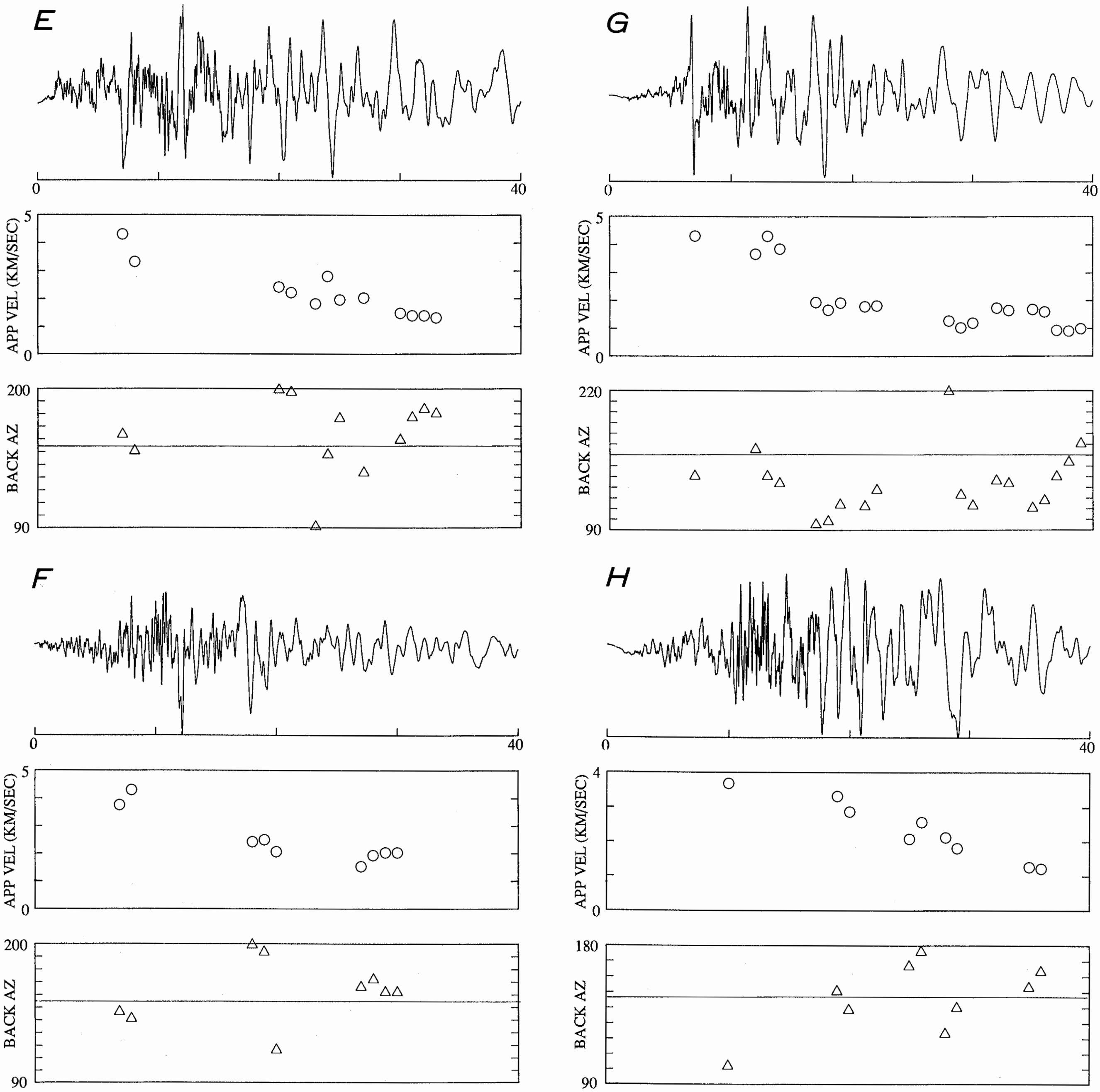

Figure 10.—Continued.

just below the alluvium in the southern part of the Santa Clara Valley near Gilroy, Calif. Thus, we would expect Love waves trapped in the alluvium to have apparent velocities of 0.3 to 2.0 km/s, similar to the range observed in the transverse-component displacement seismograms of event 1 for times later than 8 s after the *S* wave arrival.

The backazimuths for arrivals on the transverse component seismograms vary significantly (fig. 10*A*). Many of these arrivals have backazimuths essentially equal to the backazimuth to the epicenter (150°); however, from 12 to 26 s, many arrivals have backazimuths of 090°–120°. These phases are arriving from a direction 30°–60° more easterly than the source. These offazimuth phases on the transverse component are either Love waves or Rayleigh waves.

Several explanations are possible for these offazimuth arrivals. They could have been refracted by horizontal velocity gradients in the sedimentary deposits, or scattered from features to the southeast of the array. Figure 1 shows outcrops of bedrock extending into the valley to the southeast of the array: There is an "island" of exposed bedrock at Oak Hill, and another outcrop in the Santa Teresa Hills (fig. 1). These outcrops could reflect surface-wave energy from the source or convert incident *S*-wave into surface-wave energy (see section below entitled "Discussion").

One of the more striking features of these seismograms is the long-period ($T\approx4$–6 s) arrivals starting at about 10 s (fig. 10*A*). This packet appears to be dispersed, with the longer period part ($T\approx6$ s) arriving before the shorter period part ($T\approx4$ s). This long-period wavetrain is observed only on the transverse component. In the moving-window analysis above, the slowness determinations generally represent the slowness of pulses with periods of 1 to 2 s that arrive within each 2-s window. To constrain the slowness of the longer period (4–6) s wavetrain, we used a 10-s window starting at 20 s. The maximum cross-correlation was found at an apparent velocity of 1.6 km/s and a backazimuth of 143°, similar to the backazimuth to the epicenter. The low apparent velocity indicates that this wavetrain is a Love wave. In the section below entitled "Discussion," we show that a plane-layered crustal model does not produce such Love waves for a source at the depth (10 km) and distance (37 km) of event 1. Instead, these Love waves may have been generated by a conversion of *S* waves incident on the southern margin of the Santa Clara Valley.

The results of the moving-window analysis of the radial-component displacement seismograms for event 1 are plotted in figure 10*B*. Again, we have plotted the values only when the cross-correlation was at least 0.9. For a 2-s window, the direct *S* wave has an apparent velocity of about 3 km/s. The arrivals at 9 to 12 s have high apparent velocities (3–4 km/s). The arrivals with periods of about 1 s in these time windows are probably body waves that are either multiply reflected under the station or reflected by crustal interfaces.

The apparent velocity declines sharply at about 14 s, after which it is lower than 2.1 km/s. These low apparent velocities support the idea that the arrivals are Rayleigh waves, with most of their energy trapped in the shallow crust. In general, the apparent velocities at 25 to 40 s are somewhat higher than those on the transverse component at the same times. The apparent velocities on the radial component are higher than 1.2 km/s.

As with the arrivals on the transverse components, there are significant differences in the backazimuths of the arrivals on the radial component; many of these arrivals have backazimuths 30° more easterly than the backazimuth to the epicenter. One such arrival is the conspicuous negative phase at 17 s, with an apparent velocity of about 2.0 km/s and a backazimuth of 120°. The low apparent velocity of this arrival indicates a surface wave. The arrivals at 35 to 40 s have backazimuths similar to the backazimuth to the epicenter.

The radial component record shows a long-period ($T\approx5$ s) arrival immediately after the *S* wave, between 7 and 17 s. Using a 10-s window starting at 7 s, we found an apparent velocity of 3.5 km/s and a backazimuth of 141°. This long-period arrival appears to be a Rayleigh wave with a relatively high apparent velocity coming approximately from the direction of the epicenter. In the section below entitled "Discussion," we show that such an arrival is predicted by a plane-layered crustal model.

We also applied the moving-window analysis to the uncorrected radial-component seismograms (fig. 10*C*), which are essentially proportional to velocity. Because of their higher frequency content, these records show a lower coherence between stations, and so we have plotted the values only when the cross-correlation was at least 0.7. The long-period (1 s) arrival at 10 s has a high apparent velocity of 3.5 to 4.0 km/s, similar to that on the radial-component displacement seismograms. The conspicuous long-period phase at 17 exhibits a much lower apparent velocity of 2.2 km/s, The apparent velocity and backazimuth (120°) of this arrival, which appears to be a Rayleigh wave, correspond well to those in the same time window on the displacement seismograms. Later phases show apparent velocities of about 1.7 to 2.0 km/s, similar to those on the radial-component displacement seismograms. In contract, the backazimuths of the arrivals at 34 to 40 s are somewhat greater than those in the same time window on the displacement seismograms.

The results of the moving-window analysis of the vertical-component displacement seismograms for event 1 are plotted in figure 10*D*. The arrivals in the first 4 s have apparent velocities at 5.8 km/s; these windows contain the *P*-wave coda. Interestingly, the backazimuth of the *P*-wave coda differs by about 20° from the backazimuth to the epicenter. The dominant arrival at 8 s has an apparent velocity of about 3.0 km/s, indicating an *S* wave. Between 11 and 30 s, only two windows show cross-correlations of at least 0.9; these windows also show slow apparent velocities of about 1.5 km/s. The long-period arrivals at 30 to 40 s have apparent velocities of 1.0 to 2.0 km/s. The low apparent velocities and long-period characteristics of these arrivals suggest that they are Rayleigh waves. Again, the backazimuth differs somewhat from the backazimuth to the epicenter.

EVENT 2

Event 2 had a magnitude of 3.7 and a depth of 17 km, significantly deeper than event 1. The results of the moving-window analysis of the transverse component displacement for this event are plotted in figure 10*E*. The arrivals for this event were less coherent across the array than for event 1, and so we have plotted the values only when the cross-correlation was at least 0.85, to include more windows. The initial *S* wave has an apparent velocity of 4.1 km/s, and the arrivals at 20 to 35 s generally have apparent velocities decreasing over time from 2.5 to 1.2 km/s. Several arrivals have backazimuths of 180°–200°, significantly more westerly than the backazimuth to the epicenter, in contrast to the backazimuths of the arrivals from the shallower event 1, which were generally more easterly than the backazimuth to the epicenter.

The slowness for the conspicuous arrival at 11 s could not be determined because the pulse width of this arrival varied substantially across the array. An arrival with similar timing from event 1 showed an apparent velocity similar to that of the *S* wave, and so we concluded that it was a near-site reverberation.

The results of the moving-window analysis of the radial-component displacement seismograms for event 2 (fig. 10*F*) are similar to those for the other records. The arrivals at 18 to 30 s have apparent velocities of 1.5 to 2.5 km/s. As with the transverse component of event 2, some arrivals have backazimuths significantly greater than that of the backazimuth to the epicenter. The distinct pulse at 17 s has a backazimuth 70°–80° greater than that of a phase with the same arrival time relative to the *S* wave on the radial component for event 1 (see fig. 10*B*).

EVENTS 3 AND 4

For events 3 and 4, the slownesses of arrivals on the transverse components could not be determined because one of the horizontal components at station SUNJ (fig. 3) was not recorded, owing to an intermittent instrument malfunction. The results of the moving-window analysis of the radial-component displacement seismograms for event 3 are plotted in figure 10*G*. Apparent velocities decrease over time and range from 1.0 to 2.0 km/s at later than 10 s after the *S*-wave arrival. These slow arrivals have significantly longer periods than the direct *S* wave, and so we surmise that they are surface waves. The major phase at 17 s has a backazimuth about 60° less than the backazimuth to the epicenter and within 30° of that for a phase with the same arrival time relative to the *S* wave observed on the radial component for event 1 (fig. 10*B*). Interestingly, the phase at 28 s is arriving from the southwest, with a backazimuth of 220°; this phase is a surface wave that may have been generated at the west edge of the valley.

The results from the moving-window analysis of the vertical-component displacement seismograms for event 4 are plotted in figure 10*H*. This event is much more distant (63 km) than the other aftershocks studied and is significantly shallower (5.7 km). A window encompassing the initial part of the *S* wave displays an apparent velocity of 3.7 km/s and a backazimuth of 100°, in contrast to the backazimuth to the epicenter of 147°. Arrivals at 20 to 40 s have apparent velocities that decrease over time from about 3 to 1 km/s. The long-period characteristics of the arrivals with apparent velocities of 2 km/s and lower indicate that they are Rayleigh waves. The backazimuths of the later arrivals vary somewhat, although they are all within 30° of the backazimuth to the epicenter.

SYNTHETIC SEISMOGRAMS FOR EVENT 1

We computed synthetic seismograms by using the reflectivity method (Kind, 1978) to determine whether the observed waveforms for event 1 could be explained by propagation in a plane-layered structure. The parameters of the crustal model used are listed in table 2. The structure below layer 1 (alluvium) is a composite of that found from traveltimes of the *P* waves of earthquakes (Dietz and Ellsworth, 1990) and that determined from a seismic-refraction study of the southern part of the Santa Clara Valley by Mooney and Colburn (1985). We assumed that the sedimentary deposits are 400 m thick. Although the shear-wave *Q* value of 100 that we used in the model is higher than those calculated for alluvium (for example, Joyner and others, 1981), we wanted to see whether this crustal model produced surface waves at this distance for event 1. Lower *Q* values for the alluvium would attenuate the surface waves. The focal

Table 2.—*Parameters of crustal model used to generate synthetic seismograms.*

Layer	Depth at bottom of layer (km)	V_P (km/s)	V_S (km/s)	Q_P	Q_S
1	0.4	2.0	0.6	100	100
2	1.0	3.5	2.0	500	500
3	3.0	5.0	2.9	500	500
4	5.0	5.6	3.2	500	500
5	7.0	5.9	3.4	500	500
6	18.0	6.3	3.6	500	500
7	25.0	6.7	3.9	500	500
8	---	8.0	4.6	500	500

mechanism used was derived by Oppenheimer (1990) from *P*-wave first motions from this event (strike, 125° SW.; rake, 100°). We used a ramp source-time function with a duration of 0.5 s. We were particularly interested in duplicating the longer period characteristics of the observed waveforms.

The synthetic seismograms for the transverse and radial components at an epicentral distance of 37 km, corresponding to that of the Sunnyvale dense array (fig. 1), are plotted in figure 11, along with the seismograms recorded at station SUNC (fig. 3). The synthetic seismogram for the transverse component, however, does not reproduce the long-period (4–6 s) Love waves observed on the transverse-component displacement seismogram for event 1 at 10 to 30 s. A comparison of the synthetic with the observed seismogram highlights the absence of significant long-period Love waves on the synthetic seismogram. The depth-to-distance ratio (10 km/37 km) is too large to produce sizable Love waves on the synthetic seismogram.

There is some correspondence between the arrival at about 10 s on the synthetic seismogram for the transverse component and the large positive arrival at 11 s on the observed seismogram. On the synthetic seismogram, this arrival is largely produced by a free-surface reflection that is reflected upward by the boundary at 1-km depth between the layers with *P*-wave velocities of 3.5 and 5.0 km/s. As mentioned above, this arrival was observed on the transverse-component displacement seismograms for events 1, 2, and 3 (fig. 4*A*), always with the same delay time after the direct *S* wave. This similarity in delay time for events with different depths also indicates that this phase is a multiple reflection in the shallow crust near the receiver.

The synthetic seismogram for the radial component displays some of the long-period characteristics of the observed seismogram. The negative pulse at 10 s and the positive swing at about 13 s on the recorded seismogram (fig. 11*C*) are reproduced on the synthetic seismogram (fig. 11*D*). This long-period ($T{\approx}5$ s) arrival is a Rayleigh wave, which was also produced in a crustal model without the two top layers of the model listed in table 2. The synthetic seismograms indicate that this Rayleigh wave has an apparent velocity somewhat lower than that of the *S* wave, in accord with the results from the Sunnyvale dense array, which showed this long-period phase to have an apparent velocity of 3.5 km/s. The synthetic seismogram for the radial component, however, does not exhibit the 1- to 2-s energy observed on the observed seismogram at later than 16 s (fig. 11*C*). These arrivals were demonstrated to be surface waves by their low apparent velocities across the array.

DISCUSSION

It is clear from this study that surface waves are largely responsible for the long duration of shaking observed in the aftershock seismograms recorded by the Sunnyvale dense array. The observations presented here demonstrate that it is sometimes inadequate to model shaking in sedimentary basins by plane *S* waves propagating through a stack of horizontal layers. Multiple reflections in such horizontally layered media will have the same apparent velocity as the initial *S* wave. Most of the later arrivals on the observed seismograms, however, have an apparent velocity significantly lower than that of the *S* wave. Although some of this energy may represent body waves reflected by or transmitted through dipping interfaces, the low-frequency characteristics and low apparent velocities of these arrivals indicate that they are surface waves. Nonetheless, synthetic seismograms generated by models incorporating point sources, such as reflectivity, can produce surface waves when the distance is sufficiently large relative to the source depth.

The inability of our synthetic transverse-component seismograms to duplicate the observed seismograms for event 1 suggests that the long-period Love waves observed for event 1 were produced by a crustal structure that is not simply plane layered. As mentioned in the section above entitled "Introduction," numerical simulations have shown how surface waves in a sedimentary basin can be produced by the conversion of *S* waves incident on the edge of the basin. The Loves waves observed for event 1 may have been generated by such conversion along the southern and southeastern margins of the Santa Clara Valley. Furthermore, a Rayleigh wave obliquely striking the dipping edge of a basin would probably have some of its energy converted to Love waves. In addition, the observed Rayleigh waves with low apparent velocities (>15 s; fig. 10*B*) could also be produced by the conversion of body waves at the edges of the basin. Our future work will center on finite-difference simulations using two- and three-dimensional velocity models for the Santa Clara Valley; synthetic seismograms from these simulations will be compared with the observed seismograms from the Sunnyvale dense array (fig. 1).

When we deployed our array, we expected to see surface waves arriving from the west edge of the valley; however, most offazimuth arrivals were found to come from a direction more easterly than the sources. Figure 1 shows that the direct paths from the hypocenters to the array almost parallel the west edge of the valley. This grazing angle of incidence may preclude any conversion of body waves to surface waves at the west edge of the valley for these aftershocks. Numerical studies will be needed to confirm this conclusion.

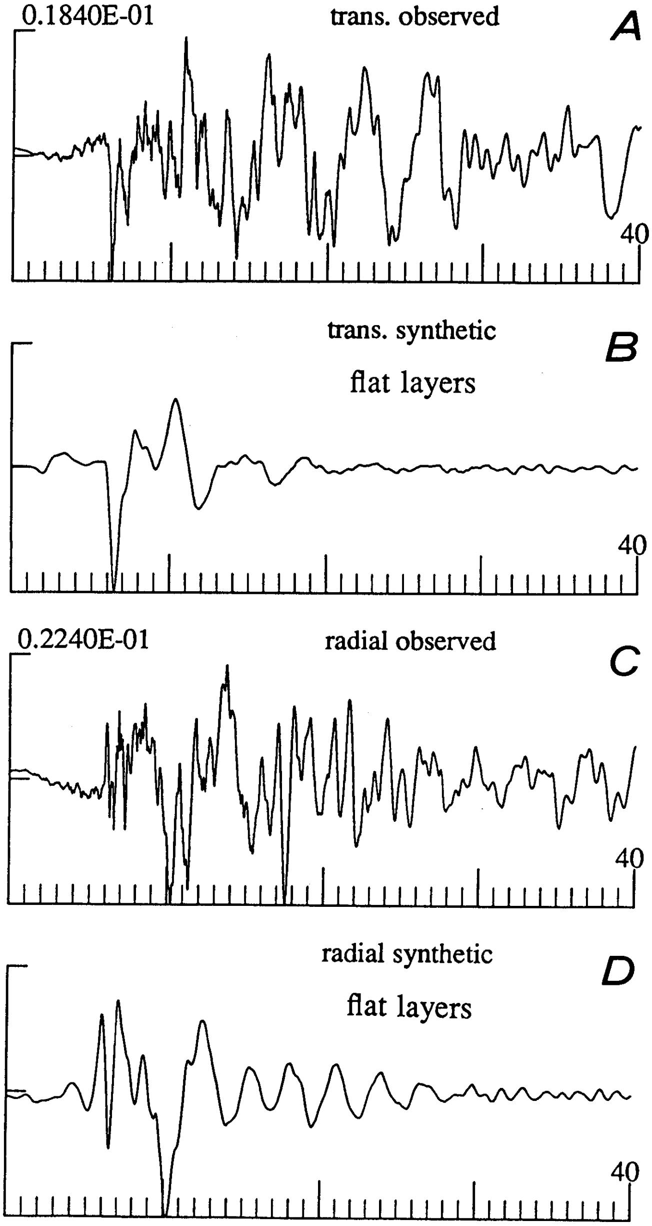

Figure 11.—Observed (*A*, *C*) and synthetic (*B*, *D*) seismograms of event 1 for transverse (*A*, *B*) and radial (*C*, *D*) components. Synthetic seismograms were generated by reflectivity method (Kind, 1978), using plane-layered crustal model listed in table 2. Initial *S* wave arrives at about 6 s. Amplitudes of synthetic seismograms in arbitrary units.

The closely spaced aftershocks (events 1–3, table 1) produced significantly different waveforms at the array (fig. 4). We note that event 1 generated substantial long-period (4–6 s) Love waves, whereas event 3 did not, even though it was located only 6 km to the west and 2 km deeper than event 1. The conversion of body waves to surface waves at the edge of the basin may be sensitive to azimuth and angle of incidence. Alternatively, the source duration for event 1 (M_L=4.4) had a long-period component lasting longer than 1 s that was absent in event 3 (M_L=3.6). Differences in focal mechanism may also be a factor. Further analysis of the waveforms and numerical-simulation studies should help to explain these observations.

This study has not attempted to demonstrate that the long-period surface waves observed for the main shock at Sunnyvale and Agnews State Hospital (fig. 1) were produced by the conversion of *S* waves at the edge of the Santa Clara Valley. These arrivals differ somewhat from the surface waves observed from event 1. On the main-shock records at Sunnyvale (fig. 2), the largest long-period displacements and velocities end about 11 s after the largest *S*-wave arrival, as identified from the acceleration traces. In contrast, the long-period motion for event 1 continues until 20 s after the direct *S* wave. The long-period energy observed at 13 to 21 s on these records may represent surface waves generated at the source. The long-period arrivals at 25 to 40 could be produced by scattering at the margins of the basin. Analysis and modeling of the main-shock records would help resolve these issues.

This study demonstrates how a small-aperture array with only four stations can be effectively used to determine the apparent velocity and backazimuth of seismic waves in sedimentary basins. We recommend that similar small-aperture arrays of strong-motion instruments be installed in sedimentary basins near the sites of expected large earthquakes (for example, Santa Clara Valley, Los Angeles Basin). Such arrays would provide sorely needed information about the long-period (T≥1 s) shaking in sedimentary basins generated by major earthquakes. This information is required to ensure that tall buildings and extended structures in sedimentary basins are adequately designed to withstand the seismic shaking from large earthquakes.

ACKNOWLEDGMENTS

We thank Leif Wennerberg, Art McGarr, and William Joyner for their helpful reviews of the manuscript; comments by David Boore and Edward Cranswick were also useful. We are grateful to the homeowners who graciously allowed us to locate our instruments on their property. The Reftek recorders were provided by Incorporated Research Institutions for Seismology, and the seismometers by the National Center for Earthquake Engineering Research. Lawrence Shengold helped maintain the dense array. David Oppenheimer provided the locations, magnitudes, and focal mechanisms of aftershocks, based on determinations from the U.S. Geological Survey. Harley Benz helped measure the distances between array stations.

REFERENCES CITED

Bard, P.Y., Campillo, Michel, Chávez-García, F.J., and Sánchez-Sesma, F.J., 1988, The Mexico earthquake of September 19, 1985—a theoretical investigation of large- and small-amplification effects in the Mexico City valley: Earthquake Spectra, v. 4, no. 3, p. 609–633.

Borcherdt, R.D., and Gibbs, J.F., 1976, Effects of local geological conditions in the San Francisco Bay region on ground motions and the intensities of the 1906 earthquake: Seismological Society of America Bulletin, v. 66, no. 2, p. 467–500.

California Department of Water Resources, 1967, Geology, app. A *of* Evaluation of ground water resources, South [San Francisco] Bay: Bulletin 118–1, 153 p.

California Division of Mines and Geology, 1969, Geologic atlas of California: Sacramento.

Dietz, L.D., and Ellsworth, W.L., 1990, The October 17, 1989, Loma Prieta, California, earthquake and its aftershocks; geometry of the sequence from high-resolution locations: Geological Research Letters, v. 17, no. 9, p. 1417–1420.

Frankel, Arthur, Filson, J.R., Borcherdt, R.D., and Vidale, J.E., 1989, Numerical simulations of strong ground motions in the Leninakan basin produced by the 1988 Armenian earthquake and its aftershocks [abs.]: Eos (American Geophysical Union Transactions), v. 70, no. 43, p. 1200.

Harmsen, S.C., and Harding, S.T., 1981, Surface motion over a sedimentary valley for incident plane *P* and *SV* waves: Seismological Society of America Bulletin, v. 71, no. 3, p. 655–670.

Haskell, N.A., 1960, Crustal reflection of plane *SH* waves: Journal of Geophysical Research, v. 65, no. 12, p. 4147–4150.

Joyner, W.B., Warrick, R.E., and Oliver, A.A., III, 1976, Analysis of seismograms from a downhole array in sediments near San Francisco Bay: Seismological Society of America Bulletin, v. 66, no. 3, p. 937–958.

Joyner, W.B., Warrick, R.E., and Fumal, T.E., 1981, The effect of Quaternary alluvium on strong ground motion in the Coyote Lake, California, earthquake of 1979: Seismological Society of America Bulletin, v. 71, no. 4, p. 1333–1349.

Kanai, Kiyoshi, 1952, Relation between the nature of surface layer and the amplitudes of earthquake motions: Tokyo University, Earthquake Research Institute Bulletin, v. 30, no. 1, p. 31–37.

Kawase, Hiroshi, and Aki, Keiiti, 1989, A study on the response of a soft basin for incident *S*, *P*, and Rayleigh waves with special reference to the long duration observed in Mexico City: Seismological Society of America Bulletin, v. 79, no. 5, p. 1361–1382.

Kind, Rainer, 1978, The reflectivity method for a buried source: Journal of Geophysics, v. 44, no. 6, p. 603–612.

Maley, R.P., Acosta, A.V., Ellis, F., Etheredge, E.C., Foote, L.J., Johnson, D.A., Porcella, R.L., Salsman, M.J., and Switzer, J.C., 1989, U.S. Geological Survey strong-motion records from the Northern California (Loma Prieta) earthquake of October 17, 1989: U.S Geological Survey Open-File Report 89–568, 85 p.

Mooney, W.D., and Colburn, R.H., 1985, A seismic-refraction profile across the San Andreas, Sargent, and Calaveras faults, west-central California: Seismological Society of America Bulletin, v. 75, no. 1, p. 175–191.

Ohtsuki, Akira, and Harumi, Kasaburo, 1983, Effect of topographies and subsurface inhomogeneities on seismic *SV* waves: Earthquake Engineering & Structural Dynamics, v. 11, no. 4, p. 441–462.

Oppenheimer, D.H., 1990, Aftershock slip behavior of the 1989 Loma Prieta, California earthquake: Geological Research Letters, v. 17, no. 8, p. 1199–1202.

Vidale, J.E., and Helmberger, D.V., 1988, Elastic finite-difference modeling of the 1971 San Fernando, California earthquake: Seismological Society of America Bulletin, v. 78, no. 1, p. 122–141.

STRONG GROUND MOTION

A THREE-DIMENSIONAL SIMULATION OF SEISMIC WAVES IN THE SANTA CLARA VALLEY, CALIFORNIA, FROM AN AFTERSHOCK

By Arthur Frankel and John E. Vidale,
U.S. Geological Survey

CONTENTS

ABSTRACT

We use a finite-difference method to propagate elastic waves through a three-dimensional model of the Santa Clara Valley, an alluvium-filled basin that underlies the city of San Jose, Calif. The model is based on depth-to-bedrock information from water wells in the area. The simulation corresponds to an area 30 km (east-west) by 22 km (north-south) by 6 km (depth), containing about 4 million grid points. Synthetic seismograms from the simulation are accurate at frequencies up to 1 Hz. We model the motions from an M=4.4 aftershock at the 1989 Loma Prieta earthquake. The simulation illustrates S-wave to surface-wave conversion at the edges of the basin, and the large amplitude and long duration of ground motion in the basin relative to the surrounding bedrock. Love waves produced at the edge of the basin are the largest arrivals in the transverse-component synthetic seismograms. Because of the slow group velocity of these Love waves, sites near the center of the basin show longer durations of significant motions than do basin sites near the valley edges; sites near the center of the basin also show larger peak amplitudes on the transverse component. Array analysis of the synthetic seismograms indicates that Love waves tend to propagate parallel to the east and west edges of the valley. Rayleigh waves are produced along the southern margin of the basin from incident S waves. Large radial motions occur where a Rayleigh wave impinges on the northeastern margin of the valley. Some Rayleigh waves travel westward across the basin after being scattered from the east edge of the valley. Synthetic seismograms calculated from the simulation have peak amplitudes similar to those on seismograms recorded by the Sunnyvale dense array for this aftershock, although the duration of the transverse component is not matched in the synthetic seismogram, using this basin model. The simulation indicates that the Love waves observed on the recorded seismograms were produced by conversion of incident S waves at the southern margin of the Santa Clara Valley. Two-dimensional simulations show how the S-wave to Love-wave conversion is affected by the angle of incidence of the S wave and the sharpness of the velocity transition between alluvium and bedrock. As more accurate basin models are developed, three-dimensional simulations should become valuable for predicting ground motions in sedimentary basins for future large earthquakes.

INTRODUCTION

With the increasing speed and memory of computers, large-scale numeric simulations involving three-dimensional variations in crustal structure are now feasible. A myriad of seismologic applications are available for such three-dimensional simulations. In this paper, we consider one such application: the propagation of seismic waves in sedimentary basins. Many population centers are situated in sedimentary basins near the rupture zones of expected large earthquakes. It is well known that such sites sustain larger ground motions with longer durations than do sites on bedrock (for example, Borcherdt and Gibbs, 1976); however, modeling of shaking in basins has been largely limited to crustal models that vary in only one or two dimensions. One-dimensional crustal models (horizontal-plane layers) show the effects of multiple reverberations of body waves in the sedimentary layers (Kanai, 1952; Haskell, 1960). Numeric simulations for media with velocity variations in two dimensions have demonstrated the importance of *S*-wave to surface-wave conversion at the edges of basins (Aki and Larner, 1970; Bard and Bouchon, 1980a, b, 1985; Harmsen and Harding, 1981; Ohtsuki and Harumi, 1983; Bard and others, 1988; Vidale and Helmberger, 1988; Kawase and Aki, 1989). These surface waves can substantially increase the duration and amplitude of shaking at sites in the basin, relative to that expected from a horizontal-plane layer over a half-space. It has been suggested that such surface waves were responsible for much of the damage to Mexico City in the 1985 earthquake (Kawase and Aki, 1989). There has been some work on three-dimensional wave propagation for simple symmetrical basin models (for example, Sánchez-Sesma, 1983; Rial, 1989; Sánchez-Sesma and others, 1989).

Ultimately, three-dimensional simulations will be used to predict seismic shaking in sedimentary basins for future large earthquakes. Accurate prediction of ground motions in basins requires three-dimensional simulations for several reasons. Lateral variation in sedimentary thickness and velocity could cause site response to depend on the azimuth to the earthquake. In closed basins, resonant modes can be set up by waves multiply reflected by the edges of the basin (Rial, 1989). In addition, the three-dimensional curvature of the alluvium-bedrock contact could cause focusing of body waves at certain places in the basin. For irregular basins, *S*-wave to surface-wave conversion could occur along several parts of the border of the basin, producing surface waves traveling in different directions across the basin. Three-dimensional simulations would also be useful for studying shaking from extended ruptures, where the azimuth and angle of incidence of *S* waves impinging on a basin vary for waves from different parts of the rupture zone.

This paper applies a three-dimensional finite-difference computer program to propagate seismic waves in the Santa Clara Valley, Calif. (fig. 1), an alluvium-filled basin south of San Francisco. This area was chosen partly because recordings of aftershocks of the 1989 Loma Prieta earthquake were available from a small-aperture dense array located in this valley in the city of Sunnyvale. Analysis of the seismograms from this array revealed that large motions after the *S* wave were produced by surface waves traveling in the basin (Frankel and others, 1991). Much of the surface-wave energy was propagating from directions substantially different from the source direction, indicating that this energy had been scattered from the edges of the basin. The presence of offazimuth arrivals emphasizes the need for a three-dimensional model of the basin to simulate the observed waveforms. This part of the Santa Clara Valley contains the city of San Jose and is a major population center. The area is also important because of its substantial computer-related industry, for which it is commonly referred to as Silicon Valley. Thus, understanding and predicting earthquake ground motions in this valley are important to society.

We simulated the seismic wavefield produced by the aftershock designated event 1 by Frankel and others (1991) that was recorded on the Sunnyvale dense array. This M_L=4.4 aftershock occurred at 0127 G.m.t. October 25, 1989 (fig. 1), and had a source depth of 10.2 km. The event exhibited a large Love wave at the array that could not be explained by a plane-layered velocity model. Many of the arrivals following the *S* wave for this event had backazimuths substantially more to the east than the backazimuth to the epicenter.

We use a three-dimensional model to illustrate the types of effects that occur in irregular sedimentary basins. Specifically, we seek to explain observations from the Sunnyvale dense array, such as the large surface waves and the presence of offazimuth arrivals.

METHOD

The three-dimensional finite-difference method propagates the complete elastic wavefield in a medium with

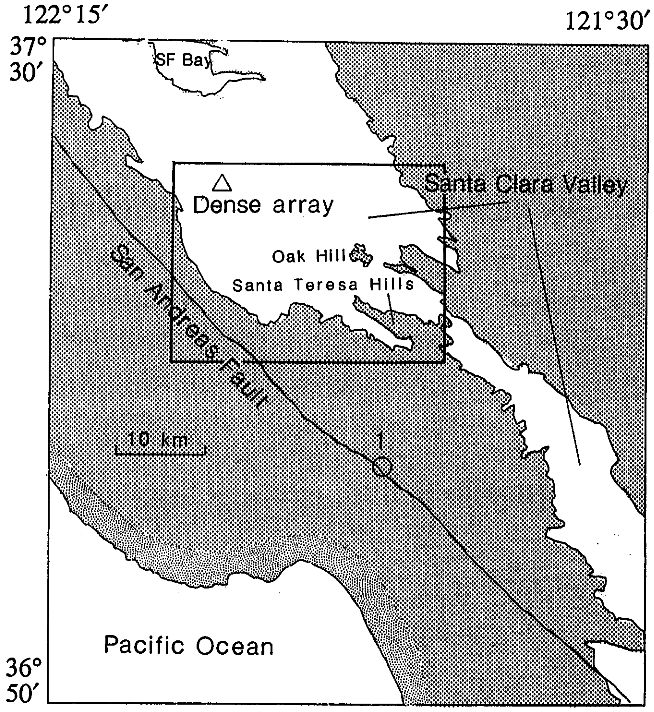

Figure 1.—Loma Prieta area, northern California, showing locations of the Santa Clara Valley, Sunnyvale dense array (triangle), and epicenter (circle) of aftershock modeled by three-dimensional simulation. Boundary of valley is contact between alluvium and consolidated rocks (from California Division of Mines and Geology, 1969). Shading indicates areas where bedrock is exposed at surface. Box denotes area used in three-dimensional simulation.

arbitrarily complex velocity structure. This wavefield includes conversions of *P* to *S*, *S* to *P*, body to surface, and surface to body waves, as well as head waves, diffractions, and multiple scattering. A general discussion of the finite-difference method for two-dimensional media was provided by Kelly and others (1976). For the three-dimensional case, let u, v, and w be the displacements in the x, y, and z directions, respectively; ρ is the density, and λ and μ are the Lamé constants. These medium properties vary with position. The three coupled wave equations are

$$\rho u_{tt} = [(\lambda+2\mu)u_x+\lambda w_z+\lambda v_y]_x + [\mu u_y+\mu v_x]_y + [\mu u_z+ \mu w_x]_z \,,$$

$$\rho v_{tt} = [(\lambda+2\mu)v_y+\lambda w_z+\lambda v_x]_x + [\mu v_x+\mu u_y]_x + [\mu v_z +\mu w_y]_z \,,$$

and

$$\rho w_{tt} = [(\lambda+2\mu)w_z+\lambda w_x+\lambda v_y]_x + [\mu w_x+\mu u_z]_x + [\mu w_y+ \mu v_z]_y \,,$$

where the subscripts denote partial derivatives, which are replaced by their finite-difference approximations for a three-dimensional grid with equal spacing in x, y, and z. At each gridpoint, the vector displacement for the next time step can be found from the displacements at adjacent points for the present time step and from the displacements at that gridpoint for the present and previous time steps. Thus, the complete wavefield is advanced in discrete time steps by applying the algorithm at each gridpoint for each time step. Synthetic seismograms can be calculated for any gridpoint.

The finite-difference method used in this paper is accurate to the fourth order in space and the second order in time. The fourth-order algorithm that approximates the spatial derivatives is an extension of that of Vidale (1990) for the two-dimensional case. Absorbing boundaries based on those described by Clayton and Engquist (1977) were applied on all sides of the grid except the top. A one-sided difference scheme (Alterman and Rotenberg, 1969) was used for the free surface because a two-sided difference scheme (Alterman and Karal, 1968) was found to be unstable for the case of a layer over a half-space when there was a large contrast in seismic velocity across the interface. The above equations do not include anelastic attenuation. Below, we approximate the effects of anelastic attenuation by convolving the synthetic seismograms with a Q operator that varies over time (Vidale and Helmberger, 1988).

The grid size for the Santa Clara Valley simulation was 300 points in the east-west direction, 220 points in the north-south direction, and 60 points in the vertical direction. The grid spacing used was 100 m, so that the simulation corresponded to a space 30 by 22 by 6 km deep. There are 3.96 million gridpoints. The displacements (three components) at two time steps are continually saved, requiring 23.76 million words of memory; additional memory is required for the medium parameters. The code was vectorized for use on a Cray computer. We achieved a speed of about 6 s per time step; each time step represented 0.015 s. The simulation was for 3,000 time steps, corresponding to 45 s. This run required about 5 hours of processing time on the Cray YMP at the University of California, San Diego.

We were particularly concerned with the accuracy of the three-dimensional model for the case of a basin with a relatively thin sedimentary fill. The Santa Clara Valley is large in horizontal extent relative to its thickness. Although it is not known precisely, the maximum thickness of the sedimentary deposits is thought to be about 500 m (E.J. Helley, oral commun. 1990). With a grid spacing of 100 m, the maximum thickness of the sedimentary deposits is only five gridpoints. To evaluate the accuracy of the three-dimensional model for such thin layers, we considered the case of a thin horizontal layer over a half-space. Synthetic seismograms calculated by the three-dimensional finite-difference method were compared with those generated by the reflectivity method of Saikia and Sen (1989), which does not have the numeric inaccuracies of the finite-difference method. Both methods include near-field terms in the synthetic seismograms.

We calculated synthetic seismograms for a model with a low-velocity surface layer (V_P=1.1 km/s, V_S=0.6 km/s, ρ=2.0 g/cm^3) over a half-space (V_P=3.5 km/s, V_S=2.0 km/s, ρ=2.6 g/cm^3). These are the same velocities used later in the Santa Clara Valley simulation. The low velocity was assigned to the top four grid levels in the model, starting at the free surface. The grid spacing was 100 m, the same as used in the Santa Clara Valley simulation. Because interfaces in the finite-difference method are located halfway between gridpoints, we would expect the finite-difference model to correspond to a 400-m-thick surface layer. The reflectivity synthetic seismograms were computed for a layer thickness of 400 m; the source was at a depth of 1 km, and the receiver at an epicentral distance of 3 km. Two cases were considered: an explosion, and a strike-slip earthquake with vertical dip and strike perpendicular to the azimuth to the receiver. The source was inserted in the grid by specifying displacements at the gridpoints adjacent to the source location; these displacements correspond to the equivalent-force system appropriate to that type of source. For the explosion, these displacements are outward directed, specified at the six points surrounding the source location. Two force couples are required for the strike-slip earthquake. For each method, the source-time function was an isosceles triangle with a base of 1.0 s. The synthetic seismograms generated by each method were low-pass filtered, with a corner frequency at 1.0 Hz. We used a high Q value of 2,500 for the reflectivity run because the three-dimensional simulation does not include anelasticity.

The synthetic velocity seismograms generated by the three-dimensional finite-difference method and the reflectivity method for the explosion (radial and vertical components) and a strike-slip earthquake (transverse component) are plotted in figure 2. For the explosion, the radial-component synthetic seismograms are nearly identical in both shape and amplitude by the two methods (fig. 2*A*). The vertical-component synthetic seismograms for the explosion start off nearly identical in amplitude and waveform for the *S* wave (fig. 2*B*). On this component, there is a progressive delay of the peaks in the Rayleigh waver over time on the finite-difference synthetic seismogram relative to the reflectivity synthetic seismogram. By the end of the seismogram, a peak of the Rayleigh wave is arriving about 1.5 s later on the finite-difference synthetic seismogram on the reflectivity synthetic seismogram, probably owing to grid dispersion in the finite-difference method, which tends to reduce the propagation speed of waves in the grid (see Alford and others, 1974).

There is generally good agreement between the two methods for the transverse-component velocity waveforms from a strike-slip earthquake (fig. 2*A*). The peak amplitude on the finite-difference synthetic seismogram is about 80 percent that on the reflectivity synthetic seismogram. The long-period Love waves are delayed somewhat on the finite-difference synthetic seismogram relative to the synthetic seismogram. Again, this delay increases over time, reaching about 1 s at about 10 s into the record (fig. 2*C*). This delay is likely due to grid dispersion from the finite-difference method. From these synthetic seismograms, we estimate that grid dispersion produces an error of about 10 percent in the velocity of the slow Rayleigh waves and Love waves in the finite-difference simulations. Thus, the synthetic seismograms plotted here probably overestimate the total duration of motion by about 10 percent.

Despite having a surface layer only four gridpoints thick, the finite-difference method generates synthetic seismograms comparable to those generated by the reflectivity method, indicating that the finite-difference synthetic seismograms are sufficiently accurate for our purposes up to frequencies of about 1 Hz. We note that a frequency of 1 Hz corresponds to a wavelength of six gridpoints for shear waves in the alluvium. A wavelength-to-grid-spacing ratio of 6 is near the minimum needed to achieve adequate accuracy for a two-dimensional fourth-order finite-difference simulation, according to Alford and others (1974). The "accuracy" of the finite-difference synthetic seismograms is also determined by the accuracy of the velocity model with respect to the true velocities.

THREE-DIMENSIONAL MODEL OF THE SANTA CLARA VALLEY

A major obstacle to applying the three-dimensional simulation to actual basins is the absence of detailed velocity models for most basins. In areas without extensive oil exploration, the thickness of the alluvium in deep basins is generally unknown. To construct a three-dimensional model of the Santa Clara Valley, we used depth-to-bedrock data from water wells. The locations of the water wells used and the depth to bedrock for each well are shown in figure 3 (California Department of Water Resources, 1967). The depth to bedrock is largely unknown in the central part of the valley because water wells do not reach bedrock there. We assigned an alluvium thickness of 457 m (1,500 ft) for points near the center of the valley, consistent with the contour for this thickness from conjectured by the California Department of Water Resources. A depth of 400 m was specified under the Sunnyvale dense array (SUN, fig. 3), on the basis of the depth of nearby wells. In a few places, the depth to bedrock was approximated as the depth of the well, even if it did not reach bedrock. A minimum-tension surface was fitted to the basement depths from the well data and the assigned points used in the simulation. The resulting depth contours of the alluvium-bedrock contact used in the three-dimensional simulation are shown in figure 3.

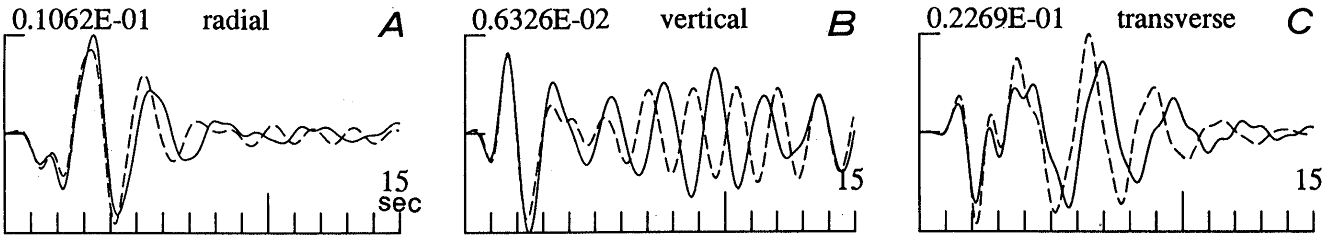

Figure 2.—Synthetic seismograms generated by finite-difference method (solid curves) and reflectivity method (dashed curves) for an explosion (*A*, *B*,) and a strike-slip earthquake (*C*). *A*, Radial component. *B*, Vertical component. *C*, Transverse (*SH*) component. Model is a 400-m-thick horizontal layer over a half-space, with source at 1-km depth; epicentral distance, 3 km.

We used a simple two-component velocity model consisting of one set of velocities for bedrock and another set for alluvium. Given the absence of detailed velocity information on the alluvium, we considered it premature to specify layering in the alluvium. We used a shear-wave velocity of 60 m/s for the alluvium, similar to the average shear-wave velocity found by Joyner and others (1981) for alluvium in the southern part of the Santa Clara Valley. Velocity logging of a shallow borehole just north of the study area found a lower shear-wave velocity in the top 30 m of the alluvium (Joyner and others, 1976). Using such a lower velocity, however, would reduce the accuracy of the finite-difference method for a given frequency. Reflectivity synthetic seismograms generated from a plane-layered model show that adding a 100-m-thick layer with a very low velocity (300 m/s) on top of the 600-m/s alluvium can significantly increase the duration of motion. This result implies that the finite-difference synthetic seismograms may underestimate the duration of shaking because of the relatively high shear-wave velocity chosen for the alluvium in the model.

We chose a *P*-wave velocity (V_P) of 1.1 km/s for the alluvium, lower than the 1.8-km/s velocity for the alluvium found in refraction surveys to the north of the study area (Hazlewood, 1976). Using this larger V_P value in the simulation caused an instability in the free-surface boundary condition (see Vidale and Clayton, 1986). The difference between the V_P value used in the model and the measured value will alter somewhat the dispersion curve of the Rayleigh waves (see fig. 6). For a plane-layered model with an alluvium thickness of 400 m, we found that the group velocity of the Airy phase of the fundamental-mode Rayleigh wave increases from 0.22 to 0.30 km/s for V_P values of 1.1 and 1.8 km/s, respectively (see below).

We chose a *P*-wave velocity of 3.5 km/s and an *S*-wave velocity of 2.0 km/s for the bedrock, similar to the velocity found by Joyner and others (1981) for Franciscan bedrock at the base of a 180-m-deep borehole in the southern part of the Santa Clara Valley. Our V_P value is comparable to the 4.0-km/s velocity for the bedrock found in refraction profiles to the north by Hazlewood (1976). In summary, the model used in our simulation had a shear-wave-velocity contrast of 0.6 to 2.0 km/s at the alluvium-bedrock contact. No smoothing was applied; this transition occurred over one grid spacing.

We assigned a velocity that was uniform with depth for the bedrock because of the way the source was incorporated

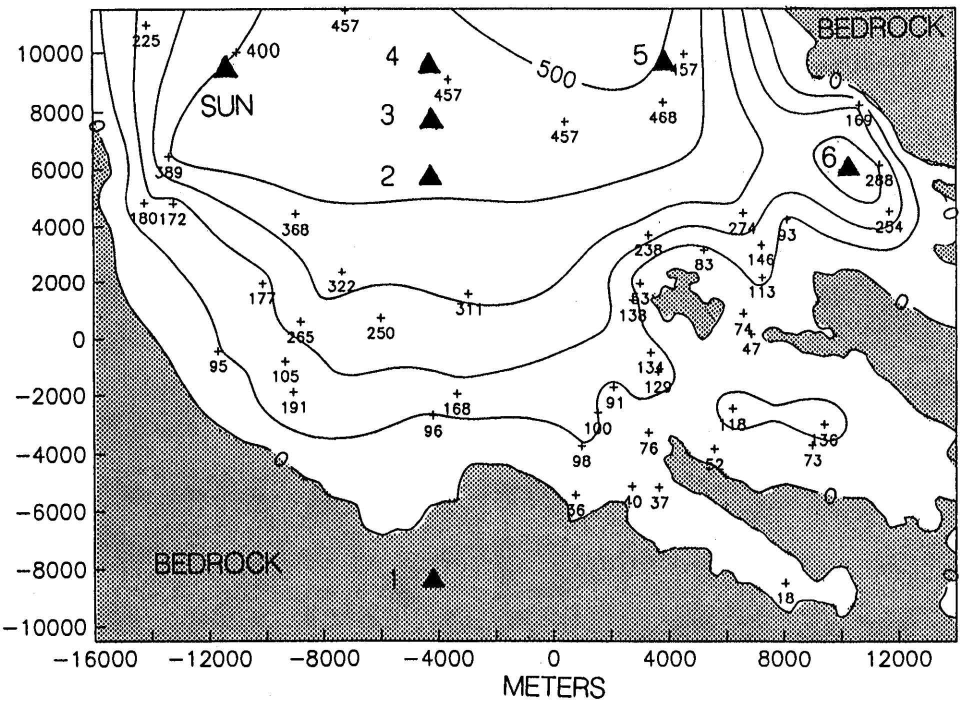

Figure 3.—Model of the Santa Clara Valley used in three-dimensional simulation. Area corresponds to box in figure 1. Contours denote depth of alluvium derived from fit to water-well data and assigned depth points; contour interval, 100 m. Shading indicates areas where bedrock is exposed at surface. Most crosses in basin show locations of water wells; numbers indicate depth to bedrock (in meters) (from California Department of Water Resources, 1967). Crosses with 400-m depth near Sunnyvale dense array (SUN) and 457-m depth in center of valley show locations of wells with postulated depths not obtained from water-well information (see text). Triangles show locations of stations used for synthetic seismograms plotted in figures 5 through 8. Line with zero depth is alluvium-bedrock contact.

into the simulation. The grid was not large enough to include the hypocenter, and so we specified the source by imposing synthetic seismograms along the south side and bottom of the grid. Each synthetic seismogram was a simple two-sided velocity pulse whose peak amplitude was determined by the far-field *S*-wave solution for an earthquake in a whole space. For each gridpoint on these two sides, the radiation pattern for an earthquake with the focal mechanism and location of event 1 was calculated on the basis of the angle of incidence for a uniform whole space. The focal mechanism for this aftershock was mainly thrusting (strike, 125°; dip, 25°; rake, 100°; Oppenheimer, 1990). The peak amplitude of each velocity seismogram inserted into the grid was specified so that its corresponding displacement pulse had an area Ω_0 given by (Aki and Richards, 1980)

$$\Omega_0 = \frac{M_0 R_{\theta\phi}}{4\pi(\beta_r \rho_r \rho_s)^{1/2} \beta_s^{5/2} R}, \qquad (1)$$

where M_0 is the seismic moment, $R_{\theta\phi}$ is the radiation-pattern coefficient, R is the distance between gridpoint and hypocenter, β is the *S*-wave velocity, and ρ is the density. The subscripts "s" and "r" denote values at the source depth and the receiver, respectively. In our case, the receivers are located along the south side and bottom of the grid, in bedrock. Equation 1 accounts for the amplitude difference caused by the impedance contrast between the source velocity and the receiver velocity. We used β_r=2.0 km/s, β_s=3.4 km/s, and $\rho_r=\rho_s$ g/cm^3. The shear-wave velocity at the source depth (10.2 km) for event 1 was estimated from the *P*-wave-velocity model of Dietz and Ellsworth (1990).

The seismic moment for event 1 was determined from *S*-wave-displacement spectra derived from recordings by General Earthquake Observation System (GEOS) instruments at stations KOI and DMD (fig. 1; see Mueller and Glassmoyer, 1990), located at hypocentral distances of 11 and 23 km, respectively. Long-period spectral levels of Ω_0 were estimated from both horizontal components and summed vectorially. The seismic moment was calculated from the expression

$$M_0 = \frac{4\pi(\beta_r \rho_r \rho_s)^{1/2} \beta_s^{5/2} R \Omega_0}{F R_{\theta\phi}}, \qquad (2)$$

where F is the free-surface correction, here taken to be 2. For the moment calculation, we used an average radiation-pattern coefficient of 0.67 (Boore and Boatwright, 1984) and a shear-wave velocity at the receiver of 2.0 km/s. β_s was set at 3.4 km/s, as above. On the basis of these values, we calculated a seismic moment of 5.2×10^{22} dyne-cm for event 1. This value was used in equation 1 to specify the amplitudes of the synthetic waveforms inserted into the finite-difference grid.

SNAPSHOTS AND SYNTHETIC SEISMOGRAMS FROM THREE-DIMENSIONAL SIMULATION

Color snapshots of the east-west component of velocity at four times in the three-dimensional simulation are shown in figures 4*A* through 4*D*. Both a map view (right) and a vertical cross section (left) are shown for each time; the cross section left is for a north-south slice 12 km from the west edge of the simulation, through the part of the basin with the greatest north-south extent in the grid. Both the map views and the cross sections show the location of the alluvium-bedrock contact in the basin. The snapshot for 5 s after the start of the simulation (fig. 4*A*) displays the initial *S*-wave pulse that was inputted along the south side and bottom of the grid. This is a two-sided pulse, with westward motion (green) followed by eastward motion (dark blue) of equal amplitude and duration; the input pulse has a period of 1.6 s. Note the node in the radiation pattern near the east side of the grid. There is some motion out ahead of the *S* wave traveling westward in the lower left part of the grid that appears to be *S*- to *P*-wave conversions from the south border of the basin. Minor motions are also observed out in front of the *S* wave in the basin, which are *S*- to *P*-wave conversions from the bottom of the basin. Because the source is located well to the south of the grid, most of the input *S*-wave energy on the east-west component consists of *SH* waves.

The snapshot at 11 s (fig. 4*B*) illustrates seismic energy reverberating in the basin. We see several east-west-trending wavefronts south of the initial *S* wave. The northernmost dark-blue band is wider than the initial green wavefront because it contains the blue wavefront from the backswing of the initial *S* wave, followed immediately by the blue band from the *S* wave that was reflected first by the free surface and then by the alluvium-bedrock contact. Each reflection at this interface produces a polarity reversal. The basin reverberations are confined to areas of the basin at least 100 m thick, where the basin is at least two gridpoints thick (counting the free-surface gridpoint). The wavefronts curve around the Oak Hill area (fig. 1) and generally parallel the contour lines of basin depth (compare fig. 3); trapped energy can also be observed in the subbasin just to the north of the Santa Teresa Hills. In the vertical cross section for 11 s (fig. 4*B*), the free-surface reflection of the initial *S* wave forms the right side of the inverted-V shape in the northern part of the map view. Energy from multiple reflections within the alluvium leak out into the bedrock, as shown by the tails extending below the alluvium in the cross section.

The snapshot at 11 s (fig. 4*B*) displays the beginning of a Love wave produced along the southern part of the basin (narrow red band near middle of map view). Successive *S*-wave reflections within the southern part of the basin have decreasing phase velocities because of the northward dip of the alluvium-bedrock contact. Eventually, these multiple reflections are critically trapped within the alluvium, producing Love waves. The Love waves have shorter periods with decreasing phase velocity, producing a dispersed wavetrain with long-period waves followed by a large, short-period Airy phase. This Airy phase can be identified by its low group velocity in the time slices and in the synthetic seismograms discussed below. The Airy phase of the Love wave contains the largest amplitude in the simulation for the east-west component and comprises the red band in the time slices. Note how the separation between wavefronts decreases from north to south in the snapshot, exhibiting normal dispersion. This pattern is maintained as the wavefronts propagate northward.

In the snapshot at 17 s (fig. 4*C*), the initial *S*-wave pulse has propagated out of the grid to the north. Now, the energy in the basin consists of multiple body-wave reflections and surface waves. The Airy phase of the Love wave (red area) has propagated farther north at a much lower speed than the initial *S* wave and its multiple reflections.

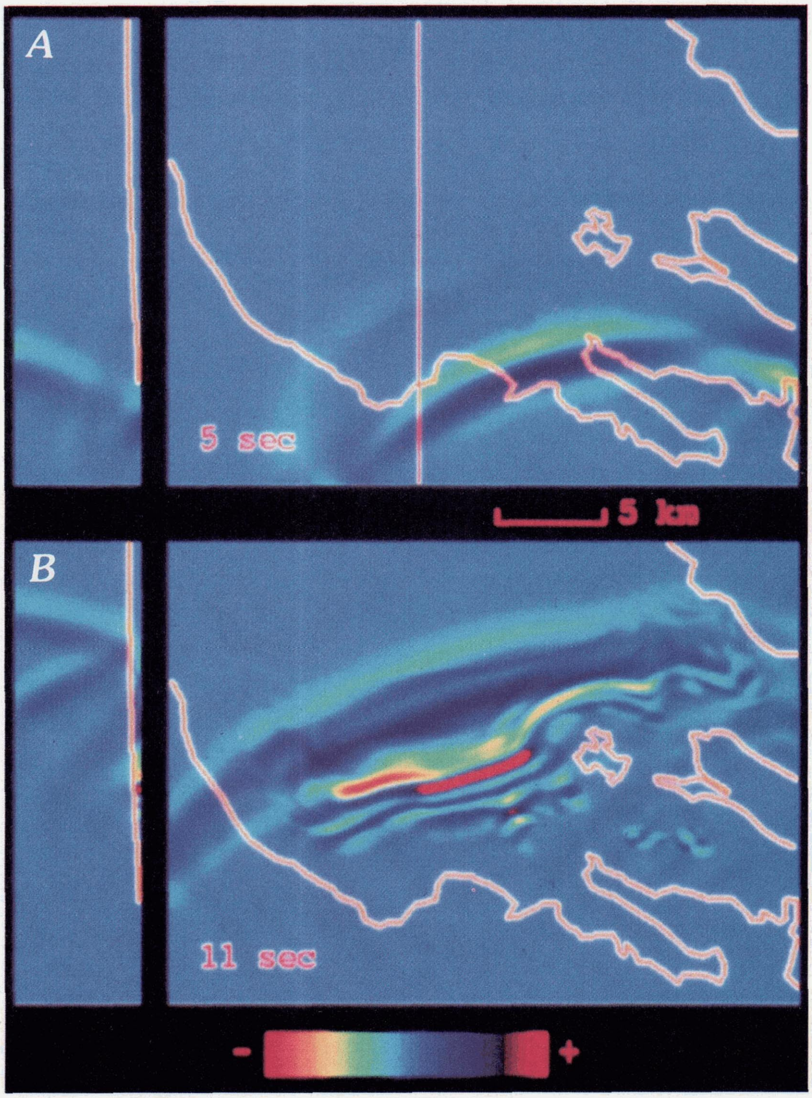

Figure 4.—Snapshots of east-west (*A–D*) and north-south (*E, F*) components of velocity from three-dimensional simulation of event 1 (Frankel and others, 1991), showing map view (right; 22 by 30 km) and cross section (6 by 22 km) at each time step. Amplitude of ground velocity is color keyed to palette at bottom: eastward motion, positive; westward motion, negative. Vertical line in figure 4*A* denotes location of cross sections, intersecting line of stations 1 through 4 (fig. 3). Depth in cross sections increases to left. Orange outlines denote location of alluvium-bedrock contact. Maximum velocity: 0.25 cm/s (*A–D*), 0.34 cm/s (*E, F*).

As before, this Love wave forms the largest amplitude on the east-west component. The vertical cross section shows that the energy in the southern part of the basin is trapped within the alluvium. The northernmost green wavefront has energy extending southward below the alluvium, indicating that it is precritically reflected at the alluvium-bedrock contact.

In the snapshot at 23 s (fig. 4*D*), the wavefronts are more segmented in space, and the wavefield in the basin is even more complex than before. The Airy phase of the Love wave (red band in upper middle of map view) is, as before, the largest motion in the snapshot. We also see north-south-trending wavefronts in the northeastern part of the basin. This is surface-wave energy that has been produced along the steep northeast edge of the basin by conversion of incident *S* waves and scattering of Rayleigh waves traveling northward in the eastern part of the basin (see below). The scattered surface-wave energy is traveling westward across the basin and, because it is radially polarized, consists of Rayleigh waves. We discuss these significant arrivals further below.

Snapshots of the north-south motions at 12 and 16 s are shown in figures 4*E* and 4*F*, respectively. At 12 s, the initial *S* wave is near the north end of the grid (fig. 4*E*). Several bands follow the initial wavefront, consisting of body waves multiply reflected in the alluvium. The bright-yellow-green band just north of Oak Hill (fig. 1) is a Rayleigh wave. As the *S* wave multiply reflects within the alluvium, its phase velocity decreases because of the northward dip of the alluvium-bedrock contact. Eventually, the body waves become critically reflected and form Rayleigh waves within the alluvium. We show below that the Rayleigh waves manifested in the north-south motions are probably first-higher-mode Rayleigh

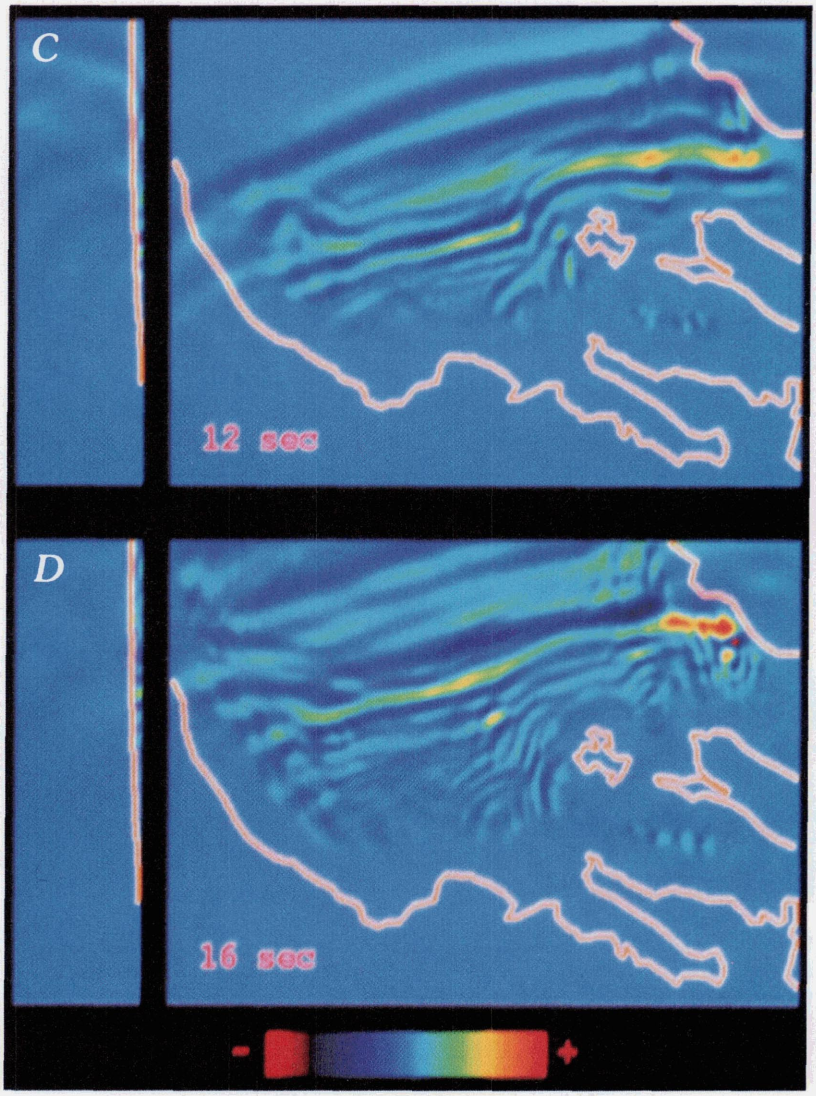

Figure 4.—Continued.

waves. Note that the north-south amplitudes increase eastward in the time slices shown in figures 4*E* and 4*F*, owing to the radiation pattern of the earthquake.

The snapshot of north-south motion at 16 s (fig. 4*F*) contains the largest horizontal motion observed in the simulation (0.34 cm/s). These large motions occur along the northeastern margin of the valley and show up as the red areas. The Rayleigh wave produced in the basin impinges on the edge of the basin and increases in amplitude, indicating that large amplitudes can occur when surface waves within the valley meet the far edges of the basin. Scattering of the Rayleigh wave at the northeastern margin of the basin produces much of the westward-propagating Rayleigh waves observed in the snapshot of east-west motion at 23 (fig. 4*D*). Another notable feature in figures 4*E* and 4*F* is the energy scattered from Oak Hill (fig. 1) that propagates northwestward; the wavefronts for this scattered energy are oriented approximately north-south.

The synthetic velocity seismograms for four surface sites on a north-south line (see fig. 4 for locations) are plotted in figure 5. Site 1 is located on bedrock, and the other sites on alluvium in the basin. The synthetic seismograms of the east-west, north-south, and vertical components are plotted with the same amplitude scale. The synthetic seismograms of the east-west and north-south components approximately represent the transverse and radial components of motion, respectively. These synthetic seismograms document the large amplitude and prolonged duration of shaking for basin sites relative to bedrock sites. The east-west component of the initial *S*-wave pulse is about twice as large at the basin sites as at the bedrock site, whereas the north-south and vertical components have similar initial *S*-wave amplitudes at the basin and bedrock sites.

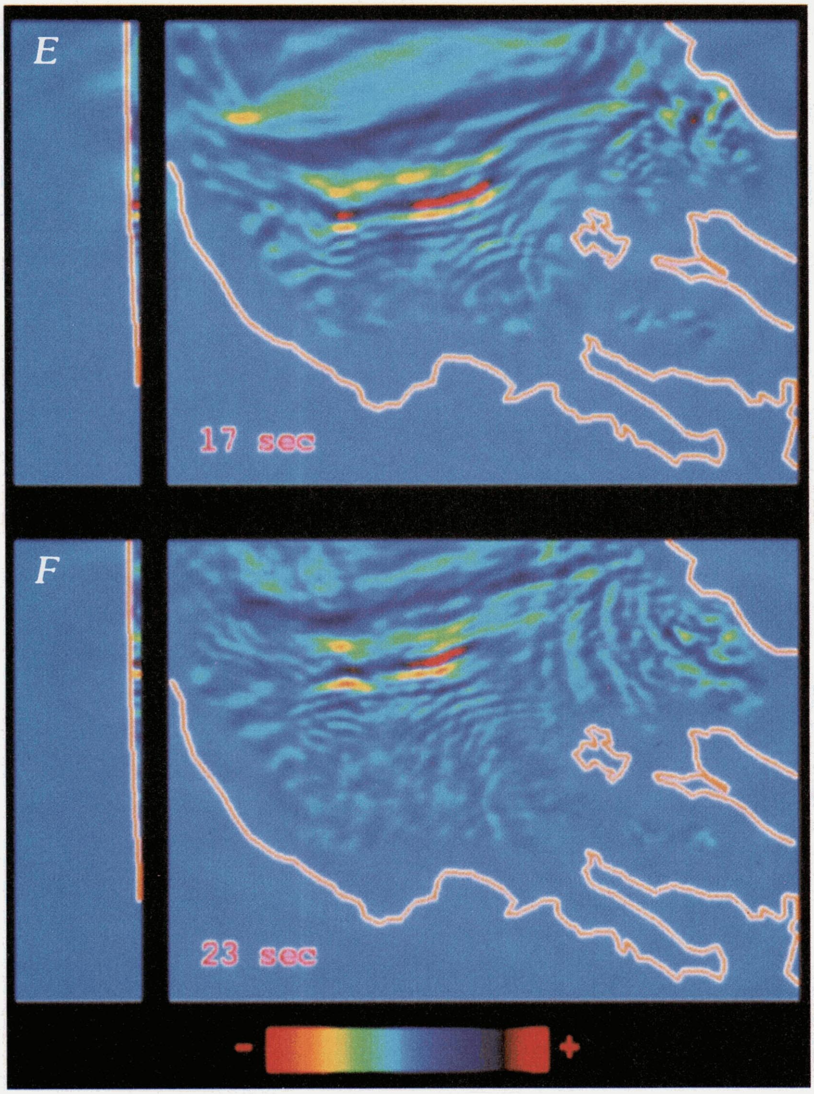

Figure 4.—Continued.

The Airy phase of the Love wave produced near the south edge of the basin is clearly visible on the east-west-component synthetic seismograms for the basin receivers; this phase represents the largest amplitude in these synthetic seismograms. At the northernmost receiver (site 4, fig. 4), the Airy phase controls the overall duration of significant ground motions on the east-west-component synthetic seismograms. Thus, sites near the center of the basin sustained longer durations of motion than basin sites near the border of the valley.

We compared the group velocities of the Love and Rayleigh waves observed in the simulations with those predicted by using a flat-layered model for the basin. We used an alluvium thickness of 400 m. Alluvium and bedrock velocities were the same as those used in the simulations; phase and group velocities and eigenfunctions for Love and Rayleigh waves were computed by using the method of Saito (1967). The dispersion curves calculated from this model for Love waves and fundamental-mode and first-higher-mode Rayleigh waves are plotted in figure 6. We found that the flat-layered model produces a Love-wave Airy phase at a period of 2.5 s with a group velocity of 0.41 km/s. We measured a group velocity of about 0.5 km/s on the synthetic seismograms plotted in figure 5 for the part of the Love wave with the largest amplitude, consistent with the group velocity for the flat-layered model. Thus, the east-west-component synthetic seismograms are characterized by a dispersed Love wavetrain with short-period energy following longer period energy and culminating in an Airy phase.

Anelastic attenuation will reduce the amplitude of the Love wave as it propagates in the basin. Using a shear-wave Q value of 20 for the alluvium, a traveltime of 10 s, and a period of 2 s reduces this amplitude by a factor

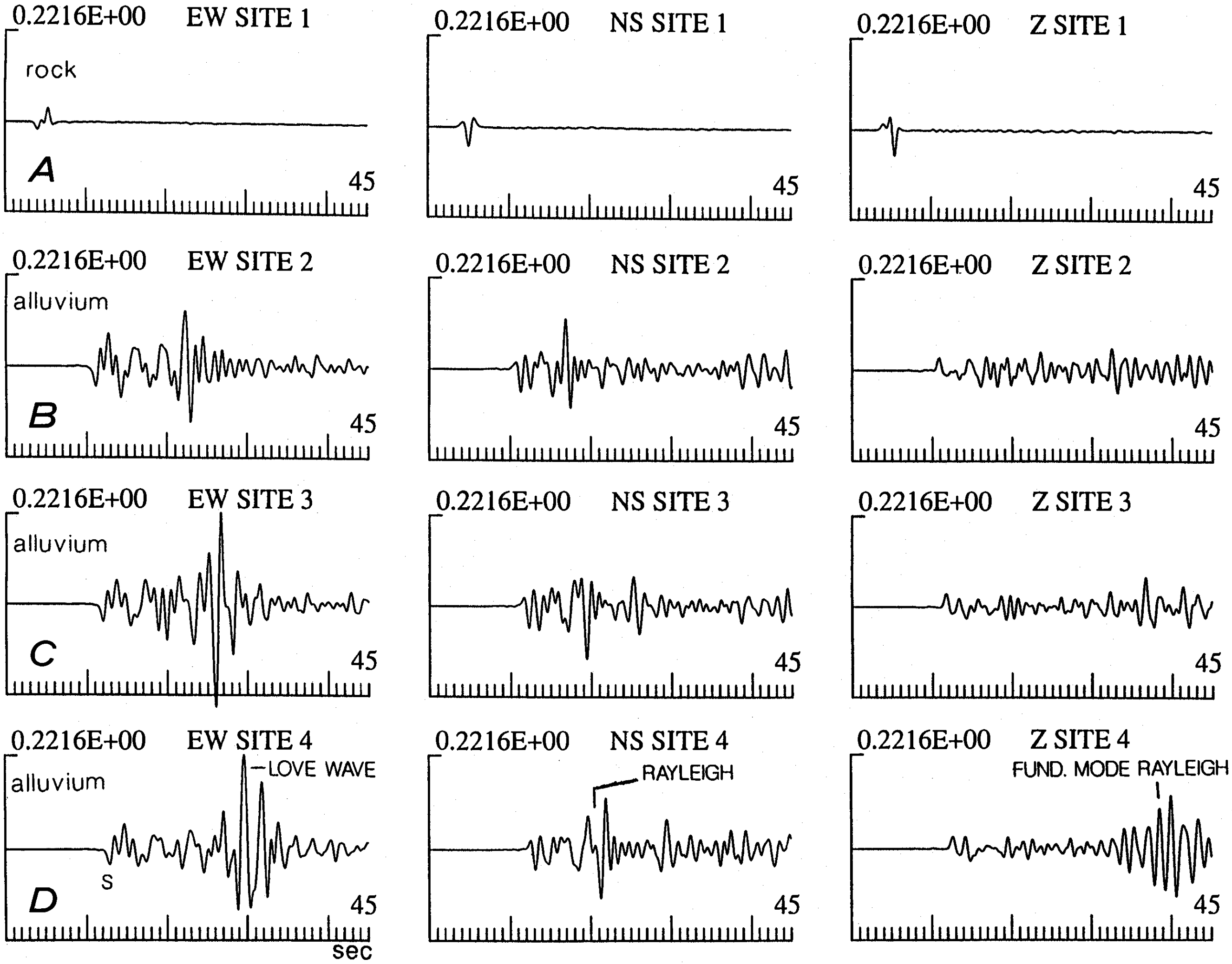

Figure 5.—Synthetic seismograms of east-west (left), north-south (middle), and vertical (right) components of velocity at stations 1 (*A*), 2 (*B*), 3 (*C*), and 4 (*D*) (see fig. 3 for locations). Note small amplitude and short duration of waveform at rock site (sta. 1) relative to basin sites (stas. 2–4), and that Love wave on east-west component has largest amplitude on seismograms and is increasingly delayed with respect to initial *S* wave as epicentral distance increases.

of 0.46. The Love wave, however, would still be comparable in amplitude to the direct *S* wave. Even with low *Q* values in the alluvium, the Love wave substantially increases the duration of shaking at basin sites.

Surface waves are also observed on the synthetic seismograms of the north-south and vertical components (fig. 5). A long-period phase arrives 4 to 7 s after the *S* wave on the north-south component at the basin sites. This is the arrival seen as a bright-yellow-green band in the snapshots shown in figures 4*E* and 4*F* and comprising the peak amplitude on the north-south-component synthetic seismograms (fig. 5). At site 4 (fig. 3), this arrival appears to be dispersed, with longer period energy preceding shorter period energy. We estimate the group velocity of this arrival at about 1.0 km/s, on the basis of the synthetic seismograms plotted in figure 5. This arrival is probably a mixture of fundamental-mode and first-higher-mode Rayleigh waves, on the basis of a comparison with the dispersion curves and eigenfunctions calculated for a flat-layered model. Both types of Rayleigh waves have similar group velocities to the synthetic arrivals and, for these periods, larger theoretical amplitudes on the radial than on the vertical component, also in agreement with the synthetic seismograms. The flat-layered model predicts a level segment of the group-velocity curve for the first-higher-mode Rayleigh wave at periods between 1.0 and 1.5 s with a group velocity of about 0.9 km/s (see fig. 6), comparable to that found in the synthetic seismograms. The eigenfunctions calculated for this higher mode Rayleigh wave indicate that its amplitude at those periods should be about 3 times larger on the radial than on the vertical component. This result may explain why the Rayleigh wave is observed mainly on the north-south-component synthetic seismograms and is conspicuous on the vertical-component synthetic seismograms (fig. 5). The fundamental-mode Rayleigh wave also has a group velocity of about 1.0 km/s for periods of 1.75 to 2.5 s (fig. 6). For these periods, the fundamental-mode Rayleigh wave has a predicted amplitude on the radial component 4 and 6 times that on the vertical component. We show below that the phase velocity of this arrival calculated from the synthetic seismograms is consistent with either the fundamental-mode or higher mode Rayleigh waves. We conclude that the largest arrival on the north-south-component synthetic seismograms is a Rayleigh wave generated by conversion of the incident *S* wave along the southern margin of the valley.

The vertical-component synthetic seismogram for site 4 (fig. 5*D*) shows a sizable Rayleigh wave near the end of the record. It is difficult to estimate the group velocity of this arrival because the arrival is distinct only at site 4 (fig. 3). The late arrival time indicates that it has a very low group velocity, much lower than the 0.5 km/s measured for the Love wave. The flat-layered model predicts the Airy phase of the fundamental-mode Rayleigh wave to have a period of 1.5 s and a very low group velocity of 0.22 km/s (see fig. 6). Furthermore, the Airy phase in the flat-layered model should be 2.1 times larger on the vertical than on the radial component, on the basis of its eigenfunctions. This prediction is consistent with the synthetic seismograms, where this arrival is clearly visible on the vertical component at site 4 but not on the north-south component. We conclude that this late arrival is a fundamental-mode Rayleigh wave in the alluvium, produced by conversion of the incident *S* wave. Analysis of the arrival times on synthetic seismograms at points adjacent to site 4 indicate that this arrival is propagating northward and is not a reflection from the north edge of the grid. This Rayleigh wave is indistinct at sites 2 and 3, implying that it may require a flat part of the alluvium-bedrock contact to develop.

The synthetic seismograms are compared with the records for event 1 from station SUNC of the Sunnyvale dense array (fig. 1) in figure 7. Both the synthetic seismograms and the observed data are rotated to the transverse and radial components and are low-pass filtered

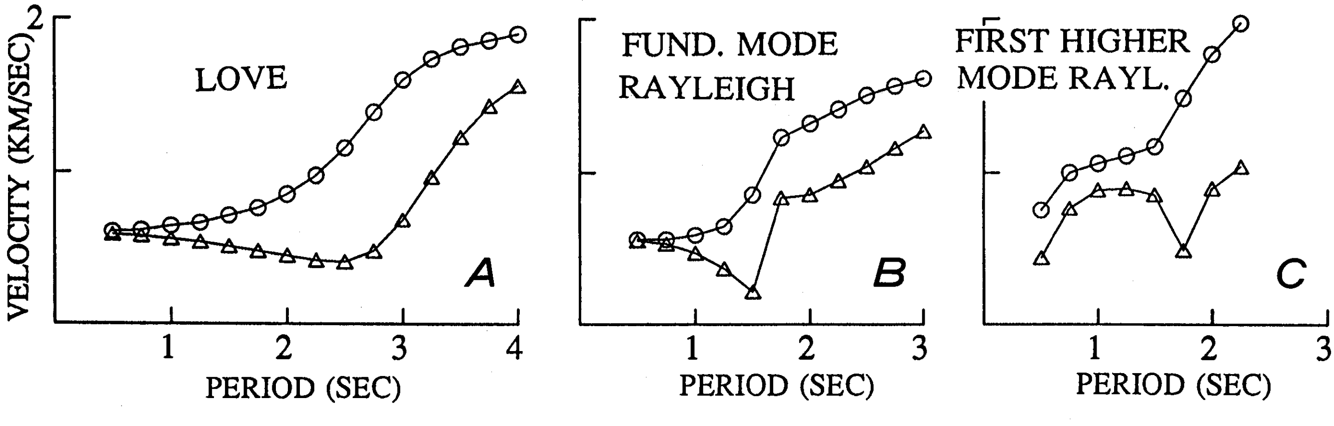

Figure 6.—Theoretical dispersion curves for Love wave (*A*), fundamental-mode Rayleigh wave (*B*), and first-higher-mode Rayleigh wave (*C*) in a 400-m-thick alluvium layer above a half-space (see text). Circles, phase velocities; triangles, group velocities.

with a corner frequency at 1 Hz. A high-pass filter with a corner frequency at 0.04 Hz was applied to the synthetic seismogram to remove a steplike artifact in the displacement seismograms. A Q operator that changes over time in the record was convolved with the synthetic seismograms to approximate the effect of anelastic attenuation on the waveforms (see Vidale and Helmberger, 1988). A different Q operator was applied to each 1.5 s window of the synthetic seismograms. Letting t denote time in the record, the t^* value for this operator was calculated from the relation

$$t^* = t^*_S + \frac{t - t_S}{Q} \ ,$$

where t_S is the arrival time of the direct S wave on the synthetic seismogram and Q is the value for alluvium. Note that $t^*_S = \int Q^{-1} dt$, where the integral is taken over the S-wave traveltime from source to receiver, assuming that the energy arriving at t has traveled t-t_S s in the alluvium. This method does not use separate P- and S-wave Q values. The Q value used here corresponds to the shear-wave Q value in the alluvium because the attenuation of surface waves (Love and Rayleigh) trapped in the alluvium is controlled by this shear-wave Q value.

The synthetic seismograms plotted in figure 7 were derived by using t^*_S=0.03 and Q=50 in the alluvium. This relatively high Q value for alluvium was chosen so that later-arriving Rayleigh waves would not be completely removed, in keeping with observations of late arrivals from the Sunnyvale dense array (see below).

In figure 7, the synthetic seismograms for the Sunnyvale dense array (SUN, fig. 3) are comparable to the recorded seismograms. The transverse-component synthetic seismograms contain a long-period Love wave after the S wave, analogous to the long-period Love wave observed on the recorded seismograms. However, the Love wave on the synthetic seismograms arrives only 8 s after the initial S wave, whereas the largest part of the observed Love wave arrives 17 s after the initial S wave (see Frankel and others, 1991). Thus, the transverse-component synthetic seismograms underestimate the duration of ground motions. This discrepancy may be due to using a shear-wave velocity for the alluvium that is too high or to underestimating the thickness of the alluvium south of the array. Frankel and others (1991) demonstrated that a flat-layered structure cannot produce the observed Love waves. Although our simulation does not duplicate the timing of these arrivals, it does demonstrate that the observed Love waves were likely pro-

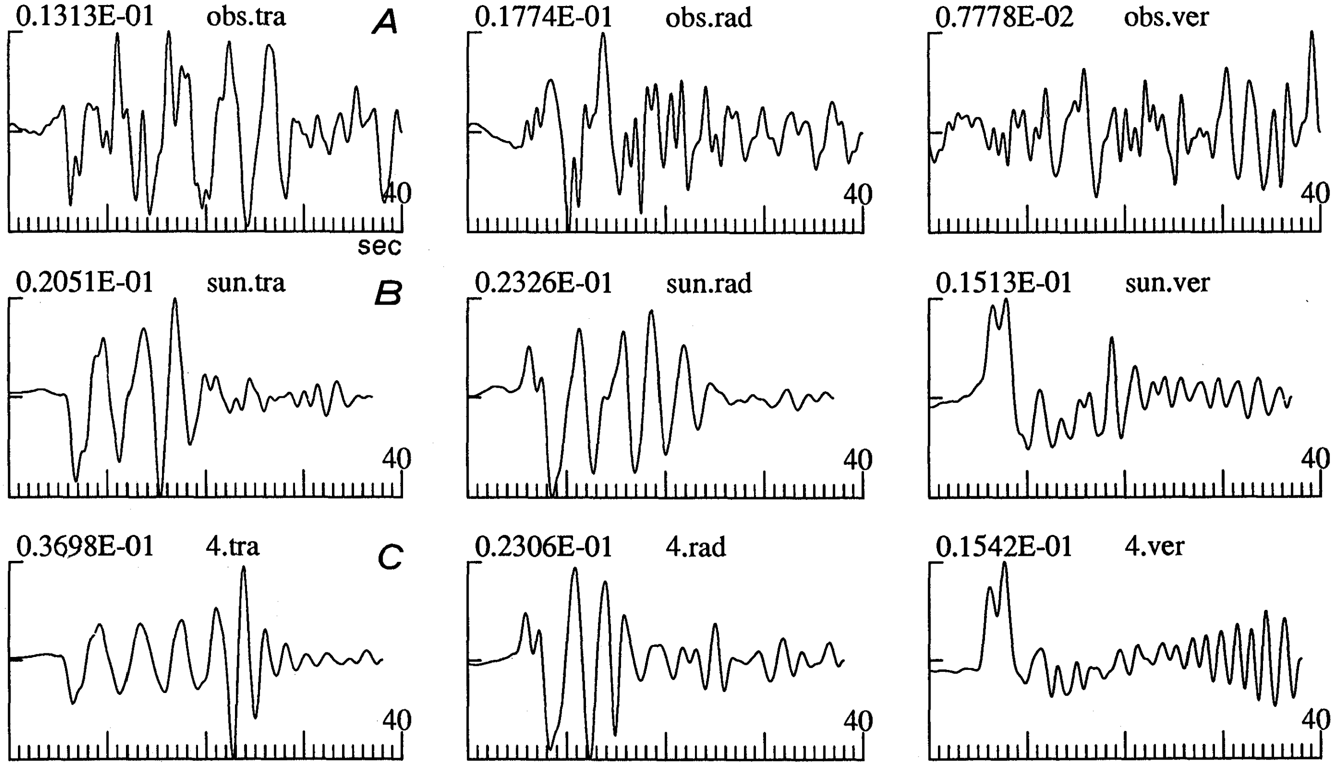

Figure 7.—Seismograms of transverse (left), radial (middle), and vertical (right) components of displacement recorded at station SUNC in Sunnyvale dense array (SUN, fig. 3) (*A*) and synthesized for that site (*B*) and station 4 (*C*). Seismograms were processed with a Q operator that varies over time.

duced by conversion of the incident *S* wave near the southern margin of the valley.

The radial-component synthetic seismograms for the Sunnyvale dense array (SUN, fig. 3) are similar in duration to the recorded seismograms. The long-period Rayleigh wave at about 2 s after the *S* wave on the recorded seismogram arrives at a similar time on the synthetic seismogram. This is the first-higher-mode Rayleigh wave described above, produced by conversion of the incoming *S* wave. There is little correspondence between the vertical-component synthetic and recorded seismograms. The direct *S*-wave arrival is conspicuous on the vertical-component synthetic seismogram but not on the recorded seismogram, possibly owing to overestimation of the shear-wave velocity in the near-surface. Using a lower *S*-wave velocity would cause the *S* wave to be more steeply incident at the surface, reducing its amplitude on the vertical component.

The peak amplitudes on the transverse- and radial-component synthetic seismograms for the Sunnyvale dense array (SUN, fig. 3) are 1.6 and 1.3 times those on the recorded seismograms, respectively. Considering the simplistic velocity model used in the simulations, this similarity is encouraging.

To gain insight into how differences in site location affect the synthetic seismograms, the synthetic displacement seismograms for station 4, located about 7 km east of the Sunnyvale dense array (SUN, fig. 3), are plotted in figure 7*C*. These seismograms were processed with the same time-varying *Q* operator as the synthetic seismograms for the dense array. The Love waves have a longer travel path to station 4 in the basin than to the dense array. The Love wave on the transverse component at station 4 is delayed more than at the dense array, and the overall duration of strong motions is similar to that on the recorded seismogram for the dense array. Thus, if we had thickened the alluvium or decreased its velocity in our model south of the Sunnyvale dense array, we could have delayed the arrival of the Love wave on the synthetic seismograms for the dense array so that its arrival time matched that on the recorded seismograms. Our knowledge of the structure of the basin, however, is insufficient to accurately predict the duration of transverse motion at basin sites.

Another notable feature of the synthetic seismograms for station 4 is the fundamental-mode Rayleigh wave on the vertical component (fig. 7*C*). As mentioned above, this Rayleigh wave was converted from the *S* wave incident along the southern margin of the basin. Some late, long-period arrivals on the vertical-component recorded seismogram (fig. 7*A*) may correspond to such an *S*-wave to Rayleigh-wave conversion. If we had used *Q* values much smaller than 50, this Rayleigh wave would have an insignificant amplitude on the synthetic seismogram. The presence of such late arrivals in the recorded seismograms may place a lower limit on the effective *Q* value for Rayleigh waves in the alluvium.

Synthetic seismograms for stations along an east-west line across the valley, along with station 6 located within the eastern part of the valley, are plotted in figure 8. These are the original synthetic velocity seismograms and do not incorporate anelastic attenuation. The east-west motions have a longer duration of shaking and larger peak amplitudes at station 4 in the center of the valley (fig. 3) than at the other stations closer to the edges of the basin. In contrast, the north-south motions have about the same duration of shaking, regardless of the location of the station within the valley. Both the north-south and vertical motions are relatively large at station 6 in the eastern part of the valley, within a part of the basin model that has a depth of 300 m, with shallower depths surrounding it. Although some of this amplitude difference may be due to radiation pattern, much of it must be caused by propagation effects, such as focusing or resonance, within this enclosed, deeper part of the basin.

MOVING-WINDOW ANALYSIS OF SYNTHETIC SEISMOGRAMS

We calculated the synthetic seismograms for closely spaced receivers so that we could use a moving-window analysis to determine the apparent velocity and direction of propagation for various arrivals. Three arrays were considered, each with nine receivers arranged in a square, with three stations on a side; the station spacing in both the north-south and east-west directions was 200 m. We used the cross-correlation method for determining vector slowness that was applied by Frankel and others (1991) to seismograms of the Loma Prieta aftershock recorded by the Sunnyvale dense array. This method finds the maximum cross-correlation of waveforms over a range of north-south and east-west slownesses for a windowed portion of the seismograms. The vector slowness corresponding to the maximum cross-correlation represents the slowness of arrivals in that window.

The results from the moving-window analysis of the east-west-component synthetic seismograms for an array located around the Sunnyvale dense array (SUN, fig. 3) are plotted in figure 9*A*. Only the results for windows with cross-correlation of at least 0.8 are shown. A window size of 2 s was used. The initial *S* wave has an apparent velocity of 1.7 km/s and a backazimuth of 153°, essentially the same as the backazimuth to the epicenter (measured clockwise from north). The apparent velocity is about equal to that expected for the direct *S* wave, considering propagation across the north-dipping alluvium-bedrock contact. Transmission of the direct *S* wave across an alluvium-bedrock contact dipping 5° N.

would produce an *S* wave with an apparent velocity of 1.6 km/s.

The apparent velocities of arrivals on the synthetic seismograms generally decrease over time (fig. 9*A*). These results are qualitatively similar to those from the Sunnyvale dense array for the four Loma Prieta aftershocks studied by Frankel and others (1991). For times between 20 and 40 (fig. 9*A*), the apparent velocities are generally from 1.0 to 1.1 km/s, significantly lower than that of the initial *S* wave. These low apparent velocities indicate that these later arrivals are surface waves. Because the east-west component is oriented approximately transverse to the direction of propagation, these surface waves are Love waves. The Love wave comprises the largest phase on the synthetic seismogram, at 24 s. A flat-layered basin model predicts a phase velocity of 1.2 km/s for the Airy phase of the Love wave, similar to the phase velocity obtained in the moving-window analysis. This result lends further support to our interpretation of the largest arrival in the east-west synthetic seismograms as the Airy phase of the Love wave.

The arrivals between 10 and 25 s have backazimuths somewhat greater than the backazimuth to the epicenter (fig. 9*A*), indicating that these surface waves are coming from a direction more southerly than the source. This direction is also apparent in the snapshots (fig. 4), where the surface waves at the west edge of the basin are propagating northward, nearly parallel to the west edge of the valley.

Later surface-wave arrivals on the synthetic seismograms for the Sunnyvale dense array (SUN, fig. 3) are propagating westward. Figure 9*A* shows that the arrivals at 37 to 41 s have backazimuths of 080°–100°. These arrivals represent surface waves scattered at the northeast edge of the valley by incident *S* waves and Rayleigh waves; these scattered surface waves then travel westward across the valley. The apparent velocity of these arrivals is about 1.0 km/s, indicating that they are sur-

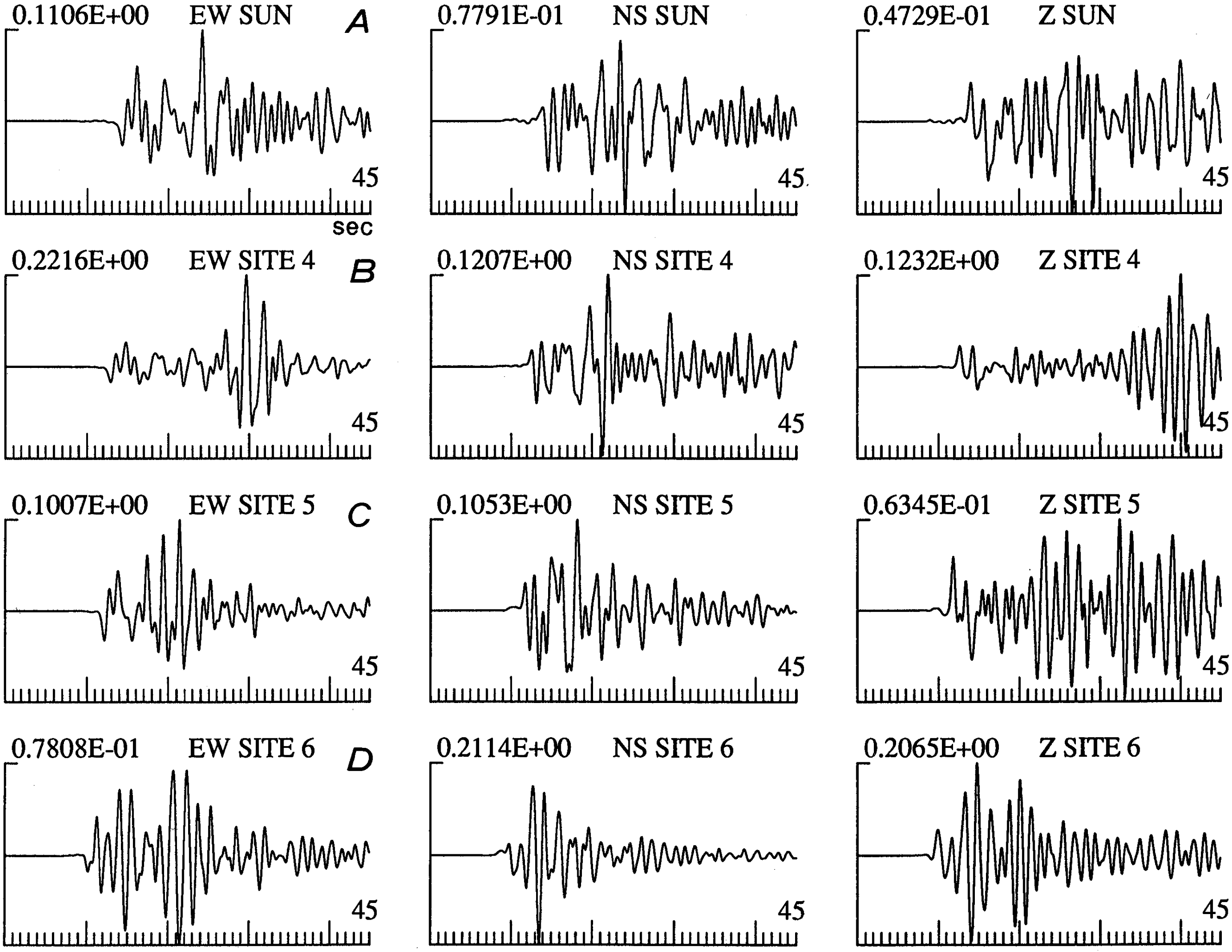

Figure 8.—Synthetic seismograms of east-west (left), north-south (middle), and vertical (right) components of velocity of Sunnyvale dense array (*A*) and stations 4 (*B*), 5 (*C*), and 6 (*D*) (see fig. 3 for locations). Seismograms do not include anelastic attenuation.

face waves. Because the east-west component nearly parallels the direction of propagation of these arrivals, we conclude that they are Rayleigh waves. These surface waves are apparent in the eastern part of the valley in the snapshot at 23 s (fig. 4*D*). Frankel and others (1991) found some surface-wave arrivals propagating northwesterly across the Sunnyvale dense array on the recorded seismograms for event 1; however, these arrivals occurred earlier on the recorded seismograms than on the synthetic seismograms. Westward-propagating surface waves start at about 10 s after the initial *S* wave on the transverse-component recorded seismograms, but not until 24 s after the *S* wave on the synthetic seismograms. Frankel and others suggested that the westward-propagating

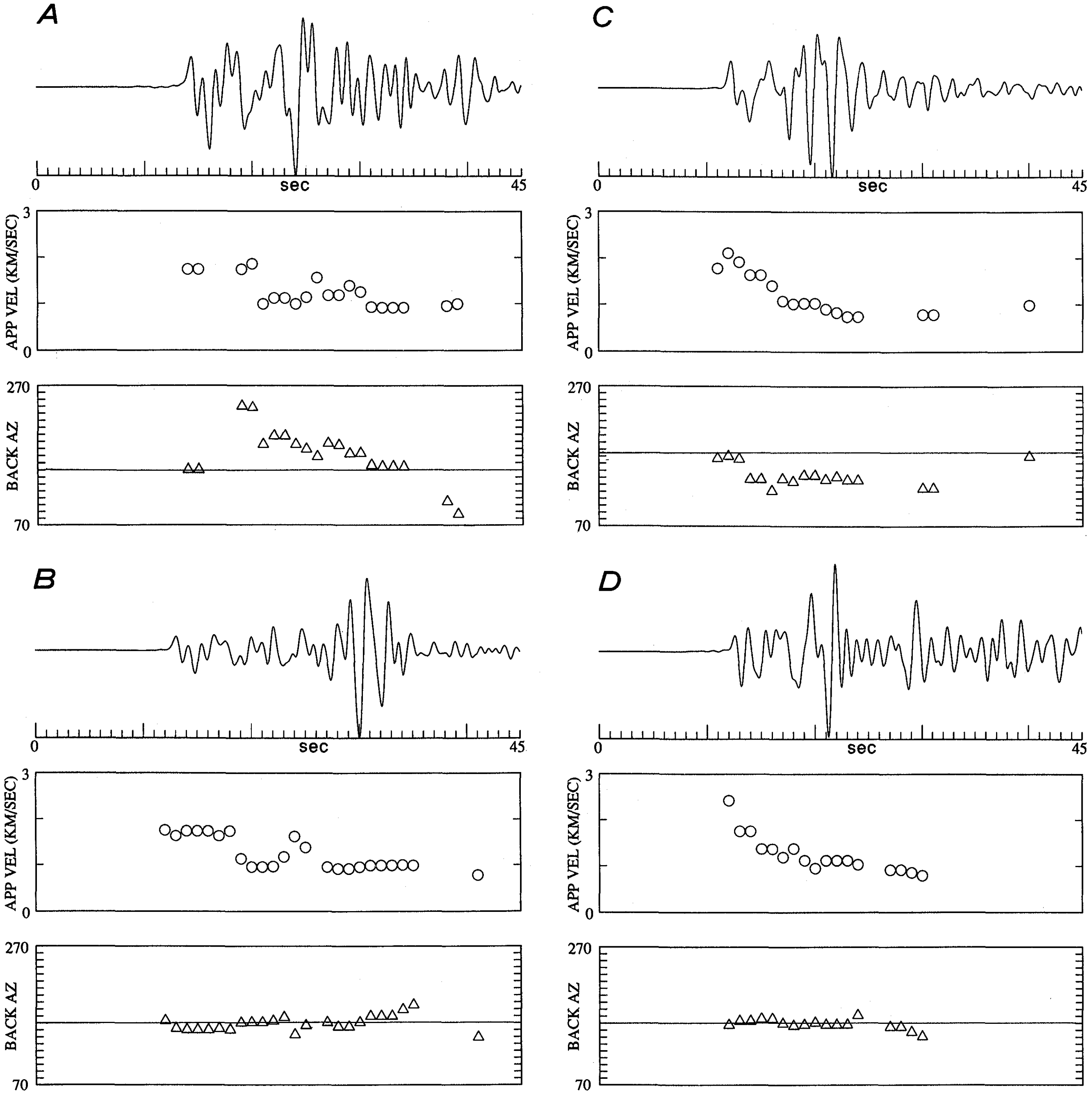

Figure 9.—Results from moving-window analyses of synthetic seismograms from small-aperture arrays in study area (see fig. 3 for locations). Top, one of nine synthetic velocity seismograms used in each analyses; middle, apparent velocity; backazimuth, bottom measured clockwise from north. Only data with a cross-correlation of at least 0.8 are plotted. Horizontal line in backazimuth plots indicates backazimuth to epicenter. *A*, Sunnyvale dense array (SUN, fig. 3), east-west component. *B*, Station 4, east-west component. *C*, Station 5, east-west component. Note decrease in apparent velocity over time indicating arrival of surface waves after direct *S* wave, *D*, Station 4, north-south component.

arrivals on the recorded seismograms may have been scattered from the vicinity of Oak Hill (fig. 1). Although the snapshots (fig. 4) show energy scattered around Oak Hill, some of it northwestward, it is unclear whether this energy has significant amplitude by the time it reaches the Sunnyvale dense array. Certainly, the moving-window analysis does not identify this energy. The large surface waves from the west edge of the basin appear to overwhelm the energy scattered from Oak Hill on the synthetic seismograms. The recorded seismograms for event 1 do not show the late-arriving energy from the east side of the basin apparent on the synthetic seismograms.

The results from the moving-window analysis of the east-west-component synthetic seismograms for an array located around station 4 (fig. 3) are plotted in figure 9*B*. Again, the apparent velocity decreases over time on the synthetic seismograms, indicating the transition from direct *S* wave through multiply reflected *S* waves to Love waves. The large arrival at 30 s, which has an apparent velocity of 1.0 km/s, is the Airy phase of the Love wave. Most arrivals are coming approximately from the source direction.

The results from the moving-window analysis of the east-west-component synthetic seismograms for an array located around station 5 near the east edge of the valley (fig. 3) are plotted in figure 9*C*. The apparent velocity decreases over time, and a large Love wave with a low apparent velocity arrives at 20 s. Most of the arrivals after the initial *S* wave have backazimuths less than the backazimuth to the epicenter, indicating that these arrivals propagate parallel to the northeast edge of the valley and along the long axis of the subbasin near that edge of the valley (see fig. 3).

In summary, the largest arrivals in the east-west-component synthetic seismograms consist of Love waves produced by conversion of the incident *S* wave at the edges of the basin. These arrivals can be identified by their low group velocity in snapshots of the wavefield (figs. 4–6) and on synthetic seismograms from widely separated receivers (fig. 5), as well as by their low apparent (phase) velocities found from measurements on arrays in the finite-difference grid (fig. 9). The arrival of the Airy phase of the Love waves determines the duration of strong motions at sites in the basin. Sites near the center of the basin (for example, sta. 4, fig. 3) have a longer duration than those near the edges of the basin (SUN, sta. 5) because of the increased delay of the Airy phase propagating into the basin (fig. 8).

The results from the moving-window analysis of the north-south-component synthetic seismograms for an array located around station 4 (fig. 3) are plotted in figure 9*D*. The apparent velocity decreases over time, and the largest arrival (at 21 s) has a phase velocity of about 1.1 km/s. Earlier in this paper, we identified this arrival as a Rayleigh wave. This apparent velocity is essentially the same as that found for a first-higher-mode Rayleigh wave for periods of 1.0 to 1.5 s, on the basis of a flat-layered basin model (fig. 6). The longer period energy just preceding the largest arrival has a slightly higher apparent velocity of 1.2 to 1.4 km/s (fig. 9*D*), approximately consistent with the phase velocities for the fundamental-mode Rayleigh wave for periods of 1.75 to 2.5 s (fig. 6). The measured phase velocities of the largest phase on the north-south component support our interpretation that it is a Rayleigh wave. Figure 9*D* also shows that the backazimuth of this arrival is about the same as the backazimuth to the epicenter.

The finite-difference synthetic seismograms and calculations for flat-layered models document that the Love and Rayleigh waves can have different periods than those predicted for *S* waves multiply reflected in the alluvium. For a 400-m-thick layer of alluvium (β=0.6 km/s), we would expect a resonant period of 2.7 s for multiply reflected *S* waves with vertical incidence. Here, the resonant period is given by $4H/V_S$, where H is the layer thickness and V_S is its shear-wave velocity (Haskell, 1960). Figure 7*C* shows that the Love wave contains significant amounts of longer period energy (≈4 s) preceding the Airy phase. The flat-layered basin model predicts that the Airy phase of the fundamental-mode Rayleigh wave will have a period of 1.5 s (fig. 6), significantly different from the resonant period for a vertically incident *S* wave. Thus, the frequency content of surface waves must be accounted for in the design of long-period structures located in sedimentary basins.

EFFECTS OF ANGLE OF INCIDENCE AND SHARPNESS OF VELOCITY TRANSITION

To assess how the *S*-wave to surface-wave conversion is affected by the angle of incidence, we used a two-dimensional *SH*-wave finite-difference program. The two-dimensional velocity model was a vertical cross section along a north-south slice 12 km from the left side of the grid. The cross sections on the left side of the time slices in figure 4 show the geometry of the alluvium-bedrock contact used in the two-dimensional model. The grid spacing for the two-dimensional runs was 100 m, the same as in the three-dimensional simulation. The grid was 220 gridpoints across and 100 gridpoints deep. The source was an isotropic point source situated in bedrock 4 km south of the south edge of the basin. Shear-wave velocities in bedrock and alluvium were 2.0 and 0.6 km/s, respectively, as in the three-dimensional simulation. By varying the depth of the source, we altered the angle of incidence of *S* waves on the edge of the basin;

source depths of 1, 5, and 9 km were considered. The angles of incidence (measured from upward vertical) at the south edge of the basin were 76°, 39°, and 24°, respectively.

The *SH*-wave synthetic seismograms for a receiver located in the basin 2 km from the north end of the grid (epicentral distance, 16 km) are plotted in figure 10. These synthetic seismograms are qualitatively similar to the east-west-component synthetic seismograms from the three-dimensional simulation for station 4 (see fig. 5). The *S* wave is followed by multiple reflections in the alluvium and then by a large, shorter period Love wave. As the source depth and angle of incidence increase, the Love wave becomes smaller relative to the direct *S* wave (fig. 10). We would expect that trapping of Love waves in the basin would be more efficient for shallow angles of incidence. We emphasize that, even with the steep angle of incidence for the 9-km-deep source, the Love wave is substantial and has a greater amplitude than the direct *S* wave, demonstrating that *S*-wave to Love-wave conversion at the edge of basins is important even for steeply incident *S* waves (see Bard and Bouchon, 1980a).

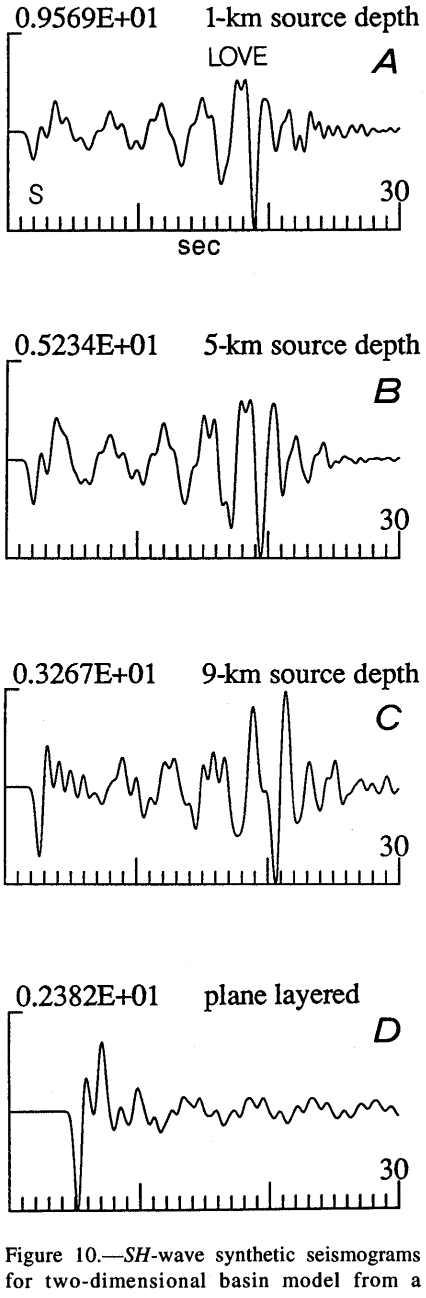

Figure 10.—*SH*-wave synthetic seismograms for two-dimensional basin model from a north-south vertical cross section located 12 km from wet edge of basin (see fig. 3). Source is located 4 km south of south edge of basin at depths of (*A*) 1 km, (*B*) 5 km, and (*C*) 9 km. Note large Love wave at 18 to 20 s for all source depths. Figure 10 *D* shows synthetic seismogram for plane-layered alluvium-bedrock contact at source depth of 5 km; no Love wave is observed.

It is enlightening to compare these synthetic seismograms with that from a flat-layered crustal model. Figure 10*D* shows the synthetic seismogram for the case where the source is at 5-km depth and the alluvium-bedrock contact is horizontal at 400-m depth; the receiver is located at an epicentral distance of 16 km, as in the above examples. Now, we see that in a flat-layered model, effectively no Love wave is produced at this distance for a source at this depth. This synthetic seismogram has much less duration of shaking than for the cases with a dipping interface. It is the dip of the alluvium-bedrock contact away from the source that produces the Love wave. As the *S* wave is multiply reflected within the alluvium, its angle of incidence becomes more grazing, and so eventually the *S* wave is critically trapped in the alluvium, forming the Love wave.

Another critical question is how the *S*-wave to surface-wave conversion is affected by the sharpness of the transition between the alluvium and bedrock. To address this question, we specified a region of transitional velocity between the alluvium and bedrock. We started with the original model, with a 0.6-km/s alluvium and 2.0-km/s bedrock. We then added two layers just below the basin and along its south edge; each transitional layer was 200 m thick. The layer closest to the basin had a shear-wave velocity of 1.0 km/s, and the next-outer layer a shear-wave velocity of 1.5 km. The synthetic seismograms for both the original, abrupt boundary and the transitional boundary, for a source depth of 5 km, are plotted in figure 11. Because of the presence of more layers, the transitional structure produces a more complex seismogram. The Love-wave conversion from the incident *S* wave still occurs with the transitional boundary, exhibiting large amplitudes at about 20 s. This result indicates that *S*-wave to surface-wave conversion is still significant when there is a transitional boundary between the alluvium and bedrock. Wider transition zones may reduce the amplitude of this conversion, especially if the transition occurs over a distance much greater than a wavelength.

DISCUSSION

The three-dimensional simulation provides important insights into how seismic waves propagate in a sedimentary basin with a realistically complex geometry. The synthetic seismograms show that the duration of shaking depends strongly on position within the basin, with sites near the edge sustaining less duration than sites in the middle of the basin. Probably the most important feature is the conversion of incident *S* waves to surface waves at the edges of the basin. This conversion has been previously reported for two-dimensional simulations, but the three-dimensional simulation illustrates how the wavefronts are distorted and scattered by the irregular bedrock topography. The three-dimensional simulation also shows that body-wave to surface-wave conversion occurs not only at the south edge of the valley but also at the northeast edge. The results of this simulation qualitatively explain the presence of surface waves in the seismograms recorded by the Sunnyvale dense array (SUN, fig. 3) and the variation in backazimuth observed for later arrivals on these seismograms (see Frankel and others, 1991). The prolonged duration of shaking due to these surface waves increases the seismic hazards to long-period structures located in sedimentary basins, such as highway overpasses, tall buildings, and pipelines. Therefore, synthetic seismograms from three-dimensional simulation should, in the future, have an important role to play in the design of such structures.

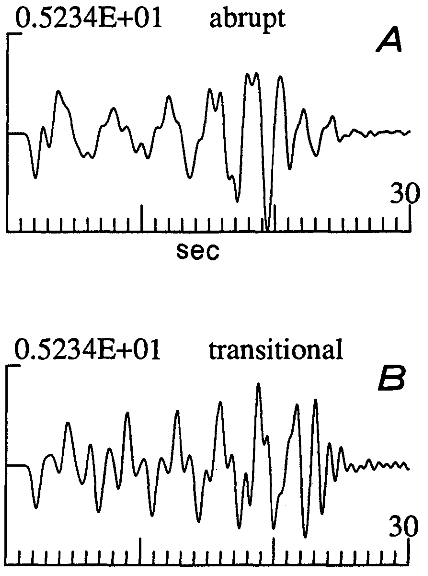

Figure 11.—*SH*-wave synthetic seismograms for two-dimensional models with abrupt (*A*) and transitional (*B*) boundary between the alluvium and bedrock (see text for explanation). Source-receiver configuration same as in figure 10; source depth, 5 km.

We have shown that large-scale three-dimensional simulations are computationally feasible for realistic basin models. A major limitation is the absence of detailed three-dimensional velocity models for many basins of interest. There is a critical need for a more detailed model of the Santa Clara Valley if progress is to be made on matching the observed waveforms and predicting shaking for future earthquakes by using three-dimensional simulations. The depth of the alluvium in the Santa Clara Valley is not known except along the edges of the basin, and so the dominant periods of multiple body-wave reflections and surface waves cannot be predicted. Analysis of the dense-array data for the Loma Prieta aftershock indicates surface-wave arrivals from the southeast, starting about 10 s after the direct *S* wave (Frankel and others, 1991). The east-west-component synthetic seismogram for the Sunnyvale dense array (SUN, fig. 3) shows face-wave arrivals from the east, but only at much later times of 24 s after the *S* wave (fig. 9*A*). The early, observed surface-wave arrivals may have been scattered from some feature situated northwest of Oak Hill (fig. 1) There is aeromagnetic evidence that the material which composes Oak Hill extends northwestward under the alluvium (see Brabb and Hanna, 1981). This material may form a horst under the central part of the basin (E.J. Helley, oral commun, 1990) that could scatter surface waves. Clearly, seismic refraction and reflection studies are needed to develop a model for the basin sufficiently accurate to predict ground motions from future earthquakes on the basis of three-dimensional simulations.

ACKNOWLEDGMENTS

David Boore and Erdal Safak reviewed the manuscript. Robert W. Clayton of the California Institute of Technology wrote the original framework of the two-dimensional finite-difference program that served as the starting point for the three-dimensional program. Lawrence Baker of the U.S. Geological Survey provided useful tips for improving the speed of the program on the Cray computer. Chandan Saikia provided his reflectivity code. We benefited from discussions with Paul Okubo, Don Helmberger, Susan Hough, and John Filson.

REFERENCES CITED

Aki, Keiiti, and Larner, K.L., 1970, Surface motion of a layered medium having an irregular interface due to incident plane *SH* waves: Journal of Geophysical Research, v. 75, no. 5, p. 933–954.

Aki, Keiiti, and Richards, P.G., 1980, Quantitative seismology; theory and methods: San Francisco, W.H. Freeman and Co., 2 v.

Alford, R.M., Kelley, K.R., and Moore, D.M., 1974, Accuracy of finite-difference modeling of the acoustic wave equation: Geophysics, v. 39, no. 6, p. 834–842.

Alterman, Z.S., and Karal, F.C., Jr., 1968, Propagation of elastic waves in layered media by finite difference methods: Seismological Society of America Bulletin, v. 58, no. 1, p. 367–398.

Alterman, Z.S., and Rotenberg, A., 1969, Seismic waves in a quarter plane: Seismological Society of America Bulletin, v. 59, no. 1, p. 347–368.

Bard, P.-Y., and Bouchon, Michel, 1980a, The seismic response of sediment-filled valleys. Part 1. The case of incident *SH* waves: Seismological Society of America Bulletin, v. 70, no. 4, p. 1263–1286.

———1980b, The seismic response of sediment-filled valleys. Part 2. The case of incident *P* and *SV* waves: Seismological Society of America Bulletin, v. 70, no. 5, p. 1921–1941.

———1985, The two-dimensional resonance of sediment-filled valleys: Seismological Society of America Bulletin, v. 75, no. 2, p. 519–541.

Bard, P.-Y., Campillo, Michel, Chávez-Garcia, F.J., and Sánchez-Sesma, F.J., 1988, The Mexico earthquake of September 19, 1985—a theoretical investigation of large and small-amplification effects in the Mexico City valley: Earthquake Spectra, v. 4, no. 3, p. 609–633.

Boore, D.M., and Boatwright, John, 1984, Average body-wave radiation coefficients: Seismological Society of America Bulletin, v. 74, no. 5, p. 1615–1621.

Borcherdt, R.D., and Gibbs, J.F., 1976, Effects of local geological conditions in the San Francisco Bay region on ground motions and the intensities of the 1906 earthquake: Seismological Society of America Bulletin, v. 66, no. 2, p. 467–500.

Brabb, E.E., and Hanna, W.F., 1981, Maps showing aeromagnetic anomalies, faults, earthquake epicenters, and igneous rocks in the southern San Francisco Bay region, California: U.S. Geological Survey Geophysical Investigations Map GP–932, scale 1:125,000, 3 sheets.

California Department of Water Resources, 1967, Geology, app. A *of* Evaluation of ground water resources, South [San Francisco] Bay: Bulletin 118–1, 153 p.

California Division of Mines and Geology, 1969, Geologic atlas of California: Sacramento.

Clayton, R.W., and Engquist, B., 1977, Absorbing boundary conditions for acoustic and elastic wave equations: Seismological Society of America Bulletin, v. 67, no. 6, p. 1529–1540.

Dietz, L.D., and Ellsworth, W.L., 1990, The October 17, 1989, Loma Prieta, California, earthquake and its aftershocks; geometry of the sequence from high-resolution locations: Geophysical Research Letters, v. 17, no. 9, p. 1417–1420.

Frankel, Arthur, Hough, S.E., Friberg, P.A., and Busby, Robert, 1991, Observations of Loma Prieta aftershocks from a dense array in Sunnyvale, California: Seismological Society of America Bulletin, v. 81, no. 5, p. 1900–1922.

Harmsen, S.C., and Harding, S.T., 1981, Surface motion over a sedimentary valley for incident plane *P* and *SV* waves: Seismological Society of America Bulletin, v. 71, no. 3, p. 655–670.

Haskell, N.A., 1960, Crustal reflection of plane *SH* waves: Journal of Geophysical Research, v. 65, no. 12, p. 4147–4150.

Hazlewood, R.M., 1976, Contour map and interpretive cross sections showing depth and configuration of bedrock surface, South San Francisco Bay region, California: U.S. Geological Survey Miscellaneous Field Studies Map MF–796, scale 1:62,500, 2 sheets.

Joyner, W.B., Warrick, R.E., and Fumal, T.E., 1981, The effect of Quaternary alluvium on strong ground motion in the Coyote Lake, California earthquake of 1979: Seismological Society of America Bulletin, v. 71, no. 4, p. 1333–1349.

Joyner, W.B., Warrick, R.E., and Oliver, A.A., III, 1976, Analysis of seismograms from a downhole array in sediments near San Francisco Bay: Seismological Society of America Bulletin, v. 66, no. 3, p. 937–958.

Kanai, Kiyoshi, 1952, Relation between the nature of surface layer and the amplitudes of earthquake motions: Tokyo University, Earthquake Research Institute Bulletin, v. 30, no. 1, p. 31–37.

Kawase, Hiroshi, and Aki, Keiiti, 1989, A study on the response of a soft basin for incident *S, P,* and Rayleigh waves with special reference to the long duration observed in Mexico City: Seismological Society of America Bulletin, v. 79, no. 5, p. 1361–1382.

Kelly, K.R., Ward, R.W., Treitel, Sven, and Alford, R.M., 1976, Synthetic seismograms; a finite-difference approach: Geophysics, v. 41, no. 1, p. 2–27.

Mooney, W.D., and Colburn, R.H., 1985, A seismic-refraction profile across the San Andreas, Sargent, and Calaveras faults, west-central California: Seismological Society of America Bulletin, v. 75, no. 1, p. 175–191.

Mueller, C.S., and Glassmoyer, G.M., 1990, Digital recordings of aftershocks of the October 17, 1989 Loma Prieta, California, earthquake, U.S. Geological Survey Open-File Report 90–503, 147 p.

Ohtsuki, Akira, and Harumi, Kasaburo, 1983, Effect of topographies and subsurface inhomogeneities on seismic SV waves: Earthquake Engineering & Structural Dynamics, v. 11, no. 4, p. 441–462.

Oppenheimer, D.H., 1990, Aftershock slip behavior of the 1989 Loma Prieta, California earthquake: Geophysical Research Letters, v. 17, no. 8, p. 1199–1202.

Rial, J.A., 1989, Seismic wave resonances in 3–D sedimentary basins: Royal Astronomical Society Geophysical Journal, v. 99, no. 1, p. 81–90.

Saikia, C.K., and Sen, M.K., 1989, Long range and high-frequency synthetic seismograms using 1–D techniques [abs.]: Eos (American Geophysical Union Transactions), v. 70, no. 43, p. 1200–1201.

Saito, Masanori, 1967, Excitation of free oscillations and surface waves by a point source in a vertically heterogeneous Earth: Journal of Geophysical Research, v. 72, no. 14, p. 3689–3699.

Sánchez-Sesma, F.J., 1983, Diffraction of elastic waves by three-dimensional surface irregularities: Seismological Society of America Bulletin, v. 73, no. 6, pt. A, p. 1621–1636.

Sánchez-Sesma, F.J., Pérez-Rocha, L.E., and Chávez-Pérez, Sergio, 1989, Diffraction of elastic waves by three-dimensional surface irregularities. Part II: Seismological Society of America Bulletin, v. 79, no. 1, p. 101–112.

Vidale, J.E., 1990, Comment on "A comparison of finite-difference and Fourier method calculations of synthetic seismograms" by C.R. Daudt *et al.*: Seismological Society of America Bulletin, v. 80, no. 2, p. 493–495.

Vidale, J.E., and Clayton, R.W., 1986, A stable free-surface boundary condition for two-dimensional elastic finite-difference wave simulation: Geophysics, v. 51, no. 12, p. 2247–2249.

Vidale, J.E., and Helmberger, D.V., 1988, Elastic finite-difference modeling of the 1971 San Fernando, California earthquake: Seismological Society of America Bulletin, v. 78, no. 1, p. 122–141.

THE LOMA PRIETA, CALIFORNIA, EARTHQUAKE OF OCTOBER 17, 1989:
STRONG GROUND MOTION AND GROUND FAILURE

STRONG GROUND MOTION

SITE-RESPONSE MODELS FROM HIGH-RESOLUTION SEISMIC REFLECTION AND REFRACTION DATA RECORDED IN SANTA CRUZ, CALIFORNIA

By Robert A. Williams, Edward Cranswick, Kenneth W. King, David L. Carver, and David M. Worley,
U.S. Geological Survey

CONTENTS

ABSTRACT

We compare earthquake site-response estimates derived from digital recordings of aftershocks recorded in Santa Cruz, Calif., with synthetic site-response estimates calculated from models of the sites' seismic-impedance structure. The impedance structure of each site is determined, first, from interpretations of high-resolution *P*-wave seismic-reflection and *P*- and *S*-wave seismic-refraction data, and, second, from published data on the regional geology and geophysics. This study is motivated by an assumption that the impedance structure of a given site, and its seismic response, can be estimated from geophysical and geologic data other than direct recordings of weak or strong ground motion. Our results suggest only limited success in predicting the seismic response and point out the critical importance of highly accurate seismic-velocity data.

Ground-motion data from as many as eight aftershocks were recorded using three-component digital seismographs, and converted to Fourier spectra. We estimated the seismic response by averaging the eight spectral ratios recorded at a given site relative to a reference station located on crystalline bedrock. We calculated the synthetic site response by forward-modeling the vertical-, radial-, and tangential-component seismic response. We use the synthetic spectral ratio (up to 10 Hz) between the two sites for comparison with the observed spectral ratio.

Spectral ratios generated by perturbing the ray parameter, *Q* value, and the layer density, depth, and velocity were computed to estimate their importance in shaping the spectral ratio. Our results indicate that layer velocities are most influential on spectral-ratio shape and probably should be known to within about 5 percent to accurately predict the ground response at frequencies above 5 Hz. Poor seismic-velocity control (especially for *S* waves) on materials between 30- and 250-m depth was found to be a major weakness in this study.

Comparison of the synthetic and observed spectral ratios at two sites about 200 to 300 m apart shows mixed results: The synthetic amplitudes are 2 to 4 times smaller than the observed, there is good agreement in curve shape below 5 Hz for both vertical and one tangential components, and there is poor agreement for both radial and one tangential components. A resonance of 1 Hz on the horizontal components and about 3.5 Hz on the vertical components, between the ground surface and a high-impedance crystalline-basement reflector at about 200-m

depth, is successfully estimated on the synthetic data. Smaller amplitude and higher frequency (5–10 Hz) resonance peaks are not accurately estimated by the synthetic data. Below 5 Hz, smoothed resonance-peak amplification of ground motion at sites located on unconsolidated sedimentary deposits (non-rock sites) on the stacked, observed data is 5 to 13 times greater than at the reference station.

The synthetic tangential-component (*SH* wave) data agree best with the observed data in both amplitude and resonance-peak location, suggesting that phase conversions and reflections from other interfaces (three-dimensional-scattering effects) are too complex to accurately simulate with the *P* and *SV* components. The relatively large distances between the stations used in this study probably violate the important "identical path" assumption used in site-response studies. Therefore, unknown effects due to differences in seismic wave path probably exist for frequencies above about 2 Hz. Also, differences in site geology between the aftershock-recording stations and the reflection/refraction sites may account for some of the discrepancy. Future studies of this type should include *S*-wave-reflection data and better *P*- and *S*-wave-velocity control on near-surface materials.

INTRODUCTION

The geographic variation of building damage and the fatal consequences of structural failure caused by locally amplified ground shaking (site response) from the earthquake have been observed before in the San Francisco Bay region and elsewhere. The 15 s of strong ground motion generated by the earthquake, which had its epicenter about 80 km south of San Francisco, resulted in the most costly single natural disaster in U.S. history, with 61 fatalities and $6 billion to $7 billion in damages, as estimated by the California Office of Emergency Services. Most of the heavy damage occurred in parts of the bay region underlain by known deposits of unconsolidated materials, which, as predicted (Borcherdt and Gibbs, 1976), locally amplified the intensity of ground shaking (U.S. Geological Survey staff, 1990).

Although the ground motion at a given site is affected by the seismic source mechanism, earthquake distance and size, seismic-wave travelpath, and near-surface geologic materials, numerous studies in the San Francisco Bay region (Wood, 1908; Borcherdt, 1970), Venezuela (Espinosa and Algermissen, 1972), Los Angeles (Rogers and others, 1985), Mexico City (Singh and others, 1988), and Olympia, Wash. (King and others, 1990b), have demonstrated that near-surface geologic conditions are the most influential factor in determining the amplitude of ground shaking. The underlying assumption in several of these studies is that the site-response estimates generated from weak-motion (low strain) data predict strong-motion behavior, although it is known that this assumption is not true in all cases. For example, Sadigh (1983), Idriss (1985), and Chin and Aki (1991) suggested that nonlinear site response invalidates weak-motion-amplification predictions in the epicentral area; Kawase and Aki (1990) showed that topographic effects must also be considered; and other investigators (for example, Jarpe and others, 1989) demonstrated discrepancies between weak-motion predictions and observed strong-motion behavior.

Despite the limitations of weak-motion data, several studies have successfully predicted strong-motion behavior from these data. Borcherdt (1970), who was one of the first workers to transfer weak-motion data into strong-motion predictions, studied the amplification factor of weak-motion recordings at soft-soil sites in the San Francisco Bay region from nuclear explosions at the Nevada Test Site and found good correlations between the amplification factor and intensity measurements from the 1906 and 1957 San Francisco earthquakes.

This study tests the usefulness of incorporating high-resolution seismic-reflection data into the plane-layered-model site-response-estimation technique to constrain surface ground motions from synthetic seismic-impedance models of the near-surface structure. The general approach of this study is similar to the modeling work by, for example, Joyner and others (1981), King and Tucker (1984), and Seale and Archuleta (1989), in which the seismic models were based on borehole or refraction data. The advantage of seismic reflection and refraction data for response studies is that they eliminate the need for local seismic sources. Successful application of this approach would demonstrate that variations in seismic ground response can be calculated from detailed knowledge of only the upper 200 to 300 m of surficial geology.

To test this approach, we used data from a site-response study that was conducted in Santa Cruz, Calif., a city located only about 12 km from the epicenter of the earthquake (fig. 1) but not previously analyzed for site-response effects. Within Santa Cruz, the amount and degree of structural damage varied widely (King and others, 1990c). Some buildings, particularly those in the downtown area (built on unconsolidated alluvium), were severely damaged by the earthquake, whereas other structures located on firm ground or bedrock sustained little or no damage (King and others, 1990c). This surficial geologic variation appears to greatly influence the amount of building damage observed in Santa Cruz. Part of the structural-damage variation is related to age and building type; however, as established by Cranswick and others (1990), the downtown alluvial-flood-plain area does amplify ground motion relative to sites outside of the alluvial basin.

The apparent correspondence of building damage to surficial geology in Santa Cruz prompted the U.S. Geological Survey (USGS) to start a three-phase site-response investigation immediately after the main shock. In phase 1, the city was surveyed for damage (King and others, 1990c). In phase 2, aftershocks were recorded with portable seismographs at 43 different sites in Santa Cruz distributed over widely differing geologic conditions (Carver and others, 1991). In phase 3, high-resolution seismic refraction and reflection data were obtained in flat-lying areas as near as possible to some of the aftershock-recording sites to determine the relation between near-surface (<200-m depth) geophysical parameters (layer thickness, *P*- and *S*-wave velocity) and observed ground motion (King and others, 1990a).

Using the aftershock data, in conjunction with the seismic-reflection data, this paper evaluates (1) the usefulness of the seismic reflection and refraction data in site-response studies; (2) the effect on synthetic site-response calculations of such factors as density, velocity, layer thickness, *Q* value, and incidence angle; and (3) the accuracy of the site response models at two sites in Santa Cruz (fig. 2). We used the phase 3 reflection and refraction data, along with published gravity and refraction data, to construct one-dimensional plane-layer impedance models and generate synthetic surface seismograms for these two sites.

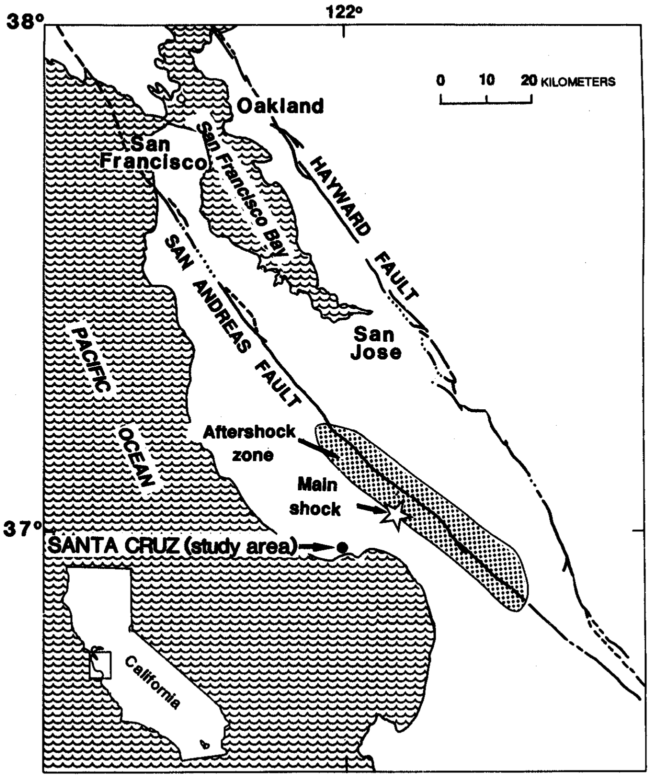

Figure 1.—San Francisco Bay region, showing locations of study area, Loma Prieta main shock, aftershock zone, and major faults (dotted where inferred).

Comparing the predicted and observed site responses (derived from phase 2 aftershock recordings) in terms of spectral ratios tests the influence of the above-mentioned factors and the accuracy of these predictions. Our results suggest that only part of the site response can be explained by the technique and data used in this study. Potentially damaging resonance frequencies are successfully predicted, but their amplitudes are underestimated in the synthetic data. The reflection profiles themselves prove to be valuable because, as representations of a site's impedance structure, they allow accurate estimates of resonance frequencies to be calculated directly from the two-way traveltime of reflections.

SPECTRAL-RATIO TECHNIQUE AND ASSUMPTIONS

The spectral-ratio technique is used to analyze three important features of ground motion during an earthquake: which frequencies were amplified, the total amplification

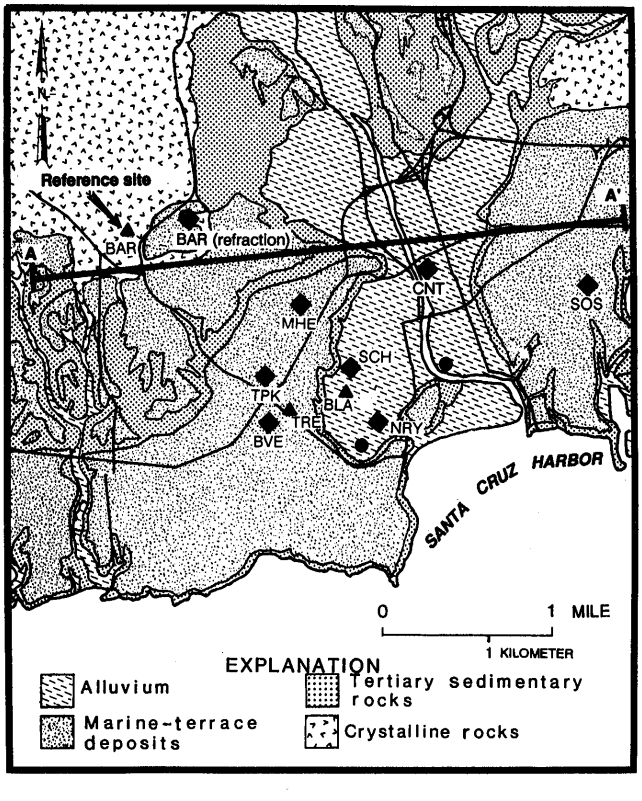

Figure 2.—Geologic map of Santa Cruz area, showing locations of seismic-reflection/refraction sites (diamonds), aftershock-recording stations (triangles), boreholes (dots), and line *A–A′* in figure 7. Stations MHE, TPK, BVE, and TRE are located on same marine terrace; stations CNT, SCH, and NRY are located in San Lorenzo River alluvial basin. Area of map is wholly within Santa Cruz city limits.

factor at a given site, and the effects of near-surface geologic conditions on seismic records (Borcherdt, 1970; Espinosa and Algermissen, 1972; Joyner and others, 1981; Rogers and others, 1985; King and others, 1990b). In most spectral-ratio studies, a reference site is selected on a bedrock outcrop (as in this study), and the Fourier spectra of the seismogram for this site $F_1(w)$, which is generally low in amplitude, are compared with those for all other stations $F_n(w)$ by a spectral ratio, as in the relation

$$F_n(w)/F_1(w) = [S(w)P_n(w)I_n(w)T_n(w)]/[S(w)P_1(w)I_1(w)T_1(w)] \ , \quad (1)$$

where $S(w)$ is the source function, $P(w)$ is the path effect incurred by waves traveling to the station, $I_n(w)$ is the instrument response, and $T_n(w)$ is the transfer function of the near-surface material beneath station n. Spectral-ratio computations assume that instrument responses are identical, and because the recording stations are located close together relative to the hypocentral distance, wave paths are assumed to be identical except near the recording station. Thus, the only element in equation 1 changing between stations is $T_n(w)$, thereby forming the expression

$$F_n(w)/F_1(w) = T_n(w)/T_1(w) = A_{n,1}(w) \ , \quad (2)$$

where $A_{n,1}(w)$ is the spectral-amplification function of the system.

All of the assumptions described above appear to be satisfied in this study except "close" station spacing relative to hypocentral distance. Menke and others (1990) empirically found that when the distance between stations is greater than one-third to one-half of a wavelength, the observed signal coherency is not statistically different from that between two recorded signals of random noise. Applying this distance criteria leads to the following derivation:

$$\begin{aligned} D &= {}^1\!/_2 L \\ L &= v/f_c \\ f_c &= v/2D, \end{aligned} \quad (3)$$

where D is the distance between stations, L is the wavelength, v is the seismic-wave velocity, and f_c is the cutoff frequency. Assuming P- and S-wave velocities of 6 and 3.4 km/s, respectively, and D=2.5 km for the distance between the hard-rock reference site and the stations located on unconsolidated sedimentary deposits, "identical paths" are limited to frequencies below 1.5 Hz for P waves and 0.85 Hz for S waves. Despite this empirical limitation, we continued the study because of some promising preliminary results for frequencies above f_c and the ability to use other stations as the reference site, which will decrease D.

GEOLOGIC SETTING

LOCAL GEOLOGY

Santa Cruz is located on the California coast at the foot of the Santa Cruz Mountains (fig. 1). The surficial geology in the city tends to divide the developed areas into three parts (fig. 2): (1) the downtown business district, located on unconsolidated Holocene alluvium deposited by the north-south-running San Lorenzo River; (2) marine terraces (Bradley and Griggs, 1976), where most of the residential housing is located, at elevations of about 10 to 20 m above the central alluvial plain; and (3) a less densely populated highlands area containing both older marine terraces and exposed crystalline-basement rocks. The important geologic units described above are summarized in figure 3.

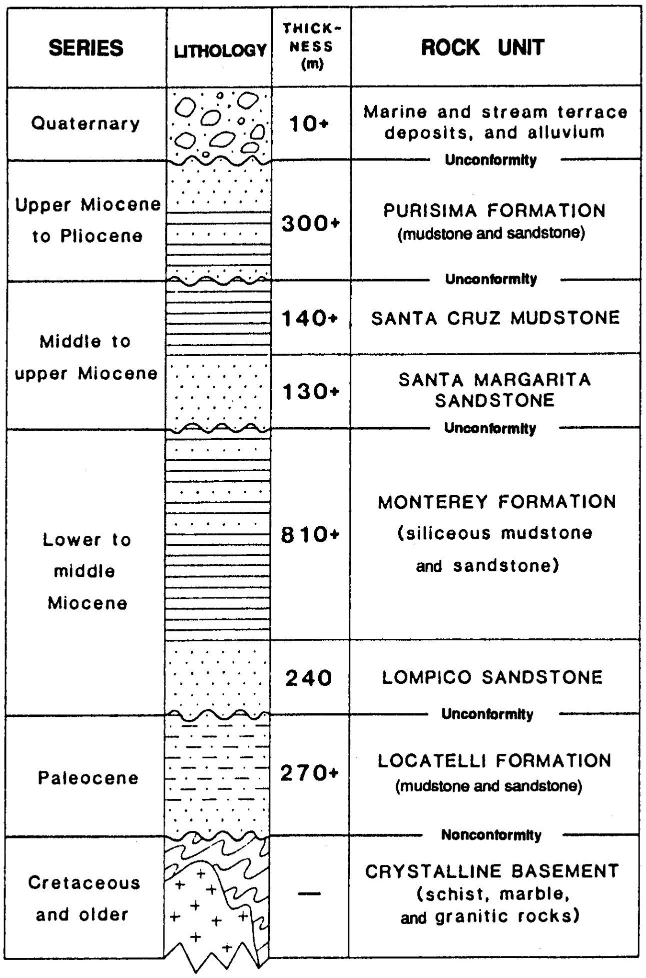

SERIES	LITHOLOGY	THICKNESS (m)	ROCK UNIT
Quaternary		10+	Marine and stream terrace deposits, and alluvium
			Unconformity
Upper Miocene to Pliocene		300+	PURISIMA FORMATION (mudstone and sandstone)
			Unconformity
Middle to upper Miocene		140+	SANTA CRUZ MUDSTONE
		130+	SANTA MARGARITA SANDSTONE
			Unconformity
Lower to middle Miocene		810+	MONTEREY FORMATION (siliceous mudstone and sandstone)
		240	LOMPICO SANDSTONE
			Unconformity
Paleocene		270+	LOCATELLI FORMATION (mudstone and sandstone)
			Nonconformity
Cretaceous and older		—	CRYSTALLINE BASEMENT (schist, marble, and granitic rocks)

Figure 3.—Generalized stratigraphic column for Santa Cruz area. The Monterey, Lompico, and Locatelli Formations are apparently absent in immediate vicinity of study area (see text). From Stanley and McCaffrey (1983).

CRYSTALLINE-BASEMENT ROCKS

Santa Cruz is located about 20 km from the San Andreas fault (fig. 1). The crust beneath Santa Cruz is a batholithic terrain composed primarily of Cretaceous granitic rocks and pre-Cretaceous schist and marble (Clark, 1981). Walter and Mooney (1982) determined from an east-west seismic-refraction profile a few kilometers north of Santa Cruz that the *P*-wave-velocity structure of these crystalline-basement rocks can be subdivided into four crustal layers. Layer 1, which comprises only the upper 2 km of the crust, has velocities of 3.6 to 4.6 km/s; the 3.6 km/s velocity is correlated with areas of Cenozoic sedimentary rocks. Laboratory velocity studies on crystalline-rock samples from the region support the 4.6-km/s velocity for layer 1 (Lin and Wang, 1980). The rest of the crust (layers 2–4), from 2- to 25-km depth, is made up of rocks with velocities of 5.3 to 6.55 km/s.

Shear-wave-velocity information on these basement rocks is less abundant. Hamilton and others (1964) reported a shear-wave velocity of 3.42 km/s from quarry-blast refraction data that represents a poorly constrained average velocity for midcrustal depths. Using this *S*-wave velocity and the midcrustal *P*-wave velocity results in a Poisson's ratio of 0.3. Using this Poisson's ratio for the other layers suggests *S*-wave velocities of 1.9 to 2.5 km/s (layer 1), 2.8 km/s (layer 2), 3.2 km/s (layer 3), and 3.4 km/s (layer 4). Focal depths for the Loma Prieta aftershocks used in this study were all in the depth range 8–14 km (U.S. Geological Survey staff, 1990).

On the basis of average rock densities of 2.6 to 2.8 g/cm^3 for granite and marble samples from around the world (Daly and others, 1966), we use a density of 2.7 g/cm^3 for the synthetic models. Additional support for this range of densities comes from a study by Gibbs and others (1976), who determined a density of 2.52 g/cm^3 for a sample of quartz diorite, similar to igneous rocks in the Santa Cruz area, from 29-m depth in a borehole located on a terrace about 40 km north of the city. Because this sample was probably disturbed during drilling and the density was not measured in place, and because of the presence of metamorphic rocks in the Santa Cruz area that generally are denser, a density of 2.7 g/cm^3 was deemed reasonable.

CENOZOIC SEDIMENTARY ROCKS

Three major formations of marine Cenozoic sedimentary rocks form a thin cover overlying crystalline basement in the Santa Cruz area, from oldest (late Miocene) to youngest (late Miocene to Pliocene): the Santa Margarita Sandstone, the Santa Cruz Mudstone, and the Purisima Formation of Stanley and McCaffrey (1983). Underlying these formations are the Monterey Formation, the Lompico Sandstone, and the Locatelli Formation of Stanley and McCaffrey (1983), but because of an absence of outcrops (and evidence from the seismic-reflection data to be described below), these strata appear to be absent in the study area. The lithology of the formations present in the Santa Cruz area, which varies slightly throughout the area, was described in detail by Clark (1981). In the study area, these units range from 10 to 300 m in thickness and dip about 3°–8° S.

Shallow refraction data of King and others (1990a) reveal that the near-surface *P*- and *S*-wave velocities of these strata as measured on the marine terraces can vary by 50 percent over distances of 500 m. *P*-wave velocities range from 1.7 to 3.0 km/s. Shallow *S*-wave velocities of the Cenozoic rocks are not well defined, but the data from one site indicate a 1.0-km/s velocity.

The densities of sedimentary rocks from around the world range from 2.2 to 2.7 g/cm^3 (Daly and others, 1966); Cretaceous rocks generally are less dense than Paleozoic sedimentary rocks. Because Clark (1981) described the Cenozoic sedimentary rocks in the Santa Cruz area as generally friable, we use a lower density of 2.3 g/cm^3 for these rocks in the synthetic seismic models.

MARINE-TERRACE DEPOSITS

Much of Santa Cruz is located on a thin layer of marine-terrace deposits overlying Cenozoic rocks (fig. 2); a small area in the northwestern part of the city is on granitic and metamorphic basement rocks. In most parts of Santa Cruz, the Cenozoic sedimentary deposits are unconformably overlain by the marine-terrace deposits, which were described by Clark (1981) as a thin (1.5–6.0 m thick), discontinuous cover of Pleistocene sand and thin pebble beds. Seismic-refraction data indicate that these marine-terrace deposits, with *P*- and *S*-wave velocities of about 1.5 and 0.3 km/s respectively, are as much as 10 to 12 m thick in some localities (King and others, 1990a). These refraction data also indicate a soil layer, about 1 to 2 m thick, with *P*- and *S*-wave velocities of about 0.25 and 0.15 km/s, respectively, overlying the marine-terrace deposits in most places (King and others, 1990a).

We use a density of 1.9 g/cm^3 for the marine-terrace deposits in the synthetic seismic models. This value was determined by Gibbs and others (1976) on a sample from a borehole located on a coeval marine terrace about 40 km north of Santa Cruz.

ALLUVIAL-BASIN DEPOSITS

The primary exception to the coverage of marine-terrace deposits is found in the San Lorenzo River flood plain, where the major Santa Cruz commercial property is located. The flood-plain material is composed of Quaternary alluvium, consisting of unconsolidated Holocene silt and sand, discontinuous lenses of clay and silty clay, and locally large amounts of gravel (Dupre, 1975). Borehole data at two locations (fig. 2) indicate that the alluvial basin is at least 30 m deep (Harding Lawson Associates, unpub. data, 1985, 1989; Haro, Kasunich & Associates, unpub. data, 1988). From refraction data, a high-velocity basin-bottom event (that is, bedrock) was not interpreted, but minimum depths appear to be about 30 m near the middle south end of the basin (King and others, 1990a). From these same data, the *P*- and *S*-wave velocities of the basin-fill material were determined to be about 1.4 and 0.15 km/s, respectively, typical of saturated, unconsolidated materials found in other parts of the San Francisco Bay region (Gibbs and others, 1976) and Mexico City (Figueroa, 1964). Shallow-borehole data from the basin also indicate saturation, with water-table depths of 1 to 1.5 m. Our results indicate a basin depth of about 40 m (see subsection below entitled "Reflection Data").

The density of the unconsolidated alluvium ranges from 1.7 to 2.1 g/cm^3 (Daly and others, 1966; Gibbs and others, 1976). We use a density of 1.7 g/cm^3 for these materials in the synthetic seismic models.

SEISMIC DATA

REFRACTION DATA

The seismic-refraction data of King and others (1990a) were acquired to determine the thickness and seismic velocity of geologic layers from the surface to a depth of about 20 or 30 m. This maximum depth was imposed by space limitations at most sites, which restricted geophone spread lengths and source offsets.

The seismic-refraction data were acquired along linear profiles on flat terrain in sod-covered schoolyards (stas. MHE, BVE, SCH, fig. 2; table 1), sod-covered city parks (stas. CNT, SOS, TPK), and an open, undeveloped field of wild grasses with a soil pervasively churned by gopher burrowing (sta. NRY). Except for station CNT, which appeared to be underlain by about 3 m of dry sand, the sod-covered areas seemed to provide relatively good source and geophone coupling. The surficial dry sand at station CNT and the gopher burrows at station NRY apparently hurt data quality, thus preventing detection of the alluvial-basin bottom by refraction methods.

The limited depth penetration of the refraction data of King and others (1990a) restricted detection to only three very shallow layers at each site for both *P*- and *S*-wave data: a 1- to 2-m-thick soil layer at the ground surface, underlain by a 2- to 10-m-thick marine-terrace deposit at terrace sites, or by saturated alluvium (*P*-wave velocity, approx 1.4 km/s) at sites in the alluvial basin, in turn underlain at 6- to 20-m depth by apparently more consolidated materials that could be the Purisima Formation, with *P*- and *S*-wave velocities of 2.05 to 3.0 km/s and 0.6 to 0.9 km/s, respectively. In contrast, at sites in the alluvial basin, no materials with a velocity higher than 1.77 km/s were observed, suggesting that strata beneath the alluvium were not detected.

Possibly the most important result for the synthetic seismic models comes from a comparison of the *S*-wave-refraction velocities in the alluvial basin with those determined on the marine terraces. In the alluvial basin, *S*-wave velocities range from about 0.08 to 0.17 km/s down to about 20-m depth, whereas on the marine terraces the *S*-wave velocity increases to 0.5 km/s at about 5-m depth (fig. 4). This contrast in *S*-wave velocity between sites in the alluvial basin and on the marine terraces is probably their most distinguishing difference, as shown in figure 5.

An additional reversed *P*-wave-refraction survey was performed on crystalline rocks in an abandoned marble quarry near station BAR (fig. 2). The data indicate that these rocks have a seismic velocity of 4.0 km/s within about 2 m of the surface, significantly higher (by at least 25 percent) than in the other refraction or reflection surveys and distinguishing station BAR from all the other sites used in this study. Significant uncertainty exists, however, concerning the velocity structure from about 30-m depth to the crystalline-basement interface. The refraction data at the quarry suggest a maximum *P*-wave velocity of 4.0 km/s, and data from other sites indicate a minimum *P*-wave velocity of about 2.5 to 3.0 km/s. Conceivably, the velocities within this interval could vary by as much as 50 percent, although it is reasonable to expect that the velocities of the Tertiary rocks never reach as high as 4.0 km/s because of the relatively strong reflector at the Tertiary rocks/crystalline-basement interface.

REFLECTION DATA

Because of the 35-m-depth penetration achieved in the refraction surveys, reflection profiling was used to extend the depth penetration and detect the alluvial-basin bottom. Indeed, high-amplitude reflections were obtained from depths ranging from 30 to 250 m at all sites, and the basin bottom was detected, making these data the primary information source used to construct the geologic models. Six *P*-wave-reflection profiles were used in this study, which, except for stations SCH and NRY (fig. 2), were collected along the same refraction lines, and so the surface materials are the same. The reflection lines at stations SCH and NRY were moved to nearby

Table 1.—*Station names, locations, and recorded data types*

[Do., ditto]

Station (fig. 2)	Location	Data type
BAR	Reference Station	Aftershock recording/refraction.
BLA	223 Blackburn Street	Aftershock recording.
BVE	Bay View Elementary School	Reflection/refraction.
CNT	Santa Cruz County Building	Refraction.
MHE	Mission Hill Elementary School	Reflection/refraction.
NRY	East side of Nearys Lagoon	Do.
SCH	Santa Cruz High School	Do.
SOS	Star of the Sea Park	Do.
TPK	Trescony Park	Do.
TRE	154 Trescony Street	Aftershock recording.

locations in an attempt to improve source and geophone coupling and to avoid possible seismic-signal complications with the edge of the alluvial basin at station SCH. We acquired the reflection data by using a standard common-depth-point (CDP) acquisition method (Mayne, 1962) with end-on source-receiver geometry, where source offsets from the near trace ranged from 15.2 to 30.5 m and geophone/shot intervals from 0.6 to 1.2 m. We used a modified 12-gage-shotgun seismic source that fired a 0.03-kg slug vertically into a 15-cm-deep hole

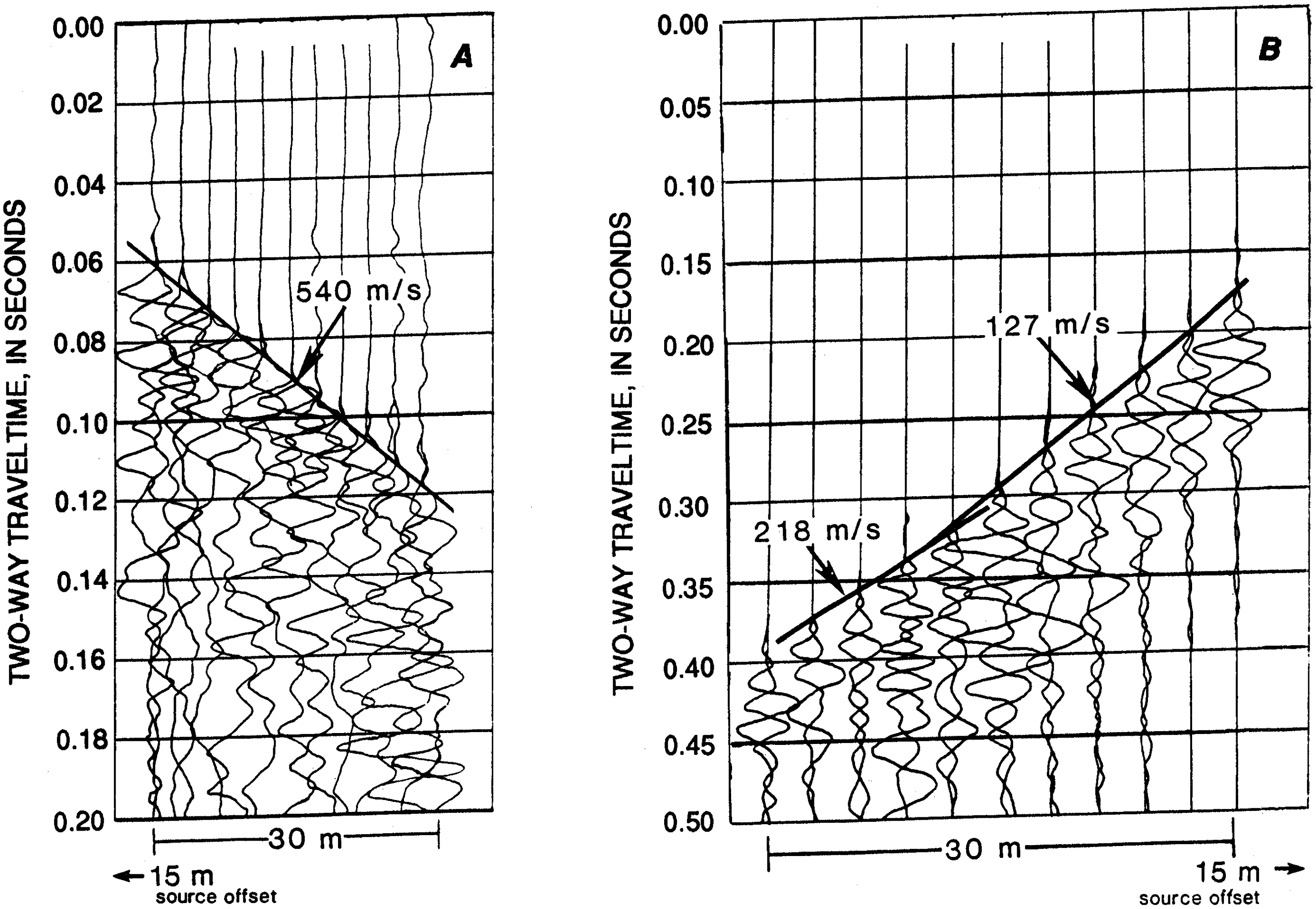

Figure 4.—*S*-wave refraction profiles, showing lower near-surface velocities at alluvial-basin site (*A*, sta. SCH) relative to marine-terrace site (*B*, sta. BVE). See figure 2 for locations.

Table 2.—*Acquisition parameters for seismic-reflection data*

Parameter	Instrument model	
	DHR–2400	ES–2401
Number of channels	24	24
Geophone natural frequency (Hz)	100	40
Geophone interval (m)	0.6–1.2	1.2
Sample interval (ms)	.5	.2
Source type	12-gage shotgun	12-gage shotgun
Source depth (cm)	15	15
Number of shots per shotpoint	1	1
Near source-receiver distance (m)	15.2	30.5
Far source-receiver distance (m)	29	58
Recording filters	180 Hz (low cut)	None.
Recording format	SEG–Y: magnetic tape	SEG–2: floppy disk

which was punched into the ground at each shotpoint. The recording parameters resulted in 12- to 24-fold CDP coverage and dominant reflection frequencies ranging from about 60 to 200 Hz. The data-acquisition parameters are summarized in table 2.

Some of the data (for example, at stas. MHE, TPK, BVE, and SOS, fig. 2) were recorded on an Input/Output 24-channel seismograph model DHR 2400 with single 100-Hz geophones at each station. At stations SCH and NRY, an EG&G model ES–2401 24-channel seismograph was used with single 40-Hz geophones at each station.

Reflection energy can be identified on the raw, unprocessed field files from each site. In addition, the general reflection characteristics of the seismic data on these field files do not vary greatly along any of the profiles, suggesting a grossly similar near-surface geologic structure along the profiles. CDP stacked sections were generated for the six profiles on the USGS computer, equipped with DISCO software, using identical data-processing parameters where possible. The high-quality reflection data required only simple, standard processing (table 3). Datum-static corrections were not needed because of the flat topography along the profiles. The data have not been corrected for geometric-spreading losses or attenuation.

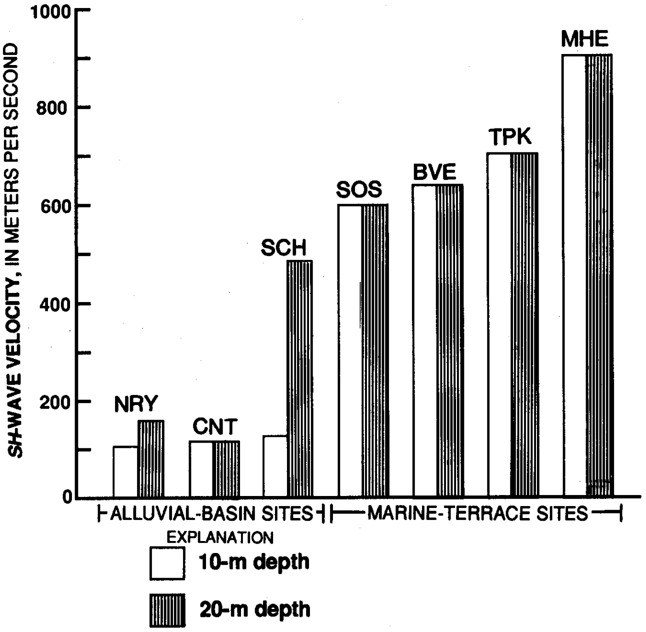

Figure 5.—Comparison of *S*-wave velocities at four marine-terrace sites and three alluvial-basin sites at 10- and 20-m depth. Velocities at alluvial-basin sites are no higher than 200 m/s at 20-m depth. Because survey at station SCH (fig. 2) was conducted near edge of alluvial basin, 500-m/s velocity there probably represents detection of basin-bounding Tertiary rocks.

Table 3.—*Seismic-reflection-data-processing steps*

[See figure 2 for locations of stations. CDP, common depth point]

Step	Description
1	Geometry definition.
2	Trace edit.
3	Coherent-seismic-noise filters to attenuate airblast and surface-wave noise.
4	CDP sort.
5	Normal moveout correction.
6	Bandpass filter, generally 100, 120–300, 400 Hz; at station SCH, 30, 60–150, 300 Hz; at station NRY, 40, 80–160, 320 Hz.
7	CDP stack.
8	Predictive deconvolution at stations MHE, NRY, SCH, SOS, and TPK.
9	Bandpass filter, generally 60,120–240,400 Hz; at station SCH, 30, 60–150, 300 Hz; at station NRY, 40, 80–160, 320 Hz.
10	Automatic gain control, generally 100- to 125-ms gate length.

The accuracy of seismic velocities for reflections occurring deeper than about 0.1 s two-way traveltime is limited, owing to the short length of the geophone spread and the relatively high seismic velocities measured. Little or no hyperbolic moveout was observed for reflections within this range and deeper; thus, the velocity model's accuracy is degraded on deep reflectors. Despite this velocity-control weakness and because the reflectors are relatively flat, we assumed that the reflection stacking velocities are equivalent to layer rms velocities; this assumption allows for calculation of the layer interval velocities (Dix, 1955) and, thus, estimation of layer thicknesses.

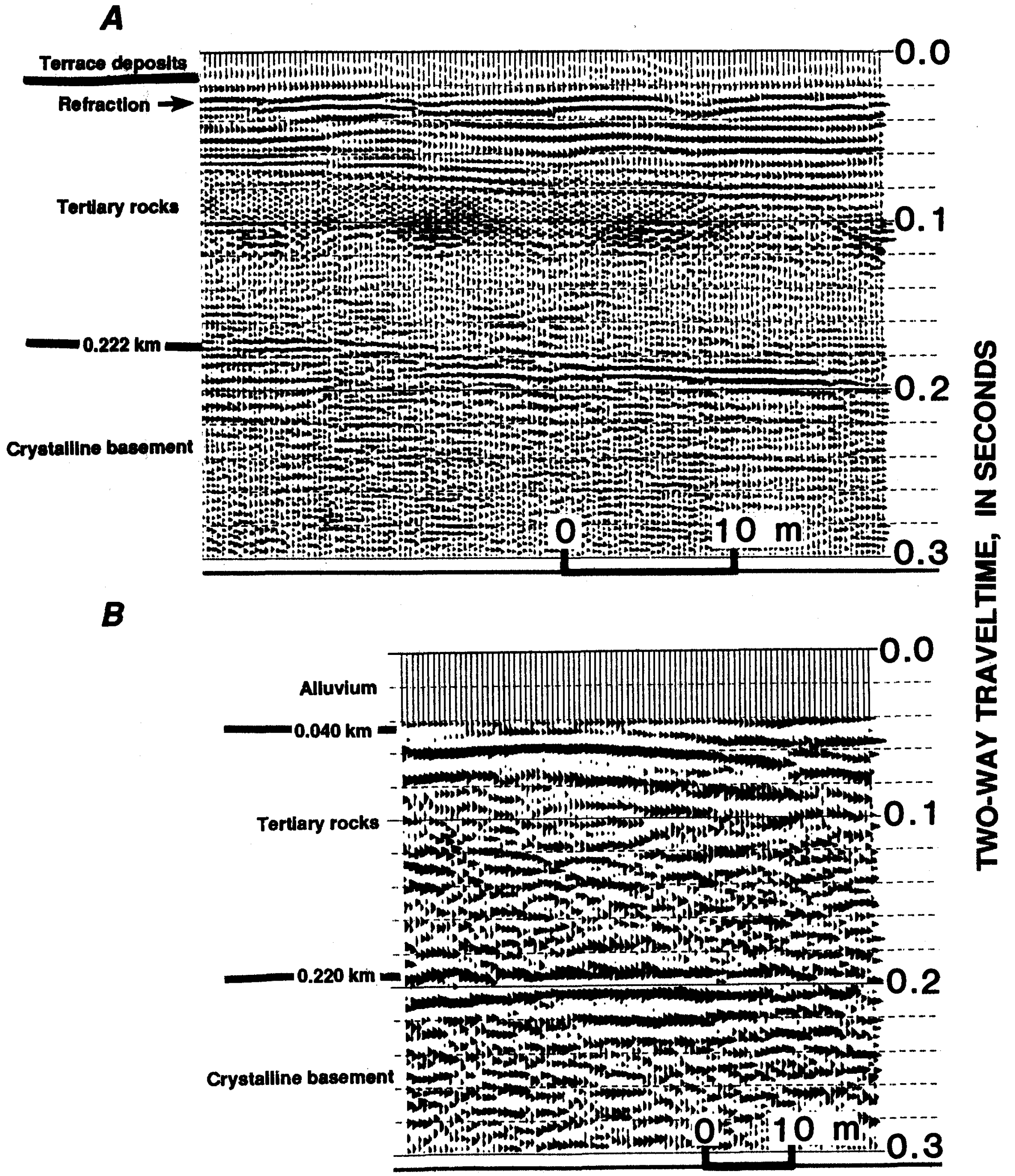

Figure 6.—Stacked seismic-reflection profiles from stations BVE (*A*), SCH (*B*), MHE (*C*), TPK (*D*), SOS (*E*), and NRY (*F*) (see fig. 2 for locations). High-frequency, diagonally trending, coherent signal between 0.09 and 0.12 s in figure 6A is airblast noise from gun. Note absence of continuous high-amplitude reflectors for crystalline basement between 0.1 and 0.2 s in figures 6*C* and 6*D*; this event may be faulted to about 0.08 s, as indicated on profiles.

INTERPRETATION

Although only two of the reflection/refraction sites are synthetically modeled in this study, we use all six sites to assess the variation of seismic velocity and to verify regional structure. The six stacked reflection profiles are shown in figure 6. On each profile, except that for station TPK (fig. 2), are generally two conspicuous zones of reflectivity and one transparent zone that lacks reflectivity. The upper zone (above 0.1 s) of reflectivity contains several reflections that evidently form high-impedance contrasts and may represent the thick intervals of semifriable sandstone that are common in the Purisima Formation (Clark, 1981), interbedded with diatomaceous shale. This upper zone of reflectivity represents about 20 to 50 m of materials. The reflector at the top of the upper zone of reflectivity was selected as the uppermost interface in the synthetic seismic model of the marine terrace at station BVE.

The shallowest layer detected ranges in depth from about 20 m at station BVE (fig. 2) to about 30 m everywhere else. This shallowest layer is probably an interval within the Tertiary strata at the sites on marine terraces. On the two sections from the alluvial basin, however, high-amplitude reflections near the top at stations SCH (at approx 0.05 s) and NRY (at approx 0.065 s) probably represent the reflection generated at the alluvium/Tertiary rocks interface. These traveltimes for stations SCH and NRY correspond to about 40- and 44-m depth, respectively. This basin-bottom reflector was selected as

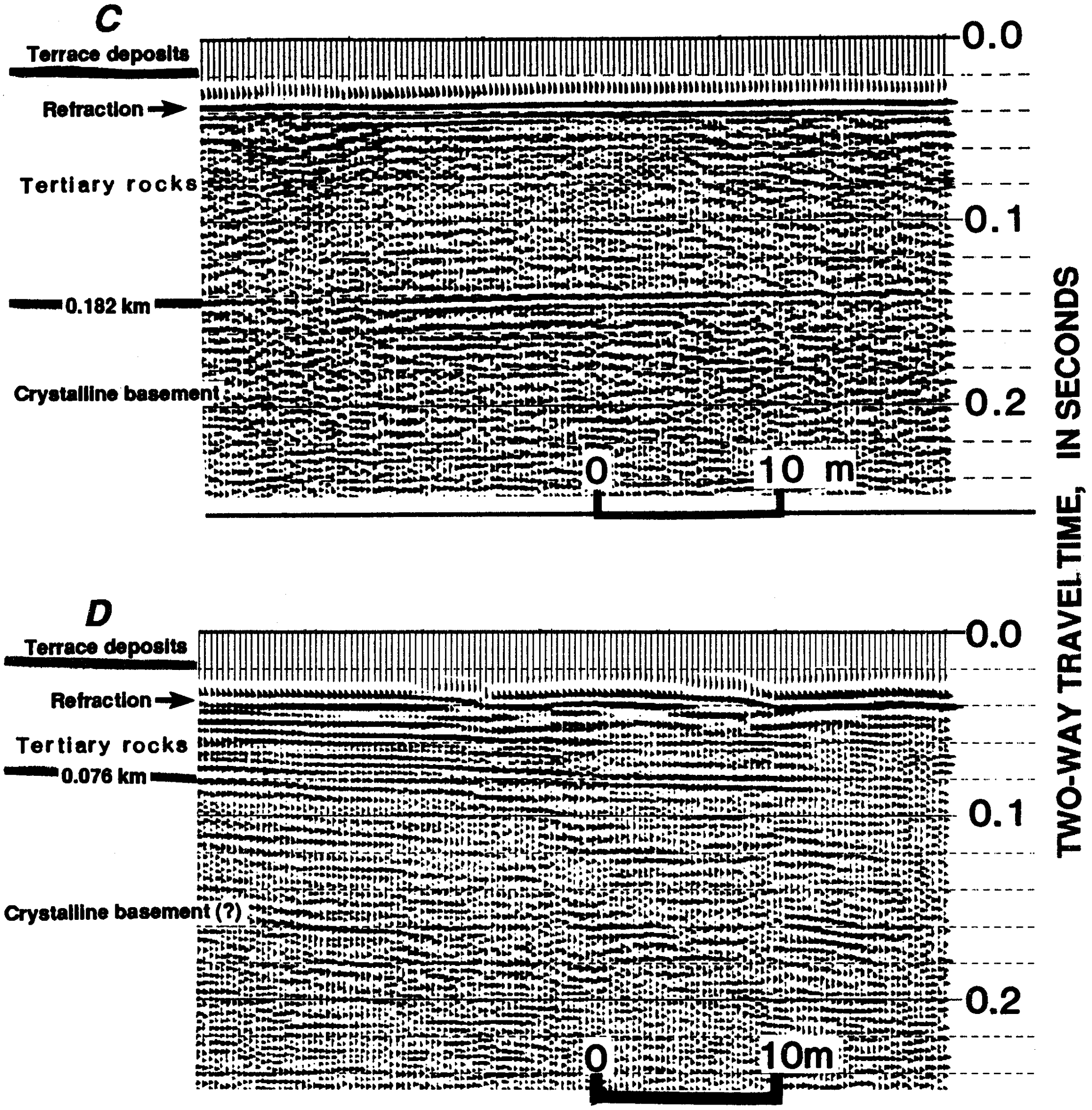

Figure 6.—Continued.

the uppermost interface for the alluvial-basin model at station SCH.

The upper zone of reflectivity is underlain by a zone 60 to 150 m thick that lacks reflections. This low-reflectivity zone could be the Santa Cruz Mudstone because it underlies the Purisima Formation and consists of medium- to thick-bedded siliceous mudstone with no notable interbeds (Clark, 1981).

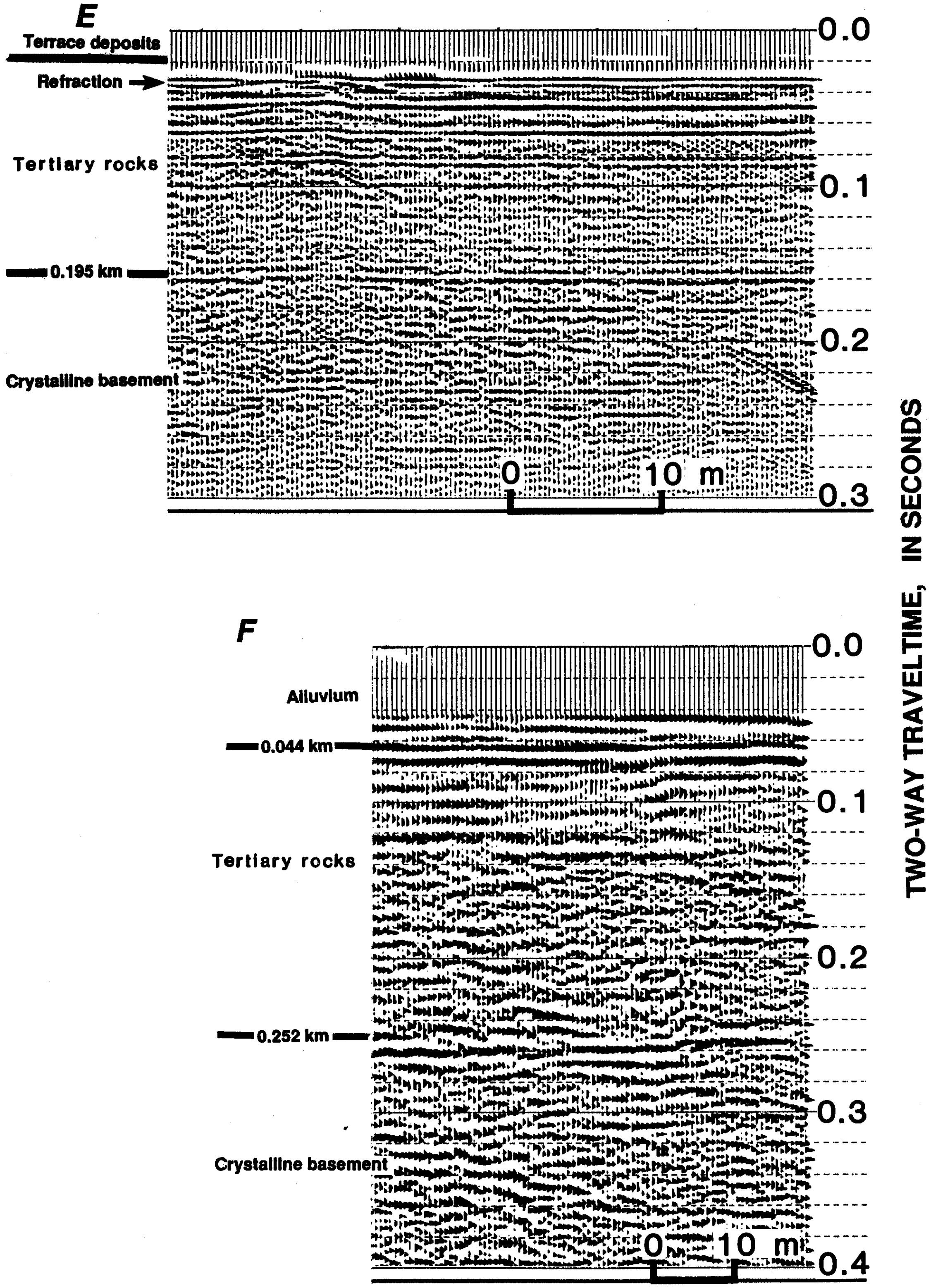

Figure 6.—Continued.

Underlying the low-reflectivity zone at all stations except TPK (fig. 2) is a distinct high-amplitude reflector that commonly appears as a doublet. This reflector, which occurs between 0.14 and 0.25 s (140–250-m depth), generally deepens from north to south, in accordance with the regional dip of about 3°–8° S. (Clark, 1981). Two possible units that could produce this reflector are the Monterey Formation (interbedded siliceous mudstone and sandstone) and crystalline basement (schist, marble, and granitic rocks).

Several lines of evidence, however, argue against the Monterey Formation as a candidate; the seismic-velocity analysis of the reflection data cannot be used as a discriminator because of the relatively small normal moveout correction on this reflector. First, the Monterey is composed of interbedded mudstone and sandstone, but on the profiles there are no other clear reflections below the primary that would suggest interbedding like that in the overlying Purisima Formation. Second, Clark's (1981) geologic map of the Santa Cruz area shows that the Monterey does not crop out in the immediate vicinity, even though older crystalline rocks do. Third, the Monterey is not expected to have an adequate impedance difference from the Santa Cruz Mudstone, because they are both siliceous, to produce this strong reflector. For example, reasonable velocities and densities for an interface between the Santa Cruz Mudstone (2.9 km/s, 2.2 g/cm^3) and the Monterey Formation (3.1 km/s, 2.3 g/cm^3),

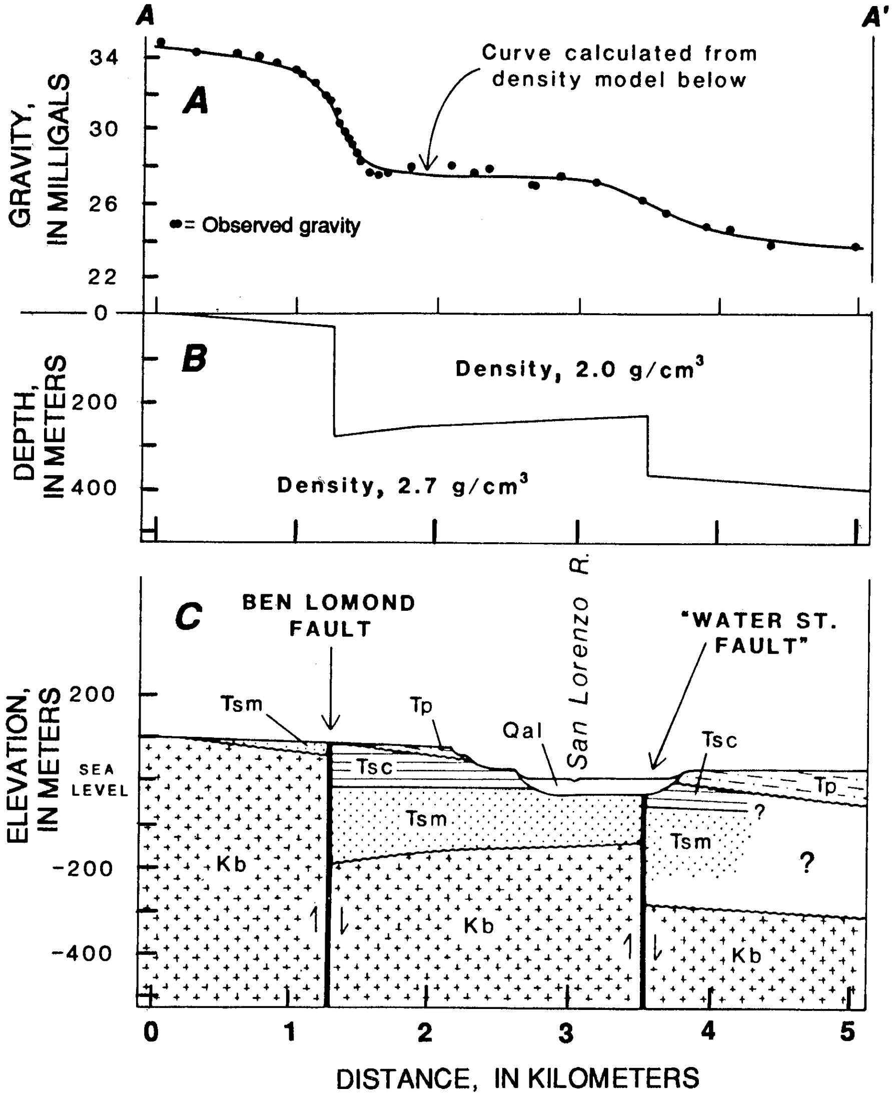

Figure 7.—Bouguer gravity (*A*), density model (B), and interpretative west-east geologic cross section (*C*) along line *A–A'* (fig. 2). Units: Kb, Cretaceous crystalline basement rocks; Qal, Quaternary alluvium; Tp, Tertiary Purisima Formation; Tsc, Tertiary Santa Cruz Mudstone; Tsm, Tertiary Santa Margarita Sandstone. Vertical exaggeration, 3:1. Paired arrows indicate direction of movement on faults. From Stanley and McCaffrey (1983).

versus an interface between the Santa Cruz Mudstone (2.9 km/s, 2.2 g/cm^3) and crystalline basement (4.0 km/s, 2.7 g/cm^3), generate reflection coefficients of 0.06 and 0.26, respectively; the Santa Cruz Mudstone/Monterey Formation reflection coefficient is characteristic of weak reflections, whereas the Santa Cruz Mudstone/crystalline-basement reflection coefficient is above average (Sheriff and Geldart, 1982). Finally, a gravity study within the city of Santa Cruz by Stanley and McCaffrey (1983) placed crystalline basement at depths almost identical to that determined for this strong reflector (fig. 7). This basement reflector was selected as an interface in the synthetic seismic models for stations BVE and SCH (fig. 2).

The gravity study also helped resolve an interpretation of the reflection data at station TPK (fig. 2). The reflection record at this site, which is only 0.4 km from a more typical record at station BVE, is anomalous because it lacks the low-reflectivity zone and underlying Tertiary rocks/crystalline-basement reflector. The gravity study places the Ben Lomond fault between stations TPK and BVE. The presence of this normal fault, with about 250 m of down-to-the-east displacement (Stanley and McCaffrey, 1983), suggests that the Purisima Formation and the low-reflectivity zone are missing at station TPK and that crystalline basement is probably much shallower there. A strong reflector on the profile for station TPK (fig. 6*D*) at about 0.07 s (approx 75-m depth), therefore, could be crystalline basement, and about 150 m of offset from the basement reflector at station BVE is indicated. The stepped appearance of the basement reflector at station BVE also suggests that the Ben Lomond fault may be represented by a series of faults over a narrow zone.

AFTERSHOCK RECORDINGS

In October and November 1989, the USGS deployed 43 portable Sprengnether DR200 digital seismographs in Santa Cruz to record aftershocks of the earthquake for a site-response study. For security reasons, most of these seismographs had to be installed on the grounds of private residences, sites that did not permit adequate space for the exploration seismic surveys. Other than the reference station (BAR, fig. 2), the aftershock-recording stations used in this study and listed in table 1 (stas. BLA, TRE) were selected because they were close to the surface seismic surveys (fig. 2). Also, to maintain a consistency between the observed and synthetic spectral ratios, each spectral ratio formed in this study incorporates data from station BAR. In this study, we used eight aftershocks from the USGS site-response study; these aftershocks range in magnitude from 2.1 to 3.6 and have hypocentral depths of 5 to 14 km (table 4), as determined by the USGS' northern California seismic network (Calnet). The aftershocks used in this study are identified by Julian day (for example, day 303 = 30 October) and hour of origin (G.m.t.). The locations of epicenters are shown in figure 8.

The seismographs were equipped with Sprengnether S6000 2.0-Hz triaxial seismometers, whose actual natural frequencies range from 1.6 to 2.5 Hz, according to the manufacturer's calibrations. The data were sampled at intervals of 5 ms (200 samples per second), antialias filtered at 50 Hz, amplified by a factor of 10, and written onto magnetic tape. In general, the seismometers were buried in soil at 0.3- to 0.6-m depth. The seismometer at the reference station (BAR, fig. 2) was buried within centimeters of the marble outcrop; seismometer-leveling requirements prevented affixing it to the marble. All the seismometers were leveled and oriented so that the north-south component is aligned with respect to magnetic north.

Selected seismograms were analyzed on a personal computer, using spectral-analysis software written by Cranswick and others (1989). First, the two horizontal-component seismograms were rotated to the backazimuth of the epicenter. To avoid possible complexities with *P*- to *S*-wave conversions and surface waves, and to allow for a more nearly equivalent comparison with similar phases on the synthetic data, each time window on the vertical and two horizontal components emphasized the first-arrival *P*- and *S*-wave signals (fig. 9). We selected a 5.12-s time window (1,024 samples) over a 512- and a 2,048-sample window because the smaller window produced spectra with broader spectral holes than the 1,024-sample window and because the 2,048-sample window was judged to be contaminated with converted phases and surface waves. As shown in figure 9, the 5-s window emphasizes the first arrivals of the selected component.

To remove a mean value (dc offset) from the synthetic seismograms, a baseline dc average was determined from 5 s of preevent signal and subtracted from the time series before calculating the spectra. Although a 0-Hz spectral-ratio amplitude is not plotted in any of the figures, the observed ratio generally does not appear to be declining toward zero for frequencies below 0.5 Hz, as would be expected if the dc bias were removed. The "high" values near 0 Hz could be caused by poor low-frequency instrument response at the reference station (BAR, fig. 2) relative to the other stations' instruments.

After the dc bias was removed, the data time window was tapered with a bell curve (Hanning window), as shown in figure 9, before transformation into the frequency domain, where the spectra are divided. To reduce the effect of spectral holes, the spectral-ratio amplitudes were smoothed before division, using a symmetrical, five-point (1.0 Hz)-triangular moving-average window. This window size does not significantly change the

Table 4.—*Source parameters of eight aftershocks used in this study*

Event	Date	Latitude N.	Longitude W.	Depth (km)	Magnitude
302–13	10–29–89	37°02.97′	121°54.47′	14.3	2.9
302–21	10–29–89	37°04.54′	121°53.83′	9.7	2.9
303–04	10–30–89	37°03.56′	121°54.02′	13.6	2.5
303–06	10–30–89	36°55.58′	121°40.78′	11.4	2.9
303–11	10–30–89	37°03.42′	121°48.57′	9.4	3.6
304–02	10–31–89	37°06.91′	121°56.33′	8.6	2.1
304–02	10–31–89	37°07.86′	121°59.53′	12.4	2.2
304–08	10–31–89	37°03.83′	121°48.26′	8.2	3.3

overall characteristics of the observed and synthetic spectra (fig. 10).

To minimize the effects of scattering, incidence angle, and azimuth, smoothed spectral ratios at stations BVE and SCH relative to reference station BAR (fig. 2) were determined for each of the eight aftershocks listed in table 4 and averaged for comparison with the synthetic ratios. The eight individual spectral ratios for the vertical, radial, and tangential components at station SCH relative to reference station BAR are plotted in figure 11. The ratios display an order-of-magnitude range of amplitude, but the frequency response varies less and has an observably repeating shape. Thus, the average of the eight ratios (heavy curve, fig. 11) appears to be a reasonable representation of the average ground motion to compare with the synthetic ratios.

The spectral ratios are displayed only up to 10 Hz because this frequency band is important in structural engineering: 10 Hz approximately corresponds to the natural frequency of a 1-story structure, and 1 Hz to that of a 10-story building. Also, extremely poor agreement was obtained in a comparison of the spectral ratios from the synthetic and observed data up to 20 Hz, and so these data are not shown here.

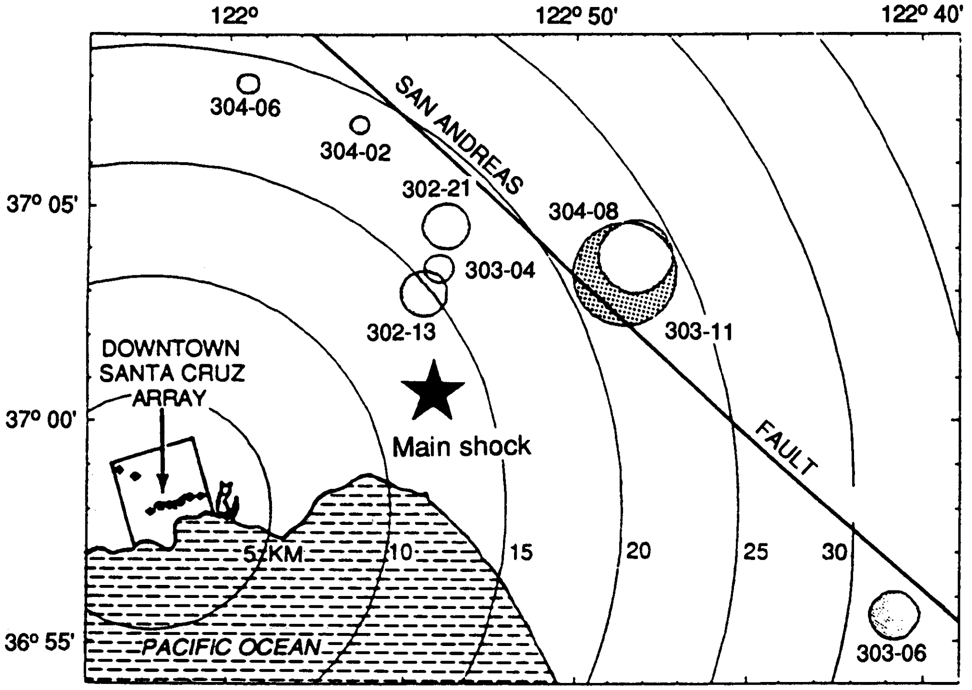

Figure 8.—Santa Cruz area, showing locations of aftershocks used in this study (see table 4). Size of circle indicates relative magnitude of aftershock. After Cranswick and others (1990).

SYNTHETIC MODELING

MODEL DEFINITION

Because the dominant frequency of the reflection/refraction data (approx 50 Hz) permits higher resolution of subsurface interfaces than do the aftershock data (dominant frequency, <5 Hz), several interfaces were imaged that would probably have no effect on the earthquake signal. Therefore, as described in a previous section, only the most conspicuous reflectors were selected. The velocity models are each 10 km thick and composed of nine horizontal interfaces over a half-space. Combining the published data with the seismic refraction and reflection data permits construction of the models (fig. 12). There is considerable uncertainty, however, regarding the *S*-wave-velocity structure because *S*-wave velocities

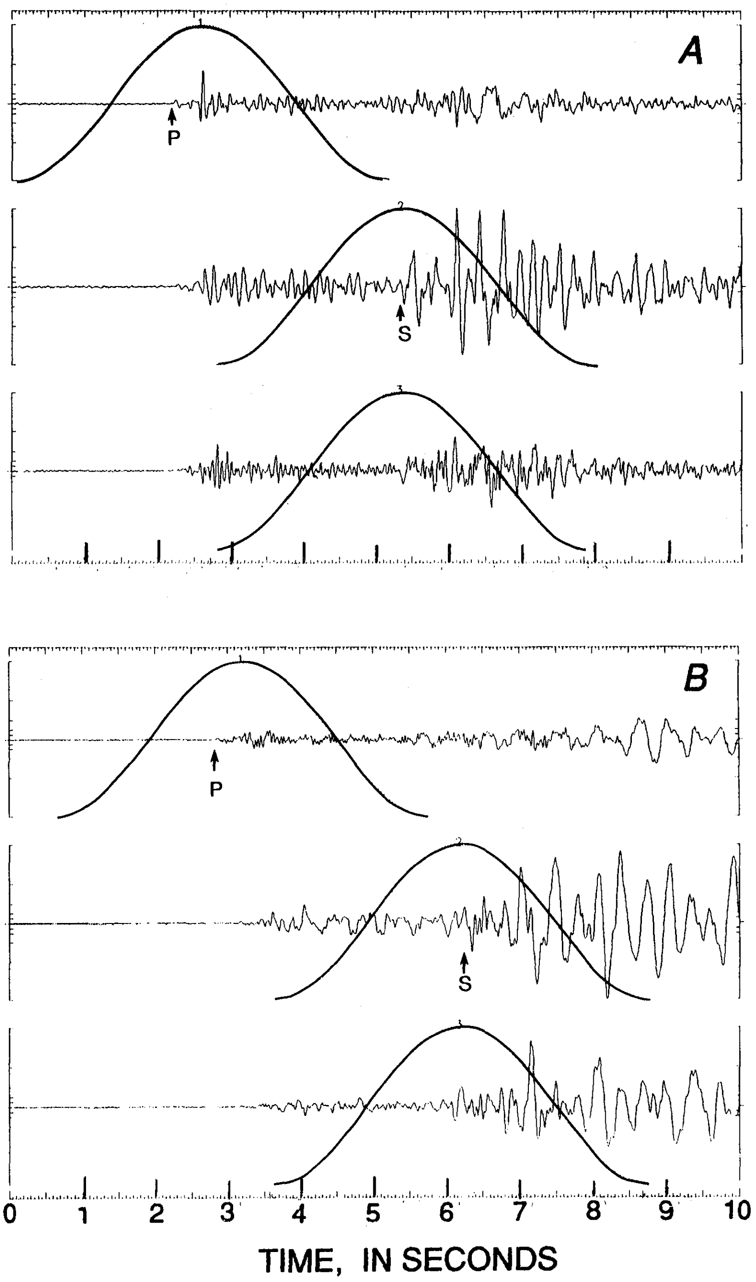

Figure 9.—Seismograms of vertical (upper curve), radial (middle curve), and tangential (bottom curve) components at stations BAR (*A*) and BLA (*B*) (see fig. 2 for locations). Bell curve shows position of 1,024-sample window on data used to generate spectrum. P, *P*-wave first arrival; S, *S*-wave first arrival.

were not directly measured in the rocks in the depth range 30–250 m. Only two indirect methods of estimating *S*-wave velocity are available. The first method is from the Santa Cruz aftershock study by Cranswick and others (1990), in which first-motion *P* waves on horizontal components are time delayed with respect to those on vertical components. Cranswick and others (1990) believed that these delays result from *P*- to *S*-wave conversions at the Tertiary rocks/crystalline basement contact; and because the delays are absent at the reference station (BAR, fig. 2) and nearly the same at the other stations (0.2–0.3 s), the traveltime through this layer is inferred to be about 3 times the *P*-wave traveltime observed in the reflection data. The second method is from an examination of *S*-wave resonance peaks (see subsection below entitled "Synthetic Versus Observed Spectral Ratios"), which convert to a 3:1 ratio of *P*- to *S*-wave traveltimes in the material overlying crystalline basement.

We assumed that the same basement structure underlies each of the sites; therefore, each model has the station BAR (fig. 2) structure as its foundation. Other than the refraction information from the quarry site, which identified the 4.0-km/s *P*-wave velocity at the surface, all the layers at station BAR were determined from published data, as described above in the subsection entitled "Refraction Data." As shown in figure 12, the velocities at station BAR range from 4.0 to 6.35 km/s at 10-km depth over six layers.

DATA GENERATION

Synthetic seismograms were generated with a seismic-response model that uses propagator matrices, according to Haskell's (1953, 1960) matrix methods. Incident homogeneous plane waves are assumed as input to each models (although inhomogeneous wavefields are also accounted for in the propagator matrices). This assumption seems reasonable in this study only for frequencies above about 3 Hz; below 3 Hz, the aftershock-recording

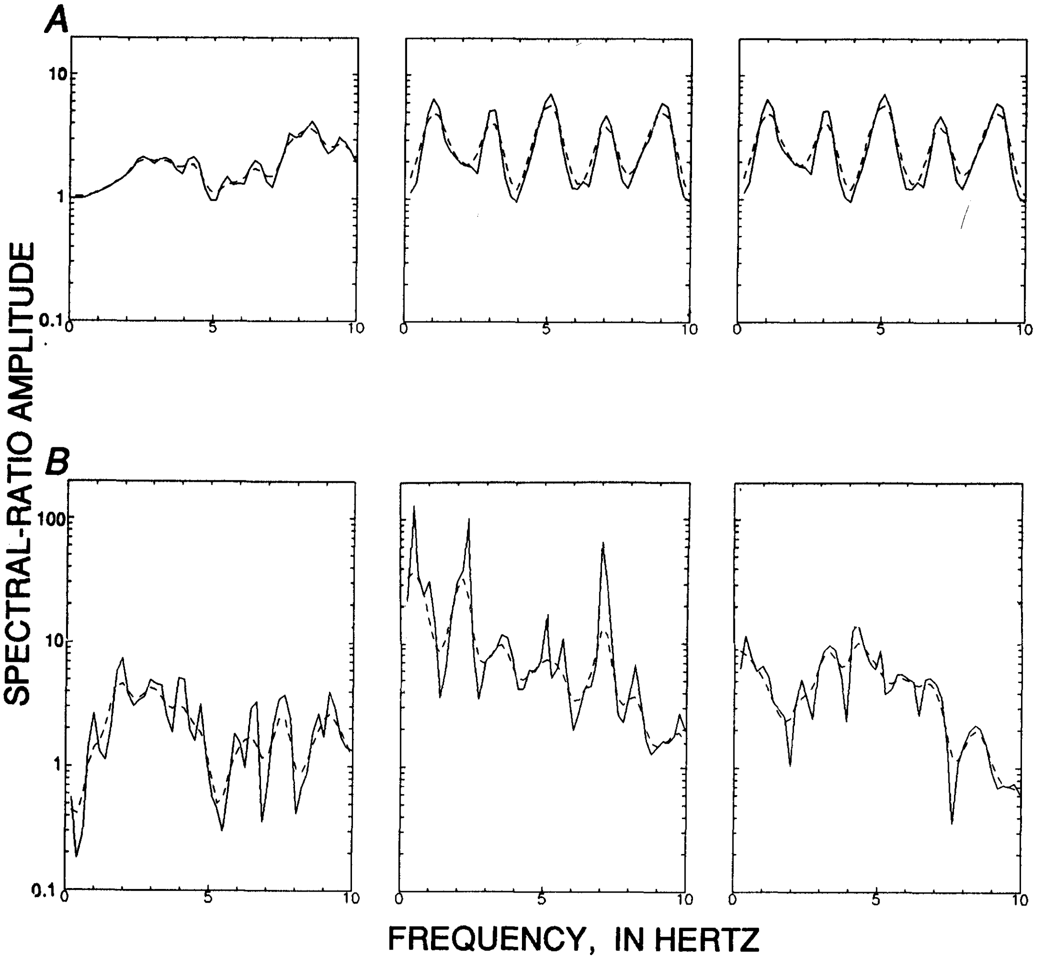

Figure 10.—Smoothed (dashed curve) and unsmoothed (solid curve) spectral ratios for vertical (left plot), radial (middle plot), and tangential (right plot) components of synthetic data at station SCH (*A*) and observed data at station BLA (*B*) with respect to reference station BAR (see fig. 2 for locations). Smoothing is by a symmetrical five-point (1.0 Hz)-triangular moving-average window.

stations are probably less than 10 wavelengths from the sources. The model program also assumes a δ-function input waveform and calculates the response from the impedance structure of the geologic model. Then, a 1,024-sample length of the resulting displacement seismogram, centered on the peak value of each phase (to emphasize direct arrivals), was extracted, detrended, tapered with a bell curve (Hanning window, identical to the observed data window), and then transformed to the frequency domain. Wraparound noise in the seismograms was not a problem with the 4,096 data points used and the 100-Hz Nyquist frequency (equal to the Nyquist frequency of the observed data). The spectra were smoothed with the same five-point-triangular spectral-smoothing window applied to the observed data.

Synthetic spectral ratios are also produced by comparing the non-rock sites to the synthetic reference station (BAR, fig. 2). The amplitude spectrum for the reference station is relatively flat in comparison with those for the non-rock sites, and so the purpose of ratioing the synthetic spectra was simply to duplicate the observed data-processing scheme and thereby remove free-surface effects, remove source effects, and permit the use of synthetic displacement spectra.

Assuming horizontal layers, the incidence angle at the base of each model was determined by calculating a ray parameter of about 0.13 for *P* waves and about 0.2 to 0.3 for *S* waves from the aftershock data. A non-zero ray parameter introduces *P–S* mode conversions at each interface in the model. The ray parameters used in this study translate to an incidence angle of about 30° for *P* waves and 30° for tangential components at the surface of the reference station. The ray parameter was determined for the same phase arrival at two stations (for example, TRE and SBR) by dividing the observed traveltime difference for this phase by the distance between these stations. For event 304–08 (table 4), these two stations were within about 8° of being along the backazimuth to the epicenter, and so correcting for this angular difference results in an error of only about 8 percent, assuming that the two stations are along the backazimuth from station TRE to the epicenter.

The calculated *S*-wave ray parameters vary more widely than the *P*-wave ray parameters because (1) it was difficult to pick identical phases at different stations, (2) clock-correction errors may exist, and (3) varying site delays could cause timing problems. Despite the uncertainty in calculating a ray parameter for the horizontal components, a value of 0.25 seems reasonable because it is about twice the *P*-wave value and reflects the approximately 2:1 published velocity ratio between *P* and *S* waves in this region. A ray parameter of 0.25 was used for the tangential components, and of 0.16 for radial components. Values higher than 0.16 form postcritical incidence angles for *P* and *SV* waves at the base of the model and generate extremely high amplitude, inhomogeneous *P* waves and associated numeric errors. For precritical arrivals, however, as described below, the ray parameter was found to have no significant effect on model response.

MODELING RESULTS AND DISCUSSION

Before comparing the synthetic and observed data at stations BVE and SCH (fig. 2), we examine the effect on seismic response of variations in individual model parameters, such as incidence angle, density, attenuation (*Q* value), seismic-wave path, and seismic velocity, to clarify the relative importance of these parameters. Except for the seismic-wave-path test, which uses stations BVE, SCH, and BAR, and unless otherwise specified, all

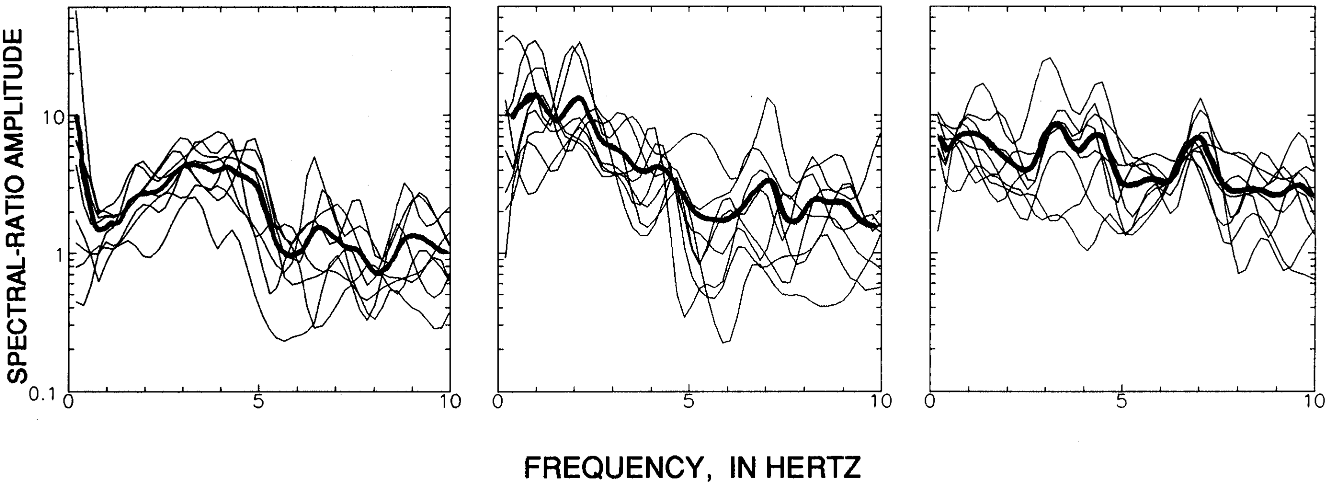

Figure 11.—Spectral ratios for vertical (left plot), radial (middle plot), and tangential (right plot) components of observed data from eight aftershocks listed in table 4, and their component average (heavy curve), at station BLA with respect to reference station BAR (see fig. 2 for locations).

tests were conducted by using spectra generated with normal incidence angles and *Q* values of 1,000 for each model layer from stations SCH and BAR.

RAY PARAMETER

Two synthetic spectral ratios generated with differing ray parameters for the vertical and tangential components are compared in figure 13. These synthetic ratios were generated by using a vertical incidence angle and the nonzero ray parameters specified in the preceding subsection. The amplitudes of the spectral ratios derived from nonzero incidence angles differ (over narrow frequency bands) by as much as 23 percent (vertical component) from those derived from a vertical incidence angle, in somewhat-unexpected fashion—that is, increased amplitudes were unexpected. Overall, the relative amplitudes differ little, and the relative positions of the spectral peaks are virtually unchanged; therefore, it appears that the synthetic model can be adequately described with a vertical incidence angle. Joyner and others (1976) also found a negligible effect on seismic response with variations of incidence angle.

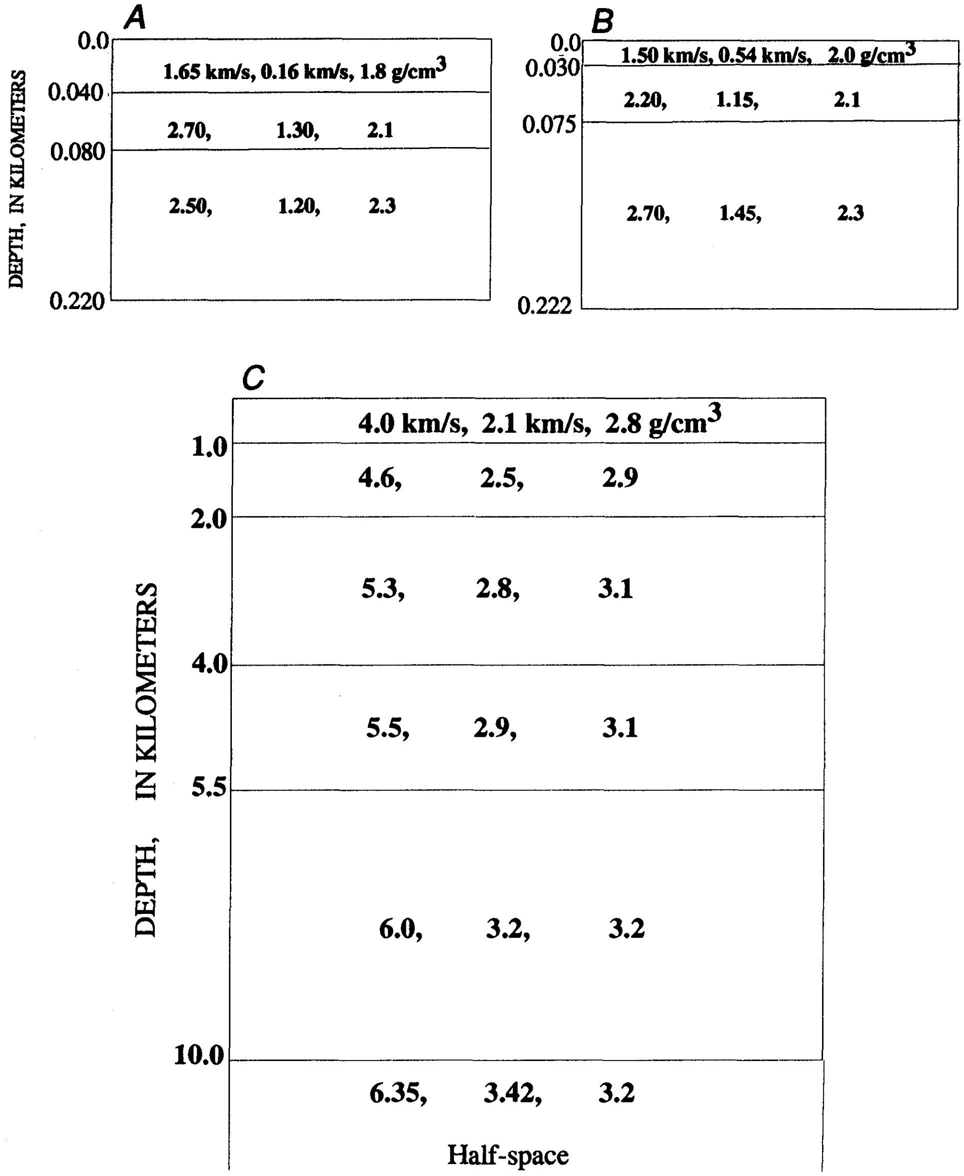

Figure 12.—Depth models for stations SCH (*A*), BVE (*B*), and BAR (*C*) (see fig. 2 for locations), showing layer depths, assigned *P*- and *S*-wave velocities, and densities. In models, structure at reference station BAR is attached to base of structures at stations SCH and BVE as the foundation.

DENSITY

The spectral ratios generated by using a ±10-percent change in the preferred densities reported in the literature are compared in figure 14. A 10-percent increase in density causes as much as a 7-percent decrease in amplitude at some frequencies, and as expected, a 10-percent decrease has the opposite effect. Generally, the amplitudes are little affected, and the frequencies of spectral peaks are unchanged, and so highly accurate densities are not essential for this modeling technique.

ATTENUATION (*Q* VALUE)

The relatively minor effects, in comparison with the error between the synthetic and observed site-response data, of including reasonable *Q* values for the surficial layers at station SCH (fig. 2) are illustrated in figure 15. As described earlier, no direct measurement of *Q* was available, and so the variable-*Q* model values were selected to be comparable to published data for saturated unconsolidated alluvium (Q=25), sedimentary rocks (Q=100), and crystalline rocks (Q=1,000). Results using *Q* values of 300 to 500 for the crystalline rocks are indistinguishable from those shown in figure 15 and are not presented here. Despite the low *Q* value for the alluvium, the variable-*Q* model results are virtually the same as for the vertical component in the constant-*Q* model but significantly different for the horizontal components, especially for frequencies above 5 Hz. We incorporate the *Q* value into the propagator matrix by way of a Futterman operator, as illustrated by Aki and Richards (1980, p. 182). As expected, above 5 Hz on the horizontal components, low *Q* values cause a decrease in amplitude with increasing frequency and help generate a spectral ratio that more closely fits the general amplification level, but they attenuate the resonance peaks too severely at about 7 Hz. For frequencies below 3 Hz that have a potentially high level of amplification relative to the reference station, variable *Q* values have a negligible effect on the spectra and thus indicate that the *Q* value is not an essential parameter at these frequencies. Generally, our results indicate that it could be an important parameter for higher frequencies at sites without strong resonances. Joyner and others (1976) and Shearer and Orcutt (1987), who studied similarly derived seismic-response models, also reported that the response was not highly sensitive to the *Q* value. Seale and Archuleta (1989), however, found the *Q* value to be important in their modeling, although including an attenuation factor also suppressed the model response above 10 Hz too severely in comparison with the observed data.

VELOCITY

Comparisons of the synthetic and observed spectral ratios with ±20-percent changes in seismic velocity from the preferred model show that velocity uncertainties are a major source of error (fig. 16). Velocity changes were applied only to the layers overlying crystalline basement. As described above in the section entitled "Seismic

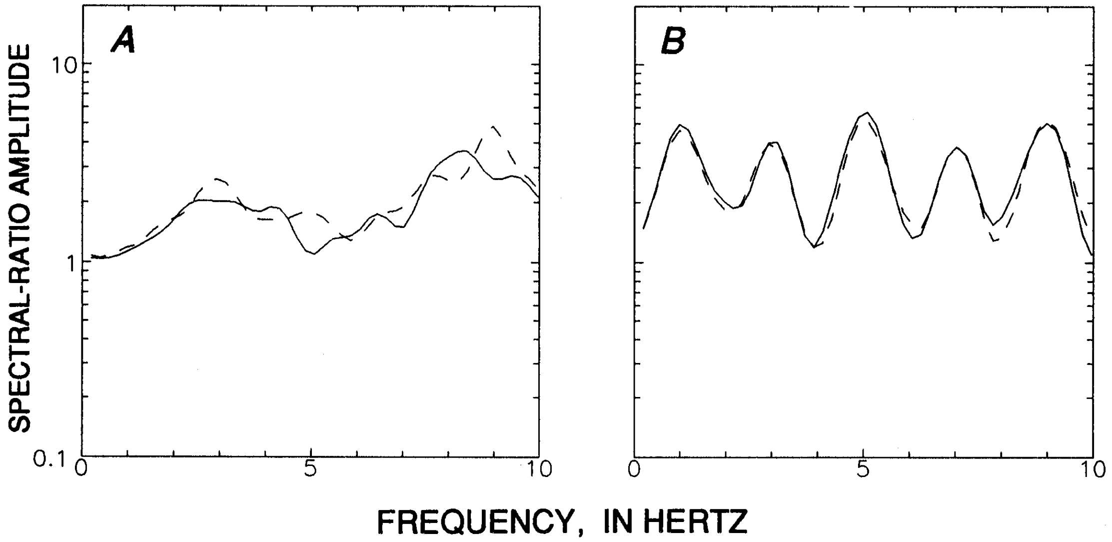

Figure 13.—Synthetic spectral ratios for *P* wave (*A*) and *S* wave (*B*) at station SCH with respect to reference station BAR (see fig. 2 for locations), generated by using vertical incidence angle (solid curve) and preferred values of ray parameter (dashed curve) of 0.13 for *P* wave and 0.25 for the *S* wave, as estimated from aftershock data.

Data," the reflection and refraction data indicate that near-surface seismic velocity can vary by 50 percent occur over distances of 0.3 to 0.5 km. Considering that the aftershock-recording sites are separated from the reflection/refraction sites by 0.2 to 0.3 km, the velocity structures could differ significantly. A 20-percent decrease in velocity causes a gradational shift to lower frequencies of all the spectral peaks, with the frequencies above 5 Hz showing the greatest shift (almost 2 Hz); a 20-percent increase in velocity has the opposite effect. This shift in frequency is comparable to an equivalent change in layer depth. Peak amplitudes are not so severely affected by these velocity changes. Thus, the results shown in figure 16 indicate that even a 20-percent variation in velocity can significantly change the spectral ratio and that the model parameters described above are of secondary importance in comparison with seismic velocity. Most other studies (for example, Joyner and others, 1976; Shearer and Orcutt, 1987; Seale and Archuleta, 1989) that involve site-response modeling derive their velocity data from borehole studies and thus appear to have better velocity control than this study.

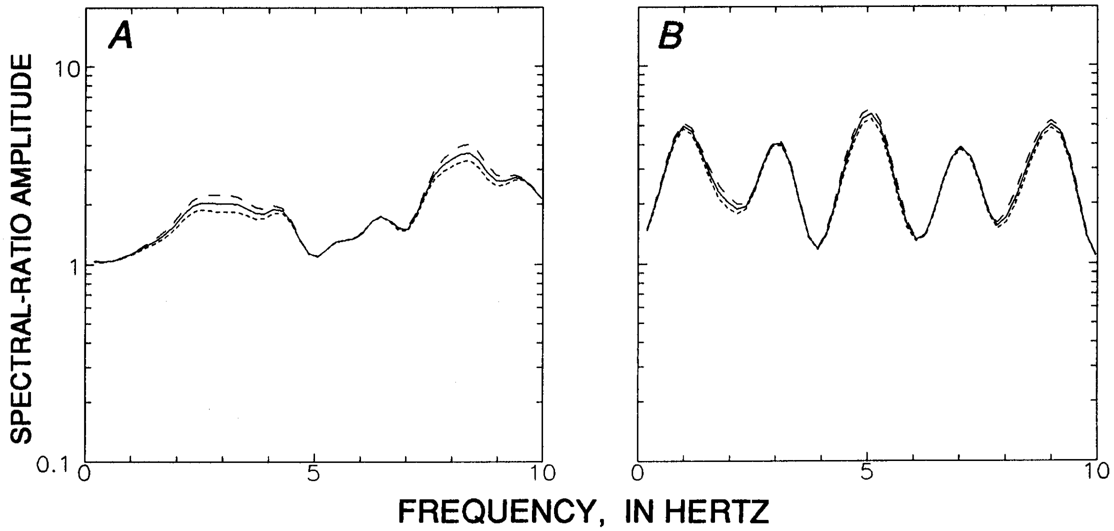

Figure 14.—Synthetic spectral ratios for vertical (*A*) and tangential (*B*) components at station SCH with respect to station BAR (see fig. 2 for locations), generated by using vertical incidence angle with preferred density model (see fig. 12) (solid curve) and density changes of +10 percent (short-dashed curve) and −10 percent (long-dashed curve).

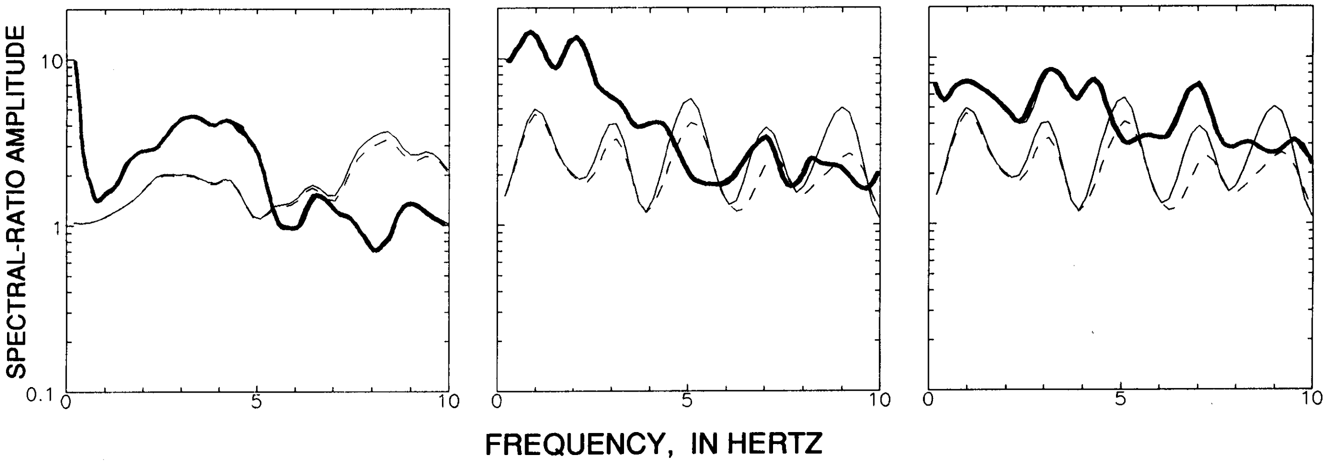

Figure 15.—Synthetic spectral ratios for vertical (left plot), radial (middle plot), and tangential (right plot) components at station SCH with respect to reference station BAR (see fig. 2 for locations), generated by using *Q* values of 1,000 in each layer (light solid curve) and estimated *Q* values of 25, 100, and 1,000 in top three layers (dashed curve), in comparison with observed spectral ratio at station BLA with respect to reference station BAR (heavy solid curve).

SYNTHETIC VERSUS OBSERVED SPECTRAL RATIOS

Given the relative importance of the modeling parameters described above, we can now test the overall effectiveness of this technique in predicting the site response at two sites. We summarize our results by comparing the observed aftershock spectral ratios with the synthetic ratios at the nearest reflection/refraction sites (fig. 17).

AMPLIFICATION LEVELS AND RESONANCE PEAKS

For the frequency band 1–5 Hz, the synthetic spectral ratios underestimate the amplification of the observed data by a factor of 2 to 4 (figs. 17*A*, 17*B*). The highest resonance peaks also occur on all three components within the frequency band 1–5 Hz of the observed data. On the vertical components, the strongest resonance occurs at about 3.5 Hz, suggesting an amplification factor of 4 to 6 over the reference station for the observed data (figs. 17*A*, 17*B*). The synthetic ratios also predict a resonance with an amplification factor of about 2 at this same frequency. On the horizontal components, a strong resonance peak typically occurs at about 1–2 and 7 Hz. The peak amplification for these frequencies at station BLA (fig. 2) is between 10 and 15. The synthetic ratios approximately duplicate the 1- and 7-Hz resonance peaks, but with about 1/3 to 1/2 the amplification of the observed data (figs. 17*A*, 17*B*). On the observed spectra, horizontal ground motion at an alluvial-basin site (sta. BLA) is amplified 2 to 5 times relative to a marine-terrace site (sta. TRE) over the entire frequency band 1–10 Hz (fig. 17*C*). The synthetic horizontal-component data also show higher amplification in the alluvial basin by a factor of as much as 3, but only at frequencies of 1, 3, 5, and 7 Hz (fig. 17*C*). The poor agreement of amplification levels between the synthetic and observed data is a common occurrence in studies of this type. For example, Joyner and others (1976, 1981), generated synthetic response data that underestimated their observed data by about the same amount as in this study.

Between 5 and 10 Hz, agreement breaks down between the synthetic and observed ratios for the vertical and horizontal components at station BVE (figs. 17*A*, 17*B*). In the observed vertical-component data, the amplification declines to below 1. The synthetic vertical-component spectral ratios do not follow this decline and continue to predict a mild amplification of about 2 to 4 at non-rock sites. For the radial component between 5 and 10 Hz, agreement between the synthetic and observed ratios is generally poor, except for one resonance peak at about 7 to 8 Hz that suggests an amplification of about 3 on both the radial and tangential components at station SCH (fig. 17*A*).

Among all three of the components compared in this study, the best agreement between the synthetic and observed ratios is obtained for the tangential component (figs. 17*A*, 17*B*). Despite the overall trend of agreement, however, the synthetic spectral ratio still underestimates the maximum peak amplification between 1 and 5 Hz by a factor of about 2 to 4. Maximum observed peak-amplification factors range from 10 to 15 within this frequency band, whereas the synthetic spectral ratio estimates a factor of only 2 to 5.

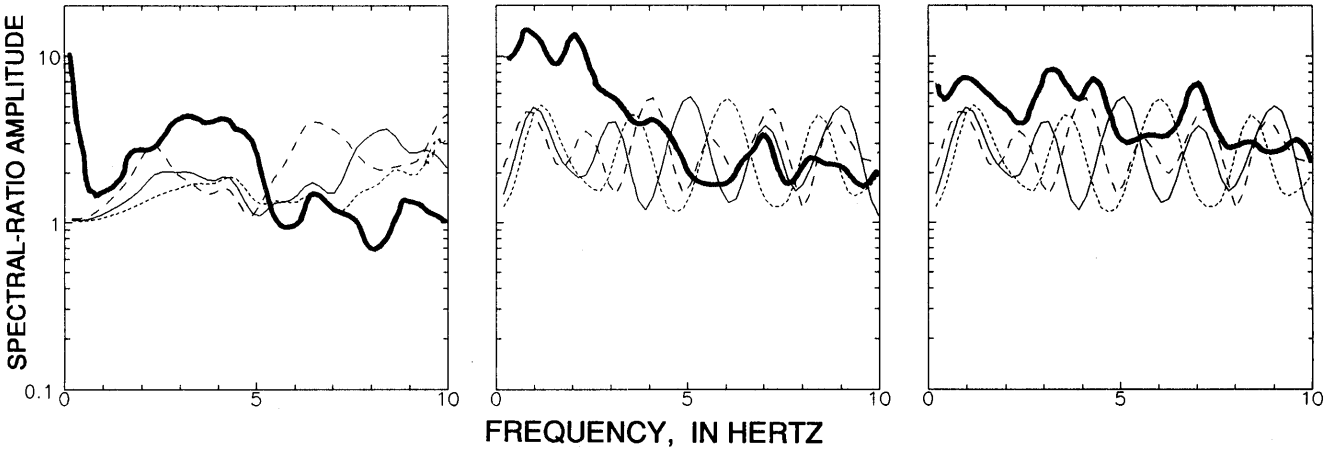

Figure 16.—Synthetic spectral ratios for vertical (left plot), radial (middle plot), and tangential (right plot) components at station SCH with respect to reference station BAR (see fig. 2 for locations), generated by using preferred velocity model (see fig. 12) (light solid curve) and velocity changes of +20 percent (small-dashed curve) and −20 percent (large-dashed curve), in comparison with observed spectral ratio at station BLA with respect to station BAR (heavy solid curve).

SOURCES OF DISCREPANCY

The good agreement between the synthetic and observed data for the tangential component might be explained by complexities in the observed waveforms caused by waves, especially *P–S* converted phases, arriving from many directions. Converted *P* and *SV* waves scattered from other interfaces, such as the alluvium/Tertiary rocks interface, outside of the assumed two-dimensional plane of analysis are not incorporated into the model. The tangential component is not complicated by these converted phases and thus is easier to model. Joyner and others (1981) compared synthetic radial-component data with observed data up to 10 Hz and found, similar to our results, that the frequency agreed at only one resonance at about 1 Hz and that the synthetic amplitude underestimated the observed by about 40 percent. Seale and Archuleta (1989) examined synthetic and observed data for only the tangential component up to 20 Hz and found, unlike our results, relatively good agreement in amplitude; resonance-peak prediction was about as successful as in this study at station SCH (fig. 2).

Both the synthetic and observed spectral ratios appear to display two types of amplification: broadband and

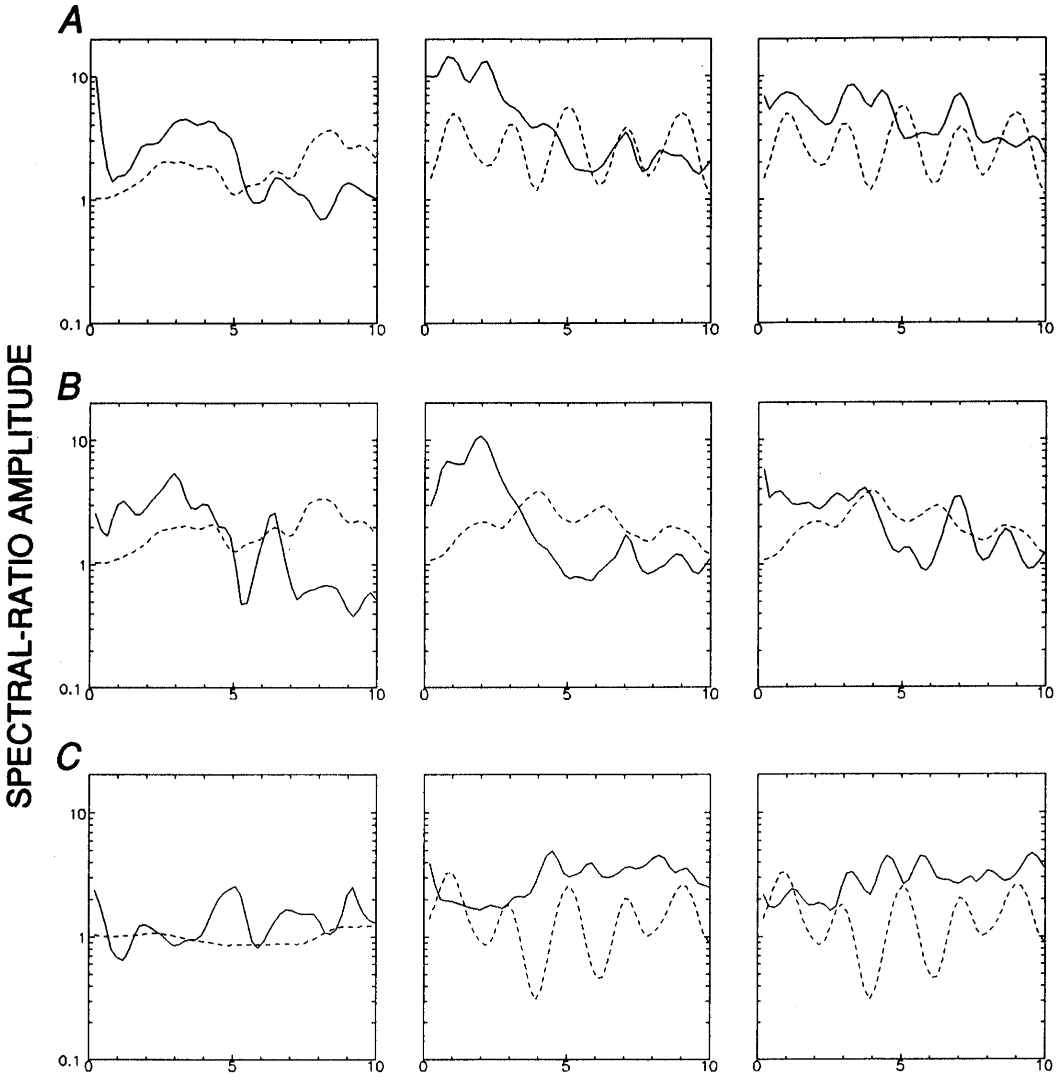

Figure 17.—Synthetic spectral ratios for vertical (left plot), radial (middle plot), and tangential (right plot) components at stations SCH (*A*, *C*) and BVE (*B*) with respect to reference stations BAR (*A*, *B*) and BVE (*C*) (see fig. 2 for locations), generated by using preferred model (see fig. 12) (dashed curve), in comparison with stacked observed spectral ratios at an alluvial-basin site (sta. BLA; *A*, *C*) and a marine-terrace site (sta. TRE; *B*) with respect to reference stations BAR (*A*, *B*) and TRE (*C*) (solid curve).

resonance. The broadband ground-motion amplification, which results from impedance-contrast amplification across a smoothly varying velocity gradient, tends to raise the overall amplification above 1 at non-rock sites between 1 and 10 Hz. A simple impedance-contrast relation can be used to estimate the broadband amplification factor A_1/A_2 caused when a wave with amplitude A_2 leaves a layer with impedance $\rho_2 V_2$ and enters a layer with impedance $\rho_1 V_1$ (Shearer and Orcutt, 1987):

$$A_1/A_2 = (\rho_2 V_2/\rho_1 V_1)^{1/2} . \tag{4}$$

If the wave enters lower velocity material, seismic amplitudes will generally increase. This calculation assumes that the wave is totally transmitted from one material to another. Applying equation 4 to the study area—for example, at station SCH (fig. 2)—indicates an amplification of about 1.5 for *S* waves at the alluvium/Tertiary rocks interface—close to the minimum amplification observed in figure 17 within the frequency band 1–5 Hz at station SCH.

The resonance-peak amplification, however, is much stronger than the broadband amplification. Strong resonance peaks indicate possible reverberations between the ground surface and high impedance contrasts in the subsurface. For resonance conditions between a surface layer 1 over a half-space (layer 2), Shearer and Orcutt (1987) developed the following simple relation for estimating wave amplification at the surface:

$$A_1/A_2 = \rho_2 V_2/\rho_1 V_1 . \tag{5}$$

Applying equation 5 to *S* waves at station SCH (fig. 2) and considering the Tertiary rocks and alluvium as a single unit, with a velocity of 0.75 km/s and a density of 2.1 g/cm^3, over the crystalline rock (half-space), with a velocity of 2.5 km/s and a density of 2.8 g/cm^3, gives an amplification of about 4.5, similar to that obtained, for example, in figure 17*A* for the synthetic radial and tangential components at 1 Hz.

CALCULATION OF RESONANCE PEAKS DIRECTLY FROM SEISMIC-REFLECTION DATA

The most useful product of this study may be the ability to predict the frequency of damaging resonances directly from reflection data. As described above, a strong resonance occurs at about 3.5 Hz on the vertical component and at about 1 to 2 Hz on the two horizontal components. These resonance frequencies could be predicted from the reflection data by using the method of Backus (1959), in which the fundamental frequency—in this case, the resonance peaks at 1 to 2 Hz on the horizontal components—is given by

$$f_n = {}^1/_4T,$$

where f_n is the frequency of the *n*th harmonic and T is the one-way traveltime for an event on the reflection records. The two-way traveltime of the crystalline-basement reflector at, for example, station SCH (fig. 6*B*), occurs at 0.19 s. Equation 6 predicts that this structure would produce a fundamental resonance peak at about 2.6 Hz—very close to the observed spectral peak at about 3 Hz in figures 17*A* and 17*C*. The same procedure can be used to predict *S*-wave resonances. Lacking *S*-wave-reflection data, however, we constructed a hypothetical *S*-wave-reflection profile, using the *P*-wave-reflection data and *S*-wave-velocity data from this study, which suggests a *P*- to *S*-wave-velocity ratio of 3:1. Applying this approximate velocity structure to the reflection profile at station SCH suggests that the basement reflector on an *S*-wave-reflection profile would occur at about 0.57 s. This reflector corresponds to a fundamental resonance frequency of about 0.9 Hz—very close to the 1.0-Hz peak observed on the radial and tangential components at station BLA and close to the broad resonance peak at 1 to 2 Hz observed at station TRE (figs. 17*A*, 17*B*). Higher harmonics should then occur at 3, 5, 7, . . . Hz. These modes are present on the tangential component at station SCH, but the presence of the harmonics at 3 and 5 Hz on the radial component is unclear.

Following the same procedure, we also modeled a few other sites, but with generally less success than described above. The uncertainties in the velocity data and the mixed results with the fit of the models, especially for the horizontal components at station BVE (fig. 2), suggests that a reevaluation of the data is needed to perform this type of study more successfully. The original intent of this procedure was to estimate the site response from interpretations of the reflection and refraction data. Nevertheless, we attempted to duplicate the observed site response at station BLA relative to reference station BAR by making several changes to the model for station SCH. Despite many iterations, however, the agreement could not be improved, probably because of surface waves.

VIOLATION OF IDENTICAL-PATH EFFECTS?

The generally poor agreement in curve shape between the synthetic and observed ratios for stations SCH and BVE (fig. 2) relative to reference station BAR (figs. 17*A*, 17*B*) could be caused by a violation of a key assumption in site-response studies: identical seismic-wave paths except for the surficial material near the receiver. As described above in the subsection entitled "Spectral-Ratio Technique and Assumptions," for the frequencies used in this study the identical-path assumption is certainly violated. To test for this violation, we calculated a ratio of the responses at stations SCH and BVE; these two stations are associated with aftershock-recording stations BLA and TRE, respectively, which were also ratioed. These stations are separated by less than a 1 km, in contrast to the 2.0- to 2.5-km distance between them and reference station BAR. Our results show, however, that the synthetic horizontal-component ratios for station SCH/BVE are a worse fit to the observed ratios for station BLA/TRE (fig. 17*C*) than the station SCH/BAR–BLA/BAR and BVE/BAR–TRE/BAR combinations (figs. 17*A*, 17*B*). The synthetic vertical-component ratio for station SCH/BVE agrees relatively well with the observed ratios, relative to the horizontal-component ratios. The vertical-component ratio for station SCH/BVE is relatively flat because the near-surface *P*-wave-velocity structures are nearly the same. The observed ratio for station BLA/TRE is also relatively flat out to about 4 Hz, beyond which the synthetic and observed responses diverge slightly. Beyond 4 Hz, the synthetic vertical-component ratio remains relatively flat, whereas at about 5 Hz, the observed ratio for station BLA/TRE shows a ground-motion amplification of about 2.5 at station BLA relative to station TRE. The relatively good agreement of the vertical-component ratios for the station SCH/BVE–BLA/TRE combination up to about 4 Hz is not unexpected because this frequency band was fairly well predicted for the station SCH/BAR–BLA/BAR and BVE/BAR–TRE/BAR combinations. The synthetic horizontal-component ratios for station SCH/BVE are a much poorer fit to the observed ratios for station BLA/TRE, probably as a result of the poor estimate of the *S*-wave-velocity structure at station BVE, as shown by a comparison of the ratios for the station BVE/BAR–TRE/BAR combination.

Owing to the smaller distance between stations BVE/TRE and SCH/BLA relative to reference station BAR (fig. 2), these ratios were expected to have fewer complications with paths effects and, therefore, to agree better with the observed ratios. However, only the vertical-component ratios (up to 4 Hz) for station SCH/BVE shows a close agreement, indicating that path effects may be an important factor. Other than this limited observation, our results contradict expectations, and so the problem of path-effect complications remains unresolved.

CONCLUSIONS

The primary objective in this study was to develop and evaluate a technique capable for predicting a site's seismic ground response, using geologic models derived primarily from high-resolution seismic reflection and refraction data. A successful development of this technique would provide a valuable, relatively low cost tool for zoning earthquake ground-shaking hazards in urban areas. As used in this study, however, the technique appears to have seismic-velocity-control weaknesses, and so it produced inconsistent results. Nonetheless, in comparison with other techniques that utilize borehole data to calculate the models, this technique rated no worse in predicting the amplitude and spectral position of low-frequency resonances.

To evaluate the technique, estimates of synthetic spectral ratios were calculated for two sites and compared with an average of eight observed spectral ratios derived from aftershock recordings over the frequency band 1–10 Hz. The synthetic spectral ratios were produced from planar multilayer models over a half-space with constant velocity and density in each layer. The reflection data revealed an impedance structure with several conspicuous reflections down to a depth of about 250 m. The most important event on the reflection data is the crystalline-basement interface at 200- to 250-m depth; this reflector was connected to a fundamental resonance in the aftershock data by a simple quarter-wavelength traveltime calculation.

The technique of comparing synthetic with observed spectral ratios showed only limited success, generally below 5 Hz on the vertical components at both sites, as a broad resonant peak predicted between 3 and 5 Hz; however, the synthetic amplitude was about a factor of about 2 below the observed data. For the radial components, only the position, not the amplitude, of resonances at about 1 and 7 Hz was successfully predicted at one site. Only one tangential component also was reasonably well predicted in amplitude and frequency of resonances at 1, 3, and 7 Hz; the amplitudes of these resonances were underestimated by a factor of about 2. An important success of this study was that, like the observed data, the synthetic data showed an increase in amplification at the alluvial-basin sites, an area of high damage and one death during the earthquake, relative to nearby, generally low damage marine-terrace sites.

We also evaluated the effects of incidence angle, density, attenuation (*Q* value), and seismic velocity on seismic response. In comparison with seismic velocity, the other effects were of only secondary importance. A test for a violation of the identical-path assumption, used in spectral-ratio studies of this type, was inconclusive; apparently, a poor *S*-wave-velocity model and surface-wave contamination at one of the sites were to blame.

Given the available data, the technique proved useful in estimating low-frequency resonances on the horizontal and vertical components at only one of two sites. Nonetheless, because this limited success is intriguing, abandoning the technique seems inappropriate. Therefore, future applications of this technique should include (1) better control of seismic velocity at depth, especially *S* waves, by way of longer geophone spreads; (2) *S*-wave seismic-reflection data; and (3) a plan to install aftershock-recording seismographs at the reflection/refraction sites.

REFERENCES CITED

Aki, Keiiti, and Richards, P.G., 1980, Quantitative seismology; theory and methods: San Francisco, W.H. Freeman, 2 v.

Backus, M.M., 1959, Water reverberations—their nature and elimination: Geophysics, v. 24, no. 2, p. 233–261.

Borcherdt, R.D., 1970, Effects of local geology on ground motion near San Francisco Bay: Seismological Society of America Bulletin, v. 60, no. 1, p. 29–61.

Borcherdt, R.D., and Gibbs, J.F., 1976, Effects of local geological conditions in the San Francisco Bay region on ground motions and the intensities of the 1906 earthquake: Seismological Society of America Bulletin, v. 66, no. 2, p. 467–500.

Bradley, W.C., and Griggs, G.B., 1976, Form, genesis, and deformation of central California wave-cut platforms: Geological Society of America Bulletin, v. 87, no. 3, p. 433–449.

Carver, D.L., King, K.W., Cranswick, Edward, Worley, D.M., Spudich, Paul, and Mueller, C.S., 1991, Digital recordings of aftershocks of the October 17, 1989, Loma Prieta, California, earthquake—Santa Cruz, Los Gatos, and surrounding areas: U.S. Geological Survey Open-File Report 90–683, 204 p.

Chin, B.-H., and Aki, Keiiti, 1991, Simultaneous study of the source, path, and site effects on strong ground motion during the 1989 Loma Prieta earthquake—a preliminary result on pervasive nonlinear site effects: Seismological Society of America Bulletin, v. 81, no. 5, p. 1859–1884.

Clark, J.C., 1981, Stratigraphy, paleontology, and geology of the central Santa Cruz Mountains, California Coast Ranges: U.S. Geological Survey Professional Paper 1168, 51 p.

Cranswick, Edward, King, K.W., and Banfill, Robert, 1989, A program to perform time and frequency domain analysis of vector timeseries recorded by portable autonomous digital seismographs: U.S. Geological Survey Open-File Report 89–172, 43 p.

Cranswick, Edward, King, K.W., Carver, D.L., Worley, D.M., Williams, R.A., Spudich, Paul, and Banfill, Robert, 1990, Site response across downtown Santa Cruz, California: Geophysical Research Letters, v. 17, no. 10, p. 1793–1796.

Daly, R.A., Manger, G.E., and Clark, S.P., Jr., 1966, Density of rocks, *in* Clark S.P., ed., Handbook of physical constants: Geological Society of America Memoir 97, p. 19–26.

Dix, C.H., 1955, Seismic velocities from surface measurements: Geophysics, v. 20, no. 1, p. 68–86.

Dupre, W.R., 1975, Maps showing geology and liquefaction potential of Quaternary deposits in Santa Cruz County, California: U.S. Geological Survey Miscellaneous Field Studies Map MF–648, scale 1:62,500, 2 sheets.

Espinosa, A.F., and Algermissen, S.T., 1972, A study of soil amplification factors in earthquake damage areas, Caracas, Venezuela: U.S. National Oceanic and Atmospheric Administration Technical Report ERL–280–ESL 31, 201 p.

Figueroa, J., 1964, Determinación del las constantes del la arcilla del Valle de México por prospección sísmica [Determination of constants of the clay of the Valley of Mexico for seismic prospecting]: Sociedad Mexicana de Ingeniería Sismologica Boletino, v. 2, p. 57–66.

Gibbs, J.F., Fumal, T.E., and Borcherdt, R.D., 1976, In-situ measurements of seismic velocities in the San Francisco Bay region—part 2: U.S. Geological Survey Open-File Report 76–731, 145 p.

Hamilton, R.M., Ryall, Alan, and Berg, Eduard, 1964, Crustal structure southwest of the San Andreas fault from quarry blasts: Seismological Society of America Bulletin, v. 54, no. 1, p. 67–77.

Haskell, N.A., 1953, The dispersion of surface waves on multilayered media: Seismological Society of America Bulletin, v. 43, no. 1, p. 17–34.

———1960, Crustal reflection of plane *SH* waves: Journal of Geophysical Research, v. 65, no. 12, p. 4147–4150.

Idriss, I.M., 1985, Evaluating seismic risk in engineering practice: International Conference on Soil Mechanics and Foundation Engineering, 11th, San Francisco, 1985, Proceedings, p. 255–320.

Jarpe, S.P., Hutchings, L.J., Hauk, T.F., and Shakal, A.F., 1989, Selected strong- and weak-motion data from the Loma Prieta earthquake sequence: Seismological Research Letters, v. 60, no. 4, p. 167–176.

Joyner, W.B., Warrick, R.E., and Fumal, T.E., 1981, The effect of Quaternary alluvium on strong ground motion in the Coyote Lake, California, earthquake of 1979: Seismological Society of America Bulletin, v. 71, no. 4, p. 1333–1349.

Joyner, W.B., Warrick, R.E., and Oliver, A.A., III, 1976, Analysis of seismograms from a downhole array in sediments near San Francisco Bay: Seismological Society of America Bulletin, v. 66, no. 3, p. 937–958.

Kawase, Hiroshi, and Aki, Keiiti, 1990, Topography effect at the critical *SV*-wave incidence; possible explanation of damage pattern by the Whittier Narrows, California, earthquake of 1 October 1987: Seismological Society of America Bulletin, v. 80, no. 1, p. 1–22.

King, J.L., and Tucker, B.E., 1984, Observed variations of earthquake motion across a sediment-filled valley: Seismological Society of America Bulletin, v. 74, no. 1, p. 137–151.

King, K.W., Carver, D.L., Williams, R.A., Worley, D.M., Cranswick, Edward, and Meremonte, M.E., 1990a, Santa Cruz seismic investigations following the October 17, 1989 Loma Prieta earthquake: U.S. Geological Survey Open-File Report 90–307, 59 p.

King, K.W., Tarr, A.C., Carver, D.L., Williams, R.A., and Worley, D.M., 1990b, Seismic ground-response studies in Olympia, Washington, and vicinity: Seismological Society of America Bulletin, v. 80, no. 5, p. 1057–1078.

King, K.W., Williams, R.A., Carver, D.L., Cranswick, Edward, and Worley, D.M., 1990c, Site response and building damage in Santa Cruz, California [abs.]: Seismological Research Letters, v. 61, no. 1, p. 13.

Lin, Wunan, and Wang, Chi-yuen, 1980, *P*-wave velocity in rocks at high pressure and temperature and the constitution of the central California crust: Royal Astronomical Society Geophysical Journal, v. 61, p. 379–400.

Mayne, W.H., 1962, Common reflection point horizontal data stacking techniques: Geophysics, v. 27, no. 6, pt. 2 (supp.), p. 927–938.

Menke, William, Lerner-Lam, A.L., Dubendorff, Bruce, and Pacheco, Javier, 1990, Polarization and coherence of 5 to 30 Hz seismic wave fields at a hard-rock site and their relevance to velocity heterogeneities in the crust: Seismological Society of America Bulletin, v. 80, no. 2, p. 430–449.

Rogers, A.M., Tinsley, J.C., and Borcherdt, R.D., 1985, Predicting relative ground response, *in* Ziony, J.I., ed., Evaluating earthquake hazards in the Los Angeles region—an earth-science perspective: U.S. Geological Survey Professional Paper 1360, p. 221–247.

Sadigh, Khrosrow, 1983, Considerations in the development of site-specific spectra, *in* Hays, W.W., ed., Proceedings of Conference XXII; a workshop on "site-specific effects of soil and rock on ground motion and the implications for earthquake-resistant design": U.S. Geological Survey Open-File Report 83–845, p. 423–458.

Seale, S.H., and Archuleta, R.J., 1989, Site amplification and attenuation of strong ground motion: Seismological Society of America Bulletin, v. 79, no. 6, p. 1673–1695.

Shearer, P.M., and Orcutt, J.A., 1987, Surface and near-surface effects on seismic waves—theory and borehole seismometer results: Seismological Society of America Bulletin, v. 77, no. 4, p. 1168–1196.

Sheriff, R.E., and Geldart, L.P., 1982, History, theory, and data acquisition, v. 1 *of* Exploration seismology: Cambridge, U.K., Cambridge University Press, 323 p.

Singh, S.K., Mena, Enrique, and Castro, R., 1988, Some aspects of source characteristics of the 19 September 1985 Michoacan earthquake and ground motion amplification in and near Mexico City from strong motion data: Seismological Society of America Bulletin, v. 78, no. 2, p. 451–477.

Stanley, R.G., and McCaffrey, Robert, 1983, Extent and offset history of the Ben Lomond fault Santa Cruz County, California, *in* Anderson, D.W. and Rymer, M.J., eds., Tectonics and sedimentation along faults of the San Andreas system: Los Angeles, Society of Economic Paleontologists and Mineralogists, Pacific Section, p. 79–90.

Walter, A.W., and Mooney, W.D., 1982, Crustal structure of the Diablo and Gabilan Ranges, central California—a reinterpretation of existing data: Seismological Society of America Bulletin, v. 72, no. 5, p. 1567–1590.

Wood, H.O., 1908, Distribution of apparent intensity in San Francisco, *in* Lawson, A.C., chairman, The California earthquake of April 18, 1906; report of the State Earthquake Investigation Commission: Carnegie Institution of Washington, Publication 87, v. 1, p. 220–246.

U.S. Geological Survey staff, 1990, The Loma Prieta, California, earthquake—an anticipated event: Science, v. 247, no. 4940, p. 286–293.

THE LOMA PRIETA, CALIFORNIA, EARTHQUAKE OF OCTOBER 17, 1989:
STRONG GROUND MOTION AND GROUND FAILURE

STRONG GROUND MOTION

VARIATION OF SEISMIC SITE EFFECTS IN THE SANTA CRUZ MOUNTAINS, CALIFORNIA

By Grant T. Lindley and Ralph J. Archuleta,
University of California, Santa Barbara

CONTENTS

ABSTRACT

The Fourier amplitude spectra of *P* and *S* waves reveal the variation of site effects with site geology, site topography, and ray azimuth. The data are digital recordings of aftershocks recorded in the Santa Cruz Mountains. The Fourier spectra were studied by calculating nonlinear least-squares best fits to 6,282 *P*- and *S*-wave spectra. Site-to-site variations of amplification and attenuation are found to be controlled by site geology and not by site topography. The relative amplification between sites was measured from the low-frequency spectral asymptotes of the Fourier spectra corrected for geometric spreading and attenuation. The lowest-amplification sites were located on the Franciscan Complex, and the highest-amplification sites on latest Tertiary (Miocene and Pliocene) sedimentary rocks. The average amplification at these Miocene and Pliocene sedimentary rock sites exceeded that at the Franciscan Complex sites by a factor of 3.3 for *P* waves and 3.9 for *S* waves. Amplification was less at ridgetop relative to valley sites, probably because most ridgetop sites are on the Franciscan Complex. Attenuation was calculated through the relation $t^*=\int dt/Q$. Frequency-independent *S*-wave t^* site averages range from approximately 0.025 to 0.055 s, and *P*-wave t^* site averages from about 0.015 to 0.045 s. The lowest t^* values were determined at the Franciscan Complex sites, and the highest t^* values at the Miocene and Pliocene sedimentary-rock sites.

Azimuthal variations of site amplification were studied from the residuals of the spectral fits; the residual is the difference between the Fourier spectrum and the fit to the spectrum. Average site residuals show broad peaks, from a few hertz to as much as 10 hertz wide, that appear to be due to site effects because they are consistent for different ray paths and earthquakes. The heights of these broad peaks are as great as a factor of 4 in amplitude. *Q* values were estimated from the widths of the broad peaks in the residuals, assuming that the broad peaks are due to resonances in near-surface layers. Estimated *Q* values are typically 5 to 12 for both *P* and *S* waves. Sharp peaks in the residuals (less than approx 1 Hz) are also observed, but they vary with the ray path and earthquake source. The cause of these sharp peaks in the residuals is unknown, although they may be due to scattering in the crust.

INTRODUCTION

The variation of seismic site effects has important implications for earthquake hazard. One important factor that causes site effects to vary is site geology. The variation of seismic site effects with site geology has been decisively demonstrated by the varying damage caused by several recent large earthquakes, including the 1985 Michoacán, Mexico, earthquake (for example, Anderson and others, 1986; Celebi and others, 1987), the 1985 Chile earthquake (for example, Celebi, 1987), and the 1989 Loma Prieta earthquake (for example, Bennett, 1990; Celebi, 1990; Seekins and others, 1990; Boatwright and others, 1991a; Bonilla, 1991; Chameau and others, 1991; Hanks and Brady, 1991; Borcherdt and Glassmoyer, 1992).

Several previous studies have examined the variation of site effects with site geology, using aftershocks of the 1989 Loma Prieta earthquake. Hough and others (1991) used an empirical Green's function analysis to determine

P-wave site attenuation for aftershocks recorded in the Santa Cruz Mountains, using the same data set as ours. Bonamassa and Vidale (1991) examined azimuthal site effects in the Santa Cruz Mountains. Boatwright and others (1991b) jointly inverted the Fourier spectra of *P* and *S* waves of Loma Prieta aftershocks in the Marina District of San Francisco and at accelerograph sites near the epicenter to determine attenuation and amplification. Fletcher and Boatwright (1991) jointly inverted Fourier spectra to determine attenuation, geometric spreading, and amplification along the San Francisco peninsula. Boatwright and others (1991a) examined the spectral ratios of aftershock recordings in the Marina District to determine how site amplification varied with site geology. King and others (1990) also measured the spectral ratios of aftershocks to determine the variation of site effects with site geology in and near Santa Cruz, Calif. This paper complements these previous studies by analyzing the variation of *P*- and *S*-wave amplification and attenuation from Loma Prieta aftershocks at 22 sites in the near-source region of the Santa Cruz Mountains.

One way this study differs from previous studies of Loma Prieta aftershocks is in our consideration of site topography along with site geology. We might expect that seismic site effects would vary with simple topography, by which we mean topographic highs and lows. Effects due to sediment-filled valleys are not considered here. Numerical calculations (Boore, 1972, 1973; Bouchon, 1973) and foam-rubber modeling (Anooshehpoor and Brune, 1989) have shown that significant amplification or deamplification can be caused by topography. Several studies have also measured amplifications as high as a factor of 10 that were attributed to topographic effects (for example, Davis and West, 1973; Griffiths and Bollinger, 1979; Tucker and others, 1984). Furthermore, there is evidence for topographic amplification at ridgetops in the Santa Cruz Mountains from the Loma Prieta main shock, on the basis of observations of fissures on ridgetops (Hart and others, 1990; Ponti and Wells, 1991). Because the aftershock-recording sites in the Santa Cruz Mountains were located in rugged topography at both ridgetop and valley sites, the data set is useful to measure seismic topographic effects. We show below, however, that site geology appears to be much more important than site topography in controlling site effects.

Finally, this paper addresses the causes of the "roughness" of seismic spectra. The Fourier spectra of earthquakes always exhibit numerous peaks and holes. We find that broad peaks (from a few hertz to 10 Hz wide) in the spectra occur consistently at a particular site for different earthquakes and ray azimuths. The *Q* value is estimated from the widths of these broad peaks by assuming that the broad peaks are due to resonances in near-surface layers. These *Q* values compare favorably with those determined in the near surface from surface and downhole recordings (for example, Seale and Archuleta, 1989; Aster and Shearer, 1991; Blakeslee and Malin, 1991). Sharp peaks in the spectra (less than approximately 1 Hz wide) also occur, but these peaks vary with earthquake and azimuth; the cause of these sharp peaks is uncertain. According to Ihaka (1985), the cause of these peaks may be scattering of seismic waves in the crust.

DATA

Aftershocks of the 1989 Loma Prieta earthquake were recorded in the Santa Cruz Mountains as part of an IRIS/PASSCAL experiment (Simpson and others, 1989). The aftershocks were recorded by Reftek recorders with Mark Products 2-Hz L–22 geophones. Most of the data were recorded at 200 samples per second with a 90-Hz antialias filter; some data were recorded at 100 samples per second with a 45-Hz antialias filter. Magnitudes range from 1.2 to 4.4, most from 1.5 to 3.2. Earthquake locations (fig. 1) are from the U.S. Geological Survey. A total of 22 stations were used, and a total of 6,282 *P*- and *S*-wave spectra were analyzed.

All the sites had unconsolidated material (soil, alluvium, or both) in the near surface. The rocks directly beneath the unconsolidated material were either Tertiary sedimentary rocks or Franciscan Complex (Clark, 1970; Dibblee and Brabb, 1978, 1980; Dibblee and others, 1978; Brabb and Dibblee, 1979). The Franciscan Complex sites in this study are underlain by graywacke.

SPECTRAL-FITTING METHOD

The Fourier amplitude spectra of *P* and *S* waves were analyzed by calculating nonlinear least-squares best fits to the spectra. The Fourier spectra were fitted to the logarithm of the functional form (Boatwright, 1978)

$$D(f) = \frac{\Omega_0 \exp(-\pi f t^*)}{[1 + (f/f_c)^{2\gamma}]^{1/2}} \qquad (1)$$

or

$$\log D(f) = \log \Omega_0 - 0.5 \log\,[1+(f/f_c)^{2\gamma}] - 0.434\pi f t^*, \qquad (2)$$

where $D(f)$ is the Fourier displacement amplitude, Ω_0 is the low-frequency spectral asymptote, f is the frequency, f_c is the corner frequency, g is the source-spectral falloff, and t^* is the traveltime divided by the quality factor of attenuation, Q. In addition, t^* was determined by two parameters according to the relation $t^*=t_0^* f^{-\alpha}$, where t_0^* and α are parameters determined by the fits. The negative sign was placed before α for agreement with the convention used in studies, which commonly take $Q=Q_0f^{\alpha}$ (for example, Aki, 1980). The best fit for a particular spectrum is the specific combination of parameters that minimizes the sum of squared residuals; the residual at each point of the Fourier spectrum is the spectrum minus the fit to the spectrum. The best-fitting combination of parameters is identically the same, whether fitting to the displacement, velocity, or acceleration spectrum.

The five parameters that can be varied to find the best fits are Ω_0, f_c, γ, t_0^*, and α. All five parameters could not be fitted at once because there were many possible parameter combinations that produced similar values for the sum of squared residuals. Generally, a unique solution could be determined when four of the five parameters were allowed to vary. When only three of the five parameters were allowed to vary, a unique best-fitting combination of these three parameters could always be determined. The fits in this study were calculated with the three parameters Ω_0, f_c, and t_0^*, varying and the parameters g and a fixed. The best-fitting combination of parameters was found by iteration from a starting model, using the Simplex algorithm (Nelder and Mead, 1965; Caceci and Cacheris, 1984) which has the advantage over most other iteration schemes that convergence toward a minimum sum of squared residuals is guaranteed. Two typical fits are shown in figure 2.

Analysis of the Fourier spectrum of locally recorded earthquakes by finding least-squares best fits to the spectra has been previously studied by numerous investigators (Boatwright, 1978; Ihaka, 1985; de Natale and others, 1987; Rovelli and others, 1988; Scherbaum, 1990; Boatwright and others, 1991b; Fletcher and Boatwright, 1991). Other studies that have used automated methods to determine the parameters of local earthquakes include those by Andrews (1986), Fehler (1985), Snoke (1987), Dysart and others (1988), and Fehler and Phillips (1991).

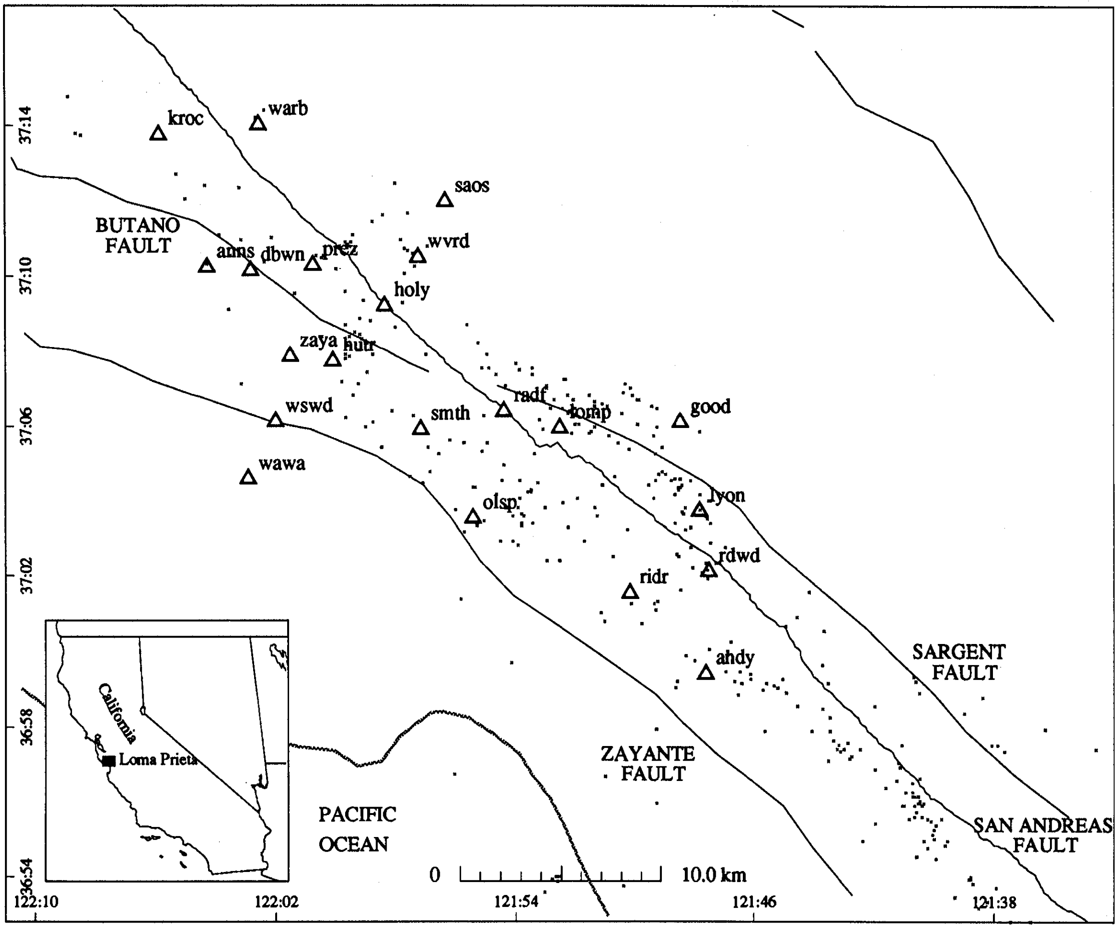

Figure 1.—Loma Prieta, Calif., region, showing locations of aftershock-recording stations (triangles) and selected aftershocks (dots).

AMPLIFICATION AND ATTENUATION

The relative amplification between sites was determined by first calculating the log average ratio of the low-frequency spectral asymptote between each site, according to the relation

$$R_{ij} = \left[\sum_{k=1}^{n} \log \left(\Omega_{0i}^{k} / \Omega_{0j}^{k} \right) \right] / n, \tag{3}$$

where R_{ij} is the relative amplification at site i relative to site j, Ω_{0i}^{k} is the low-frequency asymptote for the kth earthquake at site i, and n is the number of earthquakes recorded in common between the two sites. The Ω_0 values were normalized to 10-km hypocentral distance by assuming straight-line ray paths. An average relative amplification at each site was then calculated by averaging the R_{ij}'s:

$$A_i = \left[\sum_{j=1}^{N} R_{ij} \right] / N, \tag{4}$$

where A_i is the relative amplification at site i and N is the number of sites. The low-frequency spectral asymptotes were determined with γ set to 2.0 and α set to -0.5. Setting the source-spectral falloff, γ, to 2.0 is a common assumption (for example, Aki, 1967; Brune, 1970; Hanks, 1979). The parameter α was set to -0.5 because this value was observed to give better fits to the data in the low-frequency part of the spectrum (Lindley and Archuleta, 1992). Neither of these parameters is critical, however, for determination of the relative site amplification because other values give similar results and would not affect the principal conclusions of this study.

The relative site amplification, A_i, measured in this study is essentially the amplification of the low-frequency spectral asymptote at a particular site relative to an average low-frequency asymptote for all the sites. The low-frequency spectral asymptotes used in the calculation are derived from least-squares best fits to the spectra. Because the fits to the spectra are smooth curves between the maximums and minimums of the spectra, the relative amplification determined in this study is an amplification of the average spectral level.

The P-wave relative site amplification is plotted versus the S-wave relative site amplification in figure 3. The P- and S-wave site amplifications vary from site to site by a factor of as much as 6. The depths and velocity

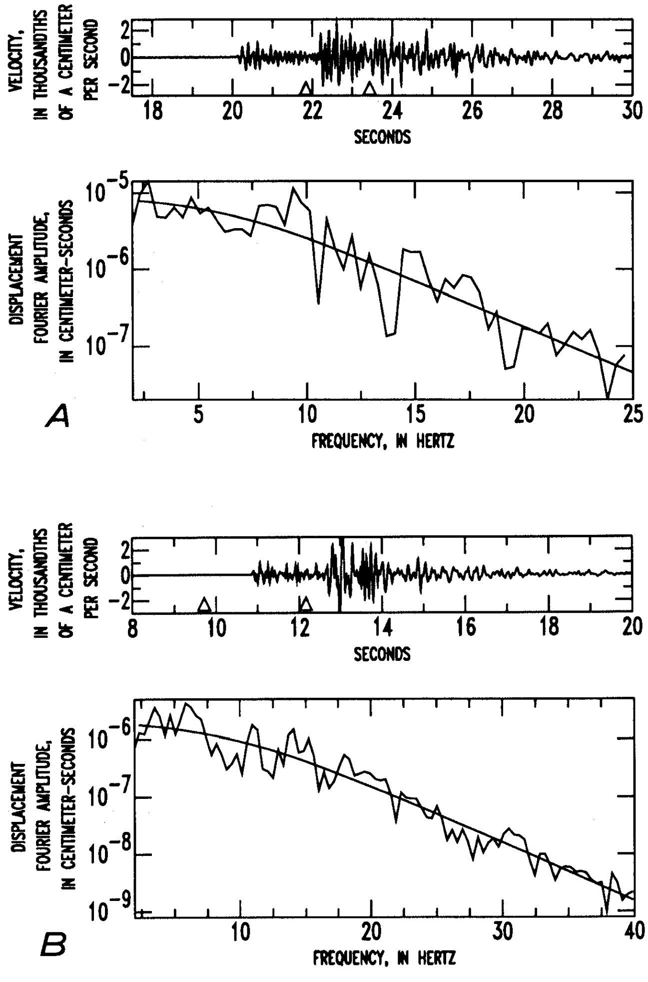

Figure 2.—Typical fits to Fourier amplitude spectrum (lower curve). Triangles (upper curve) mark beginning and ending of window for which fast Fourier transform was calculated. A 10-percent cosine taper was applied to each window. *A*, *S* wave (M=1.6) at station OLSP (fig. 1). The best fit parameters are $\Omega_0=8.8\times10^{-6}$ cm-s, f_c=9.5 Hz, and t_0^*=0.0085 s. *B*, *P* wave (M=1.5) at station RDWD. Best-fit parameters are $\Omega_0=1.9\times10^{-6}$ cm-s; f_c=14.7 Hz; and t_0^*=0.0065 s. Parameters α and γ were set to -0.5 and 2.0, respectively, in fits.

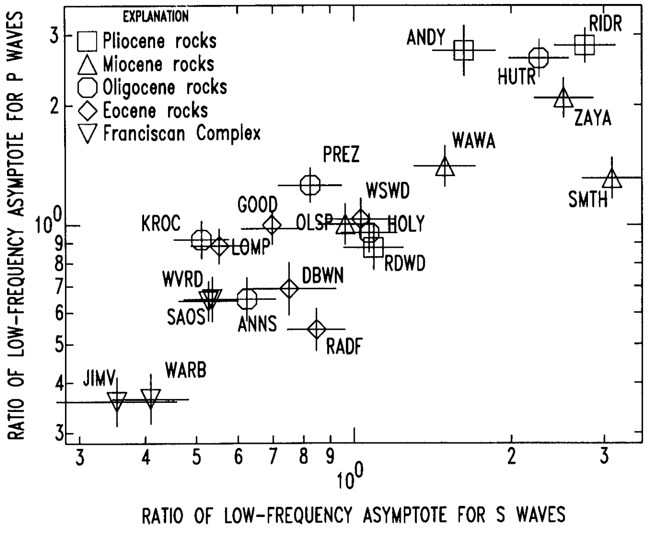

Figure 3.—*P*- versus *S*-wave relative site amplifications (see table 1). Site amplification varies systematically with site geology; lowest-amplification sites are on the Franciscan Complex, and highest-amplification sites on latest Tertiary (Miocene and Pliocene) rocks. See text for explanation of calculation of relative site amplification.

profiles of the unconsolidated material at each site are unknown, making detailed comparisons between sites difficult. Grouping the sites according to underlying rock type, however, yields a systematic variation of amplification with site geology (fig. 3; table 1). The Miocene and Pliocene sedimentary-rock sites have the largest, and the Franciscan Complex sites the smallest, amplifications. The average amplification at the Miocene and Pliocene sites exceeds that at the Franciscan Complex sites by a factor of 3.3 for *P* waves and 3.9 for *S* waves; the average amplification at the Miocene and Pliocene sites exceeds that at the Eocene and Oligocene sites by a factor of 1.7 for *P* waves and 2.1 for *S* waves; and the average amplification at the Eocene and Oligocene sites exceeds that at the Franciscan Complex sites by a factor of 2.0 for *P* waves and 1.8 for *S* waves.

We can discern no comparable correlation between simple topography and amplification. On the basis of observations of fissuring on ridgetops from the 1989 Loma Prieta earthquake (Hart and others, 1990; Ponti and Wells, 1991), amplification at ridgetop (high elevation) sites was expected, but these high-elevation sites (fig. 4) show the opposite effect—a reduced amplification, probably because many of them are on the Franciscan Complex. Site amplification appears to be controlled by site geology, not site topography.

According to Anderson and Hough (1984), attenuation can be thought of as a combination of a path effect and a site effect. The site effect is limited to the top several kilometers of the Earth's surface. On a plot of t^* versus hypocentral distance, the intercept of t^* at zero distance is the site effect, and the increase in t^* with distance is the path effect (fig. 5). To estimate the site effect, t^* values for all events within 20 km of each recording site were averaged together. t^* was calculated with the parameter α set to zero to facilitate comparisons with other studies of attenuation in local earthquakes that commonly assumed Q to be frequency independent.

As with amplification, attenuation is observed to vary systematically with site geology. *S*-wave t^* values range from about 0.025 to 0.055 s (fig. 6), and *P*-wave t^* values from about 0.015 to 0.045 s. The lowest t^* values are observed at the Franciscan Complex sites, and the highest t^* values at the Miocene and Pliocene sedimentary-rock sites (fig. 6; table 1). The Franciscan Complex sites have an average *P*-wave t^* value of 0.0178 s and an average *S*-wave t^* value of 0.0266 s; the Eocene and Oligocene sites have an average *P*-wave t^* value of 0.0251 s and an average *S*-wave t^* value of 0.0377 s; and the Miocene and Pliocene sites have an average *P*-wave t^* value of 0.0316 s and an *S*-wave t^* value of 0.0411 s (table 1).

t^* values decrease slightly at the higher elevation sites (fig. 7). As for amplification, the smaller t^* values at ridgetop sites can be explained by the fact that the higher elevation sites are generally on the Franciscan Complex. These results indicate that site amplification and attenuation are determined more strongly by site geology than by site topography.

COMPARISON OF SPECTRAL FITS AND SPECTRAL RATIOS

The method used in this study to determine the relative site amplification from low-frequency asymptotes of spectral fits is new. Therefore, it is appropriate to compare the amplification determined by this new method with that determined by a more traditional method. For this purpose, spectral ratios were calculated for earthquakes that were recorded at two stations, ZAYA and WVRD (fig. 1). These stations were chosen because they are relatively close together: Station ZAYA is in a Miocene valley, and station WVRD is at a ridgetop on the Franciscan Complex. On the basis of the spectral-fitting results, we expected an amplification at station ZAYA over station WVRD by a factor of 3 to 6 at low frequencies. Then, because of the greater attenuation at station ZAYA, we expected the spectral ratio to drop at higher frequencies.

Spectral ratios were calculated for each aftershock recorded at both stations. The spectral ratios of all the aftershocks were then log-averaged together to determine an average spectral ratio. No smoothing was done to the spectral ratios because averaging the 161 ratios produced a reasonably smooth average spectral ratio (fig. 8).

The average spectral ratio shows an amplification at frequencies below 10 Hz by a factor of about 4 at station ZAYA relative to station WVRD, (fig. 1). This amplification factor is typical for a Miocene or Pliocene sedimentary-rock site relative to a Franciscan Complex site (fig. 6; table 1). Above about 10 Hz, the spectral ratio drops steadily until at 30 Hz it is nearly 1. This drop in the spectral ratio at high frequencies is consistent with a larger t^* value at station ZAYA relative to station WVRD.

NEAR-SURFACE RESONANCES

Near-surface resonances were studied from the spectral residuals (fig. 9). To the extent that the Fourier spectrum is correctly modeled, the residual is the spectrum with the high-frequency falloff due to the source and attenuation removed. The residual consists of variations in the Fourier spectrum that range from sharp (less than approx 1 Hz wide) to broad (max 10 Hz wide).

The broad peaks in the residuals (greater than approx 1 Hz) tend to occur consistently for different aftershocks and ray azimuths (figs. 9, 10). Because these peaks are

Table 1.—*Attenuation and amplification in the Santa Cruz Mountains*

[t^* values are averages for all earthquakes within a 20-km hypocentral distance of each site. Amplification is the relative amplification between sites (see text for explanation). Franciscan Complex sites: JIMV, SAOS, WARB, and WVRD; Eocene and Oligocene sedimentary-rock sites: KROC, PREZ, ANNS, HOLY, HUTR, DBWN, GOOD, LYON, WSWD, RADF, and LOMP; Miocene and Pliocene sites: RDWD, RIDR, ANDY, ZAYA, OLSP, WAWA, and SMTH (see fig. 1 for locations). Errors are standard deviation of the mean. Numbers in parentheses are the number of t^* values averaged]

Site geology	*P*-wave t^* value	*S*-wave t^* value	*P*-wave attenuation	*S*-wave attenuation
Miocene and Pliocene rocks -----	0.0316±0.0005 (795)	0.0411±0.0009 (608)	$1.59^{+0.08}_{-0.07}$	$1.77^{+0.09}_{-0.09}$
Eocene and Oligocene rocks -----	.0251±0.0004 (749)	.0377±0.0010 (607)	$.96^{+0.05}_{-0.04}$	$.83^{+0.04}_{-0.03}$
Franciscan Complex --------------	.0178±0.0005 (333)	.0266±0.0010 (240)	$.48^{+0.04}_{-0.03}$	$.45^{+0.04}_{-0.04}$

consistent for different sources and ray paths, we interpret the broad peaks to be site effects. The heights of these broad peaks can be a factor of as great as 4 in amplitude, typically from 2.0 to 3.5. Broad peaks appear at sites with all types of site geology; the most likely cause for these broad peaks are resonances in near-surface layers of unconsolidated material.

If we assume that the broad peaks in the residuals are single-resonance peaks in near-surface layers, we can estimate the Q values in these near-surface layers from the widths of the peaks. The shape of a peak is given by (see for example, Clough and Penzien, 1975)

$$A(f) = A_0\{[1 - (f_0/f)^2]^2 + (f_0/fQ)^2\}^{-1/2}\,, \quad (5)$$

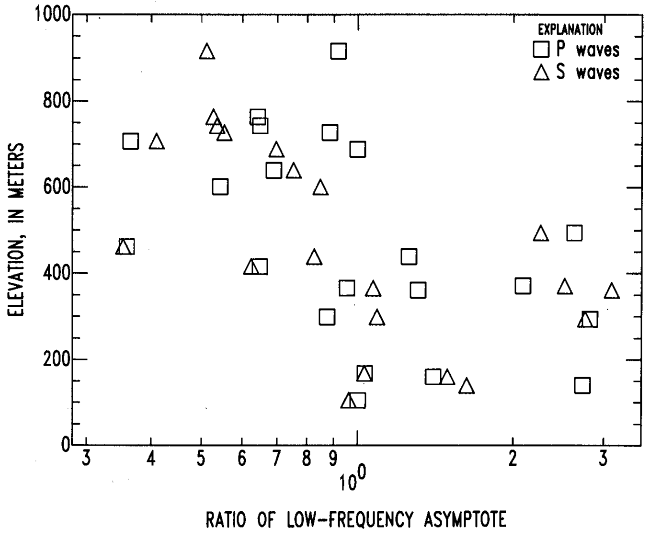

Figure 4.—*P*- and *S*-wave amplification versus site elevation. Higher-elevation sites have lower amplifications. High-elevation sites are predominantly on the Franciscan Complex.

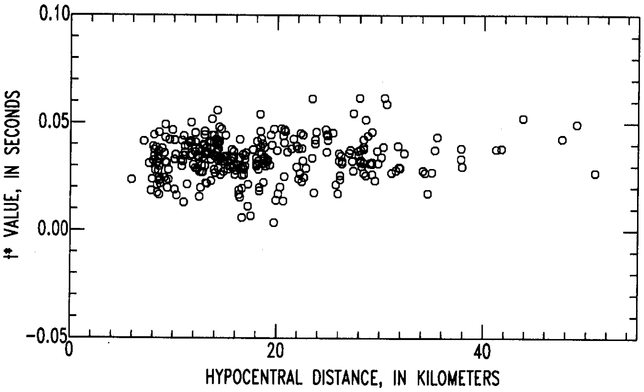

Figure 5.—*P*- wave t^* value versus hypocentral distance at station OLSP (fig. 1). As at most sites in the Santa Cruz Mountains, t^* value increases only slightly with distance, indicating that most attenuation is coming from near surface, through which all ray paths must travel.

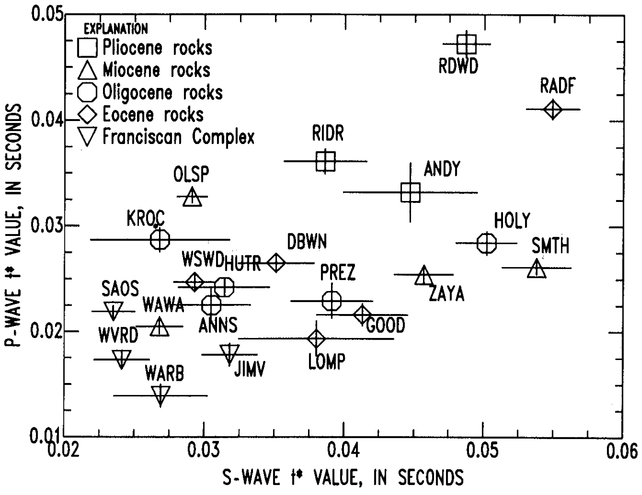

Figure 6.—*P*- versus *S*-wave t^* values (see fig. 1 for locations). In general, lowest t^* values occur at Franciscan Complex sites, and highest t^* values at Miocene and Pliocene sedimentary-rock sites (see table 1).

where $A(f)$ is the amplitude, f is the frequency, A_0 is the peak amplitude, and f_0 is the resonance frequency. The Q values estimated by this method typically range from 5 to 12 for both P and S waves (fig. 11; table 2), in agreement with borehole Q measurements in the near surface from borehole studies (for example, Seale and Archuleta, 1989; Aster and Shearer, 1991; Blakeslee and Malin, 1991). However, the Q values estimated here should be treated with some caution because some or all of the broad peaks used to determine them are multiple-resonance peaks. If so, then the Q estimates in table 2 are all too small. Other possible complicating factors are the loss of energy from near-surface layers to the crust below and the loss or addition of energy due to lateral heterogeneities.

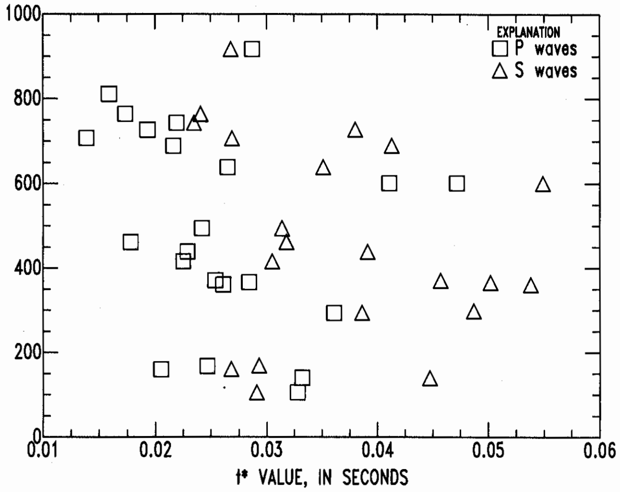

Figure 7.—Average t^* value for each site versus site elevation. Slight decrease of attenuation at higher elevation sites is probably because most high-elevation sites are on the Franciscan Complex.

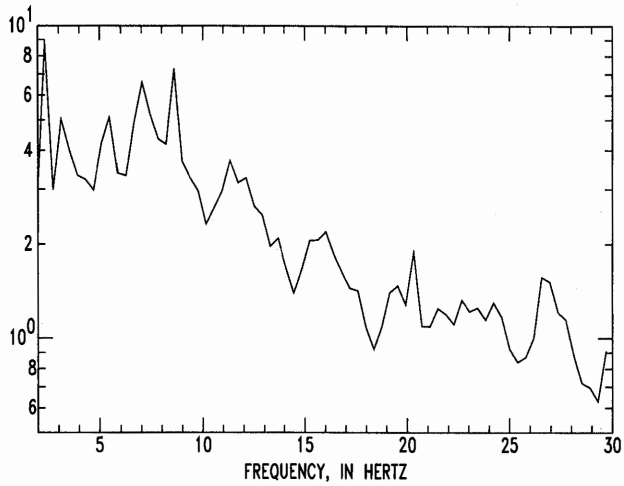

Figure 8.—S-wave spectral ratio at station ZAYA (Miocene sedimentary rocks) relative to station WVRD (Franciscan Complex) (see fig. 1 for locations). Spectral ratio is average of 161 spectral ratios of aftershocks recorded at both stations ZAYA and WVRD. Below 10 Hz, S waves at station ZAYA are amplified by a factor of about 4 relative to station WVRD; above 10 Hz, spectral ratio falls off, owing to greater attenuation at station ZAYA.

Sharp peaks in the residuals less than approximately 1 Hz wide are also observed (fig. 9). These sharp peaks are not consistent from one earthquake to the next, as shown by comparing an average residual with the residual for a single aftershock (fig. 9). They could still be due to site effects because relatively small changes in the ray azimuth or incidence angle could change the site effect. Alternatively, the sharp peaks could be due to scattering at depth, as postulated by Ihaka (1985). Echoes in a time series of itself will produce a spectrum that has peaks and holes, even if the original time series had a Fourier spectrum that was perfectly smooth. Scattering at depth would effectively produce echoes in a seismogram and could explain the sharp peaks observed in the spectrum.

CONCLUSIONS

Probably the most interesting result of this study is the strong correlation of site effects with site geology and the apparent absence of any correlation with site topography. We had expected to see a relative amplification at ridgetop sites relative to other sites; instead, a relative deamplification was observed at ridgetop sites, apparently because most ridgetop sites are on the Franciscan Complex. The amplification is lowest at sites on the Franciscan Complex and highest at sites on Miocene and Pliocene sedimentary rocks; the average amplification at the Miocene and Pliocene sites exceeds that at the

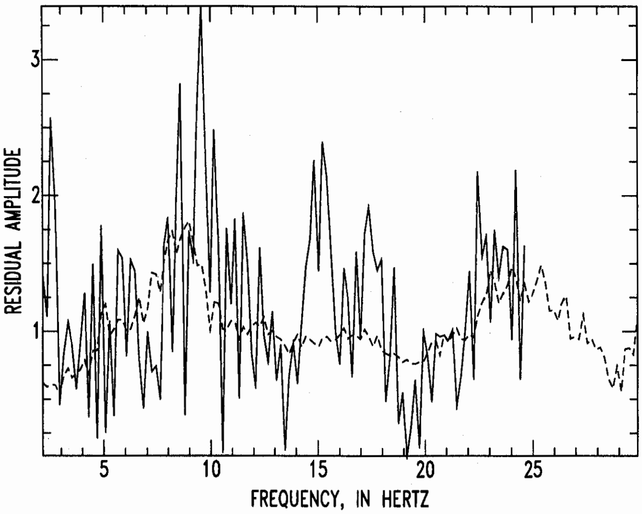

Figure 9.—Residual amplitude for a specific earthquake (solid curve) and average residual (dashed curve; average of 185 earthquakes) at station OLSP (fig. 1). Residual is spectrum minus fit to spectrum.

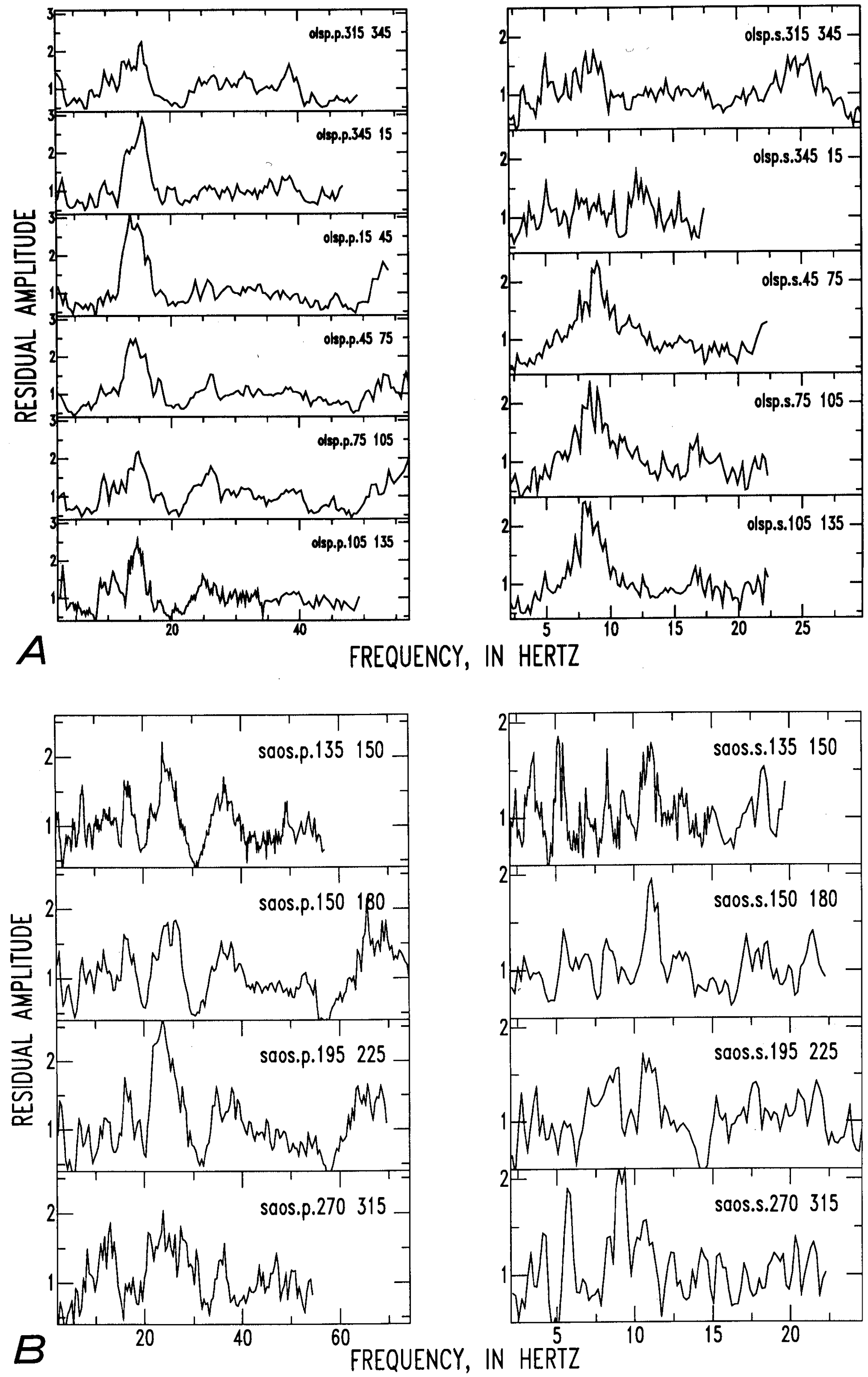

Figure 10.—Variation of *P*-wave (left) and *S*-wave (right) spectral residuals with azimuth at stations OLSP (*A*), SAOS (*B*), and RADF (*C*). Labels in upper right-hand corner of each plot indicate station name, *S* or *P* wave, and backazimuths for which average residual was calculated; for example, "olsp.p.315 345" refers to average *P*-wave residual at station OLSP for incoming rays between azimuth 315° and 345°.

Franciscan Complex sites by a factor of 3.3 for *P* waves and 3.9 for *S* waves.

S-wave t^* site averages range from approximately 0.025 to 0.055 s, and *P*-wave t^* site averages from about 0.015 to 0.045 s. The attenuation is lowest at the Franciscan Complex sites and highest at the sites on Miocene and Pliocene sedimentary-rock sites. The Franciscan Complex sites have an average *P*-wave t^* value of 0.0178 s and an average *S*-wave t^* value of 0.0266 s; the Miocene and Pliocene sites have an average *P*-wave t^* value of 0.0316 s and an average *S*-wave t^* value of 0.0411 s (table 1). Attenuation decreases slightly with site elevation, an effect most easily explained as the result of site geology because many of the ridgetop sites in this study are on the Franciscan Complex. We conclude that variations of site geology are more important than variations in site topography in determining seismic site effects in the Santa Cruz Mountains.

Peaks in the Fourier amplitude spectra were studied from the residuals. We found that the average site residuals had broad peaks from a few hertz to about 10 Hz wide that were predictable from one aftershock to the next, although there was some variation with azimuth. The heights of these broad peaks range as high as a factor of 4 in amplitude. *Q* values in the near surface were estimated from the widths of the broad peaks by assuming that the broad peaks are due to resonances in near-surface layers. Typical *Q* estimates range from 5 to 12 for both *P* and *S* waves. Sharp peaks in the residuals (less than approx 1 Hz wide) are also observed but are not predictable from one aftershock to the next. The

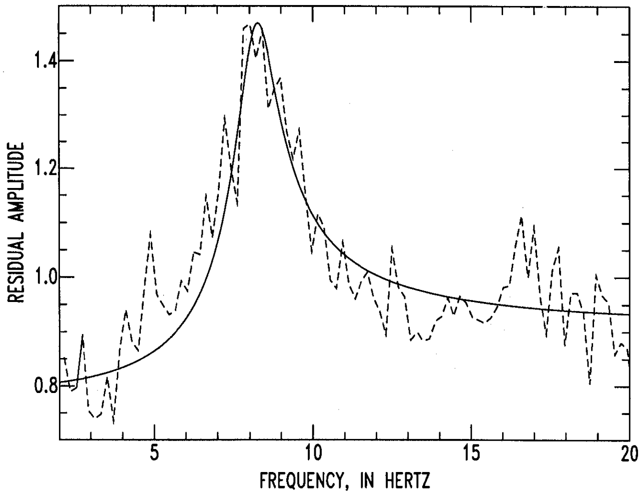

Figure 11.—*S*-wave residual (dashed curve) and fit to residual (solid curve) for resonance peak of 8.2 Hz and *Q* value of 6.0 at station OLSP. If residual peaks are resonance peaks, *Q* value can be estimated from width of resonance peak, as shown here. Fit to residual assumes that it results from harmonic resonance (see Clough and Penzien, 1975, chap. 4).

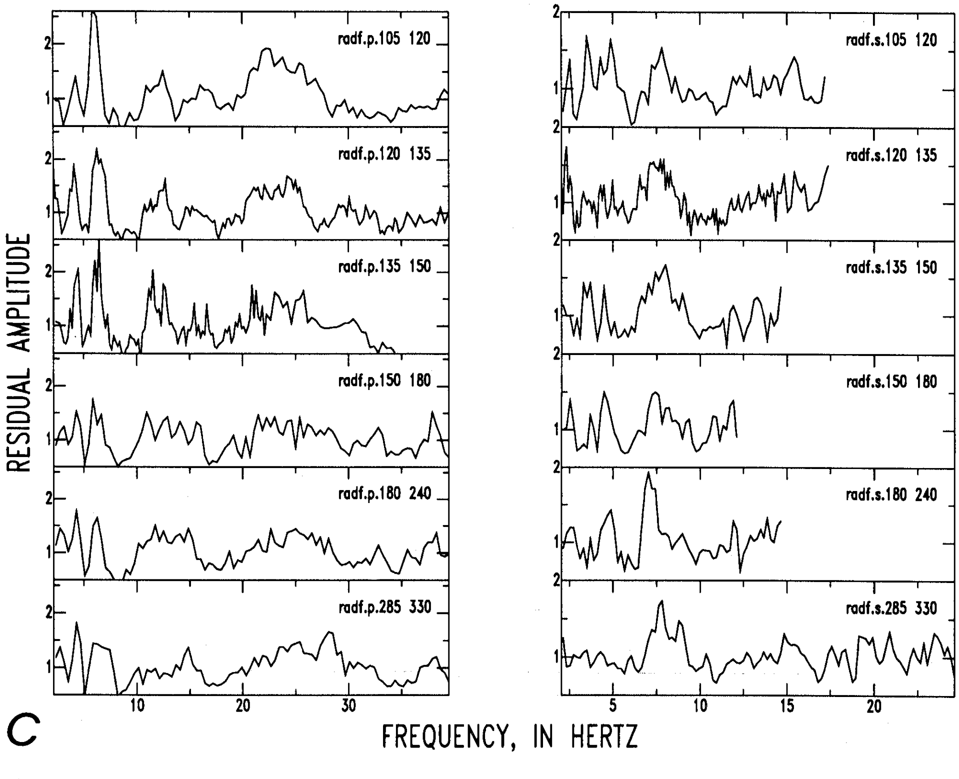

Figure 10.—Continued.

Table 2.—*Q estimates based on the width of resonance peaks, using the half-power (bandwidth) method*

[$Q=f/\Delta f$, where f is the peak resonance frequency and Δf is the width of the resonance peak at $1/\sqrt{2}$ of the peak amplitude (see Clough and Penzien, 1975, p. 72–73)]

Site	*S* or *P* wave	Back-azimuth (°)	Peak amplitude	Frequency at peak amplitude (Hz)	Half-power bandwidth (Δf) (Hz)	*Q* estimate
OLSP	*S*	105–135	2.8	8.2	1.4	5.9
OLSP	*S*	315–345	2.5	24.9	3.4	7.3
OLSP	*P*	All	3.3	14.0	3.2	4.9
SAOS	*S*	135–140	3.5	5.3	.7	7.6
SAOS	*P*	135–140	1.9	7.5	1.1	6.8
SAOS	*P*	135–140	3.0	16.5	1.4	11.8
SAOS	*P*	135–140	3.5	25.0	3.6	6.9
SAOS	*P*	135–140	1.9	36.5	5.1	7.2

cause of these sharp peaks is unknown; they may be due to scattering at depth in the crust.

ACKNOWLEDGMENTS

This research was supported by U.S. Geological Survey grant 14-08-0001-G1857. Helpful reviews were provided by John Vidale, Roger Borcherdt, and Sandra Seale. Jonathan Lees provided the map of the Loma Prieta area; the rest of the figures were produced with the help of the seismic-analysis code developed at Lawrence Livermore Laboratory, Livermore, Calif.

REFERENCES CITED

Aki, Keiiti, 1967, Scaling law of seismic spectrum: Journal of Geophysical Research, v. 72, no. 4, p. 1217–1231.

———1980, Attenuation of shear-waves in the lithosphere for frequencies from 0.05 to 25 Hz: Physics of the Earth and Planetary Interiors, v. 21, no. 1, p. 50–60.

Anderson, J.G. and Hough, S.E., 1984, A model for the shape of the Fourier amplitude spectrum of acceleration at high frequencies: Seismological Society of America Bulletin, v. 74, no. 5, p. 1969–1993.

Anderson, J.G., Bodin, Paul, Brune, J.N., Prince, Jorge, Singh, S.K., Quaas, Roberto, and Onate, Mario, 1986, Strong ground motion from the Michoacan, Mexico, earthquake: Science, v. 233, no. 4768, p. 1043–1049.

Andrews, D.J., 1986, Objective determination of source parameters and similarity of earthquakes of different size, *in* Das, Shamita, Boatwright, John, and Scholz, C.H., eds., Earthquake source mechanics: American Geophysical Union Monograph 37, p. 259–268.

Anooshehpoor, Abdolrasoor, and Brune, J.N., 1989, Foam rubber modeling of topographic and dam interaction effects at Pacoima Dam: Seismological Society of America Bulletin, v. 79, no. 5, p. 1347–1360.

Aster, R.C., and Shearer, P.M., 1991, High-frequency borehole seismograms recorded in the San Jacinto fault zone, southern California. Part 2. Attenuation and site effects: Seismological Society of America Bulletin, v. 81, no. 4, p. 1081–1100.

Bennett, M.J., 1990, Ground deformation and liquefaction of soil in the Marina District, chap. D *of* Effects of the Loma Prieta earthquake on the Marina District, San Francisco, California: U.S. Geological Survey Open-File Report 90–253, p. D1–D36.

Blakeslee, S.M., and Malin, P.E., 1991, High-frequency site effects at two Parkfield downhole and surface stations: Seismological Society of America Bulletin, v. 81, no. 2, p. 332–345.

Boatwright, John, 1978, Detailed spectral analysis of two small New York State earthquakes: Seismological Society of America Bulletin, v. 68, no. 4, p. 1117–1131.

Boatwright, John, Fletcher, J.B., and Fumal, T.E., 1991a, A general inversion scheme for source, site, and propagation characteristics using multiply recorded sets of moderate-sized earthquakes: Seismological Society of America Bulletin, v. 81, no. 5, p. 1754–1782.

Boatwright, John, Seekins, L.C., Fumal, T.E., Liu, H.-P., and Mueller, C.S., 1991b, Ground motion amplification in the Marina District: Seismological Society of America Bulletin, v. 81, no. 5, p. 1980–1997.

Bonamassa, Ornella, and Vidale, J.E., 1991, Directional site resonances observed from aftershocks of the 18 October 1989 Loma Prieta earthquake: Seismological Society of America Bulletin, v. 81, no. 5, p. 1945–1957.

Bonilla, M.G., 1991, The Marina District, San Francisco, California; geology, history, and earthquake effects: Seismological Society of America Bulletin, v. 81, no. 5, p. 1958–1979.

Boore, D.M., 1972, A note on the effect of simple topography on seismic *SH* waves: Seismological Society of America Bulletin, v. 62, no. 1, p. 275–284.

———1973, The effect of simple topography on seismic waves; implications for the accelerations recorded at Pacoima Dam, San Fernando Valley, California: Seismological Society of America Bulletin, v. 63, no. 5, p. 1603–1609.

Borcherdt, R.D., and Glassmoyer, G.M., 1992, On the characteristics of local geology and their influence on ground motions generated by the Loma Prieta earthquake in the San Francisco Bay region, California: Seismological Society of America Bulletin, v. 82, no. 2, p. 603–641.

Bouchon, Michel, 1973, Effect of topography on surface motion: Seismological Society of America Bulletin, v. 63, no. 2, p. 615–632.

Brabb, E.E., and Dibblee, T.W., Jr., 1979, Preliminary geologic map of the Castle Rock Ridge quadrangle, Santa Cruz and Santa Clara Counties, California: U.S. Geological Survey Open-File Report

79–659, scale 1:24,000.

Brune, J.N., 1970, Tectonic stress and the spectra of seismic shear waves from earthquakes: Journal of Geophysical Research, v. 75, no. 26, p. 4997–5009 [Correction, 1971, Journal of Geophysical Research, v. 76, no. 20, p. 5002].

Caceci, M.S., and Cacheris, W.P., 1984, Fitting curves to data: Byte, v. 9, no. 6, p. 340–360.

Celebi, Mehmet, 1987, Topographical and geological amplifications determined from strong-motion and aftershock records of the 3 March 1985 Chile earthquake: Seismological Society of America Bulletin, v. 77, no. 4, p. 1147–1167.

Celebi, Mehmet, Prince, Jorge, Dietel, Christopher, Onate, Mario, and Chavez, G., 1987, The culprit in Mexico City—amplification of motions: Earthquake Spectra, v. 3, no. 2, p. 315–328.

———1990, Types of structural damage, chap. B *of* Effects of the Loma Prieta earthquake on the Marina District, San Francisco, California: U.S. Geological Survey Open-File Report 90–253, p. B1–B6.

Chameau, J.L., Clough, G.W., Reyna, F., and Frost, J.D., 1991, Liquefaction response of San Francisco bayshore fills: Seismological Society of America Bulletin, v. 81, no. 5, p. 1998–2018.

Clark, J.C., compiler, 1970, Preliminary geologic and gravity maps of the Santa Cruz-San Juan Bautista area, Santa Cruz, Santa Clara, Monterey, and San Benito Counties, California: U.S. Geological Survey Open-File Map, scale 1:125,000.

Clough, R.W., and Penzien, J., 1975, Dynamics of structures: New York, McGraw-Hill, 634 p.

Davis, L.L., and West, L.R., 1973, Observed effects of topography on ground motion: Seismological Society of America Bulletin, v. 63, no. 1, p. 283–298.

de Natale, Giuseppe, Madariaga, Raul, Scarpa, Roberto, and Zollo, Aldo, 1987, Source parameter analysis from strong motion records of the Friuli, Italy, earthquake sequence (1976–1977): Seismological Society of America Bulletin, v. 77, no. 4, p. 1127–1146.

Dibblee, T.W., Jr., and Brabb, E.E., 1978, Preliminary geologic map of the Los Gatos quadrangle, Santa Clara and Santa Cruz Counties, California: U.S. Geological Survey Open-File Report 78–453, scale 1:24,000, 3 sheets.

———1980, Preliminary geologic map of the Loma-Prieta quadrangle, Santa Cruz and Santa Clara Counties, California: U.S. Geological Survey Open-File Report 80–944, scale 1:24,000.

Dibblee, T.W., Jr., Brabb, E.E., and Clark, J.C., 1978, Preliminary geologic map of the Laurel quadrangle Santa Cruz and Santa Clara Counties, California: U.S. Geological Survey Open-File Report 78–84, scale 1:24,000.

Dysart, P.S., Snoke, J.A., and Sacks, I.S., 1988, Source parameters and scaling relations for small earthquakes in the Matsushiro region, Southwest Honshu, Japan: Seismological Society of America Bulletin, v. 78, no. 2, p. 571–589.

Fehler, Michael, 1985, Locations and spectral properties of earthquakes accompanying an eruption of Mount St. Helens: Journal of Geophysical Research, v. 90, no. B14, p. 12729–12740.

Fehler, Michael, and Phillips, W.S., 1991, Simultaneous inversion for Q and source parameters of microearthquakes accompanying hydraulic fracturing in granitic rock: Seismological Society of America Bulletin, v. 81, no. 2, p. 553–575.

Fletcher, J.B., and Boatwright, John, 1991, Source parameters of Loma Prieta aftershocks and wave propagation characteristics along the San Francisco Peninsula from a joint inversion of digital seismograms: Seismological Society of America Bulletin, v. 81, no. 5, p. 1783–1812.

Griffiths, D.W., and Bollinger, G.A., 1979, The effect of Appalachian mountain topography on seismic waves: Seismological Society of America Bulletin, v. 69, no. 4, p. 1081–1105.

Hanks, T. C., 1979, *b* values and $\omega^{-\gamma}$ seismic source models; implications for tectonic stress variation along active crustal fault zones and the estimation of high-frequency strong ground motion: Journal of Geophysical Research, v. 84, no. B5, p. 2235–2242.

Hanks, T.C., and Brady, A.G., 1991, The Loma Prieta earthquake, ground motion, and damage in Oakland, Treasure Island, and San Francisco: Seismological Society of America Bulletin, v. 81, no. 5, p. 2019–2047.

Hart, E.W., Bryant, W.A., Wills, C.J., Treiman, J.A., 1990, The search for fault rupture and significance of ridgetop fissures, Santa Cruz Mountains, California, *in* McNutt, S.R., and Sydnor, R.H., eds., The Loma Prieta (Santa Cruz Mountains), California, earthquake of 17 October 1989: California Division of Mines and Geology Special Publication 104, p. 83–93.

Hough, S.E., Seeber, Leonardo, Lerner-Lam, A.L., Armbruster, J.C., and Guo, H., 1991, Empirical Green's function analysis of Loma Prieta aftershocks: Seismological Society of America Bulletin, v. 81, no. 5, p. 1737–1753.

Ihaka, G.R., 1985, Ruaumoko: Berkeley, University of California, Ph.D thesis, 68 p.

King, K.W., Williams, R.A., Carver, D.L., Cranswick, Edward, and Worley, D.M., 1990, Site response and building damage in Santa Cruz, California [abs.]: Seismological Research Letters, v. 61, no. 1, p. 13.

Lindley, G.T., and Archuleta, R.J., 1992, Earthquake source parameters and the frequency dependence of attenuation at Coalinga, Mammoth Lakes, and the Santa Cruz Mountains, California: Journal of Geophysical Research, v. 97, no. B10, p. 14137–14154.

Nelder, J.A., and Mead, R., 1965, A simplex method for function minimization: Computer Journal, v. 7, p. 308.

Ponti, D.J., and Wells, R.E. 1991, Off-fault ground ruptures in the Santa Cruz Mountains, California; ridge-top spreading versus tectonic extension during the 1989 Loma Prieta earthquake: Seismological Society of America Bulletin, v. 81, no. 5, p. 1480–1510.

Rovelli, Antonio, Bonamassa, Ornella, Cocco, Massimo, Di Bona, Massimo, and Mazza, Salvatore, 1988, Scaling laws and spectral parameters of the ground motion in active extensional areas in Italy: Seismological Society of America Bulletin, v. 78, no. 2, p. 530–560.

Scherbaum, Frank, 1990, Combined inversion for the three-dimensional *Q* structure and source parameters using microearthquake spectra: Journal of Geophysical Research, v. 95, no. B8, 12423–12438.

Seale, S.H., and Archuleta, R.J., 1989, Site amplification and attenuation of strong ground motion: Seismological Society of America Bulletin, v. 79, no. 6, p. 1673–1696.

Seekins, L.C., Lew, Frank, and Kornfield, Lawrence, 1990, Areal distribution of damage to surface structures, chap. C of Effects of the Loma Prieta earthquake on the Marina District, San Francisco, California: U.S. Geological Survey Open-File Report 90–253, p. C1–C5.

Simpson, D.W. , Hough, S.E., Lerner-Lam, A.L., and Phinney, Robert, 1989, Earthquake response [abs.]: Eos (American Geophysical Union Transactions), v. 70, no. 44, p. 1450.

Snoke, J.A., 1987, Stable determination of (Brune) stress drops: Seismological Society of America Bulletin, v. 77, no. 2, p. 530–538.

Tucker, B.E., King, J.L., Hatzfield, Denis, and Nersesov, I.L., 1984, Observations of hard-rock site effects: Seismological Society of America Bulletin, v. 74, no. 1, p. 121–136.

THE LOMA PRIETA, CALIFORNIA, EARTHQUAKE OF OCTOBER 17, 1989:
STRONG GROUND MOTION AND GROUND FAILURE

STRONG GROUND MOTION

A POSTEARTHQUAKE REEVALUATION OF SEISMIC HAZARD IN THE SAN FRANCISCO BAY REGION

By Janice M. Murphy and Steven G. Wesnousky,
University of Nevada, Reno

CONTENTS

ABSTRACT

Several years before the earthquake, seismic-hazard maps were constructed for California on the basis of the magnitudes and locations of historical earthquakes and the slip rates of Quaternary faults, each interpreted within the framework of the concept of elastic rebound. These maps showed the estimated probability that onshore Quaternary faults would generate peak horizontal ground accelerations ≥0.1 *g* at hard-rock sites during the subsequent 50 years. In this paper, we use the same method to illustrate the effect of (1) the possible release of crustal strain along the San Andreas fault associated with the 1989 Loma Prieta earthquake and (2) the acquisition of further geologic and geodetic data bearing on the slip rates and paleoearthquake history of faults in the San Francisco Bay region. Although these new observations allow for a more complex interpretation of San Andreas fault behavior than was previously recognized and thus introduce an added uncertainty into the calculations, a general result is that the probability for ≥0.1-*g* ground motions during the next 50 years remains high for most of the bay region. The original and reconstructed maps are of limited utility because they consider only relatively low levels of ground motion at hard-rock sites. For that reason, we further use empirical relations between local site geology and ground-motion amplification to construct maps showing the probability of peak ground velocities ≥40 cm/s and peak ground accelerations ≥0.5 *g* during the next 50 years. A consequence is that the largest predicted levels of ground motion commonly do not lie directly adjacent to mapped fault zones but, instead, in areas of weakly consolidated Quaternary alluvium along the margins of San Francisco Bay.

INTRODUCTION

Before the earthquake, the probability of strong ground motions due to earthquakes in the southern part of the San Francisco Bay region was considered to be high, in apparent accord with the occurrence of the 1989 Loma Prieta earthquake (fig. 1; Wesnousky, 1986). This high probability was in part due to then-current geologic and geodetic estimates that the average accumulation of slip along the San Andreas fault was 12 mm/yr (Wesnousky, 1986) and that it last ruptured in 1906, when it produced coseismic surface offsets ranging from 0.5 to 1.5 m along the Loma Prieta section of the fault (Lindh, 1983; Sykes and Nishenko, 1984; Scholz, 1985). In that regard, when figure 1 was constructed, the amount of slip that had accumulated along the Loma Prieta section of the San Andreas fault was estimated to equal about 1 m ([1986–1906] yr × 12 mm/yr), comparable to the fault slip that occurred in 1906. Thus, that section of the fault was viewed to be in the later stages of the strain-accumulation cycle, and, in turn, the seismic hazard within the vicinity was considered to be high (Wesnousky, 1986).

In accord with the concept of elastic rebound, the seismic hazard, or the probability of strong ground shaking due to an earthquake on a specific fault, excluding probable aftershocks, is generally considered lowest during the period immediately after a major earthquake—the time when accumulated strain is minimal. The 1989

Loma Prieta earthquake represents such a major earthquake. As a result, to first order, we might expect the regional seismic hazard within the San Francisco Bay region to be significantly altered in comparison with the years immediately before the October 17 event. Similarly, numerous seismic, geologic, and geodetic studies of the San Andreas and other local faults have brought new data to bear on the slip rates and paleoearthquake histories of faults within the San Francisco Bay region. In this paper, we reconstruct the hazard maps of Wesnousky (1986) to examine the effects of (1) the crustal-stress release associated with the 1989 Loma Prieta earthquake and (2) new evidence on slip rates and paleoearthquake histories for bay-region faults.

Wesnousky's (1986) map (fig. 1) was constructed from estimates of strong ground motion at hard-rock sites. That strong ground motions can be modified by local site conditions is well known (Lawson, 1908; Gilbert, 1909; Borcherdt and others, 1975b; Su and others, 1992). More recently, Borcherdt and others (1991) reported an empirical correlation between strong ground motion and specific geologic units in the San Francisco Bay region (see table 2). We incorporate these empirical relations with an existing geologic map (Borcherdt and others, 1975a) for part of the bay region (see fig. 5) to illustrate the increased resolution and, thus, utility of hazard maps that result from including site-amplification effects.

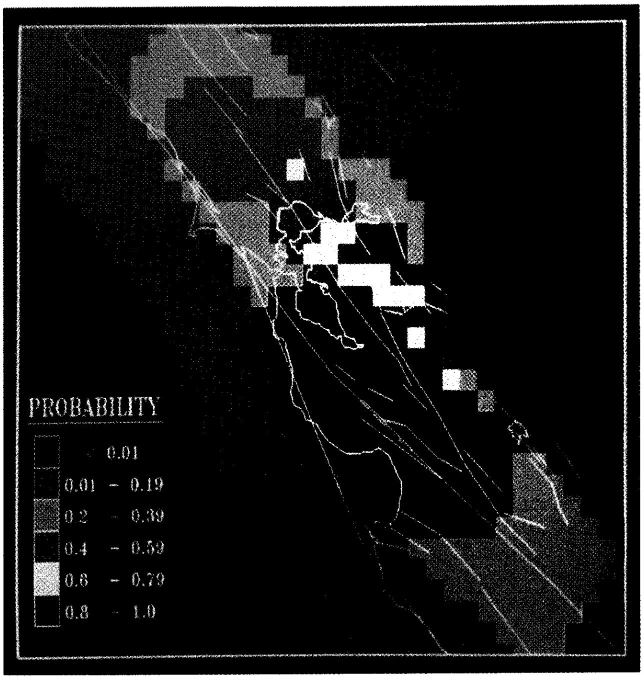

Figure 1.—Preearthquake hazard map of the San Francisco Bay region constructed by Wesnousky (1986, fig. 3b), showing estimated probability that Quaternary faults mapped in the region would generate peak horizontal ground accelerations ≥0.1 *g* during 50-yr period after 1986. Green, section of fault that ruptured in 1989 Loma Prieta earthquake.

CONSTRUCTION OF THE HAZARD MAPS

Knowledge of the slip rates and the past history of earthquakes along each fault in the bay region formed the foundation for Wesnousky's (1986) construction of hazard maps. The exact methodology, as detailed by Wesnousky and others (1983) and Wesnousky (1986), is briefly reviewed below in the supplementary section entitled "Methodology." In addition, the slip rates and earthquake histories of each fault were outlined in Wesnousky (1986). Therefore, we limit our review to those fault zones where paleoseismic studies have been made or where earthquakes have occurred since 1986. We also note that observations in Holocene materials more likely reflect current long-term activity than do estimates made from offsets in older rocks, and so we limit our discussion to studies of Holocene rocks. We focus on the San Andreas, Hayward, and Calaveras faults, which are the major fault systems in the San Francisco Bay region (fig. 2). Data and references bearing on the slip rates of all the faults used in our calculations are summarized in table 1.

FAULT-SLIP RATES

Geologic estimates of the slip rate on the San Andreas fault north of San Juan Bautista, Calif. (fig. 2*B*), range from about 7.5 to 28 mm/yr. Hall (1984) interpreted a displaced channel on the San Francisco peninsula at the north end of Crystal Springs Reservoir (fig. 2*B*) to suggest a minimum late Holocene fault-slip rate of ≥12 mm/yr. In a recent reexamination of that site, however, additional radiocarbon ages on multiple new samples showed that the original age of 1,130±160 yr B.P. on which the 12-mm/yr slip rate was based is incorrect (N.T. Hall, oral commun., 1990). The new data suggest a minimum slip rate of ≥7.5 mm/yr. Farther north, near Olema, Calif. (fig. 2*B*), Niemi and Hall (1992) determined a minimum slip rate of 24±3 mm/yr for the San Andreas fault north of its junction with the San Gregorio fault from an offset buried channel dated at 1,800±78 yr B.P., an age that is the weighted average of six tree-ring-calibrated radiocarbon ages with a 2σ range. Near Point Arena, Calif. (fig. 2*B*), Prentice (1989) interpreted a buried Holocene offset channel (2709–2356 yr B.P.) as setting a maximum slip rate of 25±3 mm/yr for the San Andreas fault (Prentice and others, 1991). The channel age is dendrochronologically calibrated and spans the 2σ error.

Estimates of slip rate over much shorter periods of time have also been made for the San Andreas fault from geodetic observations. Geodetic surveys spanning the fault from San Francisco southward to the latitude of Coyote Lake (fig. 2*B*), during the period 1970–80 show strain rates which imply that about 12±4 mm/yr of slip is accumulating along this section of the fault (Prescott and others, 1981). Geodetic surveys are also consistent with a similar slip rate near Point Reyes farther to the north (fig. 2*B*; Prescott and Yu, 1986). However, more recent analyses of geodetic data by Matsu'ura and others (1986) argue for 26±3 mm/yr of slip accumulation along the peninsular section of the San Andreas fault. A recent report by the Working Group on California Earthquake Probabilities (1990) also cited unpublished geodetic analyses that permit a slip rate of 26 to 32 mm/yr along this section of the fault. Galehouse (1991) observed no creep on the San Andreas in the past 11 years. In summary, then, geologic estimates and modeling of geodetic data allow slip rates of 7.5 to 32 mm/yr on the peninsular section of the San Andreas fault.

Figure 1 was constructed with an assumed slip rate of 12 mm/yr for the peninsular section of the San Andreas fault, an assumption supported by the apparent agreement between the late Holocene geologic slip rate of 12 mm/yr (Hall, 1984) and geodetic data (Prescott and others, 1981). Although recent developments and reanalysis of the geologic data do not rule out a 12-mm/yr slip rate, there now exists no firm basis for using this value as a preferred slip rate. We note here, as did the Working Group on California Earthquake Probabilities (1990), that (1) the 1989 Loma Prieta earthquake produced 1.6 m of lateral coseismic slip (Lisowski and others, 1990) and (2) it had been 83 years since the 1906 San Francisco earthquake ruptured this segment of the San

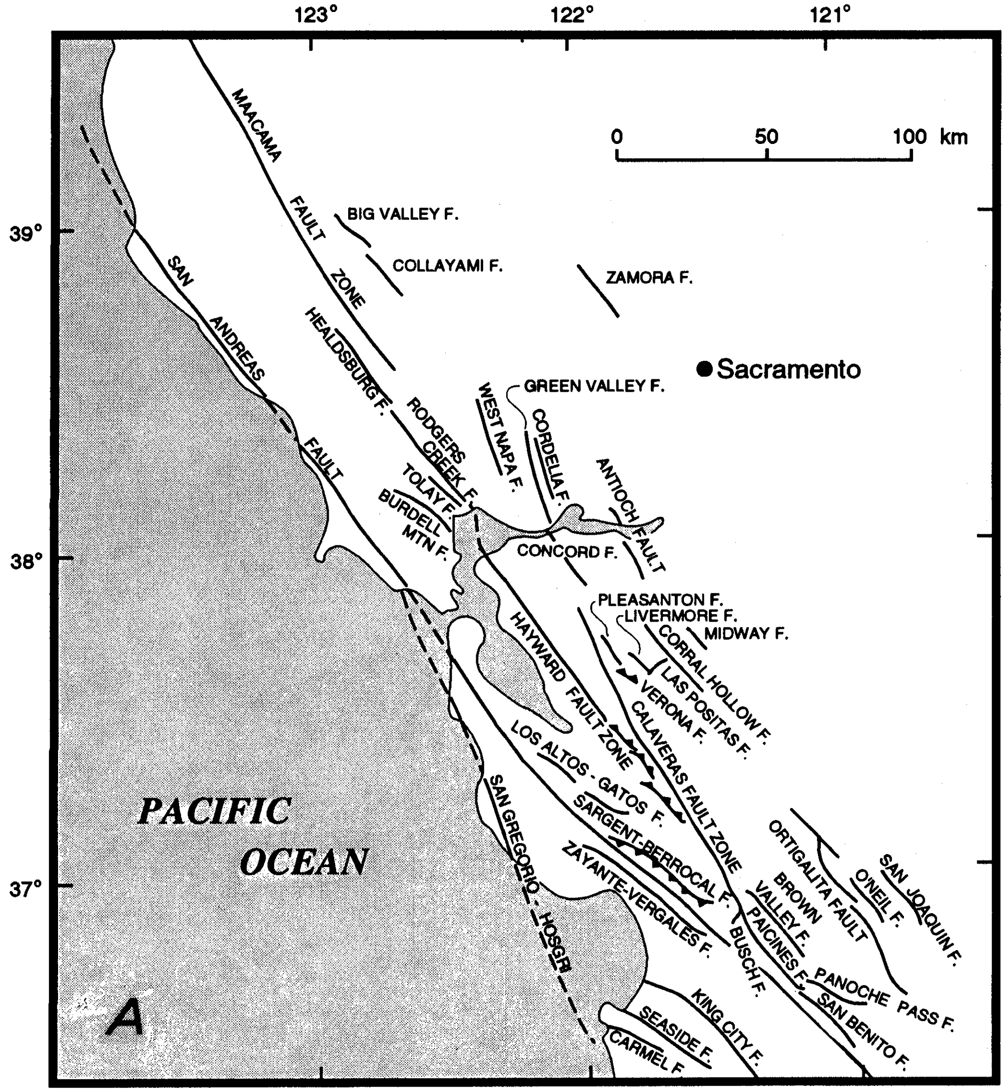

Figure 2.—Schematic maps of the San Francisco Bay region, showing locations of (*A*) Quaternary faults (dashed where inferred) and (*B*) sites discussed in text. Teeth are on hanging-wall side of thrust and reverse faults.

Andreas fault. Assuming that all the lateral slip accrued since 1906, the date of the last major earthquake along this section of the fault, we may estimate a strike-slip rate of 19 mm/yr, which is also the median of the slip rates that we reviewed. We thus assume a slip rate of 19 mm/yr for the San Andreas fault, an increase of 7 mm/yr over the slip rate assumed in constructing figure 1. We also note that the Working Group on California Earthquake Probabilities (1990) adopted a slip rate of 19±3 mm/yr.

The Hayward and Calaveras faults are subparallel to and lie east of the San Andreas fault (fig. 2*A*). The Calaveras fault splays northeastward from the San Andreas fault 30 km southeast of Hollister, Calif. (fig. 2*B*). About 10 km southwest of Hollister, Perkins and Sims (1988) determined a 9-mm/yr slip rate on the Calaveras fault from radiocarbon ages (14,425±215 calibrated yr B.P.) on an offset alluvial-terrace riser. They interpreted this age as a minimum because the terrace is south of the latitude at which slip is transferred from the San Andreas fault to the Calaveras fault system, and they further suggested a fault-slip rate of 15 to 20 mm/yr on the Calaveras fault northwest of Hollister. Geodolite measurements by Savage and others (1979) are consistent with 17±2 mm/yr of right-lateral slip across the section of the Calaveras fault south of the Hayward fault. Furthermore, Prescott and others (1981) interpreted that this slip is divided between the Hayward and Calaveras faults to the north.

Recent trenching studies along the Hayward fault near Union City, Calif. (fig. 2*B*), by Lienkaemper and Borchardt (1991) yielded an estimate of the minimum geologic slip rate of 8±0.6 mm/yr for the past 8,260±90 calibrated yr, with a 1σ range. They also noted that the average historical creep rate there has been 5 mm/yr.

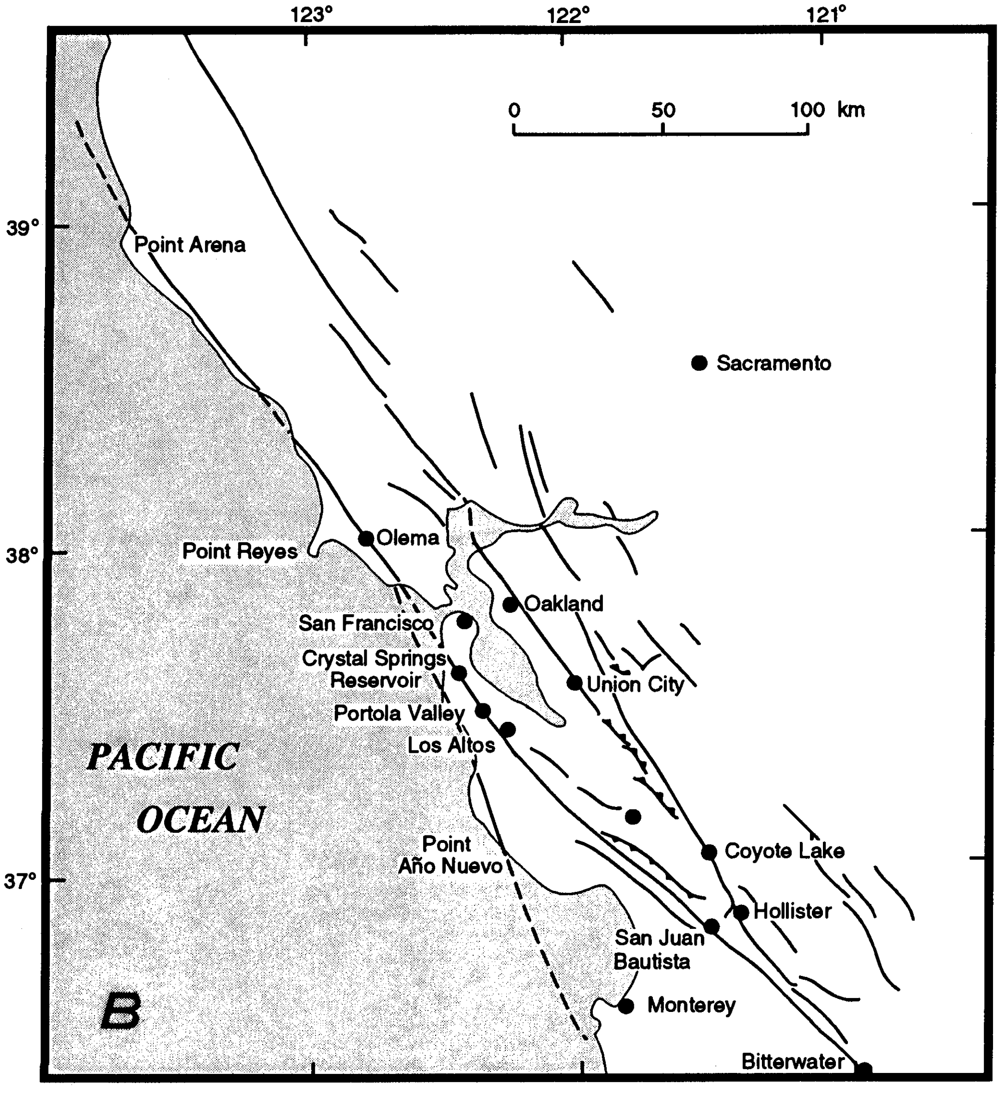

Figure 2.—Continued.

Table 1.—*Quaternary faults in the San Francisco Bay region*

[Location denotes approximate midpoint of fault. Fault types: ll, left lateral; ln, left normal; lr, left reverse; lv, left vertical; n, normal; r, reverse; rl, right lateral; rn, right normal; rr, right reverse; rv, right reverse. M_w, moment magnitude of earthquake expected from rupture of entire fault length, estimated from slip-rate-dependent empirical relations between seismic moment M_0 and rupture length (Wesnousky, 1986) in figure 7, assuming the empirical relation M_0=1.5M_w+16.1 (Hanks and Kanamori, 1979). Slip-rate classes: AA, ≥10 mm/yr; A, ≥1 mm/yr; B, ≥0.1 mm/yr; C, ≥0.01 mm/yr. A fault is assumed to be in class C when no slip-rate data are available, and is assigned a slip rate of 0.01 mm/yr for hazard-map construction. Minimum and maximum slip rates are those reported in the reference(s) listed; preferred slip rate, where listed, is used to estimate the recurrence interval, which otherwise is estimated from either the minimum, maximum, or average of the minimum and maximum slip rates, depending on which limits are set on the fault. Recurrence interval is estimated from equation 1 unless noted otherwise; intervals longer than 10,000 yr are omitted. Slip-rate determination is from predominantly the horizontal (h), vertical (v), dip-slip (d), or total (t) component of displacement. Youngest feature used to determine slip rate: h, Holocene; m, Miocene; p, Pliocene; q, Pleistocene. Letters a through c in parentheses after a reference indicate that the slip rate(s) listed are those reported by Anderson (1979) (a), Bird and Rosenstock (1984) (b), or Clark and others (1984) (c)]

Fault	Location					slip-	Slip Rate (mm/yr)			Recurrence			
	lat. (° N.)	long (° W.)	type	Length (km)	M_w	rate class	Min	Max	Prefer	interval (yr)	slip-rate determination	Youngest feature	Reference
Antioch, segment A	38.1	121.8	--	10	6.3	C	--	--	--	--	--	--	Jennings (1975).
Antioch, segment B	38.0	121.8	--	19	6.6	C	--	--	--	--	--	--	Do.
Big Valley	39.0	122.9	rl	16	6.5	B	.3	--	--	2,675	h	q	Hearn and others (1976) Clarke and others (1984)
Browns Valley[1]	36.9	121.3	--	29	6.8	C	--	--	--	--	--	--	Jennings (1975)
Burdell Mountain	38.1	122.6	--	21	6.6	C	--	--	--	--	--	--	Jennings (1975).
Calaveras, segment A (Coyote Lake).	37.0	121.5	rl	28	5.7	AA	--	--	17.0	[2]82	h	h	Wesnousky (1986), Prescott and others (1981), Savage and others (1979).
Calaveras, segment B (Morgan Hill).	37.3	121.7	rl	28	6.3	AA	7.0	17.0	--	[2]150	h	h	Do.
Calaveras, segment C	37.5	121.8	rl	31	6.3	A	--	--	7.0	[2]150		h	Wesnousky (1986).
Calaveras, segment D	37.7	122.0	rl	23	6.3	A	--	--	7.0	[2]150	h	h	Do.
Carmel [1]	36.6	121.9		28	6.8	C	--	--		--	--	--	Jennings (1975).
Collayami	38.9	122.8	rl	18	6.6	B	--	1.0	.1	--	h	q	Hearn and others (1976)(c).
Concord	38.0	122.0	rl	24	6.7	A	--	--	7.0	183	--		See text; Wesnousky (1986), Harsh and Burford (1982).
Cordelia	38.3	122.1	--	22	6.7	C	--	--	--	--	--	--	Herd and Helley (1977).
Corral Hollow[1]	37.7	121.6	--	17	6.5	C	--	--	--	--	--	--	Jennings (1975).
Green Valley	38.2	122.1	--	35	6.9	A	--	--	7.0	242	--	--	See text; Wesnousky (1986), Herd and Helly (1977), Frizzell and Brown (1976).
Greenville	37.7	121.7	rv	28	6.8	B	.1	.7	--	3,585	h	h	Wright and others (1982).
Hayward, segment A (Coyote and Silver Creek faults).	37.2	121.7	ll	18	6.6	A	--	--	9.0	118	h	h	See text; Wesnousky (1986).
Hayward, segment B (Evergreen fault).	37.4	121.8	rl	32	6.9	A	--	--	9.0	149	h	h	Do.
Hayward, segment C	37.6	122.0	rl	32	6.9	A	6.0	9.0	9.0	189	h	h	See text; Working Group on Earthquake Probabilities (1990), Lienkaemper and others (1991), Wesnousky (1986), Prescott and others (1981), Prescott and Lisowski (1982), Lawson (1908).
Hayward, segment D	37.9	122.3	rl	49	7.0	A	--	--	9.0	240	h	h	Do.
Healdsburg	38.6	122.8	rl	32	6.8	A	--	--	9.0	178	--	--	See text; Wesnousky (1986), Jennings (1975).
King City	36.0	121.6	--	57	7.1	C	--	--	--	--	--	--	Jennings (1975).
Las Positas	37.6	121.7	ln	10	6.3	B	.04	1.6		873	t	q	Carpenter and Clark (1982)(c), Herd and Brabb (1980).
Livermore	37.7	121.8	--	8	6.2	C	--	--	--	--	--	--	Jennings (1975).
Los Altos[1]	37.3	122.1	--	14	6.4	C	--	--	--	--	--	--	Do.
Los Gatos[1]	37.2	121.9	--	15	6.5	C	--	--	--	--	--	--	Do.
Maacama	39.1	123.1	--	151	7.6	A	--	--	9.0	541	--	--	See text; Wesnousky (1986), Pampeyan and others (1981), Herd (1978), Herd and Helley (1977).
Midway	37.7	121.6	r	11	6.3	B	.1	.5	--	2,651	--	--	Shedlock and others (1980)(c).
O'Neil	36.9	121.0	r	18	6.5	A	.3	1.8	--	984	--	--	Lettis (1982)(c).

Table 1.—*Quaternary faults in the San Francisco Bay region*—Continued

Fault	Location					slip-	Slip Rate (mm/yr)			Recurrence			
	lat. (° N.)	long (° W.)	type	Length (km)	M_w	rate class	Min	Max	Prefer	interval (yr)	slip-rate determination	Youngest feature	Reference
Ortigalita, segment A	37.1	121.2	?	25	6.7	C	0.01	0.04	--	[2]10,000	v	q	Anderson and others (1982), Clark and others (1984).
Ortigalita, segment B	37.0	121.1	?	18	6.6	C	.01	.04	--	[2]10,000	v	q	Do.
Ortigalita, segment C	36.9	121.0	?	18	6.6	C	.01	.04	--	[2]10,000	v	q	Do.
Ortigalita, segment D	36.7	120.9	?	21	6.6	C	.01	.04	--	[2]10,000	v	q	Do.
Paicines----------------	36.8	121.3	rl	36	6.9	A	5.0	13.0	1.0	1727	--	h	Wesnousky (1986), Harsh and Pavoni (1978), Ellsworth (1975), Savage and others (1973), Lisowski and Prescott (1981).
Panoche Pass[1]---------	36.6	121.1	--	22	6.6	C	--	--	--	--	--	--	Jennings (1975).
Pleasonton-------------	37.7	121.9	--	9	6.2	C	--	--	--	--	--	--	Do.
Rinconada-------------	35.8	120.9	rl	136	7.6	A	2.4	12.0	2.4	1,883	h	p	Durham (1965)(b), Hart (1976)(b).
Rodgers Creek---------	38.3	122.6	--	51	7.0	A	2.1	10.0	9.0	248	--	--	See text; Budding and others (1991), Schwartz and others (1992).
San Andreas, segment A (Shelter Cove to Crystal Springs).	38.5	122.8	rl	420	7.8	AA	7.5	30.0	19.0	[2]200	h	h	See text; Niemi and Hall (1992), Prentice (1989), Matsu'ura and others (1986), Prescott and Yu (1986).
San Andreas, segment B (Crystal Springs to Los Gatos).	37.4	121.1	rl	53	6.8	AA	7.5	30.0	19.0	[2]131	h	h	See text; Thatcher an Lisowski (1987), Matsu'ura and others (1986), Hall (1984), Prescott and others (1981).
San Andreas, segment C (Los Gatos to Hecker Pass).	37.1	121.9	rl	37	6.6	AA	7.5	30.0	19.0	[2]83	h	h	See text; Thatcher an Lisowski(1987), Matsu'ura and others (1986), Prescott and others (1981).
San Andreas, segment D (Hecker Pass to Bitterwater).	36.6	121.2	rl	86	7.0	AA	7.5	39.0	5.0	262	h	h	Wesnousky (1986), Burford and Harsh (1980), Clark and others (1984).
San Benito-------------	36.6	121.1	rl	24	6.7	A	5.0	13.0	1.0	1,291	--	--	Wesnousky (1986), Harsh and Pavoni (1978), Ellsworth (1975), Savage and others (1973), Lisowski and Prescott (1981).
San Gregorio-Hosgri	37.1	122.3	rl	190	7.7	A	7.0	19.0	7.0	824	h	q	Weber and Cotton (1981)(c), Weber and Lajoie (1980)(c), Clark and others (1984) (c).
San Joaquin------------	36.9	120.8	?	21	6.6	A	.2	2.0	--	1,083	v	q	Lettis (1982)(c).
Sargent-Berrocal-------	37.0	121.7	rr	51	7.1	A	--	4.0	1.0	2,225	--	h	Savage and others (1979), Hay and others (1980).
Seaside[1]----------------	36.5	121.7	--	23	6.7	C	--	--	--	--	--	--	Jennings (1975).
Tolay-------------------	38.2	122.5	--	14	6.5	C	--	--	--	--	--	--	Do.
Vaca--------------------	38.3	122.0	rl	7	6.1	A	.3	4.0	--	260	h	q	Knuepfer (1977)(c).
Verona-----------------	37.6	121.8	r	8	6.2	B	.02	.1	.1	9,735	t	q	Herd and Brabb (1980)(c).
West Napa-------------	38.3	122.3	--	17	6.5	C	--	--	--	--	--	--	Herd and Helley (1977).
Zamora-----------------	38.8	121.9	n	21	6.6	A	.2	.5	.3	4,631	v	q	Harwood and others (1981)(c), Harwood and Helley (1982)(c).
Zayante-Vergales------	37.0	121.8	rr	50	7.1	B	.1	1.3	--	3,140	t	q	Coppersmith (1979)(c), Dupre (1975)(c).

[1] Fault name assumed without reference to earlier studies.

[2] Based on historical information, trenching studies, or other geologic inferences, rather than equation 1. Cases discussed in the text.

Measurements by Galehouse (1991) confirm a creep rate of 4 to 5 mm/yr on the Hayward fault for the past 11 years. Based on synthesis of historical creep rates, geodetic data, historical seismicity, and long-term geologic slip rates, Lienkaemper and others (1991) proposed a deep-slip rate of 9 mm/yr for the Hayward fault, with a locked zone between 3- and 10-km depth. Prescott and Lisowski (1982) determined strain rates from both small (1–2 km)- and large (10–30 km)-aperture geodetic networks that straddle the Hayward fault. They concluded that no more than 4 mm/yr of slip is presently accumulating as elastic strain in rocks adjacent to the fault, whereas the total rate of displacement measured geodetically is about 8 mm/yr (Prescott and others, 1981). Subsequently, however, the strength of their conclusion has been questioned (William Prescott, oral commun., 1991). Thus, the relation between surface creep and crustal-stress accumulation is not well understood for the Hayward fault. Wesnousky (1986) assumed that a 4-mm/yr slip rate is characteristic of the strain-accumulation rate on the Hayward fault, on the basis of the analysis by Prescott and Lisowski (1982). Because it is unclear whether significant crustal strain is being released by aseismic creep, we follow Lienkaemper and others (1991) in assuming a slip rate of 9 mm/yr.

The Rodgers Creek-Healdsburg and Maacama fault zones (fig. 2*A*) are right-stepping northward extensions of the Hayward fault zone. Budding and others (1991) interpreted offset buried-channel deposits along the Rodgers Creek fault to indicate a minimum slip rate of 2.1 to 5.8 mm/yr for the past 1,200 yr. More recently, new radiocarbon ages (dendrochronologically calibrated, with a 1σ range) from the same site suggest higher slip rates of 6.4 to 10.4 mm/yr for the past 750 yr (Schwartz and others, 1992). Galehouse (1991) found no evidence of creep on the Rodgers Creek and West Napa faults (fig. 2*A*) until late 1990, when both faults began showing some evidence of movement. For reconstructing the hazard map (see fig. 4), each of these faults was assumed to slip at the same rate as the Hayward fault (9 mm/yr).

The Calaveras fault also appears to have a complex relation between surface creep and strain accumulation. Although this fault is generally assumed to be creeping, four, possibly five, moderate historical earthquakes have occurred on it (Wesnousky, 1986). Galehouse (1991) observed a creep rate of 10 mm/yr in the Hollister, Calif., area (fig. 2*B*) but found no creep at the northwest end of the fault. We follow Wesnousky (1986) in assuming a slip rate of 7 mm/yr. The Concord and Green Valley faults (fig. 2*A*) are the right-stepping continuations of the Calaveras fault (Page, 1982), and each fault is assumed to slip at the same rate as the Calaveras fault. Although there are no geologic estimates of the slip rates for these two faults, Galehouse (1991) determined creep rates of 3 to 4 mm/yr on the Concord fault and 5 to 7 mm/yr on the Green Valley fault.

Wesnousky (1986) reviewed the meager data on the San Gregorio-Hosgri fault (fig. 2*A*). We use the same interpretation here because no new data are available. Finally, we note that the sum of slip rates across the major faults in the study area is consistent with the rate of 38±3 mm/yr measured geodetically across the San Andreas-Calaveras fault system in the Hollister, Calif., area (Matsu'ura and others, 1986).

FAULT BEHAVIOR AND RECURRENCE INTERVALS

Information regarding fault-slip rate provides a measure of the strain-accumulation rate along a fault. The paleoseismologic and historical record of earthquakes and the distribution of coseismic slip observed in those earthquakes provide some basis for hypotheses regarding the future behavior of faults. We follow Wesnousky (1986) in estimating the size of future events from fault lengths and the recurrence intervals of ruptures.

The San Andreas fault is divided into four segments (A–D, fig. 3*A*) on the basis of the historical record of earthquakes and the distribution of slip that occurred during the largest of those earthquakes. More specifically, the 1906 San Francisco earthquake produced surface ruptures along a 420-km-long section of the San Andreas fault that strikes northward from San Juan Bautista, Calif. (fig. 2*B*; Lawson, 1908; Thatcher, 1975; Prentice and Schwartz, 1991). Lawson reported average coseismic surface offsets of 2.5 to 5.0 m between Los Altos and Point Arena (fig. 2*B*) in 1906, but measurements south of Los Altos were significantly smaller—from 0.5 to 1.5 m. Reexamination of geodetic data bracketing the 1906 San Francisco earthquake confirm a decrease in the 1906 slip function south of Crystal Springs Reservoir (fig. 2*B*) but do not reflect the twofold difference indicated by surface offsets (Thatcher and Lisowski, 1987). A recent study of historical data and the surface expression of the San Andreas fault in the southern Santa Cruz Mountains (Prentice and Schwartz, 1991) suggests that the surface displacements reported by Lawson (1908) in this area were not coseismic surface faulting of the San Andreas fault but shaking-induced slope failures and fractures. Therefore, none of the reported measurements of surface offset are reliable as indicators of the fault offset in the Santa Cruz Mountains in 1906 (Prentice and Schwartz, 1991). However, Prentice and Schwartz present evidence which implies that surface rupture occurred on the San Andreas fault in 1906 as far south as San Juan Bautista, Calif. (fig. 2*B*). Best estimates of coseismic offset during the 1906 San Francisco earthquake from geodetic analysis indicate slip of 3.4 to 4.4 m north of Crystal Springs Reservoir and 2.4 to 3.8 m south of Crystal Springs Reservoir.

Segment A of the San Andreas fault (fig. 3*A*) corresponds to the part of the 1906 rupture north of Crystal Springs Reservoir (fig. 2*B*). At Point Arena (fig. 2*B*), Prentice (1989) estimated a recurrence interval of 200 to 400 yr for paleoearthquakes, on the basis of excavations into an alluvial fan where at least five earthquakes were recognized. Using Wesnousky's (1986) seismic-moment relation ($T=M_0^e/\dot{M}_0^g$; see supplementary section below entitled "Methodology"), the assumed 19-mm/yr slip rate, and the 420-km-long rupture length, the recurrence interval of 1906-type earthquakes is calculated to be 200 yr, at the lower bound of geologic estimates (Prentice, 1989). Similarly, the 3.4- to 4.4-m offsets estimated geodetically for the 1906 San Francisco earthquake along segment A may be divided by the 19-mm/yr slip rate to delimit the average recurrence interval for rupture of segment A. This calculation gives a recurrence interval of 179 to 232 years. For our reconstructions, we assumed that segment A is characterized by an earthquake of M_w=7.8 every 200 yr—less than the 300 yr previously used by Wesnousky (1986).

Historical documents provide evidence that, in addition to the 1989 Loma Prieta earthquake, a major earthquake also ruptured the San Andreas fault in 1838 (Louderback, 1947). On the basis of interpreted intensities at Monterey and San Francisco, Louderback suggested that the fault rupture extended from near San Francisco to San Juan Bautista, Calif. (fig. 2*B*). In 1865, a moderate earthquake (M_I~6.3; Toppozada and others, 1981) occurred in the south bay. Because of uncertainty concerning its location (McNutt and Toppozada, 1990; Tuttle and others, 1990), we omit it from our analysis of the San Andreas fault. Also, because of its small size (M_I=6.0), we omit the 1890 earthquake that is thought to have ruptured the San Andreas north of San Juan Bautista (Ellsworth, 1990).

The 1989 Loma Prieta earthquake was not accompanied by primary surface faulting. Geodetic observations of this earthquake have been fitted best by a fault model characterized by oblique slip on a buried 37-km-long

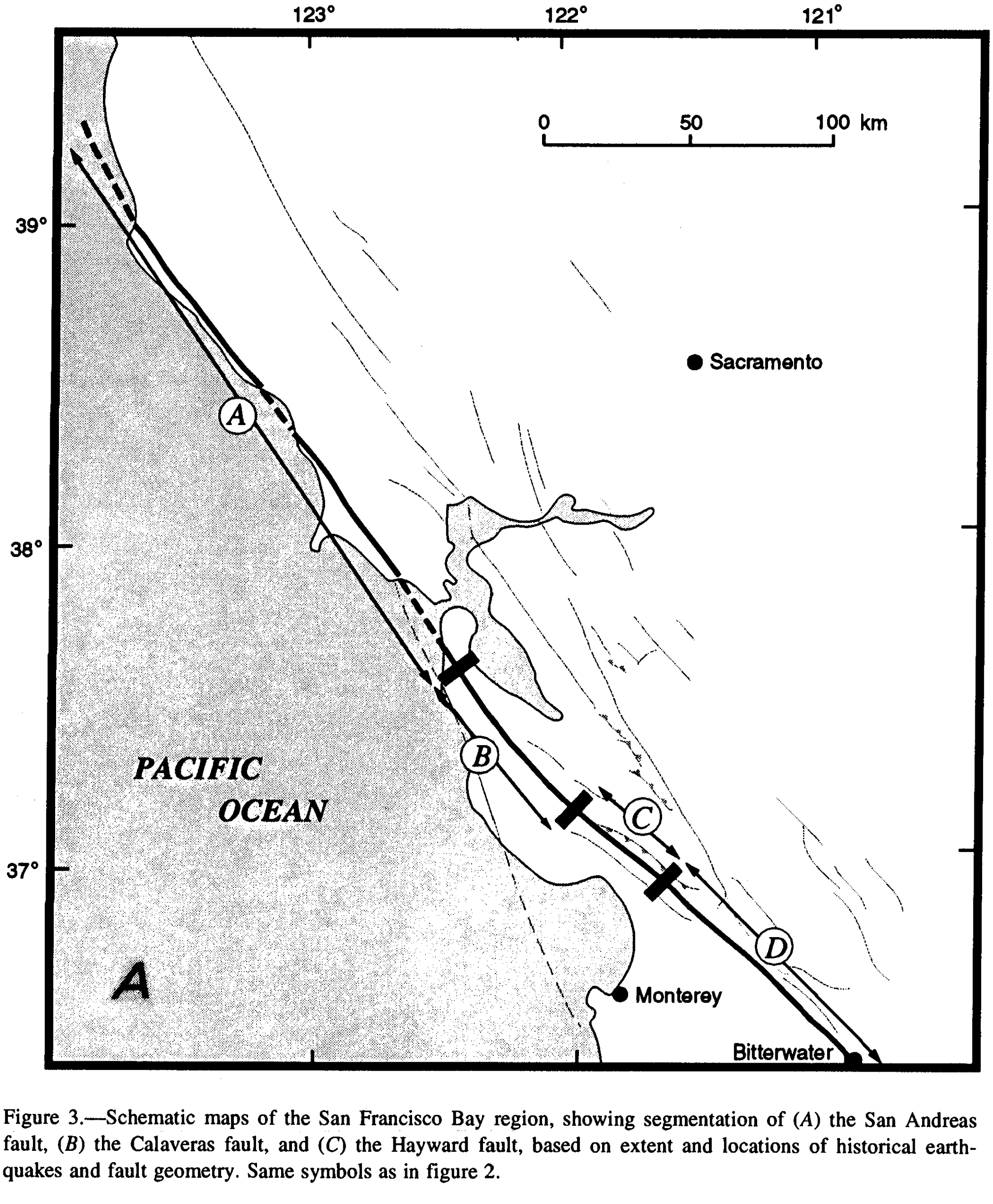

Figure 3.—Schematic maps of the San Francisco Bay region, showing segmentation of (*A*) the San Andreas fault, (*B*) the Calaveras fault, and (*C*) the Hayward fault, based on extent and locations of historical earthquakes and fault geometry. Same symbols as in figure 2.

plane dipping 70° SW. and striking N. 44° W. (Lisowski and others, 1990). Slip during the earthquake was limited to 5- to 17.5-km depth and characterized by 1.6 and 1.2 m of right-lateral and reverse slip, respectively. Analysis of preearthquake seismicity suggests that the San Andreas fault dips vertically, whereas the earthquake occurred on a dipping plane that showed no previous seismic activity (Dietz and Ellsworth, 1990; Olson, 1990). A recent geomorphic study (Prentice and Schwartz, 1991) of the San Andreas fault in the Santa Cruz Mountains showed it to be a simple, throughgoing, typical strike-slip fault that was probably defined by a simple rupture scarp in 1906. Segall and Lisowski (1990) compared geodetic data spanning both the 1906 and 1989 earthquakes and concluded that the 1989 fault model could not explain the 1906 displacements. Thus, although the 1989 Loma Prieta earthquake occurred along the San Andreas fault zone, the seismicity data and a reevaluation of the geologic data have been used to suggest that the 1906 and 1989 earthquakes did not rupture the same fault plane. However, in view of the close proximity of the Loma Prieta rupture to the vertical plane of the San Andreas fault, it cannot be ruled out that shear stress along the San Andreas fault was significantly reduced by the 1989 Loma Prieta earthquake.

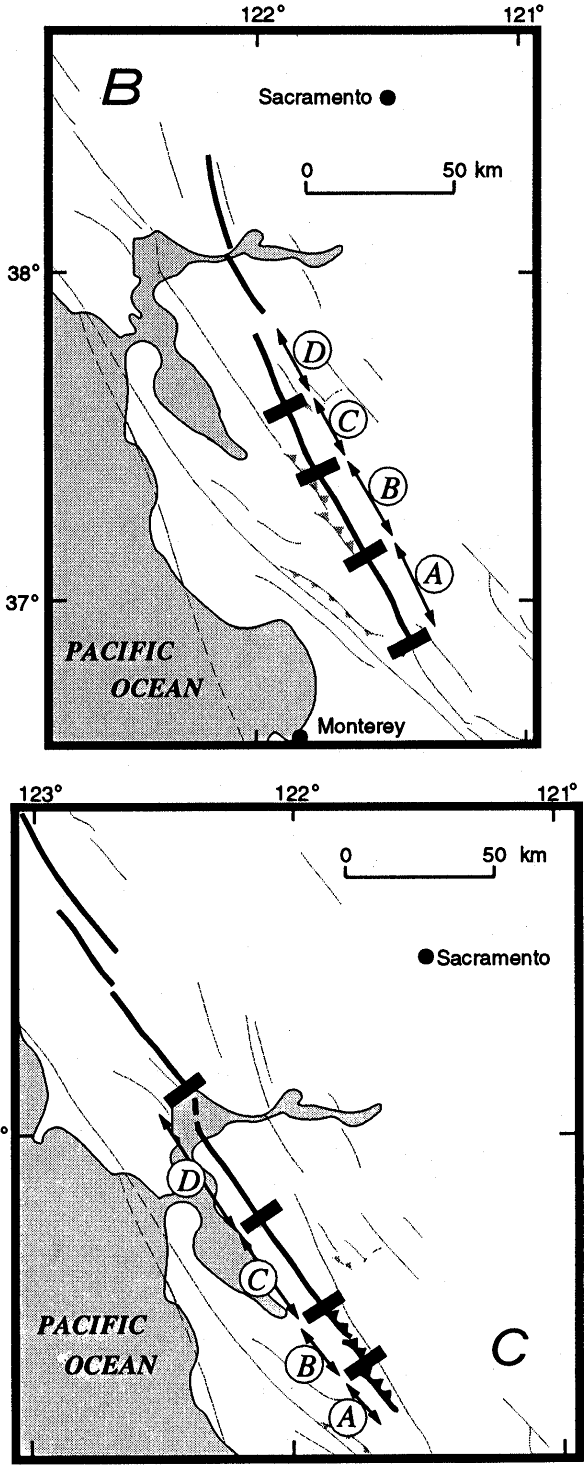

Figure 3.—Continued.

The behavior of the San Andreas fault between San Francisco and San Juan Bautista is highly complex. Large earthquakes, such as the 1906 San Francisco earthquake, nucleate northwest of this area and rupture through it, but this section of the fault also generates large earthquakes whose rupture zones are confined to it (such as the 1989 Loma Prieta earthquake). The seismicity pattern is sparse and clustered (Hill and others, 1990); seismic gaps, such as the one filled by the 1989 Loma Prieta earthquake and its aftershocks, occur between the clusters. For example, just north of the Loma Prieta rupture zone in the Portola Valley area (fig. 2*B*), a conspicuous gap currently exists (Olson, 1990). Thus, we further divide the San Andreas fault into segments based on the length and location of the Loma Prieta rupture zone and coseismic slip during the 1906 San Francisco earthquake. Segment B corresponds to the 53-km-long section of the San Andreas fault that lies between the north terminus of the Loma Prieta rupture zone and Crystal Springs Reservoir, where there was a relative drop in coseismic offset during the 1906 San Francisco earthquake (fig. 3*A*); and segment C corresponds to the approximately 37-km-long rupture length of the 1989 Loma Prieta earthquake. The Portola Valley gap lies entirely within segment B.

Because of the complexity associated with historical earthquakes along segments B and C (fig. 3*A*), estimating future recurrence intervals for moderate to large earthquakes is not straightforward. Segment B ruptured in 1838 and 1906. If we assume that the minimum coseismic slip that occurred on segment B in 1906 (2.5 m) accrued in the 68 years subsequent to 1838, a slip rate of 37 mm/yr is implied—greater than the available geologic and geodetic estimates that we have reviewed.

In that regard, 68 years is likely a minimum estimate of the average recurrence interval. Interpretation of geodetic measurements places best estimates of the coseismic offset along segment B in 1906 between about 2.5 and 3.5 m (Thatcher and Lisowski, 1987). At the assumed 19-mm/yr slip rate, from 131 to 184 yr would be required to accumulate 2.5 and 3.5 m, respectively. In our assignment of recurrence intervals, we assume 68 yr to be the minimum, 184 yr the maximum, and 131 yr the average recurrence interval for earthquakes on segment B. For segment C, we use the 83-yr period between the 1906 and 1989 earthquakes as a recurrence interval.

The extent of historical-earthquake ruptures and the locations of mapped discontinuities in fault strike were used by Wesnousky (1986) to divide the Calaveras fault zone into four segments (A–D, fig. 3*B*), each assumed to be capable of producing moderate earthquakes. The same interpretation is used here in reconstructing the hazard map (see fig. 4) because no new data on slip rate or recurrence intervals have been reported since 1986.

The Hayward fault zone splays off the Calaveras fault at a point south of San Francisco Bay, striking northwest a distance of about 120 km. Segmentation of the fault (A–D, fig. 3*C*) is similar to that described by Wesnousky (1986). Segments A and B, which include the Silver Creek-Coyote Creek and Evergreen fault systems, respectively (Aydin, 1982), show predominantly reverse motion (for example, Bryant, 1982; Page, 1982) and are 18 to 25 km long. The 36-km-long segment of the fault that ruptured in an M_I=6.8 (Toppozada and others, 1981) earthquake on October 21, 1868 (Lawson, 1908), is labeled “C” in figure 3*C*. A recurrence interval of 250 to 400 yr is inferred for this segment of the Hayward fault from offset, tilt, and liquefaction of late Holocene pond and fluvial deposits at the north end of Tule Pond in Fremont, Calif., near Union City (fig. 2*B*; Williams, 1991). An event similar to the 1868 earthquake may have also ruptured the Hayward fault in 1836 (Louderback, 1947). Although data for its location are vague, Louderback (1947) presented evidence for surface rupture in the Oakland area. Recently, the Working Group on California Earthquake Probabilities (1990) suggested that the 1868 earthquake ruptured segment D, and, as such, this suggestion is assumed in reconstructing the hazard maps (see fig. 4).

The Rodgers Creek-Healdsburg fault (fig. 2*A*) has no historical record of rupture, although geologic evidence indicates a maximum recurrence interval for M_w=7 earthquakes of 248 to 679 yr (Budding and others, 1991). More recent examination of another site along the fault provides evidence for three paleoearthquakes during the past 1,000 yr (Schwartz and others, 1992). Dendrochronologically corrected radiometric ages with a 1σ range indicate a recurrence interval of 170 to 490 yr.

DISCUSSION

HAZARD MAPS FOR STRONG GROUND MOTION AT HARD-ROCK SITES

Reconstructed hazard maps showing the probability of peak strong ground accelerations ≥0.1 *g* at hard-rock sites during the 50-yr period after the 1989 Loma Prieta earthquake are presented in figure 4. At the time of Wesnousky’s (1986) investigation, a simple model of fault behavior was allowed by the relatively few data for the recurrence behavior of this section of the fault. New data, however, imply a more complex behavior, and various scenarios exist to predict the future rupture behavior of the peninsular section of the San Andreas fault. Minimum (68 yr) and maximum (184 yr) estimates for the recurrence interval on segment B of the San Andreas fault (fig. 3*A*) are reflected in figures 4*A* and 4*B*, respectively. In both these figures, we assume that the 1989 Loma Prieta earthquake released all the strain accumulated on segment C since 1906. Given arguments to the contrary, however, we also show in figures 4*C* and 4*D* the probability of strong ground motions assuming that segment C of the San Andreas fault last ruptured in 1906, not 1989. Figures 4*C* and 4*D* are constructed similarly to figures 4*A* and 4*B*, respectively, with the exception that figures 4*C* and 4*D* assume that accumulated strain was not released in 1989.

To show how the various rupture scenarios of the San Andreas fault affect the spatial distribution of strong ground motion within the San Francisco Bay region, two extreme rupture scenarios are hypothesized. The difference in the probability of strong ground motion between figures 4*A* and 4*B* shows that uncertainties in our knowledge of the future behavior of segment B strongly influence the predicted strong ground motions within the bay region. Nonetheless, in both cases, the probability is approximately 50 percent or higher that heavily populated areas of the region will undergo strong ground motions ≥0.1 *g* during the next 50 years. The seismic hazard in the east bay and northward remains high regardless of the rupture scenario for the San Andreas fault. With respect to Wesnousky’s (1986) map, new studies of the Hayward and Rodgers Creek fault zones (fig. 2*A*) have resulted in calculating an increased probability of strong ground motions within the east bay and northward.

HAZARD MAPS INCLUDING THE EFFECTS OF LOCAL SOIL-SITE CONDITIONS

An inadequacy of our reconstructed hazard maps (fig. 4) is that they assume that all sites are on hard rock, but studies show that horizontal ground motion at the surface of a soil site can be substantially greater than that in the bedrock below (Borcherdt and others, 1975b). Studies of site amplification show that modification of ground motion is systematically related to the surficial geology (Borcherdt and others, 1975b; Borcherdt and others, 1991; Su and others, 1992); young, loosely consolidated sedimentary deposits undergo the highest amplification. Su and others (1992) used a recursive stochastic inverse method to determine the site amplification from coda

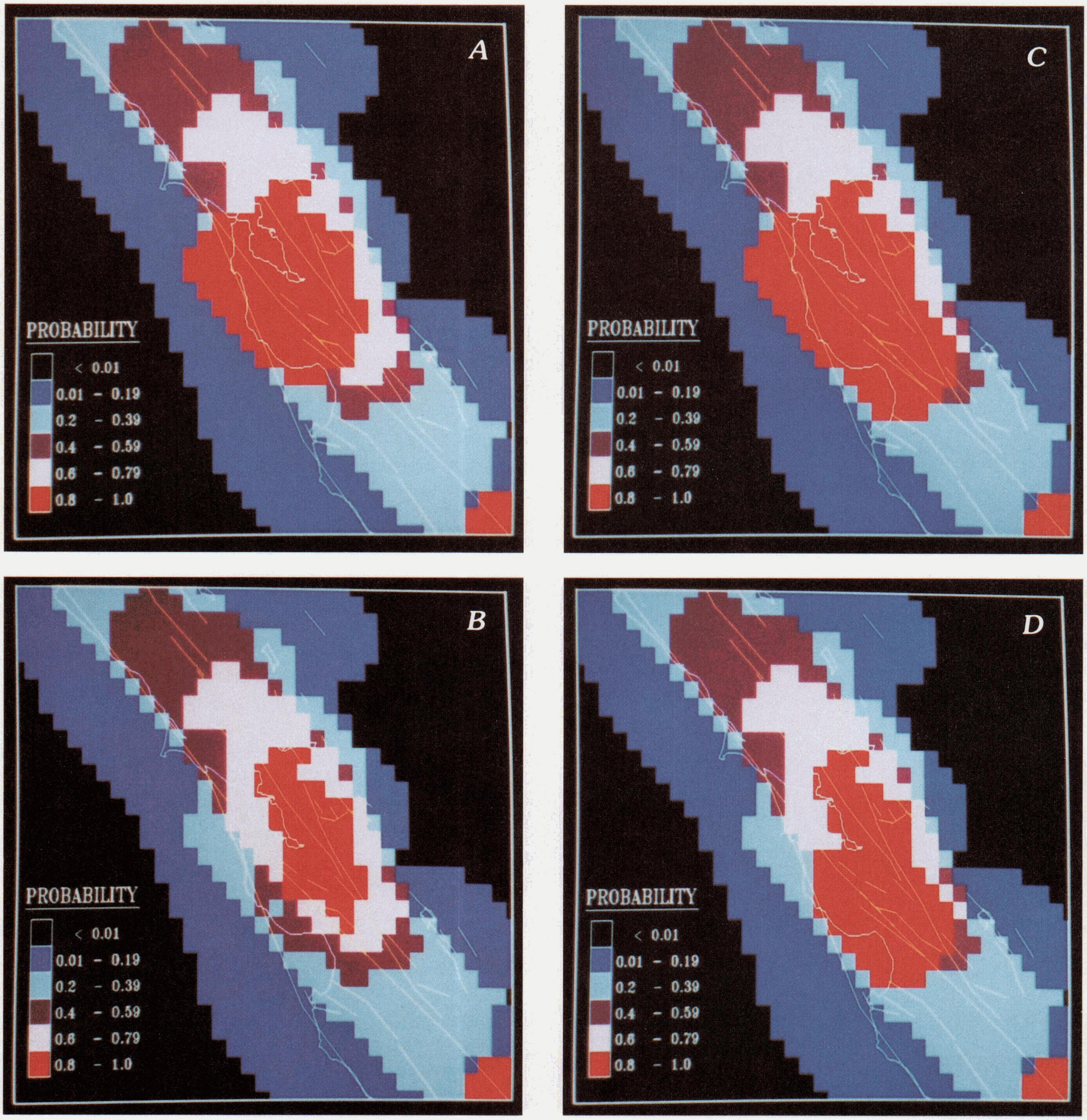

Figure 4.—Hazard maps of the San Francisco Bay region, showing estimated probability that Quaternary faults mapped in the region will generate peak horizontal ground accelerations ≥0.1 *g* at hard-rock sites during 50-yr period after the 1989 Loma Prieta earthquake. Reconstructions assume that earthquake did (*A*, *B*) or did not (*C*, *D*) release all the crustal strain accumulated since 1906; for peninsular section of the San Andreas fault, a minimum recurrence interval of 68 yr (*A*, *C*) or a maximum recurrence interval of 184 yr (*B*, *D*) is assumed.

waves in central California. They classified the numerous geologic formations into five geologic units by age; within each unit, the mean site amplification was associated with the median geologic age. Their results correlate well with strong motions observed during the 1989 Loma Prieta earthquake outside the epicentral region (50-km radius), but not within 50 km of the epicenter. They attributed this disagreement to nonlinear behavior of the sedimentary deposits. Borcherdt and others (1975b) analyzed horizontal ground motions from nuclear explosions in Nevada to determine the average amplification of geologic units in the southern part of the San Francisco Bay region. They classified six geologic units on the basis of data for seismic response to low strain. These amplifications were further refined by Borcherdt and others (1991) on the basis of average shear-wave velocities (Fumal, 1991) to a depth of 30 m and strong ground motions that occurred during the 1989 Loma Prieta earthquake (Borcherdt and others, 1991). Borcherdt and Glassmoyer (1992) reported that amplifications due to site geology during the earthquake were not statistically different from those predicted by Borcherdt and others (1991). A geologic map with six units differentiated by physical properties and geologic characteristics was compiled by Borcherdt and others (1975a). We digitized this map (fig. 5) and used the amplifications of Borcherdt and others (1991) to incorporate local site effects into the hazard maps. Descriptions and amplification values for the six generalized geologic units are listed in table 2.

Although the correlations between site amplification and geologic unit were determined from measurements of velocity response, for illustrative purposes we also use the same amplifications to construct a map showing the probability of acceleration. The probability of ground velocities ≥40 cm/s in the San Francisco Bay region during the next 50 yr is presented in figure 6*A*, and, for the same period of time, the probability of occurrence of accelerations ≥0.5 *g* is presented in figure 6*B*. In both figures, for the San Andreas fault, we assume that the 1989 Loma Prieta earthquake released the strain accumulated since 1906 along segment C (fig. 3*A*) and that the average recurrence interval for segment B is 131 yr. Clearly, the maps in figure 6 are strongly modified by incorporation of site effects; for example, the highest probabilities correspond closely to the distribution of bay mud.

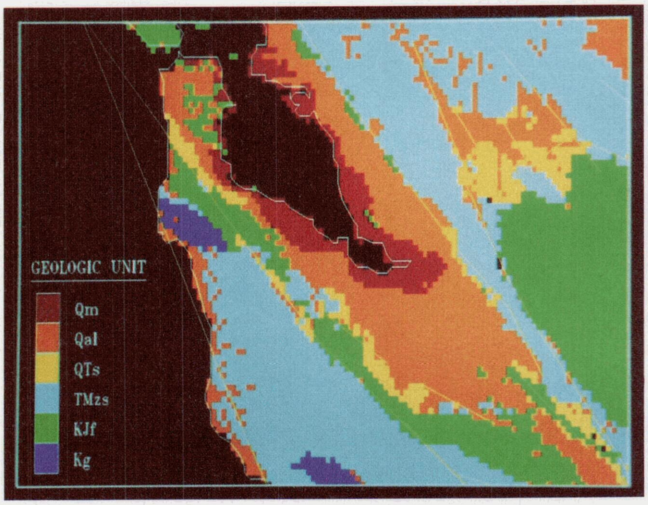

Figure 5.—Geologic map of southern part of the San Francisco Bay region, digitized from geologic map compiled by Borcherdt and others (1975a). Thin lines, faults. See table 2 for description of units.

CONCLUSIONS

To summarize, in the east bay, fault-slip rates and paleoearthquake studies are interpreted to indicate an increased level of hazard with respect to that recognized in 1986. This high level of hazard is insensitive to different rupture scenarios for the San Andreas fault. New evidence indicates a more complex behavior for the San Andreas fault than that considered in 1986. Plausible interpretations of fault behavior, however, show that the probability remains high that strong ground motions ≥0.1 *g* will occur at hard-rock sites within heavily populated areas of the San Francisco Bay region during the next 50 years. Finally, incorporation of local site geology has increased the predicted level of strong ground motion and significantly changed its distribution. Clearly, the largest advances to be made in hazard assessment will result from incorporation of site-amplification effects due to local geologic conditions.

ACKNOWLEDGMENTS

This research was supported by U.S. Geological Survey grant 14–08–0001–G1581. We thank Carol Prentice for her review of the manuscript.

REFERENCES CITED

Addicott, W.O., 1969, Late Pleistocene mollusks from San Francisco Peninsula, California, and their paleogeographic significance: California Academy of Sciences Proceedings, v. 37, no. 3, p. 57–93.

Anderson, J.G., 1979, Estimating the seismicity from geological structure for seismic risk studies: Seismological Society of America Bulletin, v. 69, no. 1, p. 135–158.

Anderson, L.W., Anders, M.H., and Ostena, D.A., 1982, Late Quaternary faulting and seismic hazard potential, eastern Diablo Range, *in* Hart, E.W., Hirschfeld, S.E., and Schulz, S.S., eds., Conference on Earthquake Hazards in the Eastern San Francisco Bay Area,

Table 2.—*Surficial geologic units in the San Francisco Bay region*

[Modified from Borcherdt and others (1975)]

Geologic unit	Symbol	Amplification factor	Description
Estuarine bay mud and Artificial fill (Holocene).	Qm	5.70	Unconsolidated, water-saturated mud. Consists of mud deposited in San Francisco Bay, artificial fill overlying bay mud, and estuarine mud at the mouths of coastal streams.
Alluvium (Quaternary).	Qal	2.50	Unconsolidated to weakly consolidated silt, sand, and gravel. Consists of late Pleistocene and Holocene alluvium. Includes minor deposits of Holocene and late Pleistocene beach and dune sand, and marine-terrace deposits.
Sedimentary rocks (Quaternary and Tertiary).	QTs	1.70	Weakly to moderately consolidated and indurated mudstone, sandstone, and conglomerate. Consists of the Santa Clara Formation along the southwestern margins of the bay basin, and the Irvington and Livermore Gravels (Rogers, 1966; Jenkins, 1943) along the northeastern margin of the bay basin.
Sedimentary rocks (Tertiary and Mesozoic).	TMzs	1.40	Moderately to highly consolidated and indurated chert, shale, sandstone, and conglomerate. Consists of all bedrock units except the Franciscan Complex and plutonic rocks. Predominantly Mesozoic marine shale and sandstone northeast of the Hayward fault, and Tertiary marine sandstone, shale, chert, and minor amounts of volcanic rocks in the upland areas throughout the south bay. Underlies parts of younger sedimentary units.
Franciscan Complex (Cretaceous and Jurassic).	KJf	1.00	Mostly well-indurated sandstone and shale but includes subordinate amounts of greenstone, chert, limestone, conglomerate, and metamorphic rocks of blueschist facies. Generally highly deformed and locally intensively sheared, containing hard blocks of various rock types in a matrix of clay materials. Constitutes the basement complex northeast of the San Andreas fault and in a small area southwest of the fault between the Pilarcitos fault and the San Andreas fault.
Granitic rocks (Cretaceous).	Kg	0.63	Consists of Montara Quartz Diorite (Curtis and others, 1958) and Ben Lomond Quartz Diorite (Baldwin, 1967). Generally jointed and deeply weathered. Constitutes the basement complex southwest of the San Andreas fault except for a small area northeast of the Pilarcitos fault.

Hayward, Calif., 1982, Proceedings: California Division of Mines and Geology Special Publication 62, p. 197–206.

Aydin, Atilla, 1982, The East Bay Hills, a compressional domain resulting from interaction between the Calaveras and Hayward-Rogers Creek faults, *in* Hart, E.W., Hirschfeld, S.E., and Schulz, S.S., eds., Conference on Earthquake Hazards in the Eastern San Francisco Bay Area, Hayward, Calif., 1982, Proceedings: California Division of Mines and Geology Special Publication 62, p. 11–21.

Baldwin, A.D., Jr., 1967, Geologic and geographic controls upon the rate of solute erosion from selected coastal river basins between Half Moon Bay and Davenport, California: Stanford, Calif., Stanford University, Ph.D. thesis, 182 p.

Bird, Peter, and Rosenstock, R.W., 1984, Kinematics of present crust and mantle flow in southern California: Geological Society of America Bulletin, v. 95, no. 8, p. 946–957.

Boore, D.M., Seekins, L.C., and Joyner, W.B., 1989, Peak accelerations from the 17 October 1989 Loma Prieta earthquake: Seismological Research Letters, v. 60, no. 4, p. 151–166.

Borcherdt, R.D., Gibbs, J.F., and Lajoie, K.R., 1975a, Maps showing maximum earthquake intensity predicted in the southern San Francisco Bay region, California, for large earthquakes on the San Andreas and Hayward faults: U.S. Geological Survey Miscellaneous Field Studies Map MF–709, scale 1:125,000, 3 sheets.

Borcherdt, R.D., and Glassmoyer, G.M., 1992, On the characteristics of local geology and their influence on ground motions generated by the Loma Prieta earthquake in the San Francisco Bay region, California: Seismological Society of America Bulletin, v. 82, no. 2, p. 603–641.

Borcherdt, R.D., Joyner, W.B., Warrick, R.E., and Gibbs, J.F., 1975b, Response of local geologic units to ground shaking, *in* Borcherdt, R.D., ed., Studies for seismic zonation of the San Francisco Bay region: U.S. Geological Survey Professional Paper 941–A, p. A52–A67.

Borcherdt, R.D., Wentworth, C.W., Janssen, A., Fumal, T.E., and Gibbs, J.F., 1991, Methodology for predictive GIS mapping of special study zones for strong ground shaking in the San Francisco Bay region, CA: International Conference on Seismic Zonation, 4th, Stanford, Calif., 1991, Proceedings, v. 3, p. 545–552.

Bryant, W.A., 1982, Southern Hayward fault zone, Alemeda and Santa Clara counties, *in* Hart, E.W., Hirschfeld, S.E., and Schulz, S.S., eds., Conference on Earthquake Hazards in the Eastern San Francisco Bay Area, Hayward, Calif., 1982, Proceedings: California Division of Mines and Geology Special Publication 62, p. 35–44.

Budding, K.E., Schwartz, D.P., and Oppenheimer, D.H., 1991, Slip rate, earthquake recurrence, and seismogenic potential of the Rogers Creek fault zone, northern California; initial results: Geophysical Research Letters, v. 18, no. 3, p. 447–450.

Burford, R.O., and Harsh, P.W., 1980, Slip on the San Andreas fault in central California from alinement array surveys: Seismological Society of America Bulletin, v. 70, no. 4, p. 1233–1261.

Carpenter, D.W., and Clark, R.J., 1982, Geologic studies for seismic hazard assessment, Las Positas fault zone, *in* Hart, E.W., Hirschfeld, S.E., and Schulz, S.S., eds., Conference on Earthquake Hazards in the Eastern San Francisco Bay Area, Hayward, Calif., 1982, Proceedings: California Division of Mines and Geology Special Publication 62, p. 147–154.

Clark, M.M., Harms, K.K., Lienkaemper, J.J., Harwood, D.S., Lajoie, K.R., Matti, J.C., Perkins, J.A., Rymer, M.J., Sarna-Wojcicki, A.M., Sharp, R.V., Sims, J.D., Tinsley, J.C., and Ziony, J.I., 1984, Preliminary slip-rate table and map of late-Quaternary faults of California: U.S. Geological Survey Open-File Report 84–106, 13 p., scale 1:1,000,000.

Coppersmith, K.J., 1979, Activity assessment of the Zayante-Vergeles fault central San Andreas fault system, California: Santa Cruz, University of California, Ph.D. thesis, 210 p.

Cummings, J.C., 1968, The Santa Clara Formation and possible post-Pliocene slip on the San Andreas fault in central California, *in* Dickinson, W.R., and Grantz, Arthur, eds., Proceedings of conference on geologic problems of San Andreas fault system: Stanford, Calif., Stanford University Publications in the Geological Sciences, v. 11, p. 191–207.

Curtis, G.H., Evernden, J.F., and Lipson, J.I., 1958, Age determination of some granitic rocks in California by the potassium-argon method: California Division of Mines Special Report 54, 16 p.

Dietz, L.D., and Ellsworth, W.L., 1990, The October 17, 1989, Loma Prieta, California, earthquake and its aftershocks; geometry of the sequence from high-resolution locations: Geophysical Research Letters, v. 17, no. 9, p. 1417–1420.

Dupre, W.R., 1975, Quaternary history of the Watsonville lowlands, north-central Monterey Bay region, California: Stanford, Calif., Stanford University, Ph.D. thesis, 232 p.

Durham, D.L., 1965, Evidence of large strike-slip displacement along a fault in the southern Salinas Valley, California, *in* Geological Survey research 1965: U.S. Geological Survey Professional Paper 525–D, p. D106–D111.

Ellsworth, W.L., 1975, Bear Valley, California, earthquake sequence of February–March 1972: Seismological Society of America Bulletin, v. 65, no. 2, p. 483–506.

———1990, Earthquake history, 1769–1989, *in* Wallace, R.E., ed., The San Andreas fault system, California: U.S. Geological Survey Professional Paper 1515, p. 153–187.

Frizzell, U.A., Jr., and Brown, R.D., 1976, Map showing recently active breaks along the Green Valley fault, Napa and Solano Counties, California: U.S. Geological Survey Miscellaneous Field Studies Map MF–743, scale 1:24,000.

Fumal, T.E., 1991, A compilation of the geology and measured and estimated shear-wave velocity profiles at strong-motion stations that recorded the Loma Prieta, California, earthquake: U.S. Geological Survey Open-File Report 91–311, 163 p.

Galehouse, J.S., 1991, Creep rates on Bay area faults during the past decade [abs.]: Seismological Research Letters, v. 62, no. 1, p. 12.

Gilbert, G.K., 1909, Earthquake forecasts: Science, v. 29, p. 121–138.

Hall, N.T., 1984, Holocene history of the San Andreas fault between Crystal Springs Reservoir and San Andreas Dam, San Mateo County, California: Seismological Society of America Bulletin, v. 74, no. 1, p. 281–299.

Hanks, T.C., and Kanamori, Hiroo, 1979, A moment magnitude scale: Journal of Geophysical Research, v. 84, no. B5, p. 2348–2350.

Harsh, P.W., and Burford, R.O., 1982, Alignment-array measurements of fault slip in the eastern San Francisco Bay area, California, *in* Hart, E.W., Hirschfeld, S.E., and Schulz, S.S., eds., Conference on Earthquake Hazards in the Eastern San Francisco Bay Area, Hayward, Calif., 1982, Proceedings: California Division of Mines and Geology Special Publication 62, p. 251–260.

Harsh, P.W., and Pavoni, Nazario, 1978, Slip on the Pacines fault: Seismological Society of America Bulletin, v. 68, no. 4, p. 1191–1193.

Hart, E.W., 1976, Basic geology of the Santa Margarita area, San Luis Obispo County, California: California Division of Mines and Geology Bulletin 199, 45 p.

Harwood, D.S., and Helley, E.J., 1982, Preliminary structure-contour map of the Sacramento Valley, California, showing major late Cenozoic structural features and depth to basement: U.S. Geological Survey Open-File Report 82–737, scale 1:250,000.

Harwood, D.S., Helley, E.J., and Doukas, M.P., 1981, Geologic map of the Chico monocline and northeastern part of the Sacramento

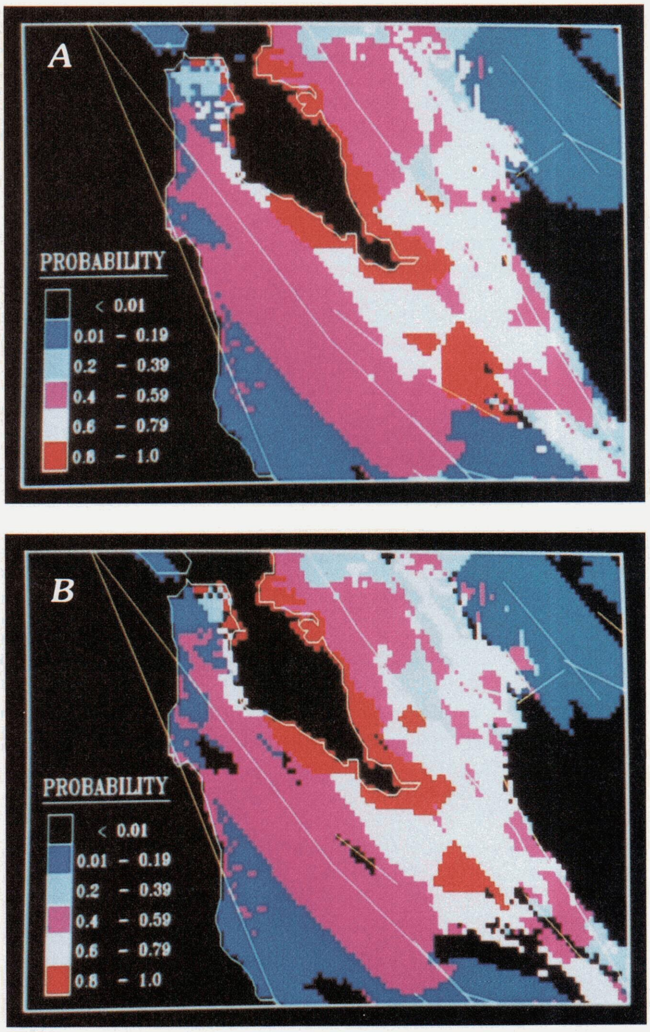

Figure 6.—Hazard maps of southern part of the San Francisco Bay region, showing estimated probability that Quaternary faults mapped in the region will generate (*A*) peak horizontal ground velocities ≥40 cm/s and (*B*) peak horizontal ground accelerations ≥0.5 *g* during 50-yr period after the 1989 earthquake, including amplification due to soil-site effects. Local geologic conditions from geologic map compiled by Borcherdt and others (1975a).

Valley, California: U.S. Geological Survey Miscellaneous Investigations Series Map I–1238, scale 1:62,500.

Hay, E.A., Cotton, W.R. and Hall, N.T., 1980, Shear couple tectonics and the Sargent-Berrocal fault system in northern California, *in* Streitz, Robert, and Sherburne, R.W., eds., Studies of the San Andreas fault zone in northern California: California Division of Mines and Geology Special Report 140, p. 41–49.

Hearn, B.C., Jr., Donnelly, J.M., and Goff, F.E., 1976, Preliminary geologic map of the Clear Lake volcanic field, Lake County, California: U.S. Geological Survey Open-File Report 76–751, scale 1:24,000.

Herd, D.G., 1978, Intracontinental plate boundary east of Cape Mendocino: California Geology, v. 6, no. 12, p. 721–725.

Herd, D.G., and Brabb, E.E., 1980, Faults at the General Electric test reactor site, Vallecitos Nuclear Center, Pleasanton, California: U.S. Geological Survey Administrative Report 77.

Herd, D.G., and Helley, E.J., 1977, Maps showing faults with Quaternary displacement northwestern San Francisco Bay region, California: U.S. Geological Survey Miscellaneous Field Studies Map MF–818, scale 1:125,000.

Hill, D.P., Eaton, J.P., and Jones, L.M., 1990, Seismicity, 1980–86, *in* Wallace, R.E., ed., The San Andreas fault system, California: U.S. Geological Survey Professional Paper 1515, p. 115–151.

Jenkins, O.P., compiler, 1943, Glossary of the geologic units of California, chap. 14 *of* Glossaries, bibliography, and index, pt. 4 *of* Jenkins, O.P., director, Geologic formations and economic development of the oil and gas fields of California: California Division of Mines Bulletin 118, p. 667–687.

Jennings, C.W., compiler, 1975, Fault map of California: California Division of Mines and Geology California Geologic Data Map Series Map 1, scale 1:750,000.

Joyner, W.B., and Boore, D.M., 1988, Measurement, characterization, and prediction of strong ground motion, *in* Von Thun, J.L., ed., Proceedings; earthquake engineering and soil dynamics II—recent advances in ground-motion evaluation: American Society of Civil Engineers Geotechnical Special Publication 20, p. 43–102.

Knuepfer, P.L., 1977, Geomorphic investigations of the Vaca and Antioch fault systems, Solano and Contra Costa counties, California: Stanford, Calif., Stanford University, M.S. thesis, 53 p.

Lawson, A.C., chairman, 1908, The California earthquake of April 18, 1906; report of the State Earthquake Investigation Commission: Carnegie Institution of Washington Publication 87, 2 v.

Lettis, W.R., 1982, Late Cenozoic stratigraphy and structure of the western margin of the central San Joaquin Valley, California: U.S. Geological Survey Open-File Report 82–526, 203 p.

Lienkaemper, J.J., and Borchardt, Glen, 1991, Holocene slip rate of the Hayward Fault at Union City, California [abs.]: Seismological Research Letters, v. 62, no. 1, p. 14.

Lienkaemper, J.J., Borchardt, Glen, and Lisowski, Michael, 1991, Historic creep rate and potential for seismic slip along the Hayward fault, California: Journal of Geophysical Research, v. 96, no. B11, p. 18261–18283.

Lindh, A.G., 1983, Preliminary assessment of long-term probabilities for large earthquakes along selected fault segments of the San Andreas fault system in California: U.S. Geological Survey Open-File Report 83–63, 14 p.

Lisowski, Michael, and Prescott, W.H., 1981, Short-range distance measurements along the San Andreas fault system in Central California, 1975 to 1979: Seismological Society of America Bulletin, v. 71, no. 5, p. 1607–1624.

Lisowski, Michael, Savage, J.C., and Prescott, W.H., 1990, Geodetic estimate of coseismic slip during the 1990 Loma Prieta, California, earthquake: Geophysical Research Letters, v. 17, no. 9, p. 1437–1440.

Louderback, G.D., 1947, Central California earthquakes of the 1830's: Seismological Society of America Bulletin, v. 37, no. 1, p. 33–74.

Matsu'ura, Mitsuhiro, Jackson, D.D., and Cheng, Abe, 1986, Dislocation model for aseismic crustal deformation at Hollister, California: Journal of Geophysical Research, v. 91, no. B12, p. 12661–12674.

McNutt, S.R., and Toppozada, T.R., 1990, Seismological aspects of the 17 October 1989 earthquake, *in* The earthquake, sec. 1 *of* McNutt, S.R. and Sydnor, R.H., eds., The Loma Prieta (Santa Cruz Mountains), California, earthquake of 17 October 1989: California Division of Mines and Geology Special Publication 104, p. 11–27.

Niemi, T.M., and Hall, N.T., 1991, Preliminary estimate of slip rate for the northern San Andreas fault at the Vedanta wind gap, Marin County, California [abs.]: Seismological Research Letters, v. 62, no. 1, p. 12.

———1992, Late Holocene slip rate and recurrence of great earthquakes on the San Andreas fault in northern California: Geology, v. 20, no. 3, p. 195–198.

Olson, J.A., 1990, Seismicity in the twenty years preceding the 1989 Loma Prieta, California earthquake: Geophysical Research Letters, v.17, no. 9, p. 1429–1432.

Page, B.M., 1982., Modes of Quaternary tectonic movement in the San Francisco Bay region, *in* Hart, E.W., Hirschfeld, S.E., and Schulz, S.S., eds., Conference on Earthquake Hazards in the Eastern San Francisco Bay Area, Hayward, Calif., 1982, Proceedings: California Division of Mines and Geology Special Publication 62, p. 1–10.

Pampeyan, E.H., Harsh, P.W., and Coakley, J.M., 1981, Preliminary map showing recent breaks along the Maacama fault zone between Hopeland and Laytonville, Mendocino County, California: U.S. Geological Survey Miscellaneous Field Studies Map MF–1217, 9 p., scale 1:24,000, 2 sheets.

Perkins, J.A., and Sims, J.D., 1988, Late Quaternary slip along the Calaveras fault near Hollister, California [abs.]: Eos (American Geophysical Union Transactions), v. 69, no. 44, p. 1420.

Prentice, C.S., 1989, Earthquake geology of the northern San Andreas fault near Point Arena, California: Pasadena, California Institute of Technology, Ph.D. thesis, 252 p.

Prentice, C.S., Niemi, T.M., and Hall, N.T., 1991, Quaternary tectonics of the northern San Andreas fault San Francisco Peninsula, Point Reyes, and Point Arena, California, *in* Geologic excursions in northern California; San Francisco to the Sierra Nevada: California Division of Mines and Geology Special Publication 109, p. 25–34.

Prentice, C.S., and Schwartz, D.P., 1991, Reevaluation of 1906 surface faulting, geomorphic expression, and seismic hazard along the San Andreas Fault in the southern Santa Cruz Mountains: Seismological Society of America Bulletin, v. 81, no. 5, p. 1424–1479.

Prescott, W.H., and Lisowski, Michael, 1982, Deformation along the Hayward and Calaveras faults: Steady aseismic slip or strain accumulation, *in* Hart, E.W., Hirschfeld, S.E., and Schulz, S.S., eds., Conference on Earthquake Hazards in the Eastern San Francisco Bay Area, Hayward, Calif., 1982, Proceedings: California Division of Mines and Geology Special Publication 62, p. 231–237.

Prescott, W.H., Lisowski, Michael, and Savage, J.C., 1981, Geodetic measurement of crustal deformation on the San Andreas, Hayward and Calaveras faults near San Francisco, California: Journal of Geophysical Research, v. 86, no. B11, p. 10853–10869.

Prescott, W.H., and Yu, S.-B., 1986, Geodetic measurement of horizontal deformation in the northern San Francisco Bay region, California: Journal of Geophysical Research, v. 91, no. B7, p. 7475–7484.

Rogers, T.H., compiler, San Jose sheet *of* Geologic map of California: Sacramento, California Division of Mines and Geology, scale 1:250,000.

Savage, J.C., and Burford, R.O., 1973, Geodetic determination of relative plate motion in central California: Journal of Geophysical Research, v. 78, no. 5, p. 832–845.

Savage, J.C., Prescott, W.H., Lisowski, Michael, and King, N.E., 1979, Geodetic measurements of deformation near Hollister, California, 1971–1978: Journal of Geophysical Research, v. 84, no. B 13, p. 7599–7615.

Scholz, C.H., 1985, The Black Mountain asperity; seismic hazard of the southern San Francisco Peninsula, California: Geophysical Research Letters, v. 12, no. 10, p. 717–719.

Schwartz, D.P., Pantosti, Daniela, Hecker, Suzanne, Okumura, Kiyoshi, Budding, K.E., and Powers, T., 1992, The Rodgers Creek fault zone; fault behavior and earthquake potential [abs.], *in* Conference on earthquake Hazards in the Eastern San Francisco Bay Area, Hayward, Calif., 1992, Program and Abstracts: El Cerrito, Calif., Earthquake Engineering Research Institute, p. 63.

Segall, Paul, and Lisowski, Michael, 1990, Surface displacements in the 1906 San Francisco and 1989 Loma Prieta earthquakes: Science, v. 250, no. 4985, p. 1241–1244.

Shedlock, K.M., McGuire, R.K., and Herd, D.G., 1980, Earthquake recurrence in the San Francisco Bay region, California from fault slip and seismic moment: U.S. Geological Survey Open-File Report 80–999, 20 p.

Su, Feng, Aki, Keiti, Teng, Ta-liang, Zeng, Yuehua, Koyanagi, S.K., and Mayeda, Kevin, 1992, The relation between site amplification factor and surficial geology in central California: Seismological Society of America Bulletin, v. 82, no. 2, p. 580–602.

Sykes, L.R., and Nishenko, S.P., 1984, Probabilities of occurrence of large plate rupturing earthquakes for the San Andreas, San Jacinto, and Imperial faults, California, 1983–2003: Journal of Geophysical Research, v. 89, no. B7, p. 5905–5927.

Thatcher, Wayne, 1975, Strain accumulation and release mechanism of the 1906 San Francisco earthquake: Journal of Geophysical Research, v. 80, no. 35, p. 4862–4872.

Thatcher, Wayne, and Lisowski, Michael, 1987, Long-term seismic potential of the San Andreas fault southeast of San Francisco, California: Journal of Geophysical Research, v. 92, no. B6, p. 4771–4784.

Toppozada, T.R., Real, C.R., and Parke, D.L., 1981, Preparation of isoseismal maps and summaries of reported effects for pre-1900 California earthquakes: California Division of Mines and Geology Open-File Report 81–11 SAC, 182 p.

Tuttle, M.P., Sykes, L.R., and Jaumé, S.C., 1990, Historic earthquakes along the Loma Prieta segment of the San Andreas fault [abs.]: Eos (American Geophysical Union Transactions), v. 71, no. 43, p. 1448.

Weber, G.E., and Cotton, W.R., 1981, Geologic investigation of recurrence intervals and recency of faulting along the San Gregorio fault zone, San Mateo County, California: U.S. Geological Survey Open-File Report 81–263, 133 p.

Weber, G.E., and Lajoie, K.R., 1980, Map of Quaternary faulting along the San Gregorio fault zone, San Mateo and Santa Cruz counties, California: U.S. Geological Survey Open-File Report 80–907, scale 1:24,000.

Wesnousky, S.G., 1986, Earthquakes, Quaternary faults, and seismic hazard in California: Journal of Geophysical Research, v. 91, no. B12, p. 12587–12631.

Wesnousky, S.G., Scholz, C.H., Shimazaki, Kunihiko, and Matsuda, Tokihiko, 1983, Earthquake frequency distribution and the mechanics of faulting: Journal of Geophysical Research, v. 88, no. B11, p. 9331–9340.

Williams, P.L., 1991, Evidence of late Holocene ruptures, southern Hayward fault, California [abs.]: Seismological Research Letters, v. 62, no. 1, p. 14.

Working Group on California Earthquake Probabilities, 1988, Probabilities of large earthquakes occurring in California on the San Andreas fault: U.S. Geological Survey Open-File Report 88–398, 62 p.

———1990, Probabilities of large earthquakes in the San Francisco Bay region, California: U.S. Geological Survey Circular 1053, 51 p.

Wright, R.H., Hamilton, D.H., Hunt, T.D., Traubenik, M.L., and Shlemon, R.J., 1982, Character and activity of the Greenville structural trend, *in* Hart, E.W., Hirschfeld, S.E., and Schulz, S.S., eds., Conference on Earthquake Hazards in the Eastern San Francisco Bay Area, Hayward, Calif., 1982, Proceedings: California Division of Mines and Geology Special Publication 62, p. 187–196.

SUPPLEMENTARY INFORMATION: METHODOLOGY

The reconstructed hazard maps (fig. 4) are based on a combined data set encompassing instrumental, historical, and geologic observations. The methodology used to reconstruct these maps was described in detail by Wesnousky and others (1983) and Wesnousky (1986). It is based on a simple model of mechanical fault behavior whereby the average recurrence interval of earthquakes on faults or fault segments is approximated by

$$T=M_0^e/\dot{M}_0^g\,, \tag{1}$$

where the seismic moment M_0^e of the expected event is determined from paleoseismic evidence, historical seismicity, or an empirical relation between fault length and seismic moment (fig. 7; Wesnousky, 1986). The geologically or geodetically determined moment rate $\dot{M}_0^g$ is a function of the fault slip rate, or, more specifically, $\dot{M}_0^g=\mu uwl$, where μ is the rigidity (3×10^{11} dynes/cm^2), u is the slip rate, w is the width (15 km), and l is the length of the fault or fault segment considered. Each fault or fault segment is assumed to rupture along its entire length in one large event. We omit small earthquakes from consideration. For faults that have some slip due to creep at depth, we use a slip rate equal to the total estimated slip rate minus the creep rate.

STRONG GROUND MOTION

Levels of strong ground motion at a gridwork of sites were calculated using the predictive strong-ground-motion relation of Joyner and Boore (1988):

$$\log y = a + b(M-6) + c(M-6)^2 + d\log r + kr \tag{2}$$

for $$5.0 \le M \le 7.7$$

and $$r = (r_0^2 + h^2)^{1/2}\,,$$

where M is the moment magnitude, r_0 is the shortest distance (in kilometers) from the recording site to the vertical projection of the earthquake fault rupture on the surface of the Earth, and the values of a, b, c, d, h, and k are listed in table 3 for predicting parameters corresponding to the larger of the two horizontal components—we use values that yield peak horizontal ground acceleration or velocity at rock sites. The moment magnitude is related to the seismic moment M_0^e through the equation $M={}^2/_3(\log M_0^e-16.1)$ (Hanks and Kanamori, 1979). As mentioned above, the seismic moment for each expected event is determined from paleoseismic evidence, historical seismicity, or an empirical relation between fault length and seismic moment (Wesnousky, 1986). Although Joyner and Boore's (1988) attenuation equation underestimated the strong ground motion during the 1989 Loma Prieta earthquake (Boore and others, 1989), for the purpose of comparison with Wesnousky (1986), we use Joyner and Boore's relation (1988). Therefore, our predicted strong ground motions may be somewhat underestimated.

For maps that include the effects of local site conditions, a two-tier method is used to estimate the strong ground motions. First, we estimate the level of strong ground motion at a hard-rock site for each gridpoint. We use values for predicting parameters corresponding to the larger of the two horizontal components (table 3). Then, we multiply the level of hard-rock strong ground motion by a local-site-amplification factor. To determine this local-site-amplification factor, we digitize the geologic map compiled by Borcherdt and others (1975a) and assign an amplification to each geologic unit (Borcherdt and others, 1991). The final estimated level of strong ground motion is a combination of the strong ground motion due to source size and source-to-site distance and the local site amplification that is related to geologic materials at the site. We do not include amplifications due to basin geometry, directivity of the rupture, or critical reflections (for example, from the Moho).

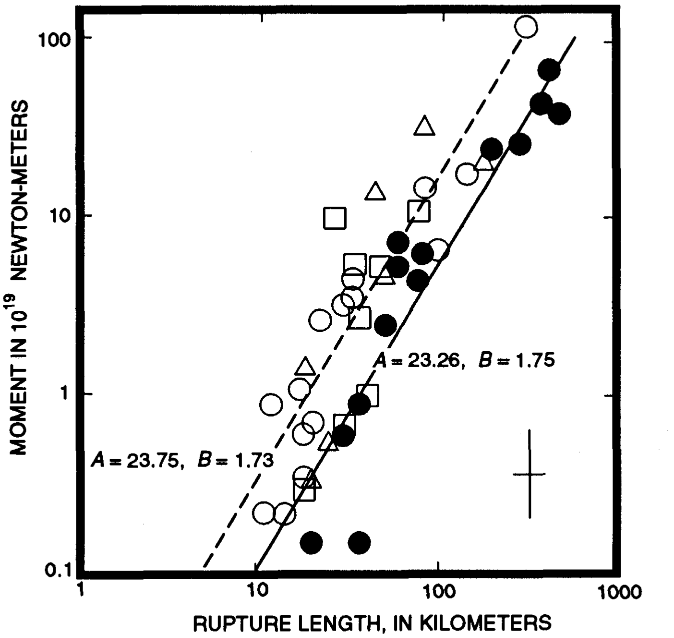

Figure 7.—Seismic moment M_0 versus rupture length l. Dots, earthquakes on major plate-boundary faults, generally characterized to have slip rates of at least 1 cm/yr; open symbols, earthquakes on faults with slip rates of less than 1 cm/yr. Squares, triangles, and dots/circles correspond to normal slip, reverse slip, and strike slip, respectively. Solid and dashed lines are curves of best fit drawn through dots and open symbols, respectively, according to equation $\log M_0=A+B\log l$.

PROBABILITY

The probability of occurrence of a given ground motion is a function of the frequency of occurrence of the specified ground motion and the time period of interest. More concisely, the probability that the occurrence time R of a certain level of strong ground motion will occur during the time period from t_1 to t_2, conditional upon t_1 yr having elapsed since the last occurrence of similar ground shaking, is generally expressed as

$$P(t_1 \le R \le t_2 \mid R > t_1) = \frac{\int_{t_1}^{t_2} f_T(t)dt}{\int_{t_1}^{\infty} f_T(t)dt}, \tag{3}$$

where $f_T(t)$ is an assumed probability-density function. To calculate $f_T(t)$, we separate the data set (Quaternary faults) into two disjoint sets—a time-independent and a time-dependent set.

For faults where we have no information regarding the past history of earthquakes, the occurrence of specific levels of strong ground motion at a site is described as a Poisson process, and so $f_T(t)$ is appropriately defined by the exponential function $\lambda e^{-\lambda t}$, where λ is the frequency of occurrence of the specified level of ground motion. Using empirical relations between seismic moment, source-to-site distance, and strong ground motions; equation 1; and data describing the length and average slip rate of faults in the San Francisco Bay region, the average expected frequency of occurrence of seismic shaking may be computed at a gridwork of sites for a range of different levels of ground motion. The frequency λ, for a given level of strong ground motion at site j, is defined by the relation

$$\lambda_j = \sum_{i=1}^{N} \frac{1}{T_i}, \tag{4}$$

where the T_i are the average recurrence intervals of the N faults that are capable of producing a specific level of ground motion at site j. Thus, for the time-independent

Table 3.—*Values of parameters used in equation 2 for predicting peak acceleration and velocity at rock sites*

Parameter	Peak acceleration	Peak velocity
a	0.49	2.17
b	.23	.49
c	.0	.0
d	-1.0	-1.0
h	8.0	4.0
k	-.0027	-.0026

case, repeated use of equations 3 and 4 for a given level of strong ground motion at a gridwork of sites provides the initial base map. Additionally, where appropriate data were available, the time dependency of seismic hazard was incorporated by taking into account the occurrence times of historical earthquakes.

Toward that end, we define the expected date T_e of rupture on a fault to equal $T_{last}+T$, where T_{last} is the date of the last earthquake rupture and T is the estimated time necessary to accumulate strain equal to that released in the previous earthquake. We also assume that the actual recurrence times distribute normally about values of T, and so T_e may be estimated with the normal-probability-density function

$$f_T(t) = \frac{1}{\sigma\sqrt{2\pi}} \exp[-(t - T)^2/2\sigma^2], \qquad (5)$$

where the standard deviation s is assigned to represent the confidence given to a predicted value of T_e. More recently studies (Working Group on California Earthquake Probabilities, 1988, 1990) have suggested the use of log-normal or Weibull distributions because they eliminate the physically unrealistic possibility of an earthquake occurring before t=0, which is allowed by equation 5. Nonetheless, for the purposes of comparison with Wesnousky (1986), we maintain use of equation 5 in this analysis. On the basis of the analysis by Sykes and Nishenko (1984) for the recurrence behavior of three fault segments in California, we assume that σ=0.33. Substitution of $f_T(t)$ in equation 3 results in an estimate of the probability that the rupture time T_e of a fault will occur during the next $\Delta t=t_2-t_1$ yr, conditional upon t_1 years having elapsed since T_{last}. This method reflects the concept that the probability of an earthquake on a specific fault or fault segment is minimal immediately after T_{last} and increases over time. The time-dependent and time-independent probabilities are combined by using established statistical methods. The hazard maps thus incorporate both conditional time-independent probability estimates for faults in the bay region about whose rupture histories we have no information, and conditional time-dependent probability estimates for faults in the bay region that have either ruptured historically or had prehistoric ruptures which have been dated by Quaternary geologic studies.